बीएआरसी न्यूज़लैटर
BARC NEWSLETTER

ISSUE NO. 309 | OCTOBER 2009

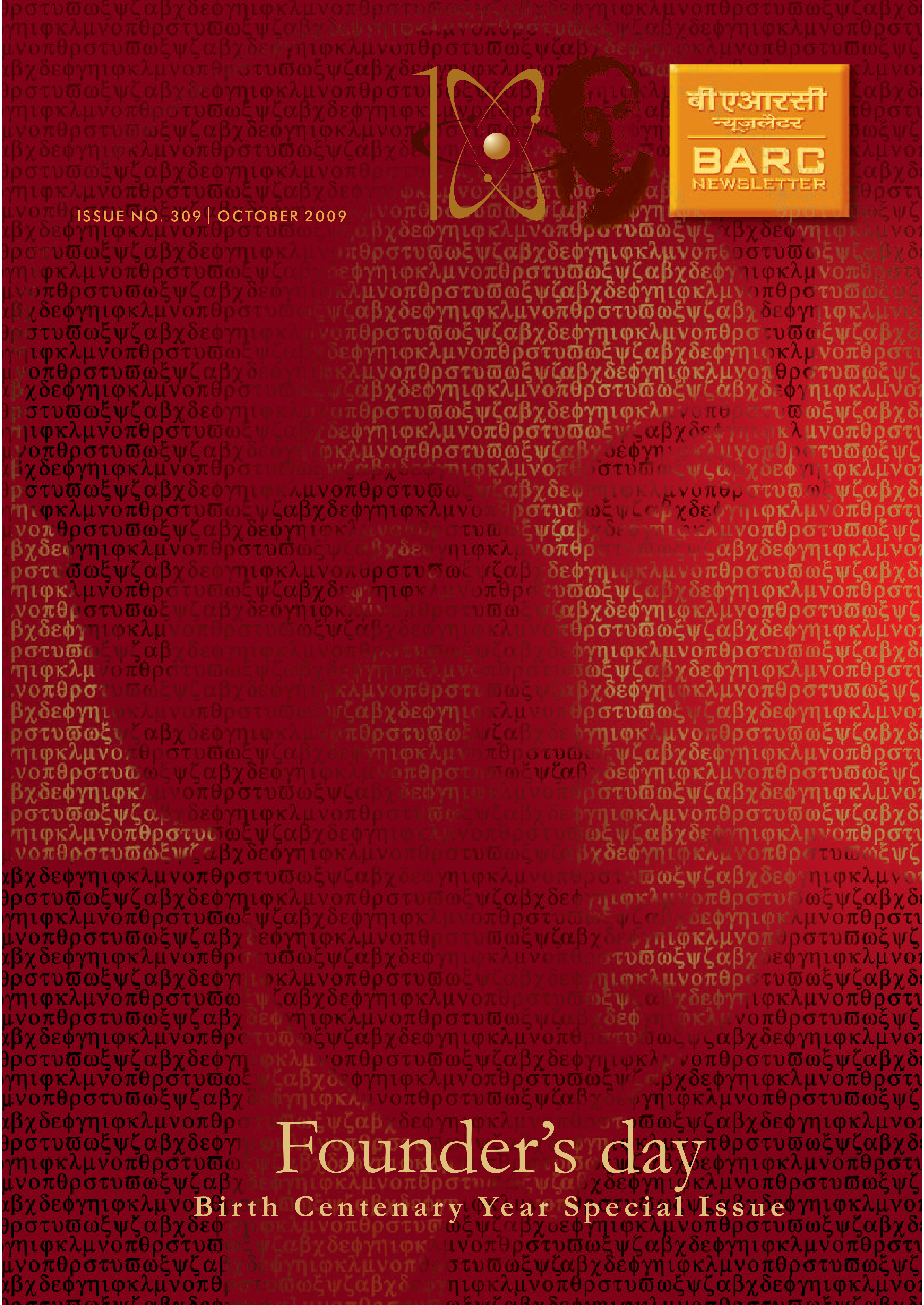

Founder's day

Birth Centenary Year Special Issue

Homi Bhabha Birth Centenary Year
30 October 2008-30 October 2009

बीएआरसी न्यूज़लैटर
BARC NEWSLETTER

Founder's day

Birth Centenary Year Special Issue

सत्यमेव जयते

भारत सरकार
Government of India

भाभा परमाणु अनुसंधान केंद्र
Bhabha Atomic Research Centre

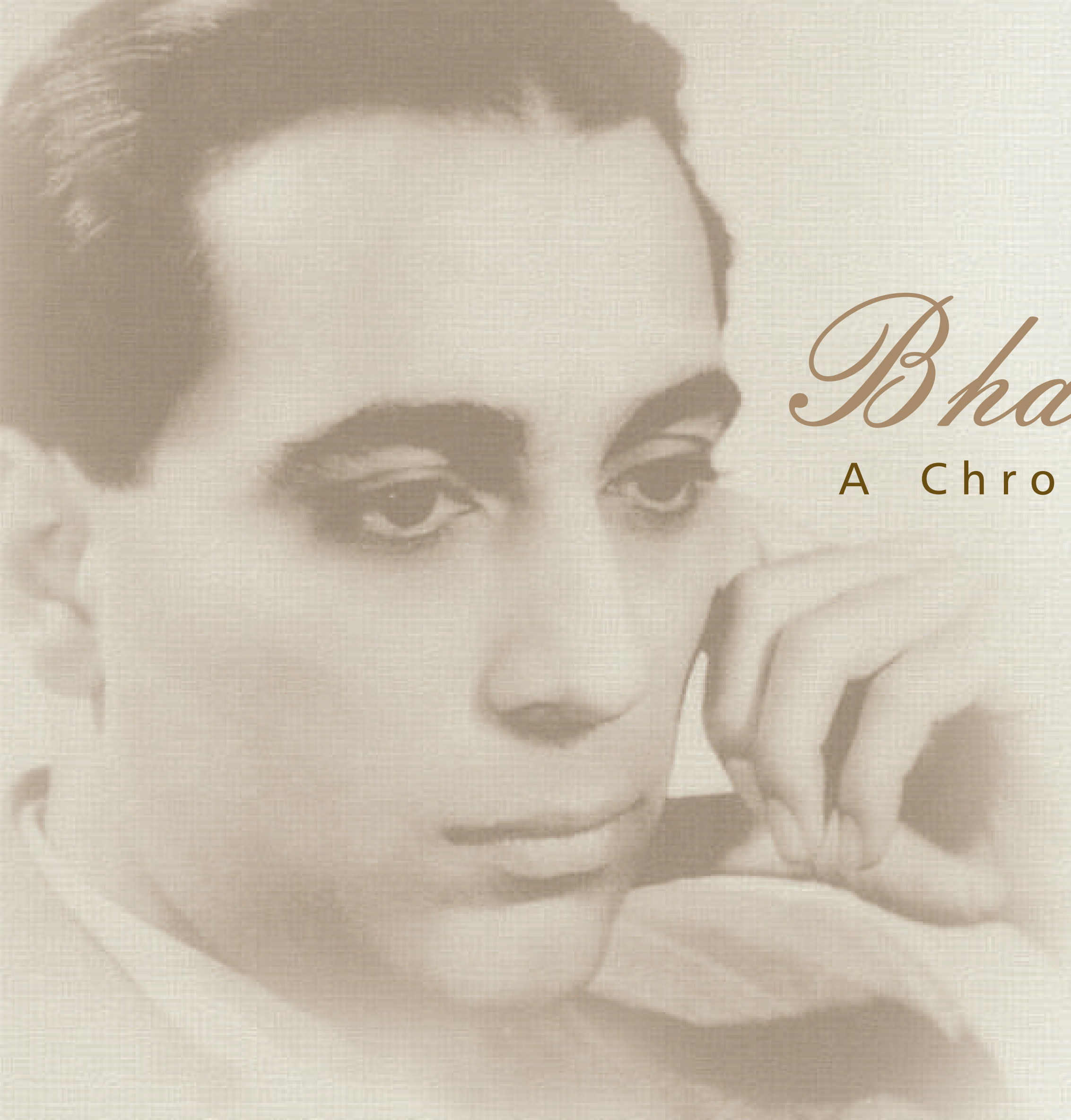

Bhabha

A Chronology

1909, October 30	Born in Mumbai (then Bombay)
1924	Passed the Senior Cambridge Leaving Examination
1925-27	Studied in Elphinstone College and the Royal Institute of Science (since he was underage for Cambridge University)
1927, October	Joined the Gonville and Caius College, Cambridge, UK
1930	Graduated in Mechanical Sciences Tripos; B.A. (Cantab) (First Class)
1931-32	Salomons Studentship in Engineering
1932	Completed Mathematics Tripos (First class) Rouse Ball Travelling Studentship in Maths, Cambridge. Visited Copenhagen and Zurich
1933	Received Isaac Newton Studentship for his first research paper
1935	Received his Ph.D. in Theoretical Physics from Cambridge University. The title of his thesis was "On cosmic radiation and the creation and annihilation of positrons and electrons". His guide was Sir Ralph H. Fowler, Physicist & Astronomer who also guided S. Chandrasekhar, Paul Dirac and D.R. Hartree
1936	Bhabha-Heitler Theory; letter published in Nature
1937	Bhabha-Heitler Cascade Theory of Cosmic Ray Showers (27 page article published in the Proceedings of the Royal Society
1939	In a short note in Nature, was the first to suggest the name "Meson" for a new particle found in Cosmic Radiation
1939	Joined as Reader in Theoretical Physics at the Indian Institute of Science (IISc.), Bengaluru
1940	Special Reader in Cosmic Ray Physics, at IISc.
1941	Elected Fellow of the Royal Society, UK
1942	Awarded the Adam's Prize, Cambridge University Full Professor, Cosmic Ray Research Unit, IISc.

1943	Sectional President (Physics), 30th Indian Science Congress Kolkata.
1944	Awarded Honorary Doctorate (Science) by Patna University
1944	Wrote a letter for the creation of a research institute in India to the Sir Dorabji Tata Trust
1945	Founded TIFR, was also its First Director
1946	Member, Atomic Research Committee, CSIR
1947	Chairman, Board of Research on Atomic Energy
1948	Hopkins Prize of the Cambridge Philosophical Society; Chairman of the newly established AEC, India
1949	Awarded Honorary Doctorate (Science) by Lucknow University
1950	Awarded Honorary Doctorate (Science) by Banaras University
1951	General President, 38th Indian Science Congress, Bengaluru
1952	Awarded Honorary Doctorate (Science) by Agra University
1954	Awarded Honorary Doctorate (Science) by Perth University
1954	Padma Bhushan; Secretary to GOI, DAE; Founding Director, AEE
1955	President, First International Conference on Peaceful Uses of Atomic Energy, Geneva
1956	Apsara swimming pool reactor becomes critical
1957	Training School established at AEET; President , National Institute of Sciences, India (NISI)
1957	Elected Honorary Fellow of Gonville and Caius College, Cambridge, UK
1957	Elected Honorary Fellowship of the Royal Society of Edinburgh, UK
1958	Awarded Honorary Doctorate (Science) by Allahabad University
1959	Awarded Honorary Doctorate (Science) by Cambridge University
1959	Elected Honorary Fellow of the American Academy of Arts and Sciences
1960	Awarded Honorary Doctorate (Science) by London University
1960	CIRUS reactor reaches criticality
1961	Awarded Honorary Doctorate (Science) by Padova University
1961	Zerlina reactor reaches criticality; Space research started under DAE
1962	New building of TIFR inaugurated
1963	Elected Foreign Associate of the National Academy of Sciences (USA)
1963	Appointed Chairman, Electronics Committee; Tarapur Atomic Power Station agreement with USA signed
1960-63	President, International Union of Pure and Applied Physics
1964	Tarapur construction started
1965	Plutonium Plant inaugurated at Trombay; Electronics Committee Report finalized.
1966, January 24	Death over Mont Blanc, Alps in the crash of Air India's plane Kanchanjunga

PUBLICATIONS:

1933-1954	Published 64 papers in the area of Theoretical Physics and Cosmic Ray Physics
1944-66	Published 15 papers on Atomic Energy in India and on Science and Technology in general; also delivered several guest lectures and invited talks at national and international fora. Out of the 79 papers published by Dr. Bhabha in his lifetime, 36 papers (mostly in the field of Theoretical and Cosmic Ray Physics) received a total of 1825 citations (Source : Web of Science for the period 1934 to Dec. 2008).

Contents

C. V. RAMAN’S SKETCH BY DR. HOMI BHABHA

HYBRID NANOELECTRONICS

D.K. Aswal
Technical Physics and Prototype Engineering Division

Dr. Aswal is the recipient of the Homi Bhabha Science and Technology Award for the year 2007

ABSTRACT

The area of hybrid nanoelectronics, wherein , organic molecules deposited on Si, exhibit electronic functionalities, is expected to extend the scaling limits of Si microelectronics, down to a few nanometers. In this article, we discuss several issues pertaining to hybrid nanoelectronics and summarize the work done in this direction at our lab. We present deposition of organic monolayers on Si substrates using self-assembly as well as electrochemical processes. The characterization of monolayers using various techniques to determine thickness, molecular ordering and orientation, surface coverage, growth kinetics etc., is presented. Finally, realization of molecular diodes, resonant tunnel diodes and resistive memories based on appropriate architecture of monolayers, comprising of alkyl-chains (σ- chains) and conjugated molecules (π-moiety) is discussed.

Introduction

One of the ultimate goals in nanotechnology, is to build electronic devices using individual molecules and this branch of research is popularly termed as molecular electronics. Molecular electronics is being proposed as an alternative to silicon-based microelectronics [1]. It is anticipated that the Si technology is likely to face scaling limits in the very near future. This is because, as the projected size of transistors goes down to 20 nm or below it, the physics of transistors leads to unacceptable power dissipation. Intense research carriedout worldwide during the last couple of years has demonstrated that, molecules exhibit unique electronic functions and the chemists around the world are synthesizing many more new molecules with desired properties. Physicists and engineers on the other hand, devised several new methods to measure the electronic transport of a single molecule. These include, break-junction, cross wire, metal nano-particle, Conductive Probe Atomic Force Microscopy (CP-AFM), Scanning Tunneling Microscopy (STM), nano-pore and planar sandwich geometry as schematically shown in Fig. 1. Among these, working with "planar sandwich geometry" is considered advantageous for molecular electronic applications as one can deposit ~10^{15} molecules/cm^2 and conveniently fabricate two-and / or three-terminal molecular devices, by choosing appropriate electrode configurations. Despite these developments, building electronics solely using molecules might take a much longer time (may be several decades!). Thus, a medium term solution, say for the next 10-15 years, is to make molecules compatible with silicon, so that, the nanoscale electronic functionality of molecules can be utilized, in silicon-based microelectronics and this research field is termed as hybrid nanoelectronics.

The advantage of molecule/Si hybrid concept is that, the inputs available from an already existing powerful silicon-based integrated circuit industry, can be used effectively, for the development of integrated hybrid devices. For the last few years, our group has been actively engaged in the development of hybrid nanoelectronics and in this brief article, we present some of our ideas and their realization [1-10]. To begin with, we describe how one can graft organic molecules on silicon to form a monolayer.

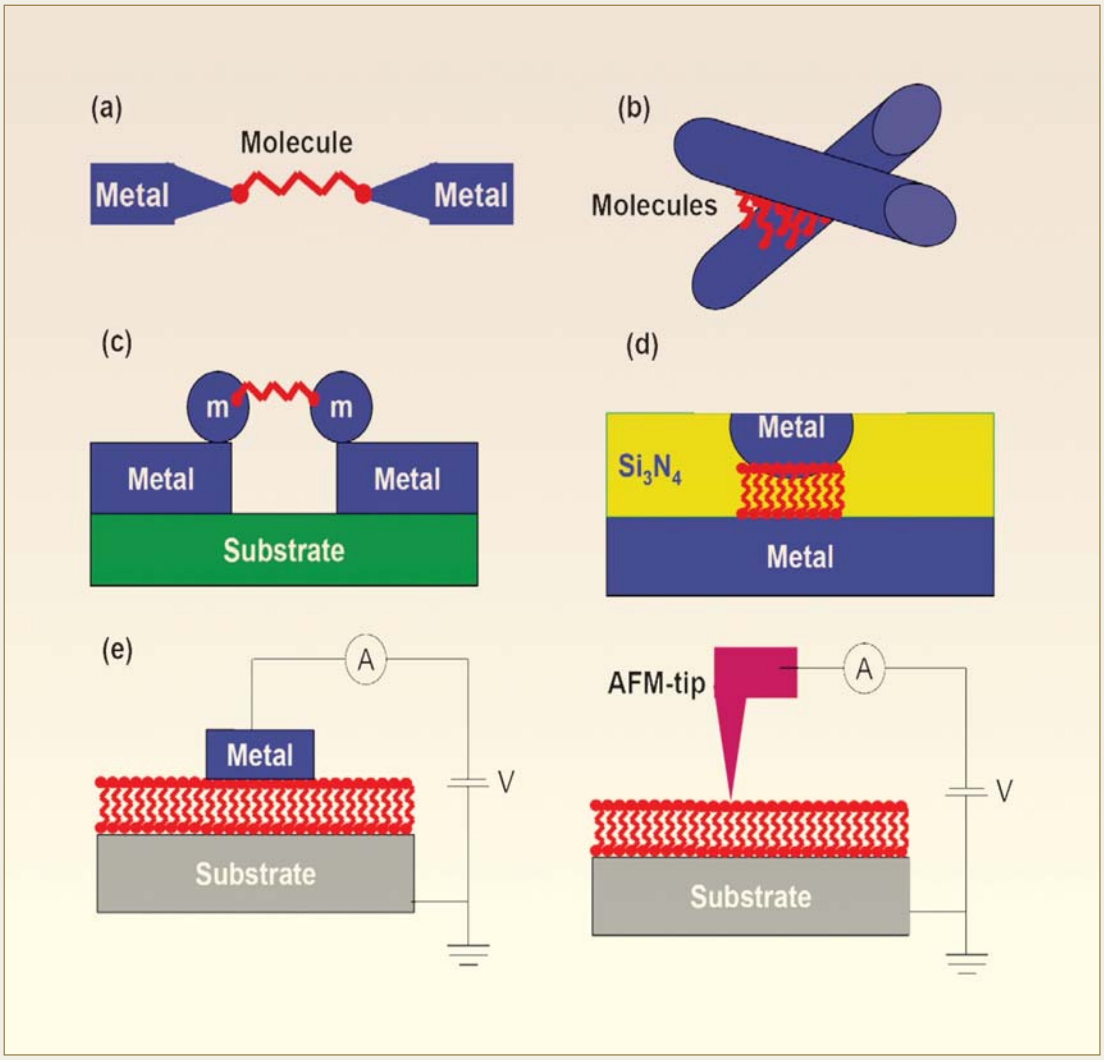

Fig. 1: Schematic of different methods used for attaching molecules to the electrodes.

(a) Break-junction method: a thin (<100 nm) metallic wire fabricated by top-down approaches is broken either by mechanical or electrical means and then molecules are deposited from a solution;

(b) Cross-wires method: organic monolayer is first deposited on an Au wire (~10μm diameter) and then a second Au wire (without molecules) is brought in close proximity to this wire using electrical and magnetic field;

(c) Metal nanoparticles method: The metal nano-particles on which a monolayer has been deposited are trapped between two closely spaced metal contacts using an alternating electric field;

(d) Nano-pore method: molecules are sandwiched between two metal layers through a small orifice or nano-pore; and

(e) Planar sandwich geometry: metal counterelectrodes are directly fabricated on monolayers deposited on conducting substrates, such as gold or highly doped Si.

The characterization of the organic monolayers is discussed. We then demonstrate functionality of various molecular electronic components such as dielectric, rectifier, resonant tunnel diode and memory.

Monolayer on Silicon

The monolayers of organic molecules on silicon, as schematically shown in Fig. 2, can be grafted by two different methods: self-assembly and cathodic electrografting method.

Self-assembly of monolayer

The Self-Assembled Monolayers (SAMs) are formed spontaneously, by immersing the Si substrates into an active solution e.g. surfactant molecules $R(CH_2)_nSiX_3$ ($X = Cl$, OCH_3 or OC_2H_5) dissolved in alkane / carbon tetrachloride [1]. The self-assembling molecule can be divided into three parts: (i) *Head group i.e.* $-SiX_3$: forms the chemical bond with surface atoms of the substrate (exothermic: ~40-45 kcal/mol or ~1.7 eV) causing the pinning of surfactant molecule to the substrate, (ii) *Alkyl chain i.e.* $-(CH_2)_n-$: the inter-chain van der Waals interactions (exothermic <10 kcal/mol or <0.4 eV) could assist in formation of ordered molecular structure which, of course, depends on the pinning density of the head groups and (iii) *Surface group i.e.* –R: this is the terminal group which is replaced with different functional groups to obtain molecular electronics devices. For a high density of head groups, chemisorbed at the surface of the substrate, – implying a good surface coverage – the alkyl chains become closer. Therefore, the inter-chain van der Waals interactions become effective, which leads to formation of a close-packed "ordered" monolayer (as schematically shown in Fig. 2). The alkyl chains, depending upon the surface coverage, have a tilt (Φ) from the surface normal. Usually higher the packing density, lower is the Φ. On the other hand, if the surface coverage is poor, the alkyl chains form a "disordered" monolayer, and the Φ can be very

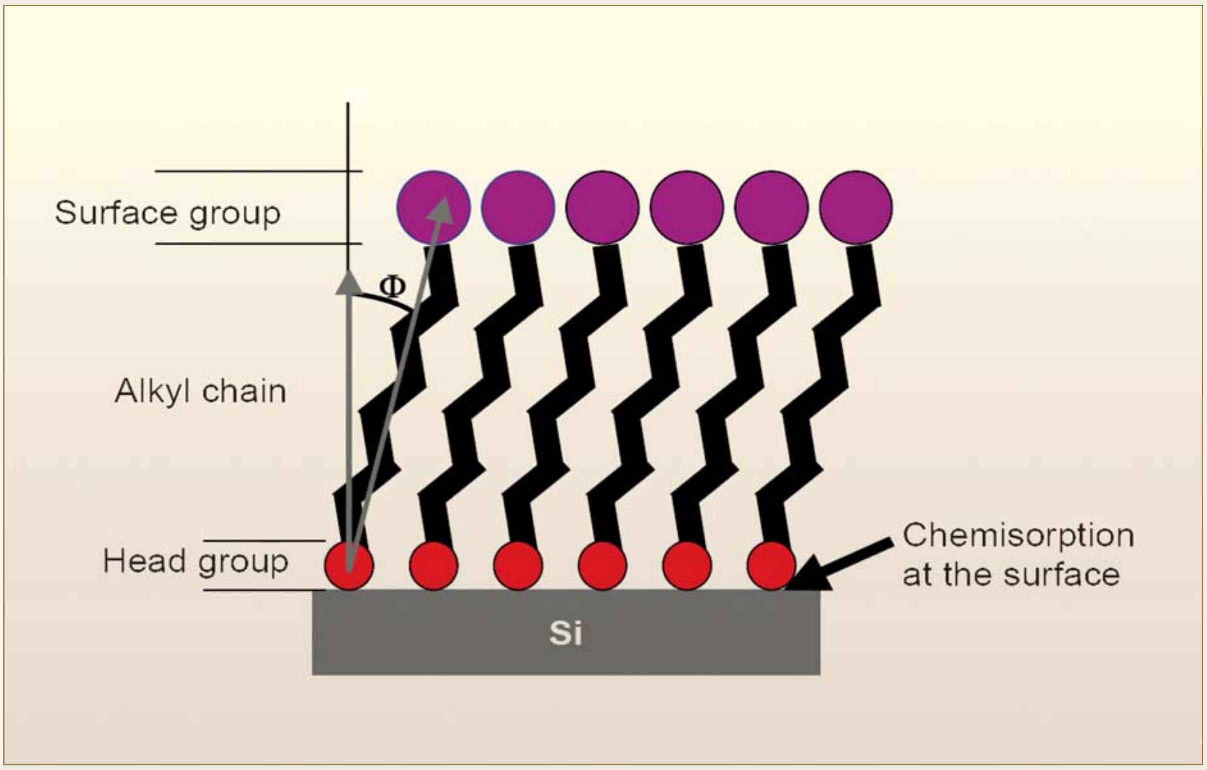

Fig. 2: A cartoon showing different parts of a self-assembled monolayer deposited on a Si-substrate suitable for molecular electronics. Φ is the tilt of the chain axis from the surface normal.

The deposition of organic SAMs on Si can be carried out using the following two approaches. (i) *Deposition of SAMs on native silicon oxide of Si (SiO_x/Si) by "silanization":* SiO_x/Si substrates are first cleaned in piranha solution (H_2SO_4/H_2O_2: 2:1 v/v) to obtain OH-terminated SiO_x/Si, which are then immersed into a solution of surfactant molecules $R(CH_2)_nSiX_3$ (X = Cl, OCH_3 or OC_2H_5) prepared using aliphatic or aromatic hydrocarbons. The chemical reaction between the hydroxylated SiX_3 and OH, results in the formation of chemical bonds. (ii) *Direct deposition of SAMs on silicon*: In this case the SiO_x layer is first etched out using 1-2% HF (aqueous) or 40% NH_4F (aqueous) to obtain an H-terminated Si surface. The SAM can be deposited by dipping the H-terminated Si substrate into a solution of 1-alkenes at 100 °C, which results in the formation of Si–C bonds. The disadvantage of self-assembly process is that, apart from the natural chemisorption of organic molecules on Si—H or Si—OH surfaces and van der Waals interactions among alkyl-chains, there is no external controlling parameter, that can force deposition of organic molecules and prevent adsorption of impurities on the Si surface.

Electrografting of monolayer

Cathodic electrografting is an emerging method for the deposition of monolayers on Si substrates [4,5]. Electrografting essentially is an electro-initiated process and it requires a charged electrode (e.g. doped Si) for the grafting of organic molecules, which takes place by formation of covalent bonds between the substrate atoms and the molecules. One of the requirements for electrografting is that, the molecule should be terminated with a cleavable electroactive group, such as, vinyl (C=C), ethynyl (C°C), halide (Cl, Br, I), tetraalkylammonium salt, diazonium salt, silane etc. Cathodic electrografting method has a distinct advantage: since a negative potential is applied to the Si substrate, the oxidation and / or hydrolysis of Si surface is out of question during the grafting of organic molecules. In fact, even if some oxide / hydroxide is present at the Si surface, it gets destroyed by a reduction process and therefore yields a clean Si surface. Moreover, the applied negative potential becomes a controlling parameter, for driving the molecules to the Si surface, which yields a highly dense monolayer.

The electrografting of organic molecules to Si surface is carried out using a three-electrode electrochemical setup. The current (I) flows between the Working-Electrode (WE) and the Counter-Electrode (CE). The Working-Electrode is the electrode on which the molecules are grafted, that is, H-terminated Si. The CE is usually a Pt wire. The potential (V) is measured between the Reference Electrode (RE) and the Working Electrode. No current passes the Reference Electrode. Reference-Electrode is an electrode which has a stable and well-known electrode potential. The high stability of the electrode potential is usually reached by employing a redox system with constant (buffered or saturated) concentrations of each participant of the redox reaction. The most common Reference Electrode is the Standard Hydrogen Electrode (SHE), which is also known as "Normal Hydrogen Electrode" (NHE). Other Reference Electrodes include saturated Calomel Electrode (SCE) ($E = +0.242V$ with respect to the SHE), Copper-Copper(II) Sulfate Electrode ($E = \sim 0.314V$) and Silver Chloride Electrode ($E = 0.225V$ saturated). The commonly used supporting electrolytes include tetrabutylammonium perchlorate (TBAP) or tetrabutylammonium hexafluorophosphate ($TBAPF_6$), prepared in dry and deoxygenated dichloromethane (CH_2Cl_2) or acetonitrile (CH_3CN). To avoid oxidation of the H-terminated Si surface, the electrografting process is generally carried out under inert ambient. The electrografting is usually carried out using either Cyclic Voltammetry (CV) (i.e. the working electrode potential is ramped linearly versus time) or constant applied potential mode.

Monolayer characterization

Once the monolayer formation is carried out on Si substrate, it is essential to characterize them [1]. The quality of the deposited monolayer is assessed by characterizing it for (i) thickness of the monolayer,

(ii) molecular orientation and ordering, (iii) uniformity and coverage, (iv) chemical composition, (v) thermal and chemical stability of the monolayer and (vi) electrical characterization. The characterization of organic monolayers typically involves a combination of multiple techniques, such as, ellipsometry, water contact angle measurement, Fourier Transform InfraRed spectroscopy (FTIR), x-ray Photoelectron Spectroscopy (XPS), atomic force microscopy etc. For chemical analysis, FTIR is commonly used. The frequencies and intensities of the vibrational modes observed in FTIR, provide detailed information about the nature of the chemical functional groups. XPS technique provides excellent information about the elements and their oxidation states present in the monolayer. Morever, XPS allows determination of thickness of the grafted organic layers. Thickness of the organic layers can also be determined using ellipsometry. Contact angle measurements provide information on the surface group of the grafted organic layer. The ordering of the monolayer can be also be assessed by imaging the surface morphology using AFM and STM. Here we present characterization of self-assembled alkane monolayers.

Thickness of alkane monolayers

Optical ellipsometry is the most routinely used technique, to determine the thickness of the monolayers, though other techniques, such as, plasmon surface polarization, X-ray reflectivity, X-ray standing waves etc. can also be employed. In fact, one can theoretically determine the length of all trans-extended *n*-alkane chains by using MOPAC software or by simply adding the bond lengths. The homologous series of methyl-terminated *n*-alkylsiloxane monolayers (n = 1-18) have been routinely deposited by reaction between *n*-alkyltricholorosilanes on native oxide of silicon. In this case, for all trans-extended chains, the length (*t*) of the monolayer containing *n* carbons (for CH_3 terminating monolayer) or (*n-1*) CH_2 units should have a linear relation [1]:

$$t = 1.26 \times (n-1) \times \cos \Phi + 4.78 \qquad (1)$$

where Φ is the tilt angle of the chain, 1.26 Å (per methylene group) corresponds to the projection of carbon-carbon bond on to the main axis of the molecule and the intercept of 4.78 is a sum of Si–O (1.33Å), C–Si (1.52Å) and length of terminating –CH_3 group (1.93Å). In Fig. 3, along with this theoretical relation at different Φ, we have plotted the experimentally measured thickness of several *n*-alkylsiloxane monolayers by different groups [11-14]. It also may be noted, as shown in the inset of Fig. 3, that the deposition temperature (T_c) required for the formation of an ordered monolayer, decreases with decreasing *n*. It is evident that the bracket of experimental values is within the theoretical one with $\Phi < 30^o$. This implies, that the methyl-terminated *n*-alkylsiloxane monolayers are deposited in all-trans conformation with a tilt angle of $<30^o$ on native oxide of Si. However, the most studied *n* = 18 i.e. octadecylsiloxane monolayer is known to exhibit a tilt angle of $<10^o$.

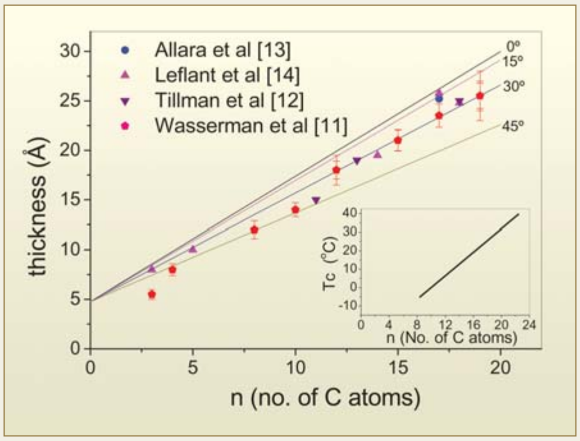

Fig. 3: Thickness of *n*-alkylsiloxane monolayers deposited on native-oxide of Si measured by different groups. The full lines are the theoretical relation of thickness as a function of n, calculated using equation 1 at different tilt angles. The inset shows the variation of the critical deposition temperature of monolayer (T_c) as a function of *n*.

Molecular orientations and ordering

TIR spectroscopy is the most powerful tool for studying the molecular orientation and ordering in organic monolayers. FTIR is usually done in two different spectroscopy modes: (i) Attenuated Total Reflection (ATR) and (ii) Reflection- Absorption (RA). In the ATR mode, individual s- and p-polarized (the parallel and perpendicular components of a plane polarized light, respectively) attenuated total internal reflection spectra are recorded. The dichroic ratio (*D*), defined as, $D = A^{s-pol} / A^{p-pol}$ (where A^{s-pol} and A^{p-pol} are *s*- and *p*- polarized absorbance, respectively) gives the information on the molecular orientation. Using *D* values of symmetric and asymmetric CH_2 stretches, one can calculate the angle between these transition dipole moments and the surface normal i.e. α_s and α_a, respectively. These two angles, in turn, allow determination of both the chain tilt angle (Φ) and chain twist angle (γ) using the relations: $\cos^2\Phi = 1 - \cos^2\alpha_s - \cos^2\alpha_a$ and $\cos\gamma = \cos\alpha_s / \sin\Phi$, respectively. It may be noted that the value of *D* has a steep dependence on α. For example, a change in *D* value from 1.04 to 1.08 would change α_a from 70 to 83° and thus extreme care is needed in interpreting data using *D* values.

The peak positions of symmetric (ν_s) and asymmetric (ν_a) stretching modes of CH_2 group give the required information about the molecular order in the monolayers. For a well ordered (i.e. crystalline) monolayers, the peak positions of ν_s and ν_a are at 2851±1 and 2918±1 cm^{-1}, respectively; while for a highly disordered (i.e. liquid) monolayers, these peak positions shift to 2855±1 and 2924±1 cm^{-1}, respectively. Typical IR spectra recorded for monolayers having different numbers of C atoms are presented in Fig. 4 (a). Since ν_a – as the monolayer goes from crystalline to liquid state – shows a maximum shift of 6 cm^{-1}, we have plotted the reported ν_a in Fig. 4 (b) for various monolayers reported by different researchers. It is evident that for $n>10$ the monolayers are in crystalline state; though for $n<10$, the disorder in monolayer increases. The information about then structure of monolayers can also be obtained by a variety of techniques, such as, X-ray, electron and neutron diffraction, high-resolution electron loss spectroscopy, Raman spectroscopy, Near-Edge X-Ray Absorption Fine structure spectroscopy (NEXRAF) etc.

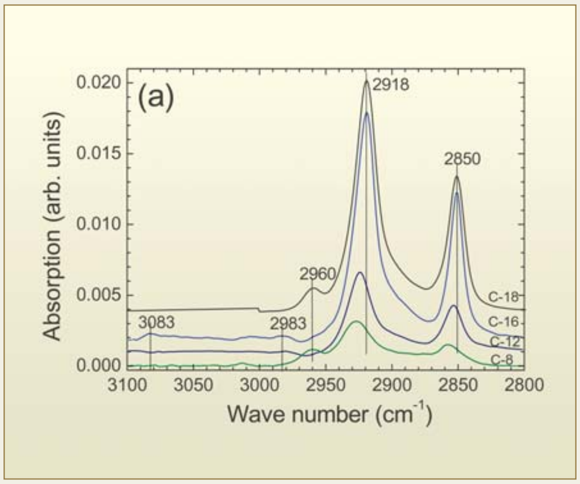

Fig. 4a: FTIR spectra for monolayers having different numbers of C-atoms: 18, 16, 12 and 8. Note a systematic shift of n_a (CH_2) peak, which is expected to be at 2918 cm^{-1} for a crystalline monolayer

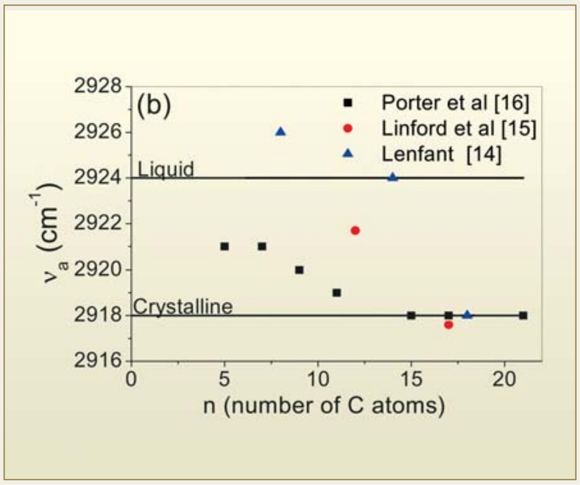

Fig. 4b: Reported value of asymmetric (n_a) stretching modes of CH_2 group for different monolayers. The values at 2918 and 2924 cm^{-1} correspond to crystalline and liquid phase of the monolayer

Uniformity and coverage

The quality and uniformity of a monolayer at various lengths (from macro to nano) can be assessed by wetting measurements and / or by directly imaging the surface topography by atomic force microscope, scanning electron microscopy and tunneling electron microscopy.

The wetting measurement is simple and effective technique because the "shape" of a liquid drop on a uniform surface depends on the free energies of the liquid and surface. A drop of liquid (de-ionized water or hexadecane, for instance) is expanded on the surface using a syringe. The "advancing" and "receding" contact angles are measured. Strictly speaking, the contact angle is determined by its properties of surface group, and not by the alkyl chain. However, alkyl chain indirectly affects the surface properties through ordering, packing and tilt. A summary of reported advancing water contact angle, measured on monolayers with different functional head groups, is presented in Table 1. It is seen that for the same surface group, but with different number of C atoms (n) in the chain, the contact angle is significantly lower for $n<10$, which indicates poor ordering of monolayer. Also for $n > 20$, the contact angle decreases, indicating the disorder arising probably due to the mingling of longer chains. Zisman showed that wettability data can be used, to determine the critical surface tension (g_c) of the monolayer surface, which is defined as the surface tension of the test liquid that completely wets the surface i.e. contact angle (Q) = 0°, and is found by plotting cos Q vs g_l (where g_l is the surface tension of a series of test liquids), and g_l value at cos Q = 1 is equal to g_c. For various surface head groups, the g_c could vary between 6 and 43 N/m at 20 °C [1].

Table 1: Water contact angle measured on different functional surface groups of SAMs.

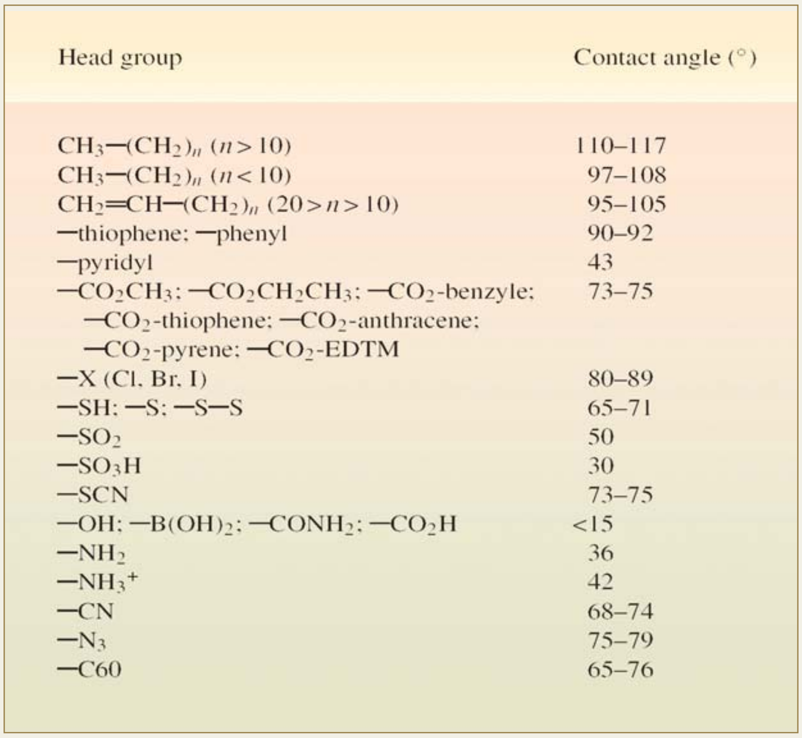

Head group	Contact angle (°)
$CH_3-(CH_2)_n$ ($n>10$)	110–117
$CH_3-(CH_2)_n$ ($n<10$)	97–108
$CH_2=CH-(CH_2)_n$ ($20>n>10$)	95–105
—thiophene; —phenyl	90–92
—pyridyl	43
$-CO_2CH_3$; $-CO_2CH_2CH_3$; $-CO_2$-benzyle; $-CO_2$-thiophene; $-CO_2$-anthracene; $-CO_2$-pyrene; $-CO_2$-EDTM	73–75
—X (Cl, Br, I)	80–89
—SH; —S; —S—S	65–71
$-SO_2$	50
$-SO_3H$	30
—SCN	73–75
—OH; $-B(OH)_2$; $-CONH_2$; $-CO_2H$	<15
$-NH_2$	36
$-NH_3^+$	42
—CN	68–74
$-N_3$	75–79
—C60	65–76

Atomic force microscopy

The surface coverage of a monolayer is usually examined by measuring the surface morphology using the Atomic Force Microscopy (AFM). The high-resolution AFM images on a scan area of 10×10 nm^2 for the crystalline octadecyltrichlorosilane monolayer, studied by Kojio et al, exhibited a periodic arrangement of the molecules, with a hexagonal array [17]. AFM is a powerful tool for understanding the growth kinetics of monolayers. For example, in Fig. 5 (a), we show AFM images of partial C18 monolayers, which were deposited by immersing the Si substrate in the octadecyltricholorosilane solution for varying amounts of time. Initially, isolated close-packed C18 islands are formed at the surface of the substrate and these islands then serve as centers for aggregation for molecules, diffusing on the surface as well as for adsorbing from solution, as schematically shown in the inset of Fig. 5 (b).

At low surface coverage, the fractal dimension of the islands increases with surface coverage, while the height remains at $\sim$25Å, indicating that C18 molecules are tilted at $\sim$30°. At higher surface coverage, the islands – height remaining at $\sim$25Å – grow by branching and eventually coalesce. With passage of time, the inter-island regions (pores or pinholes) shrink and eventually, a continuous SAM gets formed. In order to study the growth kinetics of the SAM formation, the monolayer coverage (*Q*) as a function of time, as shown in Fig. 5 (b) is determined, by analyzing the AFM images. The two regions showing different growth kinetics can be easily identified from this figure. (i) A faster and linear growth for time < 5 s (shown by solid straight line fit), indicating that the initial growth is primarily via diffusion limited aggregation. (ii) For higher times, the coverage kinetics becomes slow and can be fitted to an expression , $Q = I\sim\exp(-kt)$ suggesting that growth is limited by adsorption from the solution. The studies on the growth kinetics as a function of chain length have revealed that while long chains grow via island nucleation and growth, the short chain did not show the island growth behaviour. This has been attributed to the chain length dependent chemisorption and diffusion rates of molecules on the substrate surface, which are found to decrease with increasing chain length. However, more detailed studies are needed to confirm this mechanism. It may be noted that when the monolayer grows via island nucleation and growth mechanism, complete elimination of pinholes is not possible. These pinholes may hamper the electrical characterization of monolayer, as the counterelectrode metal particulates may diffuse through them creating short-circuits. Thus, studies on the size and distribution of pinholes in monolayer are important and must be carried out using high-resolution AFM and other techniques such as electrochemistry. In additionof this, by using a conducting AFM tip, the electrical measurements on monolayer can be carried out. Thus AFM is a unique facility in which electrical

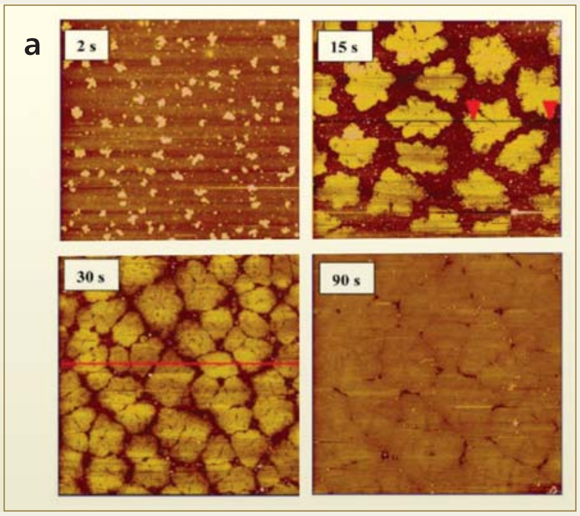

Fig. 5a:10 μm x 10 μm AFM images of partial C-18 monolayer on Si immersed in octadecyltricholorosilane solution for varying amounts of time

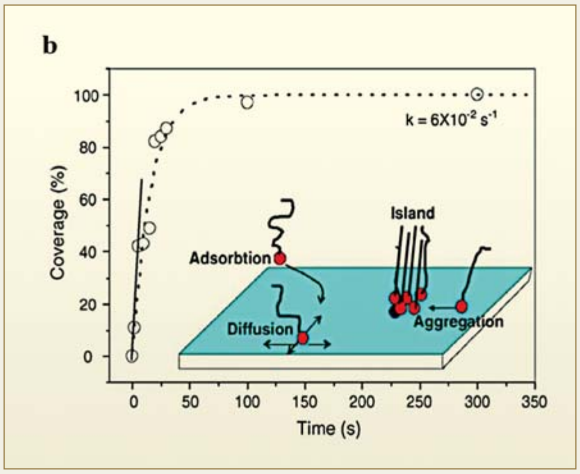

Fig. 5b: Monolayer coverage as a function of time determined using analysis of AFM images. For time < 5s, a fast and linear growth (solid line fit) indicates that growth is due to diffusion limited aggregation. For higher time, the data is fitted (dotted line) to an equation governed by adsorption-limited kinetics. Inset: Schematic showing the various processes during the monolayer growth. Once a molecule is adsorbed at the surface, it undergoes a random walk on the surface (with a certain value of 2D diffusion coefficient) until it collides with another adsorbed molecules and forms an island. Initially islands grow via diffusion-limited aggregation of adsorbed molecules followed by adsorption-limited kinetics.

measurements and the surface morphology of the monolayer can be studied simultaneously.

Thermal and chemical stability of alkane monolayer

In order to use monolayers in hybrid nanoelectronics, it is essential that monolayers must remain robust under the same daunting conditions that all existing semiconductor materials already endure. These include thermal stability upto 350°C, chemical stability under different etchants, endurance etc. Therefore, the monolayers are subjected to stability tests under a wide variety of conditions, which include high temperatures, acids, base etc. A common method to check the stability is to measure the thickness and contact angle as a function of the treatment. Most remarkably, monolayers exhibit no signature of degradation when stored in an airtight container for 18 months. Plots showing temperature, acid and base stability of C18 monolayer are presented in Fig. 6. The C18 monolayer is stable upto a temperature of ~350°C, Fig. 6 (a). The thermal stability is found to be independent of the chain length. The High-Energy Electron Loss energy spectroscopy (HEEL) measurements reveal, that at temperature higher than 350°C, the monolayer begins to decompose primarily through the cleavage of C–C bonds. The siloxane head group (Si–O) is strongly bonded to the substrate surface and begins to decompose only after 725°C. The monolayers are remarkably stable when washed using 1% detergent solution, hot tap water or organic solvents. As shown in Fig. 6(b), the C18 monolayers are stable in contact with aqueous acid at room temperature for long periods (upto a couple of days). However, monolayers get immediately deteriorated on exposing to aqueous base and a complete removal of monolayer was observed within 60 min. The destruction of monolayer in the base is due to the hydrolysis of Si–O bonds.

Molecular dielectric

The monolayer of the alkanes consisting of saturated C–C bonds has been found a good molecular dielectric. These molecules have large gaps (~9 eV) between their Highest Occupied Molecular Orbitals (HOMO) and Lowest Unoccupied Molecular Orbitals (LUMO). Typical current-voltage (*J-V*) data for CH_3-terminated *n*-alkanes (n = 3, 8, 11, 14 and 18 carbon atoms) SAMs with Al as counterelectrode are presented in Fig. 7(a). The solid lines are fit of experimental data using theoretical relationship between direct tunneling current density (*J*) and *V* for a metal-dielectric-metal like structure [6,18]:

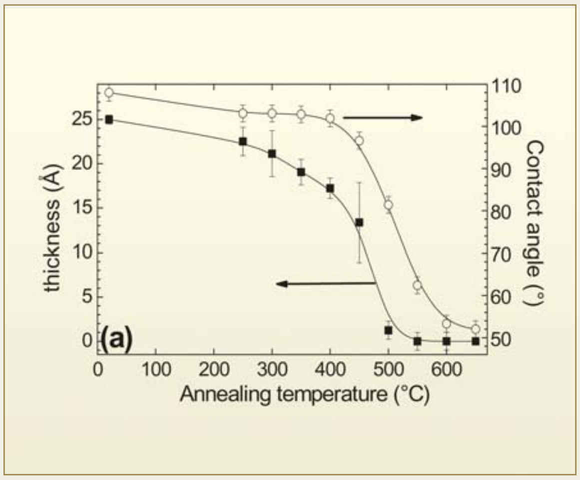

Fig. 6a: Thickness and water contact angle of C18 SAM measured as a function of annealing temperature. The annealing was carried out for 30 min under He ambient

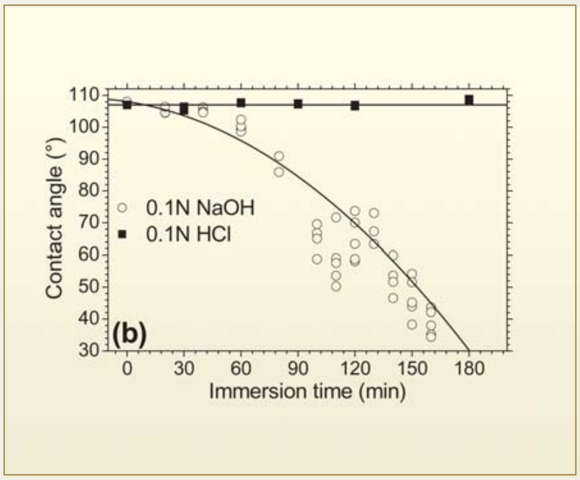

Fig. 6b: The water contact angle on C18 SAM as a function of immersion time in 0.1 N NaOH and 0.1 N HCl.

where $\alpha = \dfrac{e}{4\pi^2 \beta'^2 \hbar}$ and $A = 2\beta' \sqrt{\dfrac{2m^*}{\hbar^2}}$ e is the electron charge, m* is the effective mass of electron in the insulator, β′ is a constant and has value ~1, is the reduced Planck's constant), ϕ is average barrier height, *d* is the barrier width or molecule length and *V* voltage between the electrodes. It is seen that the ϕ value reduces with increasing chain length and becomes as low as 1.5 eV for n = 18 SAM. As shown in Fig. 7(b), the *J* through alkanes decreases exponentially with *d*, and can be described by *J* = *A*exp(– β*d*), where *A* is a constant and β is a decay constant varying between 0.4 Å^{-1} (Fig. 7 b). However, theoretical calculations predict the β value of ~0.8 Å^{-1}, and experimental values range over 0.4–0.9 Å^{-1}. The exponential decay, together with characteristic current–voltage (*I*–*V*) curves, which are temperature independent, suggest electron tunneling as the conduction mechanism for these SAMs.

From Fig. 7 it is evident that the leakage current though the alkane SAMs is quite low. However, for using them as a dielectric in electronic devices, low leakage current is not the only concern. Under high field stress, dielectric films will eventually reach breakdown, which cause an irreversible damage leading to increased leakage current and eventually fatal device failure. The physical meaning of breakdown is the destruction of the atomic structure by breaking inter-atomic bonds. Various imperfections can cause an insulating material to break down at a lower voltage than anticipated. Such events are usually

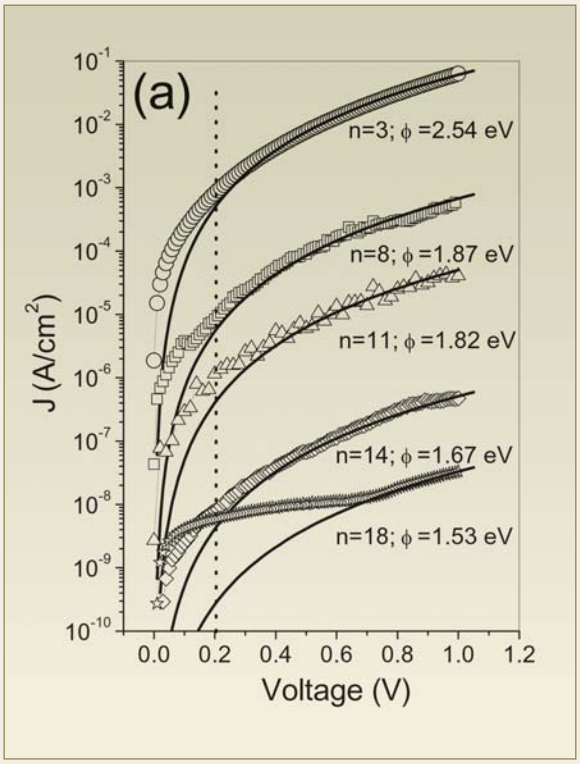

Fig. 7a: The J-V data for *n*-alkanes (n = 3, 8, 11, 14 and 18 carbon atoms) SAMs on Si. The full curves are data fit using equation 1.

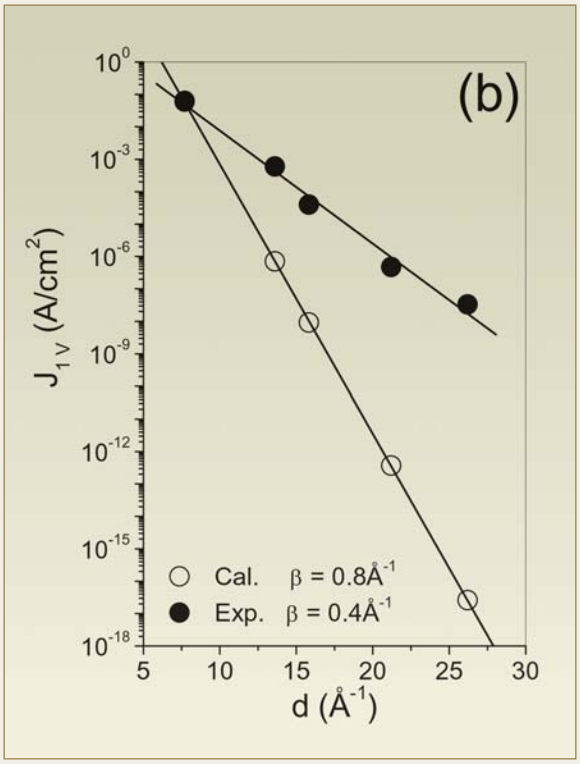

Fig. 7b: The plot of J (at 1V) as a function of molecule length. Filled circles correspond to experimentally measured; while open circles are the calculated values using equation 5 and assuming ϕ = 2.54 eV, and m* = 0.16m$_e$

$$J = \frac{\alpha}{d^2}\left[\phi e^{-Ad\sqrt{\phi}} - (\phi + eV)e^{-Ad\sqrt{\phi + eV}}\right] \qquad (1)$$

related to charge buildup for some reason, which locally increases the electric field. Thus, an insulator material is also characterized by a breakdown electric field. The simplest way of investigating the electric breakdown in an insulator is to record *J–V* data to very high voltages till one observes a breakdown. Fig. 8 presents a typical *J–V* curve for a MPTMS SAM at voltages >3.2 volts. It is seen that for voltages > 3.6 V, named as pre-breakdown region, the current jumps to either a high conduction state (i.e. high *J* values) or a low conduction state (i.e. low *J* values) or both (as in the present case). The conduction state of current jump and its occupying voltage range are random in nature. The hard breakdown of the monolayer is observed to take place between 3.6 and 4.1 V [8]. Once the hard electric breakdown of monolayer has taken place, the next voltage ramp always leads to a higher *J* and its linear relationship with *V*, suggesting creation of stress-field induced permanent defects in the monolayer during the breakdown process. Considering the fact that the native oxide does not remain a dielectric at such high voltages, the calculated breakdown field,

$$E_{BD} = \frac{V_{BD}}{d_{SAM}},$$

for the MPTMS monolayer, comes out to be ~50 MV/cm. This value is much larger than the 12-20 MV/cm reported for longer alkane chains (no. of carbon atoms > 10), suggesting that the shorter chains have higher breakdown fields. This is believed to be due to a reduction in impact ionization at reduced thickness, and needs further investigations. On the other hand, supposing that the native oxide is a perfect dielectric and we take its thickness into consideration, then the breakdown field,

$$E_{BD} = \frac{V_{BD}}{d_{ox} + d_{SAM}(\varepsilon_{ox}/\varepsilon_{SAM})},$$ is ~16

MV/cm, which is still much larger than the breakdown field of equivalent thickness (i.e. ~2 nm) of SiO_2, suggesting suitability of these monolayers for hybrid electronics.

In order to obtain an independent information on whether, apart from the monolayer, a silicon oxide layer exists at the interface or not, one can perform impedance spectroscopy. Impedance spectroscopy involves measurement of real (Z') and imaginary (Z'') parts of impedance as a function of frequency [4]. For example, a typical Z' vs Z'' plot, known as the Nyquist plot, for Al/C-8 monolayer/Si(n^{++}) structure, measured in the frequency range of 600 Hz to 1 MHz with 1 V dc bias, is shown in Fig. 9. Frequency is an implicit parameter in this curve and low frequency corresponds to points at high Z'. The data has been analyzed using the equivalent circuit shown in the inset of Fig. 9, which is assumed to be a series combination of two parallel *RC* circuits, corresponding to C-8 monolayer (R_{ML}, C_{ML}) and silicon oxide (R_{ox}, C_{ox}), respectively. The values of various parameters of the equivalent circuit obtained by fitting experimental data were $R_{ML}=30\pm0.1$ kW, $C_{ML}=1.78\pm0.08$ nF, $R_{ox}=0.11\pm0.1$ kW, and $C_{ox}=0.001\pm0.08$ nF. The physically insignificant values obtained for R_{ox} and C_{ox} confirm, that silicon oxide is absent at the interface, which is in agreement with XPS measurements. In fact, an improved fitting of data is obtained when the oxide *RC* circuit has been removed from the equivalent circuit. A capacitance of 7.12×10^{-7} F/cm^2 is obtained for the C-8 monolayer.

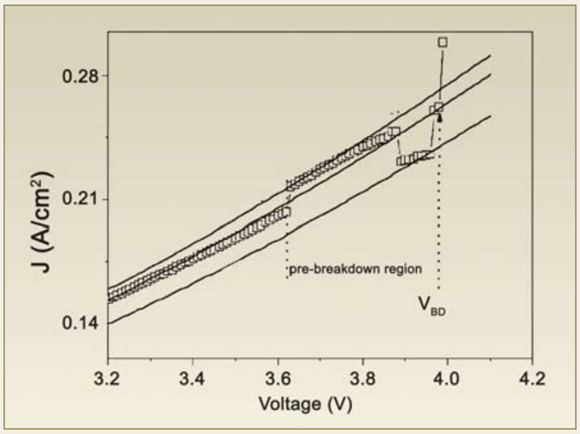

Fig 8: *J–V* plot of C3 monolayer showing the electrical breakdown. In the pre-breakdown region current jumps between the two states are shown by the solid curves

Rectification in σ–π monolayers

Aviram and Ratner proposed the first theoretical concept of single-molecule rectifier in an acceptor–bridge–donor (A–b–D) type of molecules [19]. Based on A–b–D concepts, several molecular rectifying diodes have been synthesized e.g. hexadecylquinolinium tricyanoquinodimethanide molecule ($C_{16}H_{33}$-Q-3CNQ) with donor and acceptor moieties linked by s or p bridge. Also, the molecule is ω-substituted by an alkyl chain, which is essential to allow a monolayer formation by the Langmuir–Blodgett (LB) method. These molecular diodes exhibited rectification ratio (a ratio of current density at –1V (in absolute value) and the current density at +1V) up to 2×10^4. However, in the case of $C_{16}H_{33}$-Q-3CNQ, the AR model may not be applicable as it is a D-p-A molecule and due to the π-bridge, the HOMO and LUMO may be more delocalized than expected in the AR model. Theoretical calculations show, that the direction of easy current flow (i.e. rectification current) depends on (i) the placement of the HOMO and LUMO relative to the Fermi levels of the metal electrodes before bias is applied and (ii) a shift induced in HOMO/LUMO by the applied bias. This situation is more complex than the AR mechanism and the electrical rectification can result from the asymmetric profile of the electrostatic potential across the molecule. Thus, the rectification in the $C_{16}H_{33}$-Q-3CNQ molecule can be attributed to the asymmetry profile due to alkyl tail. Prediction of a symmetric current–voltage curve in this molecule without an alkyl chain also suggests, that asymmetric electrostatic potential is the cause for rectification in $C_{16}H_{33}$-Q-3CNQ molecule. Based on the rectification due to asymmetric electrostatic potential profile in a molecular system, experimentally a simple molecular rectifier with only one donor group and an alkyl spacer chain, that is, σ-π molecules has been demonstrated [1].

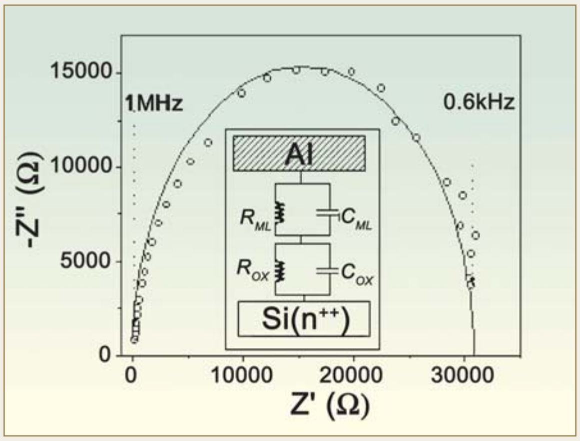

Fig. 9: Nyquist plot of Al/C-18 monolayer/ Si(n^{++}) structure recorded in the frequency range of 600 Hz to 1 MHz with a bias of 1 V. The solid line is a fit to data using a model equivalent to the *RC* circuit shown in the inset (see text).

The σ-π molecular rectifiers can be grafted on Si, using self-assembly or electrografting process either in a single step (i.e. σ-π is directed deposited on Si) or in multiple steps (i.e. first σ molecules are grafted on Si and then π groups are attached by surface modification of σ monolayers). Here we describe deposition of σ-π molecular rectifiers using three sequential self-assembly processes namely, (i) silanization, (ii) oxidation and (iii) esterification. In the first step i.e. silanization, the vinyl-terminated alkyl chains with several lengths namely, C-17, C-14 and C-8 are grafted on degenerated Si substrates by self-assembly process. In the second step, the vinyl end-groups are substituted by -COOH group using oxidation, which is carried out in aqueous solution of $KmnO_4/NaIO_4/K_2CO_3$. The yield of this oxidation has been estimated between 70 and 90 %. In the final step, the conjugated moieties are grafted onto the previously formed monolayers using esterification reactions between the COOH end-groups and different alcohols, which are shown in Fig. 10. The esterification is carried out in the presence of a water trap (dicyclohexylcarbodimide, DCCI) at room temperature for prolonged durations (120h) to enhance the reaction yield. After each step, the monolayers are characterized by contact angle, ellipsometry and FTIR, to establish the occurrence of correct chemistry at the surface of the monolayer. Unfortunately, the chemical yield of this process is around 30-40% and new chemical routes need to be explored to enhance the yield. To fabricate diode using σ–π monolayers, Al counterelectrodes (10^{-4} cm^2 area) are deposited. Aluminum is chosen to avoid any rectification effect coming from the difference between the work functions of the two electrodes (4.2 eV for Al and 4.1 eV for n-type Si, electron affinity in that latter case). This is because, as discussed earlier, a larger current is obtained when a positive bias is applied to the electrode with the smallest work function.

Fig. 11 shows typical *J-V* curves for several π-terminated monolayers made with C-17 as the alkyl spacer. In all cases, a higher current density at -1V has been measured as compared to that +1V. A similar rectifying behaviour for the s - p monolayers based on the other alkyl chains (C-8 and C-14) with similar π moieties at the end. No rectification behaviour was observed through a monolayer without π group i.e. the *J-V* curves for the C-8, C-14 and C-17 monolayers were symmetric. For every π -functionalized monolayer, a Rectification Ratio (RR) is defined as a ratio of current density at -1V (in absolute value) and the current density at 1V ($RR = \%J_{-1V}\%/ J_{1V}$). The average values of RR are in the range 3 to 13 for the functionalized monolayers. The best RR value of 37 has been obtained for the C-8/thiophene monolayer. Neither a significant

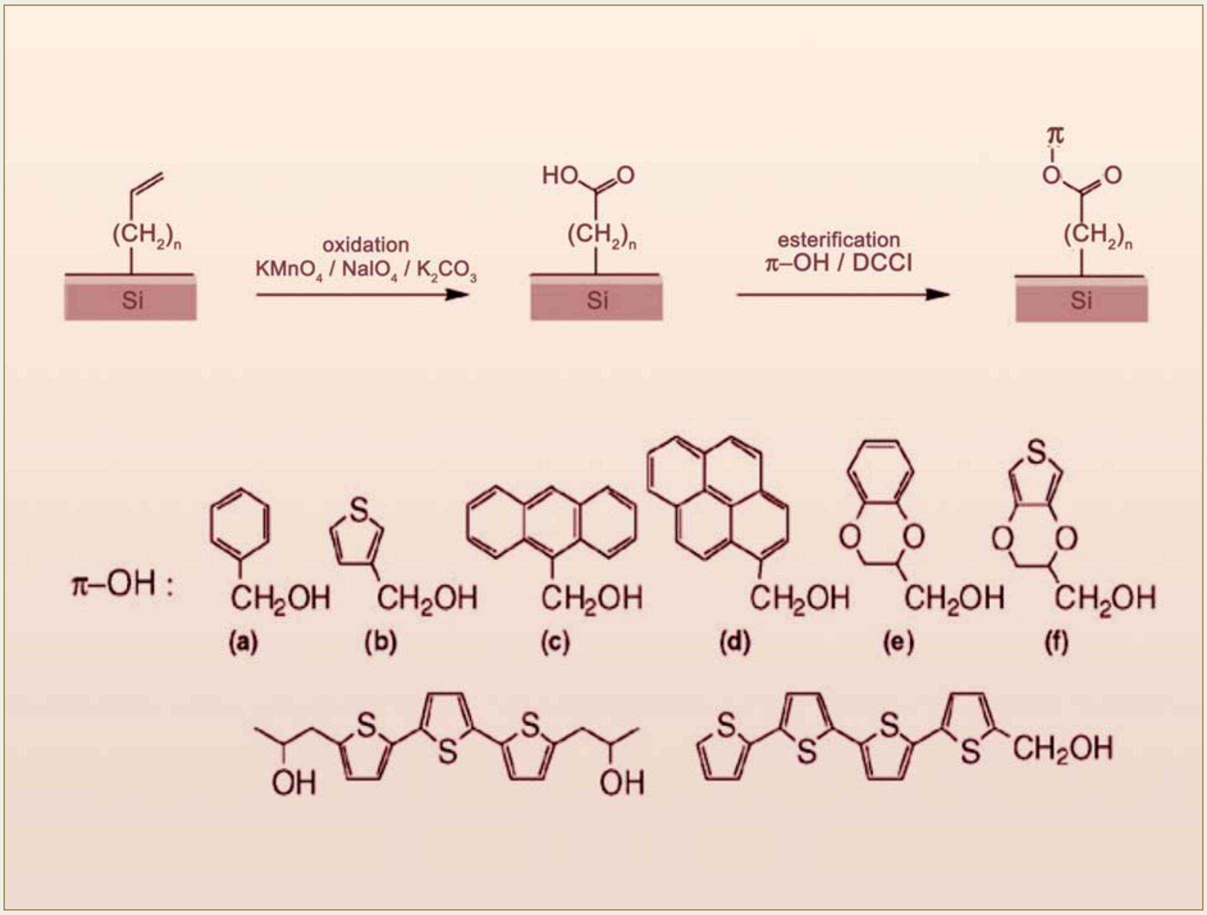

Fig. 10: The chemical synthesis of σ-π molecular diode using sequential self-assembly process. Chemical structures of π -alcohols used to functionalize the SAMs are: (a) benzyl alcohol, (b) 3-thiophenemethanol, (c) 9-anthracenemethanol, (d) 1-pyrenemethanol, (e) 3,4-ethylenedioxybenzene methanol (EDBM), (f) 3,4-ethylenedioxythiophene methanol (EDTM), (g) bis(2-hydroxypropyl)terthiophene (3T), and (h) hydroxymethyl quaterthiophene (4T).

variation of RR with the chemical nature of the end-groups nor any correlation with the alkyl spacer length has been observed.

The rectification behaviour of the σ- π molecular diodes is believed to be due to the resonant tunneling through the HOMO of the π group. The rectification effect arises for a negative bias applied on the Al electrode. because the energy difference between the Si Fermi energy (pinned at the conduction band - CB - in the degenerated Si) and the HOMO (p-orbital) is lower than that with the LUMO (π* orbital). If we assume that the π-end group is almost at the Al electrode potential (since this group is at a close contact with the electrode) and that a large part of the potential is dropped in the alkyl chains, a lower threshold (in absolute value) is required, to have a resonance between the Si CB and the HOMO when applying a negative bias on the metal electrode than between the Si CB and the LUMO for a positive bias. To determine the experimental position of the HOMO level, the *J-V* curves were fitted by a one-level model (i.e. a model in which the conduction is dominated by charge transport through a single energy level located at energy E_0 from the electrode Fermi energies). As discussed above, we assume here a resonant effect through the HOMO, then $E_0<0$, and the current density is given by [1]

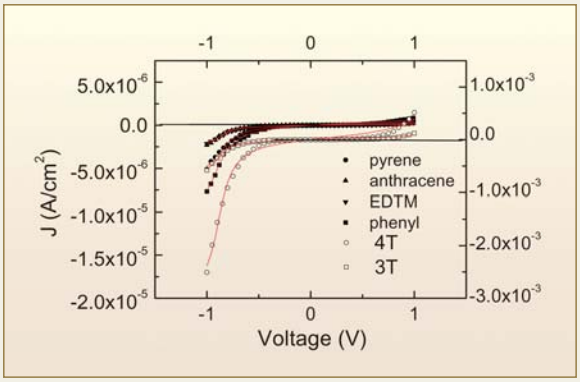

Fig. 11: Typical current density - voltage characteristics of the Si/ σ-π monolayer /Al junctions: C-17/pyrene; C-17/anthracene; C-17/EDT; C-17/phenyl ; C-8/3T and C-8/4T. Left scale = C-17 based junctions; right scale= C-8 based junctions. Solid lines are fits by equation (2)

$$J=\frac{2J_0}{\pi}\left\{\tan^{-1}\left[\theta\left(\left|E_0\right|+\eta eV\right)\right]-\tan^{-1}\left[\theta\left(\left|E_0\right|-(1-\eta)eV\right)\right]\right\} \quad (2)$$

where V is the applied potential on the metal electrode (Si is grounded), e is the electron charge, η is the fraction of the potential on the π moiety (i.e. the potential seen by the center of gravity of the π moiety), J_0 is the saturation current and θ is an electrode/molecule coupling parameter. It is observed that E_0 does not depend on the alkyl chain length. Also the threshold voltage V_T, which is defined as the intercept between a linear fit of the current at high negative voltages and the zero current y-axis, does not depend on the nature of the π group. These observations warrant further theoretical as well as experimental investigations on the electronic transport in such molecular diodes.

Molecular σ-π-σ Rresonant Tunnel Diode

Basic concept of Molecular Resonant Tunnel Diode (MRTD) is analogous to its solid-state counterpart: a potential well separated from the electrodes by two tunnel barriers. Molecules with σ-π-σ architecture are expected to act as MRTD, in alkyl-chains act as tunnel barriers and p-moiety as potential well. Self-assembly of σ-π-σ, MRTD can be carried out, using two different processes. In the first chemical process, Fig. 12 (a), the synthesis is made in five steps i.e. silanization with vinyl terminated trichlorosilane, oxidation, esterification, demethylation and repeated silanization with aliphatic trichlorosilane. The first three steps are same as those described for the synthesis of molecular σ-π diodes on Si surface. In the fourth step, i.e. demethylation, the end $-OCH_3$ group of s-p molecules is replaced by OH group by reacting with BBr_3. The terminating –OH group then can be utilized for grafting another alkane chain by silanization process. In the other chemical process, as shown in Fig. 12 (b), σ-π-σ MRTD, can be synthesized in just three steps i.e. silanization, oxidation and esterification in the presence of s-p alcohols. The J-V characteristics of these σ-π-σ MRTDs exhibited a very faint Negative Differential Resistance (NDR) effect, with ratio J_{Peak}/J_{Valley} being only ~1.01. The poor electrical characteristics are attributed to the very low yields of the formation of σ-π-σ monolayer. While the synthetic routes discussed above are well established; low yield of the reaction may lead to other chemical byproducts, which are likely to hamper the device characteristics. NDR effect has been observed in a single p-molecule namely, styrene and 2,2,6,6-tetramethyl-1-piperidinyloxy (TEMPO), deposited on degenerately doped Si(100) 2×1 reconstructed surfaces using ultrahigh vacuum STM. For styrene molecules on n-type Si(100), NDR is observed only for negative sample bias, while positive sample bias leads to electron stimulated desorption. For 2,2,6,6-tetramethyl-1-piperidinyloxy molecules, electron stimulated desorption was not observed at either bias polarity. In this case, NDR has been observed only for negative sample bias on n-type Si(100) and for positive sample bias on p-type Si(100). This unique behaviour is consistent with a resonant tunneling mechanism between the bulk silicon band structure and the discrete orbitals of the adsorbed molecule, and opens new possibilities for silicon-based molecular electronic devices. However, this interpretation subsequently has been ruled out both experimentally and theoretically, indicating that RTD molecular device has not yet been demonstrated unambiguously. Thus, synthesis of new types of σ–π–σ molecules, suitable for grafting to Si, is required.

A specially synthesized σ–π–σ molecule, that is, *N*-(2-(4-diazoniophenyl)ethyl)-*N'*-hexylnaphthalene-1,8:4,5-tetracarboxydiimide tetrafluoroborate (DHTT), as shown in Fig. 13 (a), was electrografted to the Si using its diazonium salt. A typical *J-V* recorded for a 12 nm thick σ–π–σ multilayer is shown in Fig. 13 (b). The *J-V* exhibits very small NDR effects in both positive and negative bias with peaks occurring at +1.2 and 1.6 V, respectively. Also the hysteresis is very little. The observation of very small NDR effect is attributed to the loss of σ–π–σ character owing to the formation of an inhomogeneous multilayer. These studies show that in order to achieve pronounced NDR effect, it is essential that ordered s-p-s monolayers are grafted on Si.

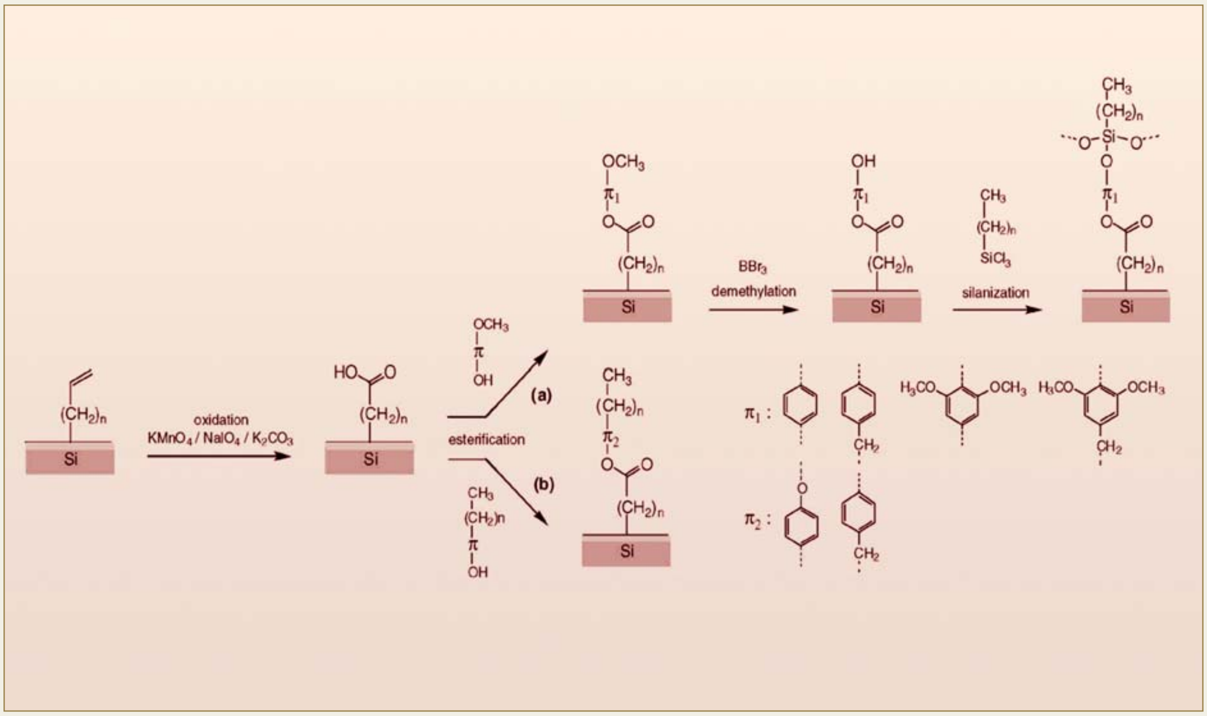

Fig. 12: Self-assembly of σ-π-σ molecular resonant tunnel diodes in (a) five - and (b) three steps

Molecular resistive memories

The redox-active molecules, such as, metallocene, porphyrin, and triple-decker sandwich coordination compounds have been found to act as charge storage elements. It has been demonstrated that porphyrins molecules (i) offer the possibility of multibit storage at relatively low potentials (below about 1.6 V), (ii) can undergo trillions of write/read cycles, (iii) exhibit charge-retention times that are long (minutes) compared with those of the semiconductor elements in dynamic random access devices (tens of milliseconds) and (iv) are extremely stable under harsh conditions (e.g. monolayer of porphyrin molecules covalently attached to a silicon substrate are stable, when subjected to temperatures of 400 °C for half an hour) and, therefore, meet the processing and operating challenges required for use in semiconducting devices. It is thus anticipated that the first generation of molecular devices will be hybrid designs where molecules are integrated with semiconductors. However, further investigations on the search of other types of redox-active molecules and understanding the factors that control parameters such as, electron transfer rate, which limits write/read times and charge retention time, which determines refresh rates, are needed. Here we present an example of the resistive memory effect in a specifically designed molecule i.e. 5-(4-undecenyloxyphenyl)-10,15, 20-triphenylporphyrin (TPP-C11), as shown in Fig. 14, which was deposited on doped n-Si substrates by an electrochemical process via formation of Si–C bonds [4].

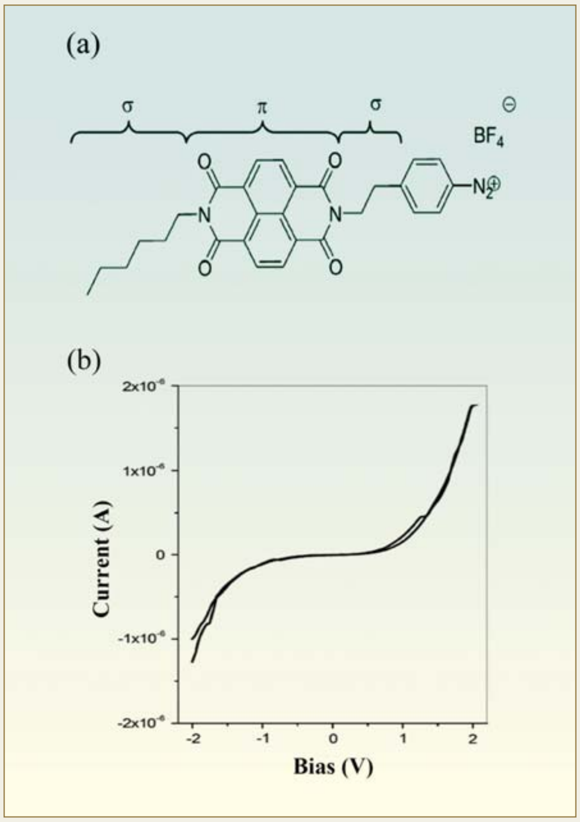

Fig. 13: (a) Molecular structure of a diazonium salt of a σ–π–σ molecule namely, N- (2-(4-diazoniophenyl)ethyl)-N′-hexylnaphthalene-1,8:4,5-tetracarboxydiimide tetrafluoroborate (DHTT). (b) Current–voltage characteristic of the σ–π–σ layers grafted on Si.

Typical *J–V* plots recorded for TPP-C11 monolayers is shown in Fig. 15. *J–Vs* are slightly asymmetric, which is attributed to the different work functions of the electrodes, i.e. Si (4.1 eV) and Hg (4.5 eV). It may be noted that the *J–Vs* of C11 monolayer did not exhibit any hysteresis; whereas for TPP-C11 monolayer a pronounced hysteresis is observed, indicating a predominant role-played by porphyrin ring. In the positive bias scan, i.e. from 0 to +0.8 V, current jumps by an order of magnitude at +0.6 V. However, on the reverse scan (+0.8 to 0 V) the current does not retrace the curve and remains at higher values. Thus, the *J–V* in the voltage range –0.6 V to +0.6 V exhibits two conduction states: one with low current (OFF) and other with higher current state (ON). The electrical bistable behaviour of TPP-C11 molecules has also been demonstrated for molecular memory effects. The memory phenomenon in electrically bistable devices is best demonstrated under 'write–read–erase–read' operations. In such a sequence of cycles, the low-conducting ('write') and high-conducting ('erase') states are induced repeatedly and the states are monitored ('read') in between. In the present case, 0 and +0.8 V pulses for 10 s were applied, respectively, to 'write' the low-conducting state and

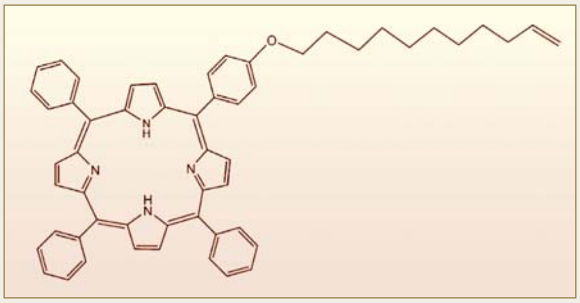

Fig.14: Molecular structure of 5-(4-undecenyloxyphenyl)-10,15,20-triphenylporphyrin (TPP-C11) specifically designed and synthesized for molecular memory effect

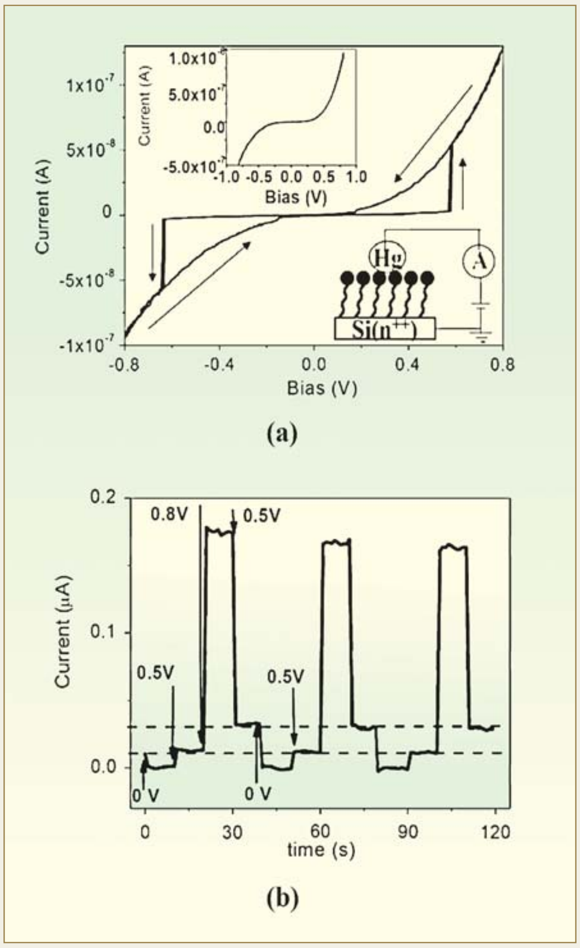

Fig. 15 (a) Reproducible J–V characteristics exhibiting hysteresis recorded for a TPP-C11 monolayer. Lower inset shows schematic of the device structure. Upper inset shows the J-V characteristics of C11 monolayer. (b) Demonstration of the memory effect in TPP-C11 monolayers. Dotted lines are guide to eye to distinguish between 'read' currents (measured at 0.5 V) after application of 'write' (0 V) and 'erase' (0.8 V) pulses.

monitored ('read') by measuring the device current (at 0.5 V), for more than 50 reading operations and a section of 'write–read–erase–read' operation recorded for such a device is shown in Fig. 15 (b). The magnitude of the device current under the 'read' voltage pulse is ~130% higher for high-conducting state ('erase') as compared to that for low-conducting state ('write').

Summary

At present, molecular electronics is one of the fastest growing fields and has brought together scientists and engineers from different disciplines. Much has been learned about the fundamental electron transport in molecules and niche applications in selected areas are emerging, but many of the remaining challenges are still formidable. It is anticipated that the first generation of molecular devices will be hybrid designs where molecules are integrated with Si- based microelectronics. Some of the passive and active molecular devices (dielectric, diodes, resonant tunnel diodes and memory) compatible to Si-microelectronics have been demonstrated. However, functional molecular transistors have not been demonstrated so far and a breakthrough in this direction is expected in the very near future.

Acknowledgements

We thank J.V. Yakhmi, S.K. Gupta, S.P. Koiry, A.K. Chauhan, S.K. Nayak, V. Saxena, N. Padma, S. Lenfant, D. Guerin, D. Vuillaume, B. Jousselme and S. Palacin for their active support.

References

1. D.K. Aswal, S. Lenfant, D. Guerin, J.V. Yakhmi and D. Vuillaume, *Anal. Chim. Acta*, 568 (2006) 84.
2. D. K. Aswal, S.P. Koiry, V. Saxena, N. Padma, S.K. Gupta, J.V. Yakhmi, S. Nayak A. Singh, and C. Suergers, in "Physics, Chemistry and Applications of Nanostructures: Reviews and

Short Notes to Nanomeeting 2007", eds. V. E. Borisenko, S. V. Gaponenko V. S. Gurin, World Scientific, Sinagpore.

3. D.K. Aswal, S.P. Koiry, B. Jousseleme, S. Palacin and J.V. Yakhmi, *Physica E* 41 (2009) 325.
4. S.P. Koiry, D.K. Aswal, A.K. Chauhan, V. Saxena, S.K. Nayak, S.K. Gupta and J.V. Yakhmi, *Chem. Phys. Lett.* 453 (2008) 68.
5. S.P. Koiry, D.K. Aswal, Vibha Saxena, N. Joshi, S.K. Gupta J.V. Yakhmi and D. Vuillaume, *Appl. Phys. Lett.* 90 (2007) 113118.
6. D. K. Aswal, S. Lenfant, D. Guerin, J. V. Yakhmi and D. Vuillaume, *Small 1* (2005) 725.
7. D. K. Aswal, C. Petit, G. Salace, S. Lenfant, D. Guerin, J.V. Yakhmi and D. Vuillaume, *Phys. Stat. Sol.* 203 (2006) 1464.
8. D.K. Aswal, S. Lenfant, D. Guerin, D. Vuillaume and J.V. Yakhmi, *Nanotechnology* 16 (2005) 3064.
9. A.K. Chauhan, D.K. Aswal, S.P. Koiry, S.K. Gupta and J.V. Yakhmi, C. Suergers, D. Guerin, S. Lenfant and D. Vuillaume, *Appl. Phys. A* 90 (2008) 581.
10. A. K. Chauhan, D.K. Aswal, S.P. Koiry, S. K. Gupta and J.V. Yakhmi, *Phys. Stat. Sol.* (a) 205(2008) 373.
11. S.R. Wasserman, Y.-T. Tao, and G.M. Whitesides, *Langmuir* 5 (1989) 1074.
12. N. Tillman, A. Ulman, J.S. Schildkraut and T.L. Penner, *J. Am. Chem. Soc.* 110 (1988) 6136.
13. D.L. Allara, A.N. Parikh, and F. Rondelez, Langmuir 11(1995) 2357.
14. S. Lenfant, Ph.D. Thesis, Organic self-assembled monolayers for molecular diodes, 2001, University of Science and Technology, Lille, France.
15. M. R Linford, P. Fenter, P.M. Eisenberger, and C.E.D. Chidsey, *J. Am. Chem. Soc.* 117 (1995) 3145.
16. M.D. Porter, T.B. Bright, D.L. Allara, and C.E.D. Chidsey, *J. Am. Chem. Soc.* 109 (1987) 3559.
17. K. Kojio, S. Ge, A. Takahara, and T. Kajiyama, *Langmuir* 14 (1998) 971.
18. J. G. Simmons, *J. Appl. Phys.* 34 (1963) 2581.
19. A. Aviram and M.A. Ratner, *Chem. Phys. Lett.* 29 (1974) 277.

ABOUT THE AUTHOR

Dr. D.K. Aswal joined BARC in 1986 through the 30th Batch of Training School after completing M.Sc. (Physics) from Garhwal University. His area of scientific interest is condensed matter physics, specializing in device-oriented research leading to hybrid molecule-on-Si nanoelectronics, thermoelectric devices and gas sensors. He has made several original contributions in the fields of high-temperature superconductors, colossal magnetoresistive manganites, metallic-multilayer grown by molecular-beam-epitaxy and thermoelectric devices. He is a recipient of several international fellowships including, JSPS fellowship, Japan (1997-99), IFCPAR fellowship, France (2004-05), BMBF fellowship, Germany (2006) and CEA fellowship, France (2008). He is a recipient of several awards, including "Homi Bhabha Science and Technology Award -2007", "DAE-SRC Outstanding Research Investigator Award-2008", and "Paraj: Excellence in Science Award, 2000". He has edited a book on "Science and Technology of Chemiresistive Gas Sensors" and authored more than 120 scientific publications in peer reviewed international journals. He is editorial board member as well as technical reviewer of several international journals.

SHAPE MEMORY ALLOYS

M. Krishnan
Materials Science Division

Dr. Madangopal Krishnan is the recipient of the Homi Bhabha Science and Technology Award for the year 2007

Deformed and distorted articles made of shape memory alloys (SMA) recover their original shape and dimensions, when temperature is raised. Usually, SMAs can only memorize the shape of the article at the higher temperature (the "recovered" shape) and, when "trained", can also memorize the shape to be assumed at the lower temperature (the "deformed" shape). This natural tendency of SMA, is a result of the reversible diffusionless phase transformation of the high temperature phase to the low temperature phase ("thermoelastic-martensitic transformation").

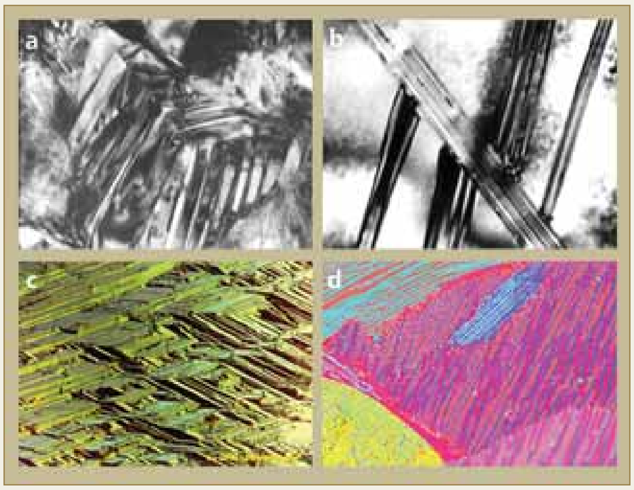

Self accommodating martensitic microstructures of SMA: a) transmission electron microscope(TEM) bright field image of triangular 3-variant B19' martensite plate group in Ni-Ti alloys; b) TEM bright field image of the plate epsilon martensite in Fe-Mn-Si-Cr-Ni alloys; c) Polarized light micrograph of 4-varien plate of 18R martensite in Cu-Zn-Al alloys; d) 4-varient plate groups in Ni-Mn-Ga ferromagnetic SMA revealed by electron backscattered diffraction.

Shape memory effect (SME) is the cumulative result of the two characteristic properties of thermoelastic martensites: pseudoplasticity and microstructural reversibility. These properties are manifestations of unique crystallographic inter-relationships found in the microstructure

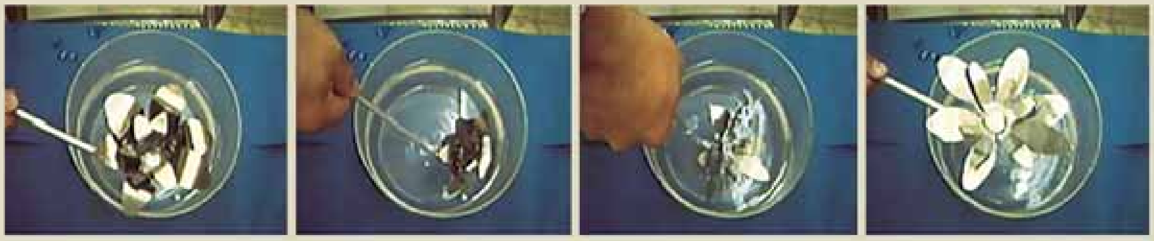

Flower made of equiatonic Ni-Ti alloy, demonstrating the shape memory phenomenon. At ambient temperature, the "flower" is easily deformed into a bud, but rapidly "blossoms" to its original shape on being immersed in hot water of SMAs. The figures shown above provide examples of the self-accommodating nature of martensite orientation variants and manner in which inter-variant interfaces in microstructures, with B19' internally twinned martensites, transform into twin interfaces.

Of a reasonably large number of alloys which show the "shape memory effect", the Ni-Ti based alloys are the best in terms of shape memory properties and their viable engineering applications. At this point in time, a very wide gamut of medical, engineering, nuclear and space applications have been created, that successfully exploit the excellent biocompatibility, superelasticity, shape recovery, damping characteristics and the high recovery stress of the Ni-Ti based shape memory alloys. However, these alloys are expensive and relatively difficult to prepare and fabricate. On the other hand, Cu-based and the Fe-based shape memory alloys, which cannot match Ni-Ti alloys in terms of all these properties, are lot easier to fabricate and a lot cheaper. Thus, these alloys are increasingly being used, where cost is a major factor.

There are a few ways in which the shape memory characteristics could be utilized. "Free recovery" applications are where the shape memory phenomenon is utilized, merely to recover the original shape, such as in case of the "flower" in the figure above. On the other hand, if a shape memory alloy object is deformed and then constrained in a manner so as to prevent free recovery, an increase in temperature will cause a large "reversion" stress to be generated, in proportion to the extent to which the deformed object strains to regain its original shape. This phenomenon of "constrained recovery" is widely employed in static applications such as fasteners, sleeves, couplings and reinforcement, and also in dynamic applications such as heat engines and actuators. The shape memory effect presents itself in another useful phenomenon known as "superelasticity". Here, a large recoverable strain is obtained, when martensite is induced above recovery temperature, by applied load. Thus, SMAs can show large elastic deformation (about 10% in Ni-Ti alloys and 30% in Cu-Be-Al alloys), a property which has been successfully utilized in engineering and medical applications like self-expanding stents, brace wires, retrieval baskets, deformable instruments, filters and springs, etc. In medical applications, the appeal of Ni-Ti alloys is its excellent biocompatibility and corrosion resistance in human body environment. Ni-Ti alloys, particularly porous materials created by combustion synthesis, have an elastic modulus close

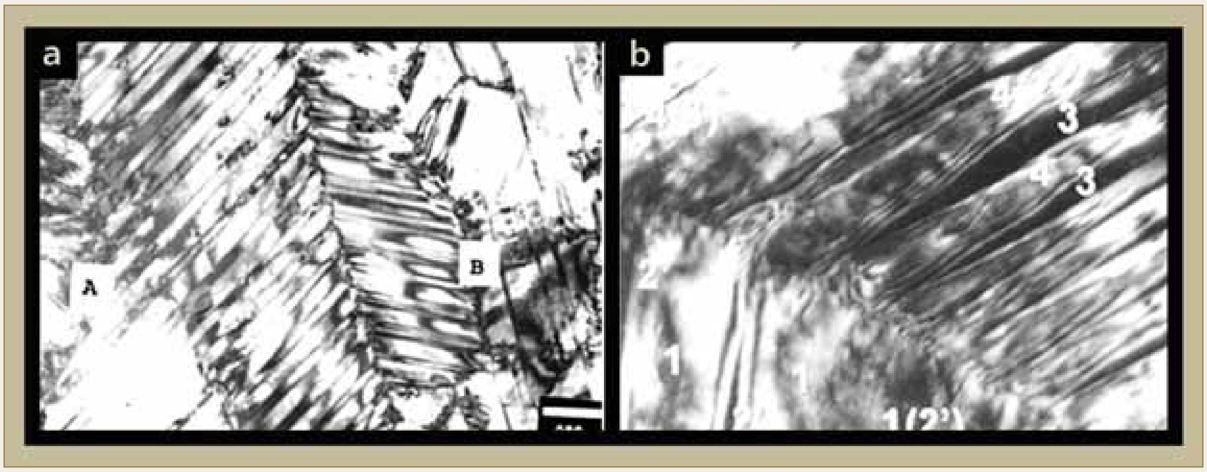

The microstructural reversibility is ensured by the formation of twin interfaces derived from mirror planes of the parent phase: a) the B19 intervariant interface fulfils this eriterion as both major and minor twin fractions of each martensite plate are twin related across the interface; b) in this case the twin intervariant interface is obtained by tapering off the minor twin fractions which are not in twin relation across the interface.

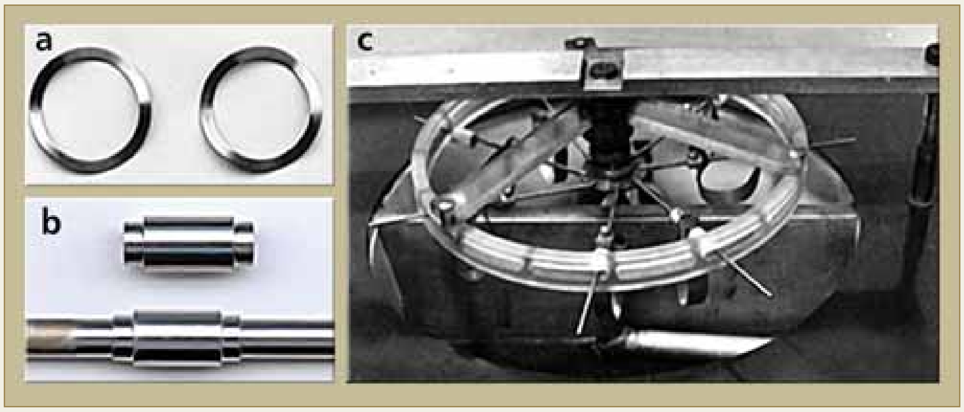

a) Ni-Ti superelastic 3-wave spring; b) Ni-Ti-Fe heat shrinkable hydraulic coupling rated for 4500 psi joints and c) heat engine with Ni-Ti SMA working elements. The Ni-Ti elements are first deformed in cold water and then recovered under constraint in hot water: The reversion stress generated during constrained recovery is used to rotate the wheel

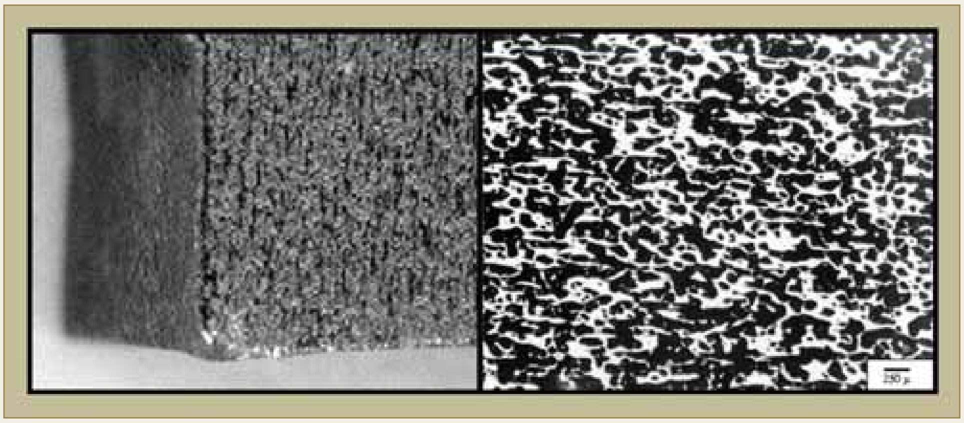

Porous Ni-Ti produced by combustion synthesis at BARC, The interconnected large open pores make porous Ni-Ti an excellent superelastic bone prosthesis material. The superelastic porous Ni-Ti materials is biocompatible and has a modulus close to that of human bone

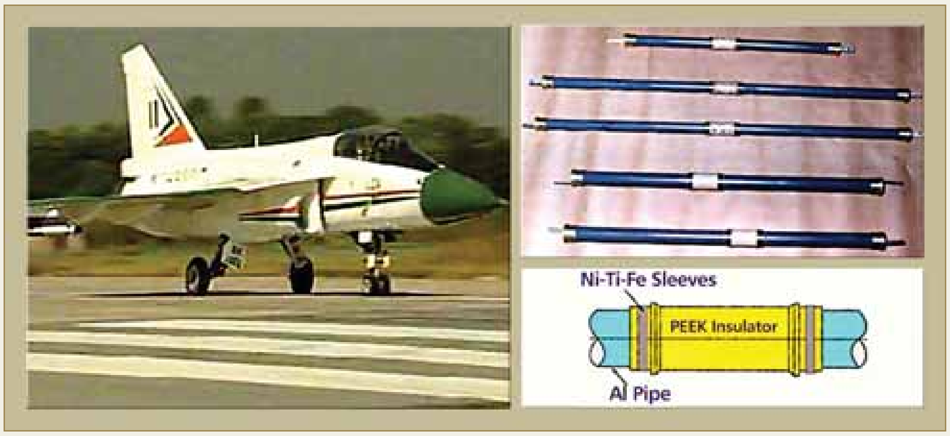

The Ni-Ti-Fe heat shrinkable sleeves developed by BARC are used as fasteners in the Light Combat Aircraft under development at Aeronautical Development Agency, Bengaluru. These sleeves have been tested and certified for airworthiness and application in combat aircrafts.

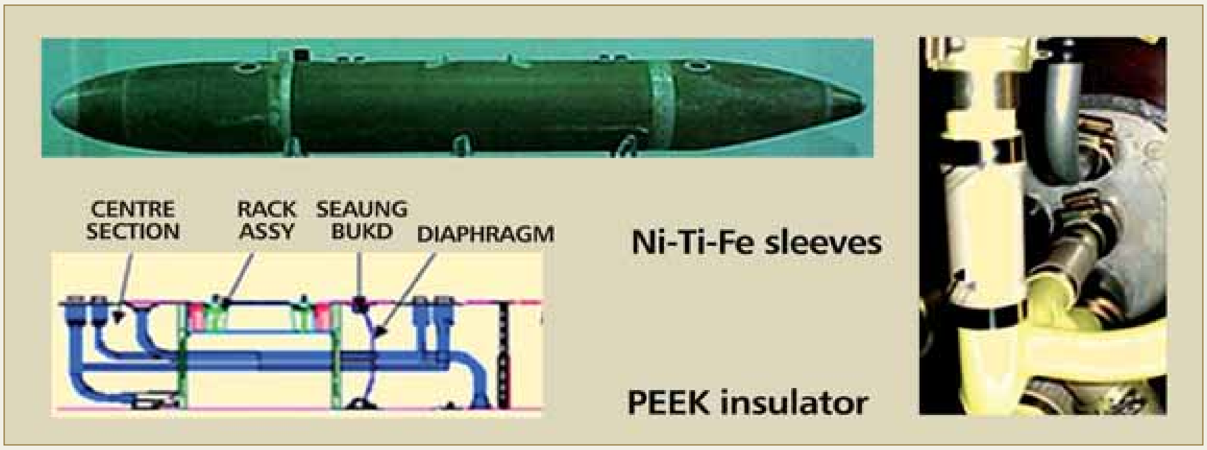

Figure shows the application of Ni-Ti-Fe heat shrinkable sleeves for fastening the polymer insulators in the drop tanks of LCA

to that of the human bone. This property is utilized in medical prosthesis where biomechanical compatibility is essential.

Research on shape memory alloys has been going on in the Materials Science Division for over two decades and has produced a number of important scientific contributions on material characterization and phase transformations, in relation to the shape memory phenomena. These include the rationalization of reversion stresses, crystallography of the martensitic transformation, the nature of self-accommodation of martensite crystals and the crystallographic interrelationships between the shape memory effect and martensitic microstructure. Alongside basic research, the development of the melting and fabrication of shape memory alloys was also pursued and this has lead to the successful development of several Ni-Ti, Cu-Zn-Al and Fe-based alloys. The most important success of this effort has been the development of Ni-Ti shape memory alloys and Ni-Ti-Fe heat shrinkable sleeves, for the Light Combat Aircraft (LCA). Both of these are not available to the defense and the nuclear industry due to import restrictions.

The flow sheet for the production of Ni-Ti-Fe sleeves for the LCA involving alloy preparation, fabrication and machining was developed at the Materials Science Division, BARC and scaled up to viable production

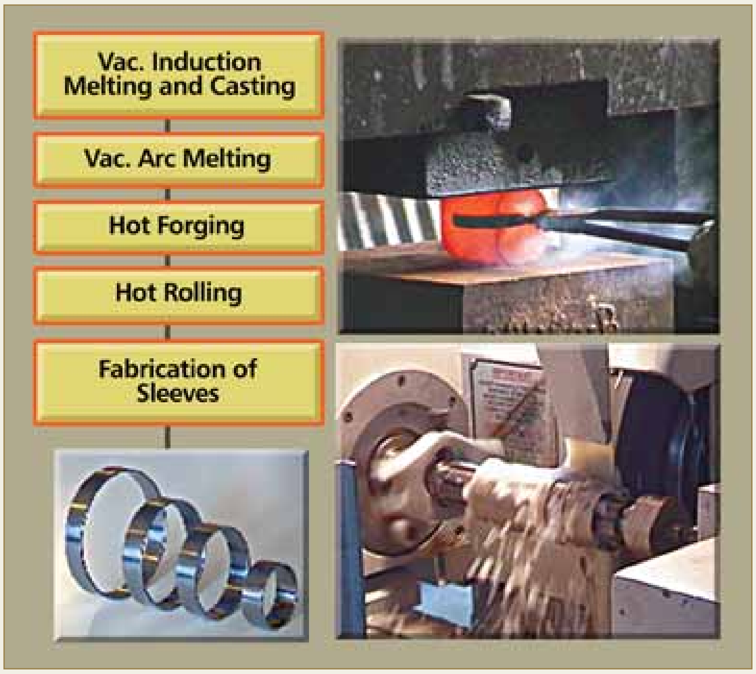

The melting, processing and fabrication flow sheet for heat shrinkable Ni-Ti-Fe SMA sleeves developed at BARC. The pictures show hot forging of Ni-Fi alloy ingots and machining of heat shrinkable sleeves from electric discharge machined blanks

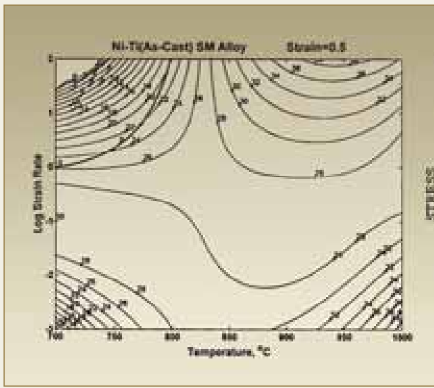

The deformation processing map for vacuum induction melted and vacuum are remelted Ni-Ti-Fe alloys. The region in the map where dynamic recrystallation occurs is preferred for hot working of the alloys

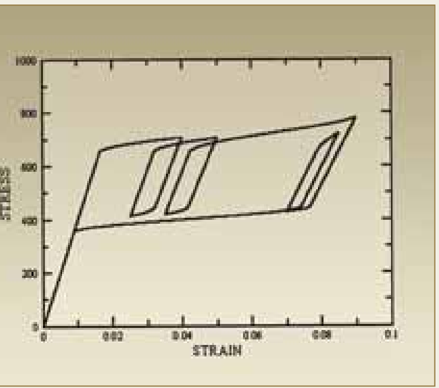

The pseudoelastic stress-strain plot generated by a I-D model of the thermoelastic behavior of Ni-Ti alloys. The model successfully reproduces the hysteresis, the transformation and the sublooping behaviour

levels. The activities of the flow sheet are spread over different work centers: the induction melting and hot rolling are done at the Atomic Fuels Division, BARC, the consumable vacuum arc melting is carried out at the Nuclear Fuel Complex, Hyderabad, hot forging at Foundry & Forge Division, HAL, Bengaluru, machining at a private workshop in Mumbai and the thermo-mechanical treatment and detailed characterization are carried out at the Materials Science Division, BARC. About 2500 sleeves have been supplied to ADA, Bengaluru. These have been used in the construction of eight LCAs and have put in more than 1000 hours of service.

The Ni-Ti-Fe heat shrinkable sleeves are used to clasp polymer insulators onto metallic conduit pipes. The sleeves are expanded in liquid nitrogen environment, using a special tool developed for this purpose and then applied to the insulator-conduit pipe joint.

The Ni-Ti-Fe SMA sleeves are used in the LCA to fasten polymer insulators to metallic conduit pipes. The sleeves are mechanically expanded in liquid nitrogen using a special tool. Soon after installation of the joint, the temperature of the sleeve rises to the ambient and shape recovery occurs. The constrained recovery generates a large stress that is sufficient to clasp the insulator onto the metallic conduit pipe. Heat shrinkable sleeves are particularly useful for joining dissimilar materials, materials sensitive to heating and where a low profile tool is required.

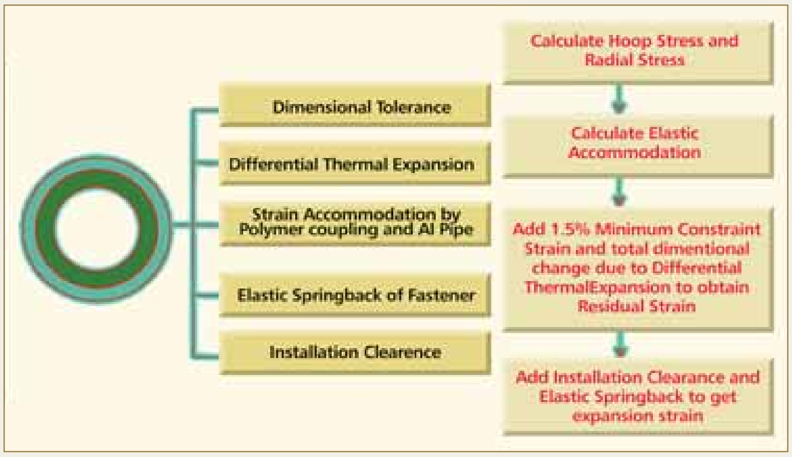

The maximum recoverable strain for polycrystalline Ni-Ti alloys is about 6%. The main objective in the design of SMA heat - shrinkable sleeves, is to deliver the force required for clasping the polymer insulator, after providing for a minimum retained strain of 1.5%, throughout service conditions

The dimensions of the sleeves and the insulator are such that, complete recovery cannot take place. Under this condition of constrained recovery, a large reversion stress is generated and the insulators are tightly fastened onto the conduit pipes. The alloy selection and mechanical design ensure, that the sleeves deliver a constant reversion stress of about 500 MPa in the temperature range of -55^{0}C to +150^{0}C. The sleeves were put through rigorous tests for airworthiness such as leakage, sealing, ultimate pressure, thermal shock, vibration, pull out and endurance (1,40,000 cycles of pressurization, under the combined action of shear and bending forces) and have been cleared for application in combat aircrafts. These performance tests ensure, that the sleeves can provide sufficient grip under conditions of temperature and pressure encountered in service. Currently, the technology for the manufacture of Ni-Ti-Fe alloys and heat shrinkable sleeves are under transfer to Foundry & Forge Division of HAL, Bengaluru, where a plant dedicated to this purpose is being set up. When operational, this plant will be the only one in the country and amongst a few worldwide that manufacture shape memory alloys and heat shrinkable fasteners. Other components currently under development for application in LCA include heat shrinkable hydraulic coupling and thermally actuated valves.

ABOUT THE AUTHOR

Dr. Madangopal Krishnan is a Homi Bhabha awardee of the 28th batch of BARC Training School. He specializes in phase transformations, especially martensitic and displacive transformations, in shape memory alloys. His major research interests include characterization of Ni-Ti, Cu-based, Fe-based and ferromagnetic shape memory materials by transmission electron microscopy, X-ray diffractometry and differential scanning calorimetry. Dr. Krishnan and his team specialize in developing the industrial scale processing of shape memory alloys and designing their engineering applications. He was also involved in developing Ni-Ti heat shrinkable fasteners and superelastic springs for the prestigious Light Combat Aircraft programme.

STUDIES ON SEISMIC SAFETY OF NUCLEAR FACILITIES

G.R. Reddy
Reactor Safety Division

Dr. Reddy received the DAE Scientific & Technical Excellence Award for the year 2007.

ABSTRACT

Nuclear facilities need to be safe during postulated earthquakes. The subject of seismic design of nuclear facilities has gained importance and substantial research was conductd apart from regular design and analysis work. The goal of achieving absolute seismic safety at optimized cost, is still being pursued. The work related to seismic safety of nuclear facilities was grouped under: Analysis and design of AHWR containment building, fuelling machine and down comers, Analysis of 32 m DSN antenna of the Chandrayan project of ISRO, Experimental programme pursued for better understanding of the structural behaviour of beam-column joints and piping components under earthquake loading, development of seismic response control devices, requalification of older facilities and retrofitting of systems such as CIRUS ball, tank, retrofitting scheme proposed for APSARA reactor building and developing Advanced Seismic Testing and Research Laboratory (ASTaR) at SERC, Chennai.

Design of AHWR Containment Building

After examining issues such as Prestressed vs RCC with Liner, connection of Inner Containment Wall (ICW) with Internal structure through Gravity Driven Water Pool and Sharing of Load by ICW and Tail Pipe tower; the AHWR containment building was designed and analyzed for dead load, prestress, accidental pressure and seismic loadings. Issues related to 100 year life and temperature control in concrete was also resolved. Finite Element model was prepared for the entire building as shown in Fig.1.1. Seismic qualification was made severe by the existence of Gravity Driven Water Pool containing 6000 m^3 of water at the top. The natural frequency of the structure coincided with the peak in the response spectrum as shown in Fig.1.2.

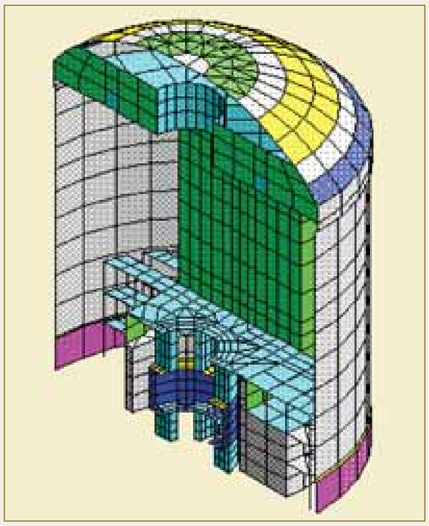

Fig.1.1 : Finite Element Model of AHWR containment

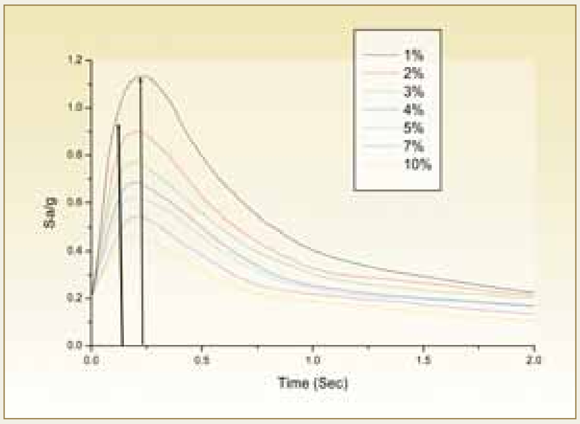

Fig. 1.2 : Response spectrum and spectral acceleration

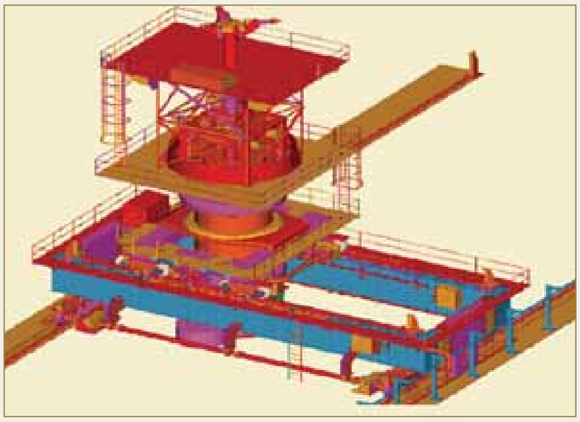

Fig. 2 : AHWR Fuelling Machine

The solution was to connect GDWP to Reactor Building. This increased the rigidity and shifted the frequency away from the peak. Combined structure with complex geometry was analyzed, using Finite Element method and shown to be safe.

Stress and Seismic analysis of AHWR Fuelling Machine

Fuelling machine of AHWR shown in Fig. 2 is a vertical type and facilitates on load fuelling. The main design was performed by RTD, BARC. The machine was analyzed for normal and accidental loads such as earthquake along with RTD and Anna University. Few design suggestions are made to avoid sliding and toppling of machine under seismic excitation.

Stress analysis of AHWR Downcomers

The downcomers forming part of Main Heat Transport System of AHWR need to have low operating stresses to avoid the risk of IGSCC. The conflicting requirements of high flexibility for reducing thermal stresses and high stiffness to reduce the seismically induced stresses required optimization of the layout. One way of achieving this is by using snubbers as shown in Fig. 3.1 which are costly and require frequent maintenance. This results in high man rem cost. The second option is making the piping system flexible by using large number of bends and conventional supports as shown in Fig. 3.2. This will increase number of welds and require large space, which eventually makes the system costly. Also, more

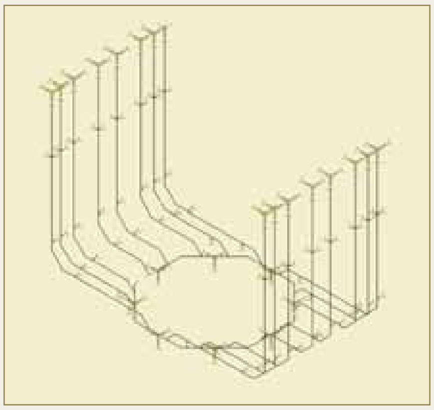

Fig. 3.1 : LAYOUT-1 Inadequate flexibility requires snubbers

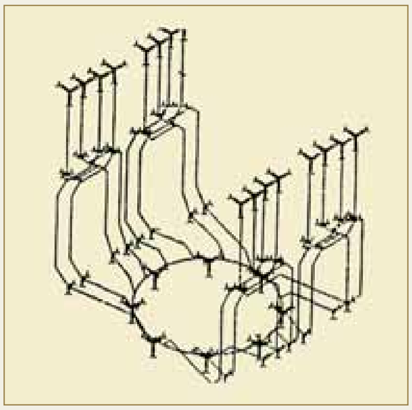

Fig. 3.2 : LAYOUT-2 Flexible but complex with too much welding

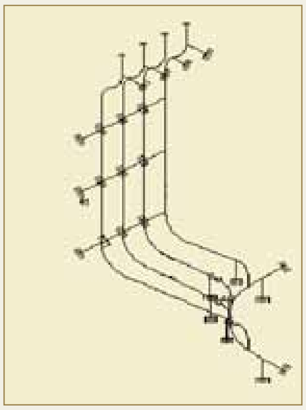

Fig. 3.3 : LAYOUT-3 Flexible, Simple uses EP dampers

number of welds result in difficulties for in-service inspection. Eliminating all the difficulties in these two layouts, an optimized layout which uses passive energy absorbers, called Elasto-Plastic Dampers (EPD) as shown in Fig. 3.3 was developed. The use of EPDs has resulted in a simpler layout with reduced number of welds and total length of the piping system.

Design and analysis of the Deep Space Network (DSN) antenna, for the Chandrayaan project

The Deep Space Network (DSN) 32 m antenna is used for communications with space craft by receiving and sending radio signals. For efficient communication, the specified optical parameters need to be maintained, considering the structural deformations under the dead weights in different orientations. Structural design and analysis of 32 Meter DSN Antenna, Chandrayaan project subjected to dead weight, thermal load, wind load and earthquake load was performed. Dead weight analysis and generated look-up table, which gives the adjustment required in sub-reflector, to compensate the structural deformation under dead weight at various elevation angles and to maintain the focal

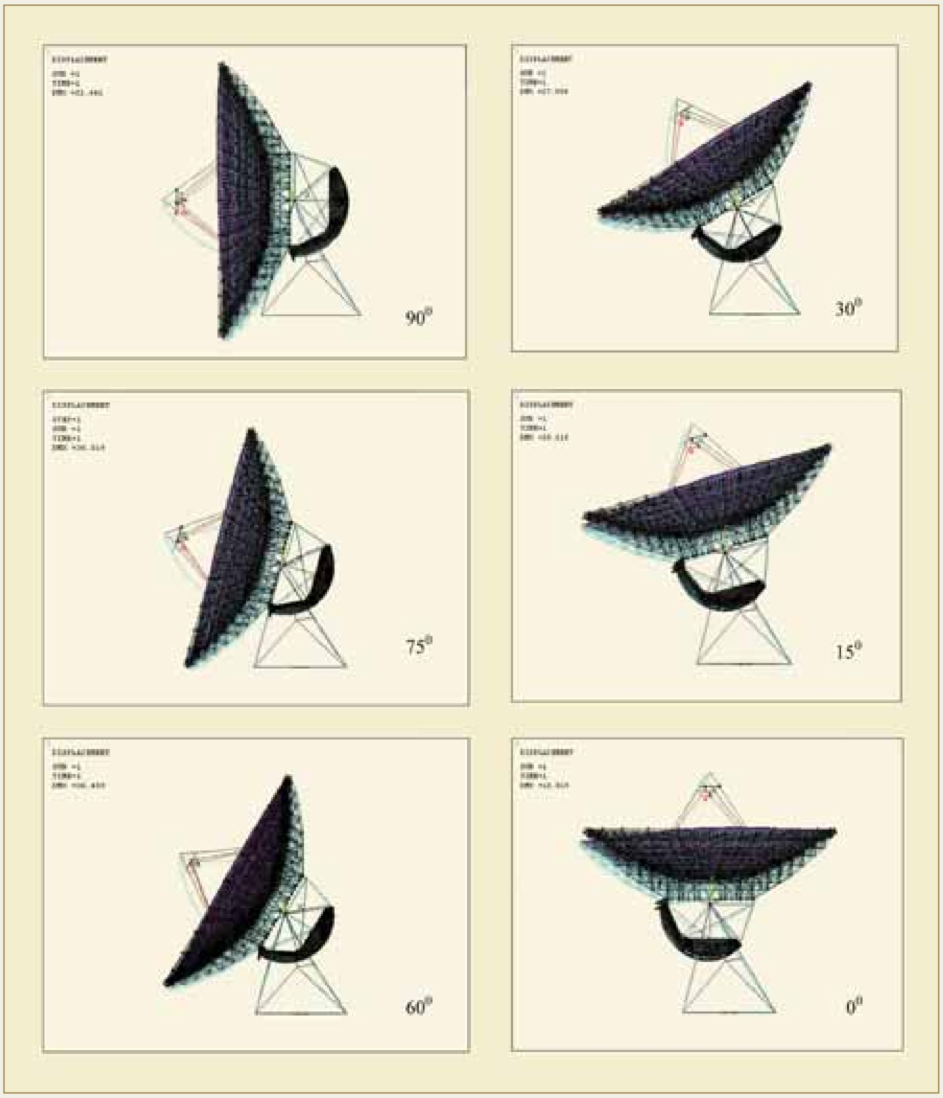

Fig. 4 : Deflected and undeflected shapes of the antenna at various elevation angles under self weight

length was performed. Deformed shapes of antenna at different elevation angles are shown in Fig. 4.

Research in RCC structures

A three-phase programme as shown in the following chart was formulated to understand the behaviour of concrete structures and its components, subjected to earthquake loading and develop realistic modeling methods, to predict the behaviour. In the first phase, about 30 joints with different sizes and detailing were tested for its load vs displacement capacity, ductility. Few results are shown in Fig. 5. It was found, that size has larger influence on the ductility of the RCC components or joints (see the bar chart). In the second phase two push over tests were conducted on frame structures of full scale and further tests on scaled models are under progress. Analysis of the structures tested was performed along with another colleague. It is concluded that while performing the analysis, failure modes such as shear, flexure+shear, confinement effects, Boundary conditions etc. shall be given due consideration for correct evaluation of seismic capacity of the structure. In the third phase, dynamic tests on the RCC structural models are planned and already one test has been completed.

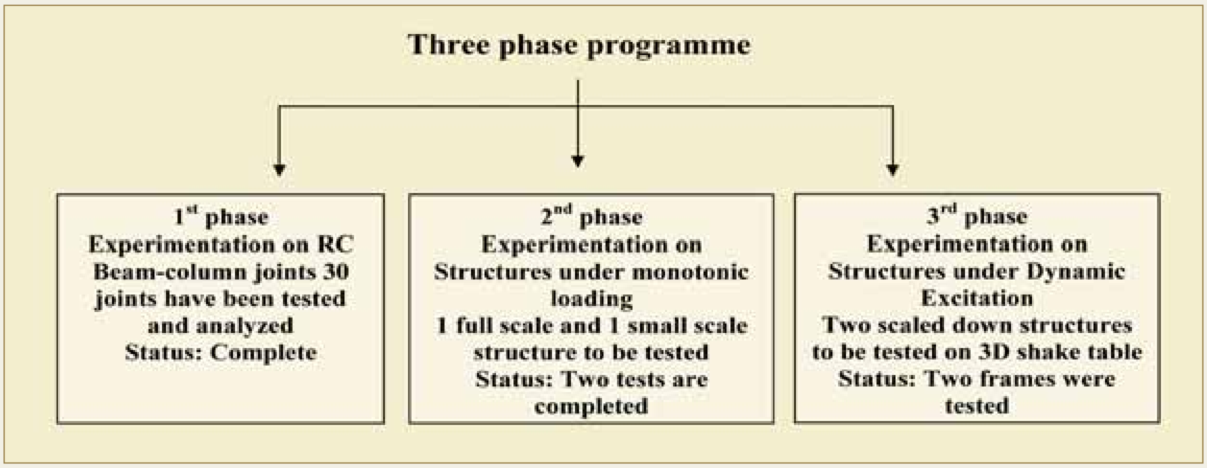

Three phase programme

1st phase
Experimentation on RC Beam-column joints 30 joints have been tested and analyzed
Status: Complete

2nd phase
Experimentation on Structures under monotonic loading
1 full scale and 1 small scale structure to be tested
Status: Two tests are completed

3rd phase
Experimentation on Structures under Dynamic Excitation
Two scaled down structures to be tested on 3D shake table
Status: Two frames were tested

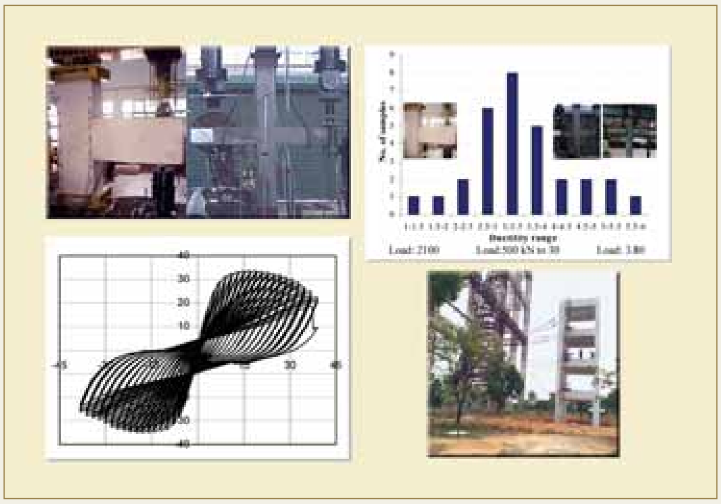

Fig. 5.1 : Load-deflection characteristics of beam-column joints

Fig. 5.2 : Pushover verification tests on RCC structures

Ratcheting studies on piping systems

ASME B & PV code has increased the allowable stress considering ratcheting modes of failures. However, it is based on limited data. Earlier the design of piping subjected to seismic excitation was based on the principle of plastic collapse. Later, it was observed that fatigue-ratcheting is a likely mode of failure of piping components. Experimental and analytical studies are carried out, to understand the changes in code and failure mechanism of piping systems. It was found that, in the static cyclic tests, the pipe with internal pressure and where maximum moment acts, starts ballooning as shown in Fig. 6.1 which results in local thinning and failure. In the case of shake table tests shown in Figs. 3.2 and 3.3, failures are noticed due to the combination of fatigue and ratcheting. At elbow and anchor weld joints, it is due to the fatigue phenomenon where as in elbow it is ratcheting. In the case of T-joints it is more like fatigue failure. It is concluded, that the failure in case of earthquake loading is by fatigue-ratcheting and for the failure to occur, the bending stress has to be in excess of the enhanced limits. Thus, the applicability of the enhanced stress limits prescribed for this type of loading was justified. Theoretical research was carried out along with IIT, Mumbai and suggested modification in the Ohno-Wang ratcheting model for better estimation of ratcheting strains, was done.

Life extension of nuclear facilities : retrofitting

While planning for extending the life of nuclear facilities, one needs to understand the design methodologies applied, including failure modes, health of Structures, Systems and Components (SSCs), present safety and design demands. The SSCs deteriorate with time. It may not be meeting the present postulated loading (e.g earthquake laoding) demands for maintaining the desired safety levels. In addition to this, the postulated failure mode may not be valid at present. For example, the soft story concept was well accepted in earlier designs, but at present it is not acceptable. For old/existing SSCs, techniques were developed for strengthening and increasing abosorbing capacity of SSCs. Some of the techiniques are steel jacketing, FRP wrapping, base isolation, using dampers etc. as shown in Fig. 7. These techniques are an inexpensive easy to accommodate and adopt into the existing SSCs. The tools base isolation, dampers can also be used for economical design, meeting the safety requirements. These also can be used for design

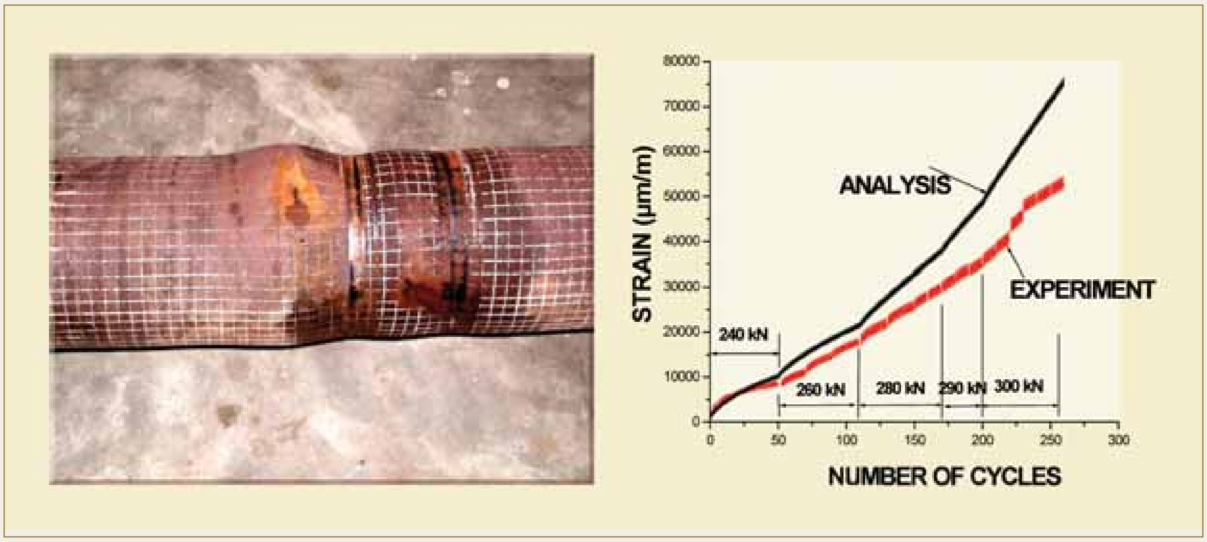

Fig. 6.1 : Slow cyclic tests on straight pipes with internal pressure

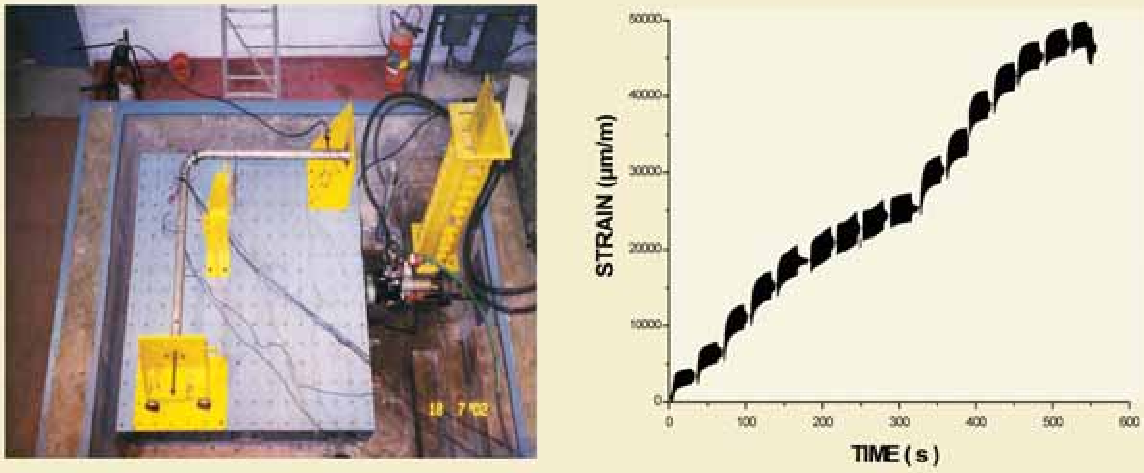

Fig. 6.2 : Shake table tests on SS piping system

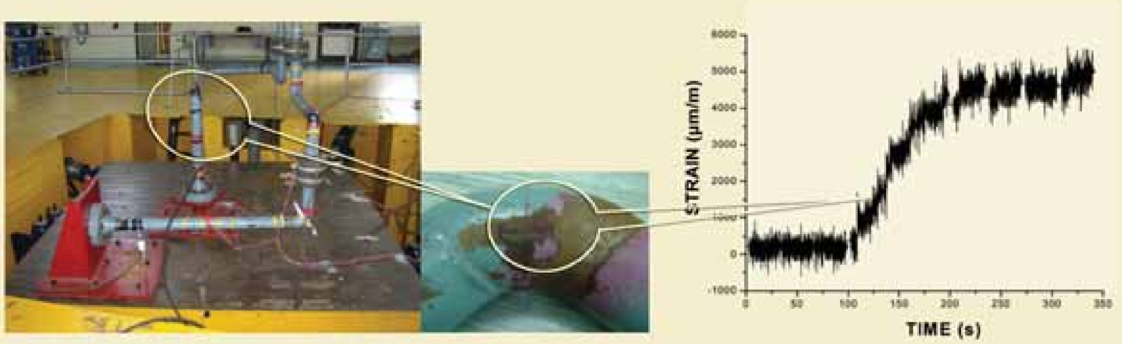

Fig. 6.3 : Shake table tests on 3-D carbon steel piping system

standardization. Along with the NRG, elasto-plastic dampers were designed and manufactured. These dampers were implemented at WIP-3A, Kalpakkam to support melter shell structures, solid waste storage cubicles. These helped to reduce the loads coming on the embedded parts. Without these tools, it would have been very difficult to qualify these structures.

Seismic Reevaluation of CIRUS research reactor

To address the concerns about the safety of research reactors, power plants and other facilities in the event of an earthquake, the Reactor Safety Division is engaged in seismic analysis of old as well as new facilities: Analyzed reactor building, Emergency storage tank (ball tanks, battery banks and dampers. It was found, that ball tank is not meeting the seismic demand as per the present requirements and proposed retrofitting scheme of steel jacketing. The scheme details as shown in Fig. 8 were given to A&CED for implementation. The retrofitting work was completed and the tank is serving as desired.

Retrofitting Schemes developed

Increase the capacity/strength of the system (Seismic Resistance Based Design)
Concrete Jacketing, Steel Jacketing, CFRP Wrapping

Reduce the demand/forces on the system (Seismic Response Control Design)
Elasto-Plastic Dampers, Base Isolators, Lead Extrusion Dampers, Tuned Liquid Dampers

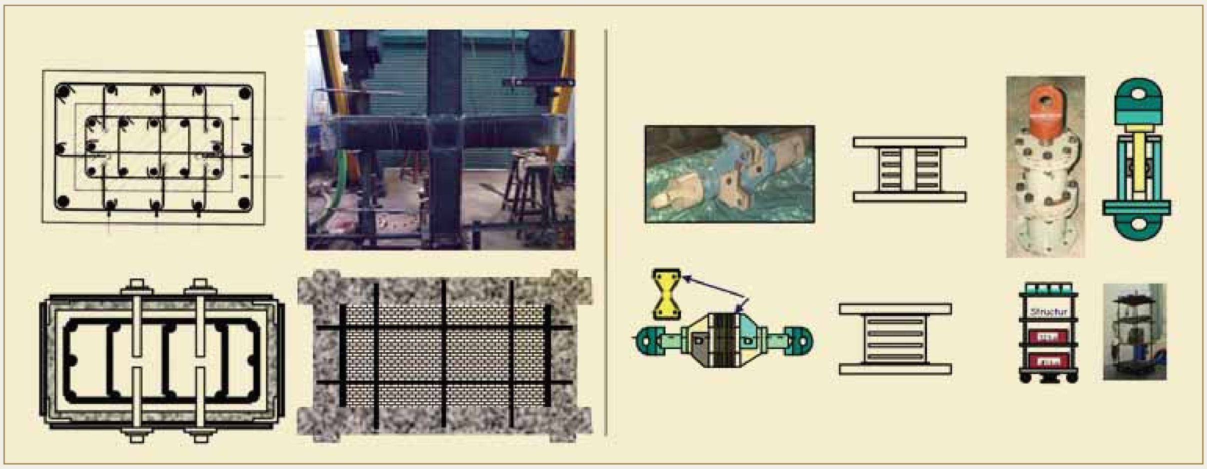

Fig. 7 : Seismic retrofitting tools

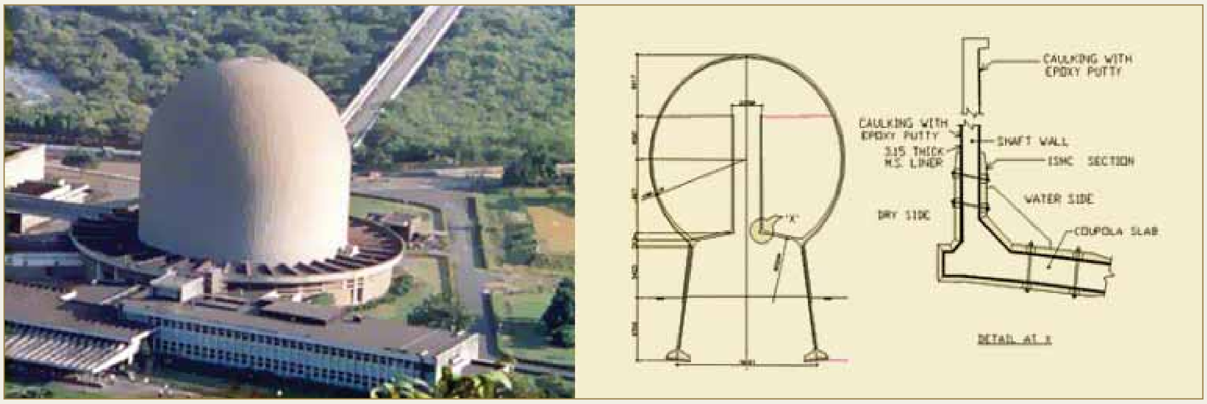

Fig. 8 : Retrofitting of ball tank central shaft with steel jacketing

Seismic Reevaluation of APSARA Reactor Building

Analyzed the reactor building of APSARA for anticipated seismic loading and proposed retrofitting measures in the form of elasto-plastic dampers. The retrofitting using dampers is only possible to meet the seismic demand in the foundation footings. Other schemes of fiber wrapping for walls and beams wherever needed were proposed. Conducted a shake

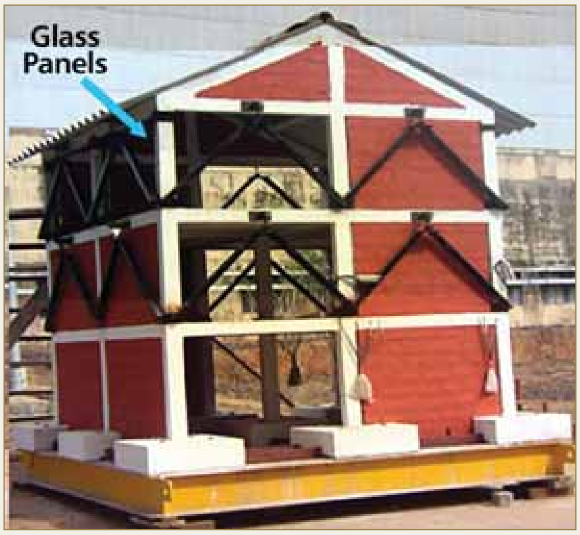

Fig. 9 : Model of APSARA building

table test on a model shown in Fig. 9 (a representation of the APSARA reactor building) to demonstrate the reduction in response, due to dampers and effectiveness of fiber wrapping for the brick walls.

Seismic proving tests on piping with dampers

A 3-D piping loop as shown in Fig.10 was tested on shake table at CPRI, Bengaluru with and without Elastoplastic dampers. Significant reduction in response due to dampers was noticed. Analysis of piping with and without dampers has been carried out and the results are found to match well with the test data.

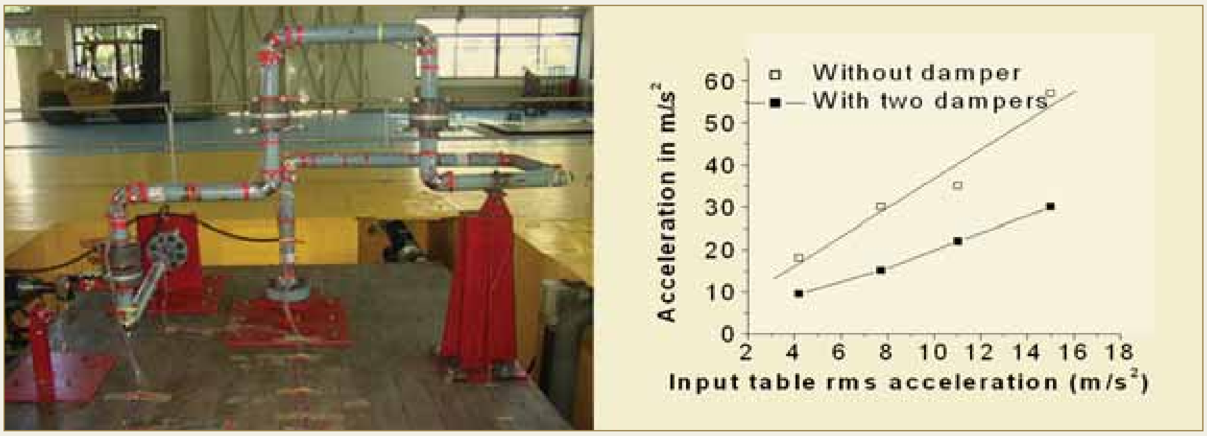

Fig. 10 : Response of complex piping system with dampers

Experimental facilities

Advanced Seismic Testing and Research (ASTaR) Laboratory at Structural Engineering Research Centre, Chennai as shown in Fig. 11 was established. This facility is unique in the country and probably in the world. It has two tables which help for multi support excitation. By using the property of synchronization of the two tables, we get a larger area for testing to support large size equipment. In addition to this, it has a feature to perform multi-support pseudo-dynamic facility, along with reaction wall to perform the tests on component levels. This facility was developed along with SERC, Chennai, IGCAR, NPCIL and BRNS.

Fig. 11 : ASTaR Laboratory

Acknowledgements

The constant support received from Ms. Y.P. Parulekar, Mr. P.N. Dubey, Mr. Akanshu Sharma, Mr. Hari Prasad to perform the above work performed is highly appreciated. The encouragement received from Head, RSS, Head RSD and Director HS&EG is acknowledged.

ABOUT THE AUTHOR

Dr. G. Rami Reddy, joinied BARC in 1984 after completion of B.E, M.Tech, PhD. He is working in the area of Structural Dynamics & Earthquake Engineering and analyzed, designed nuclear facility structures, equipment and piping systems. Made significant contributions to the design of 500 MWe PHWRs, setting of advanced seismic testing laboratory at SERC, Chennai, Component test facility at BARC, requalification of BARC facilities, 32m DSN antenna etc. and presently involved in the design of AHWR, MACE telescope, developing concrete laboratory etc. Worked in the research areas of modeling techniques of complex structures, structure-equipment interaction due to earthquakes, stochastic methods of analysis, dynamic substructure techniques, structural retrofitting etc. Mastered seismic response control methods and is involved in developing friction dampers, elasto-plastic dampers, Lead extrusion dampers, isolators and Tuned liquid dampers. He has 184 publications to his credit.

PLANAR AND VOLUME TOMOGRAPHY IMAGING FOR NDE APPLICATIONS

Umesh Kumar
Isotope Applications Division

Dr. Umesh Kumar is the recipient of the DAE Scientific & Technical Excellence Award for the year 2007

ABSTRACT

Electronic imaging devices for gamma and x-ray based Radiography Testing (RT) have shown a remarkable presence during the last decade, due to their technical adaptability to existing inspection systems and easy availability of different configurations to suit a variety of applications. The process of NonDestructive Testing or Examination (NDT or NDE) determines the existence of flaws, discontinuities, leaks, contamination, thermal anomalies or imperfections in materials, components or assemblies, without impairing the integrity or function of the inspected component. NDE is also utilized for real - time monitoring during manufacturing, inspection of assemblies for tolerances, alignment and periodic in-service monitoring of flaw/damage growth, in order to determine the maintenance requirements and to assure the reliability and continued safe operation of a particular part. Today, one can find both analog and digital imaging systems like tube-type fluoroscopy devices, solid-state Linear Detector Arrays (LDA) and two-dimensional detector arrays like Flat Panel Detectors (FPD). These devices can be adapted to suit a variety of imaging requirements like Digital Radiography (DR) operating in online and/or real-time mode and the fast emerging Industrial Computed Tomography (ICT) imaging for non-medical applications. A typical DR and ICT system may be very compact and modular for low-energy applications. However, dedicated DR/ICT systems designed and developed for specific requirements and making use of high-energy X-rays, may be a fixed installation. The Isotope Applications Division (IAD) at BARC, Mumbai has been active in the research and development activities, in the field of advanced radiation-based imaging, for industrial applications for almost a decade. IAD has demonstrated long-back, indigenous efforts in x-ray and gamma ray-based tomographic imaging systems, for various applications. It has continued its effort to modify and develop a facility for Digital Industrial Radiography (DIR) and Volume Computed Tomography (VCT) imaging systems primarily for industrial and other non-medical applications. The present paper briefly discusses research and development efforts in the planar and volume tomography imaging for NDE applications. It may be stressed here, that the work carried out so far, was primarily aimed at indigenous technology and know-how development for various applications.

Introduction

Conventional Industrial Radiography is an adaptation of the principle of latent image formation on photographic medium, by gamma rays or X-rays for non-medical applications. The conventional gamma ray and x-ray based radiography for examination of industrial specimens has been in practice for decades and it has become an indispensable tool for industrial quality control in production, maintenance and in-service inspection. Most of the applications using film-based Radiography Testing (RT) are now standardized. Though film-based RT offers probably the best spatial resolution limited by the emulsion property, there are sometimes disadvantages associated with this method, like lack of possibility of having real-time and online inspection and maximum throughput. In terms of cost-to-benefit analysis also, though film based RT may offer a simpler option in terms of initial investment, the recurring cost on consumables may be prohibitive in the long run.

The industrial applications of tomography are still picking up primarily because, one set of specifications does not cater to all problem areas. As a result, it appears that it is difficult to build a universal ICT system and standardize it. There is in general, no concern of radiation exposure to the specimen under scanning, which is in sharp contrast to the stringent regulations for medical tomography systems. In addition to this, a broad class of industrial specimens do not have any inherent motion. Some of these fundamental differences in requirements as compared to systems for medical applications provide more freedom in specifying operating parameters. Computed tomography as such, is a complex mathematical procedure involving a number of parameters.

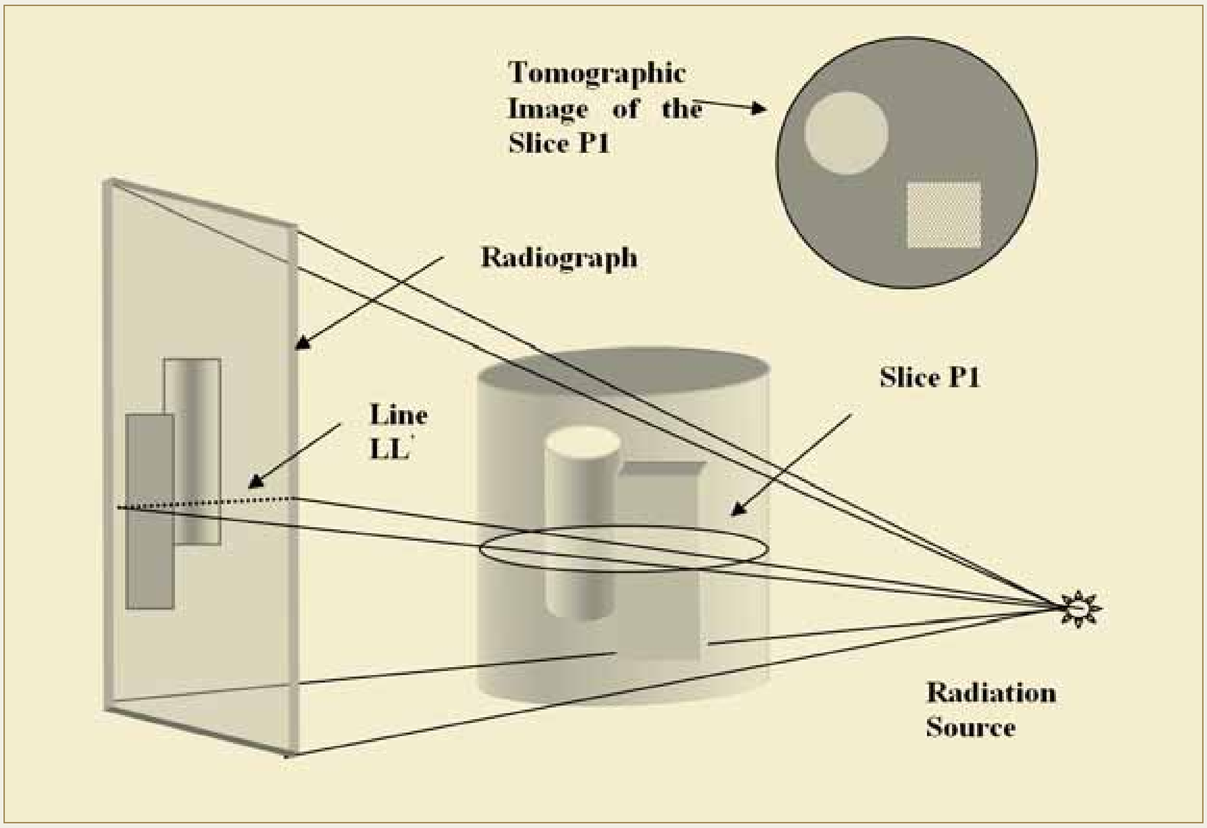

Fig. 1 : Schematic diagram of a typical radiography and tomography setup

Slight variations in the characteristics of different sub-systems, may give rise to unique problems and necessitate a thorough study. It may also need a careful solution. The fundamental difference between ICT and conventional radiography is shown in Fig. 1. In conventional radiography, information on the slice plane designated as P1, projects into a single line, $L\text{-}L'$; whereas with the corresponding tomographic image, full spatial information is preserved. CT information is derived from a large number of systematic observations at different viewing angles and an image matrix is then numerically reconstructed. Thus by using ICT, one can, in effect, slice open the test article, examine its internal features record the different attenuations, perform dimensional inspections and identify any material or structural anomalies within the system capabilities, that may exist. Moreover, by stacking and comparing adjacent tomographic slices of a test article, a three-dimensional image of the test article can be constructed. A fundamental task of CT systems, is to make an extremely large number of highly accurate measurements of gamma ray or X-ray transmission, through an object in a precisely controlled geometry.

The three important scanning geometries mainly from the point of view of industrial applications are as follows:

1. Parallel-beam geometry is technically the simplest and the easiest one, to understand the principles of tomography imaging. Multiple measurements of X-ray or gamma transmission are obtained, using a single highly collimated gamma ray or X-ray pencil beam and a detector. The beam is translated in a linear motion to obtain a projection profile. Scan times can be reduced with the use of a narrow fan beam of gamma rays or X-rays and a linear detector array. A translate-rotate scanning motion may be employed with a large rotational increment, which results in shorter scan times. The reconstruction algorithms are slightly more complicated than those for parallel-beam geometry, because they must handle narrow fan beam projection data.

2. A fan beam consisting generally of X-rays, illuminates a large number of detector elements arranged along an arc (equiangular) or a line (collinear). The object is fully covered by the fan beam. In general, an object rotation by 360^0 and no translation motion is used, to generate projection data. As a result, these rotate-only motions acquire projection data for a single image. The object can have either start-stop motion or continuous motion. There is some variation in reconstruction techniques based on different scanning mechanisms for reduced angular views.

3. A natural extension of this geometry, is to employ a two-dimensional array detector and a cone-beam of radiation such that, multiple projection lines can be acquired simultaneously and volume reconstruction can be carried out. Among various other modalities used for acquiring direct two-dimensional projections, the use of an amorphous-silicon (aSi) based Flat Panel Detector (FPD) array is common now. The FPD device can be used for direct digital radiography as well as volume tomography in an industrial imaging system.

Scintillators used in imaging applications including computed tomography can be broadly divided into two groups (a) single crystals and (b) ceramics. Single crystal scintillator such as NaI(Tl), CsI(Tl), $CdWO_4$ and $Bi_4Ge_3O_{12}$ are normally used in discrete detector configurations. The powder preparation/sintering route for the rare-earth ceramic scintillator provides high process yields, uniform scintillator quality and low cost scintillators such as gadolinium oxy-sulphide (GOS), a translucent ceramic scintillator. It is a matter of choice in terms of light output, decay time and high density for medical tomography and low-energy industrial digital radiography and tomography imaging applications.

LDA-based 2D Planar Imaging System

The use of a Linear Detector Array (LDA) in X-ray computed tomography imaging is well established. Generally, the system using an LDA, operates in a fan-beam configuration. In a non-medical tomography set-up, the X-ray source and detectors are stationary and the object is rotated for scanning. In general, equi-spaced angular projections over a complete 360^0 object rotation are required for tomography image reconstruction, using standard Convolution Back Projection (CBP) algorithm as applied to the fan-beam scanning geometry.

In non-medical imaging applications, transmission gamma or X-rays-based computed tomography, is often regarded as a supplementary Non-Destructive Testing (NDT) tool to conventional radiography. With the availability of low cost linear detector arrays and constant potential X-ray equipments, a tomographic imaging system can be developed in a cost-effective manner for experimental purpose, provided the associated problems are taken care of. The experimental ICT system for NDT applications, a block diagram of which is shown in Fig. 2, has been developed by making use of an independent scintillator-based linear detector array, commonly used for on-line radiography of low-density specimens. The specific areas which demand special attention in the development of an experimental tomographic imaging system are (a) system alignment, (b) motion instability and (c) artifacts arising due to scattering and polychromatic nature of the Bremsstrahlung X-rays. An artifact can be thought of as an artificial defect showing up in an image and which does not represent an existing flaw in the specimen. Tomography artifacts manifest themselves in somewhat different ways, since in this imaging modality, the initial measured data is subjected to a complex mathematical treatment. Third-generation tomography systems normally use a rotate-only scan geometry, with a complete view being collected by the detector array, during each sampling interval. Since all elements of a third-generation detector array contribute to each view, rotate-only scanners impose much more stringent requirements on detector performance than do second-generation units, where each view is generated by a single detector. A single detector element of a linear detector array in a rotate-only tomographic system, records transmission data corresponding to one particular ray at one particular position in the fan-beam, through a complete rotation. Therefore, all information on a circle in the reconstructed image around the center is given by one detector element. A defective or badly calibrated detector element on the sensing device will give rise to what is called ring artifacts. The term 'defective detector element' is used in a broader sense and it may indicate a dead pixel element, either an element with a different response characteristics from the rest ones or a badly calibrated element. The correction methods, which can be applied to counter the effects of such elements, depend on different factors. It is seen that if the response of majority of elements of the array is unpredictable, the correction method may be difficult to arrive at. In addition to this, when a tomography system is developed out of the available detector systems and mechanical manipulators as well as associated instrumentation, it is quite possible that a lack of synchronization among various sub-systems shows up in different artifacts in the reconstructed image. It has also been observed, that a lack of synchronization between mechanical scanning mechanism and data acquisition of a computed tomography imaging system, results in artifacts in reconstructed images. These two issues have been investigated by us in the laboratory and suitable correction methods were developed for minimization of prominent artifacts in case of planar tomography imaging using LDA. The method for correcting transmission data matrix, based on the principle of minimum of difference signal, has been tried in case of the experimental system in the laboratory. The set of multiple one dimensional transmission data profiles at different angular positions are used in the correction algorithm, to find out near-360^0 projection in a continuous rotate-only industrial CT scanning geometry. The first 1-D profile recorded is treated as the 0^0 position data and remaining profiles are then subtracted from this one. Experimental results were obtained which validate the algorithm adopted. The basic idea proposed was to identify the projection that most closely resembles the 0^0 projection and designate it as 360^0 projection, in case of a fan-beam configuration using a linear detector array. This method may be particularly useful where experimental tomographic imaging systems are designed around self-contained sub-systems and where hardware interfacing may be difficult to achieve. The algorithm suggested in the experiment may well be incorporated in the pre-processing software prior to tomographic image reconstruction.

The experimental tomographic imaging system, which was developed in the laboratory, is briefly described below. The system consists of an X-ray source though a perfectly monochromatic radiation source would be the best choice, an Xscan0.8-410 linear array detector, a computerized scanning mechanism and related instrumentation, including both hardware and software.

A section of the three-axis mechanical manipulator including the rotary mechanism, trigger component and the detector array, which is exposed to the radiation beam are seen in the photograph (Fig. 3). A 160 kV/10mA constant potential X-ray generating system with specified effective focal spots of 1.5 (large focal spot) and 0.4 (small focal spot) as per IEC 336 was used in the experiment. These are equivalent to 1.5 mm and 0.4 mm in conventional designation. The X-ray tube (MXR-160/0.4-1.5) is manufactured by M/s. Comet AG, Switzerland. The HV generator and the control unit are from M/s. Gulmay Ltd., England. The small focal spot was selected, as it was smaller than the detector resolution. The anode voltage can be set in steps of 1 kV and the tube current can be set in steps of 0.1 mA. The finer increment values of kV and mA were helpful in optimizing the detector array. X-rays coming out of the tungsten target undergo inherent filtration in the 0.8 ± 0.1mm beryllium (Be) window of the tube. The specified radiation coverage is 40^0. The high voltage unit of the constant potential X-ray generator specified short-term voltage and current stability of 0.05% / hr of set the values. The tomography system required around 10-20 seconds per scan and it was assumed that the X-ray output remained stable during this short period. Figs. 4 (a & b) show the typical graphical user interface of the reconstruction and data pre-processing routines. The profiles (Fig. 5) of the linear detector array response to varying tube currents at a fixed anode voltage of the X-ray system show spatially invariant abnormal behaviour of the detector pixels. The data pre-processing algorithm developed has been found

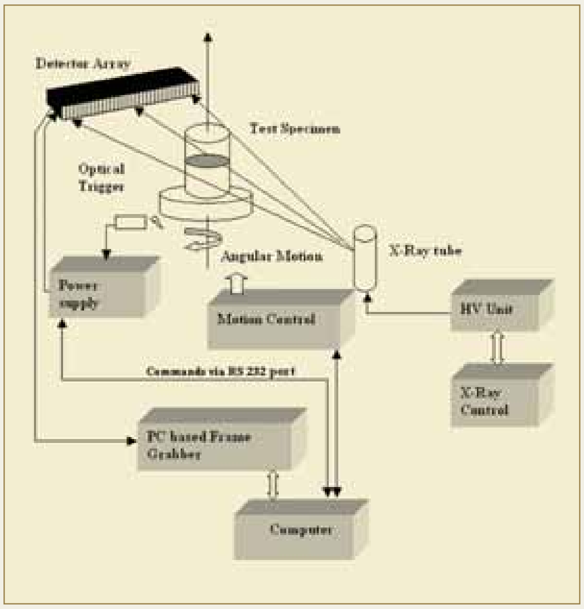

Fig. 2: An experimental low-energy tomography system using LDA

Fig. 3: Photographic view of the X-ray based experimental tomography system for industrial applications (2002)

Table 1: Linear detector array specifications

Type of the detector system :	GOS Scintillator-based linear diode array
Number of pixels :	512
Detector pixels used :	260
Pixel size :	0.8 mm(H) x 0.6 mm (W)
Detector pitch :	0.8 mm
Length of active area :	410 mm
ADC resolution :	12 bits
Control signal (PC to module) :	via RS 232 interface
Data transfer (Module to PC) :	via RS 422 interface
Onboard offset and gain calibration :	Yes
External Trigger :	Optical trigger sensor (reflecting type)

to minimize image artifacts due to such detector response in a variety of test specimens.

A three-axis PC-based stepper motor controlled mechanical manipulator was used for object manipulation and system alignment. The use of such system is a cost-effective option in place of closed loop servo-drive based manipulators. The horizontal axis is parallel to the detector length and as such it is used for beam alignment. The vertical axis is used to select scanning planes and to move the object vertically in computed radiographic scanning mode. The rotary axis provides the specimen platform to hold the object and rotate. The source to detector distance (S_D) is 1120 mm and source to centre-of-rotation distance (S_0) is set to be 920 mm. This configuration provided a geometric magnification of 1.22. In the experiment described here, only a portion of the full length of the linear array was used such that, 260 detector elements arranged symmetrically around the central ray, fully covered the circle of reconstruction. This arrangement gave a fan beam angle of approximately 10^0. This was done so that the active detector pixels receive a relatively uniform X-ray flux.

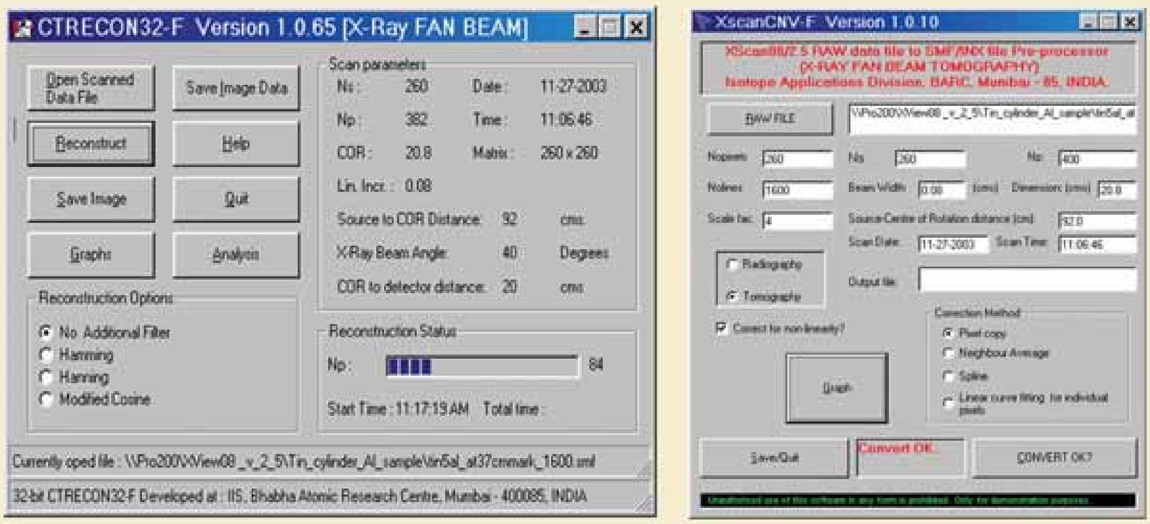

CTRECON32-F Version 1.0.65 [X-Ray FAN BEAM]

Scan parameters
Ns : 260 Date : 11-27-2003
Np : 382 Time : 11:06:46
COR : 20.8 Matrix : 260 x 260
Lin. Incr. : 0.08
Source to COR Distance: 92 cms.
X-Ray Beam Angle: 40 Degrees
COR to detector distance: 20 cms.

Reconstruction Options
● No Additional Filter
○ Hamming
○ Hanning
○ Modified Cosine

Reconstruction Status
Np : 84
Start Time : 11:17:19 AM Total time :

Currently oped file : \\Pro200\XView08 _v_2_5\Tin_cylinder_Al_sample\tin5al_at37cmmark_1600.sml
32-bit CTRECON32-F Developed at : IIS, Bhabha Atomic Research Centre, Mumbai - 400085, INDIA

XscanCNV-F Version 1.0.10

XScan88/2.5 RAW data file to SMF/INX file Pre-processor
(X-RAY FAN BEAM TOMOGRAPHY)
Isotope Applications Division, BARC, Mumbai - 85, INDIA.

\\Pro200\XView08 _v_2_5\Tin_cylinder_Al_sample\tin5al_at
Nopixels 260 Ns 260 Np 400
Nolines 1600 Beam Width 0.08 (cms) Dimension (cms) 20.8
Scale fac. 4 Source-Centre of Rotation distance (cm) 92.0
Scan Date 11-27-2003 Scan Time 11:06:46
Output file
○ Radiography
● Tomography
☑ Correct for non linearity?
Correction Method
● Pixel copy
○ Neighbour Average
○ Spline
○ Linear curve fitting for individual pixels
Convert OK

Figs. 4 (a&b): Graphical user interface of the data processing and reconstruction software for the LDA-based planar tomography imaging system

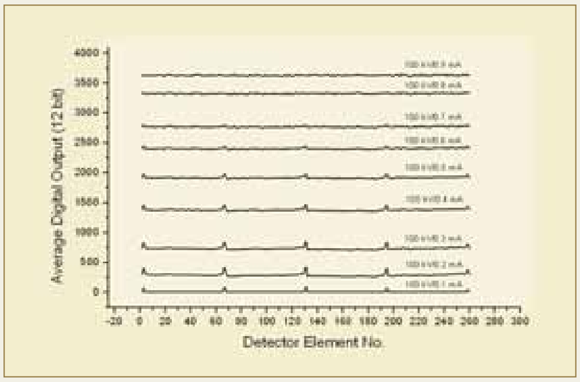

Fig. 5: LDA response to varying X-ray tube current settings at a fixed anode voltage

Combined digital radiographic and computed tomographic imaging of a test specimen

The result of digital radiographic and tomographic imaging of a typical industrial test specimen is presented here. The experiment was carried out in order to visualize the internal cross-sectional details, which would be rather difficult to see by projection method (radiography) only.

Fig. 6: Photograph of the specimen – a commercial metallic container [100mm(H) x 100mm(OD)] housing a section of welded aluminium curved tubes (12). The container was partially filled with water.

Fig. 6 shows a photograph of the specimen used in the experiment for visualizing combined digital projection radiographic and computed tomographic images. A section of twelve aluminium circular tubes welded together were housed in a thin commercial metallic container with a seam-welded joint along its length. The maximum material thickness in the beam path was found to produce projection radiographic views with sufficient contrast to visualize the aluminium structure inside the container. The digital data obtained from the linear detector array was processed to obtain the typical radiographic image

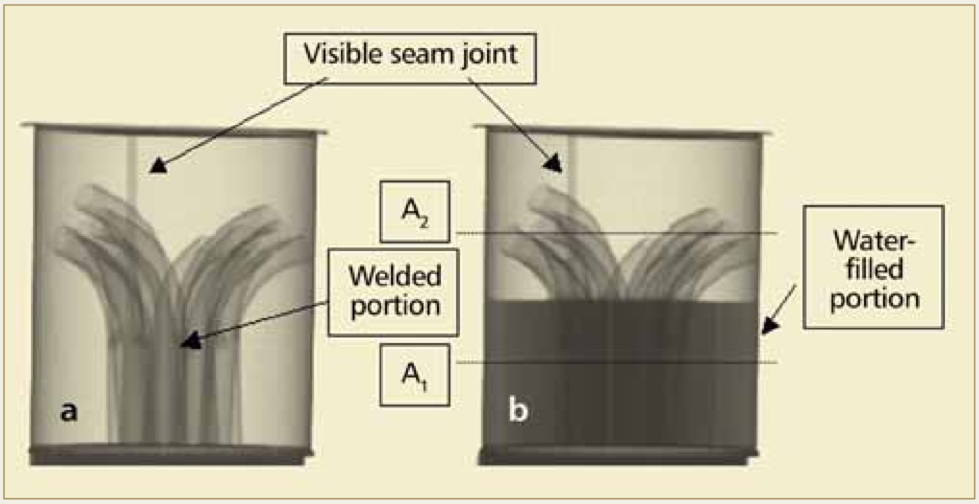

Fig. 7: (a) Radiographic view of the container assembly and (b) Radiographic view of the same specimen partially filled with water at 100 kV.

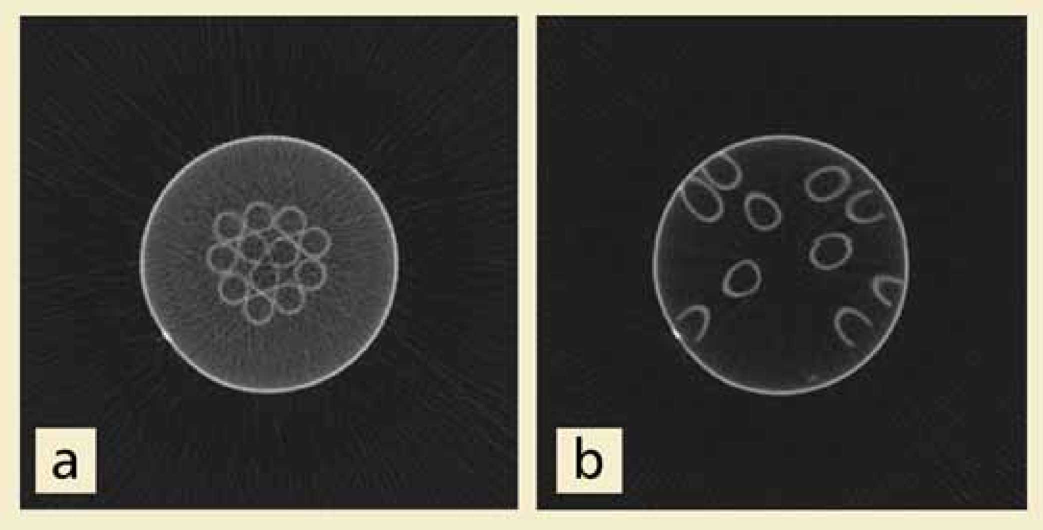

Fig. 8 : Typical tomographic images of the container-assembly cross-sections marked (a) A_1 in Fig. 7(a) and (b) A_2 in Fig. 7(b) at 100 kV.

shown in Figs. 7a & 7b. The LDA was calibrated at an X-ray tube voltage of 100 kV. The specimen was placed on the platform and it was given a vertical movement in synchronization with the data acquisition system. The acquired 12-bit digital data was scaled to 256 grey values for display purpose.

Fig. 7a shows the radiographic image of the container assembly under two different conditions. The image clearly shows the inside details of the specimen, where the seam joins the container wall, change in thickness in the welded portion of the tubes structure as well as the smooth thickness gradient due to circular shape of the container. Fig. 7b was obtained with the container partially filled with water. This was done to increase the material thickness in the beam path up to a certain height, so that, the contrast was reduced in that portion and almost no details were seen for the aluminium structure. This is due to the fact, that the energy of the X-rays is not sufficient to record details with sufficient contrast in the given configuration. The X-ray tube voltage was kept constant at 100 kV for these two images.

Fig. 8a is the computed tomographic image of a typical cross-section of the specimen in the water-filled region. This is marked as level A_1 in Fig. 7b. It can be seen that the image distinctly shows the container's thin wall cross-section, high thickness region of the seam joint in it and the aluminium tubes' cross-section inside the water. The uniform-density water region has some grainy noise visible which is due to the limited signal-to-noise ratio in the input signal. This image has significant details about the internals as compared to the radiographic image in Fig. 7b. Fig. 8b is another tomographic cross-section at a level marked A_2 above the water level. The tubes are significantly curved in this plane. This is evident from the aluminium cross-sections, which are not seen circular in shape. The selected plane has not been able to cross all the tubes and some only in parts. The relative contrast is able to distinguish all the details expected in the cross-section.

X-rays and FPD-based 3D Volume Imaging System

Development work has also continued on an integrated digital radiography and volume (direct three dimensional) imaging system, using a constant potential X-ray equipment (which can operate upto 420 kV of accelerating voltage) and an amorphous silicon-based Flat Panel Detector (FPD) assembly as its key components. Various sub-systems of the facility have recently been integrated and only some initial results have been obtained so far. The front-end software components have been developed in our

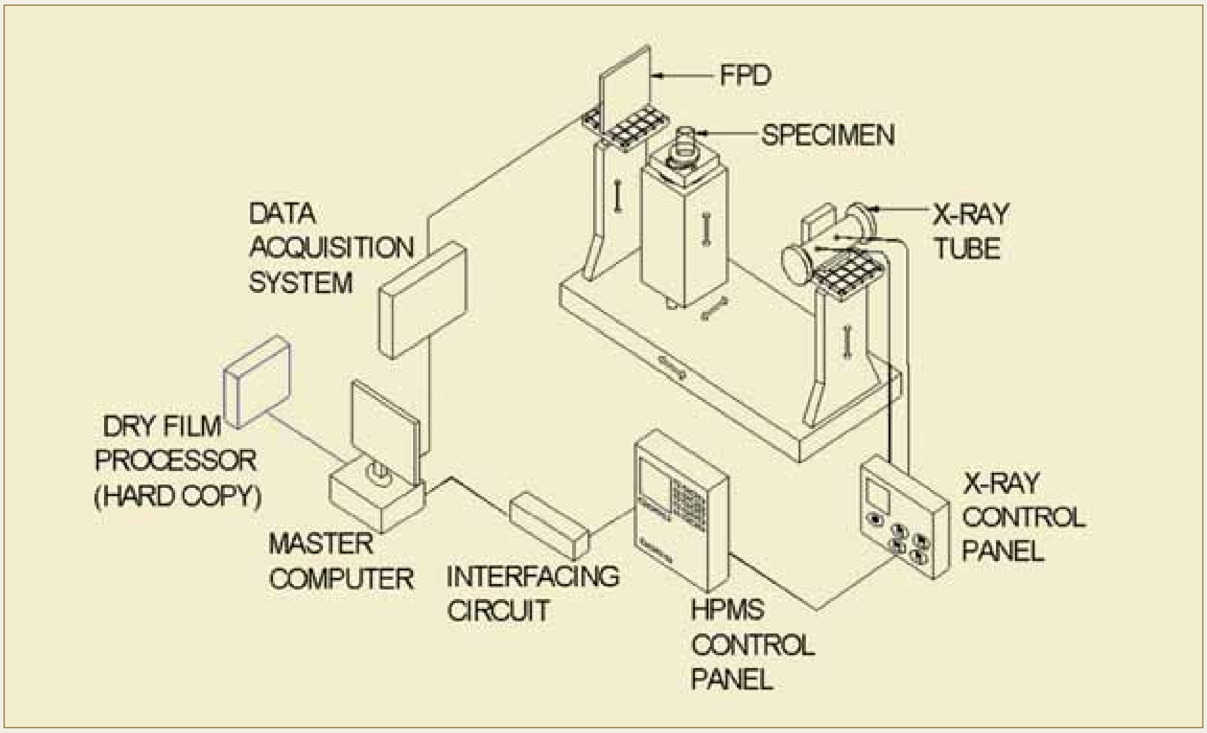

Fig. 9 : Schematic diagram of the X-ray-based Direct Digital Radiography and Volume Tomography System

laboratory, which make use of some commercial software components in the back-end. At present, performance studies on various parameters are in progress. Fig. 9 shows the schematic diagram of the complete layout. Fig. 10 shows a photographic view of the actual setup. At the extreme left in the picture is the 420kV X-ray tube head and at the far end, the FPD assembly with a shielding plate is mounted on an alignment table. Fig. 11 is the outside view of the control area in the laboratory. FPD is a fast and sensitive radiation detector and it requires exposure for a few seconds only, for general imaging applications. When the system is to be used for acquisition of large number of projection data for direct 3D tomographic reconstruction, the FPD is exposed to intense X-ray radiation continuously during the scanning sequence.

Fig. 10 : Photographic view of the X-ray based Direct Digital Radiography and Volume Tomography System housed inside a shielded enclosure

Fig. 11 : Control area of the X-ray-based Direct Digital Radiography and Volume Tomography System

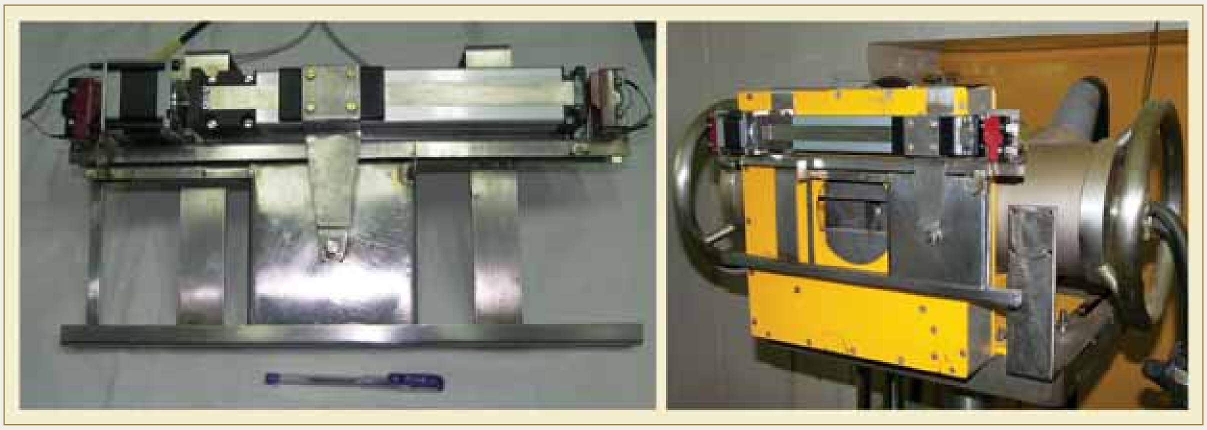

Fig. 12 : (a) Digitally controlled fast X-ray shutter mechanism (b) Shutter assembly mounted on the X-ray tube head on top of the beam collimator

The scanning sequence involves mechanical motion of rotary systems meant for object mounting. It has been observed, that the actual exposure duration is only about 10% of the total time taken by a typical scanning sequence. Due to operational difficulties, the X-ray device cannot be switched on and off rapidly. The other way to restrict exposure to the FPD in such operating cycle, is to use a fast-response beam shutter, which operates automatically and in unison with the motion and data acquisition system. Fig. 12a shows a motorized lead shutter assembly designed and developed in the laboratory and Fig. 12b shows the assembly mounted on the X-ray head on top of a beam collimator. Fig. 13 shows software interface of the master control programme used to automate the scanning sequence and data acquisition.

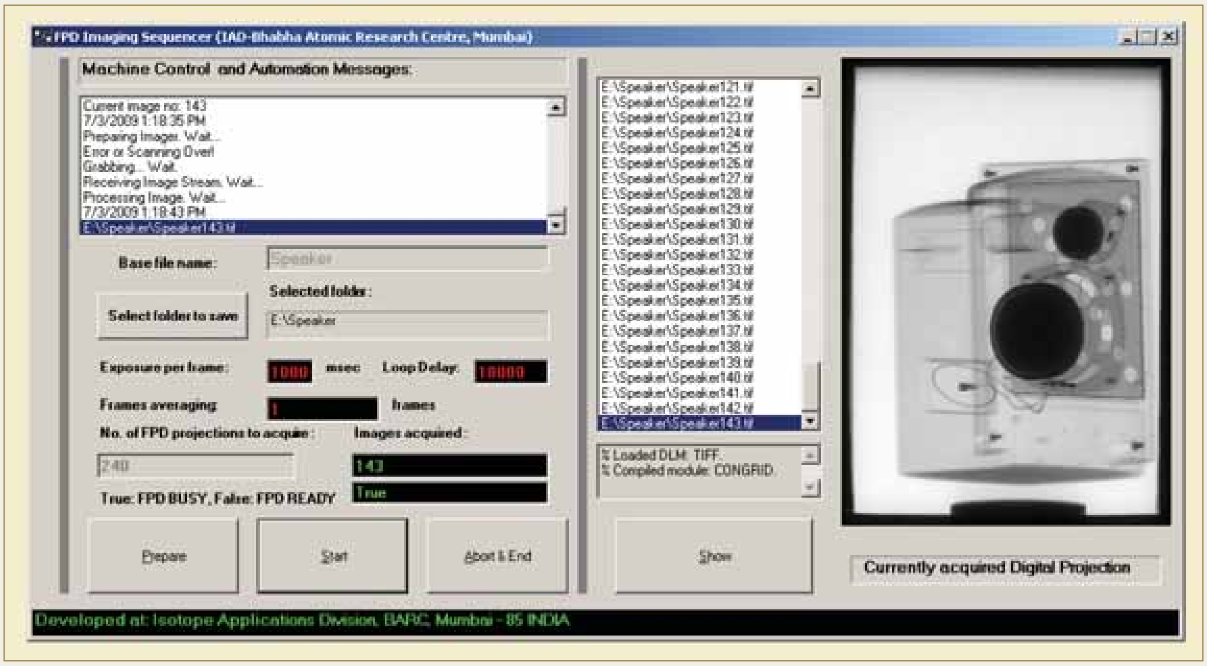

FPD Imaging Sequencer (IAD-Bhabha Atomic Research Centre, Mumbai)

Machine Control and Automation Messages:

```
Current image no: 143
7/3/2009 1:18:35 PM
Preparing Images. Wait...
Error or Scanning Over!
Grabbing... Wait
Receiving Image Stream. Wait...
Processing Image. Wait...
7/3/2009 1:18:43 PM
E:\Speaker\Speaker143.tif
```

Base file name: Speaker

Selected folder : E:\Speaker

Exposure per frame: 1000 msec Loop Delay: 10000

Frames averaging: 1 frames

No. of FPD projections to acquire : 240

Images acquired : 143

True: FPD BUSY, False: FPD READY: True

```
E:\Speaker\Speaker121.tif
E:\Speaker\Speaker122.tif
E:\Speaker\Speaker123.tif
E:\Speaker\Speaker124.tif
E:\Speaker\Speaker125.tif
E:\Speaker\Speaker126.tif
E:\Speaker\Speaker127.tif
E:\Speaker\Speaker128.tif
E:\Speaker\Speaker129.tif
E:\Speaker\Speaker130.tif
E:\Speaker\Speaker131.tif
E:\Speaker\Speaker132.tif
E:\Speaker\Speaker133.tif
E:\Speaker\Speaker134.tif
E:\Speaker\Speaker135.tif
E:\Speaker\Speaker136.tif
E:\Speaker\Speaker137.tif
E:\Speaker\Speaker138.tif
E:\Speaker\Speaker139.tif
E:\Speaker\Speaker140.tif
E:\Speaker\Speaker141.tif
E:\Speaker\Speaker142.tif
E:\Speaker\Speaker143.tif
```

```
% Loaded DLM: TIFF.
% Compiled module: CONGRID.
```

Developed at: Isotope Applications Division, BARC, Mumbai - 85 INDIA

Fig. 13 : Software Interface of the Master control programme for the X-ray-based Direct Digital Radiography and Volume Tomography System

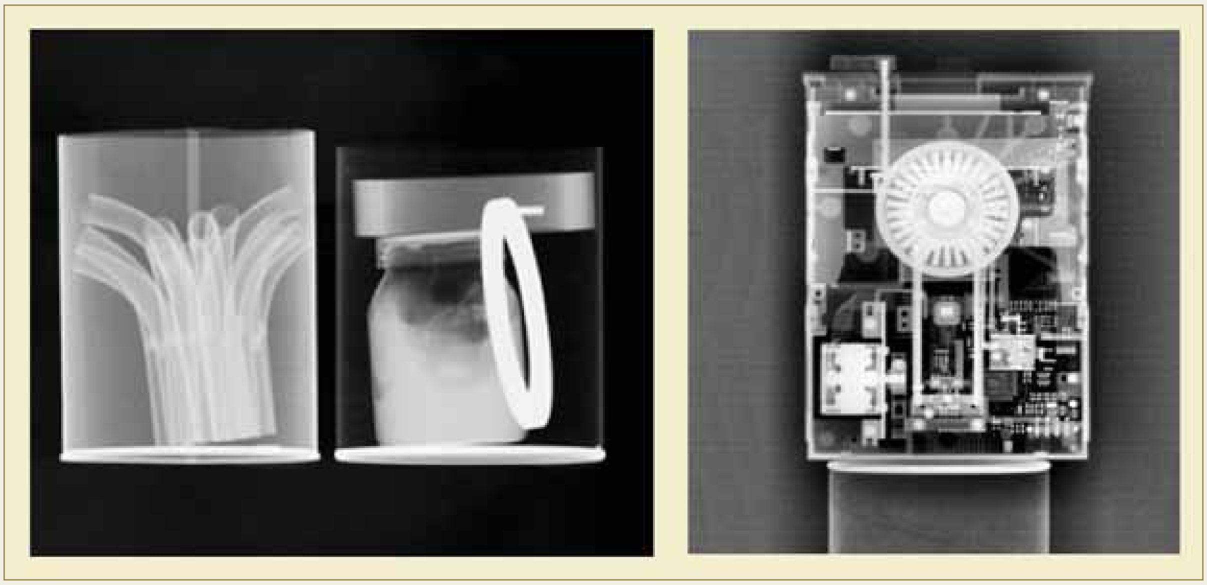

Fig. 14 : Direct digital radiography images using FPD of (a) the specimen shown in Fig. 4 and another test object showing a dried gum bottle, an adhesive tape roll and a metallic ring object (b) a 5.25" old floppy drive mechanism. These images showing spatial and contrast details have been obtained at 100-200 kV x-rays

Preliminary Volume Tomography Performance of the System

The FPD can provide good quality digital projection images with spatial and contrast details. The detector provides 16 bit/pixel data with 12-bit actual resolution. The active area of the detector is around 400mm x 2800mm. The programmed exposure can be accomplished for a variety of kV and mA combinations and the detector can be calibrated for dark current as well as beam uniformity, for correct radiographic exposures. The specially developed API functions by the manufacturers, have been used to customize the FPD operations in an automated way. This was required as for volume tomography operations; the reconstruction software requires a large number of two-dimensional projections. A variety of pre-processing corrections are required before tomography image reconstruction using Feldkemp algorithm. The test results shown here have been obtained using proprietary reconstruction software and 3D ICT data presentations have been achieved using IDL software.

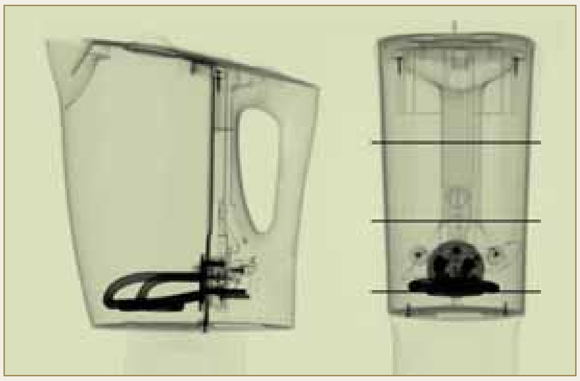

Fig. 15: Representative direct digital projection images of the test specimen, The three horizontal lines in the second image show roughly the planes for which planar tomographic images are shown in Fig. 16

The test specimen used for generating initial volume tomography data on the system was a domestic electric water boiler. The test object is made up of low-density plastic material and it contains metallic components such as heating element and screws etc. The actual projection data matrix is quite large (~ 3k x 2k pixels). Tomographic reconstruction using such a large projection data-matrix requires a very large number (> 1500) of equi-angular views. This again requires a very large scanning time. It is seen that in the present configuration, the time required for a single full-matrix digital projection, data transmission and mechanical movements is around 30-55 seconds. The number of angular scans was restricted to 100-200 projections and the projection matrix size was accordingly scaled down for suitable image reconstruction. The three figures (Fig. 16) show the projection images at 0^0 and 90^0 angular positions.

The three horizontal lines in the middle picture show roughly the planes for which planar tomographic images are shown in Fig. 16.

The three planar tomographic images seen in Fig. 14 distinctly show the internal details. The separated cross-section of the handle in the first picture, the separate water compartment in the main body and a typical cross-section of the coiled heating element is clearly visible. Fig. 15 shows the extracted three-dimensional view of the heating element, from two different perspectives.

Technology deployment

Industrial tomography may well present an example of confluence of various branches of science and engineering like radiation physics, computer science and other signal processing techniques. Tomography imaging using penetrating radiation from sealed radioisotope sources or machine-based X-rays can be applied in different ways in industrial diagnostic applications. An Industrial Process Tomography (IPT) system for fixed installation using 662 KeV gamma radiation from a sealed Cs-137 radioisotope source and multiple detectors is being designed and developed, for research applications in cold trickle bed columns, as part of a joint collaborative project under Memorandum of Understanding between BARC and an R&D laboratory of a leading petrochemical company.

Conclusion

The paper discussed development efforts in the field of planar and volume experimental tomography imaging systems for research applications in non-destructive testing and examination of industrial and other non-medical applications. Some of the advantages and configurations of industrial digital radiography and tomography imaging systems have been presented. The development work initiated under various Plan Projects was primarily aimed at technology and know-how development for different applications. The initial data generated for test scans and the reconstructed volume data using an FPD are being analyzed and it is observed, that the reconstructions show certain noise and artifacts. The optimization of various parameters like exposure time, projection resolution angular views, pre-processing of projection

Fig. 16: Representative direct digital projection images of the test specimen

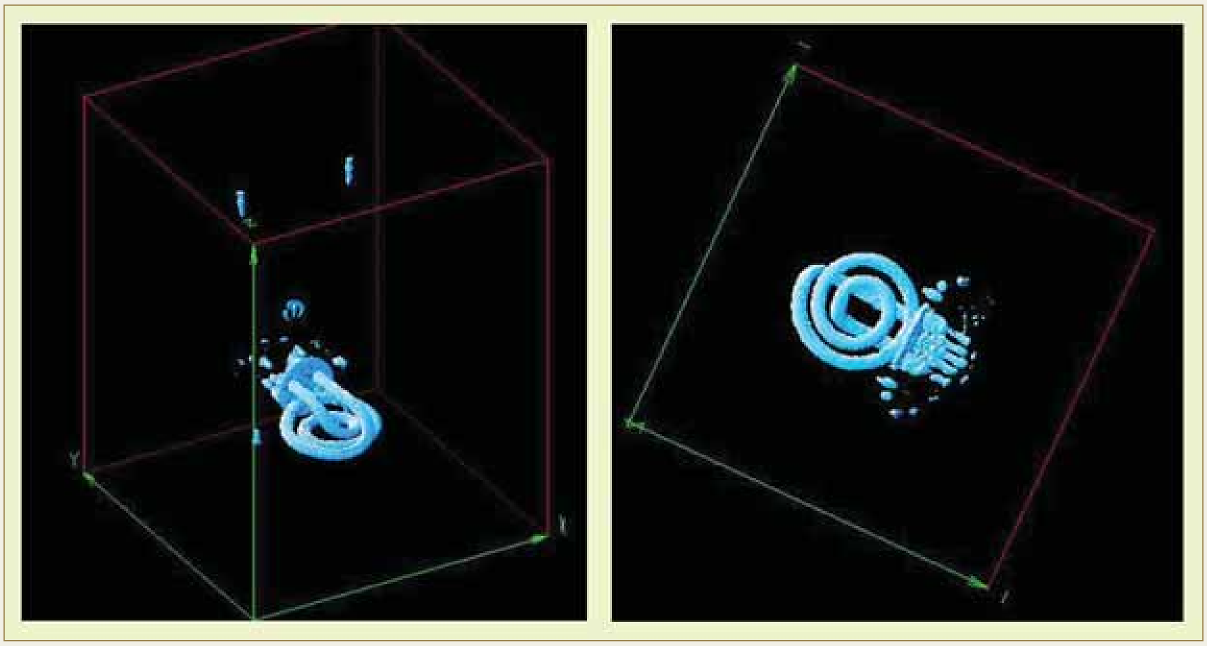

Fig. 17 : Three-dimensional views of the heating element from two different perspectives

data and overall scanning geometry are in progress. A partial bibliography is provided here for reference and further reading.

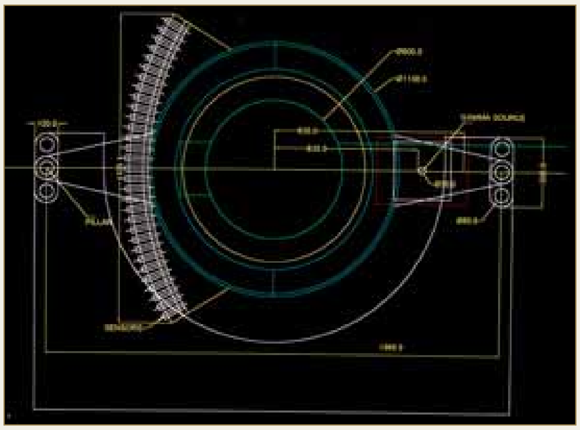

Fig. 18 : A drawing showing plan view of the Cs-137 source-based IPT system using multiple detector probes

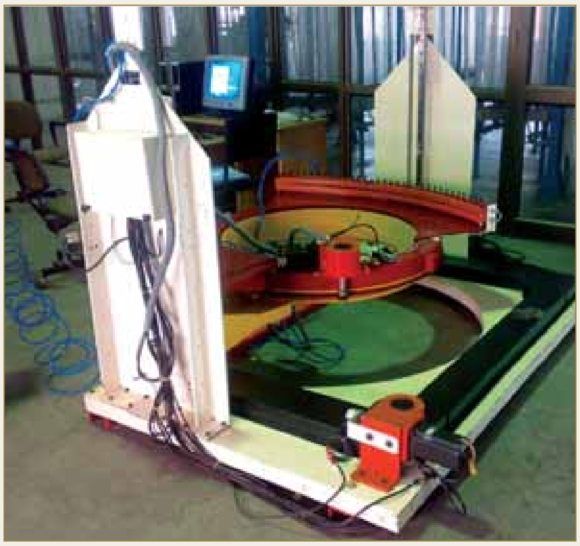

Fig. 19: Computer-controlled scanner gantry designed and developed for the IPT experiments in cold trickle bed columns

Acknowledgements

I am thankful to Dr. V. Venugopal, Director, Radiochemistry and Isotope Group and Dr. Gursharan Singh, Head, Isotope Applications Division, BARC for their continued support. Thanks are also due to all my colleagues in particular, Mr. Rajesh Acharya, Mr. Parag B. Walinjkar and Mr. Bhawanipratap S. Singh and staff of the Isotope Applications Division for their kind cooperation and help.

References

1. ASTM standards Designation: E 1441-00', American Society of Testing and Materials, USA (2000).
2. Besson G., "CT image reconstruction from fan-parallel data", *Med. Phys.,* Vol. 26, pp. 415-426 (1999).
3. Brooks Rodney A. and Di Chiro Giovanni, "Principles of Computer Assisted Tomography in Radiographic and Radioisotopic Imaging", *Phys. Med. Biol.,* Vol. 21, No. 5, pp. 689-732 (1976).
4. Carl W. E. and van Ejik, "Inorganic scintillators in medical imaging", *Phys. Med. Biol.,* Vol. 47, pp. R85-R106 (2002).
5. Carlsson Carl A., "Imaging modalities in x-ray computerized tomography and in select volume tomography", *Phys. Med. Biol.,* Vol. 44, pp. R23-R56 (1999).
6. Gilboy W. B., "X-ray and g-ray tomography in NDE applications", *Nucl. Instrum. Methods Phys. Res.,* Vol. 221, pp. 193 (1984).
7. Greskovish C. and Duclos S., "Ceramic Scintillators", Report No. 96CRD166, Technical Information Series, GE Research & Development Center (1996).
8. Kak A C and Malcolm Slaney, "Principles of Computerized Tomographic Imaging", USA (IEEE Press) (1988).
9. Kypros Kouris, Nicholas M. Spyrou, Daphne F. Jackson, "Imaging with ionising radiations, Vol 1", Surrey Univ. Press (1982).
10. Martin Spahn, Michael Stronzer, Markus Volk, Stefan Bohm, Bernhard Geiger, Gerhard Hahm and Stefan Feuerbbach, "Digital Radiography with a Large-Area, Amorphous-Silicon, Flat-Panel X-Ray Detector System", *Investigative Radiology,* Vol. 35, No. 4, pp. 260-266 (2000).
11. Metals Handbook Ninth Edition, Vol. 17, Nondestructive evaluation and quality control, ASM International, Metals park, OH 44073 (1989).
12. Rika Baba, Yasutaka Konno, Ken Ueda and Shigeyuki Ikeda, "Comparison of flat-panel detector and image-intensifier detector for cone-beam CT", *Computerized Medical Imaging and Graphics,* Vol. 26, Issue 3, pp. 153-158 (2002).
13. Tang X., Ning R., Yu. R., Conover D., "Cone beam volume CT image artefacts caused by defective cells in X-ray flat panel imagers and the artifact removal using a wavelet analysis based algorithm", *Med. Phys.* Vol. 28(5), pp. 812 (2001).
14. Umesh Kumar, Gursharan Singh, "X-rays based Experimental Direct Digital Radiography and Volume Tomography for NDT Applications", *NDT World Review* (in Russian), 2(40) (2008).
15. Umesh Kumar, G. S. Ramakrishna, A. S. Pendharkar, S. Kailas, "A statistical correction method for minimization of systemic artifact in a continuous-rotate X-ray based industrial CT system", *Nucl. Instr. and Meth. A,* Vol. 515, 829-839 (2003).
16. Umesh Kumar, G. S. Ramakrishna, "A mixed approach to artifacts minimization in a continuous-rotate X-Ray based tomographic imaging system using linear detector array", *Appl. Radiat. Isot.,* Vol. 54, Issue 4, 543-555 (2002).
17. Umesh Kumar, G. S. Ramakrishna, A. S. Pendharkar, Gursharan Singh, "Behaviour of reconstructed attenuation values with varying X-ray tube voltage in an experimental third-generation industrial CT system using linear detector array", *Nucl. Instr. and Meth. A,* Vol. 490, Isuue 1-2, 379-391 (2002).
18. Umesh Kumar, "Simulation of digital radiographic and CT imaging of a mathematically-defined phantom", *INSIGHT Journal of the British Inst. of NDT,* Vol. 44, No. 1, 40-45 (2002).
19. Umesh Kumar, G. S. Ramakrishna, S. S. Datta, Gursharan Singh, "An experimental method for ripple minimization in transmission data for industrial X-ray computed tomographic imaging system", *Sadhana* (Academy Proc. in Engg. Sciences), Vol. 27, Part 3, pp. 393-404 (2002).
20. Umesh Kumar, G.S. Ramakrishna, V. R. Ravindran, "Prototype gamma-ray computed tomographic imaging system for industrial applications", *INSIGHT* (Journal of the British Inst. of NDT), Vol. 42, No. 10, 662-666 (2000).

21. Umesh Kumar et al, "Development of an Industrial Isotopic Tomographic Imaging System CITIS-I", BARC/1993/019 (1993).
22. Umesh Kumar, "Indigenous developments in reconstructed imaging methods for industrial NDT and process examination", Special Issue on Radiation in Non-destructive Testing, Vol. XII, No. 1, *NAARRI Bulletin,* National Assoc. for Appl. of Radioisotopes and Radiation in Industry, India.
23. Zhou J., Maisl M., Reiter H. and Arnold W., "Computed laminography for material testing", *Appl. Phys. Letters,* Vol. 68, No. 24, pp. 3500 - 3502 (1996).

ABOUT THE AUTHOR

Dr. Umesh Kumar, graduated from the 32nd Batch of BARC training school and is currently serving as Head, Industrial Tomography & Instrumentation Section, Isotope Applications Division, BARC. He obtained his Ph.D. (Science) from Mumbai University. He has worked on various aspects of computed tomography for non-medical applications and image artifacts since he joined BARC in 1989. His research interests include nuclear radiation-based industrial imaging systems, digital radiography and computed tomography for NDE and radioisotope-based diagnostic techniques for industrial and medical applications. He has more than thirty publications including technical papers in peer-reviewed international journals. He is a life member of ISNT, NAARRI and INS. He and his team have been responsible for development of different tomography imaging systems, for various applications. He has been nominated by DAE as the National Project Coordinator for the IAEA sponsored projects in the Asia-Pacific Region, on advanced digital imaging techniques and industrial computed tomography for three consecutive project cycles (2005-06, 2007-08, 2009-11).

TECHNOLOGY DEVELOPMENT OF SILICON SENSORS FOR THE COMPACT MUON SOLENOID EXPERIMENT AT THE LARGE HADRON COLLIDER, CERN, FOR PHYSICS EXPERIMENTS AND FOR RADIATION MONITORING

A. Topkar, Praveenkumar S, B. Aggarwal, P.K. Mukhopadhyay and G.P. Srivastava
Electronics and Instrumentation Group

Dr. Anita Topkar received the DAE Scientific & Technical Excellence Award for the year 2007

Introduction

In recent years, silicon sensor technology has become the most preferred technology, for building detector systems of ambitious high energy physics experimental research facilities such as the LHC. Silicon sensors are being increasingly used, for detection of particles in high energy physics experiments, due to their superior performance such as fast response, good signal-to-noise ratio, compactness and their suitability to build multidetector systems, involving thousands of sensors having millions of channels. High position resolution in 1D or 2D can be easily obtained, by segmenting the sensors into strips, microstrips or pixels. Moreover, application of the well established silicon integrated technology for sensor fabrication, has enabled realization of sensors with very good uniformity and low cost. In the past few years, the Electronics Division has carried out R&D to develop the technology for various types of silicon sensors, using the fabrication facilities of the silicon foundries in our country. This programme has focused on developing the following types of sensors:

- Large area sensors for international high energy physics experimental facilities- CMS Experiment at LHC, CERN and PHENIX Experiments at RHIC, BNL, USA
- Sensors with high energy resolution for measurement of position and energy of particles in nuclear physics experiments at BARC
- Sensors for compact, low power radiation monitoring instrumentation.

A specific research and development programme was carried out, to develop the technology for 32-strip silicon strip sensors for the Compact Muon Solenoid (CMS) experiment at the Large Hadron Collider (LHC), CERN [1-8]. These sensors are used as Preshower sensors in the Electromagnetic Calorimeter of CMS for π^o/γ rejection and cover an area of $\sim$40,000 cm^2 in the CMS end caps. Developing silicon sensors with very stringent electrical specifications and uniformity over a large area of $\sim$ 40 cm^2, has been a challenging task. In view of expected radiation damage, the technology development was targeted to produce sensors with high breakdown voltage and low leakage currents, for ensuring ten years of operation in the high radiation environment of LHC. The design of the sensors, the complete mask layout and process parameter optimization was carried out by the Electronics Division. The fabrication of the sensors was carried out using the IC fabrication facility of Bharat Electronics Limited (BEL), Bengaluru as per the process outline provided by BARC. Eleven hundred silicon detector micromodules have been delivered to CERN. The silicon sensors activity was further expanded, to develop a wide variety of silicon sensors, suitable for various applications involving nuclear physics experiments and radiation monitoring [9-15]. Advanced silicon sensors such as silicon microstrip sensors with a geometry of 62 x 62mm^2 incorporating 128 strips have been developed, for the PHENIX Experiment at the Relativistic Heavy Ion Collider (RHIC) at Brookhaven National Laboratory (BNL), USA. The pitch of the strips is 470 μm and the spacing between the strips is 15 μm. Several types of silicon sensors such as silicon PIN diodes, silicon pad sensors, high energy resolution sensors for alpha and charged particle spectroscopy, large area PIN detectors for low activity counting, single and multielement silicon PIN photodiodes, radiation sensitive MOSFETs - 'XRFETs', etc. have been developed, as an outcome of R&D activity. An overview of this technology development activity is presented in the subsequent sections of this paper.

Various types of sensors developed

Silicon sensors find wide range of applications in several fields involving measurement of radiation such as charged particles, neutrons, photons, etc. The applications involve high energy particle physics, nuclear physics and astrophysics experiments, personal dosimeters, medical dosimetry, low energy X-ray spectroscopy, high resolution α and charged particle spectroscopy, detection of low activity radiation such as plutonium in air and radon monitors, contamination monitoring, area monitors, X-ray imaging, tomography, etc.

Considering the above applications, the silicon sensor R&D was targeted, to develop a wide range of sensors having different specifications in terms of sensor geometry, area, segmentation, energy resolution and dead layer. The silicon sensors developed as a result of this R&D are listed below:

- 32-strip silicon strip sensors for the CMS Experiment at LHC, CERN. These sensors are also being used for nuclear physics experiments at BARC
- 128-strip silicon microstrip sensors for the PHENIX Experiment at BNL, USA
- Silicon pad sensors with a 2 x 2 matrix and energy resolution of 18 keV for energy and position measurements of charged particles, for the 'Charged Particle Array' at BARC
- Single element silicon sensors with area ranging from 100 mm^2 to 400 mm^2 for charged particle identification and alpha spectroscopy applications

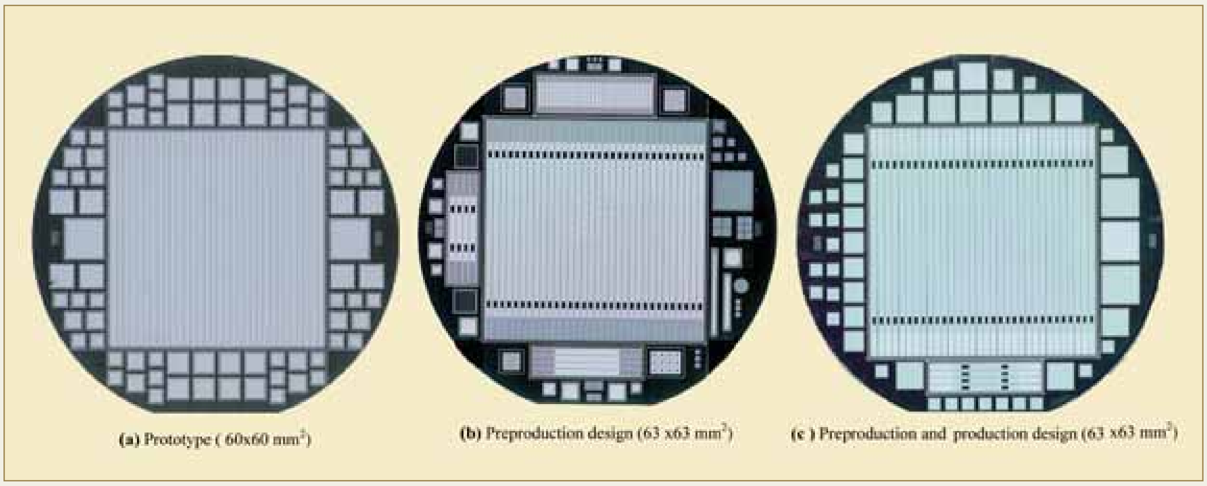
(a) Prototype (60x60 mm^2)
(b) Preproduction design (63 x63 mm^2)
(c) Preproduction and production design (63 x63 mm^2)

Fig. 1 : Wafers designed and fabricated during various phases of CMS silicon strip sensor development

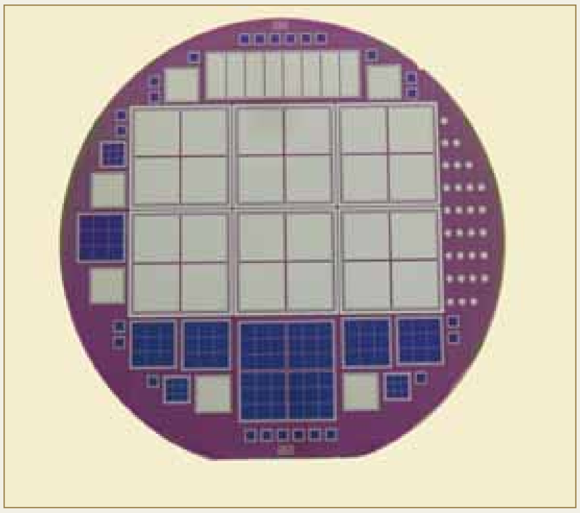

Fig. 2 : Fabricated wafer showing silicon pad sensors for Charged Particle Array

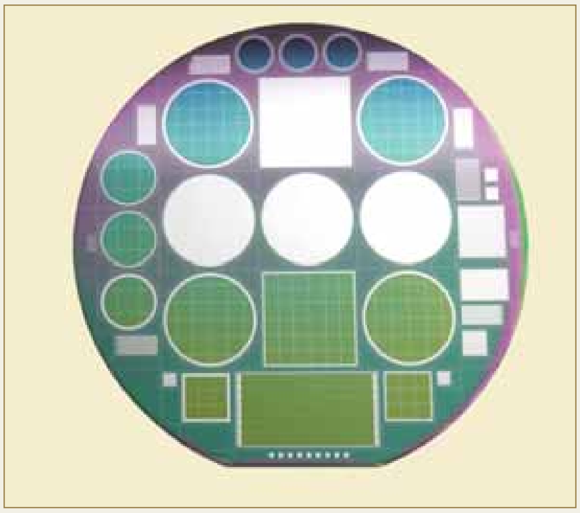

Fig. 3 : Fabricated wafer showing silicon sensors for charged particle spectroscopy and low activity counting

Figs.1-3 show fabricated wafers incorporating various types of silicon sensors.

After fabrication at wafer level, the sensors have been packaged using the facility of Bharat Electronics Limited, Bengaluru. Custom packages on ceramic substrates have been developed for this purpose. The sensors have been wire bonded using 1 mil diameter aluminum wire, using wedge bonding machines. Fig.4 shows some of the packaged sensors. An overview of the silicon sensor technology development and their performance is presented in the subsequent section of this paper.

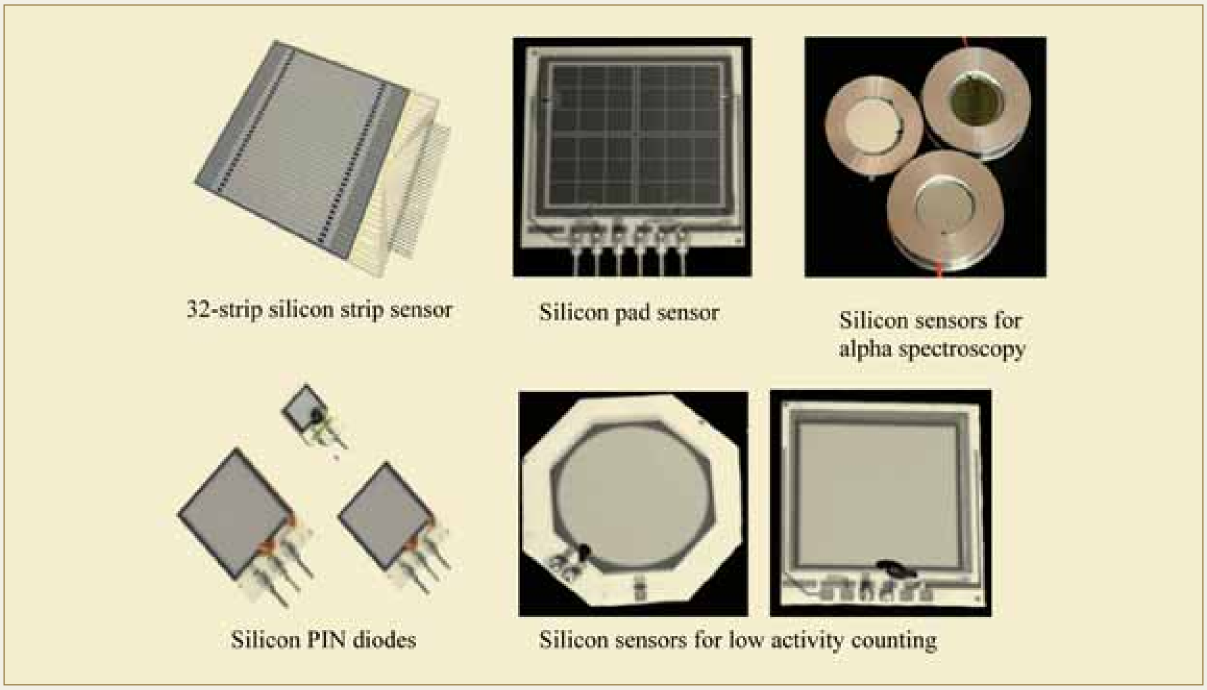

Fig. 4 : Packaged silicon sensors

Preshower silicon sensors for the CMS Experiment at LHC, CERN

The R&D for the development of technology for Preshower sensors, was carried out in various phases such as prototype development, preproduction and production. Figs.1(a)-(c) show wafers fabricated during various phases of this project. Fig. 5 and Fig. 6 show the silicon sensor after wafer dicing and the silicon sensor micromodule. The micromodule has the front end hybrid bonded to the 32 strips. The front end hybrid incorporates the PACE chip which has 32-channel preamplifier, amplifier, shaper, 196-channel analog memory along with control logic. This is a radiation hard chip developed by CERN and has been fabricated by CERN in a 0.25 micron technology at IBM.

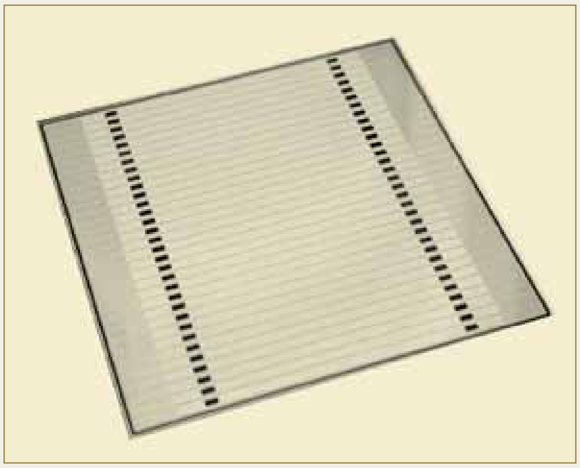

Fig. 5 : Diced 32-strip silicon sensor

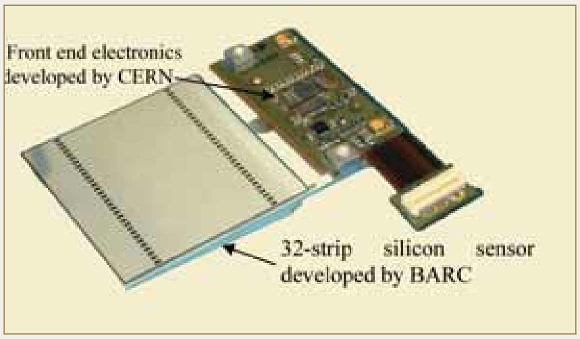

Fig. 6 : Silicon sensor micromodule along with front end hybrid

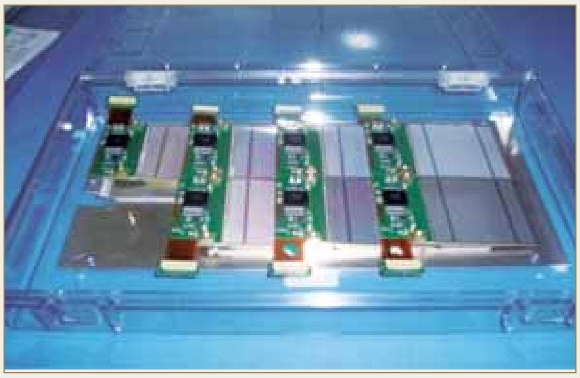

Fig. 7 : Ladder of seven micromodules

The micromodules are assembled in the form of ladders which have 7-10 micromodules and are then connected to a system motherboard which controls the micromodules and also acquires the signals from the micromodules. Fig. 7 show the ladder before integration of system motherboard.

The technology development of the silicon sensors and their production, involved several important activities such as sensor design and layout, process and device simulations, development of characterization setups and performance evaluation, fabrication process development and optimization, quality control during production and assembly of sensors into micromodules. The 4" integrated circuit fabrication facility of BEL, Bengaluru has been used, for development of the technology for fabrication of the sensors. Eight batches of silicon wafers were fabricated at BEL for optimizing the fabrication process, so as to meet the specifications. After successful development of prototype sensors and demonstration of technological capability, BARC was qualified for the production of 1000 sensors for the CMS experiment. In order to evaluate the performance of the sensors, a great deal of effort was also put in, to develop various automated setups for characterization of sensors and probe-jigs for making simultaneous contacts to the 32 strips. Various aspects such as the design of the sensors, processing issues and sensor characterization and performance of the sensors are described in the subsequent sections of this paper.

Design of the Preshower sensor

As shown in Figs.1-3, three types of mask layouts incorporating 32-strip silicon sensor along with other test structures were designed during various phases of technology development, preproduction and production. Test structures such as PIN diodes of various geometries, MOS capacitors, gated diodes, etc., were incorporated in the mask design for carrying out process diagnosis during fabrication. In addition to this, several other types of sensors such as PIN diodes of various geometries, pixel sensors, virtual pixel sensors, small area strip sensors, photodiodes, etc. were incorporated in the designs, to utilize the space around the silicon sensor.

The first version of the design used during the prototype development phase incorporated a silicon sensor with a geometry of 60mm X 60mm having 32 P^+ strips (Fig.1 (a)). A four layer mask was used for fabricating the sensors. In the initial batches, the performance of the sensors fabricated using this design was quite poor. After continuous modifications of the process parameters, in subsequent batches, sensors having very low leakage, high breakdown voltage and uniformity could be realized. As shown in Fig. 3(c), the final version of the sensor was designed for the geometry of 63mm x 63mm, with strips of width of 1.78 mm and pitch of 1.9 mm. This has been used for the production.

Features such as floating field guard rings, metal overhang over the P^+ strips and rounded corners have been incorporated in these designs, to increase breakdown voltage of the strips. All the 32 P^+ strips are enclosed by four floating field guard rings. The last guard ring is located at a safe distance from the dicing edge, so that, mechanical defects due to dicing do not affect the leakage currents.

Process and device simulations were carried out to finalize the design parameters such as width of the guard rings, spacing, length of the metal overhang, etc. As shown in Fig. 1(b) and Fig. 1(c), wafers with two types of guard ring designs, i.e., four and seven guard rings, were fabricated during the preproduction phase and the yield of the batches were compared. Since the four guard ring designs gave better yield, this design was used for the production of sensors.

Characterization of Preshower sensors

Static current vs voltage (I-V) and capacitance vs voltage (C-V) measurements were used to evaluate the performance of the sensor, i.e., leakage current, breakdown voltage and full depletion voltage. A great deal of effort was put in, to develop characterization setups, in order to carry out automated and simultaneous measurements of all 32 strips of the sensors. Probe jigs with microscopic X-Y-Z positioning to simultaneously probe all 32 strips of the unpassivated/passivated sensor were designed and fabricated at BARC.

A complete test facility for carrying out sensor qualification tests was set up in a class 10,000 clean room environment at the production center (BEL), so as to avoid transport of sensors and also because the further assembly of sensors into micromodules was to be carried out at BEL. The data of all measurements was entered in to the CRISTAL data base at CERN. The IV and CV data was used, to qualify the sensors for specifications such as full depletion voltage (V_{FD}) of the strips ($55<V_{FD}<150V$), breakdown voltage (V_{BD}) of each strip (>300V), total leakage current of the sensor (<5 µA at V_{FD} and <10µA at 300V) and uniformity of leakage current for the strips (only one strip with leakage current >1 µA at V_{FD} and >5µA at 300V). In addition to electrical characterization setups, measurement jigs for measurement of geometric parameters such as length, width and thickness were used to verify, that the dimensions of the sensors are within the specified tolerance of 100µm.

In order to ensure that the sensors would operate reliably in the radiation environment of LHC, the radiation hardness of the sensors was tested by irradiating them with fast neutrons up to a neutron fluence of $2x\ 10^{14} n/cm^2$ in a reactor (at BARC, India and at Dubna, Russia) and using a 24 GeV proton beam at CERN. As leakage currents increase excessively due to neutron radiation damage, the measurements after neutron irradiation were carried out at lower temperatures.

Fabrication technology for Preshower sensors

The development for the preshower silicon sensors was challenging as compared to the standard ICs or ASICs, because of nonavailability of standard technologies, much larger chip area causing decrease of yield and specifications requiring very low leakage currents at high operating voltages exceeding 500V.

The sensor technology was developed using high purity silicon wafers (N-type, FZ, <111>, 3-5 kΩ-cm or 5-10 kΩ-cm) supplied by TOPSIL or WACKER. These wafers had specified zero defect density and high life time of the order of a few milliseconds. This is an important specification as the quality of the wafers is a critical factor for sensor fabrication and even a single defect occurring over the sensor area, which is quite large, would result in a bad strip giving non-acceptable performance. Fabrication of the sensor was carried out, using a complex process sequence involving more than 25 process steps. Extensive process simulations were carried out to finalize the process parameters such as implantation energy and dose for boron and phosphorus, temperature and time for drive in cycles, intrinsic and extrinsic gettering cycles, etc.

The technology has been developed in a short period of about one year, by systematically optimizing various processes involved in sensor fabrication, in eight batches. During initial batches, sensors with desired specifications could not be produced by only varying process parameters such as implant dose and energy. Hence, various suite of processes were investigated, to optimize the process parameters.

Wafers from two manufacturers (WACKER and TOPSIL) with two ranges of resistivities (3-5 kΩcm and 5-10 kΩ-cm were used, to see the effect of the starting material. A number of wafers were fabricated using various combinations of process steps such as sacrificial oxide, Argon implant for extrinsic gettering, combined or separate drive in cycles for N^+ and P^+ implantations, with/without implant in scribe line, etc. Best results were obtained for wafers which were processed with sacrificial oxidation, argon implant on the back side, separate drive-in cycles for N^+ and P^+ implantations and no implant in the scribe-line region. Fig. 8 shows the reverse IV characteristics of a sensor, fabricated in the sixth batch, using the optimized process. the characteristics clearly show the remarkable improvement in the performance of the sensor in terms of leakage and break down voltage. The leakage currents have become very uniform and all strips could withstand 300V without breakdown. A double N^+ implant was incorporated at the back side of the wafer in the seventh batch, to reduce back injection. The implantation dose, energy and drive-in temperature and time, were decided on the basis of simulations, carried out to obtain a thick N^+ layer at the back side. By incorporating this process, the yield of the process significantly improved by about 50%. The typical CV and IV characteristics of all 32 strips of the sensor, fabricated using the final optimized process, are as shown in Fig.9 and Fig.10 respectively. As can be seen from the plots, sensors with very low leakage currents, high breakdown voltage and uniformity have been realized using the optimized process.

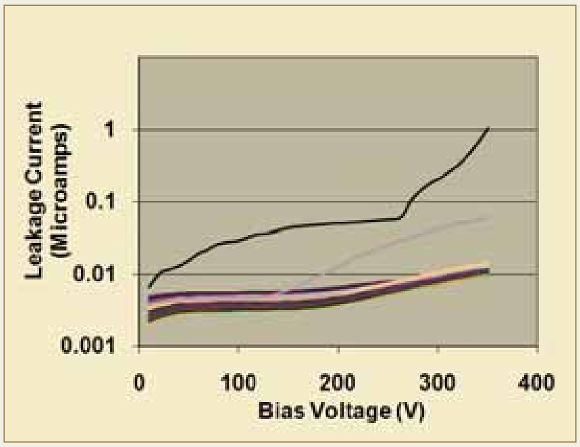

Fig. 8 : IV characteristics of a sensor fabricated in the sixth batch

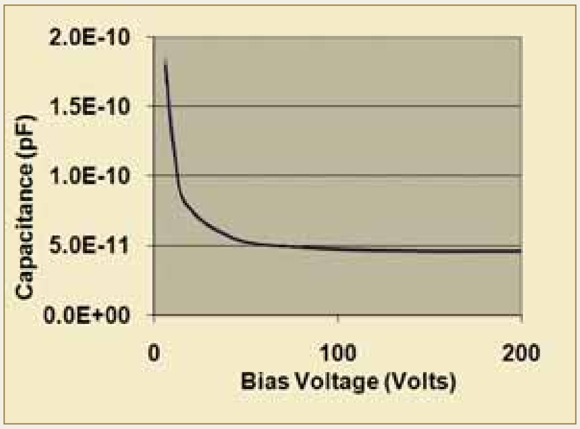

Fig. 9 : CV characteristics of all 32 strips of a sensor fabricated after process optimization

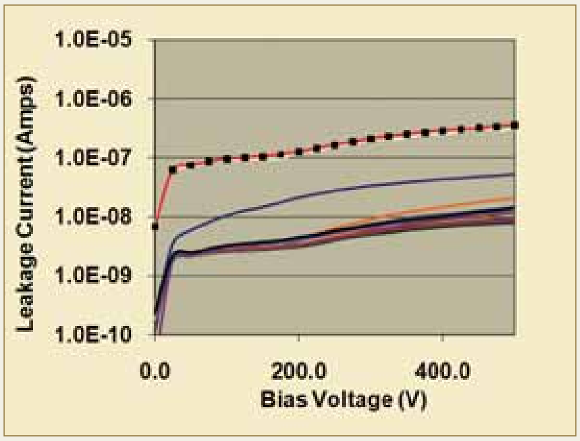

Fig. 10 : IV characteristics of all 32 strips of a sensor fabricated after process optimization, squares show total current

Production of sensors

Sensors with very good uniformity and production yield of 50% have been produced at BEL and production of eleven hundred sensors has been completed, using the optimized process as discussed earlier. The production was carried out using 300μm thick, <111>, FZ, 2-4kΩ-cm wafers manufactured by WACKER.

During the production of silicon sensors, the sensors were subjected to several quality control tests as outlined by CERN. The breakdown voltages, leakage current and capacitance of individual strips, full depletion voltage, mechanical dimensions of the sensor (thickness, length and width), dicing quality, etc., were some of the main parameters which were monitored during quality control. The data of measurement was analyzed using a LabView programme, to find various parameters for individual strips of each sensor.

The stability of the sensor was tested, by measuring the total leakage current of the sensor at different stages such as after fabrication, before micromodule assembly, after micromodule assembly, etc. The statistical distribution of various parameters such as V_{BD}, V_{FD}, total leakage current at V_{FD} and at 300V for one thousand sensors are plotted in Fig. 11 As can be seen, the breakdown voltage exceeds 500V for the majority of the sensors. The total leakage current of the sensor is of the order of 200nA at V_{FD} and is less than 1.0 μA at 300V for most of the sensors, though this tolerance is 10.0μA.

Considering the operation of LHC for ten years and high radiation background, reliability requirements were very stringent as the sensors are expected to operate without failure, once the LHC is commissioned. In order to test the stability under bias condition, few sensors were kept at 300V and the total leakage current was monitored with time. The radiation hardness tests carried out on the sensors proved, that the sensors could withstand the radiation environment of LHC.

Silicon microstrip sensors for the PHENIX Experiment at BNL, USA

After the successful development of large area silicon strip sensors for the CMS Experiment, this development activity has been taken to the next level, by developing advanced microstrip sensors for the PHENIX Experiment at BNL, USA. These sensors were designed to have 128 strips with a pitch of 470 μm and strip spacing of 15 μm. The strips will be read by a 128 channel readout

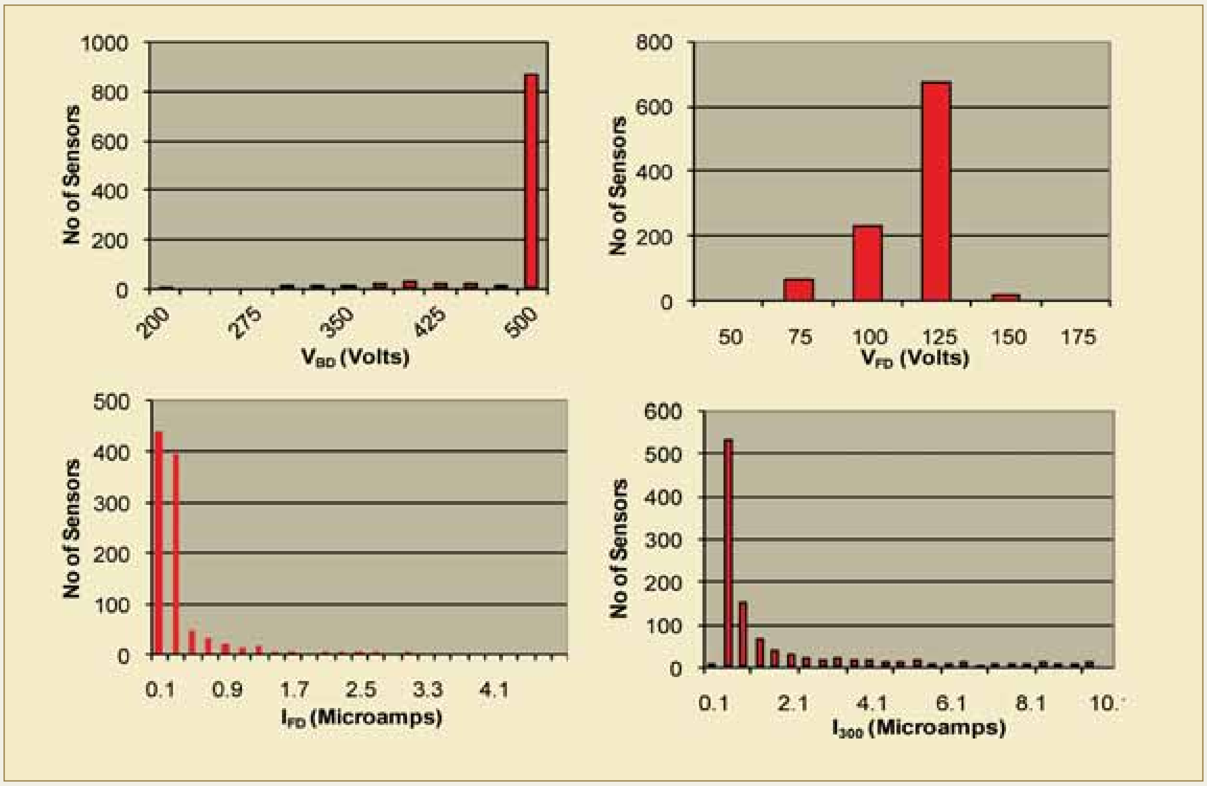

Fig. 11 : Distribution of (a) V_{BD}, (b) V_{FD}, (c) Total current at V_{FD} (I_{FD}) and (d) Total current at 300V (I_{300}) for 1000 sensors. The tolerance for I_{FD} is 5.0 µA and for I_{300} is 10 µA

chip, developed by BNL. A silicon pitch adapter to match the strip pitch of the sensor with 48 μm pitch of the readout chip has been also designed and fabricated with these sensors.

Fig. 12 (a) shows the 128-strip microstrip sensor and Fig.12 (b) shows the magnified view of the corner of the sensor. The microstrip sensors have been fabricated on 4-6 kΩ-cm, <111>, TOPSIL wafers with a thickness of 300 μm. An automated test setup incorporating a 128 pin probe card for probing the strips, a channel multiplexer and low current and capacitance measurement instruments has been developed, for the characterization of the sensor.

Fig. 12 (a) : Silicon microstrip sensor – Geometry - 62mm x 62mm, 128 strips with separation of 15 microns

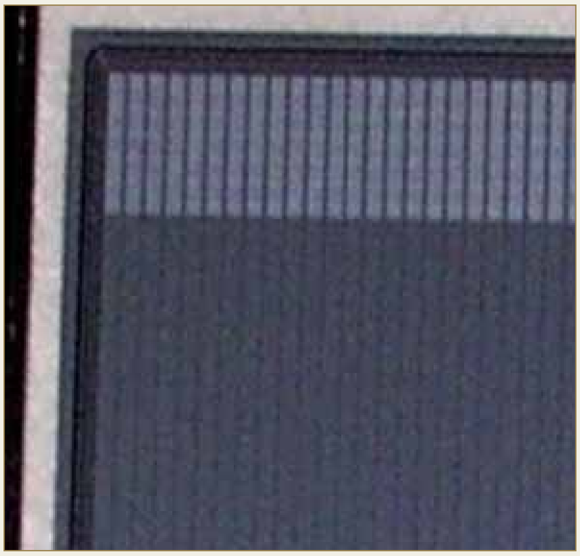

Fig. 12(b) : Magnified view of the corner of the microstrip sensor

The typical capacitance and leakage current characteristics for the 128 strips at different bias voltages are shown in Fig.13 and Fig.14 respectively. These microstrip sensors have been delivered to BNL for the PHENIX Experiment.

Silicon sensors for nuclear physics experiments and radiation monitoring

As shown in Fig. 2-4, various types of sensors have been designed and fabricated, for nuclear physics experiments, such as 'Charged Particle Array' at BARC and radiation monitoring instrumentation applications. These sensors have been designed to have circular and square geometries, with area ranging from 100 mm^2 to 400mm^2. The design has been carried out, so as to reduce the leakage currents and improve breakdown voltage of the sensors. The pad sensors have four pads each of geometry 10 mm x 10 mm and total area of 25 x 25 mm^2. These sensors have ion implanted junctions and oxide passivation. The process parameters have been initially optimized, using process simulations and then further tuned by carrying out fabrication runs in several batches. The dead layer of the window and leakage current minimization were of prime concern, in order to get the best energy resolution for charged particles. The sensors have been characterized by leakage current and capacitance measurements and by carrying out energy resolution measurements, using an alpha source of ^{239} Pu and ^{241}Am. A setup comprising of a charge sensitive preamplifier, spectroscopy amplifier, HV and MCA has been used, for energy resolution measurements. The measurements have been carried out by mounting the sensor and the source in a vacuum chamber. The leakage current characteristics of the sensors show, that the leakage currents are quite low (<10nA/cm^2 @ 100V). The pulse height spectrum obtained for the four pads of the pad sensor is shown in Fig.15. The pads show energy resolution of about 20-22 keV for ^{241}Am alpha particles of 5.486MeV. The energy

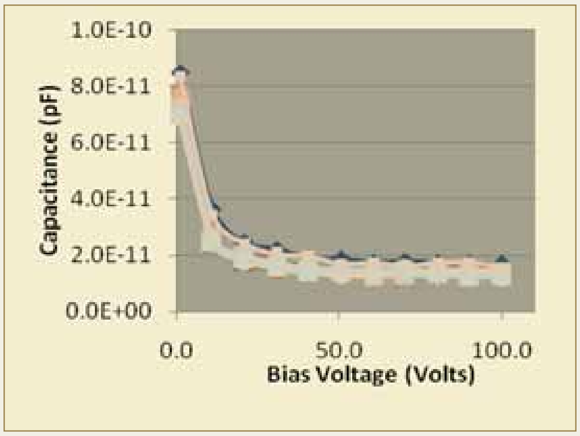

Fig. 13 : Typical CV characteristics of all 128 strips of a microstrip sensor

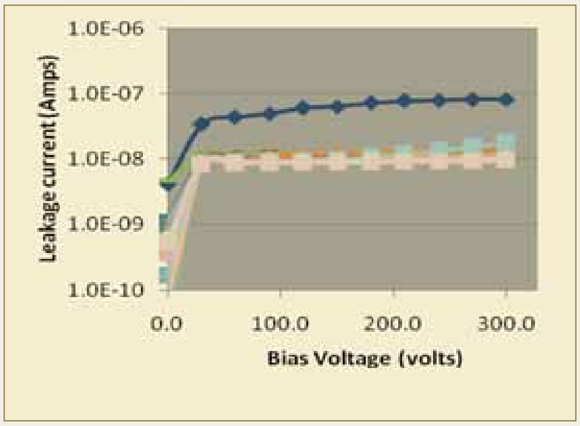

Fig. 14 : Typical IV characteristics of all 128 strips of a microstrip sensor

resolution of the sensor with area of 300mm^2 is about 18keV (Fig. 16).

Silicon PIN photodiodes

Silicon photodiodes coupled to a scintillator are used, for the measurements of X-rays or γ-radiation and charged particle spectroscopy, involving long range particles encountered in nuclear studies, laser based instrumentation, physics research and X-ray imaging. Considering the large numbers of applications of silicon photodiodes, the technology development of silicon PIN photodiodes has been carried out. Several types of photodiodes with area ranging from 0.5mm^2 to 100mm^2, quadrant detectors and 16-element array of photodiodes have been designed, using a four layer mask (Fig. 17).

The photodiodes have been fabricated using high resistivity silicon wafers, by a custom-developed low leakage current process. The dark current and capacitance of the diodes for various bias voltages has been measured up to full depletion voltage using automated setups. The dark current has been observed to be about 3-5 nA/cm^2 and the capacitance at full depletion voltage is about 45 pF/cm^2. The response of these diodes has been evaluated at different wavelengths using laser/LED and compared with a commercial photodiode having comparable area [16]. The typical responsivity of PIN photodiode of geometry

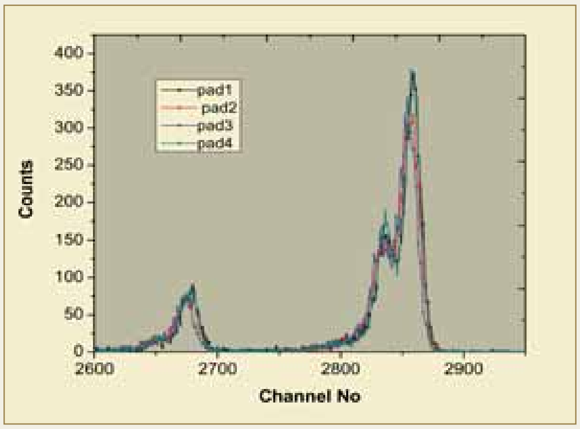

Fig. 15 : Pulse height spectrum for the four pads of the pad sensors

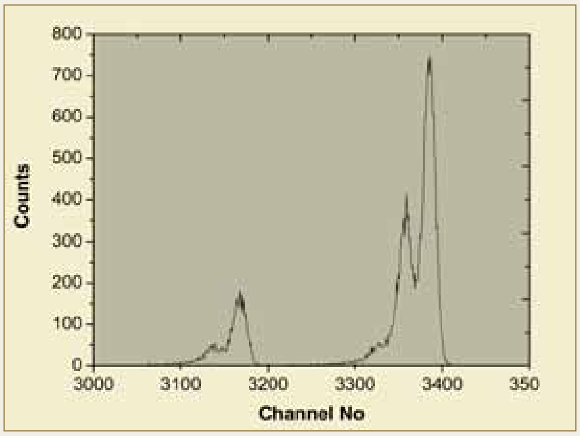

Fig. 16 : Pulse height spectrum for a sensor with 300mm^2 area

Fig. 17 : PIN photodiodes and quadrant detectors

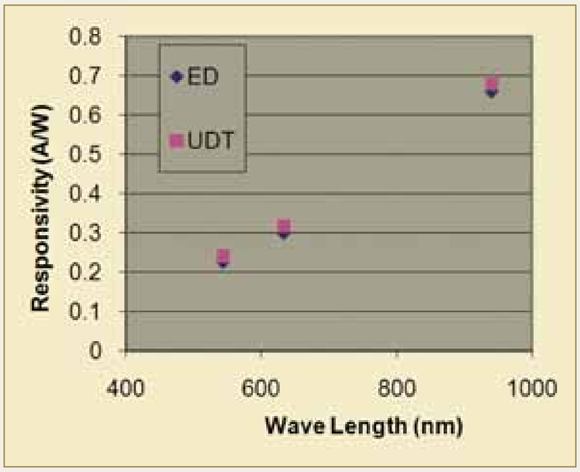

Fig. 18 : Responsivity of photodiode at various wave lengths

6mm x 6mm (marked as ED) is shown in Fig. 18. The responsivity is about 0.66 A/W at 940nm wavelength and falls to 0.24 at 453.5 nm. The performance is comparable to that of commercial photodiodes (UDT).

Summary

Demanding technology and capability for large scale production of silicon sensors with good uniformity, low leakage currents and high breakdown voltage have been developed by BARC, for the CMS Experiment at LHC, CERN. The individual strip leakage is of the order of few nA/cm^2 and the strip and total leakage currents are quite well below the specified limits. Irradiation tests carried out have shown, that the sensors meet the stringent specifications for reliable operation in the high radiation environment of LHC. Eleven hundred sensors supplied by us in the form of micromodules, have been installed in CMS preshower at LHC, CERN. The R&D carried out in the past few years has given us the technological capability for large scale production of large area sensors. Though the R&D was targeted for the development of sensors for the international experiment at CERN, this R&D triggered the indigenous development of a wide variety of high performance sensors, for nuclear physics experiments and radiation monitoring instrumentation applications at BARC. Development of new types of sensors such as silicon photomultiplier and integrated ΔE-E silicon detector telescope are underway [17].

Acknowledgement

The authors would like to thank Dr. S. Banerjee, Director, BARC, Dr. V.C. Sahni, Director, RRCAT Indore and Director, Physics Group, Mr. R.K. Patil, Associate Director (C), E&I Group, Late Dr. S.K. Kataria, former Associate Director, E&I Group, Dr. S. Kailas, Associate Director, Physics Group, Dr. R.K. Choudhury, Head, NPD, Mr. M.D. Ghodgaonkar, former Head, Electronics Division, and Prof Atul Gurtu, Spokesperson, India-CMS collaboration, TIFR for their support and encouragement in carrying out this work.

References

1. Anita Topkar, S Praveenkumar, Bharti Aggarwal, P K Mukhopadhyay and G P Srivastava, "Silicon sensors for the Compact Muon Solenoid Experiment at the Large Hadron Collider, CERN", Published in the BARC News Letter, Issue No 290, March, 2008, pp 2-14.

2. Anita Topkar, S Praveenkumar, Bharti Aggarwal and S K Kataria, "The CMS preshower silicon sensors: Technology development and production in India", Nuclear Instruments and Methods in Physics Research, A, Vol 585(2008), 121-127.

3. Anita Topkar, Praveenkumar S, Bharti Agarwal, S K Kataria and M D Ghodgaonkar, "Silicon detector technology development in India for the participation in international experiments", Pramana –Journal of Physics Vol 69 No6, December 2007, pp 1085-1088, Presented in the International Linear Collider Workshop, March 9-13, 2006, at IISc, Bengaluru India.

4. Anita Topkar, Praveenkumar S, Bharti Agarwal and S K Kataria, "Preshower Silicon Strip Detectors for the CMS Experiment at LHC" Presented in the 9th International Conference on Advanced Technology and Particle Physics, Como, Italy, October 17-21, 2005, Published in the Proceedings of the conference.

5. Anita Topkar, "Development of radiation detectors at BARC", Invited talk at the DAE-BRNS Symposium on Compact Nuclear Instrumentation and Radiation Detectors CNIRD, held at Jodhpur, March,2005, Published in the Proceedings of the symposium.

6. Anita Topkar, Praveenkumar S, Bharti Agrawal, and S K Kataria , "CMS preshower silicon strip detector for the LHC, CERN: Reliability of detectors and trials for assembly" , Proceedings of the DAE-BRNS symposium on Nuclear Physics, Vol 46B, December, 2003.

7. S K Kataria, Anita Topkar et al, “ Silicon strip detectors under India CMS collaboration”, Proceedings of DAE-BRNS symposium on Intelligent Nuclear Instrumentation, INIT 2001.

8. S K Kataria, Anita Topkar et al, “Development of technology at BEL for 32 strip silicon strip detectors and diode detectors”, Proceedings of DAE-BRNS symposium on Intelligent Nuclear Instrumentation, INIT 2001.

9. Anita Topkar and P K Mukhopadhyay, “Development of silicon detectors for charged particles”, Published in the Proceeding of DAE BRNS symposium on Nuclear Physics, Dec 2008.

10. Anita Topkar, Bharti Aggarwal and M D Ghodgaonkar et al , “Indigenous development of high performance silicon detectors”, IINC, 2005, National Conference on Microelectronics and VLSI, Dec 20-21, 2005, IIT, Bombay, Organized by International Microelectronics and Packaging Society (IMPAS), India.

11. Anita Topkar, Praveenkumar S , Bharti Agarwal, et al, “Indigenous Technology Development for High Energy Resolution Silicon PIN Diode Detectors”, Proceedings of the DAE-BRNS symposium on Nuclear Physics Vol 47B, December , 2004.

12. Seena V, Mahendra Jain, V Ramgopal Rao, Praveenkumar S and Anita Topkar, “ONO based triple dielectric passive dosimeter”, Proceedings of DAE-BRNS Symposium on Compact Nuclear Instrumentation and Radiation Detectors CNIRD, March, 2005.

13. Bency John, D C Biswas, A Saxena, B K Nayak, P K Sahu, A L Inkar ,Y K Gupta, A N Vind, A Topkar and R K Choudhury, “Pulse shape discrimination for charged particles in segmented silicon detectors”, Published in the Proceeding of DAE BRNS symposium on Nuclear Physics, Dec 2006.

14. D C Biswas, Y K Gupta, B V John, Raghav A N, A Inkar, B K Nayak, A Saxena, Anita Topkar and R K Choudhury, “Hybrid detector telescope for fission fragments and heavy ions”, Published in the Proceeding of DAE BRNS symposium on Nuclear Physics, Dec 2006.

15. R G Thomas, R P Vind, A L Inkar, A Saxena, Anita Topkar et al , “Performance of silicon strip detectors with delay line readout system”, Proceedings of the DAE-BRNS symposium on Nuclear Physics, Vol 45B, 2002, p 462-463.

16. Anita Topkar and Aseem Singh Rawat, “Indigenous Technology Development of PIN photodiodes’, Published in the Proceedings of the DAE –BRNS National Laser Symposium, December, 2006.

17. Anita Topkar, Pourus Mehta and P K Mukhopadhyay, “Development of DE-E silicon detector: Two dimensional simulation studies”, Published in the Proceeding of DAE BRNS symposium on Nuclear Physics, Dec 2008.

ABOUT THE AUTHORS

Dr. Anita Topkar acquired her PhD in 'Microelectronics' in Electrical Engineering, from Indian Institute of Technology, Mumbai. After completing her tenure as Visiting Scientist at BARC, she joined the Electronics Division, BARC in 2000. Dr. Anita Topkar received the DAE Award for Scientific and Technical Excellence for the year 2007, for her contribution in the design and technology development of silicon detectors, for the CMS Experiment at the Large Hadron Collider, CERN, for nuclear physics experiments and for radiation monitoring applications.

Mr. Praveenkumar S. acquired his M Tech in Materials Science from Indian Institute of Technology, Kanpur and he joined the Electronics Division, BARC in 2002. He has been working on the development of silicon detectors and MEMS.

Ms. Bharti Aggarwal joined the Electronics Division, BARC in 2000. She has been working in the area of silicon detectors.

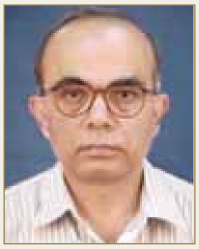

Mr. P.K. Mukhopadhyay is an Outstanding Scientist and Head, Electronics Division. He belongs to the 14th batch of BARC Training School. His area of expertise is nuclear instrumentation, hybrid microcircuits and ASICs. His fields of interest are microelectronics and nuclear radiation detectors.

Mr. G.P. Srivastava is a Distinguished Scientist and Director of Electronics and Instrumentation Group, BARC.

CAMAC INSTRUMENTATION FOR ACCELERATOR-BASED NUCLEAR PHYSICS RESEARCH EXPERIMENTS

A. Behere, S. Joy, K. Jha, S.M. Raut, M.L. Meshram,
P. Nair, S.S. Pande and Padmini S.
Electronics Division

Ms. Anita Behere is the recipient of the DAE Scientific & Technical Excellence Award for the year 2007

ABSTRACT

The Electronics Division, BARC has developed and supplied a number of CAMAC modules and systems for accelerator-based multi-parameter experiments for more than a decade. These mainly include PC-CAMAC AMPS, Nuclear ADCs and FERA-based system. These systems have been installed at Pelletron accelerator at TIFR, Mumbai and other accelerator facilities at VECC, Kolkata, IOP, Bhubaneswar, etc. They provide an indigenous solution for the high performance requirement of resolution and throughput for the experiments. A new Embedded Crate Controller has been developed, to achieve higher performance through hardware list sequencing. It has also alleviated the problem of component obsolescence in earlier versions of controllers. The recently developed and commissioned FERA system, targets higher throughput experiments spanning multiple CAMAC crates.

Introduction

For the last two decades, the Electronics Division has been involved in the development of Computer Automated Measurement And Control (CAMAC) instrumentation, for nuclear physics research. It mainly consists of CAMAC-based nuclear ADCs, TDCs, synchronization modules, programmable logic units and controllers. The delivered instrumentation is being used, for experiments in research labs of DAE such as FOTIA, BARC, Pelletron TIFR, VECC and SINP, Kolkata and also IIT Mumbai, IOP Bhubaneshwar. With the availability of higher energy accelerator beams, experiments are planned involving larger number of parameters. Improved versions of controllers and nuclear modules were developed and supplied, to support the demand for higher performance. As the experiments are getting bigger in terms of number of channels, the generated data rates are higher and CAMAC readout proved to be a bottleneck. In earlier versions of controller CC2000, the best readout time achieved was 3us per parameter and the highest data throughput obtained was 250 kBps for a single crate setup and 500 kBps for two crate setup. Increased throughput was achieved by two approaches; one with Embedded CAMAC Controller, which provides a simple solution for single crate setups and achieves throughput up to 1.5MBps. The other solution is with “Fast Encoding Readout ADC (FERA)” based system, which is a front-panel ECL readout bus, spanning multiple crates. The readout speed is 20MBps with built-in zero suppression resulting in much higher effective data throughput.

Experimental setup

A typical experimental setup consists of front-end electronics housed in NIM bins and data acquisition modules and controller in CAMAC crates. Presently, the data acquisition systems are based on CAMAC, with the controller acting as an interface between the acquisition modules and a host PC. The main acquisition modules are Analog-to-Digital Converters (ADC), Time-to-Digital Converters (TDC) and Charge to Digital Converters (QDC). The ADCs are peak sensing nuclear ADC with resolution up to 8K. The TDCs are of 4K resolution with full scale from 100ns to 1us. The commonly used QDCs have gate width from 50ns to 1us and input full scale range of 250pC. Each of these modules generally has eight, sixteen or higher number of channels. In addition to these, there may be some other modules such as coincidence, scalers, etc. in the system. Fig. 1 shows the CAMAC setup for an experiment.

A common gate is generated based on coincidence criterion for signals from selected detectors and this acts as a trigger for the acquisition modules, to start digitization. At the end of digitization, an interrupt is given to a readout controller, which reads the digital values of the parameters. An accelerator based experiment involves large number of parameters. As the number of parameters increases, the readout time increases whereas the conversion time increases only up to the number of channels multiplexed on to a single ADC. Beyond this, the conversion time does not increase since the ADC conversion happens in parallel in different ADC modules. Fig. 2 shows various timings involved in event acquisition and its dependence on the number of parameters.

CAMAC-PC Advanced Multi-parameter System

CAMAC controller CC2000 was designed around Transputer having on-board buffering of data to even out the random burst of events. It achieves a CAMAC throughput of about 3us per parameter and CAMAC-PC link at 20Mbps to a PC add-on card. MS Windows-based Advanced Multi-Parameter System (AMPS) software was built around this. Linux based version LAMPS was later developed by NPD, BARC and has been continually upgraded. The AMPS system, along with the LAMPS software, has been installed at more than 25 setups at TIFR, VECC, SINP, IOP and other labs and is being used continuously for the past many years. The sustained throughput achieved with this system was 250kBps with one crate setup. The system was later upgraded to support two crates for an improved throughput of 500 kBps. There was large demand for this setup but due to component obsolescence, its production had to be discontinued and an alternative solution became necessary.

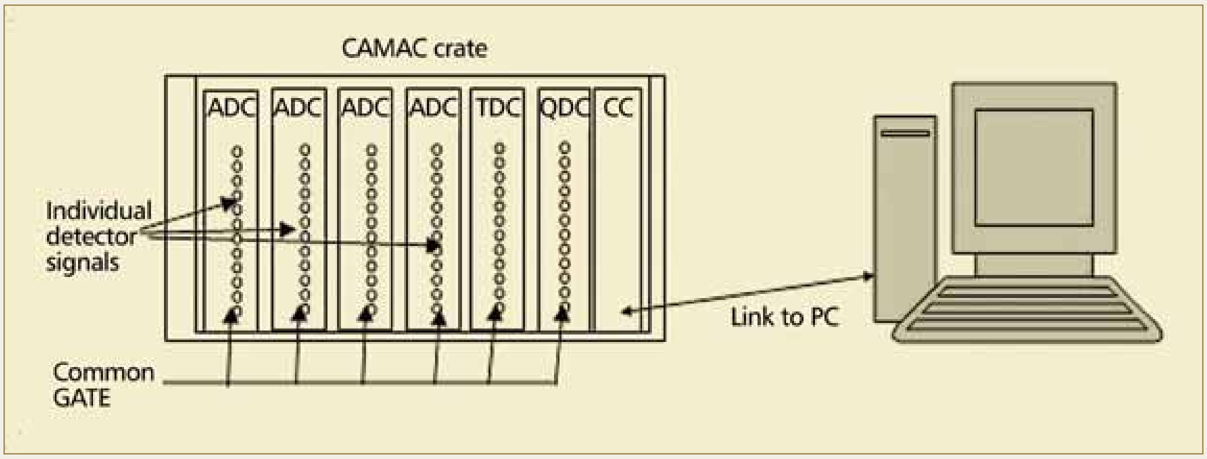

Fig. 1: Experimental setup with CAMAC ADC, TDC, QDC modules and controller having link to PC

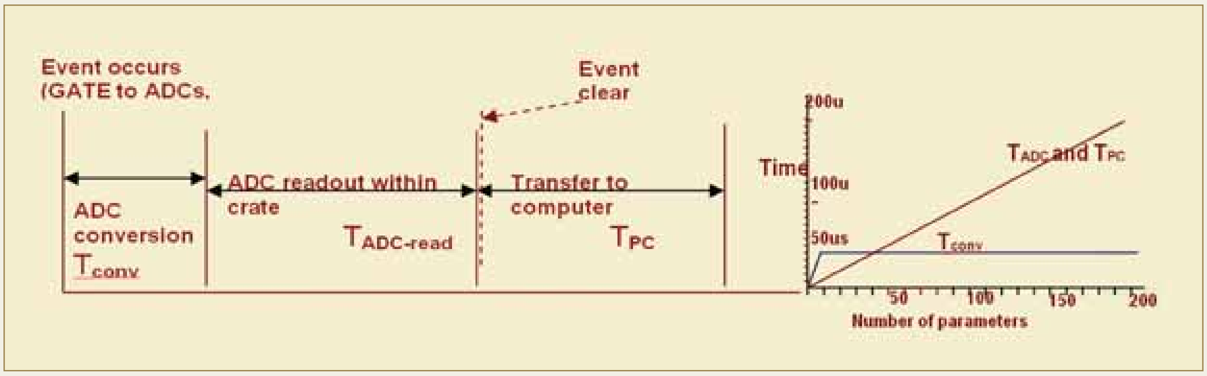

Fig. 2 : Timings involved in an event acquisition

Embedded CAMAC controller

A new Embedded CAMAC Controller (ECC) has been developed, to support CAMAC user community due to component obsolescence for CC2000 and to achieve higher performance. The major improvement is in the CAMAC readout, which has been reduced from 3us for CC2000 to 1.1us and data link to PC in the form of 100Mbps Ethernet link. With optimum embedded software using QNX operating system, sustained throughput in excess of 1.4MBps has been observed in the lab. Fig. 3 shows the Embedded CAMAC controller and its block schematic. Fig. 4 shows the throughput observed with test software at different parameters and at different event rates. These observations were carried out in the lab with a pulse generator as the source of event.

The list processing is completely implemented in FPGA hardware to achieve optimum CAMAC throughput of 1.1us. In most of the experiments, the hit ratio with timing parameters is small, thus, zero-suppressed readout from the module greatly improves the system performance. Embedded CAMAC controller incorporates sparse readout mode supported by multi-channel TDCs. The effective throughput and consequently the possible event rates will be much higher with this mode.

Fast Encoding Readout ADC (FERA) Multi-parameter System

The recently developed FERA system targets high throughput experiments, spanning multiple CAMAC crates involving large number of parameters. FERA is Lecroy proprietary ECL bus on the front side of ADCs. It has data width of 16 bits, readout speed of 100 ns per word, built-in zero suppression, small turn-around time for no valid input and support for multiple crates over single cable. The setup consists of ADCs, TDCs,

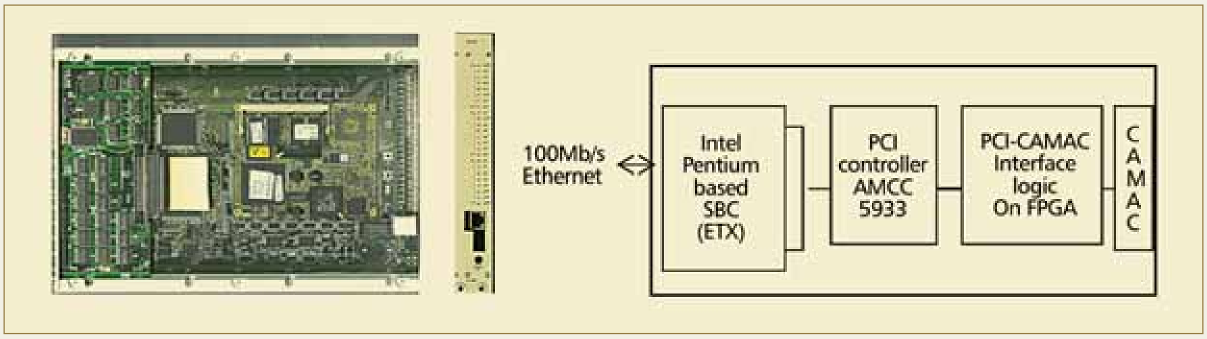

Fig. 3 : The embedded CAMAC Controller with its block schematic

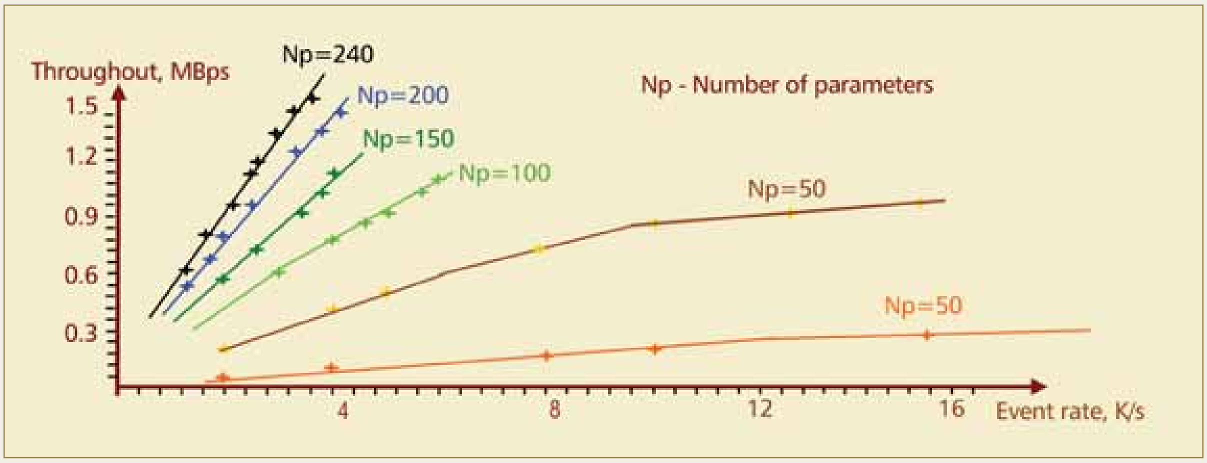

Fig. 4 : Throughput against event rates at different event sizes for embedded CAMAC controller

QDCs and other modules, with FERA interface and a FERA readout controller. There are various options for the FERA readout controller: a CAMAC module with FASTCAMAC transfer to the controller, the CAMAC controller itself or a PC add-on card. We have chosen the option of developing the FERA readout controller as a PCI add-on board as it offers direct data transfer to PC memory.

FERA Readout Controller

The FERA readout controller in the form of PCI add-on card directly transfers the data from ADCs to the PC memory. On-board FIFO is used to even-out random bursts of events and data is transferred by DMA over PCI. Programmable delays for various bus signals have been implemented, to fine tune system timings for optimum performance. Programmable timeout on critical bus signals have been implemented, to recover from error condition. Diagnostic features have been incorporated to check the healthiness of system.

Since the readout is via a front-side bus formed by multi-drop cable, the coverage of one cable segment is not limited to one crate, but can span multiple crates. The total number of ADCs on one segment is

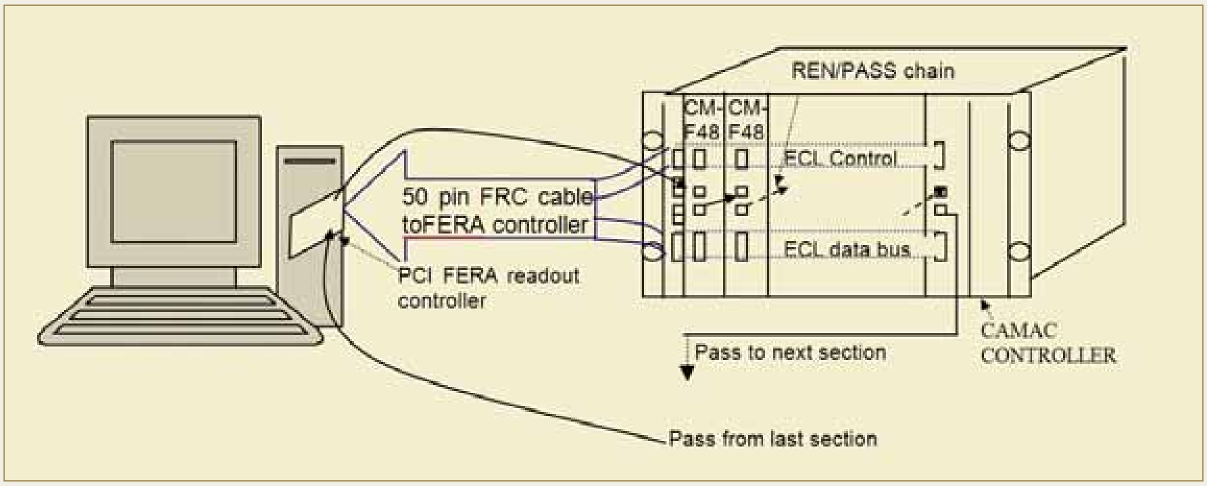

Fig. 5: FERA system setup

Fig. 6: FERA readout controller

limited by cable length and signal driver strength. Testing has been done with up to twenty ADCs in two crates. The FERA data acquisition system has been installed, commissioned and is being used in experiments.

Summary of the three setups

The three versions of CAMAC setup, namely with CC2000, Embedded CAMAC Controller and FERA cater to different experimental setups. The two crate AMPS system with CC2000 has been successfully used in many experiments and the throughput is sufficient for most of the applications. The Embedded CAMAC Controller will replace CC2000 with much improved throughput, especially in experiments with timing channels, where sparse readout mode is supported by the TDC modules. This increases the effective data throughput. The FERA system delivers throughput in setups spanning more crates, without additional hardware for synchronization. The effective throughput in terms of event rates is more than the actual rate due the built-in zero suppressed readout mode. As indicated in Fig. 7, the readout time for FERA setup is the lowest for both ADC read and for transfer to PC memory.

Data acquisition modules

The modules developed for the experiments are widely used nuclear modules such as ADC, TDC, programmable trigger unit and synchronizing module. The quad 8K FERA ADC, CM_F48, has been supplied in large numbers to the Indian National Gamma Array (INGA) experiments collaboration and other users. The octal FERA TDC module has been recently incorporated in an experimental setup. There is a large demand for both these modules.

Fig. 8 : The Quad FERA ADC, CM_F48 module

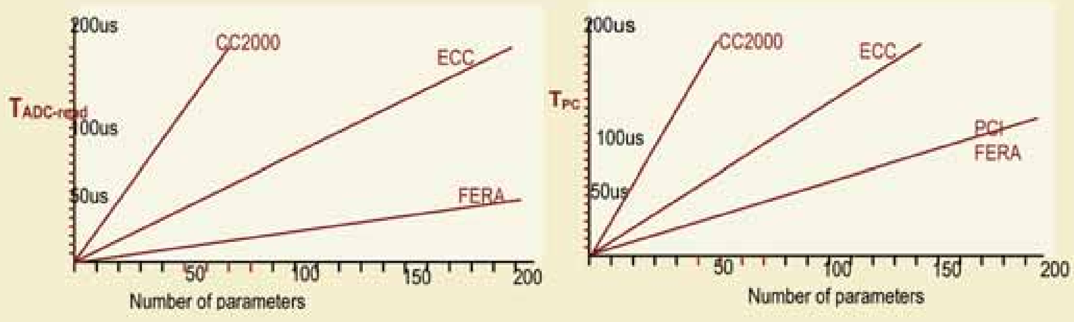

Fig. 7 : Comparison of throughput for different readout mechanisms

Quad 8K FERA ADC, CM_F48

These modules have 8K resolution with DNL of better than + 1% required for the segmented HPGe Clover detectors used in most of the INGA experiments. The conversion time is 15ms for four channels. A master gate as well as individual gate is provided, to support various modes of operation. The module can be read on CAMAC as well as FERA bus. It supports both zero suppressed and raw data mode of readout on the FERA bus. As can be seen in Fig. 9, the performance of CM_F48 is comparable with that of commercially available ORTEC ADC AD413.

Conclusion

A large number of AMPS systems and Quad FERA ADCs have been installed and commissioned at various user labs and are being used regularly in experiments. The increasing demand for higher throughput has been met with the development of higher performance FERA system. Development efforts continue towards higher density acquisition modules, suitable for the experiments with a large number of parameters and ease of maintenance.

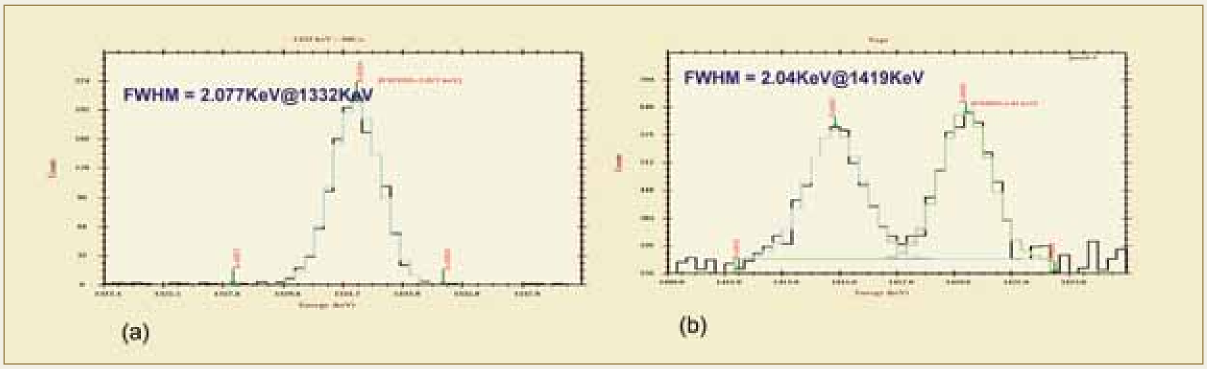

Fig. 9 : Comparison of In-beam spectrum with (a) CM-F48 and (b) ORTEC ADC, AD413 @BARC-TIFR Pelletron (Jan 07), ^{32}S + ^{78}Se @ 125 MeV

Octal FERA TDC

These modules have eight channels with 4K resolution. The conversion time is 25ms for eight channels. It has common start and individual stop signal inputs. The module can be read on CAMAC as well as FERA bus. It supports both zero suppressed and raw data mode of readout on the FERA bus. Full scale ranges of 250ns 500ns and 1mS are supported. It has INL of ± 0.05% and DNL of ±5% over upper 90% of range. Time window is selectable by means of lower and higher level discriminators through CAMAC command. Fig. 11 shows the performance of the module.

Fig. 10 : The Octal TDC module

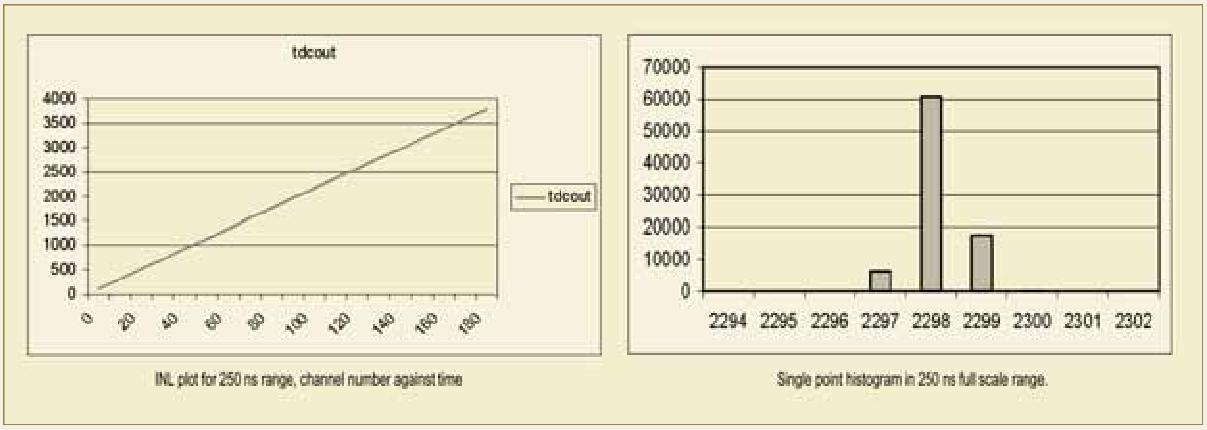

INL plot for 250 ns range, channel number against time

Single point histogram in 250 ns full scale range.

Fig. 11 : Performance of Octal TDC

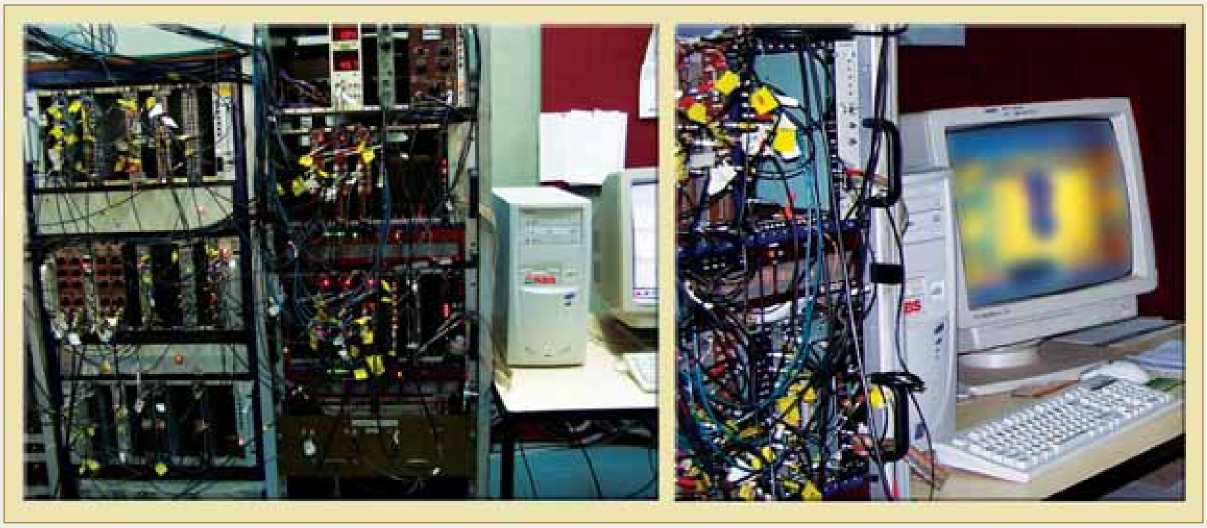

Fig. 12 : Advanced Multi-Parameter System in an experimental setup

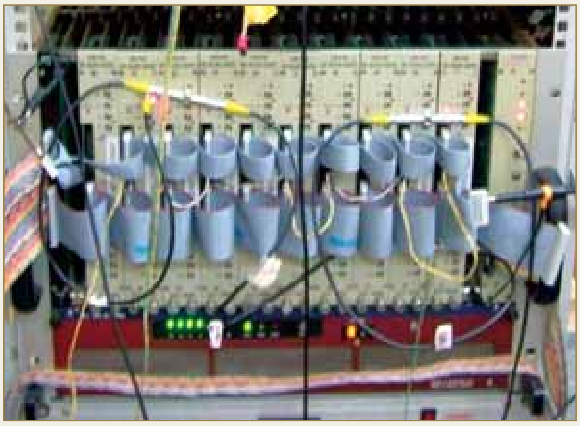

Fig 13 : FERA ADCs installed in a crate experimental setup

Acknowledgement

The authors wish to acknowledge Mr. M.P. Diwakar, Head, DAPS, ED, Mr. M. D. Ghodgaonkar, former Head, ED and Mr. P. K. Mukhopadhyay, Head, ED for their support in this development activity. The authors are also thankful to the NPD team, for the application software development, required for the systems.

ABOUT THE AUTHORS

Ms. Anita Behere, a graduate from the 27th batch of BARC Training School joined Electronics Division in 1984. She has been working in the area of design and development of CAMAC instrumentation for accelerator control and nuclear physics research and other research experiments. The design and development of the FERA based system and CAMAC controllers has been one of her major contributions.

Mr. Saju Joy, a graduate from the 36th batch of BARC Training School joined PRP, Kalpakkam. Since joining the Electronics Division in 2002, he has been working in the area of design and development of CAMAC instrumentation for nuclear physics research and accelerator control. The design and development of FERA-based nuclear ADC and TDC modules have been his major contributions.

Mr. Kuldip Jha joined the Electronics Division in 1988 and has been working in the area of design and development of CAMAC instrumentation. The design and development of FERA readout controller and Embedded CAMAC controller has been one of his major contributions.

Presently **Ms. Anita Behere, Mr. Saju Joy** and **Mr. Kuldip Jha** are involved in the design and development of camera electronics for the MACE gamma-ray telescope and instrumentation for nuclear physics research.

Mr. S.M. Raut joined the Advanced Fuel Fabrication Facility, Tarapur in 1990 and later the Electronics Division in 1996. He has been involved in the development and testing of NIM and CAMAC modules. Currently he is working on the design and development of a USB-based data acquisition system for 2-D imaging detector.

ABOUT THE AUTHORS

Mr. M. L. Meshram joined the Electronics Division in 1996. He has been involved in the development and testing of CAMAC ADCs and controllers. Currently he is working on the development of CAMAC modules for accelerator control.

Ms. Preetha Nair is a graduate from 42nd batch of BARC Training School. She joined the Electronics Division in 1999. Since then she has been involved in design and development of software for PC-based systems for nuclear reactors as well as accelerators. The design and development of embedded software for Embedded CAMAC controller has been one of her major contributions.

Mr. S.S. Pande, a graduate from the 33rd batch of BARC Training School joined Electronics Division in 1990. He has been involved in the development of application software and device drivers for PC-based CAMAC and standalone data acquisition systems. He has also developed software for plant automation systems. Currently he is developing Java application for USB based ultrasonic systems.

Ms. Padmini S., a graduate from the 31th batch of BARC Training School joined the Electronics Division in 1988. She has been involved in design and development of software for systems in Nuclear power plants and Accelerators based research. Development of software for Advanced multiparameter system, FOTIA control and information system and Embedded CAMAC Controller are her major contributions for accelerator-based research.

बीएआरसी न्यूज़लैटर
BARC NEWSLETTER

HYDRIDE INDUCED EMBRITTLEMENT OF ZIRCONIUM ALLOY PRESSURE TUBES

R.N. Singh, J.K. Chakravartty and S. Banerjee
Mechanical Metallurgy Section, Materials Group

Dr. R.N. Singh received the DAE Scientific & Technical Excellence Award for the year 2007

ABSTRACT

Tubes made of dilute Zirconium alloys, act as miniature pressure vessels in Pressurized Heavy Water Reactors (PHWRs) and are subjected to aqueous corrosion, resulting in hydrogen pick up. Hydrogen exceeding solid solubility, precipitates out as brittle hydride phase and may cause embrittlement of the host matrix. Two forms of hydride embrittlement have been recognized for dilute zirconium alloys – gross and localized. Gross embrittlement is caused due to uniformly distributed hydride precipitate, whereas localized embrittlement is caused by hydrogen migration, leading to damage accumulation within a small region over a period of time, before catastrophic failure of the component may occur. Parameters like fracture toughness, threshold stress for reorientation of hydrides, threshold hydrogen concentration for blister formation, Delayed Hydride Cracking (DHC) velocity, threshold stress intensity factor for DHC initiation, are used as fitness for service assessment of pressure tubes. In this article, some of the results generated by Materials Group, BARC, using Indian pressure tube material are highlighted.

Introduction

About ninety water-cooled nuclear reactors in the world, which are either in operation or are under construction, use pressure tubes instead of pressure vessels, to contain the hot pressurized coolant. These reactors are cooled and moderated by heavy water and hence are known as Pressurized Heavy Water Reactors (PHWRs) [1]. Each coolant channel assembly of PHWRs, comprises of a Pressure Tube (PT), a Calandria Tube (CT) and garter springs. Natural uranium oxide powder compacted and sintered in the form of pellets and encapsulated in thin cladding, forms the fuel pins of the PHWRs. Several such pins are assembled in the form of fuel bundles and are loaded in horizontal pressure tubes. Pressure tubes act as miniature pressure vessels in PHWRs, with coolant heavy water flowing through it under a pressure of around 10 MPa and at a temperature in the range of 523 to 573 K and are exposed to a fast neutron flux of 3 x 10^{17} n/m^2/s. Calandria tubes surround the pressure tubes from outside. Garter springs are provided at regular intervals in the annular space, to support pressure tube and to prevent it from contacting the cooler calandria tube, which is surrounded by low-pressure, low-temperature heavy water moderator, maintained at 333 K, in a large stainless steel vessel called calandria vessel.

The use of natural UO_2 as fuel in PHWRs demands that core structural materials such as cladding tubes (also called fuel tubes), pressure tubes (coolant tubes), calandria tubes and garter springs must have low neutron absorption cross-section and should satisfy the physical, mechanical, metallurgical and chemical requirements of radiation environment [2]. Pressure tubes being the final pressure boundary containment for hot coolant in PHWRs, their integrity is to be maintained during reactor operation. Though the specification limit for hydrogen content in the pressure tubes is 5 ppm for quadruple melted and 25 ppm by weight for double melted Zr-2.5Nb pressure tubes, part of the hydrogen / deuterium evolved during service from coolant-metal corrosion reaction, is picked up by the pressure tubes. Hydrogen present in excess of solid solubility precipitates out as hydride phase, which is known to embrittle the host matrix. The hydrogen-related problems associated with Zr-alloy components are hydride embrittlement [3] especially due to stress-reorientation of hydride, Delayed Hydride Cracking (DHC) and hydride blister formation. Considering the technological importance of hydride embrittlement of Zr-alloy in safety assessment and life management of Zr-alloy core components. The Materials Group, BARC is pursuing a comprehensive study on hydrogen / hydride induced degradation mechanisms associated with Zr-alloys, involving extensive experimentation and theoretical computations. This article highlights some of the major achievements in this area.

The pace of research and development work in this area, is controlled by hydrogen charging in Zr-alloy samples, without altering its microstructure and texture under laboratory conditions. Thus the primary focus was on the development of a reliable hydrogen charging system. Both gaseous and electrolytic hydrogen techniques are being regularly used by us and are described briefly in section 2 [4]. For fracture toughness and DHC tests, direct current potential drop system was developed in-house, to measure crack length, the salient features of which are described in [5].

The maximum amount of hydrogen which can be retained in solid solution without forming hydride precipitate is called Terminal Solid Solubility (TSS). TSS of hydrogen in zirconium alloys is observed to increase with increase in temperature. At ambient temperature, TSS of hydrogen in zirconium alloys, is less than 1μg/g. Hence, at ambient temperature almost all the hydrogen in zirconium alloy will be present as hydride. Initially, TSS was thought to be a safe limit for hydrogen concentration, below which embrittlement effect was not considered significant. However, recent studies have shown, that the threshold hydrogen concentration for DHC initiation and hydride blister nucleation are not TSS but a fraction of TSS. Thus, terminal solid solubility of hydrogen in these alloys, is an important parameter and is used by design and safety engineers, for fitness for service assessment of these components. Experimentally TSS is determined by preparing samples with known concentration of hydrogen and measuring some change in physical property, to identify transition temperature. Techniques like dilatometry [6,7], resistivity [8], internal friction [9-11], differential scanning calorimetry [12], small angle neutron scattering [13-14] and metallography [15] measure changes in dimension, resistance, damping frequency, heat flow, lattice parameter and microstructural features, respectively and are used to determine the transition temperature. The experimentally determined transition temperature is correlated with hydrogen concentration, in the form of an Arrhenius-type relationship, to obtain the pre-exponential constant and the enthalpy of the dissolution or precipitation process. With the help of these constants, TSS at any temperature can be obtained. Also, for a sample of unknown hydrogen concentration by determining the transition temperature corresponding to heating and / or cooling total hydrogen content of the sample can be estimated, using the aforementioned constant. TSS values determined for zircaloy-2 and Zr-2.5Nb alloy using dilatometry is presented in [16-17].

Hydride being brittle, makes the host matrix susceptible to embrittlement. Two forms of hydride embrittlement have been recognized for hydride forming metals - gross and localized [3]. The former requires certain minimum volume fraction of the hydride phase and results in overall reduction in tensile ductility, impact and fracture toughness. Since hydride embrittlement is a major life limiting factor for the components made from these alloys, several theoretical and experimental studies have been carried out, to understand the influence of hydrogen / hydride on the mechanical properties in general and micromechanisms assisting crack nucleation and its propagation in the presence of hydride, in particular [18]. The influence of hydrides on fracture toughness parameters of Zr-2.5Nb pressure tube material is brought out in [18].

The Zr-2.5Nb alloy pressure tubes for the Indian PHWRs are manufactured at the Nuclear Fuel Complex (NFC), Hyderabad, following a fabrication route similar to the modified route II developed by the Atomic Energy of Canada Limited (AECL) for the Pressure Tubes (PT) of CANDU reactors. The modified route II consists of two cold working steps (instead of one cold working step in the conventional route) and an intermediate annealing step. The lower extrusion ratio employed in the modified route as compared to the conventional route, ensures lower aspect ratio of grains, less intense circumferential basal pole texture and more uniform microstructure, resulting in improved irradiation resistance, reduced susceptibility to stress reorientation of hydrides, and uniform mechanical properties across the length of the tube [19]. Two minor differences in the fabrication steps of Indian tubes and modified route II developed by AECL need to be noted: viz., (i) the amount of cold work imparted during first cold working stage of tube fabrication at NFC is larger (50-55 %) as compared to the modified route II (20%) followed by AECL and (ii) compared to cold drawing practiced by AECL, at NFC, cold work is imparted using a process called pilgering, which imparts simultaneous reduction of wall thickness and diameter.

During fabrication of Cold Worked and Stress-Relieved (CWSR) Zr-2.5Nb pressure tube, majority of the α-Zr grains acquire an orientation with their basal poles, oriented predominantly along the circumferential (~55%) and radial (~43%) direction [19]. Since hydride precipitation in a-Zr grains show a habit plane nearly parallel to basal plane [20-21], for the texture of the pressure tube material, crystallographically only two orientations are permissible. These are along the circumferential-axial plane and along the radial-axial plane. Hydride platelets oriented along the circumferential-axial plane are called circumferential hydrides and those oriented along radial-axial plane are called radial hydrides [22]. Under unstressed condition, only circumferential hydrides form in Zr-2.5Nb pressure tubes. However, due to stress reorientation phenomenon, radial hydrides may precipitate and being oriented normal to hoop stress direction of the pressure tubes, can significantly increase the latter's susceptibility to failure. The phenomenon of precipitation of radial hydrides, when cooled under stress from solution annealing temperature, is known as stress-reorientation of hydrides. For dilute Zr-alloy pressure tubes, this translates to precipitation of radial hydrides under hoop stress, as compared to the precipitation of circumferential hydrides in the unstressed condition. This is usually associated with a critical stress called threshold stress below which, no reorientation occurs. The stress reorientation behaviour for Zr-2.5Nb alloy is presented in [23-25].

Delayed Hydride Cracking (DHC) [22] is a form of localized hydride-embrittlement phenomenon, which in the presence of a hydrostatic stress-field manifests itself as a sub-critical crack growth process. It is caused due to hydrogen migration up the hydrostatic stress gradient to the region of stress concentration. Once the local solid solubility is exceeded, brittle hydride nucleates normal to tensile stress. Growth of hydride nuclei continues till hydride platelet of a critical size is formed. Hydride platelet of the critical size cracks under concentrated stress, leading to the growth of the crack. This crack growth is delayed by the time required for hydrogen to reach the crack tip and form hydride platelet(s) of critical size. Hence this phenomenon is called Delayed Hydride Cracking. DHC behaviour of this material is described in section 7 [26-34] in terms of DHC velocity, activation energy and threshold stress intensity factor.

In PHWRs, Calandria Tube (CT) surrounds the PT concentrically from outside and separates the cool moderator (at $\sim$343 K) from hot coolant (at 523-563 K). Though, Garter springs are provided at regular intervals in the annulus gap between the PT and CT, to prevent PT-CT contact, either due to garter spring displacement from the designed location or due to creep or both, the PT sags and may contact CT, resulting in setting-up of thermal gradient in the PT. Hydrogen migration under thermal gradient in zirconium alloys results in formation of hydride blisters. An array of blisters makes Zirconium alloy components of nuclear reactors susceptible to fracture. The whole process of hydride blister formation and fracture of these components is very complex and involves hydrogen migration under thermal gradient, hydride precipitation, straining of the matrix, setting up of hydrostatic stress gradient, enhanced hydrogen migration under the combined influence of thermal and stress gradient, stress-reorientation of hydrides, cracking of hydrides, crack growth by delayed hydride cracking mechanism, interlinking of blisters and spontaneous fracture of the component. The stress components in hydride blisters and the surrounding matrix for certain assumed blister depths were determined for semi-ellipsoidal blister using Finite Element Method (FEM) and are described in [35-39].

Hydride acquires plate shaped morphology and the broad face of the hydride plate coincides with certain crystallographic plane of α-Zr crystal which is called habit plane. Two different theoretical approaches are used, to determine the shape and habit plane of precipitates viz., geometrical and solid mechanics [40]. For the geometrical approach, invariant plane and invariant-line criteria have been applied successfully and for the solid mechanics approach, strain energy minimization criteria have been used successfully [41-43]. Even though the aforementioned theoretical approaches are different, they often predict same shape and orientation for plate type inclusions [44]. Solid mechanics approach using strain energy computed by FEM technique have been applied to hydride precipitation in Zr-alloys, but the emphasis has been on understanding the solvus hysteresis [45-47]. A FEM based technique used to predict the habit plane of δ-hydride precipitating in α-Zr using strain energy minimization technique, is described in [48-49].

Hydrogen charging techniques [3-4]

Gaseous hydrogen charging and electrolytic hydrogen charging techniques are widely used, for introducing controlled amount of hydrogen in Zr-alloy samples. In gaseous hydrogen charging technique, Zr-alloy samples are heated in hydrogen atmosphere, either under constant pressure for different time-periods or in a constant volume system. In the former i.e. constant hydrogen partial pressure system, time-period for which the sample is exposed, determines the hydrogen concentration. In the constant volume system, the average hydrogen concentration of the sample is estimated from the product of system volume and the difference between the initial and final partial hydrogen pressures of the system. The beauty of this technique is that, the samples can be hydrided completely i.e. the amount of hydrogen charged is not limited to the terminal solid solubility of hydrogen in the alloy. Further, this technique can also be used for charging hydrogen under constant pressure. Fig. 1(a) shows photograph of gaseous hydrogen charging apparatus.

In electrolytic hydrogen charging technique, first sufficiently thick and adherent layer of hydride is deposited on the sample surface. The sample with hydride layer is homogenized at a pre-determined temperature, to attain equilibrium. After homogenization, the excess hydride layer is removed by machining. In this technique, the amount of hydrogen charged into the sample, cannot exceed the TSS at the homogenization temperature.

Direct Current Potential Drop (DCPD) technique [5]

The electrical potential drop method is one of the most commonly used techniques, for measuring crack initiation and crack growth, at elevated temperatures. In this technique, the increase in electrical resistivity

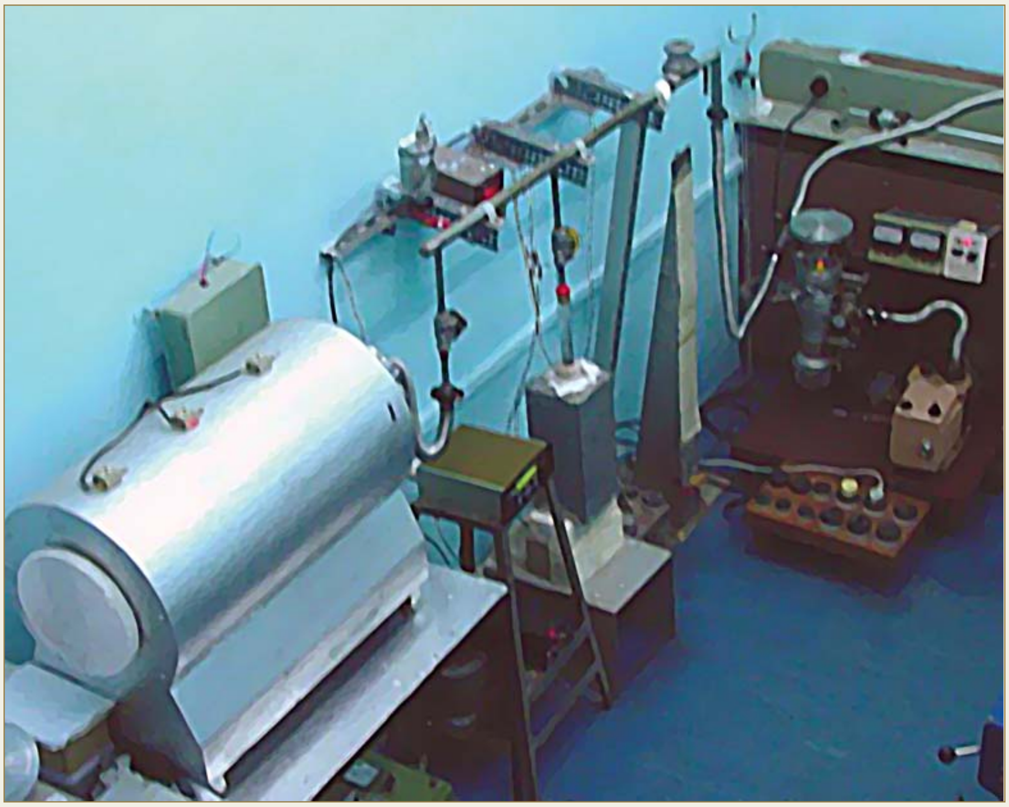

Fig.1(a): Photograph of the gaseous hydrogen charging facility set up to charge pressure tube spools of length up to 200 mm with controlled amount of hydrogen. (a) Tubular furnace for holding specimen, (b) Capacitance manometer indicator, (c) Capacitance manometer gauge head, (d) Tubular heater for heating hydrogen source and (e) Vacuum pumping system [3-4].

of a specimen to which a constant DC current is applied is used, to monitor crack extension. The main advantages of the dc potential drop method are the comparatively simple test set-ups and the capability of the technique to derive a correlation between crack length and potential drop in a certain type of specimen, by means of either analytical or numerical calculations. By measuring DCPD output across standard specimens with known crack length and by plotting the normalized DCPD output against the crack length (a) or the normalized crack length, a/W (where W is the specimen width), calibration curve can be generated. Similarly, by measuring the DCPD output as a function of temperature, the temperature dependence of the output voltage can be established. A combination of these two curves can be used, for crack growth monitoring. The main features of the DCPD system used for crack growth monitoring are described below.

DCPD system consists of a constant current unit to supply a constant dc current, an arrangement to supply this current through specimen, an arrangement to measure the potential drop across the notch/crack in the specimen and provision to record the DCPD output, temperature and current continuously. The current was supplied to the specimen through screw tightened copper lugs, welded to copper wires. The DCPD output was measured using the wire of the same material (in this case Zr–2.5Nb), to avoid error due to thermocouple effect. For this purpose, 0.5 mm diameter Zr–2.5Nb wires were spot-welded to CCT specimen, within 1mm of each side of the notch. A constant dc current was used for fracture toughness and DHC tests. The DCPD signal, specimen and furnace temperatures and current were continuously recorded on 12-channel videographic XY recorder. This DCPD system has been developed by the Materials Group, using in-house resources and expertise and is being regularly used for crack length estimation, during fracture toughness and DHC tests.

Terminal Solid Solubility (TSS) [16-17]

When a Zr-alloy sample containing hydride is heated, with increase in temperature, TSS increases resulting in dissolution of hydride in the matrix. For zirconium alloys, hydride dissolution is associated with increase in sample volume. On the other hand, when zirconium alloy sample containing hydrogen is cooled down, hydride precipitation takes place, resulting in decrease in sample volume. Using dilatometer, it is possible to detect the temperature corresponding to end of hydride dissolution during heating and beginning of hydride precipitation during cooling. For a given hydrogen concentration, the temperature corresponding to end of dissolution is called T_{TSSD} and the temperature corresponding to beginning of precipitation is called T_{TSSP}. On the other hand, for a given temperature, the amount of hydrogen in solution during heating and cooling are called TSSD and TSSP, respectively.

Both T_{TSSD} and T_{TSSP} for hydrogen in zircaloy-2 and Zr-2.5Nb pressure tube material was determined, using dilatometry from thermal strain (*e*) vs. *T* plots, its average slope (*m*) vs *T* plots and differential strain (*Diff. e*) vs *T* plots. The average slope was the ratio of change in length of the sample and temperature with respect to reference values. The differential strain was taken as the difference between the strains of the hydrogen charged sample and that of the unhydrided one. The values of the Arrhenius parameters i.e. pre-exponential constant, *A*, and heat of solution, ΔH_s, for zircaloy-2 and Zr-2.5Nb pressure tube material are listed in Table 1. As is evident from this table, the values of TSSD and TSSP, obtained by the three methods were in good agreement. Though very small scatter was observed between the TSSD values obtained in the present investigation, the TSSP values obtained from the three methods were nearly identical.

Once solid solubility is exceeded hydride phase precipitates in Zr-alloys. A typical micrograph revealing hydrides in Zr-2.5Nb pressure tube material, is shown in Fig. 2(a). For a given hydrogen content, two features of the traces of hydride on Radial-Circumferential (RC) plane and that on the Axial-Radial (AR) plane of the pressure tube, are to be noted in this figure. Firstly, the trace on radial-axial plane is straighter and longer as compared to the trace on radial-circumferential plane. This is expected because the longer α phase grain dimension along the axial direction of the pressure tube, provides uninterrupted growth along axial direction. The branching of the hydride on the

Table 1: The pre-exponential constant A and Enthalpy of the hydride dissolution or precipitation obtained during heating and cooling for zircaloy-2 and Zr-2.5Nb (in parentheses) pressure tube materials [16-17].

Transition temperature obtained from	ΔH_s (kJ/mol)	*A*	Regression coefficient
Heat up cycle			
Strain vs. temperature	30.003 (35.44)	38177.7 (63576.55)	0.9352 (0.95)
m vs. temperature	33.78	81626.0	0.9554
Differential Strain vs Temp.	34.55	94041.5	0.9192
Cool down cycle			
Strain vs. temperature	25.93 (17.21)	28536.5 (3235.6)	0.9626 (0.96)
m vs. temperature	26.00 (17.99)	29250.0 (3789.5)	0.9573 (0.94)
Differential Strain vs Temp.	26.315 (22.82)	31236.0 (12209.8)	0.9663 (0.99)

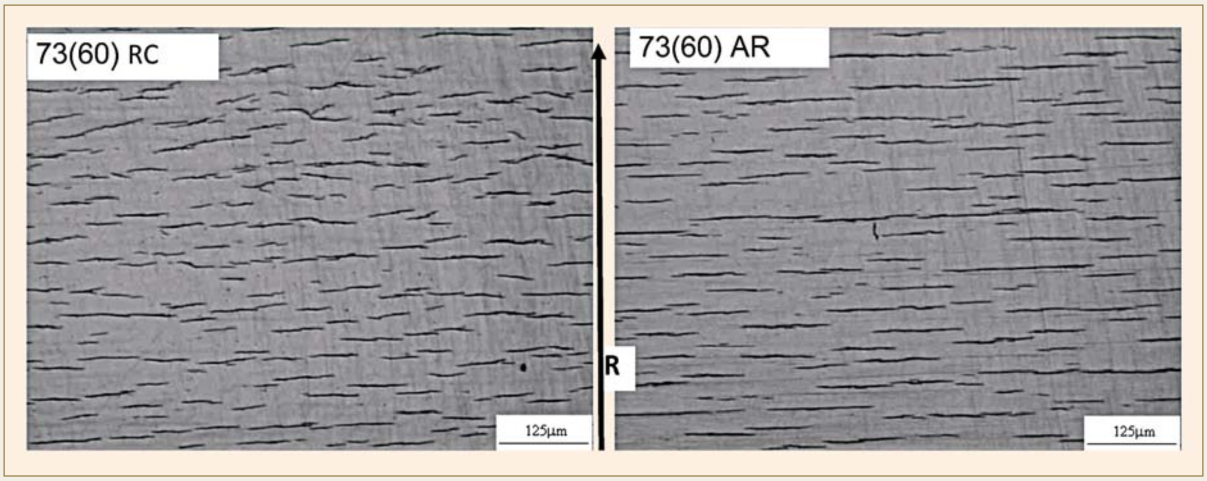

Fig. 2(a): The microstructural features of traces of hydrides on two orthogonal planes (AR and RC) of Zr-2.5Nb pressure tube alloy charged with 73 (60) ppm of hydrogen. Arrow shows the radial direction and axial or circumferential direction in these micrographs is normal to it.

radial-circumferential plane, is due to shorter grain dimension along the circumferential direction of the pressure tube. Interesting microscopic details of the circumferential hydride plates are brought out in Fig. 2(b). The hydride plates, which appear as a single entity under optical microscope, show two sub-microscopic levels of organization. At platelet level of organization, the hydride plates comprise of several smaller hydride platelets, stacked with a near parallel orientation with respect to each other. At sub-platelet level of organization, each hydride platelet was observed to be comprising of several tiny sub-platelets, stacked closely, either laterally or end to end.

Fracture Toughness [18]

The material used for fracture toughness tests were from double melted, autoclaved, unirradiated Zr-2.5Nb pressure tube spools, gaseously charged with different hydrogen concentrations. Metallographic examination suggested that, hydride plates were oriented along circumferential-axial direction of the tube. Curved Compact Toughness (CCT) specimens of width 17 mm were machined from these spools with crack plane along axial-radial plane to facilitate crack propagation along axial direction of the tube. The fracture toughness testing procedure recommended in ASTM

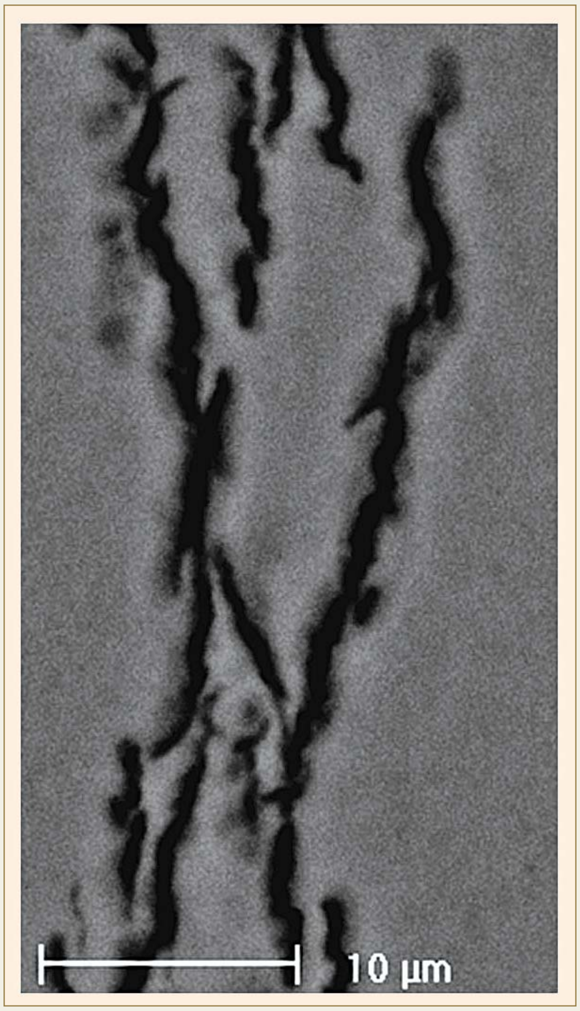

Fig. 2(b) Internal details of circumferential hydride as observed in secondary electron mode.

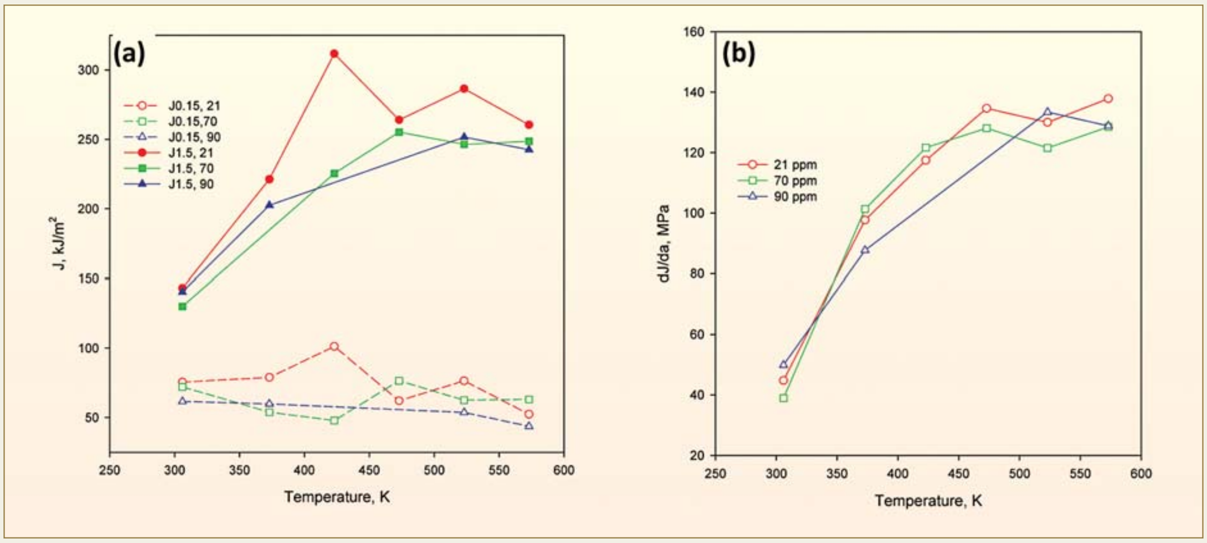

Fig. 3: Influence of test temperature on (a) $J_{0.15}$ and $J_{1.5}$ and (b) *dJ/da* values of Zr-2.5Nb pressure tube alloy containing different amounts of hydrogen [18].

standard E-813 was followed in the present investigation, except for the fact that the crack length was determined using Direct Current Potential Drop (DCPD) technique, which facilitated the use of single specimen technique, for fracture toughness parameter determination.

The Influence of test temperature on (a) $J_{0.15}$ and $J_{1.5}$ and (b) mean *dJ/da* values of Zr-2.5Nb pressure tube alloy, containing different amounts of hydrogen is shown in Fig. 3. The fracture initiation parameters $J_{0.15}$ appear to be mildly decreasing with increase in test temperature, though for the samples containing 21 wt. ppm of hydrogen, the scatter in data was large. The crack propagation parameters such as $J_{1.5}$ and mean *dJ/da,* increased with increase in test temperature and appear to be reaching a saturation value at higher test temperatures, suggesting that, this data represents the high temperature part or upper shelf of the typical S-curve, exhibited by the temperature dependence of fracture energy. It may be noted that, the mean *dJ/da* data showed least scatter as compared to other parameters. Also, the difference between crack initiation fracture toughness parameters and crack propagation parameters increases, with increase in test temperature.

The variation in critical crack length for the catastrophic failure of pressure tubes under reactor operating condition with hydrogen content and test temperature, is listed in Table 2. The value of *CCL* computed from J_Q values by iterative method, in the present investigation, was > 54 mm for all the hydrogen concentrations and test temperatures. The CCL value was highest at 423 K and for lowest level of hydrogen.

Stress-Reorientation of Hydrides [23-25]

The threshold stress for reorientation of hydrides was determined, using a hydrogen charged tapered gage tensile specimen, heating it to a solution annealing temperature, to dissolve all the hydrides, cooling from solution annealing to a reorientation temperature, applying a constant load so as to attain stress variation across the specimen axis, and allowing the specimen to cool under load. After cooling, the specimen is slit axially, examined metallographically for hydride orientation, a montaze is prepared for the entire sample, the boundary between radial and circumferential hydride is marked and local and mean threshold stresses are determined [23-25]. Leger and Donner [50], based on their observation of the existence of a marked boundary between the radial and circumferential hydrides across the thickness of the pressure tubes, concluded that, a variation in threshold stress across the pressure tube thickness, is due to residual stresses in these materials. The difference between the mean threshold stress value and the local threshold stress across the thickness, yielded the residual stress variation, across the pressure tube thickness.

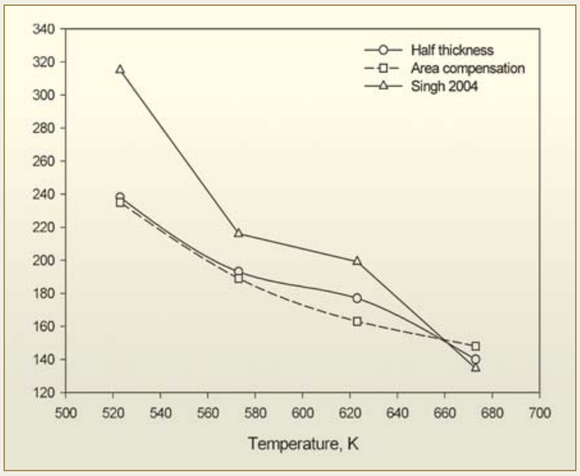

Fig. 4: Variation in mean threshold stress with reorientation temperature [24].

Fig. 4 shows the variation of the mean threshold stress with reorientation temperature and is observed to decrease with increase in reorientation temperature. The threshold stress for reorientation of hydrides in CWSR Zr-2.5Nb pressure tube material, shown in Fig. 4, were determined using a tapered gage tensile specimen, having its axis parallel to circumferential direction of tube. The tapered gage specimens were gaseously charged with controlled amount of hydrogen and subsequently allowed to cool under a constant load. A montage of the micrographs prepared by sectioning the specimen along its axis, revealed hydride plate orientation as a function of stress. A unique value of the threshold stress called mean threshold stress for reorientation of hydrides in dilute zirconium alloys, was determined by two methods, viz. half thickness methods and area compensation method [50]. Also plotted in Fig. 4 for comparison, is the mean threshold stress value for this alloy, reported by Singh et al [23]. Fig. 5 shows the variation in residual stress (difference of local threshold stress and its mean value) across the thickness of the pressure tube, at various reorientation temperatures. It was observed that the residual stresses are tensile near the inside diameter of the tube, whereas, these are compressive towards the outer diameter of the tube. Both the peak residual tensile and compressive stresses, were observed to decrease, with increase in reorientation temperature [24].

Table 2: CCL (mm) for catastrophic failure of Zr-2.5Nb pressure tubes under PHWR operating condition computed from J_Q values obtained in this work at various test temperatures and hydrogen contents [18].

S. No.	Temperature, K	21 wt. ppm	70 wt. ppm	90 wt. ppm
1.	306	57.6	56.0	56.0
2.	373	59.6	54.8	59.2
3.	423	73.0	55.0	59.2
4.	473	61.2	60.4	--
5.	523	65.6	61.8	57.2
6.	573	57.2	58.0	55.2

Delayed Hydride Cracking [5,26-34]

DHC is a discontinuous crack growth process and is usually associated with an incubation period to crack initiation, a stable crack growth velocity called DHC velocity (V_{DHC}) and a threshold stress intensity factor - SIF (K_{IH}). Below K_{IH}, V_{DHC} is negligible and above this threshold V_{DHC} increases rapidly with increase in SIF up to K_{IY} (SIF corresponding to initiation of plastic yielding at the crack tip). For SIF greater than K_{IY}, V_{DHC} is independent of the SIF. A second higher threshold SIF corresponds to fracture toughness of the material above which, crack grows in an unstable manner. V_{DHC} is influenced to a varying degree by test temperature, direction of approach of test temperature, strength of alloy, hydrogen content, crystallographic texture and microstructure of the material.

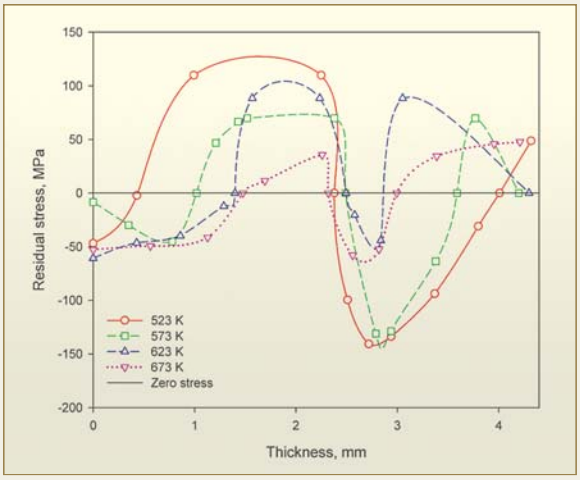

Fig. 5: Variation in residual stress across the thickness of the pressure tube at various reorientation temperatures [24].

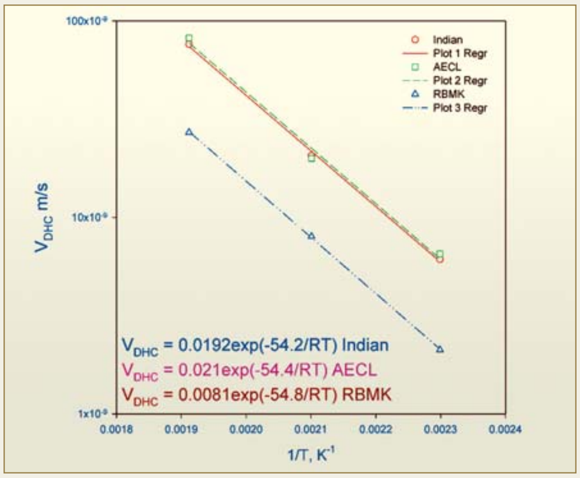

Fig. 6: The plots of DHC velocity (V_{DHC}) in Zr-2.5Nb pressure tube materials with inverse of test temperature [26].

Fig. 6 shows the plot of DHC velocity with inverse of the test temperature for CANDU, RBMK and Indian pressure tube material. The temperature dependence of V_{DHC} obtained by linear regression analysis is also shown in this figure. The superscripts denote the source of the material. At a given test temperature, the DHC velocity for the Indian and the CANDU pressure tubes, both of which are used in Cold Worked and Stress-Relieved (CWSR) condition, are comparable whereas the DHC velocity in RBMK pressure tube, which is used in quenched and aged condition, is about 2 to 3 times lower than that in CWSR pressure tubes. The variation in DHC velocity (V_{DHC}) with stress intensity factor (K_I) is shown for Indian pressure tube material in Fig. 7 as a function of test temperatures. For stress intensity factor (K_I) > 15 MPa.m$^{1/2}$, DHC velocity is practically independent of the SIF and below this value, DHC velocity decreases appreciably with decrease in K_I. The extrapolation of the plots, suggests a threshold stress intensity value of about 9-11 MPa.m$^{1/2}$ for the temperature range of 476-556K [27].

Stress Field around Hydride Blister [35-39]

For computation of stress field around hydride blister, the matrix of dimension in the ratio 1:5 was considered. Zr was modeled with transversely isotropic elastic constants [51] and zirconium hydride [52] was modeled with isotropic elastic constants. Computations were made corresponding to materials properties at 400 °C for an axisymmetric case, with the symmetry axis along vertical direction (Figs. 8 & 9) and hydride / matrix yield strength ratios of 0.2 and 1.0. The body was partitioned into several small layers, with each layer transformed sequentially (multi-step) or simultaneously (single step). 2263 number of8-node axisymmetric quadrilateral element

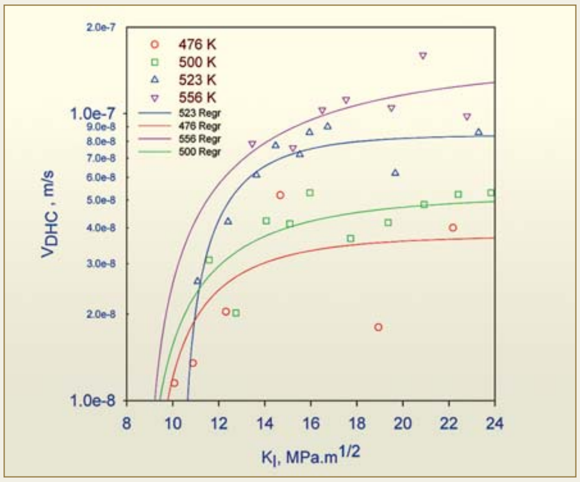

Fig. 7: Plot of DHC velocity with stress intensity factor for unirradiated cold worked and stress-relieved Zr-2.5Nb Indian pressure tube samples tested at various temperatures [27].

was used. The phase transformation of the zirconium hydrogen solid solution into hydride, was simulated by imposing a temperature rise with appropriate thermal expansion constants to obtain 17.2 % increase in volume or a linear isotropic swelling strain of 5.7%, which was imposed incrementally using ABAQUS FEM package.

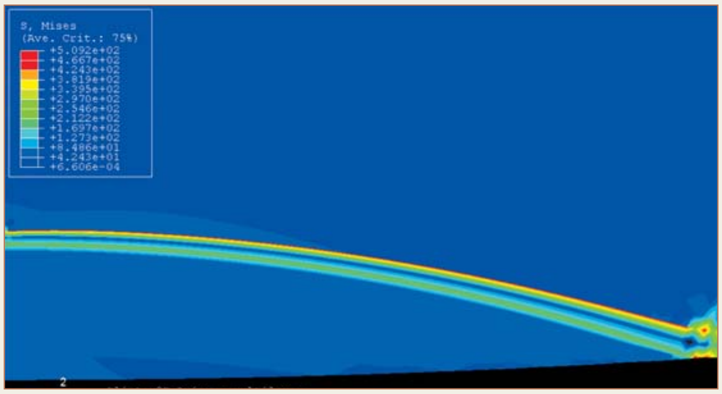

Fig. 8: Contour plot of equivalent stress in the soft blister and matrix around it. Phase transformation achieved in multiple steps [38].

The contour plot of the equivalent stress in the blister and matrix around it for the hydride / matrix yield strength ratio equal to 0.2 and computed by multi-step method is shown in Fig. 8. The scale is in units of MPa. It may be noted that the yield stress of the hydride is ~ 60 MPa and that of the zirconium is ~300 MPa [53]. As is evident from this figure, most of the regions inside the blister and matrix, are under negligible stress, with a small strip near the boundary between blister and matrix, under very high stresses. Since the hydride was considered to have lower yield strength as compared to the matrix, most of the volume change is accommodated inside the blister by the plastic flow of hydride.

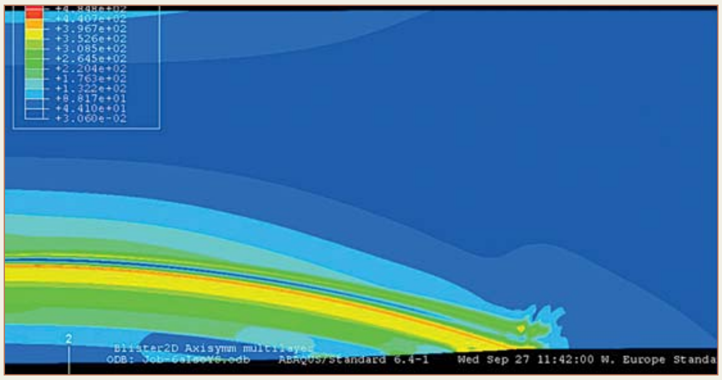

Fig. 9: Contour plot of equivalent stress in the blister and matrix around it for hydride/matrix yield stress ratio equal to unity. Phase transformation achieved in multiple steps [38].

The contour plot of the equivalent stress inside the blister and the matrix around it, with both the hydride and matrix having identical yield strengths (300 MPa) and computed by multi-step method, is exhibited in Fig. 9. The maximum value of equivalent stress was observed at the interface between blister and matrix. The stress decays as one moves away from the blister matrix interface. All earlier investigators [54-55] have simulated hydride formation by raising the temperature and allowing the phase transformation of the entire hydride in one step. For comparison, the contour plot of the equivalent stress inside the blister and inthe matrix around it, computed by single step method, is shown in Fig. 10. As is evident from Figs. 9 & 10, equivalent stresses in the blister and matrix

Fig. 10: Contour plot of equivalent stress in the blister and matrix around it for hydride/matrix yield stress ratio equal to unity. Phase transformation achieved in single step [38].

are higher for a single step transformation, than that for a multi-step transformation. The difference between the hydrostatic stress variation along direction 2 (corresponds to radial direction of tube) computed by single and multiple step methods, are shown in Fig. 11. Since hydride blisters grow sequentially, a single step phase transformation results in overestimation of the equivalent stress.

A section of the hydride blister [36] is shown in Fig.12a. It is evident from this figure, that the section of the hydride blister has three regions. Far away from the center of blister lies region I, comprised of the matrix and circumferential hydrides (horizontal dark lines). As one approaches the center of the blister, region II is reached which consists of the matrix, circumferential hydrides and radial hydrides (normal to circumferential ones). Region III comprises of single-phase hydride. The texture and microstructure of cold worked and stress relieved Zr-alloy tube is such that, under the unstressed condition of hydride precipitation, circumferential hydrides form. When hydride precipitation takes place under stress greater than a threshold value, radial hydrides may form.

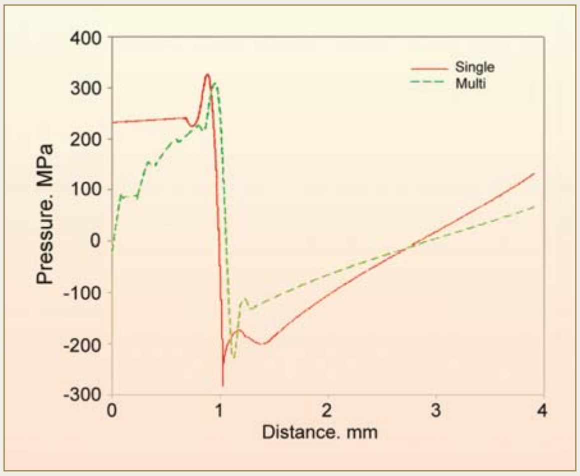

Fig. 11: Plot of pressure, $-(s_{11}+s_{22}+s_{33})/3$, variation with distance along direction 2 for single and multi step transformation of matrix to hydride [38].

In Fig. 12(b), the threshold stress variation across the sample thickness is superimposed on the plots of computed stress for σ_{11} $x_2 = 0.2, 0.5$ and 1.0mm (in the figure it is denoted as a) [36]. The hydride platelet orientation at any location in the matrix around the blister is governed by the stresses generated due to the hydride blister. For any point in the matrix where prevailing tensile stress is greater than the threshold stress for reorientation of hydrides, radial hydrides will also precipitate out.

Accommodation Energy of Hydrides and Its Habit Plane [48-49]

The accommodation energy of δ-hydride in α-Zr single crystal was computed by initial strain method. The body was partitioned into two parts viz., Hydride and matrix. Transformation of the zirconium hydrogen solid solution into δ-hydride is associated with about 17 percent positive change in volume [20]. The phase transformation was simulated by imposing a temperature rise in hydride, assigned with appropriate thermal expansion constants. The computation was carried out to determine the influence of hydride plate orientation on the accommodation energy.

The plots of normalized accommodation energy with hydride nuclei orientation for the case where hydride is isotropic elastically and matrix is transversely isotropic elastically, is presented in Fig. 13. The accommodation energy values were normalized with value corresponding to the zero degree orientation, which corresponds to the case where broad face of hydride disk is oriented normal to the c-axis of α-Zr hcp crystal. The normalized accommodation energy shows minima for zero degree orientation for fully elastic case, suggesting basal plane of α-Zr phase as the habit plane of δ-hydride. However, transformation of α -Zr-H solid solution to δ-hydride is associated with about 17 percent increase in volume. Such a large increase in volume is likely to cause plastic deformation of both hydride and the matrix surrounding it. Hence, dependence of accommodation energy on hydride

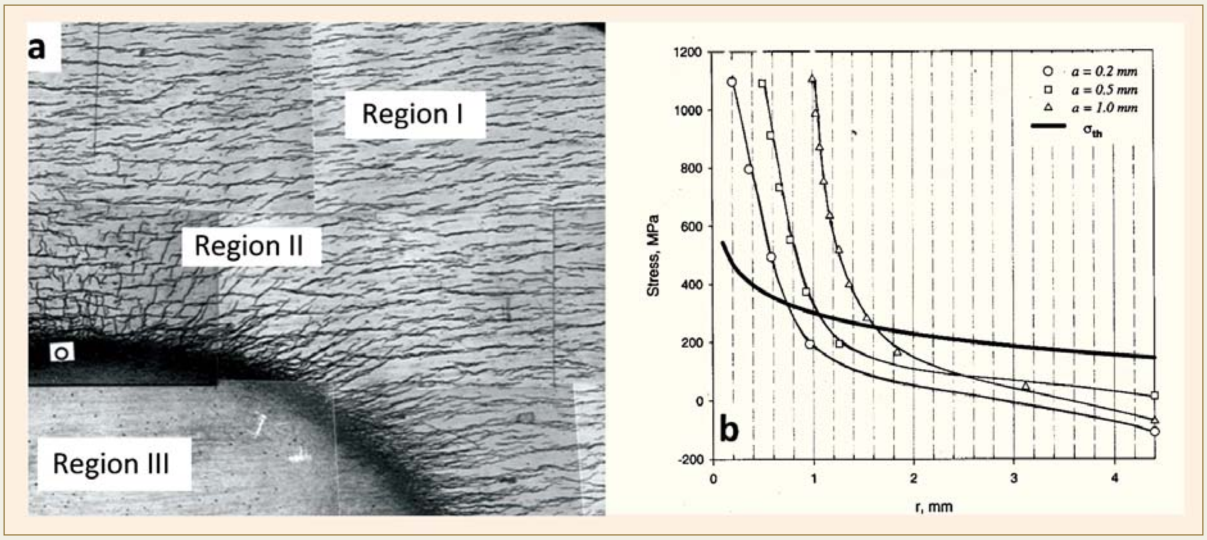

Fig. 12: (a) A section of blister in Zr-alloy. (b) Comparison of the computed stress σ_{11} and the threshold stress for reorientation of hydrides across the thickness of the plate used for growing the hydride blister [36].

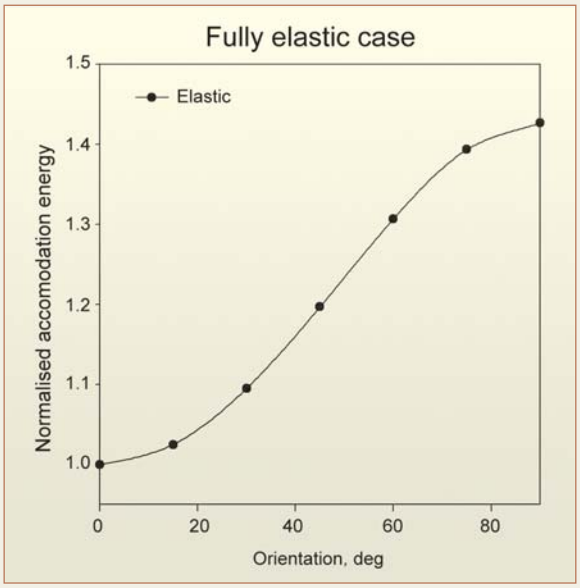

Fig. 13: Plot of accommodation energy with hydride nuclei orientation for fully elastic case [49].

nuclei orientation, was also determined for elasto-plastic case. The hydride phase was modeled to behave isotropically both elastically and plastically [52]. The matrix phase was modeled to exhibit transverse isotropic elastic behaviour [51] and either isotropic plastic behaviour (plastic or WH) or transverse isotropic plastic behaviour (Hill) [53]. Both perfect plastic behaviour (plastic) and linearly work-hardening (WH) behaviour was considered. The material model allowed linear increase in flow stress with plastic strain, resulting in ultimate tensile strength 25 percent greater than the Yield Strength (YS) of the material corresponding to a plastic strain of 10 percent.

The plots representing the variation in accommodation energies with hydride nuclei orientation for the elasto-plastic hydride and matrix is shown in Fig. 14. The plots of elastic component of accommodation energies (Fig. 14a), plastic dissipation energy (Fig. 14b) and total accommodation energy (Fig.14c) with orientation are shown for Iso-YS case, where both hydride and matrix have identical YS. The data in Fig.14 represented by circular symbols, correspond to perfect isotropic plasticity, square symbol correspond to linear work-hardening isotropic plasticity, triangular symbol correspond to perfect Hill's plasticity and inverted triangular symbol correspond to linear work-hardening Hill's plasticity behaviour of matrix. Both elastic accommodation and plastic dissipation energy values for linear work-hardening case were always higher than the corresponding values for perfect plastic case, resulting in total accommodation energy values for the former greater than the latter. The elastic accommodation energy values for Hill's plastic case

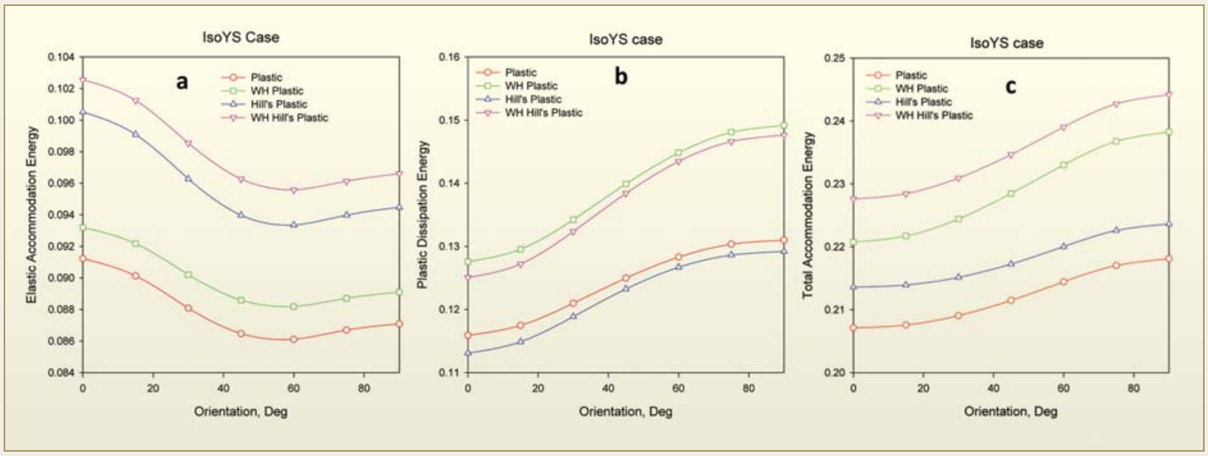

Fig. 14: Variation in accommodation energies with hydride nuclei orientation for Iso-YS case. The variation in elastic accommodation energy (a) plastic dissipation energy (b) and total accommodation energy (c) with orientation is shown [49].

was always greater than the corresponding values for isotropic plastic case, whereas plastic dissipation energy for the former was lower than the corresponding values for the latter. However, the difference between the elastic accommodation energy was greater than that for plastic dissipation energy,resulting in total accommodation energy for the Hill's plastic case being greater than the corresponding value for isotropic plasticity case.

For Iso-YS case (Fig. 14a), the elastic accommodation energy decreases with increase in orientation angle, reaches a minima at 60° and increases marginally with further increase in orientation. The plastic dissipation energy for iso-YS case (Fig. 14b) increased with increase in orientation angle. The plastic dissipation energy dominated the total accommodation energy values, ensuring that, the total accommodation energy increased with increase in orientation angle. Thus for elasto-plastic case also, accommodation energy shows minima for zero degree orientation, suggesting basal plane of α-Zr phase as the habit plane of δ-hydride.

Conclusions

Terminal solid solubility of hydrogen in Zr-alloy was determined using dilatometry and was found to be internally consistent. Up to 90 wppm of total hydrogen content, hydrides plates oriented along the circumferential-axial plane of the tube did not affect the fracture toughness appreciably. The threshold stresses were observed to decrease with increase in reorientation temperature. The difference between the local threshold stress and the mean threshold stress yielded the residual stress, which was observed to decrease with increase in reorientation temperature. For Zr-2.5Nb alloy manufactured by Q&A route delayed hydride crack growth rate (V_{DHC}) was lower as compared to those manufactured from CWSR route. Threshold stress intensity factor associated with DHC in unirradiated, cold-worked and stress-relieved Indian Zr-2.5Nb pressure tube alloy, was found to be about 9-11 $MPa.m^{1/2}$ in the temperature range of 476-556K. The stress field in the hydride blister and Zr-matrix were estimated using the finite element method. The computed effective stress obtained by carrying out the single step transformation of a hydride is higher, as compared to that obtained by a multi-step transformation. The stress field could explain the formation of radial hydrides in the matrix near the interface region. For both fully elastic case and elasto-plastic case, the accommodation energy shows minima for zero degree orientation, suggesting basal plane of a-Zr phase as the habit plane of δ-hydride.

Acknowledgements

Constant encouragement and support from Dr. A. K. Suri, Director, Materials Group, Mr. R. K. Sinha, Director, RDDG, Mr. H. S. Kamath, Director, Nuclear Fuels Group, BARC, Mr. K. B. Dixit, Director (Technical) NPCIL and Mr. S. K. Chande, Vice-Chairman, AERB is acknowledged.

It was a pleasure to discuss this work with Prof. B. P. Kashyap, of IIT Bombay, Late (Dr.) P. Rodriguez former Director, IGCAR, Dr. N. Ramakrishanan, former Director, RRL, Bhopal, Dr. P. K. De, former Head, MSD, BARC and Late (Dr.) T. K. Sinha, former Head, Mechanical Metallurgy Section, BARC.

Contribution of Dr. R. Kishore, Mr. S. Roychowdhury, Mr. S. Mukherjee, Mr. R. Kameswaran and Ms. Smita S. Sheelvantra of BARC in some of the experimental work and of Prof. P. Ståhle of Malmö University, Sweden, Prof. Matti Ristmanaa of Lunds University, Sweden, Prof. Leslie Banks-sills of Tel Aviv University, Israel and Prof. A. A. Shmakov of Moscow Engineering Physics Institute, Russia in modeling and simulation work is sincerely acknowledged.

Suggestions from Dr. M. Sundararaman, Dr. G. K. Dey, Dr. K. Madangopal, Mr. I. S. Batra, Mr. R. K. Fotedar, Dr. Raju Ramanujan (formerly) of Materials Group, BARC provided during the course of this work were indeed useful.

Help and support from Mr. Manjit Singh, Associate Director, Automation & Manufacturing Group, Mr. B. K. Shah, Head QAD, Mr. K. C. Sahoo, RRF, Mr. D. N. Sah, RRF, Dr. G. P. Tewary, RRF of BARC, Mr. B. Gopalan, formerly Control Lab. NFC and Mr. S. Vijayakumar, CE, NPCIL is acknowledged.

The authors thank all round robin participants in IAEA sponsored CRP (the results of which were published as IAEA-TECDOC 1410) for their cooperation in general and Dr. Ian Ritchie, former Scientific Secretary, Division of NFC&WT, Vienna, IAEA and Dr. C.E. Coleman, formerly of AECL in particular for their valuable support.

Authors are thankful to Mr. K. C. Majumdar, Mr. R. V. Hatwar, Mr. S. Yadav, Mr. R. Hankare for technical assistance and to Mr. A. K. Singh, Mr. Santosh Kumar and Mr. Niraj Kumar, Mr. V. P. Sinha trainee officers of HRDD, BARC for assistance in carrying out a part of the experiments. The help rendered by undergraduate summer trainees Mr. Sriram Sagar Singh, Mr. Lala Mikin R., Ms. Anuja Gupta, of IIT Roorkee, Ms. Sireesha K. and Mr. T. R. Gopinath, MGIT, JNTU, Hyderabad, K. Sairam, Salem Engg College, Tamilnadu is duly acknowledged.

References

1. R. N. Singh, S. Chatterjee and S. Banerjee, "PHWR Coolant channel safety issues – A metallurgical perspective" Chapter 3: Nuclear Reactor Safety, Eds. S. Banerjee & S. K. Gupta, Publisher: Board of Research in Nuclear Sciences, DAE, BARC, Mumbai-400085. India (2007) pp 81-123.
2. Lemaignan C., & Motta A. T., "Zirconium alloys in nuclear applications" *Materials Science & Techno. A Comprehensive treatment,* eds. R. W. Cahn, P. Haasen & E. J. Kramer, 10B chapter 7, (1994) 1.
3. R. N. Singh, Ph. D. Thesis, IIT Bombay 2002.
4. R. N. Singh, R. Kishore, S. Mukherjee, S. Roychowdhury, D. Srivastava, B. Gopalan, R. Kameswaran, Smita S. Sheelvantra, T. K. Sinha, P. K. De and S. Banerjee, "Hydrogen charging, hydrogen content analysis and metallographic examination of hydride in Zirconium alloys" BARC report No. BARC/2003/E/034.
5. Singh R. N., Kumar N., Kishore R., Roychowdhury S., Sinha T. K. and Kashyap B. P., "Delayed Hydride Cracking in Zr-2.5Nb Pressure Tube Material" *Journal of Nuclear Materials* vol. 304, (2002) pp-189-203.
6. Erickson, W. H., and Hardie, D., The Influence of Alloying Elements on Thermal Solubility of

Hydrogen in alpha Zr, *Jl. of Nucl. Mater.*, 18 254 (1964).

7. G. F. Slattery *J. Inst. of Metals*, 95 43 (1967).
8. Mishima, Y., Ishino, S., and Nakajima, S., "A resistometric study of solution and precipitation of hydrides in unalloyed zirconium", *J. of Nucl. Mater.*, 27 (1968) pp. 335-344.
9. Mishra, S., and Asundi, M. K., "Determination of solid solubility limit of hydrogen in a Zr by internal friction measurement", Zr in Nuclear Applications, ASTM STP 551, Amecrican Soc. For testing and Materials, 1974, pp. 63-71.
10. Ritchie, I. G., and Sprungmann, K. W., "Hydride precipitation in zirconium studied by low frequency pendulum techniques", *Journal de physique, Colloque C9, supplement 12, Tome 44* Dec. 1983, pp. 313-318.
11. Pan, Z.L., Ritchie, I.G. and Puls, M.P., The terminal solid solubility of hydrogen and deuterium in Zr-2.5Nb alloys, *Jl. of Nucl. Mater.*, 228(2) 227-237 (1996).
12. Khatamian, D., Pan, Z. L., Puls, M. P., and Cann, C. D., "Hydrogen solubility limits in Excel, an experimental Zr-based alloy", *J. of Alloys and Compounds*, 231 (1995) pp. 488-493.
13. Fong, R. W. L., and Spooner, S., Investigation of zirconium hydrides and hydrogen solubility limit in Zr-2.5 Nb alloy by small angle neutron scattering, *Scripta-Metall. et Mater.*, 30(5) 649 (1994).
14. Root, J. H., and Fong, R. W. L., "Neutron diffraction study of the precipitation and dissolutionof hydrides in Zr-2.5Nb pressure tube material", *J. Nucl. Mater*. 232 (1996) pp. 72-85.
15. Cann., C. D., and Atrens, A., "A metallographic study of the terminal solid solubility of hydrogen in zirconium at low hydrogen concentrations", *J. Nucl. Mater.* 88 (1980) pp. 42-50.
16. R. N. Singh, S. Mukherjee, Anuja Gupta, R. Kameswaran, Smita S. Sheelvantra, P. K. De and S. Banerjee, "Determination of Terminal Solid Solubility of Hydrogen in Zr-alloy Pressure Tube Material using Dilatometry Technique" BARC report No. BARC/2004/E/010
17. Singh R. N., Mukherjee S., Gupta A. and Banerjee S., "Terminal Solid Solubility of Hydrogen in Zr-alloy Pressure Tube Materials", *Journal of Alloys and Compounds,* 389, (2005) *pp. 102-112*.
18. Singh R. N., Ståhle P. and Srinivasan N. S., "Influence of Hydrogen Content on Axial Fracture Toughness Parameters of Zr-2.5Nb Pressure Tube Alloy in the Temperature Range of 306-573 K", Proc. of Internl. Cong. on Adv. in Nuclear Power Plants 2006 – ICAPP-06 held at Reno Hilton, Neveda, USA on June 04-08, 2006.
19. Srivastava D., Dey G.K., Banerjee S., "Evolution of microstructure during fabrication of Zr-2.5 wt. Pct. Nb alloy pressure tubes", *Metall. Trans.* A 26A (1995) 2707.
20. K. Une, K. Nogita, S. Ishimoto, K. Ogata, *Jl. of Nucl. Sci. & Techn*. 41(7) (2004) 731.
21. D. G. Westlake: *J. of Nucl. Mater.*, Vol. 26 (1968), p. 208
22. Northwood D. O., and Kosasih U., "Hydrides and delayed hydrogen cracking in zirconium and its alloys", *Interntl. Met. Rev.,* 28(2) (1983) 92-121.
23. Singh R. N., Kishore R., Singh S. S., Sinha T. K. and Kashyap B. P., "Stress-reorientation of hydrides and hydride embrittlement of Zr-2.5 wt. % Nb pressure tube alloy" *Journal of Nuclear Materials* **325** (2004) pp. 26-33.
24. Singh R. N., Lala Mikin R., Dey G. K., Sah D. N., Batra I. S. and Ståhle P., "Influence of temperature on threshold stress for reorientation of hydrides and residual stress variation across thickness of Zr-2.5Nb alloy pressure tube", *Journal of Nuclear Materials* **359** (2006) pp.208-219.
25. R. N. Singh, R. Kishore and T. K. Sinha, "Studies on stress reorientation of hydrides in Zr-2.5Nb pressure tube alloy" BARC report no. BARC/2002/E/036.

26. Singh R. N., Roychowdhury S., Sinha V. P., Sinha T. K., De P. K. and Banerjee S., "Delayed Hydride Cracking in Zr-2.5Nb Pressure Tube Material: Influence of fabrication routes", *Materials Science and Engineering A* 374 (2004) pp. 342-350.
27. R. N. Singh, P. Ståhle, J. K. Chakravartty, A. A. Shmakov, "Threshold stress intensity factor for Delayed hydride cracking in Zr-2.5%Nb pressure tube alloy" *Materials Science & Engg.* A 2009 (in press).
28. R. N. Singh and S. Banerjee (as Co-Authors from BARC) in the *Final report of a coordinated research project 1998–2002* (2004): "Delayed Hydride cracking in Zirconium Alloys in pressure tube nuclear reactors", IAEA, Vienna, 2004, IAEA-TECDOC-1410, pp. 1-92.
29. R. N. Singh, S. Roychowdhury, R. Kishore, T. K. Sinha, P. K. De and S. Banerjee, (2003): "Delayed Hydride Cracking in Zr-2.5Nb Pressure Tube Material – Part III : IAEA co-ordinated research project" BARC Report No. BARC/2003/I/03.
30. R. N. Singh, T. K. Sinha, P. K. De & S. Banerjee, (2002): "IAEA sponsored round robin test on DHC - Hydride precipitation in Zr-2.5Nb pressure tube material" Final Report No. BARC.MSD.IAEA.2002.01 submitted during 3rd RCM, Nykoping, Sweden, July 1 to 5, 2002.
31. R. N. Singh, S. Roychowdhury, T. K. Sinha, P. K. De & S. Banerjee, (2002): "IAEA sponsored round robin test on delayed hydride cracking velocity measurement in axial direction of quadruple melted Zr-2.5Nb pressure tube material",Final Report No. BARC.MSD.IAEA.2002.03 submitted during 3rd RCM, Nykoping, Sweden, July 1 to 5, 2002.
32. R. N. Singh, Niraj Kumar, R. Kishore, S. Roychaudhury and T. K. Sinha, (2001): "Delayed hydride cracking in Zr-2.5Nb pressure tube materials – part II, BARC Report No. : BARC/2001/E/026.
33. R. N. Singh, R. Kishore, T. K. Sinha, S. Roychaudhury, P. K. De and S. Banerjee (2000): "IAEA sponsored round robin test on delayed hydride cracking velocity measurement in axial direction of the Zr-2.5Nb pressure tube material" Progress Report No. BARC.MSD.IAEA.2000.01 submitted at 2nd RCM, Pitesti, Romania, 5-9 June, 2000.
34. R. N. Singh, R. Kishore, Santosh Kumar, S. Roychaudhury, M. Unnikrishnan, T. K. Sinha, P. K. De, and S. Banerjee, (2000): "Delayed hydride cracking velocity and crack growth measurement using DCPD technique in Zr-2.5Nb pressure tube material" Materials Science Division, Materials Group, BARC Report No. 2000/E/038.
35. Singh R. N., Kishore R., Sinha T. K. and Kashyap B. P., "Hydride blister formation in Zr-2.5 wt. % Nb pressure tube alloy" *Jl. of Nuclear Materials* vol. 301, (2002) pp-153-164.
36. Singh R. N., Kishore R., Sinha T. K., Banerjee S. and Kashyap B. P., "Stress field estimation around a semi-constrained inclusion and its validation by interpreting hydride platelet orientation around a blister in a Zr-2.5Nb alloy" *Materials Science and Engineering A* 339, (2003) pp. 17-28.
37. R. N. Singh, R. Kishore and T. K. Sinha, (2001): "Hydride blister formation in Zirconium-alloy pressure tubes" BARC Report No. : BARC/2001/E/012.
38. Singh R. N. and Ståhle P., "Fracture of Zr-alloy pressure tubes due to hydride blister formation", Proc. of 19th Nordic Seminar in Computational Mechanics- NSCM19 hosted by Lund University, Faculty of Engineering on 20-21 October, 2006, Lund, Sweden.
39. R. N. Singh, P. Ståhle, K. Sairam, J. K. Chakravartty and B. P. Kashyap, "Stress-field Computation for Hydride Blister Forming in Zr-alloys" Paper No. 8137 presented at 2008 Water Reactor Fuel Performance Meeting held on October 19-23, 2008, Renaissance Seoul Hotel, Seoul, Korea.
40. M. Kato, T. Fuji, S. Onaka, *Acta Mater.*, 44(3) (1996) 1263.

41. U. Dahmen, P. Furguson, K. H. Westmacott, *Acta Metall*., **32** (1984) 803.
42. U. Dahmen, K. H. Westmacott, *Acta Metall*., 34 (1986) 475.
43. D. Duly, *Acta Metall*., 41 (1993) 1559.
44. M. Kato, T. Fuji, *Acta Metall*., 42 (1994) 2929.
45. M. P. Puls, *Acta Metall*., 32 (1984) 1259.
46. Leitch B. W. and Puls M. P.,, *Metall. Trans*., 23A (1992) 797.
47. B. E. Leitch, S. –Q. Shi, *Moedlling Simul. Mater. Sci. Engg*. 4 (1996) 281.
48. R. N. Singh, P. Ståhle, K. Sairam, Matti Ristmanaa, S. Banerjee, "d-hydride habit plane determination in a-Zirconium by strain energy minimization technique at 25 and 300 °C", Paper No. 8138 presented at 2008 Water Reactor Fuel Performance Meeting held on October 19-23, 2008, Renaissance Seoul Hotel, Seoul, Korea.
49. R. N. Singh, P. Ståhle, Leslie Banks-Sills, Matti Ristmanaa, S. Banerjee "ä-Hydride Habit Plane Determination in á-Zirconium at 298 K by Strain Energy Minimization Technique" *Defect and Diffusion Forum Vol. 279 (2008) pp 105-110*.
50. Leger M. and Donner A., "The effect of stress on orientation of hydrides in zirconium alloy pressure tube materials", *Can. Metall. Q.*, 24(3) (1985) pp-235-243.
51. Fisher, E. S. and Renken, C. J. "Single crystal elastic moduli and the hcp®bcc transformation in Ti, Zr and Hf", *Phy. Rev. A* 135 (1964) 482.
52. M. P. Puls, S. Q-Shi, J. Rabier, "Experimental studies of mechanical properties of solid zirconium hydrides", *Jl. of Nucl. Mater.* 336 (2005) p-73.
53. Singh R.N., Mukherjee S., Kishore R., Kashyap B.P., "Flow behaviour of a modified Zr–2.5wt%Nb pressure tube alloy", *Journal of Nuclear Materials* 345 (2005) 146–161.
54. Kim Y. J. and Vanderglas M. L., "Elastic-plastic analysis of hydride blisters in zircaloy-2 pressure tubes",*Proc. of ASME-PVP conf*., New Orlearns, USA, June (1985) p-161.
55. Byrne T. P., Metzger D. R., Leger M., "Zirconium hydride blister modelling and the application to the P2-G16 failure", *Transactions of the 11th international conference on structural mechanics in reactor technology*. Tokyo (Japan). 18-23 Aug 1991. Shibata, Heki (ed.) Atomic Energy Society of Japan. B (1991) pp. 335-340.

ABOUT THE AUTHORS

Dr. R. N. Singh obtained his B. Sc. (Met. Engg.) from BIT Sindri in 1988. After graduating from 33rd batch of Training school, he joined Materials Group, BARC. He earned his Ph.D. (Met. Engg. & Mat. Sc.) from IIT Bombay in 2003. He was awarded prestigious AvHumboldt Foundation Fellowship in 2004, to work as a guest researcher at the Max Planck Institute for Iron research, Dusseldorf, Germany. He was awarded Marie Curie Incoming International fellowship by European Commission in 2005 to work at Malmo University Sweden. Dr. Singh had carried out extensive work covering the entire spectrum of hydrogen-induced degradation of mechanical and physical properties of zirconium alloys. The issues such as Terminal Solid Solubility (TSS) of hydrogen, influence of hydrogen content on tensile behaviour and fracture toughness, threshold stress for hydride reorientation, temperature and hydrogen content dependence of Delayed Hydride Cracking (DHC) velocity and threshold stress intensity for DHC initiation and hydride blister formation have been studied by him. His areas of research include elevated temperature deformation, Superplasticity, creep, Impact and fracture toughness with the objective of correlating microstructure with mechanical properties of structural materials. Presently, he is working on the development of heat-treated Zr-2.5Nb pressure tube material and its characterization. These studies by Dr. Singh are aimed at generating data and understanding required for safety analysis, residual life assessment and life extension of pressure tubes. The results of these studies have been/are being compiled by Dr. Singh in the form of Publications in peer-reviewed journals (35), BARC reports (14) and presented in national and international conferences (50).

Dr. J. K. Chakravartty is an Outstanding Scientist and Head, Mechanical Metallurgy Section of Materials Group, BARC. He joined from the 20th batch of BARC Training School. Since his joining BARC, he is associated with various research and development activities related to nuclear structural materials. His area of expertise is characterization of mechanical properties and he has accomplished a number of important tasks during his research career spanning over 30 years. He has contributed in the areas of structure- properties correlation in nuclear structural steels and zirconium alloys with emphasis on fatigue and fracture behaviour, optimization of hot workability and control of microstructure in various zirconium alloys. He is currently associated with hydrogen related problems in zirconium alloys and evaluation of fracture toughness of pressure vessel steels. Dr. Chakravartty has been the recipient of Research Associateship of National Research Council (National Academy of Sciences, USA). He has more than 110 technical publications to his credit.

Dr. S. Banerjee is internationaly well known for his work in the field of physical metallurgy and materials science, especially in zirconium and titanium-based alloys. A Distinguished Scientist, Dr. Banerjee has been the recipient of many awards and honours. These include: Shanti Swarup Bhatnagar Award, G.D. Birla Gold Medal, INSA Prize for Materials Science and Indian Nuclear Society Award. Notable among the international awards received by him are Acta Metallurgica Outstanding Paper Award and Humboldt Research Award. Dr. Banerjee is a Fellow of the Indian National Science Academy, Indian Academy of Sciences, Indian National Academy of Engineering and the National Academy of Sciences. Currently he is the Director of BARC.

A STUDY ON MICROSTRUCTURAL EVOLUTION, PHASE TRANSFORMATIONS AND HIGH TEMPERATURE PROPERTIES OF ZR_3AL AND ITS TERNARY DERIVATIVES FOR FUTURE APPLICATIONS IN INDIAN PRESSURIZED HEAVY WATER REACTORS

R.Tewari, G.K.Dey and S.Banerjee
Materials Science Division
and
T.R.G. Kutty
Radiometallurgy Division

Dr. Raghvendra Tiwari received the DAE Scientific and Technical Excellence Award for the year 2007

ABSTRACT

Due to the limitation imposed by existing materials on the performance of Indian nuclear reactors, Zr_3Al base intermetallics have been considered as candidate materials, for structural components in pressurized heavy water nuclear reactors, due to their attractive properties. However, these alloys could not be used for structural applications in the reactors, because of poor room temperature ductility and irradiation-induced amorphization. Our recent studies of ternary addition of niobium in Zr_3Al, have shown some promising results. The present paper reports microstructural evolution and high temperature properties of these alloys, upon long time annealing treatment. The formation of various phases, temperature regime of their stability, chemical composition and volume fraction of these phases during prolonged annealing, have also been studied. A pseudo-binary phase diagram with varying niobium concentrations has also been developed. The morphology and distribution of the Zr_3Al phase have been explained on the basis of long range diffusion, as the rate controlling step. High temperature properties are determined and suitable range of deformation as well as for applications, have been established.

Introduction

Indian Pressurized Heavy Water Reactors (IPHWRs) work at around 30% efficiency; this figure depends upon the difference in the temperatures of the water leaving the pressure tubes and the water coming out of the heat exchanger. The latter temperature is difficult to alter. In order to improve the efficiency, therefore, attempts have been made to operate the reactors at higher temperatures. These attempts are severely restricted due to a sharp drop in the strength of the current zirconium alloys temperatures above about 573 K. *Higher efficiency therefore requires stronger materials.*

In the context of the life of a reactor, radiation induced creep is one of the major issues related to structural materials. A small increment in the core temperature would increase the creep rate by several orders. In the intermediate temperature and stress range, which prevails in IPHWRs, creep is mainly governed by dislocation climb. This, in turn, depends on the rate of migration of irradiation-induced point defects to the dislocations. From the point of view of climb of dislocations, interstitials are more deleterious than vacancies. Thus a reduction in the creep rate could be achieved, by reducing the diffusion of interstitials. In this respect, an ordered structure could show a better resistance to creep as due to long range ordered structures, it effectively entraps vacancies which would result in a higher steady-state vacancy concentration. Consequently, interstitials have higher chances of combining with vacancies and getting annihilated. Some earlier theoretical studies [1,2] have shown, that even at an intermediate degree of order, which is likely to occur in the presence of irradiation under steady state condition, is sufficient to provide a substantial reduction in the creep rate. *A material with ordered structure would be better suited for it.*

In addition to this, one of the major problems encountered with existing zirconium-based reactor core structural materials, is related to hydrogen pick up. Due to the very limited solubility of hydrogen in these structural materials, various hydride phases precipitate out upon thermal cycling and particularly, during the shutting down of reactors. The anisotropy associated with the hcp structure of the low temperature α phase of these materials, causes preferential precipitation of hydride precipitates, on the basal planes. Such a preferential hydride precipitation is not desirable, since being a brittle phase it could provide an easy path for crack propagation. Irradiation growth, which is associated with the anisotropy in crystal structure, poses another formidable problem, with abnormal growth occurring in some undesirable directions. *The use of a material with an isotropic cubic structure and a high solubility for interstitials like hydrogen, therefore, could solve these problems.*

In order to address these issues, a study has been initiated, to explore the possible application of an intermetallic phase, as structural components. Due to high strength (~135 GPa at room temperature) and adequate toughness (K_{IC} ~50 MPa$\sqrt{m}$ at room temperature) Zr_3Al-based alloys have been considered as candidate materials for structural components in Pressurized Heavy Water Reactor (PHWR) [1,2]. Unlike existing structural materials which have highly anisotropic behaviour due to hcp crystal structure, Zr_3Al with its ordered fcc structure (Cu_3Au type; $L1_2$ structure) shows no preferred orientation due to higher symmetrical crystal structure [2]. Moreover, Zr_3Al has a relatively low absorption cross section for thermal neutrons, a reasonably high melting point (1723 K; operating temperature $< 0.34\ T_m$) and a moderate density (5970 Kg/m^3) and ultimate tensile strength three times that of the materials, which are currently being used in PHWRs. However, Zr_3Al based materials have some inherent problems, which could be summarized as: (i) inadequate control over the distribution of undesirable phases [2], (ii) high notch sensitivity [3] and (iii) irradiation-induced amorphization [4].

Our recent study on ternary addition of Nb to the binary Zr_3Al, have shown some promising results. It has been found that by addition of niobium, mechanical properties of these alloys can be tailored [5,6]. Addition of Nb to Zr_3Al appears to alter the sequence of phase transformation, thus providing an opportunity to generate a variety of microstructures [5,7,8]. Some of the phases encountered in the binary and ternary systems of Zr, Al and Nb elements are listed in Table 1.

To date, there has been no detailed study on microstructures of the Zr_3Al-Nb alloys, generated during various heat treatment processes. The work summarized in this paper is a part of our ongoing efforts on the development of the Zr_3Al-Nb alloy. In the present study, the temperature range of 1100- 1723 K, where most of the phase reactions are found to occur in the binary Zr-Al system has been selected, and

Table 1: Some of the phases observed in binary Zr-Al, or ternary Zr-Al-Nb systems in the Zr rich side

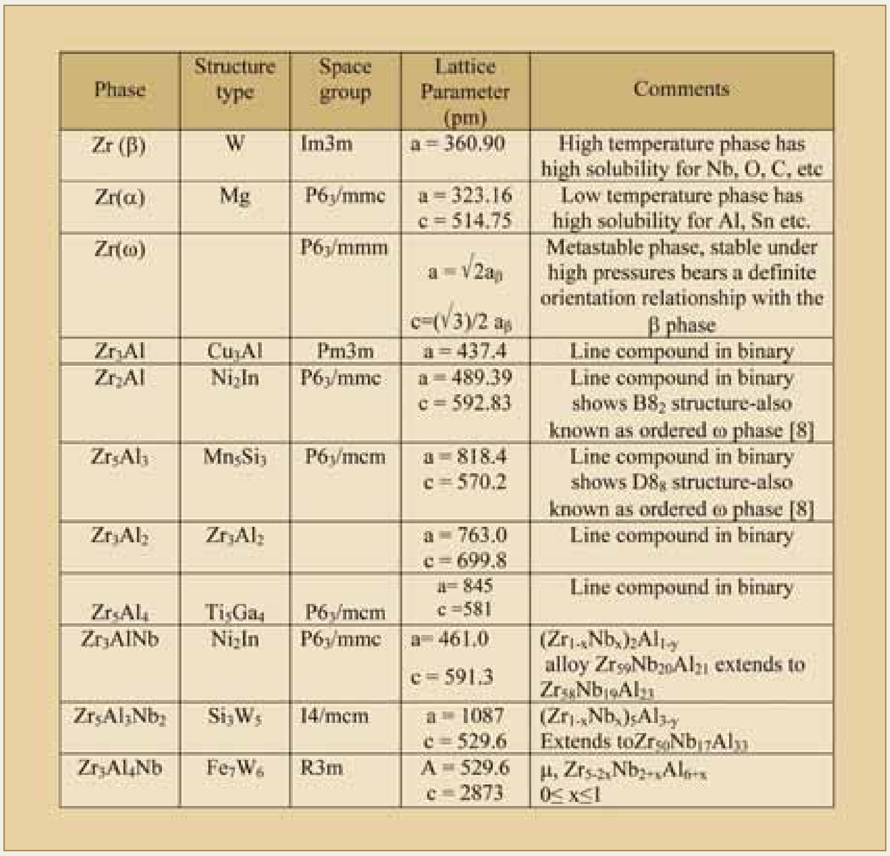

Phase	Structure type	Space group	Lattice Parameter (pm)	Comments
Zr (β)	W	Im3m	a = 360.90	High temperature phase has high solubility for Nb, O, C, etc
Zr(α)	Mg	$P6_3/mmc$	a = 323.16 c = 514.75	Low temperature phase has high solubility for Al, Sn etc.
Zr(ω)		$P6_3/mmm$	$a = \sqrt{2}a_\beta$ $c=(\sqrt{3})/2\ a_\beta$	Metastable phase, stable under high pressures bears a definite orientation relationship with the β phase
Zr_3Al	Cu_3Al	Pm3m	a = 437.4	Line compound in binary
Zr_2Al	Ni_2In	$P6_3/mmc$	a = 489.39 c = 592.83	Line compound in binary shows $B8_2$ structure-also known as ordered ω phase [8]
Zr_5Al_3	Mn_5Si_3	$P6_3/mcm$	a = 818.4 c = 570.2	Line compound in binary shows $D8_8$ structure-also known as ordered ω phase [8]
Zr_3Al_2	Zr_3Al_2		a = 763.0 c = 699.8	Line compound in binary
Zr_5Al_4	Ti_5Ga_4	$P6_3/mcm$	a= 845 c =581	Line compound in binary
Zr_3AlNb	Ni_2In	$P6_3/mmc$	a= 461.0 c = 591.3	$(Zr_{1-x}Nb_x)_2Al_{1-y}$ alloy $Zr_{59}Nb_{20}Al_{21}$ extends to $Zr_{58}Nb_{19}Al_{23}$
$Zr_5Al_3Nb_2$	Si_3W_5	I4/mcm	a = 1087 c = 529.6	$(Zr_{1-x}Nb_x)_5Al_{3-y}$ Extends to$Zr_{50}Nb_{17}Al_{33}$
Zr_3Al_4Nb	Fe_7W_6	R3m	A = 529.6 c = 2873	μ, $Zr_{5-2x}Nb_{2+x}Al_{6+x}$ $0\leq x\leq 1$

long term annealing treatment was given to obtain the equilibrium microstructure. This paper reports on the formation of various phases in the microstructures of samples of the Zr_3Al-Nb alloys, aged in the aforementioned temperature range, their chemical composition and volume fraction and establishes the role of Nb in the formation of these phases.

Physical and Mechanical Properties of Zr_3Al Based Alloys

Zr_3Al has ordered fcc structure with lattice parameter 0.437 nm. The ordered Zr_3Al phase remains stable against any thermal treatment till it decomposes above 1300 K. However, some degree of disorder can be induced by irradiation. Under extreme irradiation conditions (fluence exceeding 10^{28} n/m^2), it undergoes amorphization at low temperatures, but retains its crystalline nature in the intermediate temperatures (600-800 K). The alloys of the material are of moderate density 5.97 gm/cc with liquidus temperature of close to 1723 K but high elastic modulus, shear modulus and Poison's ratio. Some of the properties of Zr_3Al have been compared with existing alloys and are listed in Table 2 and variation in the properties of these alloys is shown in Fig. 1.

Formation of Various Phases in Zr_3Al-Based Alloys

Phase in the binary alloys

Zr_3Al, a line compound in the binary Zr-Al phase diagram (Fig. 2), contains 8.97 wt% Al. The formation of Zr_3Al occurs via a eutectic and two peritectoid reactions:

$$\text{Liquid} \rightarrow \quad \beta + Zr_5Al_3 \qquad Te = 1625K \qquad (1)$$

Table 2: Comparison of properties of Zr_3Al, Zircaloy-2 and Zr-2.5Nb

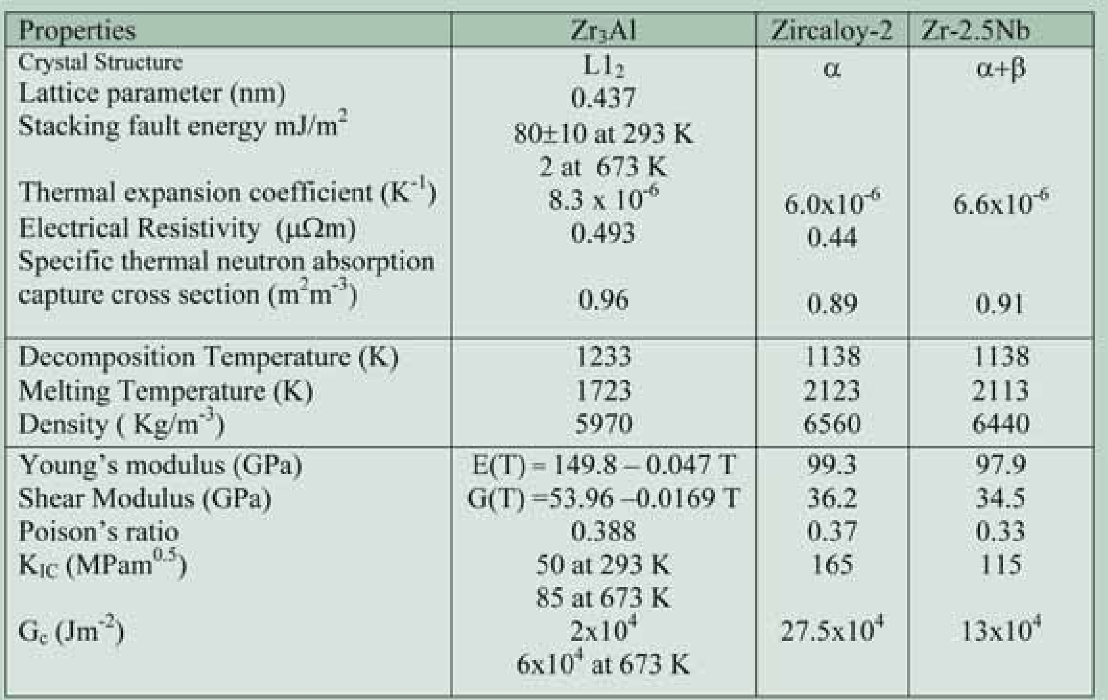

Properties	Zr_3Al	Zircaloy-2	Zr-2.5Nb
Crystal Structure	$L1_2$	α	α+β
Lattice parameter (nm)	0.437		
Stacking fault energy mJ/m^2	80±10 at 293 K 2 at 673 K		
Thermal expansion coefficient (K^{-1})	8.3×10^{-6}	6.0×10^{-6}	6.6×10^{-6}
Electrical Resistivity (μΩm)	0.493	0.44	
Specific thermal neutron absorption capture cross section (m^2m^{-3})	0.96	0.89	0.91
Decomposition Temperature (K)	1233	1138	1138
Melting Temperature (K)	1723	2123	2113
Density (Kg/m^{-3})	5970	6560	6440
Young's modulus (GPa)	E(T) = 149.8 – 0.047 T	99.3	97.9
Shear Modulus (GPa)	G(T) =53.96 –0.0169 T	36.2	34.5
Poison's ratio	0.388	0.37	0.33
K_{IC} ($MPam^{0.5}$)	50 at 293 K 85 at 673 K	165	115
G_c (Jm^{-2})	2×10^4 6×10^4 at 673 K	27.5×10^4	13×10^4

$\beta + Zr_5Al_3 \rightarrow Zr_2Al$ Tp1 = 1488K (2)

$\beta + Zr_2Al \rightarrow Zr_3Al$ Tp2 =1293K (3)

The as solidified material of this composition consists of a metastable mixture of α-Zr(Al) (hcp) (transformed from the high temperature β-Zr(Al) phase) and Zr_2Al (ordered hexagonal, $B8_2$) phases [9] and the formation of Zr_3Al occurs when the as solidified material is heated below 1248 K. The kinetics of the reaction reaches a maximum of around 1163 K (about 80 K below the transition temperature)[9].

Phases In ternary alloys

A summary of the different phases observed as a result of annealing treatment at various temperatures for the alloys Zr_3Al, Zr_3Al-1.8Nb, Zr_3Al-3Nb and Zr_3Al-10Nb is given in Table 3. Subsequent to the

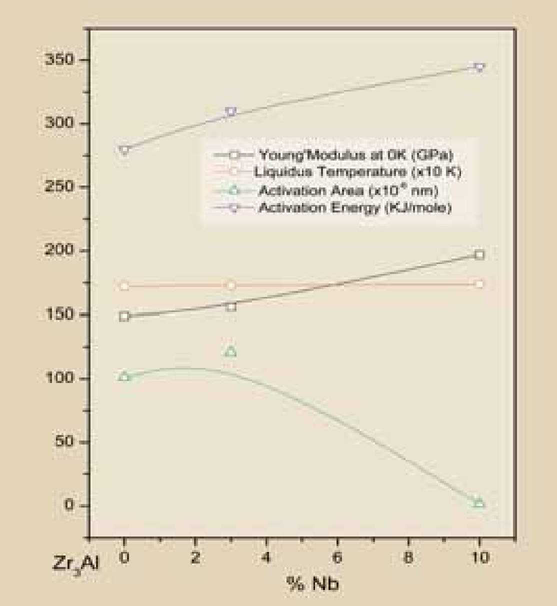

Fig. 1: Some of the properties of Zr_3Al based alloys as a function of Nb concentration

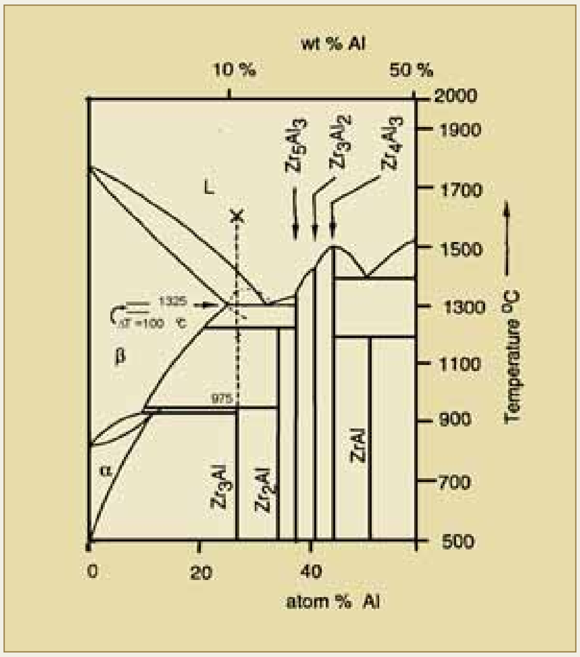

Fig. 2: Phase diagram of Zr-Al

identification of various phases, their chemical compositions and volume fractions, it is possible to propose the schematic phase diagram as shown in Fig. 3, for the Zr_3Al-Nb section. The vertical section was developed from the different phase reactions expected to occur and consequent emergence of the various phases like, β, B2, Zr_5Al_3, Zr_2Al, Zr_3Al and their ternary derivatives observed in these alloys.

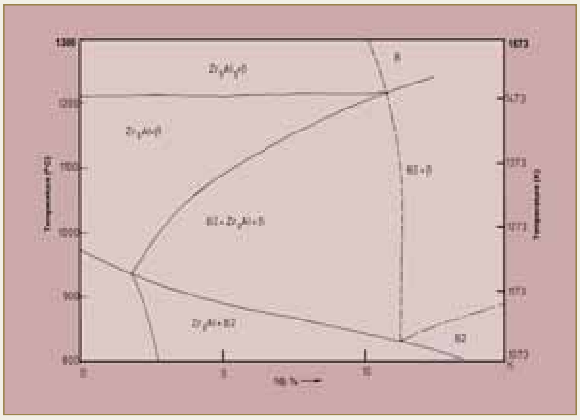

Fig. 3: Schematic pseudo-binary phase diagram of the Zr_3Al-Nb system

The sequence of phase transformation remains nearly same in the case of ternary alloys, but the phase fields of various phases change considerably. Based on the different phases encountered in the Zr_3Al-Nb alloys, the temperature range can be divided into three temperature regions; Temperature Range 1 from 1473 K to 1723 K, Temperature Range 2 from 1223 K to 1473 K and Temperature Range 3 from 1223 K and below. Annealing in the Temperature Range 1 exhibits two-phase microstructure with the matrix phase as the β phase and the second phase as the Zr_5Al_3 phase or its ternary derivatives. A typical microstructure obtained from samples annealed in Temperature range 1 is shown in Fig.4(a). The β phase in this temperature

Table 3: Summary of the different phases encountered in the Zr_3Al-Nb alloys

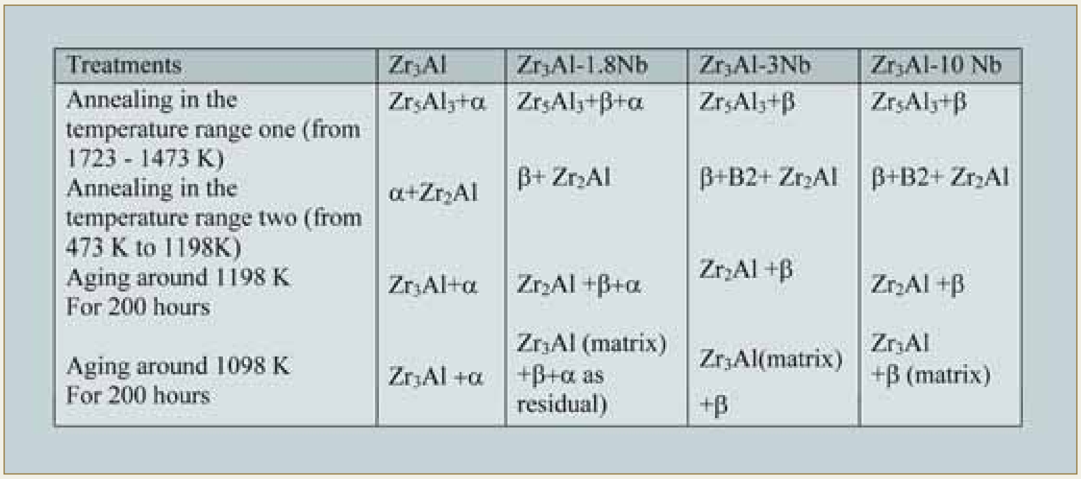

Treatments	Zr_3Al	Zr_3Al-1.8Nb	Zr_3Al-3Nb	Zr_3Al-10 Nb
Annealing in the temperature range one (from 1723 - 1473 K)	$Zr_5Al_3+\alpha$	$Zr_5Al_3+\beta+\alpha$	$Zr_5Al_3+\beta$	$Zr_5Al_3+\beta$
Annealing in the temperature range two (from 473 K to 1198K)	$\alpha+Zr_2Al$	$\beta+Zr_2Al$	$\beta+B2+Zr_2Al$	$\beta+B2+Zr_2Al$
Aging around 1198 K For 200 hours	$Zr_3Al+\alpha$	$Zr_2Al+\beta+\alpha$	$Zr_2Al+\beta$	$Zr_2Al+\beta$
Aging around 1098 K For 200 hours	$Zr_3Al+\alpha$	Zr_3Al (matrix) +β+α as residual)	Zr_3Al(matrix) +β	Zr_3Al +β (matrix)

range remains disordered. The volume fraction of the second phase decreases with increase in niobium concentration, but increases marginally with decrease in temperature.

The matrix β shows ordering tendency and the Zr_2Al phase and its ternary derivatives are encountered, when samples are annealed in the temperature range 2. The Zr_2Al phase maintains the orientation relationship with the β phase (Fig.4(b)). In the Temperature Range 3 depending upon the Nb concentration, presence of a single phase or two phase microstructure is noticed. Low concentration alloys, up to 1.8Nb, show the single $L1_2$ phase, whereas higher concentration alloys show the presence of two phase microstructures. With concentration increasing to 3%Nb, the microstructure of alloys comprises the $L1_2$ phase as the major phase and the B2 phase as a minor phase (Fig. 4(c)) The B2 phase is found mainly located at the grain boundaries of the $L1_2$ grains. The B2 phase is rich in Nb and Al whereas the $L1_2$ phase is lean in Nb. With increasing concentration to 10%Nb, the B2 phase becomes the major phase in which small precipitates of the $L1_2$ phase are found distributed (Fig. 4(d)) along the grain boundaries and in the interior of the B2 grain.

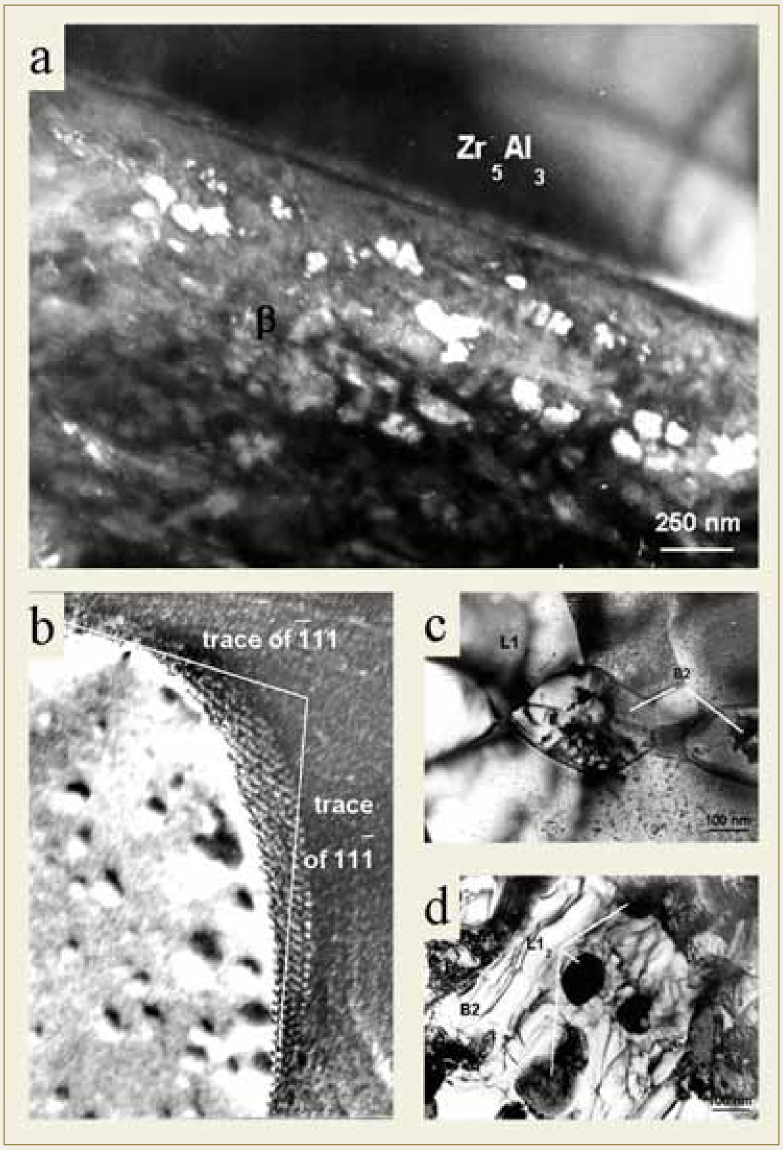

Fig. 4: Typical microstructure showing samples of Zr_3Al-Nb alloys aged (a) in the Temperature Range 1 (b) in the Temperature Range 2 (c&d) in the Temperature Range 3

The size of the β + Zr_2Al phase field is of technical importance. This is because, depending on the composition and temperature at which the phase field is obtained, thermo-mechanical treatment can be designed. As the particle size and the distribution of the Zr_2Al phase, control the rate of formation of the equilibrium Zr_3Al phase and relative volume fractions of untransformed phases, final properties and microstructures of the alloys can be controlled by suitable thermo-mechanical treatment. The morphology of the Zr_2Al particles can be altered from coarse, chunky particles, to fine uniformly distributed particles, by selecting the appropriate annealing treatment.

Selection of suitable temperature range for hot-working

The suitable temperature for any given alloy will be the temperature range in which for a given work pressure, a maximum amount of deformation can be imparted without failure. Such a condition is ensured only if the material undergoing deformation rapidly recrystallizes simultaneously. The search for a suitable temperature range for deformation, essentially reduces and determines the temperature range of recrystallization. In the present study, using the plasticity parameter of the material, after converting from hot hardness tests, a gross temperature range was determined. Microstructural examination of the hot-deformed samples helped in identifying the role of each phase during deformation and in turn, to understand the role of niobium in altering the temperature range of deformation.

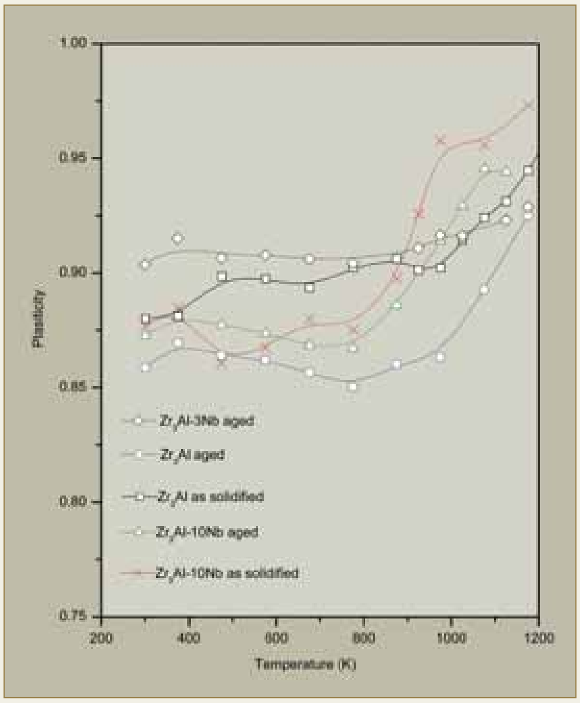

Fig. 5: Plasticity parameters as a function of temperature

Fig. 5 shows the variation in plasticity characteristics as a function of temperature for some of the Zr_3Al-Nb alloys. From the thermo-mechanical application point of view, a suitable temperature region can be identified, by observing the minimum temperature above which δ_H attains a value greater than 0.9. Based on which the temperature region where these alloys could be deformed successfully, was selected as between 1050 K - 1100K. The material in small quantity has been successfully rolled in this temperature range (Fig. 6). Typical rolled and partially cracked specimens are also shown in the figure.

The microstructural studies of the hot-rolled samples revealed, that the matrix β phase has undergone dynamic recrystallization. It has been observed that if interconnecting network of the $Zr_2(Al,Nb)$ phase forms,

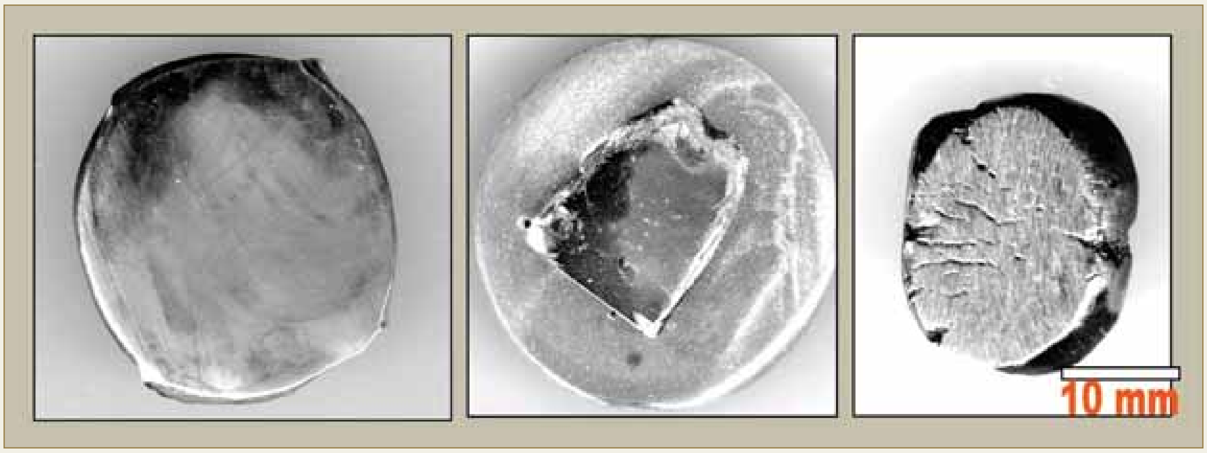

Fig. 6: Specimens obtained after hot-working

it provides an easy path for crack propagation. Therefore, in order to avoid brittle failure of the alloy, fine distribution of the Zr_2(Al,Nb) phase in the form of island morphology should be maintained. As the volume percentage and the distribution of the Zr_2(Al,Nb) can be altered by temperature and by the extent of deformation, small deformation in each step and an intermediate annealing treatment of half an hour after two successive passes, yield a uniform distribution of the Zr_2(Al,Nb) phase, in the relatively large grain size of the β phase (8 to 10 mm). In short, it can be deduced that 1100 to 1200 K is the optimum temperature range. An intermediate annealing time of 30 minutes is sufficient for producing the suitable microstructure for the successive passes.

Room Temperature and High Temperature Properties

The variation of the hardness in the Zr_3Al alloys did not show a monotonous fall as observed in many other alloy systems, but showed maxima in the intermediate temperature range. A similar phenomenon has been observed in the Zr_3Al based phases, when the yield stress of the material has been plotted as a function of temperature [9].

The microstructural study of the room temperature deformed sample has shown, that the mode of deformation is by glide of dislocation partials with burger's vectors as a/3<112> bounding superlattice intrinsic stacking faults on {111} planes. The dislocations responsible for the creation of anti phase boundaries were absent in this temperature range. Between the temperature range of 600-800 K, both the modes of deformation occur simultaneously and above 800 K, dislocations responsible for APB dominate the deformation mechanism. At temperatures close to melting point grain sliding dominates other modes of deformation.

Hardness-time relationship

The variation in hardness with time at a constant temperature, provides information of the creep behaviour of the alloy, at that temperature. The indentation creep results have shown, that the hardness of the Zr_3Al based alloys exhibit small variations with time up to 800 K. The stress exponent in this temperature range show a very high value, indicating that the dominant modes of deformation are athermal in nature.

At temperatures higher than 800 K, value of stress exponent approaches close to 5, this suggests the onset of the diffusion-assisted phenomenon. In order to decipher the dominant creep mechanism operating at different temperature regions, parameters such as stress exponent, activation energy and activation area were determined. The values of these parameters are shown in Table 4. Activation energy of creep in this temperature region, falls in the range of 250 to 350 kJ/mole (Table 4). On comparing with other alloys like zircaloys and the Zr-2.5Nb, the value of the activation energy of creep of the Zr_3Al based alloys appear higher, but these values fall within the range of activation energies of creep, shown by other aluminides such as Ti_3Al, Fe_3Al etc. [10,11]. Based on these estimates it was concluded, that the activation energy of creep in Zr_3Al based alloys is due to the self-diffusion of zirconium in the Zr_3Al alloys.

Table 4: Parameters like activation area and activation energy calculated from the derived conventional creep curves

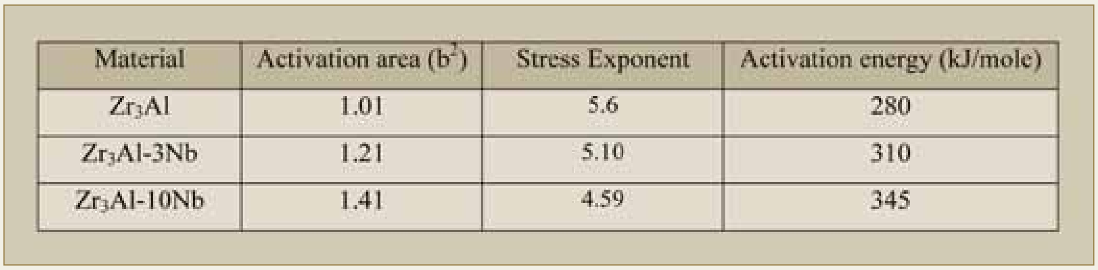

Material	Activation area (b^2)	Stress Exponent	Activation energy (kJ/mole)
Zr_3Al	1.01	5.6	280
Zr_3Al-3Nb	1.21	5.10	310
Zr_3Al-10Nb	1.41	4.59	345

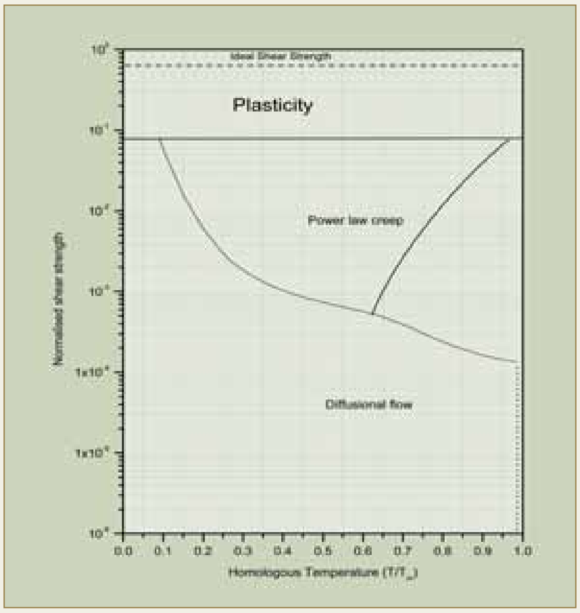

Fig. 7: Creep map for binary Zr_3Al phase

Several mechanisms have been proposed, to account for the creep rate observed at high temperature range. The mechanism based on diffusional flow (Herring-Nabarro creep) and Coble creep can be excluded, as for these processes stress exponent, n, should be equal to unity. This condition has never been observed in this alloy system in the temperature range of examination. Two other mechanisms proposed are (1) the model of climb of edge dislocations [9] and (2) the model of jogged screw dislocations [9]. The activation energy of both the mechanisms is the same, but the activation area is different for both the mechanisms. The former mechanism requires an activation area of the order of b^2, whereas the latter requires activation area of the order of hundreds of b^2. The calculated activation area for the present material is of the order of b^2 and therefore, the climb of edge dislocation is the dominating mechanism.

Based on the approach provided by Sargent and Ashbey and Li et al [12,13] a creep map for the Zr_3Al based material has been drawn. Fig.7 represents the creep map for the binary Zr_3Al alloy and the data used to generate this, is given in Table 5. The hardness data was superimposed on it. The data points pertaining to temperatures higher than 0.5 T_m are marked in the map and it may be noticed that these fall in the regime of power law creep. The values of the data points for temperature lower than $0.5T_m$ approach the plasticity region indicating that, at temperatures below this temperature region, deformation process is athermal in nature. This is in agreement with our findings.

Concluding Remarks

Zr_3Al is a novel intermetallic awaiting applications in the nuclear as well as non-nuclear industries. The present study elucidates the vast variety of microstructures possible in the Zr_3Al based intermetallics. The formation of these phases and their morphologies could be altered, using a suitable combination of thermo-mechanical and aging treatment. Mechanical properties assessed

Table 5: Relevant data used to generate creep mechanism map.

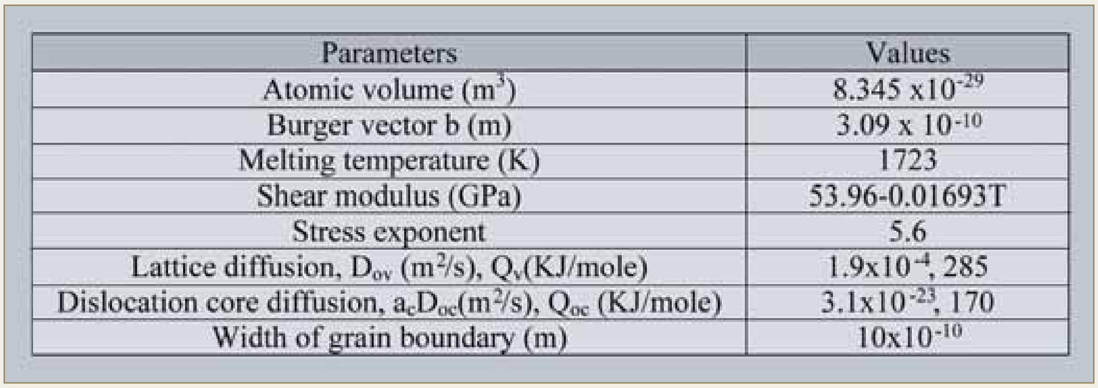

Parameters	Values
Atomic volume (m^3)	8.345×10^{-29}
Burger vector b (m)	3.09×10^{-10}
Melting temperature (K)	1723
Shear modulus (GPa)	53.96-0.01693T
Stress exponent	5.6
Lattice diffusion, D_{ov} (m^2/s), Q_v(KJ/mole)	1.9×10^{-4}, 285
Dislocation core diffusion, a_cD_{oc}(m^2/s), Q_{oc} (KJ/mole)	3.1×10^{-23}, 170
Width of grain boundary (m)	10×10^{-10}

during the present study using indentation creep mechanisms provided insight into the mechanical properties and their variation with temperature. Based on the encouraging results shown by the Zr_3Al-Nb alloys, attempts are being made to fabricate a pressure tube of smaller dimensions, which would be taken up for further studies, for structural applications.

References

1. E. M. Schulson, *J. Nucl. Mater.*, 66,p 322-324(1977).
2. E.M. Schulson, *Intermetallic Compounds*, Vol.2, Editors J.H. Westbrook and R.L. Fleischer, John Eiley and Sons Ltd., 133(1994).
3. E.M. Schulson and J.A. Roy, *J. Nucl. Mater.*,71, p.124 (1977).
4. H. E. Rosinger and B. J. S. Wilkins, *J. Nucl. Mater.*, 89, p.347-353(1980).
5. R. Tewari, G. K. Dey, R.K. Fotedar, T.R.G. Kutty and N. Prabhu, *Met. Trans.*, 35A, pp.205 (2004).
6. R.Tewari, G. K. Dey, T. R. G. Kutty, A. K. Sengupta, N. Prabhu and S. Banerjee, *Met. Trans.*, 35A, pp.189 (2004).
7. R. Tewari, N. Prabhu, G.K. Dey, P. Mukhopadhyay and S. Banerjee, *Metallurgical and Materials Transactions*, Vol.33A, p. 1919(2002).
8. R. Tewari, P. Mukhopadhyay, S. Banerjee and L. A. Bendersky, *Acta Materialia*, vol.24, p.1307(1999).
9. R. Tewari, Ph.D. thesis, Indian Institute of Technology-Bombay (2001).
10. A. H. Cottrell, *Mater. Sci. Tech.*,7,p.981(1991).
11. C. G. McKamey, P.J. Maziasz and J. W. Jones, *J. Mater. Res.*,7, p.2089(1992).
12. W. B. Li, J. L. Henshall, R. M. Hooper and K. E. Easterling, *Acta Metall. Mater.*,39,pp.3099(1991).
13. P.M.Sargent and M.F.Ashby, *Mater. Sci. Tech.*, 8,pp.594(1992).

ABOUT THE AUTHORS

Dr. R. Tewari joined BARC from the 32nd batch of BARC Training School in Metallurgy discipline and was awarded the Homi Bhabha Prize. Areas of his research interest are phase transformations in zirconium and niobium alloys, development of newer alloys for structural applications at elevated temperature and for higher burn up, structure-property correlation in these alloys. Structure related phase transformations; in particular omega phase transformation. He is a recipient of the Young Metallurgist Award and SRC-BRNS Fellowship. He has 75 scientific publications to his credit.

ABOUT THE AUTHORS

Dr. G. K. Dey joined from the 23rd batch of BARC Training School and was awarded the Homi Bhabha Prize. He has won several awards for his scientific contributions; of these mention can be made of the Young Scientist Award, Young Metallurgist Award, MRSI Gold Medal and Metallurgist of the Year Award. He is a Fellow of the National Academy of Engineering (FNAE) and the Indian Academy of Sciences (FAS). Areas of his research interest are phase transformation in zirconium and nickel-base Alloys, amorphous alloys, rapidly solidified crystalline and quasicrystalline alloys, high resolution electron microscopy. He has more than 220 scientific publications to his credit. Currently Dr. Dey is heading the Materials Science Division, BARC.

Dr. S. Banerjee is internationally well known for his work in the field of physical metallurgy and materials science specially zirconium and titanium-based alloys. A Distinguished Scientist, Dr. Banerjee has been the recipient of many awards and honours. These include Shanti Swarup Bhatnagar Award, G.D. Gold Medal, INSA Prize for Materials Science and Indian Nuclear Society Award. He has been bestowed with 'Padmashree' by the President of India. He is a Fellow of the National Academy of Engineering (FNAE) and the Indian Academy of Sciences (FAS). Currently Dr. Banerjee is Director, Bhabha Atomic Research Centre, Mumbai.

Dr. T.R.G. Kutty joined BARC in 1973. His field of expertise is evaluation of thermophysical and thermomechanical properties of materials, hot hardness, creep and fracture toughness of ceramics, dilatometry, densification, behaviour and sintering kinetics. Structure-property correlation of ceramics, development of metallic fuels and its properties.

A NOVEL ELECTROSTATIC ION TRAP AND FOURIER TRANSFORM MEASUREMENTS FOR HIGH-RESOLUTION MASS SPECTROMETRY

K. G. Bhushan, S. C. Gadkari, J. V. Yakhmi and V. C. Sahni
Technical Physics and Prototype Engineering Division

Dr.K. G. Bhushan is the recipient of the DAE Scientific & Technical Excellence Award for the year 2007

ABSTRACT

We report on the development of a novel electrostatic ion trap for high-resolution mass spectrometry. The ion trap works on purely electrostatic fields, thereby allowing simultaneous trapping and studying of multiple mass species, over a large mass range. Ions are trapped and stored as a bunch between two collinearly placed electrostatic ion mirrors and oscillate continuously. The oscillatory signals are fourier-transformed to produce the frequency spectrum, wherein each frequency corresponds to a particular mass of the trapped ions. From the initial experiments a mass resolving power ($m/\Delta m$) of about 20,000 and a storage lifetime of about 100ms is observed. This unique feature and several other important characteristics of this ion trap are presented, along with its application as a high resolution mass spectrometer.

Introduction

Since the invention of Ion trapping techniques about 50 years ago [1], ion traps have been utilized for mass spectrometric purposes. These ion traps range from small tabletop size to large ion storage rings. In general, in most of the small ion traps, ions are trapped and confined to a small region of space using a combination of magnetostatic or time-dependent (RF) fields [2]. The motion of the ions under the influence of such fields is usually a complex function of these fields and in general has been well understood. Another method of trapping and storing ions is the storage-ring technique, where ions with high kinetic energy are kept circulating with the help of magnetic steering and focusing systems. These are large systems and are particularly advantageous when used with electron-cooler inside, which the circulating ion beam can be merged with the electron beam, in nearly zero relative velocity conditions. The storage rings require external injection followed by acceleration either externally [3] with a linac or within the ring itself using synchrotron-type acceleration capabilities [4,5].

Several techniques have been put forward for time-of-flight mass spectrometry such as time-lag focusing [6] and compensating mirrors [7]. Piyadasa, et al [8] reported on a multireflecting instrument where a resolution of about 31,000 for bovine insulin was obtained. Later, Benner [9] using a similar instrument could trap and study DNA molecules. Ring et al [10] demonstrated the fourier transform capabilities of a similar ion trap using a MALDI-type source.

In this paper, we present an electrostatic ion trap, similar to the one originally reported by Zajfman et al [11], which is somewhere in between the small 'table-top' devices and large 'storage rings' and its application for mass spectrometry. The principle of working of this ion trap and its application to radiative lifetime measurements has already been established [12,13] hence only a brief description is presented here.

Design of the ion trap

'Photon-storage' devices such as 'optical resonators' have long been used in optical devices such as lasers, and their properties have been well studied. In such devices, photons can be trapped between two focusing mirrors and the stability condition is given by [14]:

$$0 \le \left(1-\frac{D}{\rho_1}\right)\left(1-\frac{D}{\rho_2}\right) \le 1 \qquad (1)$$

where D is the distance between the mirrors and ρ_1 and ρ_2 are the radii of curvature of the mirrors. In the case of a symmetric resonator $(\rho_1 = \rho_2)$ and using the relationship for focal length $f = \frac{\rho}{2}$ the above equation can be simplified to:

$$\frac{D}{4} \le f \le \infty \qquad (2)$$

The ion trap presented here, works on a similar principle in which the photon mirrors are replaced by 'electrostatic ion-mirrors' and the photon beam is replaced by a well-defined ion-beam. The main advantage with electrostatic ion mirrors is that, they are not mass limited unlike 'magnetic mirrors', which means, very massive ions can also be trapped and stored along with lighter ions provided they have the same kinetic energy.

The design of the ion trap closely follows the original design of Zajfman et al [11,12]. A photograph of the actual ion trap is shown in Fig. 1. The ion trap consists of two collinearly placed electrostatic ion mirrors, each consisting of 5 electrodes. The mirrors are arranged on an optical bench with suitable tie-rods that ensures that they are collinear. In order to have lateral confinement, an einzel lens is added before each mirror. Together with the einzel lens, the ion mirrors have both reflecting and focusing properties that obey Eqn.(2). The inner most electrodes on each mirror are grounded, thereby keeping the region between the two mirrors field-free.

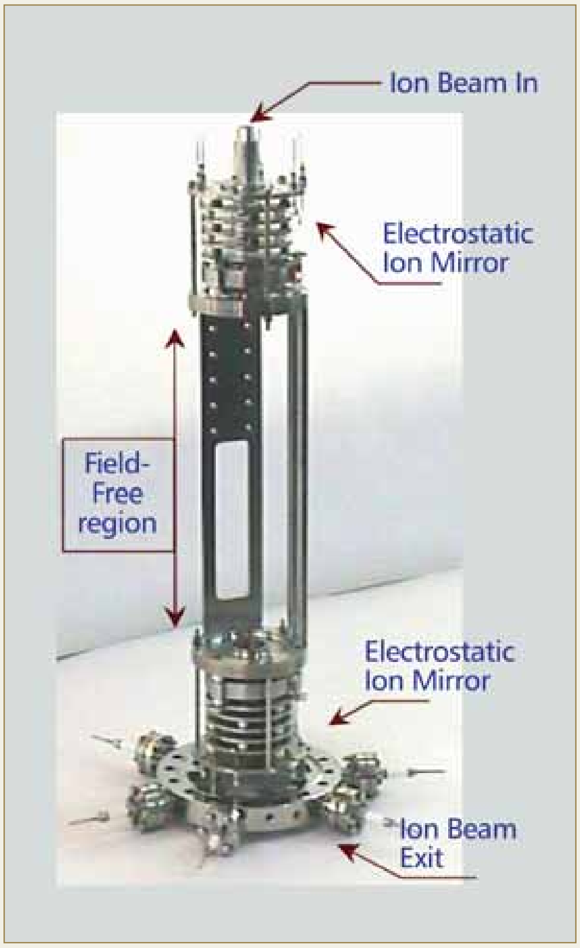

Fig. 1: Photograph of the ion trap

In order to have reflecting properties, the ion mirrors need to have a potential which is high enough to stop the ions i.e. $V_\phi > \frac{E_\mu}{q}$ where E_μ is the kinetic energy of the ion beam and q is the charge of the ions. The performance of the ion trap was simulated with SIMION v7.0 software [15]. The initial set of voltages on the ion mirrors and the einzel lenses could be obtained from the simulation, in order to determine stable conditions of trapping. However in order to perform mass spectrometry with the ion trap, it is important that the trapped ions remain bunched for a long period of time. In order to achieve this, the voltages on the ion mirrors and the einzel lenses were adjusted such that, the energy spread in the ion beam which translates into velocity spread could be compensated, by determining the turnaround points inside the ion mirror. It should be noted that this procedure only reduces the time-spread in the arrival of the ion bunch due to the energy spread in the ion beam at the centre of the ion trap, where the image charge detector is located.

Experimental setup and results

A. Storage Lifetime Measurements

A schematic of the experimental setup is shown in Fig. 2. The setup consists of an electron impact ion source followed by suitable acceleration and focusing elements. An electrostatic chopper is utilized, to pulse the DC beam with pulse widths ranging from 0.5 to 5 microseconds. In order to remove the energetic neutrals that are produced along the beamline, a zeman type 90° electrostatic deflector [16] is employed. The pulsed ion beam is allowed to enter the ion trap through a 1mm aperture with the help of suitable XY deflectors and einzel lenses. The entire beamline is kept at a very low base pressure of about 5 x 10^{-9} mbar with the help of triode sputter ion pumps, while the ion trap is pumped with the help of a 1000 l/s cryopump and a base pressure of about 7 x 10^{-10} mbar could be achieved which rises to about 1 x 10^{-9} mbar with the ion source operating. DC ion beam currents of about 50 nA could be injected into the ion trap with every injection, or about 80,000 ions equivalent per microsecond pulse.

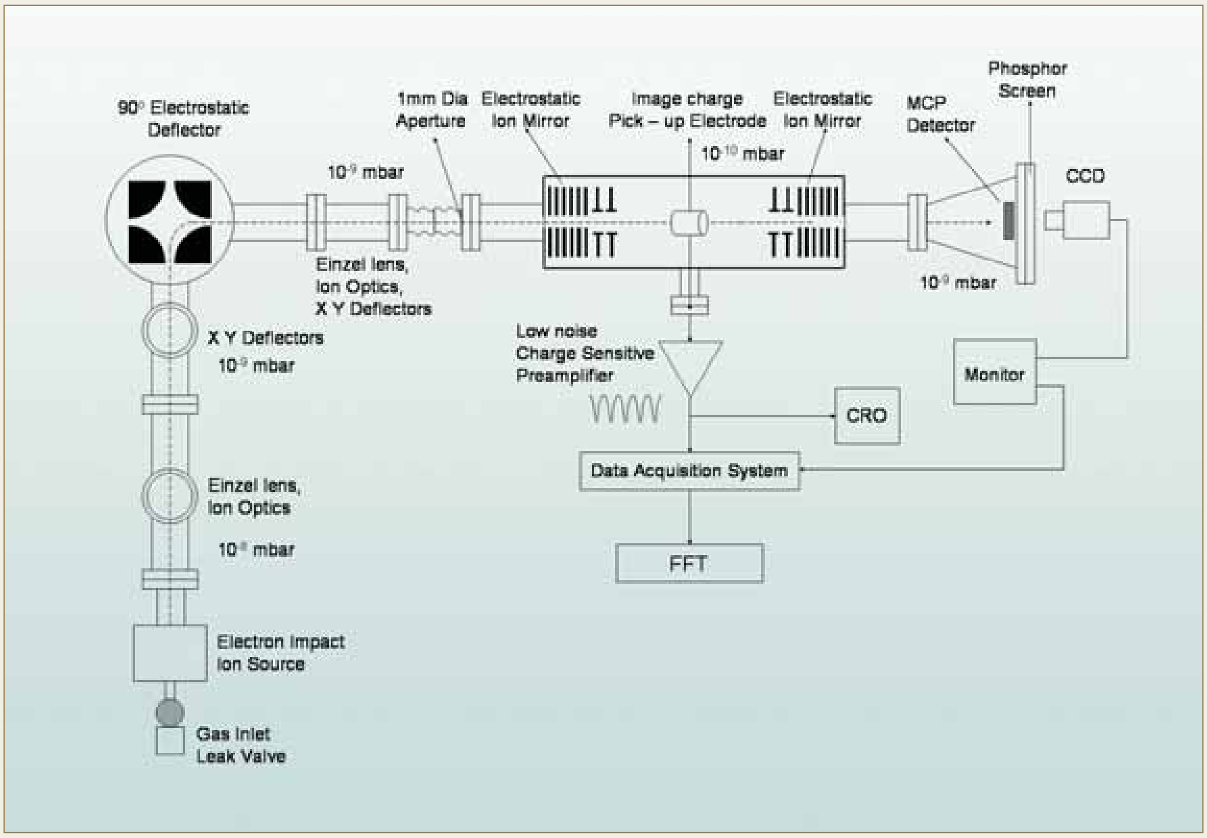

Fig. 2: Schematic of the experimental setup

The voltages on the entrance mirrors are lowered to zero while injecting the ion bunch into the ion trap and the voltages on the exit mirror are kept high all the time. The voltages on the entrance mirror are switched ON (identical to the exit mirror), as the bunch enters the image charge pickup tube, located at the center of the ion trap. This reduces any interference due to the high voltage switching. Fast high voltage switches (Behlke GmbH, Germany. HTS Series) with rise times of less than 100ns are utilized to effect the high voltage switching. The ion bunch is now trapped between the two mirrors and oscillates with a frequency that is inversely proportional to the square root of the mass of the ions. Once the ion bunch is trapped, the ions can decay either by a charge transfer type of reaction (the ions are neutralized by colliding with a residual gas molecule and are no longer trapped) or by elastically scattering off a residual gas molecule and no longer within the realm of stability condition of the trap.

The storage lifetime of the ions is given by : $\tau = \dfrac{1}{\eta \sigma \upsilon}$

where η is the number density of residual gas molecules in the ion trap, σ is the charge transfer cross section and ν is the velocity of the ions. The storage lifetime is measured by monitoring the energetic neutrals, that leave the trap (roughly about a quarter of the stored particles at any given time) are detected by a Microchannel plate detector and counted by a PC-based Multichannel scaler (FAST ComTec, Germany. Model P7887) which histograms the data given the bin sizes. The start of the multichannel scaler is slightly delayed, with respect to the start of the trapping cycle. The entire timing cycle is controlled by a specially designed 6-channel, <5ns jitter timer, whose pulse widths and delay could be adjusted for individual channels in 100ns steps. Storage lifetimes measured for different ions are shown in Fig. 3. Storage lifetimes of about 100ms or greater could be achieved routinely which was only limited by the base pressure in the ion trap. Under these conditions, an argon ion bunch oscillates with a frequency of about 332 KHz, which when measured for 50ms turns out to be 16,500 oscillations or the equivalent of a 6 Km long time-of-flight tube when unfolded.

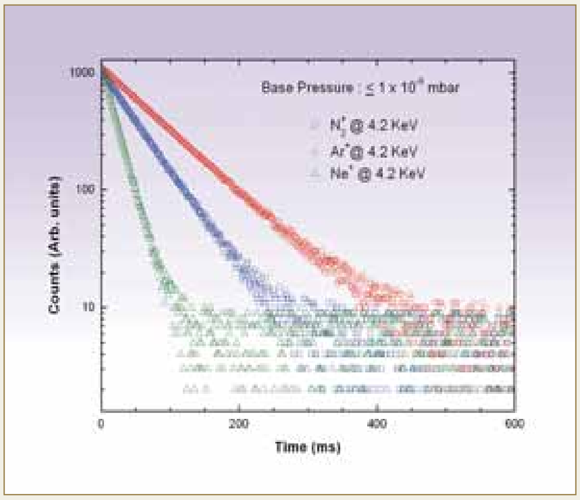

Fig. 3. Storage lifetimes of various ions

B. Mass Spectrometry

The oscillation of the ions is detected with the help of an image charge detector (a small metallic tube of 18mm length and 12mm diameter) located at the center of the ion trap. A proportional image charge is induced on the detector every time the ion bunch passes through it. This charge is then amplified with a suitable low noise charge sensitive preamplifier and the output signal of the preamplifier is digitized by a PC-based high speed digitizer card [CompuScope 82G, Gage Inc.]. A fourier transform operation is performed on the digitized signal, to obtain the frequency spectrum.

Two types of ion trapping modes were employed to optimize the oscillation signals of the ions. In the first case, the dispersive case, the potentials on the ion mirrors were chosen to be linear which made the mirror a 'hard' mirror. In the second case, the self-bunching case, a velocity compensated approach was applied to the potentials on the ion mirrors, which made the ion mirror function as a 'soft' mirror.

Fig. 4 shows an FFT spectrum obtained in the 'dispersive mode' from the oscillations of a $^{40}Ar^+$ ion bunch, which was used to calibrate the mass spectrometer. The sensitivity of the ion trap was limited by the capacitance of the image charge detector, the capacitance of the ultrahigh vacuum electrical feedthrough used to transfer the signal out of the vacuum chamber and the input capacitance and the noise levels of the pre-amplifier. Thus in the present setup, we could not observe $^{36}Ar^+$ due to its very low natural abundance. The FWHM (Δf) of the fundamental harmonic is 50Hz and using $R = m/\Delta m = f/2\Delta f$, we obtain a mass resolution of about ~ 3320. The FFT spectrum was averaged for about 100 injection cycles.

Fig. 5 shows an FFT spectrum obtained from the same $^{40}Ar^+$ ion bunches trapped in the self-bunching mode. In this case, the oscillatory signals decayed much slower than in the dispersive mode, which contributed to a better FFT spectrum. The FWHM (Δf) of the fundamental harmonic is now 20Hz and using $R = m/\Delta m = f/2\Delta f$, we obtain a mass resolution of about ~ 8300. The FFT spectrum was averaged for about 100 injection cycles.

Fig. 6a shows an 'as recorded' Xe^+ frequency domain spectrum obtained in the 'self-bunching' mode averaged for about 100 injection cycles. The peak amplitudes closely match the known natural abundances of the various isotopes. Further, even higher harmonics could be detected for longer observation times in the self-bunching mode, indicating that a very high mass resolution is possible with this type of mass spectrometer.

Fig. 6b shows a 5th harmonic from which the mass resolution is calculated as $R = m/\Delta m \sim 21{,}000$. This is mainly because the oscillations of the ion bunches in the ion trap are not affected by the usual factors that affect normal TOF instruments such as trigger jitter, time response of the MCP detector, etc. These and other interesting features such as its ability to be coupled with multiple ion sources such as MALDI ion source, Electrospray ion sources, etc., make this ion trap, a versatile instrument for mass spectrometry.

Conclusion

We have demonstrated a novel electrostatic ion trap which traps and stores ions as a well defined beam that works on the principle of an optical resonator. Storage lifetimes of about >100ms for various ions could be achieved. We have also demonstrated the capabilities of the ion trap as a high resolution mass spectrometer with mass resolutions over 20,000.

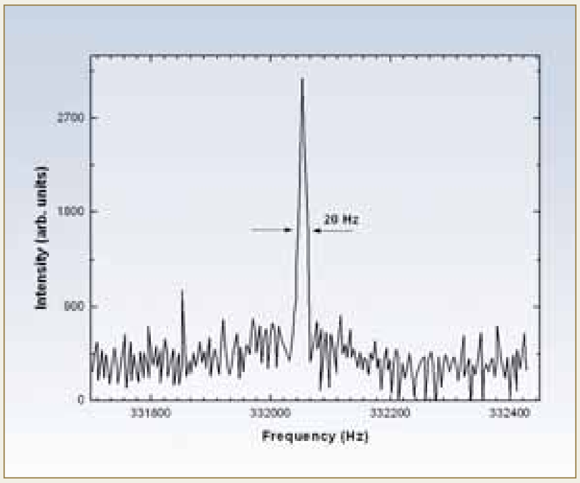

Fig. 4: Frequency domain spectrum showing the first harmonic of trapped Ar^+ ions in the dispersive mode

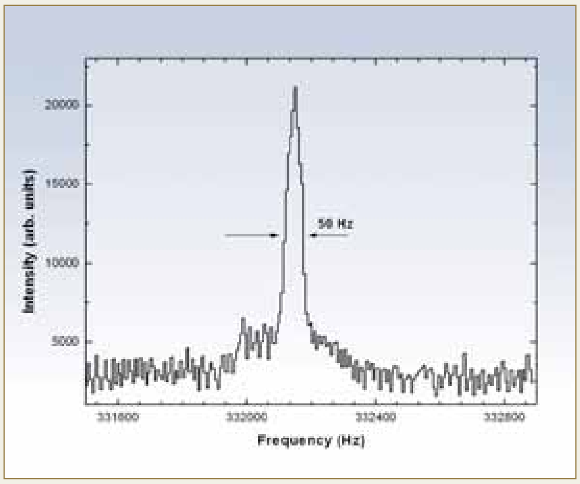

Fig. 5: Frequency domain spectrum showing the first harmonic of trapped Ar^+ ions in the 'Self-bunching' mode

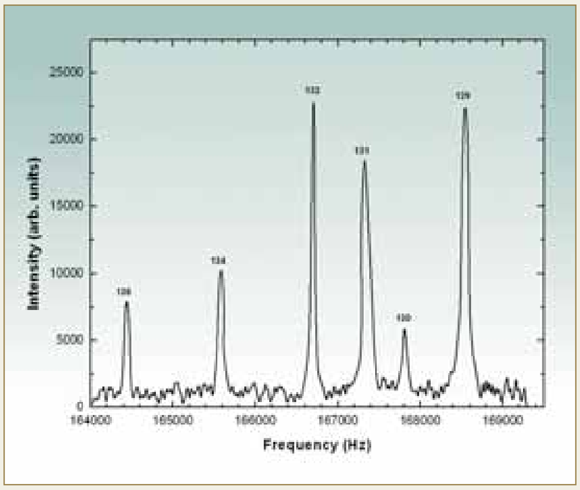

Fig. 6a: Frequency domain spectrum showing the first harmonic of trapped Xe$^+$ ions in the 'Self – bunching' mode

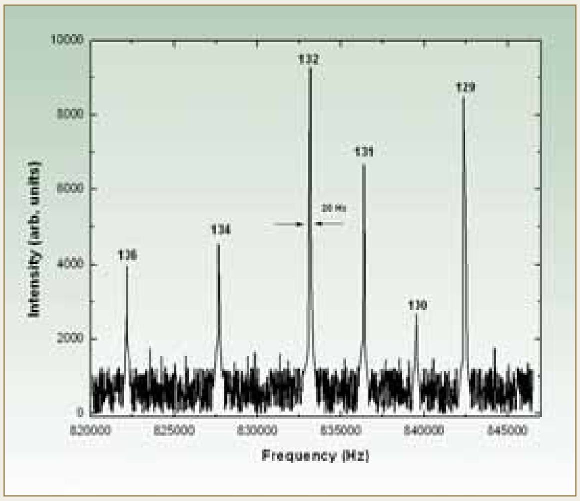

Fig. 6b: Frequency domain spectrum showing the fifth harmonic of trapped Xe$^+$ ions in the 'Self – bunching' mode

Further improvements are presently underway to enhance the mass resolution by utilizing extremely low ripple high voltage power supplies, very low noise charge-sensitive pre-amplifiers and to improve the base pressure in the ion trap. With these developments we expect this ion trap to be capable of studying large bio-molecules with particularly interesting functional properties.

Acknowledgements

This work was supported by the Dept. of Atomic Energy, Govt. of India through project grant "Programme on advanced analytical and other instruments". Technical help of Mr. V. B. Chandratre in setting up the low noise charge pre-amplifier and Mr. S M Rodrigues for assembly and alignment of the Ion trap is gratefully acknowledged.

References

1. W. Paul and H. Steinwedel, Z. *Naturforsch. A* 8, 448 (1953).
2. see for eg., *Phys. Scr.* T59 (1959) ; "Ion Traps" Pradip K Ghosh.
3. D. Habs et al., *Nucl. Instrum. Methods Phys. Res*. B 43, 390 (1989).
4. R. Stensgaard, *Phys. Scr.* T22, 315 (1988).
5. K. Abrahamsson et al., Nucl. Instrum. Methods *Phys. Res.* B 79, 269 (1993).
6. W.C. Wiley and I. H. Mclaren, *Rev. Sci. Instrum.* 26, 1150 (1955).
7. B. A. Mamyrin , V. I. Karataev, D. V. Shmikk and V. A. Zagulin, Sov. *Phys. JETP,* 37, 45, (1973).
8. C. K. G. Piyadasa, P. Hakanson and T. Ariyaratne, Rapid Commun. *Mass Spectrom.* 13, 620 (1999).
9. W. H. Benner, *Anal. Chem*. 69, 4162 (1997).
10. S. Ring, H. B. Pedersen, O. Heber, M. L. Rappaport, P. D. Witte, K. G. Bhushan, N. Alstein, Y. Rudich, I. Sagi and D. Zajfman, *Anal. Chem*. 72, (17), 4041, (2000).
11. D. Zajfman, O. Heber, L. Vejby-Christensen, I. Ben-Itzhak, M. Rappaport, R. Fishman, and M. Dahan, *Phys. Rev.* A 55, R1577 (1997).
12. M. Dahan, R. Fishman, O. Heber, M. Rappaport, N. Altstein, D. Zajfman, W. van der Zande, *Rev. Sci. Instrum.,* 69 (1), 76, (1998).
13. K G Bhushan, H B Pedersen, N Alstein, O Heber M L Rappaport and D Zajfman, *Phys. Rev. A.,* 62, 12504, (2000).
14. Yariv, in Quantum Electronics, 3rd ed. (Wiley, New York, 1989), p.142.
15. SIMION V.7.0, Ion Source Software.
16. H. D. Zeman, *Rev. Sci. Instrum.* 48 (8), 1079, (1977).

ABOUT THE AUTHORS

Dr. K. G. Bhushan joined TP&PED, BARC in 1993. Since then, he has worked primarily in the field of development of novel analytical instrumentation for Surface analysis and Synchrotron radiation based studies. He was awarded the 'Feinberg Graduate School – Post Doctoral fellowship' by Weizmann Institute of Science, Israel. He has developed a novel version of the ion trap that can be utilized as a high resolution mass spectrometer and also developed special electrodes for Triode-type sputter Ion pumps. His current research interests include development of high spatial resolution chemical imaging Secondary Ion Mass Spectrometer and special pumps for the production of extreme high vacuum.

Dr. S. C. Gadkari is presently Head, Crystal Technology Section, TP&PED, BARC. Dr. Gadkari's research interests include: Thin film based gas sensors for H_2 and H_2S, Crystal growth and characterization of high temperature superconductor, development of pulsed current-voltage characteristic measuring instrument, growth of ferroelectric Lead Germanate crystals and development of energy maters for fast laser pulses as well as growth of novel crystals for use as scintillators, synchrotron radiation based analytical systems and thin film based devices for production of ultrahigh vacuum.

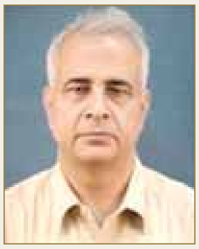

Dr. J. V. Yakhmi is presently the Associate Director(S), Physics Group, BARC. Dr. Yakhmi's current research interests range from high temperature superconductors to Molecular electronics, Self-organized systems, nano-technology and development of advanced functional materials that can be used as sensors for various applications ranging from trace-gas detection to radiation monitoring. Dr. Yakhmi heads several research committees, including BRNS Basic Sciences research committee. Dr. Yakhmi is also Head, Technical Physics & Prototype Engineering Division, BARC.

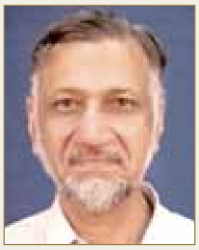

Dr. V. C. Sahni was Director, Physics Group, BARC and Director, RRCAT, Indore. Dr. Sahni's current research interests include accelerators, synchrotron radiation sources and their utilization, condensed matter physics, building and using various kinds of advanced equipment for physics research and applications including electron accelerators and lasers. He has been instrumental in the commissioning of INDUS-2, the Indian Synchrotron Radiation Source (SRS). As part of DAE/CERN collaboration, Dr. Sahni has spearheaded the design, development and delivery of prototypes of many high quality components and subsystems. Dr. Sahni is a fellow of the National Academy of Sciences and has been conferred the 'M. M. Chugani Award' for the year 2004, by the Indian Physics Association.

TECHNOLOGY DEVELOPMENT FOR THERMOELECTRIC DEVICES

A. Singh
Technical Physics and Prototype Engineering Division

Dr. Ajay Singh is the recipient of the DAE Young Scientist Award for the year 2007

ABSTRACT

Diffusion bonded very low resistance electrical contacts (specific contact resistance < 10 $\mu\Omega cm^2$) have been developed on *n*-type PbTe and *p*-type TAGS-85 ($(AgSbTe_2)_{0.15}(GeTe)_{0.85}$) thermoelements. Thermoelectric devices having two *p*-*n* couples in series (each of four elements having 7.5 mm dia) generated an output power of 1.2 W (at operating current of ~ 17 Amp) at hot side temperature $T_h = 500$ °C and a temperature difference $\Delta T = 410$ °C. Internal resistance of the devices was found to increase linearly with increase in the number of thermoelements. The efficiency of developed thermoelectric devices was found to be 6 %. The devices have been continuously operated for more than 8 months in air without any degradation of the output power.

Introduction

In view of global energy need and global warming problems, research and development in the field of thermoelectric power generation, as a means of recovering huge amount of waste heat emitted by automobiles, factories etc., has been accelerating at a fast prace. The ThermoElectric Devices (TED) convert heat into the electrical energy. These consists of several *n*- and *p*-type semiconductor thermoelements connected electrically in series and thermally in parallel. Electrical contact between these n and p-type thermoelements is usually made using metallic electrodes [1]. It is desirable that the joints between the thermoelements and the electrodes have low electrical contact resistance and resist fracture during thermal cycling. Mechanical failure due to thermal expansion mismatch may be eliminated, by inserting a buffer layer of intermediate thermal expansion between metal electrode and thermoelectric materials. In addition to this, materials should be selected so that there is no inter-diffusion between joining materials and thermoelements. In thermoelectric coolers, solder materials such as SnBi, are normally used to connect p and n–type thermoelements, via Cu metal stripes. However, for TED operating at high temperatures, diffusion related problems are significant and may lead to device performance degradation with time. A thin diffusion barrier of material such as iron, molybdenum or tungsten may prevent diffusion.

Depending on the operating temperature of TED, different kinds of *n* and *p*-type semiconductor materials are currently being used. Semiconductor alloys like *n*-type PbTe and *p*-type $(AgSbTe_2)_{0.15}(GeTe)_{0.85}$ (TAGS-85) and Si-Ge alloys are well established for electrical power generation at high temperatures [1]. Since 1961, PbTe, TAGS-85 and Si-Ge based TEDs were successfully employed for reliable delivery of power, to space mission probes. These TED's have worked successfully for more than 20 years. In the space mission TED such as n-PbTe/p-TAGS based devices, the contacts between elements and electrode (nickel stripes) were formed by Ag-Cu-In brazing alloys [1, 2]. In case of Si-Ge based devices electrical contacts were formed by tungsten as interconnect and graphite as buffer layer [1, 2]. So far there are only few reports that deal with details of fabrication of highly efficient TED. Hori et al have fabricated a stacked TED using Bi-Te and Pb-Te with are efficiency of 6.1% [2].The key to realizing an efficient TED, depends on finding good thermoelectric materials and very low contact resistance between interconnects and thermoelements [3]. So far there is not enough published literature which details interface studies of electrode / thermoelectric materials and which play a significant role in deciding the contact resistance and long-term stability of TED.

Here we report the fabrication and characterization of *n*-type PbTe and *p*-type TAGS-85 thermoelements with Ag shoes at the ends and subsequently the fabrication of devices using two p-n couples in series. The *p*-type and *n*-type thermoelements were joined by silver stripes using diffusion bonded contact using Fe powder and SnTe based interfaces. Two legs devices showed an open circuit voltage of 135 mV and a current of 17 Amp with matched load of 4 mW. In these devices, contribution of contacts to total device resistance was found to be 3.5%. The working efficiency of the devices was found to be ~6 %.

Experimental details

Single-phase polycrystalline *n*-type PbTe and *p*-type TAGS-85 materials were synthesized by vacuum melting in a rocking furnace [1, 4]. To fabricate *n*-type PbTe elements (7.5 mm dia. and 8 mm height), powder of PbTe was filled in a stainless steel (SS) die with interface layers of Fe and (50% PbTe+ 50%Fe) as shown in Fig. 1(a). The SS die had a thin graphite liner to avoid reaction with thermoelectric materials. This layered structure was then pressed in a vacuum hot press at temperature of 600°C and a load of 700 kgs. The fabrication of *p*-type TAGS-85 elements was carried out in a similar way to that of n-type PbTe using SnTe and Fe as interface materials as shown in Fig. 1(b). As the diffusion of Fe into TAGS-85 is reported to result in rapid degradation of the contacts [1, 4], SnTe was used as a diffusion barrier. For assembly of the devices, PbTe and TAGS elements were connected using silver stripes as discussed later.

The fabricated thermoelements were characterized for phase identification, microstructures, interface analysis, temperature dependence of Seebeck coefficient (*S*), electrical conductivity (σ) and power output. Conductivity was measured using a standard four-probe measurement technique on rectangular bar-shaped samples (PbTe, and TAGS) of 7x3x1 mm^3 size using silver paint contacts for voltage and current. The Seebeck coefficient was measured using seesaw method. For this purpose, two miniature Pt heaters of 2 x 2 mm^2 size were attached at two ends of the rectangular samples, using thermally conducting but electrically insulating alumina cement. The two ends of the sample were alternately heated (to yield a temperature difference of nearly 10 °C across the sample) and generated Seebeck voltages were measured using two silver pint contacts. The temperature difference across the sample was measured using a chromel- alumel (K-type) differential thermocouple, which is fixed on the sample using alumina cement. For measurements of temperature dependence of *S* and σ, the sample with contacts were placed in a furnace and temperature was controlled at different value using a Eurotherm temperature controller. Errors in the measurement of *S* and σ arise from error in measurement of sample dimensions and voltage / thermocouple contact spacings and total error is expected to be less than 10%. The measurements were repeated in 4-5 samples of each type and results agreed within ±7% of average value.

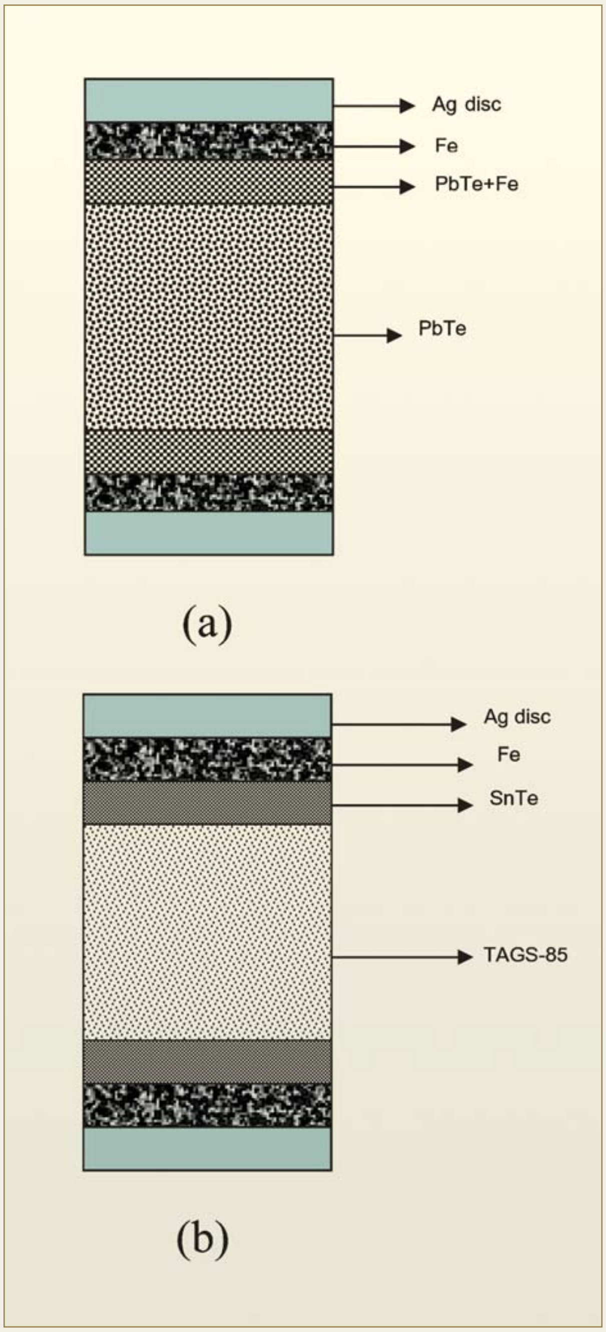

Fig. 1: Schematic diagram showing the sequence of materials inside the die set for fabrication of (a) n-type (PbTe) and (b) p-type (TAGS-85) thermoelements.

In order to characterize the devices for maximum power output, resistances of different values (0.5-30mΩ) were prepared using thick copper wires. The length of the resistance was maintained at more than 5 cm to minimize any error due to soldering at ends. Values of these resistances were accurately measured using the four-probe technique by soldering them between two thick silver stripes. For power measurement, resistances were connected across the devices and voltages across them were measured using a Keithley make nanovoltmeter. The measured voltage was used to calculate device current and power using already resistance values. Maximum power output and optimum load were determined from these data for different resistances. Errors in power output measurement were due to small errors in four probe measurement of load resistances and is expected to be less than 2%.

Results and Discussion

Fig. 2 shows X-Ray Diffraction (XRD) patterns of the synthesized compounds. These show single phase PbTe (with NaCl structure with lattice parameter of 6.463 Å) and TAGS-85 materials .TAGS-85 is found to have hexagonal structure with *a* and *c*- axis lattice parameters of 8.34 Å and 10.66 Å respectively.

The various interfaces of the PbTe and TAGS-85 thermoelements were characterized by Scanning Electron Microscopy (SEM) and Energy Dispersive X-ray analysis (EDX) techniques and the results are shown in Figs. 3 and 4 respectively. Here, we may like to add that the interface images shown here were obtained on thermoelements after continuous operation for more than 4 weeks. In order to study the interfaces, the samples were cut and polished to obtain a mirror-like surface finish. The Back-Scattered Electron (BSE) image of PbTe element (shown at the centre of Fig. 3), clearly reveals chemically sharp interfaces between Ag, Fe, (PbTe+Fe) and PbTe. This is further supported by the x-ray mapping of Ag, Fe, Pb and Te elements (shown as side images in Fig. 3). No interaction between PbTe and Fe is observed in (PbTe+Fe) layer. These results are in agreement with the reported phase diagram of

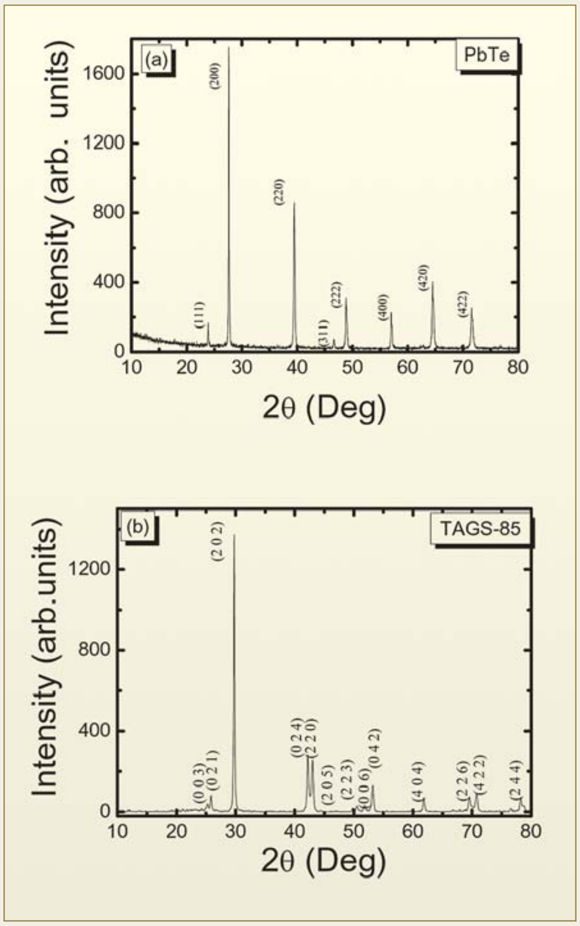

Fig. 2: X-ray diffraction pattern of (a) PbTe and (b) TAGS-85 materials

PbTe-Fe and indicate the high quality of the bonding achieved between PbTe and Fe.

Results of imaging and elemental mapping of TAGS-85 elements also showed chemically sharp interfaces (Fig. 4). We did not observe any diffusion across Fe/SnTe or SnTe/TAGS-85 interfaces which is reported to result in the loss of device strength and its failure. Due to immiscibility of Fe and Ag at equilibrium, the Fe/Ag interface is found to be chemically sharp in both type of thermoelements. On comparison with images taken for fresh elements (not shown here) no difference in interface sharpness was observed.

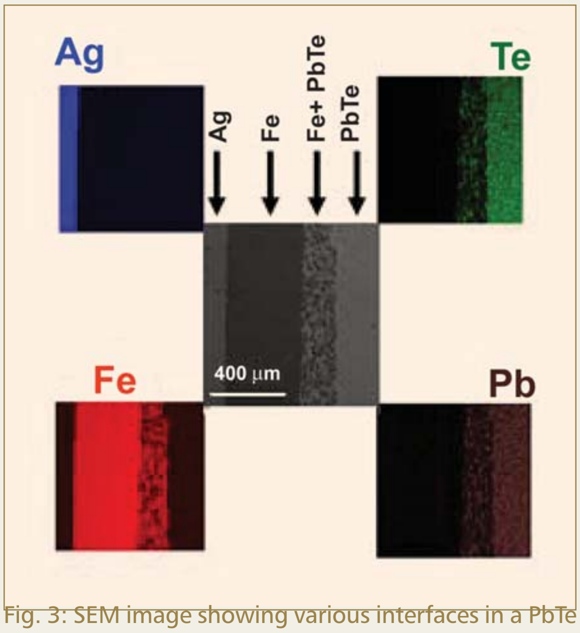

Fig. 3: SEM image showing various interfaces in a PbTe element. Side images show the elemental mapping of Ag, Fe, Pb and Te obtained using EDX

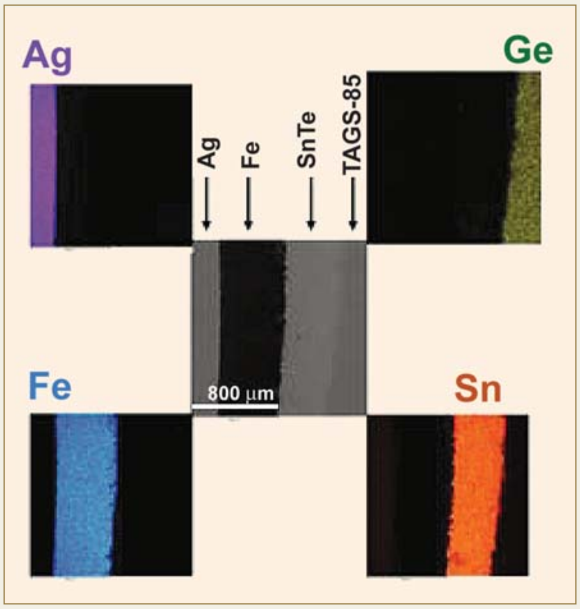

Fig. 4: SEM image showing various interfaces in a TAGS element. Side images show the elemental mapping of Ag, Fe, Sn and Ge obtained using EDX

The temperature dependence of Seebeck coefficient (*S*), electrical conductivity (σ) and power factor (S^2s) for PbTe and TAGS-85 elements are shown in Figs. 5 and 6, respectively. The electrical conductivity (σ) decreases with increasing temperature for both elements as expected for heavily doped semiconductors. The absolute value of *S* increases with increasing temperature, resulting in similar temperature dependence of the power factor ($S^2\sigma$) for both elements. The power factors at 500°C are found to be 18 μWcm^{-1}K^{-2} for PbTe and 24 μWcm^{-1}K^{-2} for TAGS-85 as compared to the best reported values of 26 and 36 μWcm^{-1}K^{-2} respectively [1]. It may be noted that synthesized PbTe and TAGS-85 materials exhibit nearly same power factor at temperature of operation and the transport properties are very close to the optimized materials synthesized by other research group.

For fabrication of the devices, thermoelements were packed in an asbestos housing that provides an enclosure to hold them and being an insulator, reduces direct flow of heat between hot and cold surfaces. Subsequently, silvers stripes were placed on the top and bottom side the thermoelements. Fig. 7 (a) shows the schematic diagram for a two legs device. The entire assembly was vacuum hot pressed (vacuum of 2 x 10^5 Torr) and optimized bonding temperature of 400 °C. Photographs of 2, 4 and 6 leg devices fabricated in this manner are shown in Fig. 7 (b).

In order to characterize the devices, they were placed in a home-made testing set up, having a spring-loaded hot surface and water-cooled copper base. The temperature of hot surface and water-cooled surface were measured by thin wire (25 μm) thermocouples placed between the hot / cold ends and device.

Characteristics for a typical two legs device as function of load resistance are shown in Fig. 8 (a) for hot end temperature of 500°C and temperature difference of 410°C. The device showed an open circuit voltage of 130 mV and maximum output power of ~ 1.15 watt (with load voltage of 68 mV and current of 17 Amp.). Similarly other devices were characterized and Fig. 8(b) shows the maximum output power for different devices as function of hot side temperature (T_h). The expected open circuit voltage was also estimated for a temperature difference of 410°C, using Seebeck coefficient (of PbTe

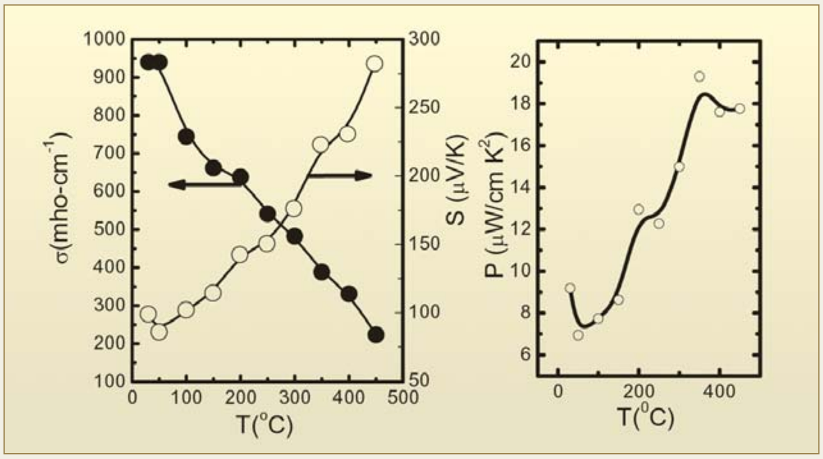

Fig. 5: Temperature dependence of electrical conductivity (σ), Seebeck coefficient (*S*) and power factor (*P*) for PbTe thermoelement.

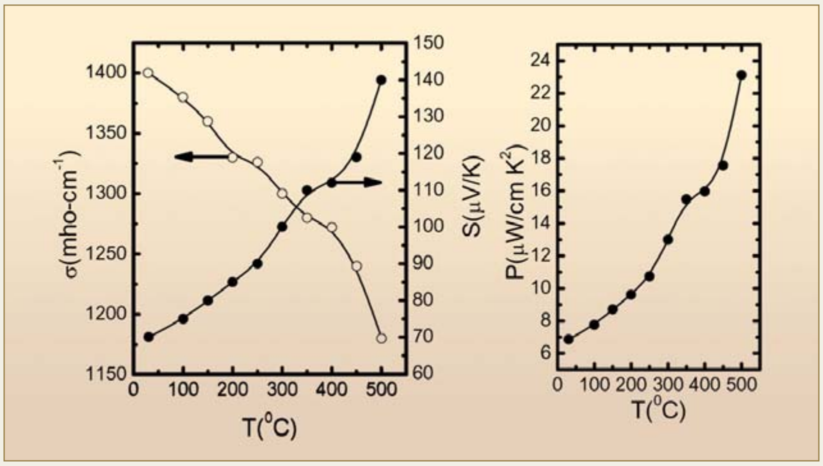

Fig. 6: Temperature dependence of electrical conductivity (σ), Seebeck coefficient (*S*) and power factor (*P*) for TAGS-85 thermoelement.

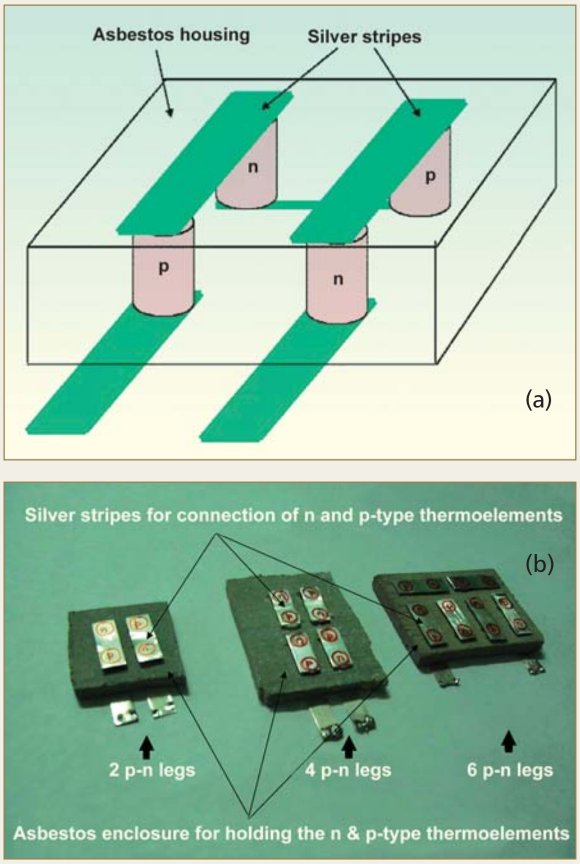

Fig. 7: (a) Schematic diagram showing the packing and interconnection between elements in two legs device (b) Photographs of two, four and six legs TED

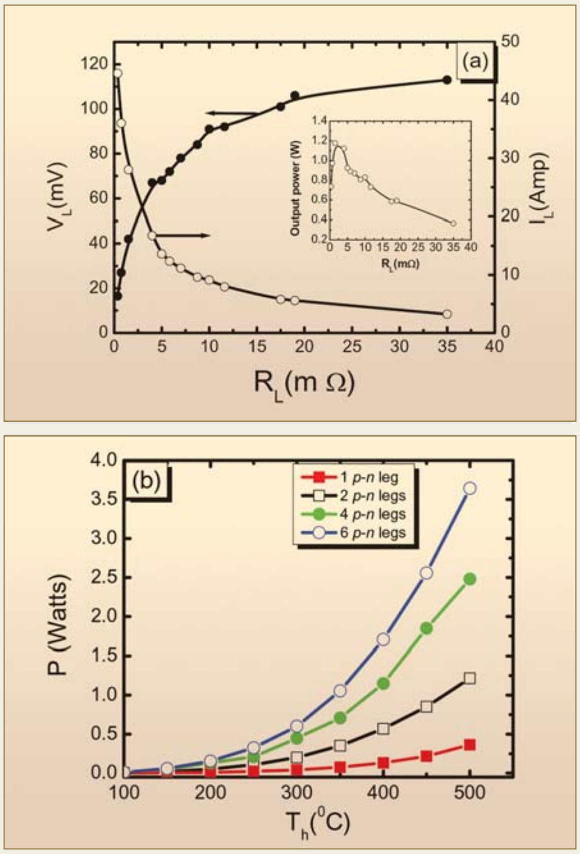

Fig. 8: (a) The load voltage (V_L) and current (I_L) as a function of load resistance (R_L). The inset shows output power of two legs device (b) Output power different devices as a function of hot side temperature (T_h)

and TAGS) at average temperature of 295^{o}C. This yielded a value of ~ 200 mV compared with the measured value of 130 mV. The difference between the measured and estimated values could be due to actual temperature difference across PbTe and TAGS part of elements in Fig. 1 being lower due to the temperature drop across the silver metal stripes and interface layers.

I-V characteristics of all the devices were found to be linear showing ohmic contacts. The internal resistance (R_{int}) of a device (See Fig. 1) has two contributions. First contribution is due to material resistance (*Rm*) contributed by (a) PbTe (R_{PbTe}) and TAGS (R_{TAGS}) cylindrical shaped layers, (b) SnTe (R_{SnTe}) or PbTe+Fe ($R_{PbTe+Fe}$) and Fe layers (R_{Fe}) in TAGS/PbTe elements and (c) silver discs and strips (R_{Ag}). The second contribution is combined contact resistance (*Rc*) of all the interfaces in each element. Contributions to *Rm* were determined by measurement of four probe resistivity of each material (using bar shaped sample described as earlier) and for a two legs device were found to be, R_{PbTe} = 1.1 μΩ, R_{TAGS} = 0.75 μΩ, R_{SnTe} = 45.4 μΩ, $R_{PbTe+Fe}$ = 5 μΩ, R_{Fe} = 0.87 μΩand R_{Ag} = 9.82 μΩ yielding a total materials resistance of *Rm* = 3.84 μΩ. The resistance of two leg device (having four elements) was measured by the four probe technique to be 3.98 mW (the resistance of complete device was also calculated by measured voltage drop across a load and open circuit voltage of the device. Both measurements yielded similar results). This yields average contact resistance for each element to be 35 μΩ (specific contact resistance = 7.6 μΩcm^2 for each contact). The contribution of contact resistance to total device resistance is found to be 3.5%. Similar results were obtained for four and six legs devices. It may be noted that the fractional loss of power due to contact resistance is approximately equal to the ratio of contact and thermoelectric material resistances. For contacts of given specific resistance, fractional loss of power is independent of element area, but is inversely proportional to element length. In some of the earlier studies a specific contact resistance value of less than 100 $\mu\Omega$cm^2 has been mentioned as desirable, for thermoelectric applications. As the four probe resistance of the device can be measured accurately ($<$ 0.1% error), errors in the measurement of contact resistance arise from errors in the measurement of resistivity of each material (10% as mentioned in the experimental section).

The efficiency of the devices was directly measured as ratio of electrical power output to heat flow through the device. For determination of heat flow through device elements, radiation loss from heater and heat flow through asbestos housing were first determined, using thermally insulating material and plain asbestos sheets. For two legs device, heat flow was found to be 20 W, yielding a typical device efficiency of ~6% [4]. The durability of the devices was investigated by their continuous operation under $T_h = 500$ °C and $\Delta T = 410$ °C in air. Three devices were operated continuously for 8 months without any measurable degradation.

Conclusions

In conclusion we have demonstrated a process for the fabrication of thermoelectric devices based on *n*-type PbTe and *p*-type TAGS-85 thermoelements. The average electrical contact resistance for each contact in the devices was found to be £10 $\mu\Omega$-cm^2. SEM images and EDX analysis of electrode and thermoelectric materials interfaces revealed chemically sharp interfaces even after long period of operation of devices. For hot end temperature of 500 °C and temperature difference of 410 °C, two legs devices exhibited typical output power of ~ 1.2 W (at current of 17 Amp) with a working efficiency of 6%. The devices have been continuously in operation for 8 months, without any degradation.

Acknowledgement

The author wishes to thank Dr. K. Bhanumurthy of MSD, BARC for the technical discussion about the diffusion-bonding of the electrical contact.

References

1. Rowe D M 1996 *CRC Handbook on thermoelectrics* (Boca Raton, FL: CRC Press).
2. Hori Y, Ito T 2006 *Proceeding of 25th International conference on Thermoelectrics* (*Vienna Austria*) p.642.
3. Abels B, Beers D S, Cody G D, Dismukhes J P 1962 *Phys. Rev.* 125 44.
4. Ajay Singh, S. Bhattacharya, C. Thinaharan, D. K. Aswal, S. K. Gupta, J. V. Yakhmi, K. Bhanumurthy 2009 *J. Phys. D: Appl. Phys.* **42** 015502.

About the Author

Dr. Ajay Singh joined Technical Physics and Prototype Engineering Division of BARC in 1999, after graduating from the 42nd Batch of the Training School in Physics discipline. He completed his Ph. D. from Mumbai University in 2004. He was a Humboldt Post doctoral Fellow at Physikalisches Institute, University of Karlsruhe Germany during 2005-2007. His field of interest are understanding the novel properties of superconductor / ferromagnet multilayer, MgB$_2$ superconductor and development of thermoelectric devices. He has published about 35 papers in peer-reviewed journals.

BARC NEWSLETTER

DIFFUSION IN CU(AL) SOLID SOLUTION

A. Laik and K. Bhanumurthy
Materials Science Division

Mr. Arijit Laik is the recipient of the DAE Young Engineer Award for the year 2007

ABSTRACT

The solid state diffusion characteristics in the Cu(Al) solid solution phase, was investigated in the temperature range of 1023–1223 K, using single phase bulk diffusion couples, between pure Cu and Cu- 10 at.% Al. The interdiffusion coefficients, *D*, were calculated using Boltzmann–Matano method and Hall's method from the concentration profiles of the couples acquired using EPMA. The calculated interdiffusion coefficients (*D*) ranged between 1.39 X 10^{-14} and 3.97 X 10^{-13} m^2/s in the temperature range of 1023 to 1223 K. The composition and temperature dependence of *D* were established. The activation energy for interdiffusion varies from 123.1 to 134.2 kJ/mol in the concentration range 1 at. % $\leq C_{Al} \leq$ 9 at. %. The impurity diffusion coefficient of Al in Cu, is determined by extrapolating the interdiffusion coeffficient values, to infinite dilution of the alloy i.e $C_{Al} \rightarrow 0$ and its temperature dependence was also established. The activation energy for impurity diffusion of Al in Cu was found to be 137.1 kJ/mol.

Introduction

The Cu-rich side of the Cu-Al system, finds commercial application in the form of aluminium bronzes, which are Cu-based alloys containing up to 16% Al. These alloys are considered as potential materials for a wide variety of applications, due to their corrosion resistance and exceptionally high strength [1]. The Cu-side terminal solid solution is single phase Cu(Al) (α-phase) and can dissolve up to 19.7 at. % of Al and can be strengthened by cold working. Additions of certain elements, such as cobalt and nickel render these single-phase binary alloys, age-hardenable. The Cu(Al) solid solution takes part in two solid state reactions in the system i.e. a eutectoid reaction $\beta \leftrightarrow \gamma_1 + Cu(Al)$ at 567 °C and a peritectoid reaction $Cu(Al) + \gamma_1 \leftrightarrow \alpha_2$ [2]. These reactions being solid state in nature, their kinetics are essentially controlled by the diffusion behaviour of the participating phases.

It is worth noting, that Sprengel et al [3] showed that the interdiffusion coefficients obtained from diffusion couple consisting of multiple phases, differ from those consisting of a single-phase. Kim and Chang [4] have reported a large difference in the activation energy for interdiffusion, determined by multi-phase diffusion couples and single-phase diffusion couples, in the NiAl phase. The large difference in the activation energy could be due to the fact, that phase boundaries formed in multi-phase diffusion couples, influence the diffusion flux to a large extent. The phase boundaries act both as source and sink for point defects and the grain boundaries in an intermediate phase, formed during annealing, may alter the overall diffusion rate in the system. Therefore, the diffusion coefficients calculated from such experiments, are not truly representative.

Besides, no published data for tracer diffusivity of aluminium (D_{Al}) in Cu is available. It is worth mentioning here, that this is due to the experimental limitations in determining the impurity diffusion coefficient of Al in Cu, primarily due to non-availability of suitable radioactive isotope of Al, which could be used as tracer. The only isotope which is suitable for such experiments is ^{26}Al ($t_{1/2}$ = 0.75 X 10^6 yr), which has low specific activity and is extremely expensive. The production and isolation of the ^{26}Al isotope, required for the radio-tracer diffusion experiments, is extremely difficult [5] and can be achieved through a (*p,pn*) nuclear reaction, with naturally occurring ^{27}Al in a cyclotron [6]. However, the impurity diffusion coefficient of Al can also be determined, from concentration-dependent interdiffuson coefficients, using diffusion couples experiments. Recently such studies on binary systems Ni-Al [7] and Zr-Al [8] have been reported.

The present study reports a detailed investigation of the diffusion behaviour in the fcc Cu(Al) solid solution, in the concentration range $0 \leq C_{Al} \leq 10$ at.% Al in the temperature range of 1023 to 1223 K. The impurity diffusion coefficient of Al in Cu, is determined by extrapolating the interdiffusivity values, to infinite dilution of the alloy i.e. $C_{Al} \rightarrow 0$ and its temperature dependence was also established.

Experimental procedure

A dilute alloy of nominal composition Cu-10 at. %Al was prepared by vacuum induction melting, using pure (99.9%) Cu and pure (99.95%) Al. Rectangular pieces of size 10 X 8 X 3 X mm^3 were cut from the rolled Cu-Al alloy and pure Cu and were encapsulated in quartz tubes in He atmosphere and annealed at 1223 K for 72 h. The 10 X 8 mm^2 surfaces of the samples were prepared, to a metallographic finish of 0.25 µm. The diffusion couples were made by keeping the polished surfaces of the pure Cu and the Cu-10 at. %Al alloy pieces in contact with each other, under a pressure of about 5 MPa in an Inconel die and then heating in vacuum better than 10^{-3} Pa at 1223 K for 1 h. Chemical analysis using EPMA across the interface of the as-bonded couples, showed a negligible diffusion width. The couples were then sealed in quartz capsules in He atmosphere and diffusion-annealed isothermally, for different time intervals, in a preheated resistance heating furnace, in the temperature range 1023–1223 K for 24–72 h. The details of the heat treatment schedule of the isothermal diffusion annealing are given in Table 1. The cross-sections of the couples were prepared to 0.25 µm finish using standard metallographic techniques as described earlier. The polished surfaces of the couples were etched with an etchant with the composition: 5 parts water, 5 parts ammonium hydroxide and 2 parts hydrogen peroxide to reveal the microstructure.

The cross-sections of the polished samples were characterized using an optical microscope and an electron probe microanalyzer (CAMECA SX100) equipped with three wavelength dispersive spectrometers. The operating voltage and beam current were kept at 20 kV and 20 nA respectively. Pure Cu and pure Al were used as standards for the analysis. Lithium fluoride and thallium acid pthalate(TAP) crystals were used, for diffraction of Cu-Kα and Al-Lα lines respectively. The standard PAP correction

Table 1: Heat treatment schedule for the diffusion couples

Couple No.	Temperature [K]	Time [hrs]
1	1023	72
2	1073	62
3	1123	48
4	1173	36
5	1223	24

programme was used for atomic number (Z), absorption (A) and fluorescence (F) corrections. Quantitative analysis on point-to-point basis was done at a regular interval of 1-2 µm, by scanning the sample across the bonding interface, to determine the concentration profile. For each sample, at least three scans were taken at different locations, to confirm the consistency of the concentration profiles.

Results and Discussion

Interdiffusion in the Cu(Al) phase

Fig. 1 shows a typical concentration profile for the couple annealed at 1223K. The plot shows typically solid solution type of concentration penetration curve across the interface. The concentration profiles for all the couples are of the same nature and is represented by Fig. 1. During the process of annealing, the initial compositions of the individual pieces of the couples are preserved at the ends, thereby fulfilling the requirement of infinite geometry. The interdiffusion coefficients for various compositions, within the diffusion zone for all the diffusion couples, were calculated by using the Boltzmann-Matano method [9,10] and Hall's method [11]. The interdiffusion coefficients (D) calculated ranges between 1.39 X 10^{-14} and 3.97 X 10^{-13} m^2/s in the present temperature range of annealing.

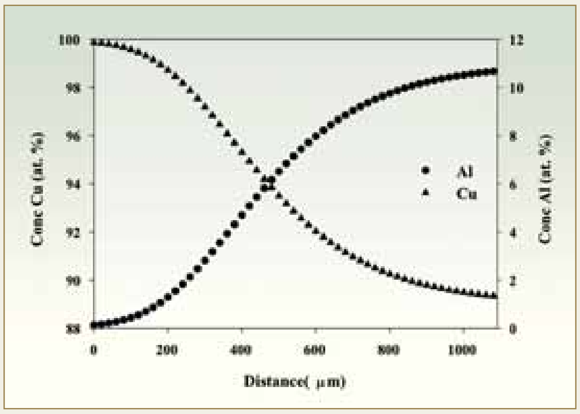

Fig. 1: Concentration profile across the interface of Cu/ Cu-10 at. % Al couple annealed at 1223K for 24 h.

The interdiffusion coefficients were calculated at compositions alloy, ranging from 0.5 at. % to 9.5 at. % at intervals of 0.5 at. %. The concentration dependence of interdiffusion coefficients at various temperatures by Boltzmann-Matano method is presented in Fig. 2. The interdiffusion coefficients at various temperatures are fitted in a cubic relation of the type:

$$D = a + b\,C_{Al} + c\,C_{Al}^{2} + dC_{Al}^{3}$$

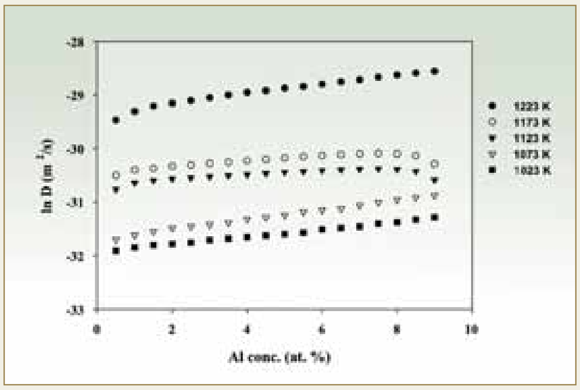

Fig. 2: Concentration dependence of interdiffusion coefficient in Cu(Al) solid solution at various temperatures

The values of the parameters a, b, c and d for various temperatures are given in Table 2.

Such enhancement in the interdiffusion coefficient D of the terminal solid solution, with the addition of Al was reported in other systems as well. For example, increase in the interdiffusion coefficient in the β-Zr(Al) solid solution phase was observed in single phase [8] as well as in multiphase [12] diffusion couple experiments. Similar behaviour was reported in the β-Ti(Al) solid solution phase by Hirano and Iijima [13]. Addition of Al to Cu decreases the solidus temperature line in the Cu–Al phase diagram [2]. The activation energy of diffusion is directly related to the solidus temperature [14]. Therefore, with increase in Al concentration, solidus temperature and hence activation energy decreases and the diffusivity increases.

Table 2: Values of the parameters *a*, *b*, *c* and *d* in the relation $D = a + b\,C_{Al} + c\,C_{Al}^2 + d\,C_{Al}^3$ (C_{Al} is in at. %).

Temperature [K]	*a*	*b*	*c*	*d* X10^{-4}
1023	-29.54	0.24	-0.03	16.21
1073	-30.48	0.04	0.01	-15.02
1123	-30.74	0.01	0.01	-10.63
1173	-31.75	0.14	-0.01	7.02
1223	-31.93	0.09	-0.01	5.04

In order to establish the temperature dependence of the interdiffusion coefficient *D*, the logarithmic values of *D* (ln *D*) is plotted against the reciprocal of the absolute temperature (*T*) of diffusion annealing for various compositions in Fig. 3. A linear relationship in this plot shows, that *D* follows an Arrhenius type of relationship, $D = D_0 \exp(^-Q/RT)$. The pre–exponential factor (D_0) and the activation energy (Q) were evaluated at various compositions, in the range 1 at. % $\leq C_{Al} \leq$ 9 at. % from the values of slope and intercept of the plots in Fig. 3. The values are tabutaled in Table 3. The activation energy for interdiffusion, Q, varies between 123.1 ± 3.9 to 134.2 ± 3.9 kJ/mol in this concentration range.

Impurity diffusion of Al in Cu

According to the Darken's relation [15], the interdiffusion coefficient in an infinitely dilute solid solution, corresponds to the impurity diffusion coefficient of the solute in the solvent matrix. The impurity diffusion coefficient of Al in Cu phase was determined, by extrapolating the *D* values in the range $0 \leq C_{Al} \leq 1$ at. %, calculated by Hall's method, to infinite dilution, i.e., $C_{Al} \rightarrow 0$. In the narrow composition range $0 \leq C_{Al} \leq 1$ at. %, *D* bears a linear relationship of the type $D = a + b\,C_{Al}$. Here the impurity diffusion of Al in Cu is denoted as D_{Al}^{Cu} (C_{Al} = 0). Table 4 shows the values of D_{Al}^{Cu} at various temperatures of investigation. The logarithm of (C_{Al} = 0) is plotted against the inverse of absolute

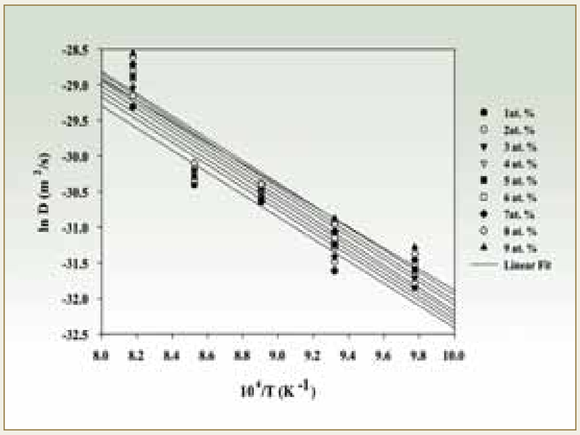

Fig. 3: Temperature dependence of interdiffusion coefficient, *D*, at various concentrations of Al

Table 3: Pre-exponential factor, D_0, and activation energy, Q, for interdiffusion in the Cu(Al) solid solution phase at various compositions of Cu and Al

Composition Al [at. %]	Pre-exponential factor (D_0 X 10^8) [m²/s]	Activation energy [kJ/mol]
1	4.88	129.5
2	7.01	131.9
3	8.22	132.8
4	9.60	133.6
5	10.83	134.2
6	9.68	132.5
7	9.97	132.3
8	8.58	130.4
9	3.82	123.1

Table 4: Impurity diffusion coefficients of Al in Cu.

Temperature [K]	Impurity diffusivity D_{Al}^{Cu} [m²/s]
1023	1.4823 X 10^{13}
1073	5.7903 X 10"^{14}
1123	4.4646 X 10^{14}
1173	1.6261 X 10^{14}
1223	1.3582 X10"^{14}

temperature in Fig. 4. The frequency factor D_0 and the activation energy Q_{Al} have been estimated by fitting a straight line to the data points in Fig. 4, by linear regression method. The activation energy of impurity diffusion is 137.1 ± 4.0 kJ/mol. The temperature dependence can be expressed by an Arrhenius relation:

$$D_{Al}^{Cu} = 1.49 \ X \ 10^{-7} \exp\left(\frac{-137.1 \pm 4.0}{RT}\right) \text{m}^2/\text{s}.$$

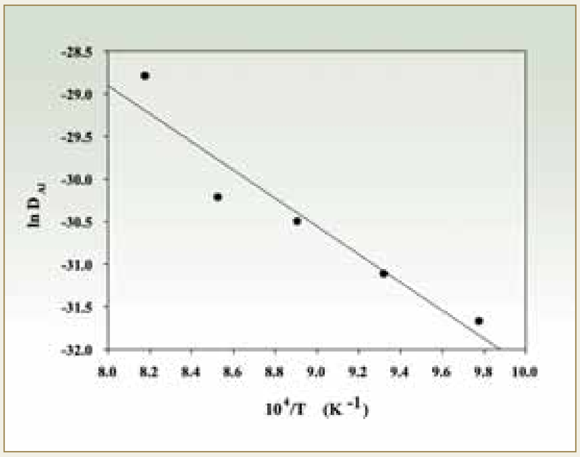

Fig. 4: Temperature dependence of impurity diffusivity of Al in Cu.

Summary

The interdiffusion coefficient for the fcc Cu(Al) solid solution phase was determined, in the temperature range of 1023–1123 K, using single phase bulk diffusion couples, between pure Cu/Cu- 10 at.% Al alloy. The interdiffusion coefficients, *D*, calculated using Boltzmann–Matano method and Hall's method, were found to range between 1.39 X 10^{-14} and 3.97 X 10^{-13} m^2/s in this temperature range. The composition and temperature dependence of the interdiffusion coefficient (*D*) were established. The interdiffusion coefficient (*D*) was found to follow a cubic relation of the type $D = a + b C_{Al} + c C_{Al}^2 + d C_{Al}^3$ with the concentration of Al in the range 1 at. % $\leq C_{Al} \leq$ 9 at. %. The interdiffusion coefficient (*D*) shows an Arrhenius type of temperature dependence and the activation energy for interdiffusion varies from 123.1 to 134.2 kJ/mol in this composition range. The impurity diffusion coefficient of Al in Cu is determined by extrapolating the interdiffusion coefficient values to infinite dilution of the alloy i.e $C_{Al} \rightarrow 0$. The temperature dependence of the impurity diffusion coefficient of Al in Cu D_{Al}^{Cu} was established and the activation energy for impurity diffusion of Al in Cu, was found to be 137.1 ± 4 kJ/mol.

Acknowledgements

The authors are grateful to Dr A. K. Suri, Director Materials Group and Dr. G. K. Dey, Head Materials Science Division, for their support and encouragement.

References

1. Metals Handbook, Vol. 2, 10th Edn., ASM International (1990), Materials Park, Ohio, p. 216.
2. J. L. Murray, in: *Binary Alloy Phase Diagrams*, edited by T. B. Massalski, H. Okamoto, P. R. Subramanian and L. Kacprzak, 2nd Edn., ASM International, Materials Park, OH (1990) pp. 141-143.
3. W. Sprengel, N. Oikawa, H. Nakajima, Proceedings of the Workshop on Defects, Dynamics and Diffusion in Intermetallics, Vienna, Austria, 1994.
4. S. Kim, Y. A. Chang: Metall. *Mater. Trans. A* Vol. 31A (2000) p. 1519.
5. H. Mehrer: *Mater Trans. JIM*, Vol. 37 (1996) p. 1259.
6. T. S. Lundy and J. F. Murdock: *J. Appl. Phys*. Vol. 33 (1962) p. 1671.
7. K. Fujiwara and Z. Horita: *Acta Mater*. Vol. 50 (2002) p. 1571.
8. A. Laik, K. Bhnaumurthy and G. B. Kale: *J. Nucl. Mater*. Vol. 305 (2002) p. 124.

9. C. Matano: *Jpn. J. Phys*. Vol. 8 (1933) p. 109.
10. L. Boltzmann: *Annal. Phys*. Vol. 53 (1894) p. 960.
11. L. D. Hall: *J. Chem. Phys*. Vol. 21 (1953) p. 87.
12. A. Gukelberger, S. Steeb: *Z. Metallkd*. Vol. 69 (1978) p. 255.
13. K. Hirano, Y. Iijima, in: Conference Proceedings of TMS-AIME Fall Meeting Detroit MI, edited by M.A. Dayananda, G.E. Murch, 7 September 1984, p. 141.
14. A. Vignes and C. E. Birchenall: *Acta Metall*. Vol. 16 (1968) p. 1117.
15. L. S. Darken: *Trans. AIME* Vol. 175 (1948) p. 184.

ABOUT THE AUTHORS

Mr. Arijit Laik joined from the 43rd batch of BARC Training School in Metallurgy discipline and was awarded the Homi Bhabha Prize. His research interest is mainly solid state diffusion in metals and alloys. His other research interests are metal-ceramic reactions, dissimilar materials joining and materials characterization using electron probe microanalysis. He has more than 30 research publications.

Dr. K. Bhanumurthy joined the 24th batch of BARC Training School. His research interest includes interdiffusion studies in metals and alloys, similar and dissimilar materials joining using advanced solid state processes, friction stir welding, materials characterization, phase diagrams study and evaluation. He has more than 110 research publications.

STUDIES ON APPLYING RISK INFORMED IN-SERVICE INSPECTION FOR INDIAN NUCLEAR POWER PLANT AND HEAVY WATER PLANT

G. Vinod
Reactor Safety Division

Dr. (Ms.) Gopika Vinod is the recipient of the DAE Young Engineer Award for the year 2007.

What is risk informed IN-SERVICE INSPECTION?

Risk Informed In-Service Inspection (RI-ISI) focuses the utilization of risk quantification in formulating an ISI plan, thereby emphasizing the importance of surveillance and maintenance activities on plant risk. This methodology has been successfully adopted by Oil & Gas industry and Chemical plants, to that extent, they were able to establish an effective structural integrity management programme, which reduces plant down time, industry and regulatory burdens and continues to maintain plant safety. Risk informed methodology has started catching up in nuclear industry as well wherein Probabilistic Safety Assessment (PSA) technique is widely used, for quantifying risk to a plant. PSA results were able to provide insights into myriads of decision making issues such as optimizing Surveillance Test Interval, Allowable Outage Time etc. Since these parameters are directly involved in analyzing the unavailability of safety systems, solutions are provided in a fairly direct manner. But the problem becomes slightly complicated while suggesting an optimum inspection interval for critical components, involved in In-Service Inspection. This paper attempts to traverse through these issues and provides a suitable solution.

Risk can be defined as the likelihood frequency of an event multiplied by the consequence of the event. Extending this definition of risk in RI-ISI [1,2], two factors, viz., failure frequency of the component and its failure consequence are required, for applying this methodology. The In-Service Inspection plan has direct impact on failure frequency of component. After estimating the failure frequency, the next issue involves the selection of systems / components to include the RI-ISI programme. In Nuclear Power Plants (NPPs), consequence is quantified using PSA methodology, whereby the Core Damage Frequency (CDF) is computed. Electric Power Research Institute (EPRI) has suggested a Risk Matrix for RI-ISI, which includes the failure frequency of the components versus its conditional core damage probability. The estimation of Conditional Core Damage Probability (CCDP) is dealt in detail in section 4. Risk Matrix has suggested 7 inspection categories, depending on risk level, which determines the inspection interval, scope of inspection and type of inspection. Many components can fall in the same category, which specifies a period of inspection interval. Proper optimization techniques should be adopted, in deciding the components to be taken up in each year, with respect to cost of inspection, risk level of plant and permissible radiation exposure. These issues and an appropriate solution are summarized below:

1. How to select the component for inspection? (Find a suitable importance measure)
2. How ISI affects component? (Use Markov model)

3. What to do when many components fall in same category? (Formulate optimization problem).

How In-Service Inspection affects the risk of plant?

In-Service Inspection checks for the structural integrity of piping components, using various Non Destructive Testing (NDT) techniques, to detect the presence of flaws or cracks in the component, which can lead to undesirable situations like leak or rupture. Failure of the piping can be termed as the probability that the component reaches these undesirable states. Even if the piping reaches the leak state, repair activity can be carried out during in-service inspection, so that, it can be made functional. In other words, in-service inspection decides the time-dependent failure probability of the component. The NDT technique used during ISI, also decides the probability of detection of flaw that can lead to undesirable state. These aspects have been efficiently handled using Markov model [3,4], so that a realistic estimate of piping failure probability can be used.

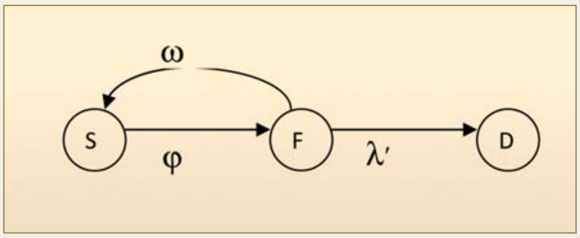

Markov model for single failure state

Piping system state

S = Success state

F = Flaw State

D = Degraded (Leak or Rupture)

State Transitions

φ = Occurrence of flaw

ω = Inspect and Repair Flaw

$\lambda' = $ Occurrence of degraded state $= \lambda_L + \lambda_R$

λ_L = Frequency of leakage

λ_R = Frequency of rupture

φ, the frequency for initiation of flaw can be chosen based on the operating experience or expert judgement. Inspect and repair flaw rate, ω is defined as

$$\omega = P_{f1} P_{FD} / (T_I + T_R) \qquad (1)$$

P_{f1} = probability that piping element with a flaw will be inspected per inspection interval. The value will be 1 if it is in the inspection programme, else it will be 0.

P_{FD} = probability that a flaw will be detected given this element is inspected. This is the reliability of inspection programme and equivalent to Probability of Detection. For most Non Destructive Examinations, the value is between 0.84 and 0.95.

T_I = Mean time between inspections for flaw, is typically 10 years for nuclear power plants

T_R = Mean time to repair once detected, is in order of days, 200 hrs.

Which System to select?

Importance measures have established their credibility in decision making issues. But the conventional importance measures are designed for applying in components from safety systems, which appear in the form of unavailability in PSA analysis. Since RI-ISI principally deals with the components from process systems, which appear as failure frequency in PSA analysis, these conventional importance measures fail to provide suitable solution. Borgonovo [5] has suggested a new measure, Differential importance measure, principally based on sensitivity methods, which has been found suitable for RI-ISI.

Differential Importance Measure (DIM) can be defined as the fraction of total change in Risk that is due to a change in parameter xi.

$$DIM_{x_i} = \frac{\delta R_{x_i}}{\delta R}$$
$$\delta R_{x_i} = R(x_i + \delta x_i) - R_0 \qquad (2)$$
$$\delta R = \sum_i \delta R_i$$

where R is the risk or Core Damage Frequency from PSA model x_i is the component appearing in the PSA model.

A detailed discussion of this measure with its application in RI-ISI can be found in reference [6].

Consequence Analysis and Risk Matrix Categorization

The risk information provides an estimate of consequence of failure of a component, using PSA models. Consequence can be quantified through the estimation of Conditional Core Damage Probability (CCDP). The risk from failure of a component on failure of a specific joint i (eg. a particular weld) is expressed in terms of $CCDP_i$. The consequence evaluation group is organized into two basic impact groups: **(i) Initiating Event and (ii) Loss of Mitigating Ability [1,7].**

In *Initiating Event (IE) impact Group*, $CCDP_i$ can be directly obtained from the PSA results, by dividing the CDF due to the specific IE by the frequency of that IE.

$$CCDP_i = \frac{CDF_{\text{due to IE}}}{IE_{\text{frequency}}} \qquad (3)$$

In the loss of mitigating ability group, the event involves the component failures in safety system. Safety system can be in two configurations, standby and demand. In standby, $CCDP_i$ is

$$CCDP_i = [CDF_{(qi = 1)} - CDF_{(BASE)}] * T_E \qquad (4)$$

and in demand

$$CCDP_i = [CDF_{(qi = 1)} - CDF_{(BASE)}] * T_t \qquad (5)$$

Where,

$CDF_{(qi = 1)}$ = CDF given the component failure from joint i
$CDF_{(BASE)}$ = Base or reference CDF
q_i = component failure/unavailability due to failure from joint i.
T_E = Exposure Time (Detection time + AOT)
T_t = Mean time between tests or demands.

Risk matrix is defined as the decision matrix that is used to categorize the components based on degradation mechanism and consequence of its failure (Fig. 1). From international experience [3], a basis has been established, for ranking components rupture

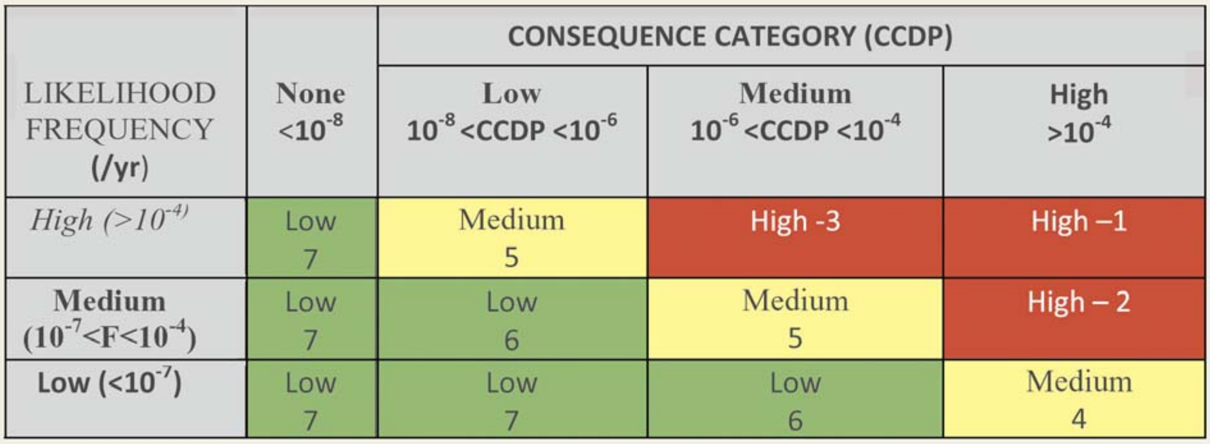

LIKELIHOOD FREQUENCY (/yr)	None $<10^{-8}$	CONSEQUENCE CATEGORY (CCDP)		
		Low 10^{-8} <CCDP <10^{-6}	Medium 10^{-6} <CCDP <10^{-4}	High $>10^{-4}$
High ($>10^{-4}$)	Low 7	Medium 5	High -3	High –1
Medium (10^{-7}<F<10^{-4})	Low 7	Low 6	Medium 5	High – 2
Low ($<10^{-7}$)	Low 7	Low 7	Low 6	Medium 4

Fig. 1 : EPRI risk matrix

potential as High, Medium or Low, simply by understanding the type of degradation mechanism present. Each component is assigned the appropriate category depending on its ΔCDF and degradation mechanism. Each category specifies inspection programme strategy, which will include prioritisation of components for inspection, inspection interval, inspection method and scope/volume of inspection.

How to optimize?

Many components may fall in the same inspection category. An optimum plan should be devised subjected to constraints such as risk to plant, cost of inspection and radiation exposure to workers, if the component is in radioactive area. A typical optimization problem can be defined as

$$\lambda_{\text{system}} = \sum_{i=1}^{n} \lambda_i \qquad (6)$$

Subject to constraints such as

$$C_j = \qquad (7)$$

$y_i = 1$ for $j = x_i$, where x_i is the year of allocation of the feeder. Else, $y_i = 0$

$$E_j = \sum_{i=1}^{n} e_i y_i \le E_{\max} \qquad (8)$$

$y_i = 1$ for $j = x_i$, where x_i is the year of allocation of the feeder. Else, $y_i = 0$
Where,

n is the number of the components in ISI programme.

C_j and E_j are constraints for cost and exposure time respectively.

The objective function itself is an implicit constraint

Case Studies in RI-ISI

(i) Heavy Water Plant- Kota

A pilot study has been carried out for first pair (CT1-HT1) of first stage of exchange towers including gas and liquid loops. Failure data collected from HWP (K) have been statistically analyzed by Bayesian updating technique and generic values are taken from API 581 [8]. ANSI /ASME B31G model has been used, to estimate the remaining strength of pipeline containing corrosion defects. First Order Reliability Method (FORM) has been used for reliability analysis of pipelines [9]. Detailed sensitivity analysis was also carried out, for identifying various critical parameters. For consequence analysis, sample quantitative factors from guidelines of API 581 have been used for consequences, due to toxic release and fire.

The study demonstrates that even at 25 years of plant life, all the Process Heat Exchangers, Coolers, Chillers, Steam Heaters and the liquid pipe line (barring one) poses Medium Risk mainly due to medium consequences. Study also demonstrates that the Towers and large diameter gas lines, fall in the High Risk Category. Prima-facie the study indicates that there is scope for optimization in the existing ISI Plan. It would be proper to put a cautionary note that the pilot study has considered certain failure models, damage mechanisms, likelihood and consequence factor, analytical technique etc. that may be improved upon, in the detailed study.

With this study, it is strongly felt that by amalgamation of ASME and API approach, statutory requirements, past experience of HWB and generic data available for similar plants, the ISI can be optimized.

(ii) Indian PHWR

In the systems considered, any failure in the components present in PHT will be an initiating event, viz., Loss of Coolant Accident (LOCA). Depending upon the area of leak or rupture, they are classified

Table 1: Results of the pilot study on RBI of Heavy Water Plant

Items	Number of items	Consequence category	Failure probability category[1]		Risk		Current ISI [10]
			15 Yrs	25 Yrs	15 Yrs	25 yrs	
Towers	2 Nos	H	H	VH	H	H	H
Process HX	4 Nos	M	VH	VH	M	M	H
Coolers, Chillers Steam Heater	5 Nos	M	VH	VH	M	M	H
Gas Lines	6 Nos	H	M	H	M	H	4H 2M
Liquid Lines	30 Nos	2H 28M	4H 24M 2L	27 VH 1H 2M	28M 2L	1H 29M	10H 20M

either as small or large LOCA events. In the case of Small LOCA, CCDP comes from the accident sequence involving failure of Reactor Protective system, where as in the case of Large LOCA, CCDP comes from accident sequence involving failure in injection and recirculation of Emergency Core Cooling System (ECCS).

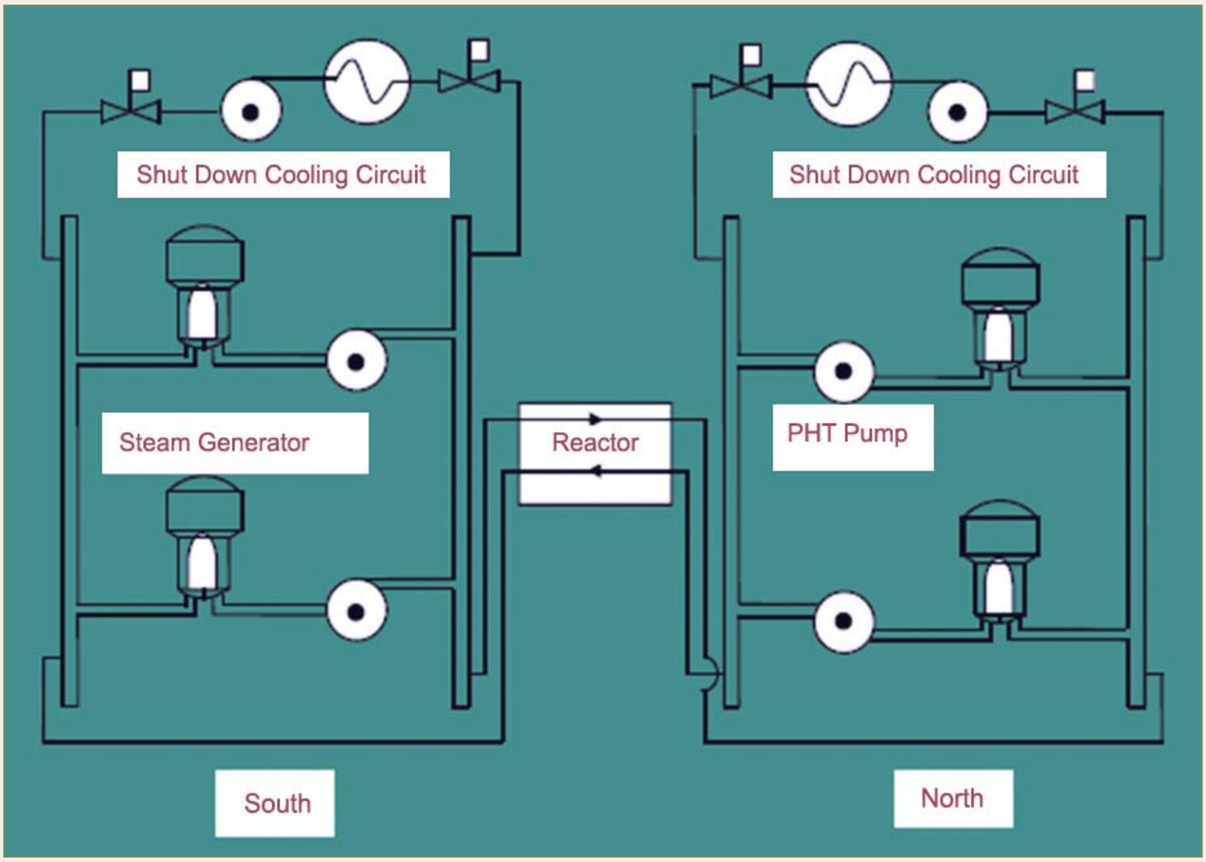

Fig. 2 : Schematic of PHTS and SDCS

For the shut down cooling system, pipelines upto the first isolation valves (MV1, MV2, MV3 and MV4) are connected with PHTS. So any leak or rupture in these pipelines will be equivalent to a LOCA event, and treated likewise. After these isolation valves, components will be in an on-demand configuration. Here, mean time between the tests / inspection interval or demand is to be considered.

Risk impact analysis essentially carries out a comparison between the existing inspection programme and risk-based inspection programme. For the components considered in the case study, these aspects were compared and summarized in Table 2.

Conclusions

Risk Informed In-Service Inspection is in itself an efficient methodology to reduce the inspection resources and plant down time. In the case of nuclear power plant, radiation exposure is also another limiting factor. By employing RI-ISI, the inspection can be focused on the high risk significant systems / components, thereby avoiding unnecessary radiation exposure during the inspection of low risk significant components. Safety is a prime concern in the nuclear industry, which can be suitably contained by the ISI programme suggested using RI-ISI methodology. There are lot of inherent uncertainties involved in PSA analysis, from the point of view of data and modeling, which needs to be properly addressed for successful implementation of RI-ISI.

Table 2 : Risk impact analysis

Sl. No:	COMPONENT DESCRIPTION	CURRENT CATEGORY	RISK CATEGORY
1	Piping from Outlet Header – Steam Generator	B	5
2	Piping from Steam Generator – Primary Coolant Pump	B	5
3	Piping from Primary Coolant Pump Valve	B	6
4	Piping from Primary Coolant Pump – Inlet Header	B	5
5	Steam Generator	A	6
6	Primary Coolant Pump	A	5
7	Reactor headers (RIH/ROH)	A	3

References

1. NUREG-1661, *"Technical Elements of Risk Informed In-Service Inspection for Piping."*
2. Gopika Vinod, Santhosh, Durga Rao.K & R. K. Saraf, "Risk Based Inspection & Decision making", workshop on Risk Management in Chemical Industry, held at AERB, Mumabi, 29th – 30th Januaury 2004.
3. K.N. Fleming, S. Gosselin, and J. Mitman, *"Application of Markov Models and Service Data to Evaluate the Influence of Inspection on Pipe Rupture Frequencies"*, Proceedings of the ASME Pressure Vessels and Piping Conference, Boston, August 1-5, 1999.
4. Gosselin, Stephen R. and Karl N. Fleming, *"Evaluation of Pipe Failure Potential via Degradation Mechanism Assessment"*, Proceedings of ICONE 5, 5th International Conference on Nuclear Engineering, May 26-30, 1997, Nice, France.
5. E. Borgonovo & G. Apostolakis, *"A new importance measure for risk informed decision*

making", Reliability Engineering and System Safety, Vol. 72: pp. 193-212, 2000.

6. Gopika Vinod, H. S. Kushwaha, A.K. Verma & A. Srividya, *"Importance Measures In Ranking Piping Components For Risk Informed In-Service Inspection "*, Reliability Engineering and System Safety, Vol. 80(2), pp 107-113 (2003).
7. EPRI, USNRC, *"Risk Informed In-Service Inspection Evaluation Procedure"*, TR-112657, July 1999.
8. API, 1998. API Publication 581, Base Resource Documentation—Risk-Based Inspection, 1st ed. Order # No.: C58101, © 1995– 1999. American Petroleum Institute.
9. Santosh, Gopika Vinod, O. P. Shrivastava, R. K. Saraf, A. K. Ghosh and H. S. Kushwaha, "Reliability analysis of pipelines carrying H_2S for risk based inspection of heavy water plants", Reliability Engineering and System Safety, pp. 163-170, 91, 2006.
10. In-Service Inspection for Heavy Water Plants, 2000.

About the Author

Dr. (Ms.) Gopika Vinod, a graduate of 37th batch of BARC Training School, joined Reactor Safety Division, BARC in 1994.

She has made significant contributions in the area of Probabilistic Safety Assessment (PSA). She has actively participated in the PSA Studies of AHWR and research reactors, Fire PSA, Risk Informed In-Service Inspection methods for piping systems in DAE facilities and in the development of Risk Monitor.

She has conducted extensive research on applicability of Risk Informed In-Service Inspection methods which have resulted in formulating a complete framework. She has successfully translated the research methods into the application framework. The most important contributions are the introduction of a new importance measure, incorporating the effects of In-service inspection through markov model and using genetic algorithm for optimizing inspection. She could later extend her research for chalking out the RI-ISI programme for nuclear power plants as well as in heavy water plants. She has co-authored a standard for applying the risk-based inspection and maintenance procedures, for European industry.

A NEW DAMAGE MECHANICS-BASED APPROACH FOR INTEGRITY ASSESSMENT OF PLANT COMPONENTS

M.K. Samal
Reactor Safety Division

Dr. M.K. Samal is the recipient of the DAE Young Engineer Award for the year 2007

ABSTRACT

It is now widely recognized in literature, that the results of the local damage model are mesh-dependent. The growth of damage tends to localize in the smallest band that can be captured by spatial discretization. Upon mesh refinement, the solution converges to a localization zone of zero width (in the limit), which results in zero energy dissipation and hence the results become physically meaningless. In this work, the Rousselier's damage model has been extended to a nonlocal form, using the nonlocal damage parameter as an additional degree of freedom of the finite element (FE) model. The mesh independent nature of the model has been demonstrated through the simulation of fracture behaviour of a standard fracture mechanics specimen, using different mesh sizes. The model has also been applied for simulation of ductile to brittle transition behaviour of ferritic steels. It is demonstrated that the temperature dependency of the Weibull parameters is observed due to the inability of the elasto-plastic and conventional damage models to predict the pre-cleavage ductile crack growth of the order of few microns. With the use of the new model, it has been possible to predict the fracture toughness master curve of a ferritic pressure vessel steel in the ductile to brittle transition regime.

Introduction

Prevention of failure of pressurized and high-energy components and systems, has been an important issue in the design of all types of power and process plants. Instead of the traditional fracture mechanics based approaches, it is now possible to go for detailed modeling of different fracture or material degradation processes. In these models (popularly known as continuum damage models or local models), the effect of material damage is usually considered as an internal variable in the expressions representing the constitutive behaviour of engineering materials [1-4]. Numerical analyses based on these local damage models, however, are often found to depend on the spatial discretisation (i.e., mesh size of the numerical method used). The increasingly finer discretisation grids can lead to earlier crack initiation and faster crack growth [5]. This non-physical behaviour is caused by the fact that the localization of damage in a vanishing volume is no longer consistent with the concept of a continuous damage field, which forms the basis of the continuum damage mechanics approach. In this paper, the author has regularized the Rousselier's model [2] with the help of a nonlocal damage parameter, the evolution of which is related to the local void volume fraction through a diffusion type equation. This damage diffusion equation has been discretised alongwith the stress equilibrium equation using finite element method.

In order to predict the cleavage fracture probability in the DBT region, Beremin's model [6] needs to be combined with continuum damage mechanics models. When simulating the crack tip stress field at a lower temperature (when stress gradients are large) using finite element (FE) method, one needs to use a very fine mesh, which cannot be used for the classical (or local) damage mechanics model as the mesh size is pre-defined for a material (which is typically of the order of 0.2mm). This order of FE mesh is too coarse to correctly capture the low temperature crack tip stress field and hence the Weibull parameters are unable to predict the fracture toughness transition curve, when the classical damage mechanics or elasto-plastic models are combined with Beremin's model. Many times, an empirical variation of Weibull parameters with temperature has been suggested [7] and used the same for prediction of the transition curve along with elasto-plastic analysis for calculation of Weibull stress. However, the problem lies in the inability to model small amounts of ductile crack growth (before unstable cleavage fracture) in the FE analysis. Again, the minimum amount of stable crack growth that can be simulated is of the order of one element size. In experiments, it is usually observed that the average stable crack growth (before instability) is of the order of 0.2 mm at -20 deg. C and hence to simulate very small amounts of crack growth (of the order of one-tenth of 0.2 mm), one requires mesh sizes of the order of 0.02 mm. It is now clear that local damage models cannot be used for these mesh sizes and hence the use of nonlocal formulation has been investigated in this work.

This paper is divided into six sections. After a brief literature survey in the introductory section, the mesh independent ductile damage model is briefly described in the second section. The third section describes the Beremin's model which uses the two-parameter Weibull statistics. The fourth section demonstrates the mesh independent nature of the nonlocal Rousselier's model where a standard 1T compact tension (CT) specimen (made of German low alloy pressure vessel steel DIN 22NiMoCr3-7) has been analyzed in 2D plane strain continuum at room temperature (upper shelf), using four different mesh sizes near the crack tip (i.e., 0.4, 0.2, 0.1 and 0.02 mm respectively). The simulation of the fracture toughness transition curve has been presented in the fifth section followed by concluding remarks in the final section.

A mesh-independent ductile damage model

Recently, the author has developed a nonlocal formulation of Rousselier's model, using nonlocal damage d as a nodal degree of freedom [8-9]. The increment of the nonlocal damage variable $\dot{d}$ in a material point $\bar{x}$ is mathematically defined as a weighted average of the increment of the local void volume fraction $\dot{f}$ in a domain Ω, i.e.,

$$\dot{d}(\bar{x}) = \frac{1}{\Psi(\bar{x})} \int_{\Omega} \Psi(\bar{y};\bar{x}) \dot{f}(\bar{y})\, d\Omega(\bar{y}) \qquad .....(1)$$

where $\bar{y}$ is the position vector of the infinitesimally small volume $d\Omega$ and $\Psi(\bar{y},\bar{x})$ is the Gaussian weight function given by

$$\Psi(\bar{y};\bar{x}) = \frac{1}{8\pi^{3/2} l^3} \exp\left(-\frac{|\bar{x}-\bar{y}|^2}{4l^2}\right) \qquad .....(2)$$

The length parameter l in Eq. determines the size of the volume, which effectively contributes to the nonlocal quantity and is related to the scale of the microstructure. The above integral nonlocal kernel holds the property that the local continuum is retrieved as $l \rightarrow 0$. By expanding $f(\bar{y})$ in Taylor's series and substituting in Eq. and doing some algebra, one can obtain the damage diffusion equation as

$$\dot{d} - \dot{f} - C_{length}\nabla^2\dot{d} = 0 \qquad ....(3)$$

where C_{length} is the characteristic length parameter of the material. The yield function of the Rousselier's model is modified by substituting the nonlocal damage d in place of the local ductile void volume fraction f as

$$\phi = \frac{q}{1-d} + D\sigma_k d \exp\left(\frac{-p}{(1-d)\sigma_k}\right) - R(\varepsilon_{eq}) = 0 \qquad .....(4)$$

where D and σ_k are the parameters of the Rousselier's model and are constants for a material. For solving the boundary value problem of the nonlocal damage continuum, one needs to solve the partial differential equation along with the mechanical equilibrium equation

$$\nabla.\sigma + f_b = 0 \qquad .....(5)$$

and the associated boundary conditions, where σ is the Cauchy stress tensor and f_b is the body force per unit volume. For the nonlocal damage degree of freedom, the additional (i.e., Neumann) boundary condition is used and is expressed as

$$\nabla\dot{d}.n\big|_{\Gamma_d} = 0 \qquad .....(6)$$

Where $n\big|_{\Gamma_f}$ is the normal to the boundary Γ_f. By discretizing the weak forms of the governing differential equations, we obtain the FE equations in matrix form as [8-9]

$$\begin{bmatrix} K_{mm} + K_{NL} & K_{ud} \\ K_{du} & K_{dd} \end{bmatrix} \begin{Bmatrix} \Delta\hat{u} \\ \Delta\hat{d} \end{Bmatrix} = \begin{Bmatrix} f_m^{ext} - f_m^{int} \\ -f_d^{int} \end{Bmatrix} \qquad ....(7)$$

It may be noted that the stiffness terms K_{ud}, K_{du} and K_{dd} in the element stiffness matrix are contributions of the nonlocal formulation and f_m^{int} and f_m^{ext} are the internal and external mechanical force vectors respectively, whereas f_d^{int} is the internal damage force vector.

Beremin's model for cleavage fracture

For initiation of cleavage fracture, several micro-mechanical models have been proposed in literature [6]. Many of these models share the common feature that no modification of the material constitutive laws is performed. It is thus assumed, that cleavage fracture occurs before any material degradation due to void growth etc. has taken place, which is true only in case of fracture in the pure lower shelf region. When treating problems of transition from ductile to cleavage fracture, combination of cleavage and degradation models is necessary. The inherently random nature of cleavage fracture, has prompted many developments of statistical models of fracture [10-11]. Most of these are based on the so-called weakest link assumption, which leads to the following expression for the probability of fracture, i.e.,

$$P_f = 1 - \exp\left(-\int_V g(\sigma_I^l)\frac{dV}{V_{ref}}\right) \qquad .....(8)$$

Where V is the volume of the plastically deformed zone (an essential condition for slip induced nucleation of cleavage micro-cracks) in the component, V_{ref} is the reference volume which is taken many times as 0.001 mm^3. The function $g(\sigma^l_I)$ expresses the probability of failure of an infinitesimal volume i (having volume dV)according to the expression

$$dP_f = g(\sigma_I^l)\frac{dV}{V_{ref}} \qquad .....(9)$$

where σ^l_I is the maximum principal stress acting at a material point in the plastically deformed region having volume. According to Beremin's model [6], the form of is defined as

$$g(\sigma_I^l) = \left(\frac{\sigma_I^l}{\sigma_u}\right)^m \qquad .....(10)$$

where m and σ_u are the Weibull's shape and size parameters respectively. Using Eq. (10) in Eq. (8), one can obtain the probability of cleavage fracture P_f at any given loading as [5]

$$P_f = 1 - \exp\left[-\left(\frac{\sigma_w}{\sigma_u}\right)^m\right] \qquad .....(11)$$

where the loading parameter is defined as the Weibull stress σ_w and is expressed as [6]

$$\sigma_w = \sqrt[m]{\sum_{i=1}^{n}\left(\sigma_I^i\right)^m \frac{V_i}{V_0}} \qquad .....(12)$$

In the present work, Eq. (11) is used to calculate the probability of cleavage fracture of the CT specimen at different loading levels and at different temperatures, where the Weibull stress will be calculated using the stress field ahead of the growing crack using Eq. (12).

Analysis of a compact tension specimen in the upper shelf region

Experiments have been conducted at MPA, Universität Stuttgart, Germany on standard 1T CT specimens (with initial crack to width ratio $a_0/W=0.522$) at different temperatures ranging from -100 to -20 deg. C in the DBT region as well as at room temperature (upper shelf) [12]. The specimens are made of German low alloy pressure vessel steel DIN 22NiMoCr3-7. The standard CT specimen has the following dimensions, i.e., width $W=50$ mm, height $H=60$ mm, thickness $B=25$ mm and net thickness (after 20% side groove) $B_n=20$ mm. Due to symmetry, only half of the specimen has been modeled with necessary symmetric boundary conditions. Four different mesh sizes (near the crack tip of the specimen) are selected for the analysis, i.e., 0.4, 0.2, 0.1 and 0.02 mm respectively. Both local and nonlocal Rousselier's models have been used. The other material properties used in the analysis are listed in Table 1. The other material properties can be found in Ref. [8-9]. Fig. 1 shows the load-CMOD (crack mouth opening displacement) results of analysis of the local model with different mesh sizes, and a comparison with experimental data. It is clear that the results are highly mesh-dependent. Fig. 2 shows the load-CMOD results of the nonlocal analysis and it can be observed that the results are nearly mesh independent and compare very well with experimental data. Even the load-CMOD result obtained using a very fine mesh of 0.02 mm near the crack tip, compares very well with the experiment. The variation of J-integral with crack growth in the CT specimen is shown in Fig. 3 for the local model and in Fig. 4 for the nonlocal model, for analysis with different mesh sizes. As can be seen from Fig. 3, the predicted fracture resistance behaviour is FE mesh independent for the nonlocal model, whereas the results are highly mesh dependent in case of the local model (Fig. 4). The results of both the analyses have been compared with those of experiment and it can be noted, that the results of nonlocal analysis compare very well with the experiment, even for the 0.02 mm mesh. Hence, this mesh size has been used for further analysis in the ductile to brittle transition (DBT) region.

Table 1: Material properties of DIN 22NiMoCr3-7

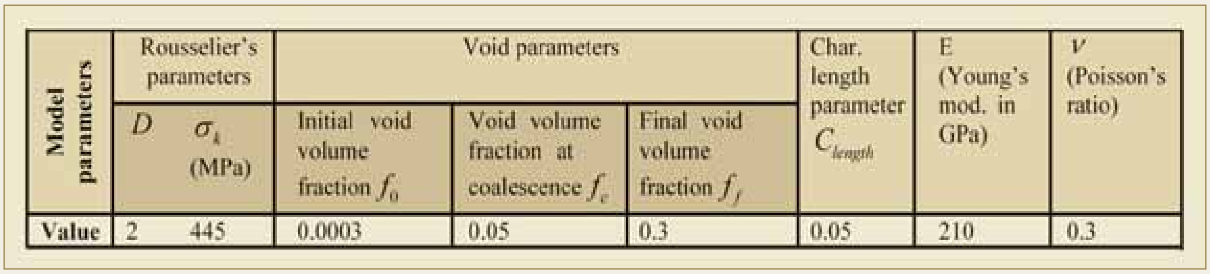

Model parameters	Rousselier's parameters		Void parameters			Char. length parameter C_{length}	E (Young's mod. in GPa)	ν (Poisson's ratio)
	D	σ_k (MPa)	Initial void volume fraction f_0	Void volume fraction at coalescence f_c	Final void volume fraction f_f			
Value	2	445	0.0003	0.05	0.3	0.05	210	0.3

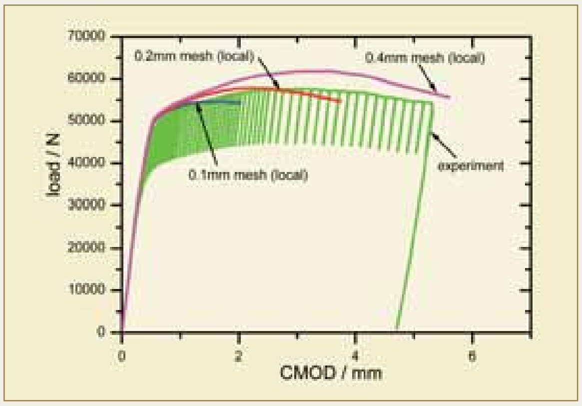

Fig. 1 : Load-CMOD response of the 1T CT specimen for different FE mesh sizes using local model

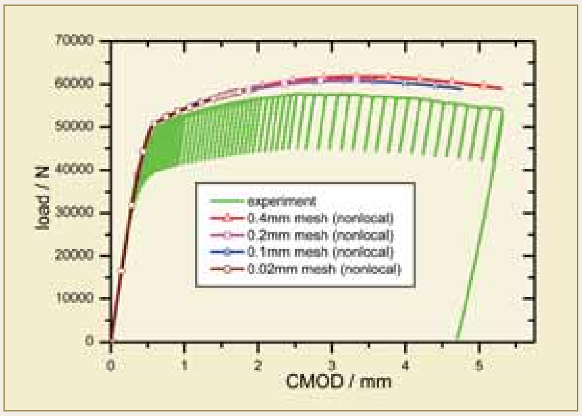

Fig. 2 : Load-CMOD response of the 1T CT specimen for different FE mesh sizes using nonlocal model

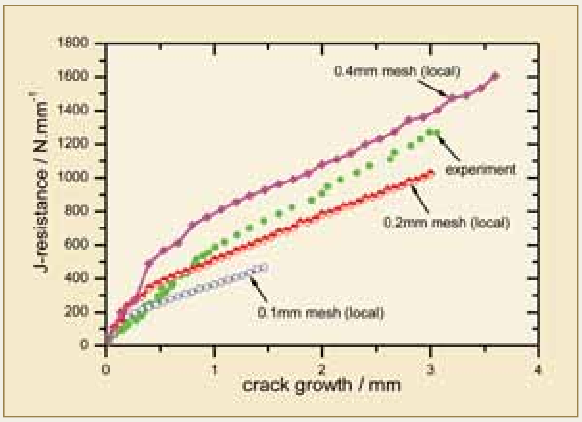

Fig. 3: J-resistance behaviour of the 1T CT specimen with crack growth for different FE mesh sizes using local model

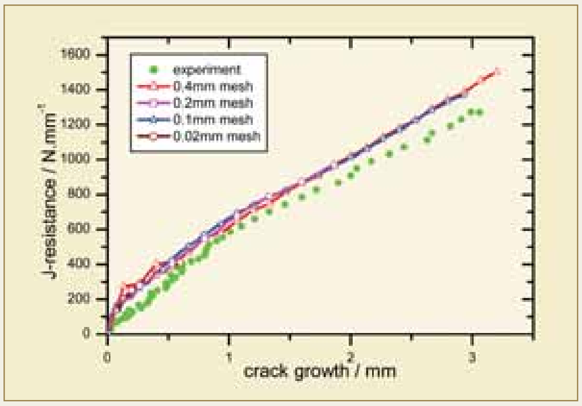

Fig. 4 : J-resistance behaviour of the 1T CT specimen with crack growth for different FE mesh sizes using nonlocal model

Analysis of a compact tension specimen in the DBT region

It was observed from experiments [13] that there is virtually no remarkable stable crack growth in the CT specimens before final fracture by cleavage in the temperature ranges of -100 to -60 deg. C and hence the fracture is nearly pure cleavage. However, at temperatures beyond -60 deg. C, there is onset of stable crack growth, which is of the order of 200 micron (average value) at -20 deg. C. The ductile crack growth alters the stress and strain distribution ahead of the crack tip in the specimens and hence it can significantly affect the probability of cleavage fracture of the specimens. In this work, simulations have been carried out using 2D plane strain analysis of the CT specimens at different temperatures in the DBT region using combined nonlocal Rousselier and Beremin's model with a very fine mesh of 0.02 mm near the crack tip.

The experimental values of fracture toughness (i.e.,K_{JC}, which has been calculated from the critical values of J -integral at unstable fracture (i.e.,J_c), Young's modulus (E) and Poisson's ration (ν) by using the conversion formula $K=[J.E/(1-\nu^2)]^{1/2}$) at which final fracture (by instability) occurred, are plotted with respect to temperature (from -100 to -20 deg. C) in Fig. 5 (open circles denote experimental points). It can be seen from Fig. 5, that the scatter in the

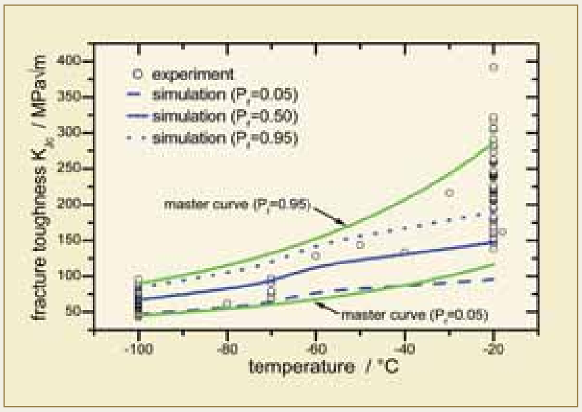

Fig. 5 : Comparison of simulated (elasto-plastic analysis) scatter of fracture toughness of CT specimen with experiment in the DBT region

experimental fracture toughness is large at -20 deg. C as compared to the scatter at -100 deg. C.

Initially, elasto-plastic analysis of the CT specimen was performed, in order to calculate the probability of cleavage fracture. This was carried out essentially to demonstrate the importance of the simulation of stable crack growth in prediction of cleavage fracture. It may be noted that a single set of Weibull parameters (m and σ_u are taken as 34.6 and 2005 MPa respectively) was used, for the whole temperature range under consideration and hence these are treated as temperature-independent in the present work. Obviously, crack growth is not simulated in the elasto-plastic analysis and hence the predicted probability P_f of cleavage fracture of the Beremin's model (without damage) could not capture the experimental scatter as shown in Fig. 5. The master curve approach [13] also provides a basis for the determination of fracture toughness values within the transition temperature regime. In this approach, the cleavage fracture toughness (K_{JC}) is defined by the equation

$$K_{JC} = \left(\ln\frac{1}{1-P_f}\right)^{0.25}\left[11+77\exp\left(0.019\left(T-T_0\right)\right)\right]\left(\frac{25}{l_{cf}}\right)^{0.25}+20\left(\mathrm{MPa}\sqrt{\mathrm{m}}\right) \qquad .....(13)$$

where P_f is the probability that a single selected specimen chosen at random from a population of specimens will fail before reaching the K_J value of interest, T is the temperature in deg. C and l_{cf} is the crack front length (measured in mm) for the defect being assessed. The master curve reference temperature T_0 is usually determined, using a standard test method [13] from a limited number of fracture toughness tests, performed on ferritic steels of a specified product form at different temperatures, in the ductile-brittle transition range.

Fig. 6 shows the comparison of predicted cleavage fracture probability (for fracture toughness) curves (with and without consideration of ductile damage or stable crack growth) with experimental scatter bands of the CT specimen. The lines (solid for 50%, dashed for 5% and dotted for 95% probability of cleavage fracture, corresponding to fracture toughness), represent simulation results of combined elasto-plastic analysis and Beremin's model (without modeling of stable crack growth) and the dots (open dots for 5%, semi-open dots for 50% and closed dots for 95% probability of cleavage fracture) represent the simulation results using combined nonlocal damage mechanics analysis and Beremin's model. The value of C_{length} parameter for the material has been taken as 0.05 and other model parameters are given in Table 1. It can be observed from Fig. 6, that predicted fracture toughness values (corresponding to 5%, 50% and 95% probability of failure) match very well with those of experimental data, except the fracture toughness corresponding to 5% probability of failure at -20 deg. C (simulation value is slightly less than that of experiment).

Conclusions

In this work, a nonlocal form of the Rousselier's damage model has been developed. The effect of stress-strain and damage history of the surrounding material region on the damage development at a material point is taken care of, though a damage diffusion equation. The FE formulation of the new model has been developed, in order to solve problems with complicated geometry and boundary conditions.

In order to predict the probability of cleavage fracture in the DBT region, simulation of small amount of stable crack growth is very important. It is important to realize the fact that the stress field gets modified ahead of a growing crack and hence prediction of the same is crucial for accurate determination of the loading parameter, i.e., Weibull stress. With the help of mesh independent nonlocal damage models, it is possible to use a very fine mesh ahead of the crack tip, in order to predict stable crack growth, of the order of few microns.

References

1. A.L. Gurson, Continuum theory of ductile rupture by void nucleation and growth: Part-I: Yield criteria and flow rules for porous ductile media, *Trans. ASME J. Eng. Mater. Technol.* 99 (1977) 2-15.G.
2. Rousselier, Ductile fracture models and their potential in local approach of fracture, *Nucl. Eng. Des.* 105 (1987) 97-111.
3. A. Needleman, V. Tvergaard, An analysis of ductile rupture in notched bars, *J. Mech. Phys. Solids* 32 (1984) 461-490.
4. V. Tvergaard, A. Needleman, Analysis of cup-cone fracture in a round tensile bar, *Acta Metall.* 32(1) (1984) 157-169.
5. F. Reusch, B. Svendsen, D. Klingbeil, A non-local extension of Gurson-based ductile damage modelling, *Comput. Mater.* Sci. 26 (2003) 219-229.
6. F.M. Beremin, A local criterion for cleavage fracture of a nuclear pressure vessel steel, *Metall. Trans. A,* 14A (1983) 2277-2287.7. H . P . Seebich, Doctoral Dissertation, Institut für Materialprüfung Werkstoffkunde und Festigkeitslehre, Universität Stuttgart, Germany (2007).
8. M.K. Samal, Nonlocal damage models for structural integrity analysis. Doctoral dissertation, Institut für Materialprüfung Werkstoffkunde und Festigkeitslehre, Universität Stuttgart, Germany (2007).
9. M.K. Samal, M. Seidenfuss, E. Roos, B.K. Dutta, H.S. Kushwaha, Finite element formulation of a new nonlocal damage model, Fin. Elem. Anal. Des. 44 (2008) 358-371.K. Wallin, The scatter in K_{JC} -results, Eng. Fract. Mech. 19 (1984) 1085-1093.
10. A. Khalili, K. Kromp, Statistical properties of Weibull distribution, *J. Mat. Sc.* 26 (1991) 6741-6752.
11. K. Wallin, Master curve method: a new concept for brittle fracture, *Int. J. Mater.* Product. Technol. 14 (1999) 342-354.
12. Eisele U. et al., 2006. Critical examination of the master curve approach regarding application in German nuclear power plants, Final Report, Reactor Safety Research -Project No. 1501 240, Materialprüfungsanstalt Universität Stuttgart, Germany.
13. ASTM-E 1921-05. Standard test method for determination of reference temperature for ferritic steels in the transition range. American Society for Testing and Materials (2005).

ABOUT THE AUTHOR

Dr. M.K. Samal is working in the Reactor Safety Division of BARC, since 1997 after passing from 40th batch of BARC Training School. He has received his Ph.D. from the University of Stuttgart, Germany. His teaching and research interests include finite element analysis, material modeling, smart structures and damage mechanics. He has also successfully implemented the online damage monitoring system at various chemical process and thermal power plants of India. He has received many awards including Homi Bhabha Gold medal from BARC training school in 1997, Ashok Chaturvedi Memorial Award for first rank among mechanical engineering masters students of IIT Mumbai in 2003, Indian Nuclear Society Medal in 2007 and DAE Young Engineer Award in 2007. He has more than 80 publications including 26 papers in various international journals.

ROOM TEMPERATURE TOXIC GAS SENSORS BASED ON TELLURIUM

S. Sen
Technical Physics and Prototype Engineering Division

Dr. Shashwati Sen received the Young Achiever Award (2008) at the 53rd DAE Solid State Physics Symposium, held at BARC, Mumbai, from Dec. 16-20, 2008

ABSTRACT

Various morphologies of Tellurium, such as thin films and films made from Te nanostructures, have been explored as toxic gas sensors, operating at room temperature. The resistance of these films was found to increase reversibly, on exposure to reducing gases, while the opposite effect was observed on exposure to oxidizing gases. The sensitivity as well as the selectivity of these sensors, with respect to different gases has been studied. Response to different gases was found to be a function of various parameters like: deposition temperature, substrate crystallinity, grain size and effect of intra-grain and grain boundary regions. Techniques like Raman spectroscopy, X-ray photoelectron spectroscopy and Impedance spectroscopy has been employed, for investigating the gas—tellurium interaction.

Introduction

In recent years, because of increasing awareness about environmental pollution, efforts have been made for the development of sensors, which can detect gases in the ppm level and are economical and roboust in operation. Routinely used semiconductor gas sensors are based on SnO_2, WO_3, ZnO and TiO_2. All these materials are n-type semiconductors and require operating temperatures in the range of (200-400 °C). High temperature operation of these sensors and associated power consumption (in the range of 200 mW to about 1W) precludes battery-driven operation and leads to problem in long term stability.

For the last few years, a lot of effort has gone into the fabrication of new materials, which can detect different gases at lower temperatures, particularly at room temperature. Recently, a group led by Tsiulyanu has reported the use of Tellurium (Te) thin films, for room temperature detection of some toxic gases such as NO_2 [1], CO and propylamine [2]. Moreover, the lower melting point (~ 723K) of Te and its elemental nature implies, that its films can easily be evaporated devoid of any stoichiometric deviations, thereby making it an attractive material for study in gas sensing properties. Tellurium is an elemental semiconductor with energy gap of 0.34 eV. Its thin films show p-type conduction due to lattice defects acting as acceptors.

We have studied the gas sensing properties of Te thin films deposited by thermal evaporation as well as Te nanotubes grown by physical vapour deposition: both at atmospheric pressure as well as under vacuum conditions. Sensitivity towards different gases has been studied and the effect of different parameters on the sensitivity of these films has been investigated. The interaction of gas was investigated using Raman spectroscopy, X-ray photoelectron spectroscopy and Impedance spectroscopy [3,4].

Experimental Details

Thin films have been typically deposited by thermal evaporation technique using molybdenum or tantalum boat at a vacuum of better than 10^{-5} Torr. Depositions were carried out at the rate of ~ 0.5 to 10 nm/s, monitored by using quartz crystal thickness monitor, to yield films of 200 nm thickness. The films have been deposited at different substrate temperatures between 77 and 373 K and on different substrates like sapphire, polycrystalline Al_2O_3 (alumina) and glass.

For the growth of Te nanotubes under vacuum conditions, deposition was carried out on Si (111) substrate at substrate temperature of 100 °C. Further Te nanotubes were also grown on metal nanoparticles like Ag and Au by the same method [6].

Growth of Te nanotube under atmospheric pressure was carried out under argon atmosphere, in a tubular furnace [7]. In brief, Te powder was loaded in an alumina boat and placed in a 1 m long quartz tube. The furnace temperature was increased to 550 °C in presence of Ar gas flow of 150 cc / min and maintained at this temperature for 2 hours. Te nanotubes were found to deposit on quartz tube in the direction of gas flow, at temperature of 30-50 °C. These nanotubes were dispersed in ethanol to make a suspension, which was painted on a glass plate to form a film.

The gas sensitivity of these films was recorded by measuring their two probe resistances in the presence of gases with varying concentrations. For resistance measurement, the electrical contacts onto the film surfaces were made, by thermally evaporating gold pads in a two-probe configuration and attaching silver wires to them, using indium solder. For sensitivity measurements, the film was loaded in an airtight housing having a volume of 250 cc. A measured quantity of the gas was taken from a canister, containing gas at 1000 ppm concentration, using a syringe and introduced in the housing, so as to yield the desired gas concentration. The response and recovery of the films exposed to different gas concentrations were obtained, by plotting their resistance as a function of time.

Results and Discussion

Tellurium thin films: The effect of deposition parameter like substrate temperature was investigated for Te films deposited on alumina substrate. The morphology of Tellurium films deposited on alumina substrate at various substrate temperatures between 77-373 K, shows a change in microstructure from amorphous to polycrystalline (supported by SEM images and XRD), accompanied by grain growth with increasing substrate temperatures. Films deposited at 77 K are smooth and do not show the presence of any grains, indicating their amorphous nature whereas films deposited at 373 K, show grain growth in the form of dendrites with an average size of ~ 800 x 155 nm^2 which are polycrystalline in nature [5]. The effect of substrate crystallinity on microstructure of films, has been investigated by *in-situ* deposition of films on amorphous (glass), polycrystalline (alumina) and single crystal (sapphire) substrates held at 373 K. All these films showed dendritic growth with smallest grain size on glass substrates. While the grain size is similar for films on sapphire and alumina substrates, coalescence of grains on sapphire, has reduced sharp grain boundaries.

The gas sensitivity of these films was measured at various temperatures for several gases like NH_3, H_2S, NO_2 etc. Response of Te films is found to reduce with increase in temperature, for both oxidizing and reducing gases and at T~ 373 K, the sensitivity drops to negligibly low values (< 10 %) for all the gases. Thus all sensitivity studies have been been carried out at room temperature.

Te films deposited at 373K on alumina were able to detect less than 0.1 ppm of H_2S. The response and recovery time for 1 ppm H_2S were 5 and 20 minutes respectively. Sensitivity of Te sensors at 10 ppm concentration of different gases as NH_3, H_2S, NO_2 etc. showed that, films are most sensitive to H_2S and have good response to NO_2 while they have no response to CO and hydrogen gases.

Response of the films deposited at different temperatures on exposure to H_2S shows that, the film sensitivity increases with the deposition temperature. Increase in sensitivity at higher deposition temperatures is attributed to low defect density in the films at higher temperatures [5]. In the presence of defects (which increase at low deposition temperatures), excess charges (holes) generated on interaction with gases are trapped on defect centers, leading to a reduced change in conductivity (hence, sensitivity). This also leads to slower response time for films deposited at lower substrate temperature.

Response of Te films deposited at 373K on glass, sapphire and polycrystalline alumina to H_2S showed that, the films deposited on glass substrate show maximum sensitivity while those on sapphire show minimum sensitivity. This is understandable, as smaller grain size for films on glass substrates provides large effective surface area for gas-film interaction, thereby improving its gas sensitivity. Coalescence of Te grains on sapphire, reduces grain boundary area, that reduces gas sensitivity.

Tellurium nanostructures: To further increase the surface-to-volume ratio, films of Te nanotubes were tested for different gases. These films were found to show maximum response towards Chlorine gas. Impedance spectroscopy studies showed that, the response to chlorine and other oxidizing gases is mainly contributed by change in grain boundary resistance and is therefore enhanced for nanotubes. On the other hand, the intergrain region resistance contributes response towards reducing gases (like H_2S), thus thin films are more suited to H_2S sensor.

Metal nanoparticles were found to act like nucleation centres for the growth of Te nanotubes, by thermal evaporation method under vacuum. This lead to the formation of dense, uniform and oriented nanotubes of Te on Si(111) substrate [6]. Sensors made from Te nanotube on Ag nanoparticles, were found to show selective response towards NO gas, because of some catalytic reaction between Ag particle and NO gas, as investigated by Raman and XPS spectroscopy.

The gas detection mechanism of tellurium was investigated using Raman and x-ray photoelectron spectroscopy. It was observed, that at room temperature, oxygen is absorbed on the surface of thin films. This oxygen traps electrons and leads to increase in the hole concentration and conductivity. On exposure to reducing gases, this oxygen is removed which leads to decrease in the hole concentration and thus increase in resistance of the film. On the other hand, on exposure to oxidizing gases, more electrons gets trapped and thus the hole concentration and the conductivity of the film increases.

Conclusions

Te thin films and nanostructures were investigated for their sensitivity towards different gases at room temperature. The thin films were found to show maximum sensitivity for H_2S. Films deposited at 373 K on glass substrates, showed maximum sensitivity towards gases such as H_2S and NO_2, because of lower defect density as well as smaller grain size. The selectivity towards NO_2 was increased by depositing Te nanotubes on Ag nanoparticles on Si (111) substrate at 100°C. Te thick film made from Te nanotubes synthesized in furnace under atmospheric pressure, was found to show high sensitivity towards chlorine gas. The sensitivity towards oxidizing gas was found to be contributed by the grain boundary part of the films while response to reducing gas is from the intragrain region.

References

1. D. Tsiulyanu, et al, *Sens. Actuators* B 73 (2001) 35.
2. D. Tsiulyanu, et al, *Sens.* Actuators B 85 (2002) *232.*
3. Shashwati Sen, et al, *Sens. Actuators* B 98 (2004) 154.
4. Shashwati Sen, et al, *Sensors and Actuators* B, 115 (2006) 270-275.
5. V Bhandarkar, et al *Materials Science and Engineering* B 131(2006) 156-161.
6. Vivek Kumar, et al, *J Nanoscience Nanotechnology* (in press).
7. Shashwati Sen, et al, *Cryst. Growth Des.*, 8 (1), 238–242.

ABOUT THE AUTHOR

Dr. (Ms) Shashwati Sen joined BARC in 1996 through the 40th batch of BARC training school. She obtained her Ph.D. degree from Mumbai University in 2003 for her work on "Dissipation mechanism in high temperature superconductors." Currently she is working on gas sensors based on elemental and metal oxide semiconductors, thin films and their nanostructures.

THERMO-PHYSICAL PROPERTIES OF OXIDE CATALYSTS PROBED BY TEMPERATURE PROGRAMMED DESORPTION/ REDUCTION/OXIDATION/ (TPDRO) TECHNIQUES

M.R. Pai
Chemistry Division

Dr. Mrinal Pai was conferred the Young Scientist Award by the Indian Thermal Analysis Society (ITAS) and TA Instruments, USA, in Feb. 2008

ABSTRACT

The structure–activity correlations of large number of substituted novel mixed oxide systems, with their catalytic activity for reactions involved in pollution control and energy related reactions, were established. Thermal behaviour, stability, reducibility and oxidizability, ease of oxygen desorptivity of oxide samples, which are important considerations to design an oxide catalyst, were probed by the Temperature Programmed Deduction /Oxidation/ Desorption (TPDRO) technique. Thermo physical properties and catalytic performances of vast number of oxide/mixed oxide catalysts as a function of extent of dopant, particle size calcinations temperatures were investigated. Different kinds of catalysts needed to meet many strategic requirements of the Department of Atomic Energy, such as the catalysts required for hydrogen-oxygen recombination in nuclear installations under emergency situations and the catalysts for sulfuric acid decomposition reaction involved in Sulfur-Iodine thermochemical cycle for hydrogen production, were also developed. In this article, the potential of TPDRO technique for thermophysical characterization of few select oxide samples used in various catalytic reactions would be discussed.

Introduction

Various mixed oxides with spinel, perovskite and pyrochlore structures have been widely investigated in order to explore their suitability as substitutes for noble metal catalysts, for applications in pollution control, electrolytic cell, water splitting reaction etc. [1-3]. Their thermal behaviour, stability, reducibility and oxidizability, ease of oxygen desorptivity are important criteria, on the basis of which an oxide catalyst is designed. With an objective to enhance thermal stability and incorporate high catalytic activity to these oxides, various mixed metal oxides, have been synthesized and investigated in detail and attempts have been made to incorporate multiple cations at A or B sites of these oxide systems, so as to further tailor their catalytic behaviour and stoichiometric stability, during actual application. The Temperature Programmed Reduction/Oxidation (TPR/TPO) cycles have been recorded, to investigate their redox behaviour, as a function of the value of x (extent of the substitution), in which T_{max} values indicated the ease of reducibility and oxidizability respectively, of the oxide samples which were further correlated with the value of x. The amount of Hydrogen consumed under TPR curves was correlated with the nonstoichiometry generated in the mixed oxide samples, as a result of alter-valent substitution. Also successive 4-5 TPR/TPO cycles were recorded, to study their reproducible behaviour and stability, during prolonged use in catalytic applications. Temperature Programmed Desorption (O_2-TPD) in the inert atmosphere upto 1000°C were recorded, to study the effect of substitution –induced oxygen-ion vacancies, generated on the ease of thermal desorption of lattice oxygen. H2-TPD helped in evaluating the active metal surface area of metal, dispersed on supported samples. H_2-TPD profiles of H_2 storage materials reveal the kinetics and ease, with which H_2 is released from storage materials on thermal activation [4]. TG/DTA has been recorded, to investigate the phase transitions and their stability in varying atmospheres, as a function of the value of x in various studies.

Recently, studies on In-Ti-O system [5] were undertaken, with the objective to monitor the thermo-physical characteristics and redox behaviour of substituted Indium titanate (In_2TiO_5) single-phased samples, which can serve as prospective catalysts. The amount of H_2 consumed under TPR curves, was correlated with the nonstoichiometry generated in the $In_2Ti_{1-x}Fe_xO_{5-\delta}$ samples. Fe/Cr substitution, induced ease in the reducibility (T_{max}) of substituted oxides, as compared to In_2TiO_5. Formation of In^{1+} and presence of Cr^{3+} in the reduced sample is confirmed, using x-ray photoelectron spectroscopy. Earlier, we have reported the structural characteristics; thermal stability, redox properties and the catalytic activity of pyrochlore or $A^{IV}B_2O_7$ type ($Th_xLa_{1-x}V_2O_{7-\delta}$) compounds; the influence of La^{3+} substitution at A-site over the redox behaviour and catalytic activity studies of these oxides for reaction of methanol was studied [6]. La substitution results in lowering of reduction temperature, as reflected by TPR profiles. The factors responsible for these catalytic and redox properties of substituted ThV_2O_7 samples, are identified as generation of nonstoichiometric phase, where involvement of lattice oxygen plays an important role as revealed by O_2-TPD. The shift of the overall TPR profile to lower temperature, indicated the ease of reduction process, due to oxygen ion vacancies generated in $V_2O_7^{4-}$ chains. DTA/TG results revealed, that the presence of La led to suppression of the polymorphic behaviour of ThV_2O_7 [7]. As compared to ThV_2O_7 and $Th(VO_3)_{4,}$ the $LaTh(VO_4)_{3-\delta}$ phase was found to reduce at higher temperatures. Similarly in the metavanadate of thorium, $Th(VO_3)_4$ as a function of substitution by La and Mn at both A and B sites respectively. In case of La substitution in $Th(VO_3)_{4,}$ the substituted samples comprised of two distinct phases, one corresponding to tetragonal thorium metavanadate with partial substitution at A-sites, i.e. $La_xTh_{1-x}(VO_{3-\alpha})_4$, and the other a new phase identified as $LaV_4O_{11+\delta}$. A definite correlation is found to exist between the microstructural defects generated in the above-mentioned two phases because of the oxygen-ion vacancies, resultant enhancement in thermal diffusitivity of lattice oxygen as revealed by lowering of temperature requirement for desorptivity of Oxygen in O_2-TPD, and finally the catalytic activity of the substituted mixed oxides. We have also studied and reported the stability, redox behaviour, and catalytic properties of $La_{0.8}Sr_{0.2}Mn_{1-x}Fe_xO_{3-\delta}$ (LSMF) oxides, as a function of cationic substitutions at B sites [8]. The lowering of T_{max} in the TPR profiles and the enhancement of catalytic activity in case of LSMF samples were governed by a combination of factors, such as (i) a smaller crystallite size - resulting from Fe substitution at B-site, (ii) and greater non-stoichiometry caused by substitution of an aliovalent cation at B site, facilitating the lattice oxygen diffusion via anionic vacancies generated in the process and (iii) a change in the symmetry around a constituent cation. Very recently we have reported the catalytic decomposition of sulphuric acid by $Fe_{2(1-x)}Cr_{2x}O_3$ oxide catalysts, an intermittent reaction in generation of hydrogen by sulphur-iodine thermochemical water splitting cycle [9]. In case of $Fe_{1.8}Cr_{0.2}O_3$, shift in T_{max} is 12°C for consecutive cycles, in contrast to 50° in case of Fe_2O_3, thus indicating that Cr substitution helped in stabilizing active Fe_2O_3 component. Thus Solid solution of 10 % Cr substitution in Fe_2O_3 lattice has not only enhanced activity and stability, but also prevented the deactivation of the catalyst during prolonged use in sulfuric acid decomposition reaction. The salient results of these systems are summarized below.

Catalytic and redox properties of nano sized $La_{0.8}Sr_{0.2}Mn_{1-x}Fe_xO_{3-\delta}$ mixed oxides

$La_{0.8}Sr_{0.2}MnO_{3-\delta}$ (LSM) reportedly is important as prospective cathode material for solid oxide fuel cells. In the present study, our objective was to investigate the catalytic and redox properties of LSM material, as a function of Fe substitution. The $La_{0.8}Sr_{0.2}Mn_{1-x}Fe_xO_{3-\delta}$ (LSMF) samples of perovskite-type structure, with the value of x ranging from 0 to 1.0 were synthesized, by using two different methods, viz. nitrate and solid state routes and by calcining at different temperatures. The samples were characterized by using techniques of powder X-Ray Diffraction (XRD) and N_2 adsorption techniques. The chemical state in these multi-metal oxides was identified using X-ray Photoelectron (XPS) and Mossbauer Spectroscopies (MB). The redox behaviour of these samples was studied by recording TPR profiles. The effect of iron substitution on particle size, reduction behaviour and catalytic activity of these materials, was evaluated for a CO oxidation as a model reaction.

The XRD studies showed, that the incorporation of iron resulted in single phase samples of orthorhombic symmetry, instead of the rhombohedral symmetry of the parent perovskite LSM phase. The Mössbauer spectra revealed that iron existed in trivalent state but in three distinctive coordinative environments. At one of these sites, iron was found to be paramagnetic in nature and the concentration of these species decreased with increasing iron content. On the other hand, XPS results (Fig.1) revealed, that the coordination of 'B' site cations Fe and Mn was different at the surfaces of the sample as compared to those in the bulk. No significant segregation of an individual metal was noticed at the surface layer. At the same time, the particles of Fe-containing samples were smaller in size as compared to LSM and it was found to have direct bearing on the lowered reduction temperature and the enhanced catalytic activity of LSMF samples. The results of comparative study of same compositions prepared by different routes revealed that subtle changes in particle morphology may also play an important role in the catalytic behaviour of the substituted perovskites, in addition to the effect of substitution-induced micro-structural defects and the synergistic effects due to valence changes of the active metal components.

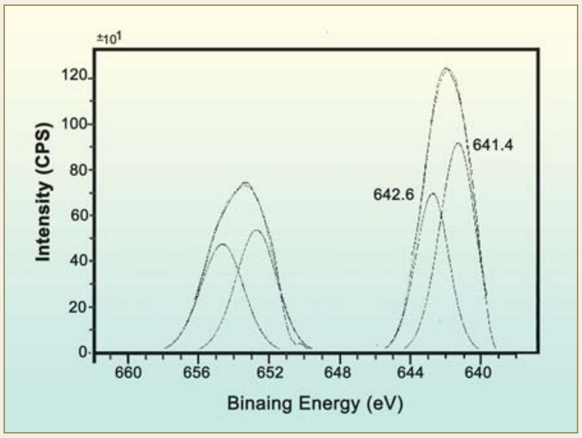

Fig.1 : Mn 2p XPS spectrum of $La_{0.8}Sr_{0.2}Mn_{0.8}Fe_{0.2}O_{3-\delta}$ (LSMF2) catalyst.

TPR/TPO studies

The reduction profiles (TPR) of LSM along with its iron-substituted analogues are presented in Fig. 2 (a-f). The reduction profile of LSM (Fig. 2a-f) shows at least two clear reduction stages, first at 350-600°C and the second stage in the wide temperature interval of 700-980°C. We may mention that Mn is the only reducible species in the case of LSM sample. This profile clearly indicates the existence of two distinct manganese sites, corresponding to XPS bands mentioned above. Such multiple reduction stages have been reported by Buciuman et al [26] in case of TPR study on $LaMnO_{3.16}$ samples, with substitution at A site with Sr, Ba, K and Cs. It has been demonstrated by these authors, that

Mn is present in +4 as well as in +3 states and the Mn^{4+} state reduces at a lower temperature as compared to Mn^{3+}. This has been interpreted in terms of lowering of the oxidative nonstoichiometry, on substitution of La^{3+} by cations at lower oxidation stage, while keeping the tetravalent manganese practically unchanged. Since our sample shows rhombohedral symmetry, the reduction of strontium substituted lanthanum manganites is likely to follow the scheme:

At 350°C

$$La^{3+}_{0.8}Sr^{2+}_{0.2}Mn^{4+}_{x}Mn^{3+}_{1-x}O_{3.16} \rightarrow La^{3+}_{0.8}Sr^{2+}_{0.2}Mn^{3+}O_{2..9}$$

At 700°C

$$La^{3+}_{0.8}Sr^{2+}_{0.2}Mn^{3+}O_{2..9} \rightarrow 0.4\,La_2O_3 + 0.4\,MnO + 0.2\,SrMn_3O_{6-\delta}$$

The XRD pattern of the TPR residue of LSM showed the presence of La_2O_3, MnO and $SrMn_3O_{6-d}$. In line with the previously reported studies, we conclude that the low temperature reduction in Fig. 6 arises due to $Mn^{4+} \rightarrow Mn^{3+}$ and at high temperature i.e. above 600°C, it is due to Mn^{3+} to Mn^{2+}.

In case of sample LSMF2 where a part of Mn is substituted by Fe, an additional shoulder band is observed at ~ 400°C and the intensity of high temperature bands (T_{max} ~ 520, 700 and 900°C) is decreased considerably (Fig. 2b). Fe^{3+} has partly replaced Mn^{4+} and Mn^{3+}. This was further supported by the XRD results showing a clear change in symmetry from rhombohedral to orthorhombic, which is known to be an oxygen deficient compound. As the concentration of Fe increases, the 520°C band shifts to a further low temperature of 494°C for the value of x = 0.2, indicating that, iron substitution facilitates the reduction of Manganese ions. For further substitution of Fe considerable decrease in reduction temperature is observed for example, LSMF4 and LSMF6 (Figs. 2c-d) shows Tmax at 395 and 308°C. TPR profiles of composition with higher concentration of Fe (Fig. 2 e-f) showed that a strong reduction band at temperature above 800°C indicating reduction of Fe^{3+} only at very high temperature. The lowering in reduction temperature in case of LSMF6 sample is attributed to synergism among metal ions of different oxidation states existing in different coordinations as mentioned above. The shift in Tmax from ~300°C to higher temperature ~500°C from LSMF6 to LSF sample respectively, is attributed to increase in symmetric ordering of Fe as we go from LSMF6 to LSF sample as indicated by Mössbauer spectroscopy results.

In addition to the role of Fe substitution, the reduction profile of a sample depended upon the particle morphology as well. Thus, a considerable shift was noticed at a higher temperature in TPR profile of a representative $La_{0.8}Sr_{0.2}Mn_{0.8}Fe_{0.2}O_{3-\delta}$ sample, synthesized by solid state route and having larger particle size. These results are shown in the dotted curve b of Fig. 2. The solid state synthesized sample reduces at ~150°C higher temperature as

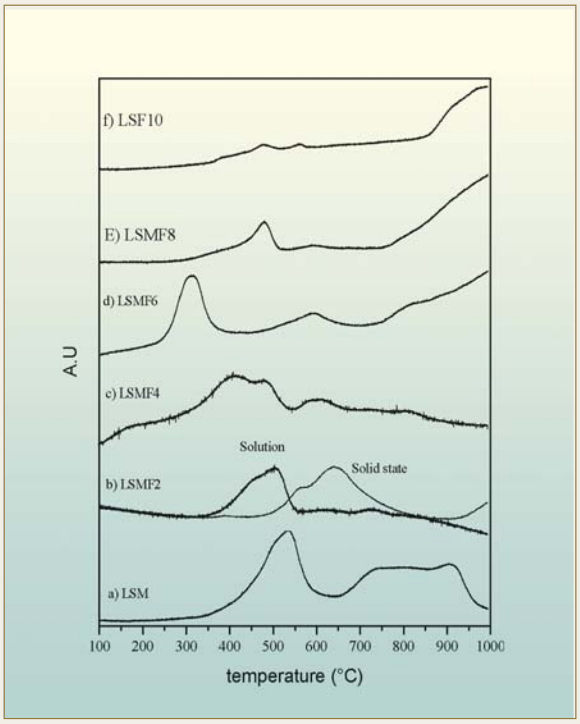

Fig. 2 : Profiles of typical 1st TPR cycle of different LSMF samples synthesized by solution route, (a) LSM, (b) LSMF2, (c) LSMF4 (d) LSMF6 (e) LSMF8 and (f) LSF. Curve (b dotted) shows TPR profile of a LSMF2 sample synthesized by solid state route.

compared to solution route synthesized sample. The increase in reduction temperature indicates that redox properties are affected significantly by particle size.

Catalytic activity

Fig. 3 presents the CO oxidation activity of Fe-substituted LSM samples, all synthesized at a calcination temperature of 900 °C. As seen in curves b, c and d of this figure, the iron containing samples exhibited better catalytic activity as compared to un-substituted LSM (curve a) or the sample of other extreme composition, i.e. LSF (curve e). For instance, Fe containing samples exhibited ca. 90 to 100% conversion of CO to CO_2 at 400°C, while only 45% conversion was observed using LSM at this reaction temperature. Not only an increase was observed in the conversion, the reaction onset temperature was also found to decrease as a result of iron substitution Fig. 3 (b-d). The highest CO conversion was exhibited by $La_{0.8}Sr_{0.2}Mn_{0.4}Fe_{0.6}O_{3-\delta}$ (LSMF6) catalyst and is in line with the considerable lowering in reduction temperature to ~300°C (Fig. 3d) as compared to 533°C of the unsubstituted sample. The decrease in CO conversion from LSMF6 to LSF sample, is attributed to increase in symmetric ordering of Fe as we go from LSMF6 to LSF sample as indicated by Mössbauer spectroscopy results.

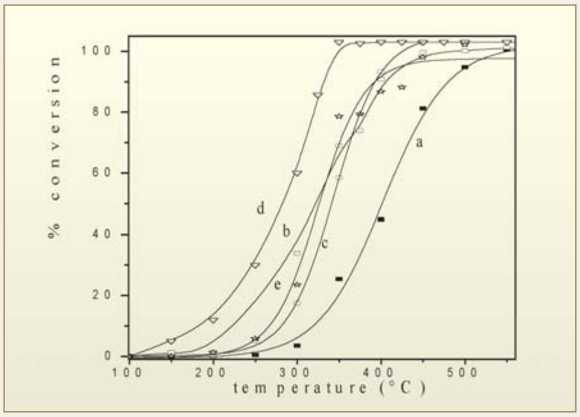

Fig. 3 : Catalytic activity for CO oxidation reaction of different $La_{0.8}Sr_{0.2}Mn_{1-x}Fe_xO_{3-d}$ catalysts. LSM (b) LSMF2 (c) LSMF4 (d) LSMF6 and (e) LSF

The results of the present study show, that the substitution of Fe in place of Mn, caused a rearrangement in the symmetry of the parent LSM perovskite. Thus, the substituted samples exhibited an orthorhombic symmetry instead of the rhombohedral symmetry of the unsubstitued counterpart. At the same time we observed the existence of multiple valence states of Mn and Fe cations at the B site in the substituted samples, validating the synergistic effects of these cations in generating the lattice vacant sites, that in turn may lead to the ease of sample reducibility. It is also important to notice a decrease in the particle size and the corresponding increase in surface area, in case of the substituted mixed oxide samples synthesized through solution route and calcined at relatively lower temperatures (Table 1). We observe direct influence of symmetry around Fe atom on the reduction behavior and catalytic activity of these samples (Figs. 1-3). The catalyst LSMF6 has three types of Fe in asymmetric environment, leading to the highest activity and lowering in reduction temperature. The decrease in CO conversion and increase in reduction temperature from LSMF6 to LSF sample, is attributed to increase in symmetric ordering of Fe as we go from LSMF6 to LSF sample, as indicated by Mössbauer spectroscopy results. Based on our experimental results, we may thus suggest that in addition to substitution induced nonstoichiometry, synergestic effects micro-structural defects arising due to cationic substitution, certain subtle changes in the particle morphology of these mixed-oxides, may also play an important role in the enhancement of their catalytic activity for oxidation reactions.

Thermo-physical characterization of Ru/Al_2O_3 catalyst samples using TPDRO

Two samples of the titled catalyst, one fresh Ru/Al_2O_3 and other used for hydrogenation of a macrocyclic compound, were characterized for their total and active metal surface area, crystal structure, redox behaviour during successive reduction-oxidation cycles, metal content, oxidation state of Ruthenium etc. In the fresh sample, XRD results showed poor crystalline features due to γ-Al_2O_3 (PCPDF- No. 47-1308). No distinct reflections due to metallic ruthenium were observed; however broad reflections at 2θ values of ~ 28, 35 and 54.4°, suggested the presence of RuO_2 in the sample (PCPDF- No. 43-1027). Whereas in the used sample features due to γ-Al_2O_3 were present but those due to RuO_2 were not there. Estimation of RuO_2 crystallite size using Scherrer's formula gave rise to a value of ~ 10 nm. However presence of particles in 2.5 – 10 μ size range were evident from SEM images. X-ray photoelectron spectroscopy revealed that Ru existed in both Ru° and Ru^{IV} state in the fresh sample, where binding energy values for Ru ($3d_{5/2}$, $3d_{3/2}$), O (1s), Al(2p) were measured. Surface area was estimated by N_2 BET found to be 102 m^2g^{-1} with a Type IV isotherm with point of inflection at p/p_0 of ~0.75 was observed in fresh sample which was unchanged after the reaction as surface area of the used sample was ~ 98.5 m^2g^{-1}. Redox behaviour of Ru/Al_2O_3, both the fresh and used samples were studied by Temperature Programmed Desorption/ Redution/Oxidation (TPDRO) system, where samples were pretreated in He at 350°C for 2h prior to measurement. Each TPR cycle (60 – 1100°C) was followed by a TPO run(60 – 800°C). The results during first cycle of Temperature Programmed Reduction (TPR) of fresh catalyst (Fig.4) sample, showed the presence of two peaks with peak maxima at ~187 and 480°C, respectively, with the latter being the prominent one. While the former peak is associated with reduction of RuO_2, the latter one was attributed to strong metal-support interaction, as reported in several studies. During the first cycle of Temperature Programmed Oxidation (TPO) after a TPR run, a peak with T_{max} at ~550°C was observed and was attributed to oxidation of Ruthenium. In the subsequent TPR cycles which followed a TPO run, gave rise to single peak with T_{max} in the range of 145 - 155°C, which is attributed to reduction of RuO_2 species. The lowering of T_{max} in subsequent TPR cycles, may arise due to difference in the RuO_2 crystallite size. While in used sample the TPR/TPO results (Fig. 5) are similar to those observed in a fresh sample except that, in the first TPR cycle, the lower temperature peak at ~187°C was not observed and this is in conformity with the absence of RuO_2, as observed during XRD examination. The active metal surface area was measured by H_2-TPD, where H_2 was adsorbed at the surface at 120° and then desorbed. The metal surface area for the fresh sample was found to be 2.8 which increased after the reaction and for the used sample it was found to be 3.2 $m^2g^{-1.}$ These results conform the fact that ruthenium is mostly present in a metallic state in the used catalyst. As a result, there is a nominal increase

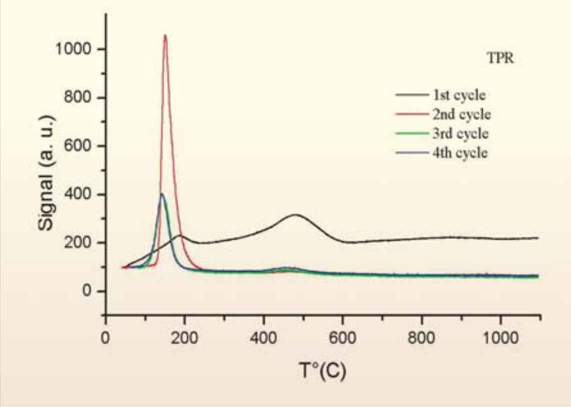

Fig. 4 : Multiple TPR/TPO cycles of Ru/Al_2O_3 fresh sample. Each TPR cycle was followed by a TPO run.

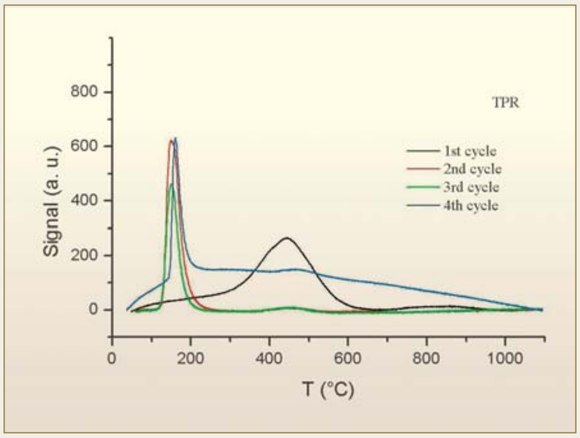

Fig. 5 : Multiple TPR/TPO cycles of Ru/Al_2O_3 used sample. Each TPR cycle was followed by a TPO run.

in the metal surface area and in metal dispersion. Both samples show similar redox behaviour except for the absence of oxide species in the used catalyst. Thus we conclude, that oxide RuO_2 species present in the fresh sample are active species and get consumed during the reaction. Also from TPO results, catalyst can be regenerated at a temperature of ~550°C in air.

Some recent studies

Studies on Sulfur-Iodine Thermochemical Cycle for Hydrogen Production

Recently work has been initiated at the Chemistry Division on Sulfur-Iodine thermochemical cycle, which deals with the development of catalyst systems, for decomposition of sulfuric acid, the most energy intensive step involved in this cycle towards decomposition of water for hydrogen production. Chromium substituted Fe_2O_3 catalysts were synthesized via solid-state route and characterized by XRD, N_2 sorption and Temperature Programmed Reduction/ Oxidation (TPR/O) techniques. Catalytic activity for decomposition of sulfuric acid in the temperature range of 400 - 800°C has shown that, onset temperatures for SO_2 formation in all samples were ~600°C. Successive TPR/O studies on these samples have revealed better sintering characteristics as compared to a pure Fe_2O_3 sample and thereby suggested a better performance of chromium substituted catalyst during prolonged use for sulfuric acid decomposition.

Temperature Programmed Reduction / Oxidation

The TPR profiles depicting the reduction behavior of $Fe_{2-x}Cr_xO_3$ samples are shown in Fig. 6. Data on pure Fe_2O_3 and Cr_2O_3 samples are also included in this figure. As seen in Fig. 6 a, the TPR profile of Fe_2O_3 sample comprises a prominent band with T_{max} at ~470°C and another broad band with onset of 530°C and having T_{max} at ~705°C. The reduction onset temperature of the main band is at 330°C. The presence of two bands suggests the two reduction steps. Since Cr^{3+} is stable towards H_2 atmosphere up to 1000°C, as evident from Fig. 6d, the reduction profile of the substituted samples is attributed to the reduction of $Fe^{3+} \rightarrow Fe^0$ species. T_{max} value of the main band at ~ 470°C shifted to higher values by ~ 25°C upon chromium substitution.

The overall TPR profiles of these samples remained same during successive TPR/TPO cycles (Fig. 7). However, the T_{max} value for the main band in case of chromium substituted samples, reduced by about 45°C during 2nd TPR run and remained unchanged during subsequent cycles. On the other hand, T_{max} for the main band was shifted to higher temperatures by ~30°C, in case of Fe_2O_3 during subsequent TPR/TPO cycles and was attributed to sintering of the sample. Thus, Cr^{3+} substitution has not only eased the reduction of iron oxide, but also enhanced the compositional stability towards multiple TPR/TPO cycles, as compared to unsubstituted sample.

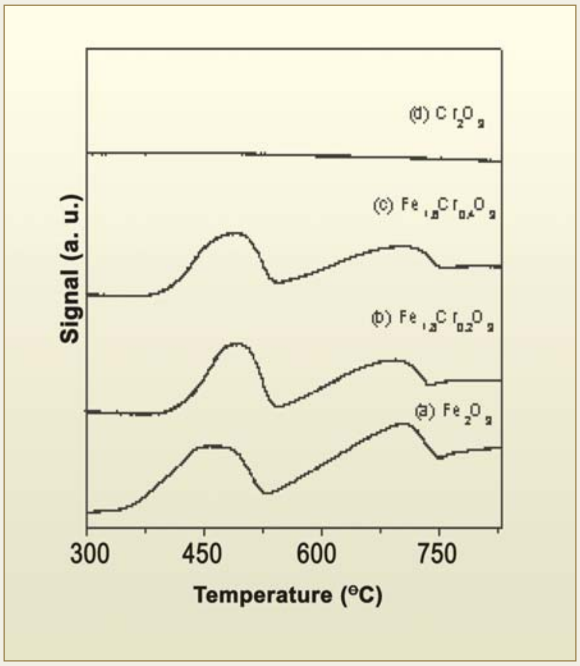

Fig. 6 : TPR profile of various chromium substituted and unsubstituted iron oxide samples

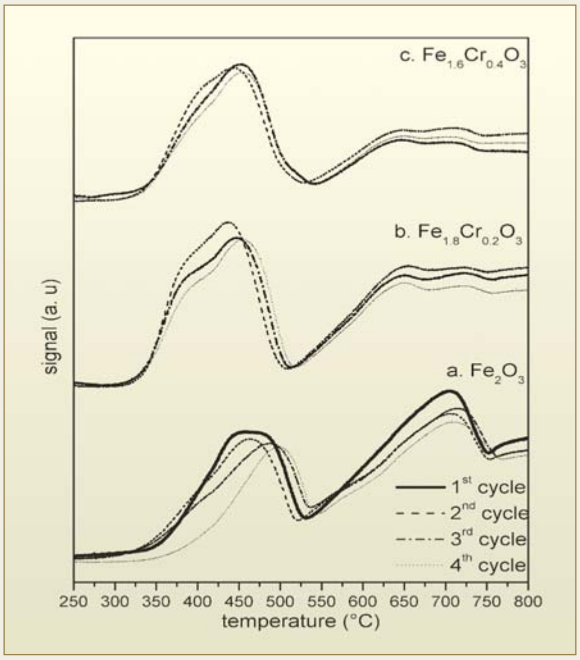

Fig. 7 : Successive TPR profiles chromium substituted and unsubstituted iron oxide

Catalytic Properties of Dispersed Metal ions (M=Ni, Co and Pt) on $La_2Ti_{2(1-X)}Fe_{2x}O_{7-\delta}$ oxides supports for N_2O Decomposition

Nitrous oxide (N_2O) is a harmful pollutant of the atmosphere, as it is a major contributor to global warming [10] and leads to stratospheric ozone destruction. To control the emission of N_2O, many catalysts have been reported for the catalytic decomposition of N_2O, including supported metals [11], pure and mixed oxides [12] and zeolites, transition metals [13] and their oxides.

Here we report, the catalytic properties of finely dispersed Metal ions on Lanthanum titanate support viz; M-$La_2Ti_{2(1-x)}Fe_{2x}O_{7-\delta}$ oxides (M=Ni, Co and Pt; x = 0 and 0.4), for catalytic decomposition of N_2O. In these samples, fine powders of Ni, Co and Pt metal ions were dispersed on Fe substituted (LF) / unsubstituted Lanthanum Titanate (LT), viz; $La_2Ti_{2(1-x)}Fe_{2x}O_{7-\delta}$ oxide supports, with an objective to decompose the N_2O efficiently at low temperature. Lanthanum titanate, $La_2Ti_2O_7$, is a Layered Perovskite and has shown several advantages as support over alumina or other conventional supports. $La_2Ti_2O_7$ is stable towards reduction and oxidation atmoshphere upto 1000°C. Also metal dispersed on perovskite surface [14] remains in dispersed state, even after prolonged use and does not suffer from the drawbacks of ageing, agglomeration and subsequent loss of activity, as observed in conventional catalysts, Pt/Al_2O_3, Pd/Al_2O_3. The metal particle moves back and forth between the B-site in the perovskite structure and the metal particle lattice site in the real catalyst when exposed to fluctuation of the oxygen content of the emission exhaust. To minimize the fluctuations in the oxygen content, if we have a perovskite support this can easily provide and withdraw oxygen. Thus, $La_2Ti_2O_7$, a layered perovskite is a preferred support for different metals like Pt, Ni, Co. etc. $La_2Ti_2O_7$ crystallizes in a monoclinic lattice, is a member of a homologous series of layered structures built from (110) perovskite slabs differing in thickness and bounded by crystallographic shears in the perovskite [100] direction. Adjacent slabs are offset from one another by half of one TiO_6 octahedron height and the octahedron connectivity is broken at the shear interface.

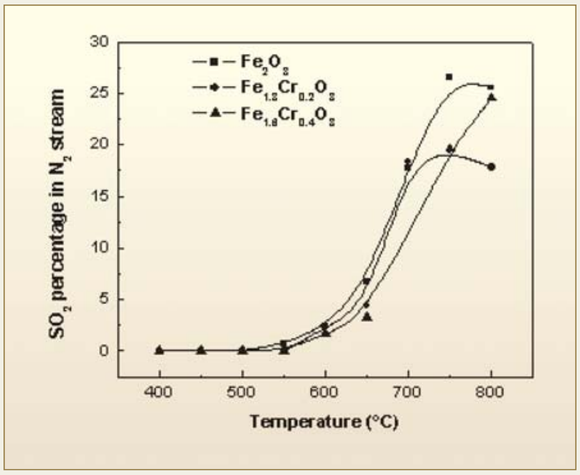

Fig. 8 : Catalytic activity for decomposition of sulfuric acid over various catalysts

Support samples with the compositions of $La_2Ti_2O_7$ (LT) and $La_2Ti_{1.2}Fe_{0.8}O_{7-\delta}$ (LF4) samples were synthesized

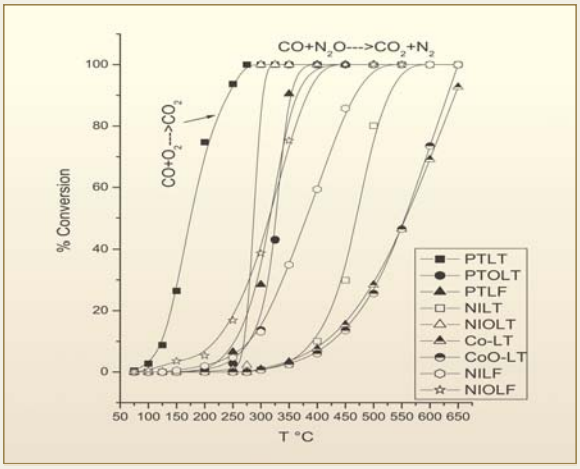

Fig. 9 : The temperature-dependent catalytic activity of M-$La_2Ti_{2(1-x)}Fe_{2x}O_{7-\delta}$ oxide samples for CO+N_2O reaction.

by Gel Combustion route (GC) followed by dispersion of metal using wet impregnation method. The samples, M-$La_2Ti_{2(1-x)}Fe_{2x}O_{7-\delta}$ oxides (M=Ni, Co and Pt; $x = 0.4$) were characterized by XRD, SEM, TEM, XPS and AAS for compositional analysis. The TPR profiles of these samples were recorded, to study their reduction behaviour. The activity of several metal supported samples was evaluated, for CO+ N_2O, N_2O decomposition reaction. The adsorption behavior of CO, N_2O gases on these catalysts samples was monitored by recording *in situ* FTIR spectra, to explore the mechanistic aspects involved in the catalytic reaction.

The XRD patterns of samples containing Ni, CO and Pt supported on $La_2Ti_{1.2}Fe_{0.8}O_{7-d}$ sample reveal, that all lines are attributed to single phase; rhombohedral $LaFeO_3$ phase having unit cell parameters a=5.566 Å, b= 7.854 Å, and c= 5.56 Å, Vol=242.81 Å^3 (JC-PDS Card. No. 37-1493). After impregnation of metals on either LTO/LF4 support, there are no additional XRD lines observed due to metal ions, suggesting that, incorporated metal ion is too small in content to be detected by XRD. Successive 4-5 TPR/TPO cycles recorded for supports alone, suggests the reorganization of oxygen excess layered perovskite, $A_2B_2O_7$ lattice to ABO_3 type lattice perovskite structure on reduction and vice versa, thus facilitates the removal and acceptance of oxygen within the same composition. In addition to peaks observed in the TPR profile of support, a low temperature peak at ~180°C and 280°C were also observed in first and second TPR cycles of Pt-LFGC and Ni-LFGC samples attributed to reduction of Pt and Ni respectively. The presence of low temperature peaks in Ni-LFGC and Pt-LFGC samples suggest that both Ni and Pt exist in oxide form, to some extent, in the impregnated samples. All these samples were found to be active as shown in Fig. 9, the decreasing order of activity of different samples as observed from activity data was; NiO-LT (PT-LT) > NiO-LF4 > PtO-LT > Ni-LF4 > Ni-LT > CoO-LT > Co-LT. For the $CO+N_2O \rightarrow CO_2 + N_2$ reaction, the maximum conversion was observed with NiO dispersed on LT support where 100% conversion was obtained at 300°C with onset of conversion at 250°C. Metal ion dispersion has considerably enhanced the activity as compared to support LTO, which showed negligible activity at 300°C and in case of LF4, 100% conversion was obtained at 400-410°C with an onset at 300°C. Particle size distribution from TEM image of NiO-LT sample (Fig. 10) reveals that, particles of average size ~10-12 nm of amorphous nickel oxide are uniformly dispersed on support, $La_2Ti_2O_7$. These nanoparticles were responsible for the considerable rise in activity, observed with the NiO-LT

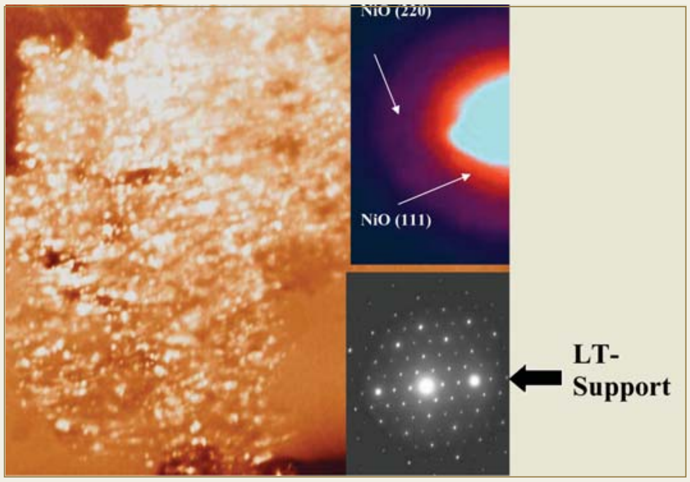

Fig.10 : TEM/ED image of NiO-LT sample.

sample, as compared to other samples. Inset of Fig.10 shows, two different electron diffraction images; rings corresponding to 220 and 111 planes of polycrystalline NiO dispersed on support, other ED image has well defined dots attributed to crystalline monoclinic lanthanum titante support. In case of PT-LT sample, Fine particles of Pt present on grain boundaries of support observed on the backscattered SEM image of Pt-LTGC has resulted in considerably high activity of 100% conversion at 275°C, with onset at 75°C only, for CO oxidation reaction alone. *In situ* IR results reveals that adsorption and decomposition of N_2O alone occurs considerably at 300° on NiO-LTGC, in contrast to support samples, LT and LF4 where no decomposition was observed even at 350°C. Overall, conclusion is that dispersion of Ni and Pt metal ions on $La_2Ti_2O_7$ support considerably modifies its properties and enhances catalytic activities of oxide samples for N_2O decomposition reaction.

Acknowledgements

My sincere thanks are due to Dr. N.M. Gupta, former, Head Chemistry Division, for his guidance, support and encouragment. I sincerely thank Dr. T. Mukherjee, Director, Chemistry Group, Dr. D. Das, Head, Chemistry Division, Dr. S. R. Bharadwaj, Head, FCM&CS, Chemistry Division for their constant support and encouragement. I thank Dr. A. K. Tyagi, Head, SSCS, Chemistry Division and senior colleagues Dr. A. D. Belapurkar, Dr. V.S. kamble, Dr. A. K.Tripathi, Dr. B. N. Wani of my section for their keen interest and useful discussions. I thank Dr. R. Tewari, MSD and Dr. G. K. Dey, Head, Materials Science Division for TEM images. I thank all my coauthors, A. M. Banerjee, K. Bhattacharyaa, S. Varma, , S. N. Achary, R. Mishra, K. Shashikala, B. P. Mandal, V. Grover, S. S. Meena, Jagganath, Shovit B., B. Sreedhar, A. S. Kerkar, R. V. Pai, P. A. Hassan for their respective contributions. I duly thank all my other colleagues, students and friends for providing moral support.

References

1. H. Tanaka and M. Misono, *Curr. Opinion in Sol. Stat. Mater. Sci.* 5 (2001), 381.
2. R.J.H. Voorhoeve, "*Advanced Materials in Catalysis*" p. 129, Academic Press, New York, 1997
3. L.G.Tejuca, J.LG. Fierro and J M D Tascon *Adv. Catal*. 36 (1989) 237
4. K. Shashikala, Seemita Banerjee, Asheesh Kumar, Mrinal R. Pai and C.G.S. Pillai, *Int. J. Hydrogen Energy,* Article in press, 2009.
5. M. R. Pai, A. M. Banerjee, S. R. Bharadwaj and S. K. Kulshreshtha, *J of Mater. Research, 22(2007)1787.*
6. M. R. Pai, B. N. Wani, A. D. Belapurkar and N. M. Gupta, *J. Molec. Catal. A: Chemical,* 223 (2004) 275.
7. Mrinal R. Pai, B. N. Wani and N. M. Gupta, *Thermochimica Acta,* 425 (2005) 109.
8. M. R Pai, B. N. Wani, B. Sreedhar, S. Singh and N. M. Gupta, *J. Molecular Catalysis A: Chemical*, 246 (2006) 128.
9. A.M. Banerjee, M.R. Pai, K. Bhattacharya, A.K. Tripathi, V.S. Kamble, S.R. Bharadwaj, S.K. Kulshreshtha; *International Journal of Hydrogen Energy,* 33 *(2008)* 319.
10. P. Ramirez, F. Kapteijn, K. Schoffel, J. A. Moulijn, *Appl. Catal. B:* 44 (2003) 117.
11. V.K. Tzitzios, V. Georgakilas, *Chemosphere* 59 (2005) 887.
12. L. Yan, T. Ren, X. Wang, D. Ji, J. Suo, *Appl. Catal. B* 45 (2003) 85.
13. A.K. Ladavos and P.J. Pomonis, *Appl. Catal. B,* 2 (1993) 27.
14. Y. Nishihata, J. Mizuki, T. Akao, H. Tanaka, M. Uenishi, M. Kimura, T. Okamoto and N. Hamada, *Nature,* 418, (2002) 164.

ABOUT THE AUTHOR

Dr. (Ms.) Mrinal R. Pai joined BARC through Training School (40th Batch) after completing her Post graduation in Chemistry from IIT Delhi, in 1996. She initiated her research activities in the field of catalysis with development of H_2 mitigation catalyst during year 1999 in the Chemistry Division. She was awarded Ph.D degree in Physical Chemistry from Mumbai University in 2005. Also, she gained experience in synthesizing fine powders of nano-size oxides/mixed oxides with spinels, perovskites and pyrochlore structures and characterizing them by various techniques for their prospective applications in pollution abatement, water splitting by photocatalysis and sulfuric acid decomposition reaction in S-I thermochemical cycle. There are sixteen publications in refereed international journals, several publications in symposia and conferences and invited talks to her credit.

BIMOLECULAR ELECTRON TRANSFER (ET) REACTIONS IN MICELLAR MEDIA: UNIQUE MARCUS INVERSION AND ITS TUNING

M. Kumbhakar
Radiation & Photochemistry Division

This lecture was given by Dr. Kumbhakar at the Young Scientist Award presentation – 2007, instituted by the National Academy of Sciences, India, at Allahabad in July 2007

Chemical reactivity and its tuning is an important aspect of research in chemical sciences. Chemical reactivity deals with various factors that govern both the reaction rates and the reaction mechanisms, by which reactions transpire. Knowing the nature of the intermediate steps is also an important aspect in understanding the chemical reactions in detail. Among all the chemical processes, electron transfer (ET) is undoubtedly the most fundamental reaction and is found to be involved as the initial step in numerous chemical systems of vast technological importance, such as information storage, energy conversion, photosynthesis, respiration, etc.[1, 2] ET is in fact ubiquitous in Chemistry and Biology and this veracity of the ET reactions that prompted Prof. R.A. Marcus to develop the theoretical understanding of ET dynamics,[3, 4] which ultimately fetched him the Nobel Prize in Chemistry in the year 1992.

According to Marcus ET theory (originally developed in 1956[3, 4]), reaction rate (k_{et}) for the reaction $D/A \rightarrow D^{+}/A^{-}$, where D and A represent the electron donor and the electron acceptor, respectively, is related to the reaction free-energy (ΔG^0) by the following quadratic equation,[5]

$$k_{et} = \frac{2\pi}{\hbar}\frac{V_{el}^2}{\sqrt{4\pi\lambda_s k_B T}}\exp\left\{-\frac{\left(\Delta G^0 + \lambda\right)^2}{4\lambda k_B T}\right\}$$

where, V_{el} is the measure of the electronic coupling between the reactant (D/A) and the product (D^{+}/A^{-}) states, k_B is the Boltzmann constant, T is the absolute temperature and λ is the total reorganization energy, given as $\lambda = (\lambda_s + \lambda_i)$, λ_s is the solvent reorganization energy and λ_i is the intramolecular reorganization energy. The most interesting feature of Marcus ET theory is the expected inversion in the ET rate as the exergonicity of the reaction ($-\Delta G^0$) exceeds total reorganization energy λ. Thus the Marcus equation predicts a bell shaped correlation (well known as the Marcus inversion behaviour) between the reaction rate and the free-energy, which can be shown graphically as in Fig. 1.

Following Marcus equation, in the exergonicity region of $-\Delta G^0 < \lambda$, the k_{et} increases with an increase in the exergonicity ($-\Delta G^0$) of the reaction (normal region) until the situation of barrierless condition is reached at $-\Delta G^0 = \lambda$, where the ET reaction proceeds without any barrier and consequently with the

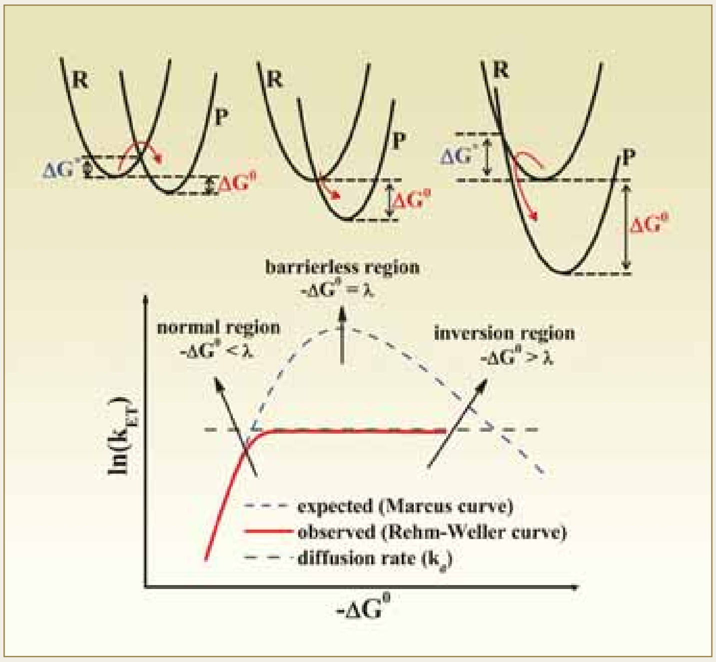

Fig. 1: Free energy curves for the reactant (R) and product (P) states for the three regions of inverted bell shaped Marcus correlation curves. Modification of Marcus correlation in the case of intermolecular ET reactions due to the limiting effect of diffusion of the reactants on the reaction rates is also shown (Rehm-Weller curve).

maximum rate. The most interesting feature of Marcus equation, is the inversion in the ET rates in exergonicity region of $-\Delta G^0 > \lambda$, known as the Marcus inversion region. This inversion region has tremendous implications in applied areas as in most ET systems following the forward charge separation reaction, the subsequent back ET reaction often also takes place, which significantly reduces the effective outcome of the ET process, if the rate of the back ET reaction is not substantially slower than the forward ET reaction. This can be easily perceived if we consider the reverse ET reaction, which produces back the ground state reactants and occurs at a much higher exergonicity than that of the forward ET reaction, such that the back ET is in the inverted region but the forward ET is closer to the barrierless region. In designing an efficient photoinduced charge separation system, it is always desired that the forward ET is carried out at a rate much higher than that of the reverse ET process. As the previous discussion suggests, this can be easily achieved if the exergonicity of the forward ET reaction is quite close to the barrierless situation such that, the exergonicity of the reverse ET invariably appears at the inversion region. Thus, by taking the advantage of this relationship, it might be possible to control or modulate the ET reactions; a classic example being the primary charge separation step in photosynthesis, that occurs in nature with its maximum efficiency.[5]

Marcus inversion region for intramolecular ET reactions (D and A moieties are chemically bound) was first realized experimentally in the mid-eighties.[6] However, for intermolecular ET reactions (D and A moieties are isolated molecules), Marcus inversion region is very difficult to demonstrate. This is primarily because the diffusion of reactants (D and A) is required in the first step, to bring the reactants together to participate in the ET reaction (*cf.* Fig. 1) and in such cases the diffusional rate effectively becomes the rate determining step. Thus in intermolecular ET reactions, the diffusion process imposes an upper limit (k_d) on the observed reaction rate and consequently masks the observation of the expected Marcus inversion behaviour, rather reaction rate saturates to k_d at higher exergonicity region, the behaviour commonly known as the Rehm-Weller behaviour.[7] At exceedingly high reaction exergonicity, there is still a possibility to observe inversion behaviour where absolute ET rate becomes lower than the diffusional rate.[8] However, finding a homologous donor-acceptor series, which can extend to very high reaction exergonicity, is very difficult to obtain.

Therefore, the challenge to chemists in ET research is to design a methodology to overcome these limiting factors, i.e. the diffusion of the reactants and the non-availability of suitable donor-acceptor series and thus to convincingly demonstrate the Marcus inversion behavior for intermolecular ET reactions.

In our studies, to surmount these limiting factors, organized assemblies such as micelles and reverse micelles have been judiciously chosen as the reaction media, for the investigation of the intermolecular ET reactions. The merits for the selection of micellar media is based on the following considerations.

(i) Reactants in micellar microenvironment get entangled within the surfactant chains and their mobility is expected to be largely reduced.[9] Therefore, diffusion of reactants can be largely prevented, which otherwise masks the Marcus inversion behaviour in homogeneous solution.

(ii) The value of λ_s for ET reaction is expected to be quite less in micellar media as compared to that in bulk homogeneous solution of similar polarity, as the solvent motion is largely retarded in micellar systems.[10-12] Therefore, Marcus inversion region ($-\Delta G^0 > \lambda$) could be achieved at relatively lower exergonicity in micellar media than in polar homogeneous media. Hence, instead of increasing the exergonicity to an unreasonably high value, Marcus inversion region could be shifted to relatively lower exergonicity in micellar media as compared to that expected in homogeneous solution.

To substantiate our proposition that micellar media can be conducive for the observation of Marcus inversion behaviour, intermolecular ET reactions were investigated between excited coumarin dyes (as electron acceptors) and aromatic amines (as electron donors) in sodium dodecyl-sulphate (SDS) micellar solutions, using fluorescence quenching measurements. Indeed, for the first time, full bell shaped Marcus correlation curve has been demonstrated by us for intermolecular ET reactions using micelles as the reaction media,[13] where similar ET systems showed the usual Rehm-Weller behaviour in homogeneous acetonitrile solution.[14] The typical results in micellar media displaying Marcus Inversion behaviour is shown in Fig. 2.

Apart from demonstration of the inverse bell shaped correlation between the reaction rate and the driving force, we also emphasized the intricate details of the micellar ET kinetics, by critical analysis of the observed results and by scrupulous scrutiny of published literature. It has been established that the standard diffusional kinetic model,[15, 16] which is used by many researchers to analyze the reaction kinetics in micelles, is not appropriate in describing the ET kinetics for the systems we studied. Rather, for our systems, it was realized that ET reactions in micelles effectively occur under nondiffusive condition[17-20] and the kinetics is determined mainly by the distant dependent quencher distribution around the excited fluorophore.[13] Moreover, in micelles, ET occurs between donor-acceptor pairs that are on an average

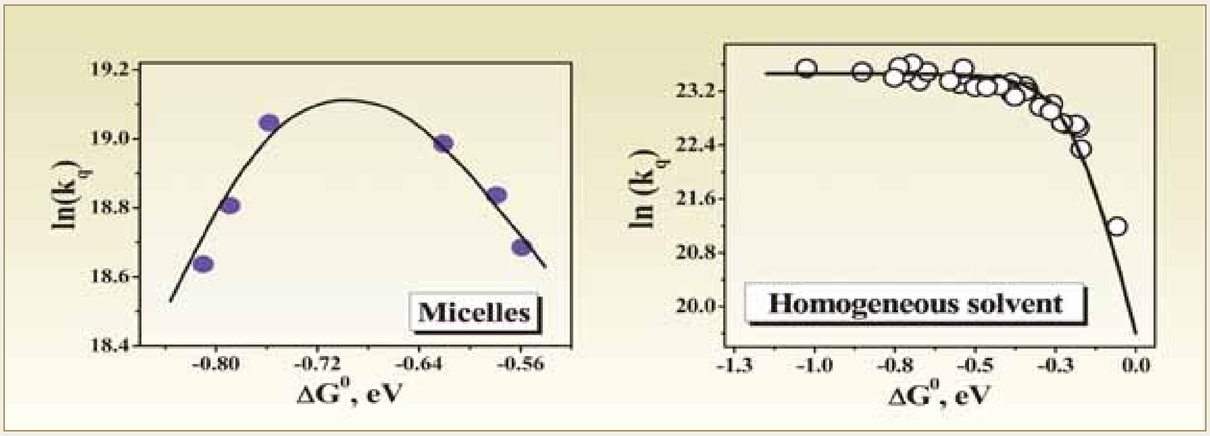

Fig. 2: Marcus correlations for the intermolecular ET reactions between coumarins and amines in micellar media (left) and in homogeneous acetonitrile solution (right).

separated by an intervening surfactant chain.[21] The most important finding of our studies on ET reaction in micellar media is the onset of Marcus inversion at around -0.6 eV, much lower in energy than that expected from the full contribution of the solvent reorganization energy λ_s ($\geq$ -1.2 eV).[22, 23] Unlike conventional ET theory, these results were better explained by the Sumi-Marcus two-dimensional ET (2DET) theory,[24] where the ET reaction is viewed to proceed through the intramolecular coordinate even when the reactants are in a non-equilibrium configuration with respect to the solvent reorganization coordinate, as shown in Fig. 3.

The successful demonstration of Marcus inversion behaviour in micellar media also raises a number of questions. Some of the important ones are,

(i) How micellar characteristics (i.e. micellar charge and size) influence the observed ET kinetics?

(ii) Is it possible to tune the exergonicity scale for the appearance of Marcus inversion region?

(iii) Whether the observation of Marcus inversion is specific to some donor-acceptor systems or it is a general phenomenon applicable to all kind of donors and acceptors involved.

(iv) Is the inversion in the ET rates at higher exergonicity due to the alteration in the diffusion parameters of the reactants or is it due to the alteration in the energetics (e.g. activation barrier) for the ET reactions ?

(v) Why are the ET rates orders of magnitude slower in micelles when compared to those of electron donor amines that are directly used as the reaction medium (non-diffusional ET) ?

To address the first question, intermolecular ET studies were also carried out in neutral micelles formed by triton-X-100 (TX100) and Pluronic tri-block copolymers

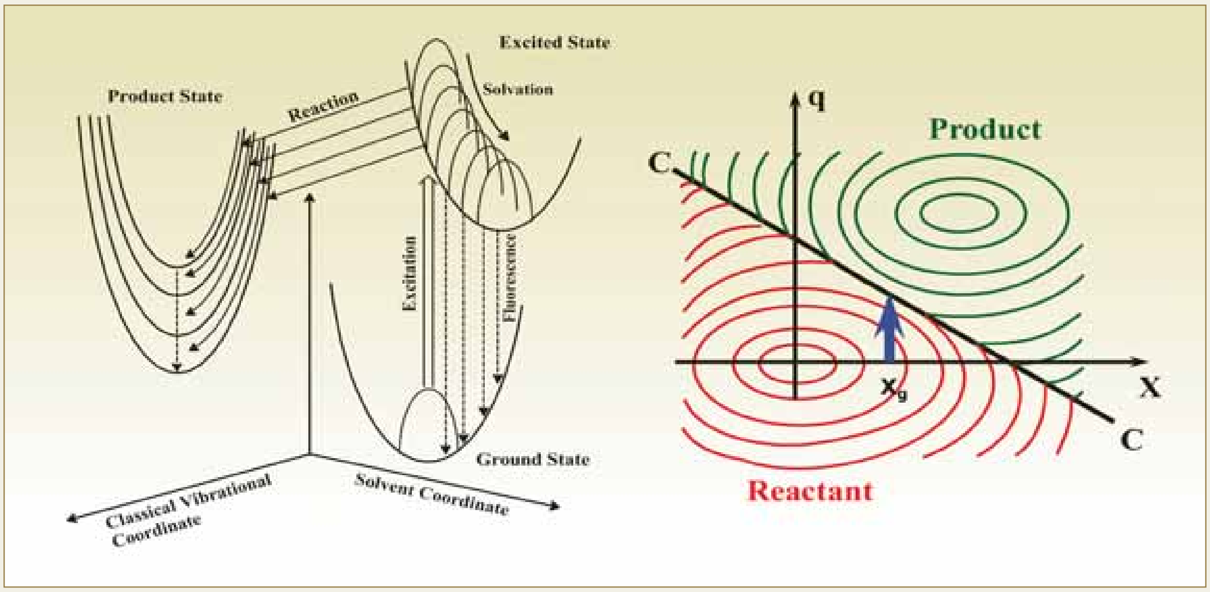

Fig. 3 : Conceptual drawing of the hybrid ET reaction as formulated in the Sumi-Marcus two dimensional ET theory (left). The solvation process occurs along the solvent coordinate, while the reaction occurs through the classical low frequency vibrational coordinate. The role of quantum mechanical high frequency vibrational levels on the ET reaction have also been indicated in the scheme. The isoenergy contours of the potential energy surfaces (right) drawn in a two-dimensional plane for the reactant and product states in relation to the two-dimensional ET model is also shown, where X represents the solvent coordinate and q represents the nuclear coordinate. The normalized X,q coordinates for the reactant and product state potential energy minima are customarily considered at (0,0) and (1,1) coordinates, respectively. The line C-C represents the transition state curve corresponding to the crossing of the reactant and product state potential energy surfaces. In this model electron transfer can occur along the q coordinate for any solvent configuration (X_g), as are shown by arrow parallel to the q coordinate.

(P123) and in cationic micelles formed by cetyltrimethyl ammonium bromide (CTAB) and dodecyltrimethyl ammonium bromide (DTAB) and the results were compared with those in anionic SDS micelle.[13, 17, 18, 21, 22, 25-27] Interestingly, Marcus inversion behaviour was clearly evident in all the micelles, irrespective of their cationic, anionic or neutral nature and the differences in their sizes. Although depending on the relative propensity of solvation and ET rates, appearance of Marcus inversion was shifted towards higher exergonicity in CTAB and DTAB micelles (~1.2 eV) as compared to that in SDS, P123 and TX100 micelles (cf. Fig. 4). Nearly 0.6 eV shift for the onset of Marcus inversion region, depending on the micellar identity for the same coumarin-amine systems is an interesting observation and suggests the possibility of tuning the ET rates, by changing the nature of the micelles. This observation in turn answers our second query on the tuning of Marcus inversion region.

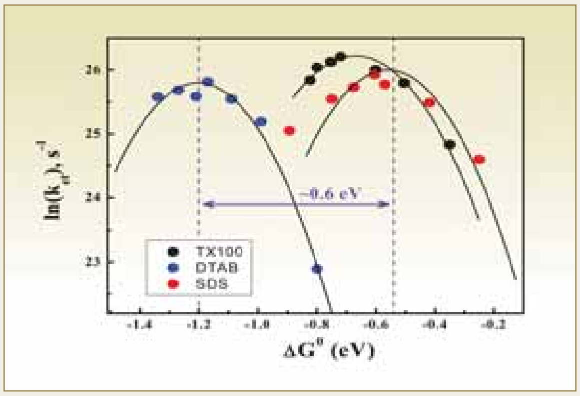

Fig. 4: Marcus correlation curves for coumarin-amine systems in different micelles. ET rates are calculated from the fast decay components

To evaluate the third point, intermolecular ET studies were further extended to other series of donor-acceptor systems, namely, quinone-aromatic amine systems in SDS micelles.[18, 23] It is seen that ET rates for quinone-amine systems also show inversion behavior above an exergonicity of 0.7 eV, quite similar to that observed earlier for the coumarin-aromatic amine systems. Marcus inversion behaviour is also seen for coumarin-aliphatic amine systems in other micelles.[25] These results substantiate the fact that Marcus inversion behaviour is a general phenomenon for intermolecular ET reactions in micellar media.

We also studied similar ET reactions in TX-100 and P123 micellar solutions as a function of temperature to answer the fourth issue.[17, 27] The results indicate an inverse bell-shaped correlation for the estimated activation energy (E_a) for the ET reactions with ΔG^0, as envisaged from the Marcus ET theory (cf. Fig. 5). The translational diffusion coefficient (D_L) of the acceptor dyes on the micellar surface, calculated from the two-step model of their fluorescence anisotropy decays in micellar systems, show nearly linear relation with ΔG^0 (cf. Fig. 5). Comprehension of these results indicates that the inversion in the ET rate at higher exergonicity is due to the alteration in the activation barrier for the ET reactions and the role of reactant diffusion is really insignificant for intermolecular ET reaction in micellar systems.

Ultrafast quenching experiments with similar donor-acceptor systems in micelles, using the state-of-the-art fluorescence up-conversion instrument (developed under the Xth Project Plan), helped us to investigate the fifth point of our queries.[22] The fastest ET rates estimated as the inverse of the shortest lifetime components (~ 4-10 ps) of the fluorescence decays ($k_{et} \cong t_{fast}^{-1}$) and the relatively slower ET rates (k'_{et}) obtained from the conventional Stern-Volmer analysis of the relatively longer time constants (~ 40-100 ps) of the fluorescence decays exhibit similar Marcus inversion behaviour. Fitting of Marcus correlation curves for k_{et} and k'_{et} indicate two largely different values for the V_{el}, which is known to have an exponential relation with the separation (r) between the reacting D and A, (i.e. $V_{el}(r) = V_{el}(r_0) \exp[-\beta(r-r_0)]$, where β is the attenuation coefficient, usually assumed as unity and r_0 is the sum of the D and A radii). It has beenindicated from the critical analysis of the results that in micellar media, the ultrafast ET (k_{et}) component arises due to the surfactant separated donor-acceptor pairs, that are oriented perfectly to give the maximum electronic

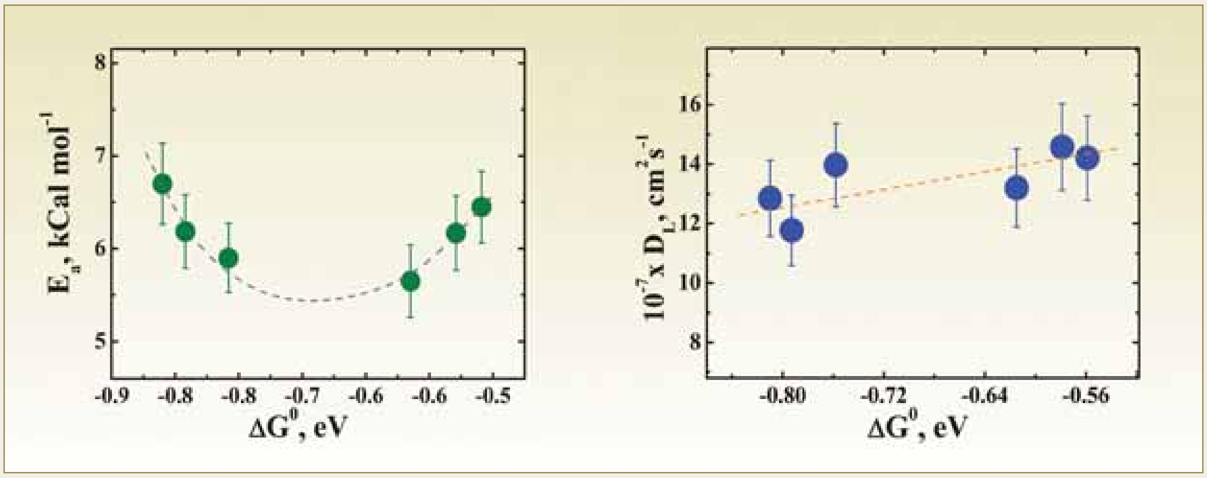

Fig. 5 : Plot of E_a vs ΔG^0 (left) and D_L vs ΔG^0 (right) for the coumarin-amine systems in P123 micelles.

coupling and the slower ET component (k'_{et}) is predicted to arise due to those pairs of D and A for which the orientations are not very suitable but still good enough to give a sizable electronic coupling. As the interacting donor–acceptor molecules are on an average separated by an intervening surfactant chain in micelle, ET rates are inherently slower in comparison to the ET reactions where they are in close contact, e.g. in experiments with coumarin dyes in the electron donating amine solvents.

In summary, the main highlight of our ET research, is the demonstration of a simple but innovative approach, to control the kinetics and mechanism of intermolecular ET reactions in micellar media and the appreciation of diverse intriguing aspects related to micellar ET dynamics, of general interest to chemists who strive to control the dynamics and mechanism of chemical reactions, for the maximum outcome of the desired effect.

Acknowledgements

I wish to record my sincere thanks to all my coauthors and collaborators for their valuable contributions. Support from all the colleagues of RCPD and TCS is also sincerely acknowledged.

References

1. J. Jortner, M. Bixon, *Electron Transfer From Isolated Molecules to Biomolecules (edited by J. Jortner and M. Bixon), Advances in Chem. Phys.*, Wiley, New York, **1999**.
2. J. R. Bolton, N. Mataga, G. L. McLendon, *Electron Transfer in Inorganic, Organic and Biological Systems*, American Chemical Society, Washington, DC, **1991**.
3. R. A. Marcus, *J.Chem.Phys.* **1956**, *24*, 966.
4. R. A. Marcus, *J.Chem.Phys.* **1956**, *24*, 979.
5. G. J. Kavarnos, *Fundamentals of Photoinduced Electron Transfer*, VCH Publishers, New York, **1993**.
6. J. R. Miller, L. T. Calcaterra, G. L. Closs, *J. Am. Chem. Soc.* **1984**, *106*(10), 3047-3049.
7. D. Rehm, A. Weller, *Israel J. Chem.* **1970**, *8*, 259.
8. M. Tachiya, S. Murata, *J. Phys. Chem.* **1992**, *96*, 8441-8444.
9. M. Kumbhakar, T. Mukherjee, H. Pal, *Photochem. Photobiol.* **2005**, *81*, 588-594.
10. M. Kumbhakar, T. Goel, T. Mukherjee, H. Pal, *J. Phys. Chem. B* **2004**, *108*, 19246.
11. M. Kumbhakar, S. Nath, T. Mukherjee, H. Pal, *J. Chem. Phys.* **2004**, *121*, 6026-6033.
12. M. Kumbhakar, T. Goel, S. Nath, T. Mukherjee, H. Pal, *J Phys. Chem. B.* **2006**, *110*, 25646.

13. M. Kumbhakar, S. Nath, H. Pal, A. V. Sapre, T. Mukherjee, *J. Chem. Phys.* **2003**, *119*, 388-399.
14. S. Nad, H. Pal, *J. Chem. Phys.* **2002**, *116*, 1658-1670.
15. M. Tachiya, *Kinetics of Non-homogeneous Processes*, Wiley, NY, **1987**.
16. M. Tachiya, *Chem. Phys. Lett.* **1975**, *33*, 29.
17. A. K. Satpati, M. Kumbhakar, S. Nath, H. Pal, *J. Phys. Chem. B* **2007**, *111*, 7550-7560.
18. M. Kumbhakar, S. Nath, T. Mukherjee, H. Pal, *J. Chem. Phys.* **2005**, *122*, 084512.
19. S. D. Choudhury, M. Kumbhakar, S. Nath, H. Pal, *J. Chem. Phys.* **2007**, *127*, 194901.
20. S. D. Choudhury, M. Kumbhakar, S. Nath, S. K. Sarkar, T. Mukherjee, H. Pal, *J. Phys. Chem. B* **2007**, *111*, 8842-8853.
21. M. Kumbhakar, S. Nath, T. Mukherjee, H. Pal, *J. Chem. Phys.* **2004**, *120*, 2824-2834.
22. M. Kumbhakar, P. K. Singh, S. Nath, A. C. Bhasikuttan, H. Pal, *J. Phys. Chem. B* **2008**, *112*, 6646-6652.
23. A. K. Satpati, M. Kumbhakar, S. Nath, H. Pal, *J. Photochem. Photobiol. A: Chem.* **2008**, *200*, 270-276.
24. H. Sumi, R. A. Marcus, *J. Chem. Phys.* **1986**, *84*(9), 4894-4914.
25. M. Kumbhakar, T. Mukherjee, H. Pal, *Chem. Phys. Lett.* **2005**, *410*, 94-98.
26. M. Kumbhakar, S. Nath, T. Mukherjee, H. Pal, *J. Chem. Phys.* **2005**, *123*, 034705.
27. M. Kumbhakar, S. Nath, T. Mukherjee, H. Pal, *J.Phot.Chem.Photobio. A: Chemistry* **2006**, *182*, 7-16.

ABOUT THE AUTHOR

Dr. Manoj Kumbhakar joined RPCD, BARC, in 2001, after successfully completing the one year orientation course in Chemistry discipline from the 44th Batch of Training School. His research interests include fast and ultrafast dynamics of electron transfer, charge transfer and solvation processes in homogeneous and heterogeneous media; photophysics of aromatic molecules and dynamics at the single molecule level. He received his PhD degree from Mumbai University in 2007. He is currently involved in developing a single molecule multi-parameter fluorescence spectroscopy setup in BARC under the XI-th Project Plan. Dr. Kumbhakar is the recipient of the Homi Bhabha Award in Chemistry for the year 2000–2001. He is also the recipient of the Elsevier PhD Photo-Scientist Award 2005 for his review article on single molecule spectroscopy. He received the Young Scientist Award - 2007 from the National Academy of Sciences India, Allahabad, for his significant contribution in the field of chemical dynamics in micro-heterogeneous media.

PHOTOINDUCED ELECTRON TRANSFER KINETICS IN CONFINED SYSTEMS AND MODULATION BY AN EXTERNAL MAGNETIC FIELD

S.D. Choudhury
Radiation & Photochemistry Division

Dr. (Ms.) S.D. Choudhury is the recipient of the "Dr. P. K. Bhattacharyya Memorial Young Scientist Award" for the year 2007, for her excellent work in the field of Photochemistry

ABSTRACT

Photoinduced Electron Transfer (PET) reactions have been studied in the presence of an external magnetic field, in order to identify the mechanism and dynamics of such reactions. It has been demonstrated that not only the structure of the participating molecules, but also the topology of the medium can have a profound influence on the magneto-dynamics of electron transfer reactions. The elusive Marcus inverted region has also been observed for bi-molecular PET reactions in some confined media.

Introduction

Photoinduced Electron Transfer (PET) is one of the most important processes underlying many photochemical and photobiological reactions.[1,2] The primary life sustaining process on earth, photosynthesis, is initiated by PET. Understanding and control of PET reactions comprise one of the broadest and flourishing areas of research today. PET reactions involve the jump of an electron from the occupied orbital of one reactant (donor), to the unoccupied orbital of another (acceptor), either of them may be photoexcited. In solution, where the molecules are free to diffuse, PET is influenced by reactant diffusion as well as solvent reorganization and different types of ion pair species are formed. Exciplex or excited state complex formation is also a manifestation of PET reactions.

PET reactions involve a change in the number of unpaired spins and thus can be affected by an external Magnetic Field (MF). The MF effect is basically an interplay between spin dynamics and diffusion dynamics.[3-5] The electron spin multiplicity of the excited state (Singlet, S or Triplet, T) is generally preserved during charge transfer and a memory of this initial spin multiplicity is retained in the resulting Radical Ion Pair (RIP) until the latter undergoes further reactions. If the RIP is in the singlet spin state, back electron transfer and geminate recombination is favoured. Conversely, if the RIP is in the triplet spin state, recombination is hindered as the radicals escape to the bulk and participate in further reactions. The spin multiplicity of the RIP is, however, not stationary and can evolve coherently between the S and T configurations. When the partners of a RIP are sufficiently separated, the exchange interaction,

$J \approx 0$, and the singlet (S) and triplet ($T_{\pm}$, T_0) states become degenerate. In this situation, Inter System Crossing (ISC) among the different spin states is possible by electron-nuclear hyperfine interaction. In the presence of an external MF, the degeneracy of the triplet states is destroyed due to Zeeman splitting and as a result $S \leftrightarrow T_+, T_-$ conversion is stopped leading to an increase in the population of the initial spin state (Scheme 1). The modulation of spin dynamics of RIPs, in the presence of an external MF, can be detected by monitoring the increase in exciplex luminescence of the singlet precursors in homogeneous solutions, by using a phase sensitive detection system.[5] For the triplet precursors, the laser flash photolysis technique is used for the detection of the transients and a MF is applied with the help of an externally placed electromagnet to see the MF effect on the dynamics of the transient radical ion species. For triplet derived RIPs, the MF effect is not observed in homogeneous media because radical separation is too rapid and geminate reaction is generally a very minor process. In organized assemblies, the RIPs are in a restricted environment and hence can retain their geminate character for a sufficiently long time so that spin flipping can occur.[35] The MF effect is thus an important tool for probing the initial spin of the reactants as well as the dynamics of PET reactions.

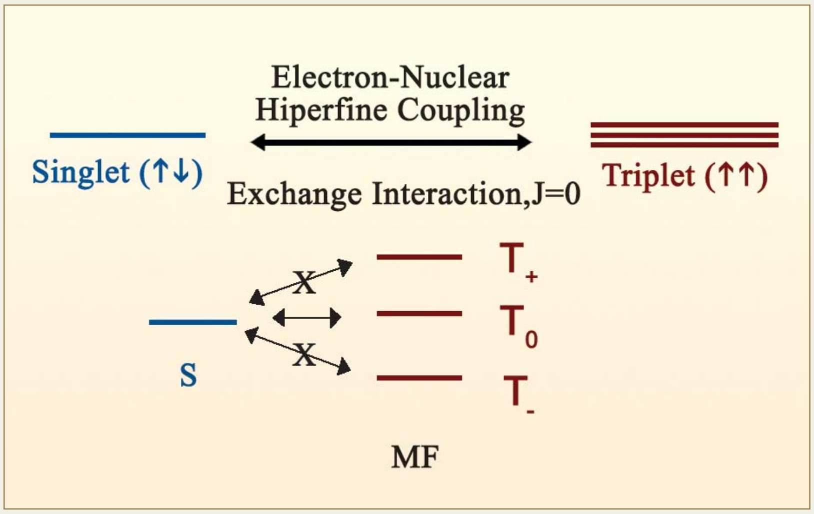

Scheme1: Spin dynamics in the presence of an external MF

Relation between structure of participating molecules and PET dynamics revealed by MF studies

Several studies have indicated the important role of molecular structure and steric effect on PET reactions and the steric encumbrance has been utilized to improve PET reactions, by reducing the energy-wasting back-electron transfer process.[6,7] We have used the MF effect to study PET dynamics from Ethyl CarbaZole (ECZ) to two structurally different acceptors, DiMethyl Terephthalate (DMT) and DiCyano Benzene (DCB). These acceptors have similar reduction potentials and the extent of charge transfer is similar in both cases. However, DCB is a planar molecule where as DMT is non planar and bulkier. It is interesting to see how this is manifested in the PET dynamics and subsequently in MF behaviour.

Exciplex luminescence is observed for both the systems indicating the formation of a charge transfer complex for ECZ-DMT and ECZ-DCB. In the presence of an external MF (~0.012 T), the exciplex luminescence increases, suggesting that the initial RIP is formed in the S state. Typically the percentage MF effect, i.e. the percentage increase in exciplex luminescence intensity in the presence of MF, varies with the dielectric constant of the medium and reaches a maximum at a medium dielectric constant value.[5] This is because at low polarity, the spin flipping is hindered and at a high polarity the geminate recombination is hindered. At an intermediate polarity, both spin flipping and geminate recombination are balanced and as a result, maximum MF effect is observed. This pattern is seen for ECZ-DMT and ECZ-DCB, as well, but the nature of the plots for % MF effect vs dielectric constant is quite different for the two systems (Fig. 1). These differences are attributed to the different structures of the acceptor molecules. Due to the greater steric bulk of DMT, the energy barrier between the solvent separated ion pair and the contact ion pair increases and hence the solvent polarity required for observing the maximum MF effect increases for ECZ-DMT. Moreover, the spin correlation is valid up to much higher polarity for ECZ-DMT, so the plot for ECZ-DMT is also much broader than that of ECZ-DCB. However, the MF effect is lower for ECZ-DMT because of the higher propensity of DMT to undergo ISC and to form free ions.

Effect of the medium on MF behaviour: micelles and reverse micelles

We have identified a new exciplex system between a heteroaromatic molecule PhenaZine (PZ) and some aromatic amines like N,N-DiMethylANiline (DMAN). In this case, however, there was no enhancement in the exciplex luminescene in the presence of an external MF. The molecule PZ undergoes rapid ISC to the triplet state. So the MF effect on triplet derived RIPs was studied using laser flash photolysis in two different heterogeneous media, namely micelles and reverse micelles.[9] A pronounced MF effect was observed in both the cases. The MF effect increases with increasing MF and then saturates at a particular value (Fig. 2). This behaviour is typical of the hyperfine coupling mechanism and the MF value at which half the saturation is reached ($B_{1/2}$), is a measure of the hyperfine coupling constant.[3-5] Interestingly, the experimental $B_{1/2}$ value observed in micellar media is much higher than the theoretically calculated $B_{1/2}$ value. Since the effective concentration of donors inside a micelle will be quite high, this could promote electron hopping and hence lead to an increase in the $B_{1/2}$ value.[10] Moreover, for donor-acceptor molecules encapsulated in micelles with restricted space, the situation can be compared to that of a linked system, so the high $B_{1/2}$ value can be explained by lifetime broadening due to frequent re-encounter within the RIP.[11]

Another interesting feature was observed in reverse micelles. It is well known that the size of reverse micelles can be easily modulated by changing the water to surfactant molar ratio ([water]/[surfactant] = w_0). It is observed that the MF effect increases with increasing water pool size, reaches a maximum and then decreases again. This result demonstrates that MF effect requires an optimum separation between the donor and acceptor molecules, which is attained at an intermediate w_0 value.

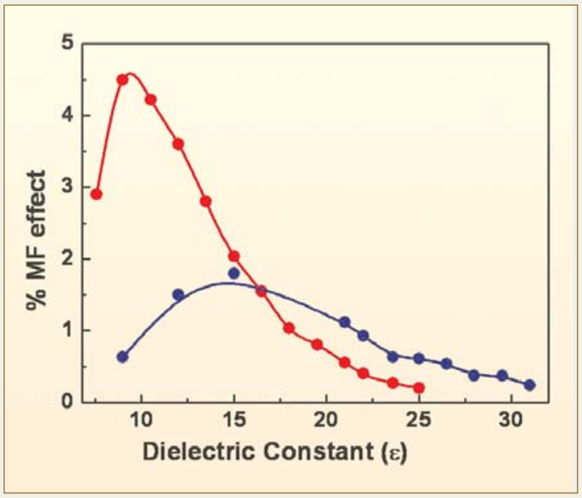

Fig. 1: Plots of percentage MF effect vs solvent dielectric constant for ECZ-DMT (blue) and ECZ -DCB (red)

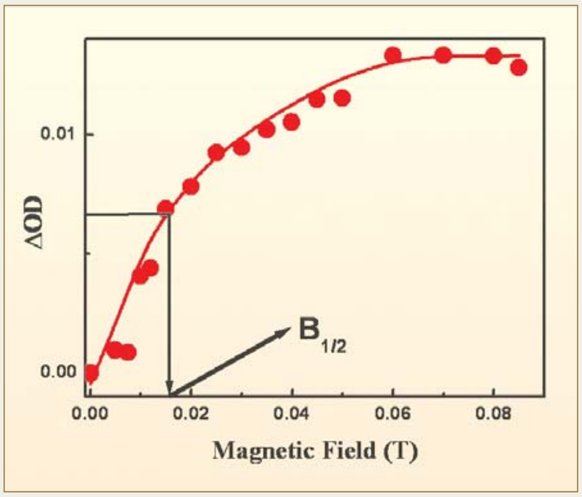

Fig. 2: Variation of ÄOD (increase in transient absorption of DMAN radical cation) with external MF for PZ-DMA

PET in model biomolecules: insights from MF effect

Interaction of a model carcinogen, 4-Nitro Quinoline-N-Oxide (NQO) has been studied with some indole derivatives, the amino acids, Tyrosine (TyrOH) and Tryptophan (TrpH) and the proteins Bovine Serum Albumin (BSA) and lysozyme. Interesting differences have been observed in the behaviour of the indole derivatives depending on their substitution. In acetonitrile medium, PET is accompanied by subsequent proton transfer from the indoles. However, in protic medium protonation from the surrounding medium is the dominating reaction following PET. Similar behaviour is observed in the case of the amino acids and the proteins. Surprisingly, 4NQO showed a preferential interaction with the TrpH residues of the proteins, although quenching rate constants of triplet 4NQO by TrpH and TyrOH are similar. This indicates that in a protein environment, the 4NQO molecule has an affinity for the TrpH residues or alternately, 4NQO is capable of destroying the native structure of the proteins such that, the TrpH residues become more exposed and hence more susceptible to the attack.

The effect of an external MF on this system has been studied for elucidating the mechanism of the reaction. It is worth fuctioning that an external MF can perturb the free radical concentration in a system and hence has immense significance in the free radical-based biochemical reactions. Indirectly, the MF can act as a co-carcinogen by enhancing the genotoxic potential of the radical carcinogen.[12] In the present cases, the MF effect was observed to be very small. This is attributed to competition between random and geminate proton transfer. When PET is accompanied by geminate proton transfer between the participating radicals, the spin correlation is preserved, hence MF effect can be observed. However, when PET is accompanied by random proton transfer from the medium, the spin correlation is destroyed and hence no MF effect can be observed.[13]

Bimolecular PET kinetics in organized assemblies

One of the most intriguing aspects of Marcus ET theory is the "Marcus inverted region". According to classical Marcus theory for outer-sphere ET reactions, the rate constant, k_{ET}, is given by

$$k_{ET} = \nu \exp\left(-\frac{\left(\Delta G^0 + \lambda\right)^2}{4\lambda k_B T} \right) \qquad (1)$$

where, ν is the frequency of motion in the reactant potential well, ΔG^0 is the free energy change for the ET reaction, k_B is the Boltzman constant, T is the absolute temperature and λ ($= \lambda_s + \lambda_i$), is the total reorganization energy, where λ_s and λ_i are the solvent reorganization energy and the intramolecular reorganization energy, respectively.[1,2] The most interesting feature of this theory is the expected inversion in the ET rates as the exergonicity of the reaction ($-\Delta G^0$) exceeds λ. Although predicted way back in 1956, the inverted region could not be detected for bimolecular ET reactions for a long time, because in these cases, the actual ET rates are masked by diffusion rates. This problem of diffusion can be circumvented by using micellar media, where diffusion of the reactants is largely retarded / prevented and thus the actual ET rates can be monitored.[14] Moreover due to slow solvation dynamics in micelles, the effective solvent reorganization energy (λ_s) will be lower, so the inverted region in the Marcus correlation (k_{et} vs ΔG^0 plot) will be shifted to the lower exergonicity, making it easy to be observed.

We have investigated the bimolecular ET kinetics between some coumarin derivatives and aromatic amines in two organized assemblies, namely, reverse micelles and Small Unilamellar Vesicles (SUVs). In reverse micelles, the coumarin dyes were found to be localized in the heptane-like phase or in the water-like phase. Clear Marcus inversion was observed in the water-like phase (Fig. 3).

However, the inversion was not apparent in the heptane-like phase because sufficient exergonicity could not be attained with the present systems.[15] In SUVs, the coumarin dyes were found to be localized

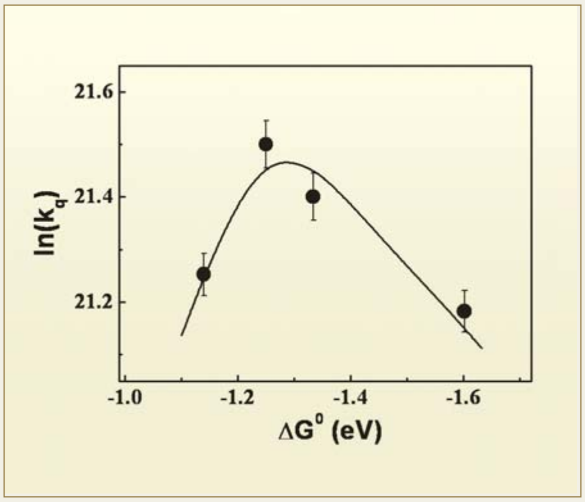

Fig. 3: Marcus correlation curve for coumarin-DMAN system in water-like phase of reverse micelles showing the inversion behaviour

in the lipid bilayer and in this case too, clear Marcus inversion could be observed.[16] These results indicate that irrespective of the nature of the system, confinement of the reactants causes bimolecular ET reactions to occur under non-diffusive condition and this helps in the easy observation of Marcus inversion behaviour, although such a behaviour is normally not observed for bimolecular ET reactions in homogeneous media.

Acknowledgement

I would like to acknowledge my Ph.D. supervisor, Prof. S. Basu, SINP, Kolkata and my mentor Dr. H. Pal, BARC, Mumbai. I am also thankful to Dr. S.K. Sarkar, Head, RPCD, Dr. T. Mukherjee, Director, Chemistry Group, BARC and all members of Molecular Photochemistry Section, RPCD for their constant encouragement and support.

References

1. G. J. Kavarnos, *Fundamentals of Photoinduced Electron Transfer;* VCH Publishers: New York, 1993.
2. Bolton, J. R.; Mataga, N.; McLendon G. L. Eds. *Electron Transfer in Inorganic, Organic and Biological Systems,* American Chemical Society: Washington DC, 1991.
3. U. E. Steiner, T. Ulrich, *Chem. Rev.* 89 (1989) 51.
4. I. R. Gould, N. J. Turro, M. B. Zimmt, *Adv. Phys. Org. Chem.* 20 (1984) 1.
5. K. Bhattacharyya, M. Chowdhury, *Chem. Rev.* 93 (1993) 507.
6. F. D. Lewis, P. E. Correa, *J. Am. Chem. Soc.* 106 (1984) 194.
7. J. Zhou, R. P. Shah, B. R. Findley, C. L. Braun, *J. Phys. Chem.* A 106 (2002) 12.
8. S. Dutta Choudhury, S. Basu, *Chem. Phys. Lett.* 408 (2005) 274-278.
9. S. Dutta Choudhury, S. Basu, *J. Phys. Chem.* A 109 (2005) 8113-8120.
10. H. W. Kruger, M. E. Michel-Beyerle, E. W. Knapp, *Chem. Phys.* 74 (1983) 205.
11. A. Weller, H. Staerk, R. Triechel, Faraday Discss. *Chem. Soc.* 78 (1984) 271.
12. J. C. Scaiano, F. L. Cozens, J. McLean, Photochem. Photobiol. 59 (1994) 585.
13. S. Dutta Choudhury, S. Basu, *J. Phys. Chem.* B 110 (2006) 8850-8855.
14. M. Kumbhakar, S. Nath, T. Mukherjee, H. Pal, *J. Chem. Phys.* 123 (2005) 034705.
15. S. Dutta Choudhury, M. Kumbhakar, S. Nath, S. K. Sarkar, T. Mukherjee, H. Pal, *J. Phys. Chem.* B 111 (2007) 8842-8853.
16. S. Dutta Choudhury, M. Kumbhakar, S. Nath, H. Pal, *J. Chem. Phys.* 127 (2007) 194901.

ABOUT THE AUTHOR

Dr. (Ms.) Sharmistha Dutta Choudhury received her M. Sc. degree in Chemistry with Gold medal from Jadavpur University, Kolkata in 2000. She carried out her Ph.D. work at Saha Institute of Nuclear Physics, Kolkata and obtained her Ph.D. degree from Jadavpur University in 2006. She joined BARC as a Dr. K. S. Krishnan Research Associate in the same year and is presently employed in the Radiation & Photochemistry Division, BARC. Her research interests include photoinduced electron and proton transfer reactions and host guest interactions.

MONTE CARLO DOSIMETRY OF CSA1 AND CSA2 ^{137}CS BRACHYTHERAPY SOURCE MODELS

T. Palani Selvam, S. Sahoo and R. S. Vishwakarma
Radiological Physics & Advisory Division

This paper received the Best Oral Paper Award at the meeting "Updates in Medical Physics", held at AIIMS, New Delhi, on Sep. 8, 2007.

Introduction

Photon emitting brachytherapy sources with average energy higher than 50 keV are being extensively used in the brachytherapy treatment of various tumours such as gynaecological, breast, prostate, head and neck and other soft tissue cancers.[1] The sources used in intracavitary brachytherapy applications include low activity (in units of mCi) stainless steel encapsulated ^{137}Cs tubes. 2D (two dimensional) dose-rate distribution in water is generally used as input data for Radiotherapy Treatment Planning System. The distributions are either in the form of 2D Cartesian look-up table or in the form of dose parameters prepared in accordance with the TG-43U1 protocol[2], recommended by the American Association of Physicists in Medicine (AAPM). There are many published studies devoted to the dosimetry of different commercial models of ^{137}Cs sources, performed in accordance with the TG-43 formalism.[3-10] Most published studies are based on the GEANT4-based Monte Carlo code[4-7,9,10] and Williamson[3] employed the Monte Carlo-based MCPT code.

The Board of Radiation and Isotope Technology (BRIT), India has indigenously developed two ^{137}Cs source models, namely, CSA1 (active length 1.5 cm) and CSA2 (active length 1 cm) for intracavitary brachytherapy applications. About 70 radiotherapy centers in India utilize these sources with a manual afterloader. The nominal activities of the CSA1 and CSA2 sources are 120 mCi and 80 mCi, respectively. The source designs are significantly different from other existing commercial models of ^{137}Cs sources. According to the TG-56 report,[11] a dose-rate dataset specific to each source model must be used. Hence, it is important that accurate dosimetry data are made available for the above-mentioned sources. The objective of the present study is to calculate dosimetry data in accordance with the TG-43U1 formalism[2] for the CSA1 and CSA2 ^{137}Cs sources including 2D (two dimensional) dose rate distribution (in cGy/(h U)) in Cartesian format. For the present work, we have employed the well-established EGSnrcMP code system[12] as it has novel electron transport mechanics.

Materials and Methods

Radioactive sources

Fig. 1 depicts the cross-section views of the CSA1 and CSA2 ^{137}Cs sources and the coordinate system employed in the Monte Carlo simulation. Both the sources have an active radius of 0.065 cm and external radius of 0.15 cm. The active lengths of CSA1 and CSA2 sources are 1.5 cm and 1 cm, respectively. The active core of these sources is composed of borosilicate glass of density 2.7 g cm^{-3}. Source particles are uniformly distributed in this active volume. The active part of the sources is sheathed in a 0.1-mm-thick platinum cylinder. There is an inactive borosilicate glass (spacer) below the active source part for both the source models. For the CSA1 source, the length of this inactive borosilicate glass is 2 mm, whereas for

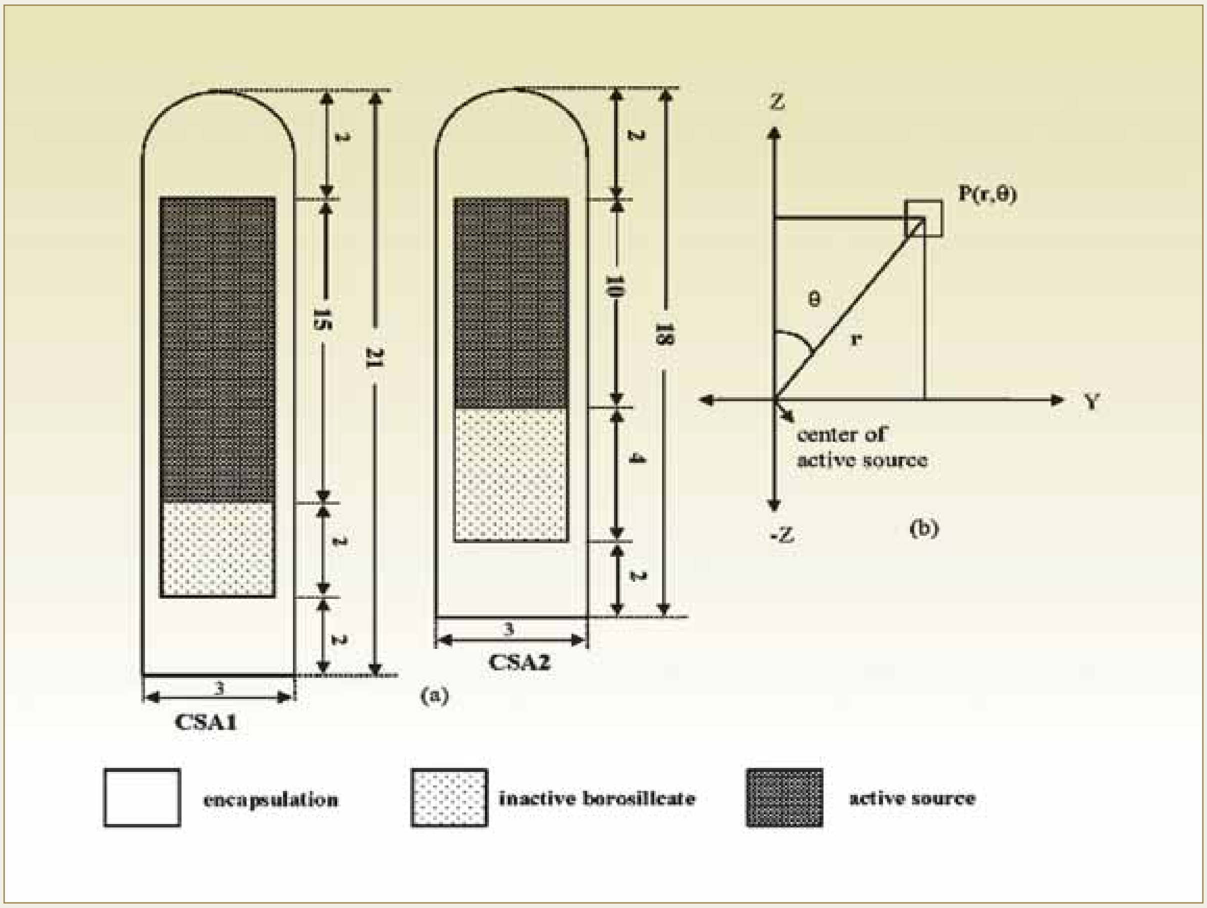

Fig. 1 : (a) Schematic diagram of CSA1 and CSA2 ^{137}Cs sources simulated in the Monte Carlo calculations. The spherical ends are modeled as flat. Dimensions shown are in mm (not to scale). (b) The coordinate system used in the Monte Carlo calculations. The origin is chosen to be at the centre of the active source.

the CSA2 source, it is 4 mm. The sources are further encapsulated in a 0.5 mm thick AISI 316L stainless steel (density is 7.8 g cm^{-3}) capsule, with an outer radius of 1.5 mm, a spherical distal end and a 2 mm thick proximal end. The distance from the distal end of the active source to the tip of the source is 2 mm. The overall lengths of the CSA1 and CSA2 sources are 21 mm and 18 mm, respectively.

Monte Carlo calculations

The PEGS4 dataset needed for Monte Carlo simulations is based on the state-of-the-art XCOM compilations.[13] We set AE=512 keV and AP=1 keV while generating PEGS4 dataset, where the parameters AP and AE are the low-energy thresholds for the production of secondary bremsstrahlung photons and knock-on electrons, respectively. Rayleigh scattering bound Compton scattering, photoelectric absorption and fluorescent emission of characteristic x-rays were all simulated. We used only the 662 keV gamma energy of ^{137}Cs emission (yield of 662 keV: 0.851 photon/disintegration).[14] In the Monte Carlo calculations, we ignored x-rays from ^{137}Ba, because in a previously published study, it was demonstrated that these x-rays did not contribute to the calculated air-kerma strength, S_{K}.[15] The density of water considered for the Monte Carlo simulations is 0.998 gcm^{-3} at 22^{0}C, which is consistent with the TG-43U1 update.

In the Monte Carlo calculations, the distal spherical surface of the CSA1 and CSA2 sources is modeled as flat (therefore distal end has a uniform stainless steel thickness of 2 mm) as the FLURZnrc and DOSRZnrc user-codes[16] cannot handle this aspect of source geometry. We used the EGSnrcMP-based DOSRZnrc user-code for calculating absorbed dose in a 80 cm diameter x 80 cm height water phantom. In the Monte Carlo calculations, absorbed dose is scored in cylindrical shell segments symmetric about the source axis. Absorbed dose is calculated as functions of away, y and axial z distances. The values of photon and electron transport cut-off parameters, PCUT and ECUT, used are 10 keV and 521 keV (10 keV kinetic energy), respectively.

The FLURZnrc code[16] calculates the particle fluence and mean energy in cylindrical regions in a cylindrical RZ geometry. Calculation of air kerma was done in vacuum (using the FLURZnrc code) avoiding the need to correct for photon attenuation and scatter by air. As described by Borg and Rogers[17,18] in their EGS4-based[19] study on calculation of fluence spectrum and S_K of ^{192}Ir sources, the photon fluence spectrum scored (10 keV interval) at y=100 cm was subsequently converted to air-kerma per initial photon, K_{air} (y=100 cm) (in cGy/initial photon) using the mass-energy-absorption coefficient of air.[20] The composition of air considered is as recommended by the TG-43U1 protocol (40% humidity)[2]. The K_{air}(y=100 cm) value was converted to S_K per unit source activity, S_K/A (in cGycm^2/(h Bq) or U/Bq)).

Monte Carlo parameters and statistical uncertainties

All Monte Carlo simulations utilized the PRESTA-II electron-step-length algorithm and EXACT boundary-crossing algorithm. The electron step size parameter is set at ESTEP=0.25. To increase the speed of the calculations, for all simulations, electron range rejection technique was used by setting ESAVE=2 MeV.

Up to 4 x 10^9 primary photon histories are simulated. All simulations were run on a 2.66 GHz PIV machine. The statistical uncertainties on the calculated estimates have a coverage factor $k=1$. For the regions containing all the y values and up to z = ± 2 cm, the statistical uncertainties on the dose and water-kerma values varied between 0.06% and 0.5%. For regions $z > 2$ cm to $z = 5$ cm and up to y= 2 cm, the uncertainties varied between 0.5% and 1.5%. For regions $z > 5$ cm to z=20 cm and up to y=2 cm, the uncertainties varied between 1.5% and 2%. For the rest, the uncertainties varied between 0.2% and 1%. The uncertainty on air-kerma was less than 0.10%. Throughout this paper, the number in parentheses following a value, represents the absolute uncertainty on the last digit of the value with a coverage factor $k=1$.

Results and Discussion

TG-43 parameters

Air-kerma strength and dose rate constant

The calculated value of S_K/A for the CSA1 and CSA2 sources is 7.393(7)x10^{-8} cGycm^2/(h Bq). This suggests that material details along the source axis (inactive borosilicate spacers of different lengths) and active length do not affect the value of S_K/A. The values of dose rate constant, Λ obtained for the CSA1 and CSA2 sources are 0.945(1) cGy/(h U) and 1.023(1) cGy/(h U), respectively.

Radial dose function

Table 1 presents the values of radial dose function, $g_L(r)$ for the CSA1 and CSA2 sources. We utilized the line source-based geometry function, $G_L(r, \theta=\pi/2)$ for calculating $g_L(r)$ The $g_L(r)$ data is fitted to two polynomial functions $g_L(r)$. The $g_L(r)$ For r = 0.2 cm – 0.5 cm, the data are fitted to a 4th order polynomial function and for r = 0.5 cm - 20 cm, to a 5th order polynomial function. The values of coefficients are given at the bottom of Table 1. The data of the CSA1 and CSA2 sources are almost identical. The fitted and actual values of agree to within 0.01 % up to 0.5 cm and agree to within 0.02% - 0.25% for r = 0.5 cm and 20 cm. Up to r = 3 mm, data of the CSA1 and CSA2 sources are significantly different from that of other sources.[4,9,10].

2D anisotropy function

The TG-43U1 protocol[2] permits the use of more complex forms of the geometry function (i.e. "exact" geometry function) for accurately estimating dose at small distances. In our study, the dose data in Cartesian format was tabulated as functions of r and q. Tables II and III present the values of 2D anisotropy function, F(r,θ) for the CSA1 and CSA2 sources for r = 0.2 cm -15 cm, respectively. We utilized the line source-based geometry function for calculating F(r,θ).

Approximating the distal spherical end of the CSA1 and CSA2 sources as flat, introduces systematic uncertainty on the dose results, for regions close to source axis. To obtain an approximate estimate of systematic uncertainty, we calculated the primary component of collision kerma analytically for the cases, spherical end and flat end. A comparison of the results suggests, that the primary component of collision kerma is comparable when $\theta = 0^0$ to 5^0. Depending upon the values of r and for $\theta = 6^0$ to 15^0, the primary component of collision kerma for the case, spherical end was higher by 0.5% to 1.5%, when compared to the case, flat end. In the analytical calculation of collision kerma, the active cylindrical source was divided into N number of discs. Exponential attenuation of 662 keV photons by the source materials (active source, platinum and stainless steel) and water for each of the photon paths in these materials, was included in the analytical calculation.

2D look-up table

The 2D dose rate distributions in water (in cGy/(h U)) around the CSA1 and CSA2 sources in along-away co-ordinates are presented in Tables V & VI respectively. Although the active length of the CSA1 source (1.5 cm) is larger than that of the CSA2 source (1 cm) dose rate at z=1 cm and y=0.2 cm for CSA1 source is higher by a factor of 1.5, when compared to that of the CSA2 source. This is because, the values of line source-based geometry function at these positions are 1.87 cm^{-2} and 1.24 cm^{-2}, respectively, for the CSA1 and CSA2 sources.

Table 1 : Monte Carlo-calculated radial dose function, g_L (r) of the CSA1 and CSA2 ^{137}Cs sources. The line source-based geometry function G_L (r,θ) was used for calculating g_L (r).

Distance	Radial dose function $g_L(r)$	
r(cm)	[a]CS1 (L=1.5cm)	[b]CSA2 (L=1cm)
0.20	0.9836	0.9830
0.25	1.0153	1.0220
0.30	1.0116	1.0169
0.40	1.0043	1.0085
0.50	1.0007	1.0029
0.75	1.0011	1.0014
1	1.0000	1.0001
1.5	0.9977	0.9968
2	0.9944	0.9921
2.5	0.9897	0.9878
3	0.9848	0.9829
3.5	0.9789	0.9777
4	0.9744	0.9721
4.5	0.9673	0.9655
5	0.9621	0.9596
6	0.9484	0.9467
8	0.9173	0.9159
10	0.8830	0.8815
12	0.8449	0.8427
14	0.8026	0.8020
15	0.7827	0.7792
18	0.7137	0.7142
20	0.6686	0.6690

[a] g_L *(r)* of CSA1 has been fitted to a 4th order polynomial between r = 0.2 – 0.5 cm and 5th order polynomial between 0.5 cm and 20 cm. The coefficients obtained were a_0= -0.7231, a_1=20.67543, a_2=-89.78567, a_3=168.52667, a_4=-115.73333 and a_0= 1.00307, a_1= -0.00168, a_2= -0.00175, a_3=1.11609e-04, a_4=-4.83893E-6 and a_5=8.81973E-8, respectively, for r = 0.2 cm to 0.5 cm and r = 0.5 cm to 20 cm.

[b] g_L *(r)* of CSA2 has been fitted to a 4th order polynomial between r = 0.2 – 0.5 cm and 5th order polynomial between 0.5-20 cm. The coefficients obtained were a_0=-1.1769, a_1=26.25577, a_2=-114.48067, a_3=215.74333, a_4=-148.73333 and a_0=1.0059, a_1=-0.00509, a_2=-9.1533e-04, a_3=2.01673e-05, a_4= -2.95412e-07 and a_5= 5.31396e-09, respectively, for r = 0.2 cm to 0.5 cm and r = 0.5 cm to 20 cm.

Uncertainty

As recommended in the TG-43U1 report[2], the uncertainties of the final dose rate values have been evaluated from contributions, the type A or statistical uncertainty and the type B or systematic uncertainty. The dose rate distribution of ^{137}Cs sources in water gives statistical uncertainties of less than 2% for the points at or close to the longitudinal seed axis and less than 0.5% for the other points. The statistical uncertainty on the simulation of the S_K/A is less than 0.1%.

The type B uncertainty is quite complex to evaluate. This uncertainty is composed of various factors: (a) the uncertainty due to volume-averaging artifacts,

Table 2 : Monte Carlo-calculated 2D anisotropy function F(r,θ) for the CSA1 ^{137}Cs source. The line source-based geometry function $G_L(r,\theta)$ was used for calculating F(r,θ).

θ (deg)	**radial distance, r (cm)**													
	0.20	**0.5**	**0.75**	**1**	**1.5**	**2**	**3**	**4**	**5**	**6**	**7**	**8**	**10**	**15**
0	-	-	-	0.952	0.928	0.919	0.906	0.901	0.893	0.898	0.901	0.899	0.909	0.907
1	-	-	-	0.953	0.931	0.924	0.911	0.902	0.902	0.910	0.896	0.906	0.897	0.899
3	-	-	-	0.994	0.919	0.883	0.866	0.852	0.857	0.866	0.861	0.861	0.883	0.894
5	-	-	-	0.912	0.866	0.850	0.838	0.833	0.838	0.844	0.852	0.861	0.871	0.892
7	-	-	-	0.896	0.856	0.845	0.840	0.841	0.839	0.848	0.852	0.859	0.874	0.896
10	-	-	-	0.895	0.869	0.861	0.854	0.857	0.863	0.872	0.879	0.882	0.886	0.905
12	-	-	-	0.918	0.883	0.875	0.873	0.874	0.884	0.889	0.889	0.897	0.899	0.918
15	-	-	0.977	0.943	0.908	0.901	0.900	0.898	0.901	0.907	0.911	0.914	0.916	0.936
20	-	-	1.006	0.963	0.944	0.936	0.926	0.930	0.928	0.932	0.949	0.932	0.938	0.948
25	-	0.998	0.996	0.976	0.963	0.957	0.948	0.944	0.948	0.953	0.947	0.951	0.957	0.954
30	-	1.017	0.995	0.987	0.970	0.965	0.962	0.956	0.960	0.960	0.961	0.963	0.965	0.962
35	-	1.014	0.994	0.986	0.980	0.976	0.972	0.972	0.972	0.973	0.971	0.978	0.975	0.976
40	-	1.008	0.993	0.990	0.990	0.984	0.980	0.977	0.977	0.977	0.979	0.978	0.987	0.985
45	-	1.002	0.994	0.993	0.989	0.990	0.986	0.986	0.987	0.989	0.986	0.986	0.989	0.986
50	-	0.999	0.992	0.994	0.990	0.990	0.990	0.987	0.991	0.990	0.990	0.990	0.991	0.998
55	0.889	0.998	0.993	0.995	0.994	0.994	0.992	0.991	0.992	0.994	0.990	0.993	0.995	0.996
60	0.926	0.999	0.995	0.995	0.995	0.995	0.992	0.990	0.993	1.000	0.992	1.001	1.000	0.996
65	0.954	0.999	0.997	0.999	1.004	0.995	0.995	0.992	0.995	0.997	0.997	0.998	1.006	0.997
70	0.980	1.001	1.010	0.998	0.996	0.999	0.996	0.994	0.994	1.000	0.998	1.002	1.001	0.998
80	0.997	1.000	0.997	0.999	1.000	1.001	1.000	0.997	0.999	1.003	1.000	1.006	1.004	1.004
90	1	1	1	1	1	1	1	1	1	1	1	1	1	1
100	0.995	0.999	0.997	0.999	1.000	1.000	1.001	0.997	0.999	1.000	0.999	1.001	1.003	1.005
110	0.974	0.999	0.997	0.998	0.999	0.998	0.998	0.997	0.998	0.999	0.996	0.999	1.002	0.999
115	0.954	0.998	0.995	0.997	0.997	0.997	0.996	0.995	0.998	0.998	0.999	0.999	1.000	1.002
120	0.931	0.999	0.994	0.996	0.995	0.996	0.996	0.992	0.994	0.997	0.996	1.004	0.997	1.003
125	0.888	0.999	0.995	0.994	0.994	0.992	0.991	0.990	0.994	0.996	0.993	0.997	0.996	0.998
130	-	1.000	0.994	0.994	0.991	0.992	0.990	0.989	0.990	0.993	0.987	0.993	0.992	0.993
135	-	1.004	0.992	0.992	0.990	0.988	0.986	0.986	0.986	0.989	0.988	0.987	0.990	0.988
140	-	1.006	0.991	0.989	0.986	0.987	0.983	0.981	0.985	0.984	0.978	0.981	0.984	0.988
145	-	1.012	0.990	0.985	0.979	0.976	0.977	0.974	0.975	0.975	0.971	0.976	0.978	0.982
150	-	1.016	0.994	0.983	0.973	0.970	0.967	0.964	0.967	0.969	0.965	0.973	0.971	0.978
155	-	0.998	0.994	0.974	0.962	0.958	0.957	0.959	0.958	0.955	0.952	0.959	0.961	0.962
160	-	-	1.009	0.965	0.948	0.940	0.936	0.930	0.939	0.937	0.939	0.940	0.943	0.954
165	-	-	0.973	0.946	0.921	0.909	0.903	0.900	0.906	0.905	0.908	0.914	0.915	0.930
168	-	-	-	0.928	0.898	0.880	0.873	0.872	0.880	0.888	0.888	0.898	0.898	0.919
170	-	-	-	0.919	0.865	0.852	0.852	0.850	0.862	0.873	0.870	0.873	0.885	0.908
173	-	-	-	-	0.837	0.822	0.823	0.823	0.838	0.839	0.844	0.854	0.862	0.891
175	-	-	-	-	0.858	0.832	0.823	0.820	0.832	0.835	0.843	0.851	0.867	0.884
177	-	-	-	-	0.898	0.863	0.842	0.835	0.850	0.856	0.855	0.864	0.865	0.881
179	-	-	-	-	0.921	0.897	0.886	0.921	0.885	0.882	0.875	0.887	0.902	0.907
180	-	-	-	-	0.911	0.899	0.887	0.887	0.895	0.904	0.897	0.894	0.899	0.917

Table 3 : Monte Carlo-calculated 2D anisotropy function F(r,θ) for the CSA2 ^{137}Cs source. The line source-based geometry function $G_L(r,\theta)$ was used for calculating F(r,θ).

θ (deg)	radial distance, r (cm)													
	0.20	0.5	0.75	1	1.5	2	3	4	5	6	7	8	10	15
0	-		-	0.947	0.939	0.925	0.938	0.925	0.918	0.928	0.919	0.915	0.917	0.934
1	-	-	-	0.951	0.936	0.931	0.939	0.923	0.921	0.927	0.944	0.915	0.917	0.931
3	-	-	-	0.947	0.929	0.908	0.898	0.892	0.891	0.895	0.900	0.894	0.897	0.922
5	-	-	-	0.927	0.894	0.882	0.881	0.883	0.879	0.881	0.890	0.898	0.895	0.905
7	-	-	-	0.904	0.882	0.874	0.871	0.870	0.877	0.879	0.878	0.886	0.892	0.912
10	-	-	-	0.897	0.875	0.876	0.876	0.875	0.881	0.887	0.892	0.892	0.902	0.922
12	-	-	-	0.888	0.880	0.881	0.884	0.884	0.887	0.895	0.896	0.902	0.908	0.919
15	-	-	0.925	0.908	0.906	0.901	0.902	0.907	0.907	0.913	0.912	0.920	0.926	0.935
20	-	-	0.956	0.941	0.929	0.927	0.928	0.936	0.934	0.934	0.933	0.935	0.939	0.949
25	-	0.987	0.969	0.961	0.949	0.948	0.946	0.948	0.948	0.947	0.947	0.951	0.952	0.953
30	-	1.010	0.979	0.968	0.964	0.964	0.961	0.958	0.962	0.959	0.958	0.959	0.965	0.967
35	-	1.005	0.988	0.979	0.975	0.974	0.974	0.970	0.972	0.973	0.969	0.970	0.972	0.989
40	-	1.001	0.989	0.984	0.981	0.984	0.979	0.978	0.978	0.977	0.977	0.980	0.984	0.983
45	-	0.997	0.994	0.993	0.989	0.988	0.987	0.987	0.985	0.987	0.983	0.982	0.988	0.986
50	-	0.991	0.994	0.993	0.987	0.989	0.990	0.991	0.991	0.992	0.990	0.987	0.990	0.991
55	0.892	0.992	0.996	0.994	0.993	0.993	0.993	0.991	0.992	0.994	0.989	0.990	0.995	0.997
60	0.930	0.992	0.997	0.995	0.994	0.993	0.996	0.993	0.994	0.991	0.991	0.995	0.998	0.990
65	0.957	0.992	0.999	0.998	0.997	0.995	0.998	0.998	0.999	1.006	0.993	0.996	1.000	0.993
70	0.977	0.992	0.999	0.998	0.997	0.997	0.998	0.996	0.997	0.998	0.995	1.000	0.997	0.995
80	0.996	0.995	1.000	1.001	1.000	1.000	1.003	0.999	1.002	1.002	0.997	1.001	1.003	0.998
90	1	1	1	1	1	1	1	1	1	1	1	1	1	1
100	0.996	0.993	1.002	1.000	1.000	1.000	1.002	1.001	1.000	0.999	0.998	0.998	1.001	0.998
110	0.977	0.994	0.999	0.998	0.997	0.998	1.001	1.000	1.002	0.998	0.998	0.996	1.003	0.995
115	0.960	0.992	0.998	0.996	0.995	0.997	0.999	0.997	1.002	0.999	0.999	1.002	1.003	0.999
120	0.929	0.994	0.997	0.995	0.995	0.994	0.996	0.994	0.994	0.995	0.995	1.000	0.997	0.995
125	0.889	0.991	0.996	0.994	0.993	0.995	0.996	0.992	0.995	0.995	0.992	0.995	0.997	0.993
130	-	0.992	0.994	0.991	0.991	0.992	0.991	0.990	0.992	0.991	0.989	0.989	0.991	0.992
135	-	0.995	0.991	0.989	0.987	0.987	0.987	0.988	0.988	0.990	0.989	0.987	0.987	0.985
140	-	0.998	0.989	0.984	0.983	0.984	0.984	0.985	0.987	0.987	0.982	1.001	0.983	0.980
145	-	1.004	0.985	0.979	0.977	0.978	0.980	0.976	0.977	0.977	0.973	0.974	0.978	0.976
150	-	1.008	0.980	0.973	0.970	0.971	0.974	0.973	0.974	0.970	0.966	0.972	0.969	0.975
155	-	0.987	0.971	0.962	0.957	0.955	0.956	0.959	0.960	0.957	0.953	0.957	0.961	0.962
160	-	-	0.960	0.953	0.940	0.937	0.937	0.938	0.941	0.966	0.941	0.941	0.946	0.946
165	-	-	0.939	0.925	0.912	0.911	0.913	0.905	0.916	0.913	0.916	0.916	0.920	0.929
168	-	-	0.923	0.907	0.887	0.881	0.878	0.883	0.887	0.898	0.894	0.899	0.907	0.922
170	-	-	-	0.885	0.860	0.853	0.859	0.862	0.870	0.880	0.878	0.877	0.892	0.914
173	-	-	-	-	0.846	0.836	0.839	0.843	0.852	0.859	0.864	0.866	0.880	0.902
175	-	-	-	-	0.875	0.866	0.852	0.847	0.863	0.860	0.868	0.867	0.876	0.905
177	-	-	-	-	0.892	0.870	0.864	0.860	0.871	0.873	0.879	0.882	0.880	0.894
179	-	-	-	-	0.900	0.888	0.922	0.897	0.896	0.887	0.893	0.890	0.902	0.899
180	-	-	-	-	0.899	0.890	0.891	0.886	0.898	0.901	0.908	0.892	0.903	0.906

(b) the uncertainty due to the energy spectrum, (c) the uncertainty due to photon cross section dataset, and (d) the uncertainty due to the geometric design of the source. The uncertainty on volume averaging is negligible. The uncertainty on the ^{137}Cs energy spectrum is negligible. Hubbell[21] assigns an uncertainty of 2% on photon cross section dataset. We assign a global uncertainty of 0.8% on cross section. We have not evaluated the contribution of the uncertainty in the internal component mobility of the source. We assign a 1% uncertainty on the dose results, for the polar angles $\theta=6^0$ to 15^0 as the distal spherical end of the source was modeled as flat. Thus, the combined type A and type B uncertainty is about 1% for all the points, except near longitudinal axis points $\theta=0^0$ to 5^0 where the combined uncertainty is about 2.2%.

Table 4 : Away and along 2D dose rate distribution in water (in cGy/(h U)) for the CSA1 ^{137}Cs source.

Distance along z (cm)	Distance away. y (cm)														
	0	0.2	0.5	0.75	1	2	2.5	3	4	5	6	8	10	15	20
20	0.00171	0.00173	0.00165	0.00166	0.00164	0.00163	0.00163	0.00161	0.0016	0.00158	0.00154	0.00143	0.00130	0.00095	0.00065
15	0.00347	0.00340	0.00332	0.00336	0.00339	0.00333	0.00336	0.00333	0.00328	0.00318	0.00303	0.00272	0.00235	0.00154	0.00096
10	0.00896	0.00860	0.00851	0.00843	0.00844	0.00841	0.00836	0.00823	0.00785	0.00730	0.00670	0.00546	0.00434	0.00240	0.00134
8	0.0143	0.0141	0.0138	0.0135	0.0134	0.0136	0.0133	0.0130	0.0120	0.0108	0.00953	0.00729	0.00551	0.00278	0.00149
6	0.0269	0.0255	0.0249	0.0247	0.0248	0.0243	0.0234	0.0222	0.0193	0.0164	0.0138	0.00966	0.00685	0.00318	0.00163
5	0.0387	0.0371	0.0361	0.0364	0.0364	0.0347	0.0326	0.0301	0.0249	0.0203	0.0165	0.0110	0.00757	0.00336	0.00169
4	0.0631	0.0596	0.0573	0.0580	0.0584	0.0518	0.0471	0.0419	0.0325	0.0252	0.0196	0.0124	0.00820	0.00351	0.00174
3	0.119	0.109	0.106	0.107	0.105	0.0826	0.0700	0.0591	0.0421	0.0306	0.0229	0.0137	0.00881	0.00365	0.00178
2.5	0.175	0.162	0.159	0.157	0.150	0.106	0.0861	0.0704	0.0477	0.0335	0.0244	0.0142	0.00909	0.00369	0.00179
2	0.293	0.265	0.262	0.250	0.228	0.137	0.106	0.0826	0.0530	0.0361	0.0259	0.0148	0.00930	0.00375	0.00180
1.5	0.604	0.589	0.543	0.463	0.380	0.179	0.129	0.0966	0.0584	0.0387	0.0272	0.0152	0.00949	0.00377	0.00182
1	—	1.88	1.19	0.812	0.586	0.216	0.148	0.107	0.0623	0.0403	0.0281	0.0154	0.00959	0.00382	0.00183
0.75	—	5.12	1.82	1.077	0.717	0.234	0.157	0.111	0.0638	0.0412	0.0283	0.0156	0.00969	0.00381	0.00182
0.5	—	8.36	2.43	1.321	0.837	0.249	0.164	0.115	0.0655	0.0417	0.0287	0.0157	0.00969	0.00378	0.00183
0.25	—	9.26	2.78	1.485	0.917	0.258	0.168	0.117	0.0660	0.0420	0.0288	0.0157	0.00971	0.00382	0.00184
0.15	—	9.39	2.85	1.521	0.936	0.261	0.169	0.118	0.0661	0.0420	0.0288	0.0157	0.00969	0.00382	0.00183
0	—	9.45	2.89	1.539	0.945	0.262	0.169	0.118	0.0663	0.0421	0.0289	0.0157	0.00970	0.00383	0.00184
0.15	—	9.39	2.85	1.521	0.936	0.261	0.169	0.118	0.0661	0.0420	0.0288	0.0157	0.00969	0.00382	0.00183
-0.25	—	9.26	2.78	1.485	0.917	0.258	0.168	0.117	0.0660	0.0420	0.0288	0.0157	0.00971	0.00382	0.00184
-0.5	—	8.36	2.43	1.320	0.837	0.249	0.164	0.115	0.0655	0.0417	0.0287	0.0157	0.00969	0.00378	0.00183
-0.75	—	5.11	1.82	1.076	0.717	0.234	0.157	0.111	0.0638	0.0412	0.0283	0.0156	0.00968	0.00381	0.00182
-1	—	1.94	1.19	0.813	0.586	0.215	0.148	0.107	0.0623	0.0403	0.0281	0.0154	0.00959	0.00382	0.00183
-1.5	0.595	0.578	0.547	0.464	0.381	0.179	0.129	0.0967	0.0584	0.0387	0.0272	0.0152	0.00949	0.00377	0.00182
-2	0.288	0.260	0.263	0.252	0.229	0.137	0.106	0.0826	0.0530	0.0361	0.0259	0.0148	0.00931	0.00375	0.00180
-2.5	0.172	0.159	0.158	0.158	0.151	0.106	0.0862	0.0704	0.0477	0.0335	0.0244	0.0142	0.00910	0.00369	0.00179
-3	0.115	0.107	0.105	0.107	0.106	0.0828	0.0701	0.0592	0.0421	0.0306	0.0229	0.0137	0.00881	0.00365	0.00178
-4	0.0618	0.0586	0.0562	0.0576	0.0583	0.0520	0.0472	0.0420	0.0325	0.0252	0.0196	0.0124	0.00820	0.00351	0.00174
-5	0.0386	0.0366	0.0354	0.0358	0.0362	0.0348	0.0327	0.0301	0.0250	0.0203	0.0165	0.0110	0.00758	0.00335	0.00169
-6	0.0264	0.0252	0.0245	0.0243	0.0246	0.0244	0.0235	0.0223	0.0194	0.0164	0.0138	0.00966	0.00685	0.00318	0.00163
-8	0.0142	0.0138	0.0137	0.0133	0.0134	0.0135	0.0133	0.0130	0.0120	0.0108	0.00958	0.00730	0.00551	0.00279	0.00149
-10	0.00886	0.00853	0.00843	0.00833	0.00831	0.00839	0.00833	0.00824	0.00786	0.00733	0.00671	0.00547	0.00435	0.00240	0.00134
-15	0.00347	0.00352	0.00331	0.00338	0.00333	0.00332	0.00332	0.00330	0.00328	0.00318	0.00303	0.00273	0.00236	0.00155	0.00096
-20	0.00168	0.00169	0.00165	0.00166	0.00164	0.00162	0.00162	0.00161	0.00159	0.00157	0.00154	0.00144	0.00130	0.00095	0.00065

For $\theta = 6^0$ to 15^0, the combined uncertainty is about 2.4%.

Conclusions

The dose rate distribution in water for the indigenously developed CSA1 and CSA2 ^{137}Cs source models has been calculated using the EGSnrcMP-based Monte Carlo code system. The dose rate distributions are presented in AAPM TG-43U1 recommended parameters and in a 2D Cartesian look-up table. These dose rate values can be used as input data for treatment planning, for the indigenous development of treatment planning software.

Acknowledgements

The authors are grateful to Mr. H. S. Kushwaha, Director, Health Safety & Environment Group, BARC, Dr. Y. S. Mayya, Head, Radiological Physics & Advisory Division, BARC and Dr. G. Chourasiya, BARC for their constant encouragement throughout the project. The authors are also grateful to the Board of Radiation and Isotope Technology, India and the Radiopharmaceuticals Division, BARC for providing geometric details of the sources.

Table 5 : Away and along 2D dose rate distribution in water (in cGy/(h U)) for the CSA2 ^{137}Cs source.

Distance along z (cm)	Distance away. y (cm)														
	0	0.2	0.5	0.75	1	2	2.5	3	4	5	6	8	10	15	20
20	0.00172	0.00169	0.00167	0.00166	0.00170	0.00164	0.00166	0.00161	0.00160	0.00158	0.00153	0.00144	0.00130	0.00095	0.00065
15	0.00354	0.00339	0.00348	0.00345	0.00352	0.00343	0.00338	0.00334	0.00329	0.00318	0.00304	0.00272	0.00236	0.00154	0.00097
10	0.00896	0.00871	0.00881	0.00865	0.00868	0.00844	0.00834	0.00820	0.00783	0.00731	0.00668	0.00548	0.00434	0.00240	0.00134
8	0.0148	0.0144	0.0144	0.0140	0.0138	0.0137	0.0133	0.0130	0.0120	0.0108	0.0095	0.00728	0.00550	0.00278	0.00149
6	0.0271	0.0262	0.0256	0.0251	0.0252	0.0242	0.0233	0.0221	0.0192	0.0163	0.0137	0.00962	0.00685	0.00317	0.00163
5	0.0397	0.0382	0.0374	0.0368	0.0365	0.0344	0.0324	0.0300	0.0249	0.0203	0.0164	0.0110	0.00757	0.00336	0.00169
4	0.0633	0.0606	0.0580	0.0581	0.0577	0.0514	0.0465	0.0415	0.0323	0.0251	0.0196	0.0124	0.00820	0.00351	0.00175
3	0.115	0.110	0.105	0.104	0.102	0.0813	0.0695	0.0587	0.0421	0.0307	0.0229	0.0137	0.00884	0.00364	0.00178
2.5	0.169	0.161	0.153	0.150	0.144	0.104	0.0855	0.0699	0.0474	0.0335	0.0245	0.0143	0.00907	0.00368	0.00179
2	0.279	0.253	0.244	0.234	0.216	0.135	0.105	0.0824	0.0531	0.0362	0.0259	0.0148	0.00929	0.00376	0.00180
1.5	0.514	0.509	0.475	0.423	0.360	0.178	0.129	0.0967	0.0588	0.0388	0.0273	0.0152	0.00948	0.00378	0.00182
1	1.39	1.23	0.981	0.747	0.563	0.217	0.149	0.107	0.0627	0.0405	0.0281	0.0155	0.00965	0.00381	0.00182
0.75	3.38	2.63	1.571	1.030	0.712	0.237	0.158	0.112	0.0646	0.0414	0.0283	0.0156	0.00966	0.00380	0.00184
0.5	—	7.40	2.432	1.359	0.864	0.253	0.166	0.116	0.0654	0.0419	0.0289	0.0157	0.00971	0.00383	0.00183
0.25	—	12.07	3.200	1.631	0.980	0.265	0.171	0.119	0.0664	0.0421	0.0289	0.0158	0.00970	0.00382	0.00184
0.15	—	12.70	3.378	1.697	1.009	0.267	0.172	0.119	0.0666	0.0422	0.0289	0.0157	0.00970	0.00383	0.00183
0	—	12.99	3.478	1.733	1.024	0.268	0.172	0.119	0.0667	0.0422	0.0290	0.0158	0.00972	0.00382	0.00185
0.15	—	12.70	3.377	1.697	1.009	0.267	0.172	0.119	0.0666	0.0422	0.0289	0.0157	0.00970	0.00383	0.00183
-0.25	—	12.07	3.199	1.631	0.980	0.265	0.171	0.119	0.0664	0.0421	0.0289	0.0158	0.00970	0.00382	0.00184
-0.5	—	7.39	2.430	1.359	0.864	0.253	0.166	0.116	0.0654	0.0419	0.0289	0.0157	0.00971	0.00383	0.00183
-0.75	—	2.72	1.573	1.030	0.712	0.237	0.158	0.112	0.0646	0.0414	0.0283	0.0156	0.00965	0.00379	0.00184
-1	—	1.26	0.986	0.748	0.564	0.217	0.149	0.108	0.0627	0.0405	0.0281	0.0155	0.00965	0.00380	0.00182
-1.5	0.496	0.488	0.481	0.425	0.362	0.178	0.129	0.0967	0.0588	0.0389	0.0273	0.0152	0.00949	0.00378	0.00182
-2	0.261	0.244	0.245	0.236	0.217	0.135	0.105	0.0825	0.0532	0.0362	0.0259	0.0148	0.00929	0.00375	0.00181
-2.5	0.162	0.156	0.152	0.151	0.145	0.105	0.0856	0.0699	0.0475	0.0335	0.0245	0.0143	0.00908	0.00368	0.00181
-3	0.110	0.106	0.102	0.104	0.102	0.0817	0.0697	0.0589	0.0421	0.0307	0.0229	0.0137	0.00885	0.00365	0.00178
-4	0.0605	0.0588	0.0560	0.0570	0.0575	0.0517	0.0467	0.0416	0.0323	0.0251	0.0196	0.0124	0.00821	0.00351	0.00175
-5	0.0381	0.0370	0.0362	0.0358	0.0361	0.0345	0.0325	0.0301	0.0250	0.0203	0.0164	0.0110	0.00758	0.00336	0.00169
-6	0.0264	0.0255	0.0250	0.0243	0.0247	0.0243	0.0234	0.0222	0.0193	0.0164	0.0137	0.00963	0.00686	0.00317	0.00163
-8	0.0142	0.0139	0.0139	0.0136	0.0134	0.0136	0.0133	0.0130	0.0120	0.0108	0.00952	0.00729	0.00551	0.00279	0.00152
-10	0.00884	0.00859	0.00855	0.00848	0.00844	0.00837	0.00834	0.00821	0.00786	0.00735	0.00671	0.00549	0.00435	0.00240	0.00134
-15	0.00348	0.00346	0.00342	0.00342	0.00342	0.00336	0.00334	0.00332	0.00329	0.00318	0.00304	0.00272	0.00236	0.00154	0.00097
-20	0.00167	0.00166	0.00163	0.00167	0.00168	0.00163	0.00164	0.00161	0.00159	0.00158	0.00154	0.00144	0.00130	0.00096	0.00065

References

1. Z. Li, R. K. Das, L. A. DeWerd, G. S. Ibbott, A. S. Meigooni, J. Pérez-Calatayud, M. J. Rivard, R. S. Sloboda, and J. F. Williamson, "Dosimetric prerequisites for routine clinical use of photon emitting brachytherapy sources with average energy higher than 50 keV," *Med. Phys.* **34**, 37-40 (2007).
2. M. J. Rivard, B. M. Coursey, L. A. DeWerd, W. F. Hanson, M.S. Huq, G. S. Ibbot, M. G. Mitch, R. Nath, and J. F. Williamson, "Update of AAPM Task Group No. 43 Report: A revised AAPM protocol for brachytherapy dose calculations," *Med. Phys.* **31**, 633–674 (2004).
3. Jeffrey F. Williamson "Monte Carlo-based dose-rate tables for the Amersham CDCS.J and 3M model 6500 ^{137}Cs tubes", *Int. J. Radiat. Oncol. Biol. Phys.* **41**, 959-970 (1998).
4. E. Casal, F. Ballester, J. L. Lluch, J. Pérez-Calatayud, and F. Lliso, " Monte Carlo Calculations of dose rate distributions around the Amersham CDCS-M-type ^{137}Cs source," *Med. Phys.* **27**, 132-140 (2000).
5. F. Ballester, J.L. Lluch, Y. Limami, M.A. Serrano, E. Casal, J. Pérez-Calatayud, and F. Lliso, "A Monte

Carlo investigation of the dosimetric characteristics of CSM11 ^{137}Cs sources from CIS," *Med. Phys.* **27**, 2182–2189 (2000).

6. J. Pérez-Calatayud, F. Ballester, M. A. Serrano-Andrés, J. L. Lluch, V. Puchades, Y. Limami, and E. Casal "Dosimetric characteristics of the CDC-type miniature cylindrical ^{137}Cs brachytherapy sources, " *Med. Phys.* **29**, 538-543 (2002).
7. ^{7}J. Pérez-Calatayud, D. Granero, F. Ballester, V. Puchades, and E. Casal, "Monte Carlo dosimetric characterization of the ^{137}Cs selectron/ LDR source: Evaluation of applicator attenuation and superposition approximation effects," *Med. Phys.* **31**, 493–499 (2004).
8. Lizhong Liu, Satish C. Prasad, and Daniel A. Bassano, "Determination of ^{137}Cs dosimetry parameters according to AAPM TG-43 formalism," *Med. Phys.* **31**, 477-483 (2004).
9. J. Pérez-Calatayud, D. Granero, E. Casal, and F. Ballester and V. Puchades, "Monte Carlo and experimental derivation of TG-43 dosimetric parameters for CSM-type Cs-137 sources," *Med. Phys.* **32**, 28-36 (2005).
10. J. Pérez-Calatayud, D. Granero, F. Ballester, E. Casal, R. Cases, and S. Agramunt, "Technical note: Monte Carlo derivation of TG43 dosimetric parameters for radiation therapy resources and 3M ^{137}Cs sources," *Med. Phys.* **32**, 2464-2470 (2005).
11. R. Nath, L. L. Anderson, K. J. A. Meli, A. J. Olch, J. A. Stitt, and J. F. Williamson, ''Code of practice for brachytherapy physics: Report of the AAPM Radiation Therapy Committee Task Group No. 56,'' *Med. Phys.* **24**, 1557–1598 (1997).
12. I. Kawrakow and D. W. O. Rogers, "The EGSnrc Code System: Monte Carlo simulation of electron and photon transport," Technical Report No. PIRS–701, National Research Council of Canada, Ottawa, Canada, 2006.
13. M.J. Berger and J. H. Hubbell, 1987. XCOM, Photon cross sections on a personal computer, Report No. NBSIR87–3597, NIST, Gaithersburg, MD 20899.
14. National Nuclear Data Center. Nuclear data from NuDat, a web-based database maintained by the National Nuclear Data Center, Brookhaven National Laboratory, Upton, NY, USA; http://www.nndc.bnl.gov/nudat2/. Last access on June 15, 2009.
15. T. Palani Selvam, K. N. Govinda Rajan, P. S. Nagarajan, B. C. Bhatt, and P. Sethulakshmi, "Room scatter studies in the air kerma strength standardization of the Amersham CDCS-J-type ^{137}Cs source: a Monte Carlo study," *Phys. Med. Biol.* **47**, N113-N119 (2003).
16. D. W. O. Rogers, I. Kawrakow, J. P. Seuntjens, and B. R. B. Walters, "NRC User Codes for EGSnrc," Technical Report No. PIRS-702, National Research Council of Canada, Ottawa, Canada, 2006 (see http://www.irs.inms.nrc.ca/inms/irs/EGSnrc/EGSnrc.html). Last access on June 15, 2009.
17. Jette Borg and D. W. O. Rogers, "Spectra and air-kerma strength for encapsulated ^{192}Ir sources," *Med. Phys.* **26**, 2441–2444 (1999).
18. J. Borg and D. W. O. Rogers, Monte Carlo Calculations of Photon Spectra in Air from ^{192}Ir Sources, NRC Report PIRS-629r (see http://www.irs.inms.nrc.ca/inms/irs/papers/PIRS629r/pirs629r.html), 1998. Last access on June 15, 2009.
19. W. R. Nelson, H. Hirayama, and D. W. O. Rogers, The EGS4 Code System, Report SLAC-265, Stanford Linear Accelerator Center, Stanford, California, 1985.
20. J. H. Hubbell and S. M. Seltzer, ''Tables of x-ray mass attenuation coefficients and mass energy-absorption coefficients 1 keV to 20 MeV for elements $Z=1$ to 92 and 48 additional substances of dosimetric interest,'' NISTIR 5632 (1995).
21. J. H. Hubbell, "Review of photon interaction cross sections data in the medical and biological context," *Phys. Med. Biol.* **44**, R1–R22 (1999).

ABOUT THE AUTHORS

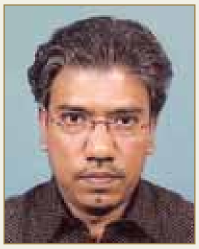

Dr. T. Palani Selvam is a Medical Physicist working in the Radiological Physics & Advisory Division of BARC. His research interest is related to radiotherapy research applications including radiotherapy treatment planning using analytical and Monte Carlo techniques. He was a Post Doctoral fellow at the Carleton Laboratory for Radiotherapy, Carleton University, Ottawa, Canada during 2004-2006. He is a faculty member for one-year Dip. R.P. Course, conducted by the Division under the aegis of HBNI.

Mr. Sridhar Sahoo is a Medical Physicist working in the Radiological Physics & Advisory Division of BARC. He is involved in R&D activities in the field of Medical Physics such as dosimetry of radiotherapy sources using Monte Carlo methods, indigenous development of radiotherapy treatment planning system and radiation protection in medical application of radioisotopes. He is a faculty member for various radiation safety related short-term programmes. He is also a faculty member for one-year Dip.R.P. Course, conducted by the Division under the aegis of HBNI.

Mr. R. S. Vishwakarma is a Medical Physicist working in the Radiological Physics & Advisory Division of BARC. He is involved in R&D activities in the field of Medical Physics such as dosimetry of radiotherapy sources using Monte Carlo methods, indigenous development of radiotherapy treatment planning system and radiation protection in medical application of radioisotopes. He is a faculty member for various radiation safety related short-term programmes. He is also a faculty member for one-year Dip.R.P. Course, conducted by the Division under the aegis of HBNI.

ROLE OF DILUENT ON STRONTIUM TRANSPORT ACROSS SUPPORTED LIQUID MEMBRANE USING DTBCH18C6 AS CARRIER

D.R. Raut, P.K. Mohapatra and V.K. Manchanda
Radiochemistry Division

This paper was given the Best Oral Presentation Award (Analytical & Environmental Chemistry Section) at the 26th Indian Council of Chemists' Annual Conference, held at H.S. Gaur University, Sagar, Madhya Pradesh, during February 26-28, 2008

ABSTRACT

Solvent extraction and Flat Sheet Supported Liquid Membrane (FSSLM) transport studies for radiostrontium separation from nitric acid medium were carried out, using 4,4'(5')-di-*tert*-butyl-dicyclo hexano-18-crown-6, (DTBCH18C6) as the extractant. Role of diluent on the extraction and transport of Sr(II) was investigated. Encouraging results were obtained during the solvent extraction investigations, using 0.1M DTBCH18C6 in a diluent mixture, comprising 80% toluene – 20% 1-octanol as the solvent, which displayed significantly lower nitric acid extraction, as compared to pure 1-octanol as the diluent.

Introduction

Due to high heat output and long half life (($t_{1/2}$ = 28.5 yrs), separation of ^{90}Sr from High Level Waste (HLW) eases its vitrification and subsequent safe management. Further, the separated radiostrontium can be used as a source, for thermoelectric and thermomechanical power generators [1].

Crown ethers have been used as size selective complexing agents for the alkali / alkaline earth metal ions [2,3]. In the SREX flow sheet developed at the Argonne National Laboratory, USA 4',4"(5")-di-*tert*-butyldicyclohexano-18-crown-6 (DTBuCH18C6) in 1-octanol has been used as extractant, for the selective removal of Sr from high level waste. However, due to the high cost of the ligand, Supported Liquid Membrane (SLM)-based separation method with low solvent inventory, is a viable alternative to the solvent extraction method for radiostrontium recovery from nuclear waste solution [4]. However, though the SREX solvent extracts Sr(II) efficiently, it also co-extracts large amount of acid [4]. The present work deals with development of alternative solvent with reduced acid uptake, by using binary mixtures of 1-octanol with different diluents and subsequent use of the modified solvent, for the carrier extractant in supported liquid membrane studies.

Experimental

All reagents including DTBuCH18C6 (Fluka, Switzerland) were of AR grade. PTFE membranes (0.45 µm pore size, 64% porosity) used in the present study were procured from Sartorius, Germany. ^{85,89}Sr obtained from BRIT, Mumbai was used (as a surrogate for ^{90}Sr), after ascertaining its radiochemical purity by gamma spectrometry. The distribution data for Sr was obtained by mixing 1 mL of the ligand solution in the suitable diluent mixture, with an equal volume of the aqueous phase containing the required concentration of HNO_3 and spiked with $^{85,89}Sr$ tracer in a thermostated water bath at 25±0.1°C for about1hour. After centrifugation, the phases were separated and assayed radiometrically, using a well-type NaI(Tl) scintillator counter. The SLM transport studies were carried out using 25 mL glass transport cells, with feed / strip solutions stirred at 200 rpm. Usually, the feed compartment contained $^{85,89}Sr$ tracer in 3.0 M HNO_3 , while the strip solution was distilled water. Assay of the strontium tracer was made as described above from the feed as well as the receiver compartment at different time intervals, to calculate the permeability coefficients and % transport data. The transport studies were carried out at ambient temperature (24±1°C). The material balance in these studies was found to be within ±5%.

Results and Discussion

Solvent extraction studies

Solution of DTBuCH18C6 in 1-octanol, when used as the solvent, though showed high distribution coefficient from acidic feed, its acid uptake reduces process efficiency. On the other hand, poor solubility of the crown ether in solvents with low acid uptake, necessitates the use of polar diluents such as 1-octanol, as a modifier solvent. Accordingly, in the present work 1:1 mixture of 1-octanol with aromatic diluents viz. toluene, tert-butyl benzene (TBB) and tri-isopropyl benzene (TIB) were used. The D_{Sr} values observed using 0.01 M DTBuCH18C6 were 1.03 ± 0.02, 1.03 ± 0.02, 1.22 ± 0.01, 0.76 ± 0.03 with 100% 1-octanol, 50% 1-octanol + 50% tert-butyl benzene, 50% 1-octanol + 50% toluene and 50% 1-octanol + 50% tri-isopropyl benzene, respectively. The acid uptake in these diluent mixtures was 11%, 7%, 3%, 1%, respectively, suggesting that 1-octanol-toluene mixture can be used as a suitable alternative. The aqueous phase used in these studies was 3 M HNO_3, which is the acidity of the HLW. All subsequent studies were carried out using binary mixtures, of toluene and 1-octanol. The concentration variation studies carried out in all these diluent mixtures, revealed the 1:1 stoichiometry of extracted complex. The results of diluent variation studies carried out with 1-octanol and toluene are presented in Table 1. Though the data indicated no significant change in D_{Sr} value with varying diluent proportion, acid uptake was found to decrease with increase in proportion of toluene. This was attributed to the decreasing content of water (which may be playing a crucial role for the acid uptake by hydrogen bonding) with decreased 1-octanol proportion in the diluent mixture. This was confirmed by carrying out the Karl Fisher Titration with all diluent mixtures. The

Table 1: Behaviour of DTBuCH18C6 dissolved in different diluent mixtures, [DTBuCH18C6] = 0.01M, aq. phase: 3M HNO_3

Diluent mixture	D_{sr}	% Acid uptake
100% 1-octanol	1.03 ± 0.02	11±1
80% l-octanol+ 20 % toluene	1.02 ±0.01	8±1
60% l-octanol+ 40 % toluene	1.16 ±0.01	6±1
50% l-octanol+ 50 % toluene	1.22 ±0.01	3±1
40% l-octanol+ 60 % toluene	1.30 ± 0.04	3±1
20% l-octanol+ 80 % toluene	1.18 ±0.02	1±1
100 % toluene	-	-

Table 2: % of moisture content obtained by Karl Fisher titration method in different diluent mixtures pre-equilibrated with 3M HNO$_3$, temperature: 25 ^{0}C

Diluent composition	% moisture	% acid uptake
100% 1-octanol	7.51 ± 0.09	11±1
80% l-octanol+ 20 % toluene	3.33 ±0.07	8±0
60% l-octanol+ 40 % toluene	2.31 ±0.12	6±1
50% l-octanol+ 50 % toluene	2.29 ±0.15	3±0
40% l-octanol+ 60 % toluene	1.50 ± 0.24	3±1
20% l-octanol+ 80 % toluene	1.10 ±0.10	1±1
100 % toluene	0.00 ± 0.00	-

results presented in Table 2 confirmed the decreased content of water with decrease in the 1-octanol content in binary mixture.

Supported Liquid Membrane(SLM) studies

Using 3 M HNO$_3$ as the feed solution and distilled water as the strip solution, SLM studies were carried out using 0.01 M DTBCH18C6 in toluene + 1-octanol in different proportions. The transport data profile is presented in Fig. 1. The transport rate was slow when 100% 1-octanol was used as diluent while enhancement in transport rate was observed for binary mixture of 1-octanol and toluene. Highest transport rate was observed when 20% 1-octanol + 80% toluene was used as the diluent mixture. This was attributed to the transport of acid by the diluent mixtures as presented in Fig. 2. Surprisingly, with 20% 1-octanol + 80% toluene as diluent, after 55% transport of Sr(II), transport of acid with a higher rate was observed. With all binary diluent mixtures, transport of acid was fast enough to affect the transport of Sr(II). As a result, as shown in Figs. 1 and 2, the Sr(II) transport attained a plateau value of about 55% after 24 hours, when acid transport was ~50% in all diluent mixtures. Though the solvent extraction studies indicated a decrease in the acid uptake with decreasing 1-octanol content, the SLM studies indicated transport ~50% acid in all diluent mixtures employed. Use of buffer solution in the receiver phase did not suppress the acid transport. To study the effect of H$^+$ ion concentration, Sr(II) transport studies were carried out at fixed nitrate ion concentrations with varying amounts of H$^+$ ion concentration. It was observed that the permeability coefficient deceased to about one third of the value obtained with 1 M HNO$_3$ as the feed. However, Sr(II) transport was found to

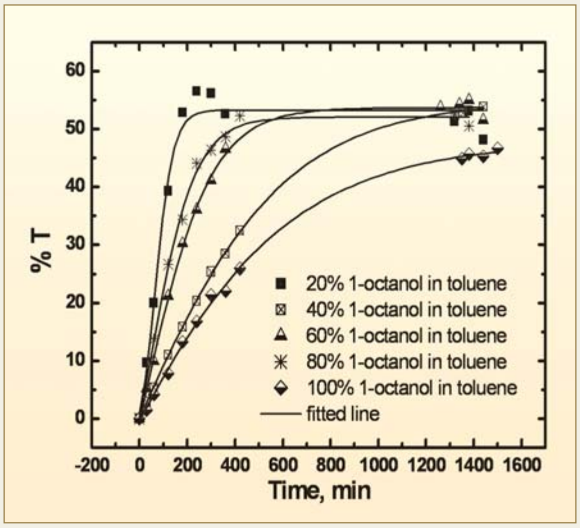

Fig. 1: % Transport of Sr(II)in by 0.01M DTBuCH18C6 in different diluent compositions feed: 3MHNO$_3$, strip: distilled water

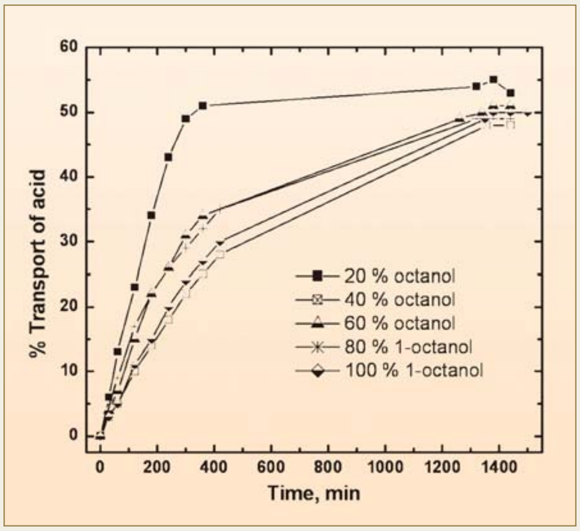

Fig. 2: Transport of acid in supported liquid membrane studies by 0.01M DTBCH18C6 different diluent mixtures, feed solution: 3M HNO_3, strip solution: distilled water

saturate to ~50% which improved significantly when the feed solution contained 3M $NaNO_3$.

Conclusions

Use of binary mixture of 1-octanol with toluene showed significantly lower acid uptake as compared to pure 1-octanol as the diluent in solvent extraction studies. The SLM studies, however, did not indicate quantitative transport of Sr(II) when 3 M HNO_3 was used as the feed. Sr(II) transport in all cases containing acidic feed solutions saturated to slightly more than 50% which was ascribed to the competitive acid transport phenomena.

References

1. IAEA Technical Data Series No. 356, IAEA, 1993.
2. Y. Takeda; *Topics in Current Chemistry*, 121 (1984)1.
3. E. P. Horwitz, M. L. Dietz, D. E. Fisher; *Solv. Extr. Ion Exch*. 1991 (9) 1.
4. N. Rawat, P.K. Mohapatra, D.S. Lakshmi, A. Bhattacharyya and V. K. Manchanda; *J. Membr. Sci.*, 275, 82 (2006).
5. D.R. Raut, S.A. Ansari, P.K. Mohapatra and V.K. Manchanda; pp 343, NUCAR-2009.

ABOUT THE AUTHOR

Dr. P. K. Mohapatra joined the Radiochemistry Division, BARC in 1987, after graduating from the 30th Batch of BARC Training School. His research interests include separation of actinides and fission products using liquid membranes. He has developed hollow fiber liquid membrane separation method for the recovery of actinides and fission products from radioactive waste samples. Dr. Mohapatra has to his credit about 100 publications in reputed international journals.

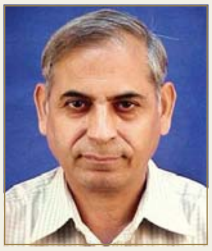

Dr. V.K. Manchanda has research interests in the areas of separation science of actinides, actinides' speciation, CQC of plutonium-based fuels, complexation of actinides and fission products with macrocyclic ligands. He has more than 190 publications in reputed international journals to his credit. He is the past President of IANCAS and Founder President of ASSET. He is on the Advisory Board of international journals such as *Radiochimica Acta* and *Solvent Extraction & Ion Exchange*. He currently heads the Radiochemistry Division, BARC.

SYNTHESIS AND CHARACTERIZATION OF MIXED METAL OXIDES FOR ENERGY AND ENVIRONMENT-RELATED REACTIONS

A.M. Banerjee, M. R. Pai and S. R. Bharadwaj
Chemistry Division

This paper was conferred the Best Paper Award (Second) for Oral Presentation at the National Symposium for Materials Research Scholars, held at IIT Mumbai, on 17th & 18th May, 2008

ABSTRACT

A series of aliovalent and isovalent ions were substituted at A and B-site in Indium titanate, $In^{3+}_2Ti^{4+}O_5$ (A=Ni^{2+} and Nd^{3+}, B =Fe^{3+} and Cr^{3+}, x/y=0.0-0.2), with an objective to evaluate their photoactivity for water splitting reaction, as a function of substitution under actual sunlight and sunlight-like irradiation. Samples were prepared by means of a solid state reaction, the surface and bulk properties of the substituted samples were characterized by X-Ray Diffraction (XRD), Brunauer–Emmett–Teller (BET) N_2 sorption method, FTIR and DRUV techniques. The analytical results of DRUV show that Nd^{3+} doping did not shift the main absorption band edge significantly, but some new absorption peaks attributable to 4f internal electron transition existed in the visible region. In case of Ni, Fe and Cr band edge was shifted in visible range.

Introduction

In view of global energy and environmental issues, significant efforts have been made, to develop suitable catalysts for the efficient splitting of water. Water splitting can be achieved through thermochemical, photocatalytic and other methods. With these aspects in view, we propose to develop Indium titanate based mixed oxides, for splitting of water stoichiometrically, under visible light irradiation.

Experimental

Catalyst Synthesis

Mixed oxides with nominal compositions $In_{2(1-x)}Nd_{2x}TiO_5$, $In_{2(1-x)}Ni_{2x}TiO_{5-\delta}$, $In_2Ti_{1-x}Fe_xO_{5-\delta}$, $In_2Ti_{1-x}Cr_xO_{5-\delta}$, were synthesized through ceramic route by using pre-dried In_2O_3, TiO_2, NiO Nd_2O_3, Fe_2O_3 and Cr_2O_3 (99.99% purity), as starting materials, mixing them in appropriate stoichiometry as depicted by the following equations:

$(1-x)In_2O_3 + TiO_2 + xNd_2O_3 \rightarrow In_{2(1-x)}Nd_{2x}TiO_{5-\delta}$ (2x = 0.0, 0.1, 0.2, 0.3 and 0.4)

$(1-x)In_2O_3 + TiO_2 + 2xNiO \rightarrow In_{2(1-x)}Ni_{2x}TiO_{5-\delta}$ (2x = 0.0, 0.1, 0.2, 0.3 and 0.4)

$In_2O_3 + (1-x)TiO_2 + x/2Fe_2O_3 \rightarrow In_2Ti_{1-x}Fe_xO_{5-\delta}$ (x = 0.0, 0.05, 0.1, 0.15 and 0.2)

$In_2O_3 + (1-x)TiO_2 + x/2Cr_2O_3 \rightarrow In_2Ti_{1-x}Cr_xO_{5-\delta}$ (x = 0.0, 0.1, and 0.2)

The pellets of homogeneous mixtures were calcined, first at 700°C for 65 h and then at 1000°C for 64 h and finally at 1250°C for 24 h, with intermittent grindings, so as to ensure the uniformity and the completion of the reaction. All samples are abbreviated in text as M(x), where M is the dopant ion and x is the extent of substitution.

Catalyst Characterization

The Powder XRD patterns were recorded on a Philips diffractometer (model PW 1710), equipped with a graphite monochromator and Ni-filtered Cu-Kα radiation. The patterns were indexed using powderx programme for determination of the unit cell parameters of the substituted samples. The crystallite size, *D*, was calculated from XRD line width according to the Scherrer equation.

The SEM images were recorded on Model Tescan Vega MV 2300T/40, using an accelerating voltage of 25KV at the working distance ~10mm. EDS was recorded with Inca Crystal IC 250 at a working distance of 23 mm spectra.

Band Gap Measurements: Diffusion Reflectance Spectra (DRS)

Band gap measurements of all semiconductor oxide samples was estimated, by recording their Diffuse reflectance UV-Visible spectra using spectrophotometer of JASCO model V-530, Japan, scanned in the range of 200-1000 nm at the scanning speed of 200nm/min.

Results and Discussion

Crystal structure by XRD

The powder XRD patterns of all the doped and undoped samples are shown in Fig. 1. The $In_2TiO_{5,}$ is isostructural with In_2VO_5. It crystallizes in the orthorhombic space group, with a = 0.7241 nm, b= 0.3427 nm c= 1.4878 nm, cell volume = 0.3692 nm^3 and Z = 4. The lines due to reactant oxides are missing in all substituted patterns thus confirming the completion of the solid-state reaction. Following are the XRD results as a function of individual dopants at A site by Nd and Ni, and at B-site by Fe and Cr.

A-site substitution, $In_{2(1-x)}Nd_{2x}TiO_{5:}$

The XRD patterns of all Nd^{3+} substituted In_2TiO_5 compositions, are presented in Fig. 1, as a function of x, where the XRD pattern of x = 0, 0.1 and 0.2 composition matches with that of orthorhombic In_2TiO_5 (JCPDS card No.30-0640) oxide. The XRD patterns as shown in Fig. 1 reveal that substitution by isovalent metal ion, Nd^{3+} at A-site in In_2TiO_5 has resulted in single-phase compositions isomorphic to In_2TiO_5 phase. Weak reflections present at 2q= 28.5°, 28.8°, 33.21°, attributable to new secondary phase are also visible in $In_{1.7}Nd_{0.3}TiO_{5-\delta}$ The lines corresponding to a new secondary phase were identified and attributed to the Nd_2TiO_5 JCPDS card No. 37-0944). The intensities of XRD lines due to this new phase, increased with increase in Nd content of $In_{1.7}Nd_{0.3}TiO_{5-\delta}$ and $In_{1.6}Nd_{0.4}TiO_{5-\delta}$ substituted samples. A-site substitution by isovalent cation, Nd^{3+} has induced a mixed phase formation beyond 10% of dopant comprising of both parent $In_2TiO_{5-\delta}$ and $Nd_2TiO_{5-\delta}$ phases, whereas samples with $In_{1.9}Nd_{0.1}TiO_{5-\delta}$ $In_{1.8}Nd_{0.2}TiO_{5-\delta}$ compositions were single phase isomorphic to In_2TiO_5 phase.

$In_{2(1-x)}Ni_{2x}TiO_5$

Fig. 1 also shows the powder XRD patterns of In_2TiO_5 and corresponding patterns observed due to aliovalent substitution of Ni^{2+} in place of In^{3+} at A-site. The XRD patterns of samples with $In_{1.95}Ni_{0.05}TiO_{5-\delta}$, $In_{1.9}Ni_{0.10}TiO_{5-\delta}$ and $In_{1.8}Ni_{0.2}TiO_{5-\delta}$ compositions, match with the XRD pattern of unsubstituted indium titanate sample, asshown in Fig. 1. Thus in these samples Ni substitution resulted in single phase due to formation of solid solution of Ni with the lattice of the parent compound, indium titanate. However, for samples, having Ni content higher than 10%, some low intensity lines in addition to parent phase were also observed.

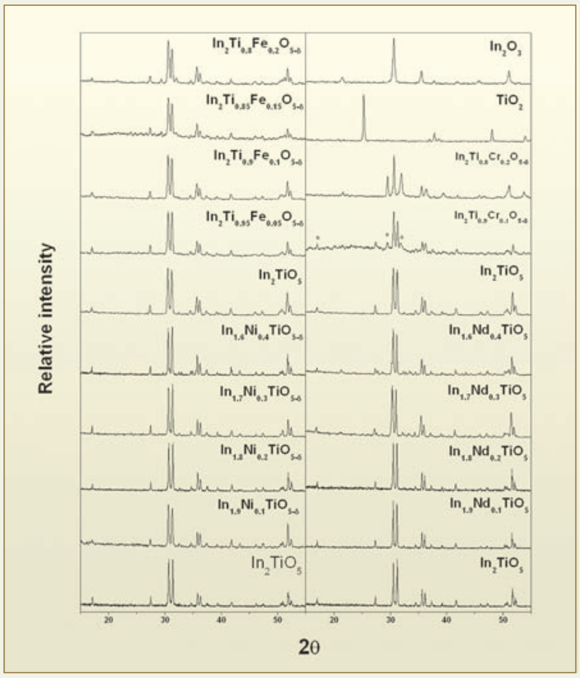

Fig. 1 : XRD patterns of In_2TiO_5, $In_{2(1-x)}Nd_{2x}TiO_5$, $In_{2(1-x)}Ni_{2x}TiO_{5-\delta}$, $In_2Ti_{1-x}Fe_xO_{5-\delta}$ $In_2Ti_{1-x}Cr_xO_{5-\delta}$ (x = 0.0-0.2) as a function of substitution.

These weak lines present at 2θ= 43.33°, 35.71° and 63.02° are attributed to the formation of secondary phase in the samples having compositions of $In_{1.7}Ni_{0.3}TiO_{5-\delta}$ and $In_{1.6}Ni_{0.4}TiO_{5-\delta}$. The secondary phase was identified to be $Ni_{0.75}Ti_{0.125}O$ (JC-PDS card No. 31-0916).

B-site substitution $In_2Ti_{1-x}Fe_xO_{5-d}$

The XRD pattern (Fig. 1), of x = 0, composition matches well with that of orthorhombic In_2TiO_5 (JCPDS card No.30-0640) oxide. The XRD patterns of Fe substituted compositions, i.e. 0.05≤ x ≤ 0.2 are presented in Fig.1 (c & e). All these patterns reveal that Fe substitution has resulted in single-phase material comprised of In_2TiO_5 phase. Table 1 lists the change in lattice parameters and cell volume as a function of Fe content as generated by indexing the XRD patterns of substituted samples. This data reveals that as Fe content increases the cell volume decreases, which can be explained by inclusion of smaller cation, Fe (0.64 Å) in place of relatively larger size cation, Ti (0.68 Å).

$In_2Ti_{1-x}Cr_xO_{5-d}$

Fig. 1 presents the XRD patterns of B-site substituted $In_2Ti_{1-x}Cr_xO_{5-\delta}$ compositions. The XRD pattern of composition with $In_2Ti_{0.9}Cr_{0.1}O_{5-\delta}$, shows weak reflections attributable to new phase (marked as *) are also visible which indicates the formation of secondary phase. Thus Cr substitution has resulted in mixed phases. The lines corresponding to new secondary phase were identified and attributed to be $Cr_{0.286}Ti_{0.714}O_{1.857}$ (JCPDS card No. 30-416).

Thus, cationic substitution of Fe^{3+} at B-site has resulted in single-phase material, isomorphic to In_2TiO_5 phase, whereas Ni^{2+}, Nd^{3+} and Cr^{3+} resulted in mixed phases due to limited solubility of these ions in In_2TiO_5 lattice. Fe^{3+} and Cr^{3+} are transition elements of same valence and ionic radii when substituted at B-site in In_2TiO_5 under identical conditions; their implications in the lattice were varied and cannot be generalized. Thus, the nature of cation, its transport properties and diffusion characteristics play an important role in solid-state reaction.

Table 1 : Lattice parameters of $In_2TiO_{1-x}Fe_xO_{5-\delta}$ samples

Sr. No.	Sample		Lattice parameters (Å)			Cell Volume (Å³)
			a	b	c	
1	$In_2Ti_{1-x}Cr_xO_{5-\delta}$ orthorhombic	X = 0.0	7.241 (2)	3.427 (2)	14.878 (6)	369.24
2		X = 0.1	7.227 (8)	3.425 (8)	17.873 (6)	368.26
3		X = 0.2	7.225 (6)	3.408 (5)	14.853 (1)	365.82

Though Fe substituted samples are single-phase compositions, there is a slight distortion of lattice as may be caused either by the generated substitution-induced non-stoichiometry or due to decrease in crystallinity of these samples. This data indicates that even on substitution of upto 20% Fe in place of Ti the structure remains intact despite of the incorporated distortion. This may be attributed to the almost identical ionic radii of Ti^{4+} and Fe^{3+}.

Diffuse Reflectance Spectroscopy (DRS)

The metal ion substitution affects the electronic structure of the semiconducting photocatalysts which is manifested in their DRUV-Vis spectra. Fig. 2a. illustrates the light absorption properties for the In_2TiO_5 and metal ion substituted at A and B-site. The band gap of these compounds can be estimated from plots of the Kubelka-Munk functions F(R) versus photon energy. One of the most characteristic features is that, the Eg value (Eg is band gap) is narrowed with Fe and Cr doping. The band gap is changed from 3.2eV (In_2TiO_5) to 2.1eV ($In_2Ti_{0.8}Fe_{0.2}O_{5-\delta}$) and 1.9 in case of Cr doping ($In_2Ti_{0.8}Cr_{0.2}O_{5-\delta}$). This is considered largely to be a consequence of the Fe 3d or Cr 3d level. Ni has also resulted in lowering of band gap from 3.02 to 2.0 eV. The band gap change in Ni-doped compounds can be attributed to internal transitions in a partially filled d shell. The wavelength at the absorption edge, λ was determined as the intercept on the wavelength axis for a tangent line.

Fig. 2b shows the UV–VIS diffuse reflectance spectrum of $In_{2(1-x)}Nd_{2x}TiO_{5-\delta}$, as a function of x. The spectrum indicates that In_2TiO_5 has an optical gap of 3.02 eV. The presence of several peaks at 529.5, 588.5, 741, 802, 866 and 879 nm in the spectra of Nd substituted samples, reveals that the Nd^{3+} substitution has enabled the sample to absorb in visible region considerably. These peaks are attributed to possible charge transfer transitions between Nd 4f and other bands. The intensity of peaks was found to increase with increase in Nd content. The band gap is likely to occur between the top of the oxygen 2p band and the bottom of the

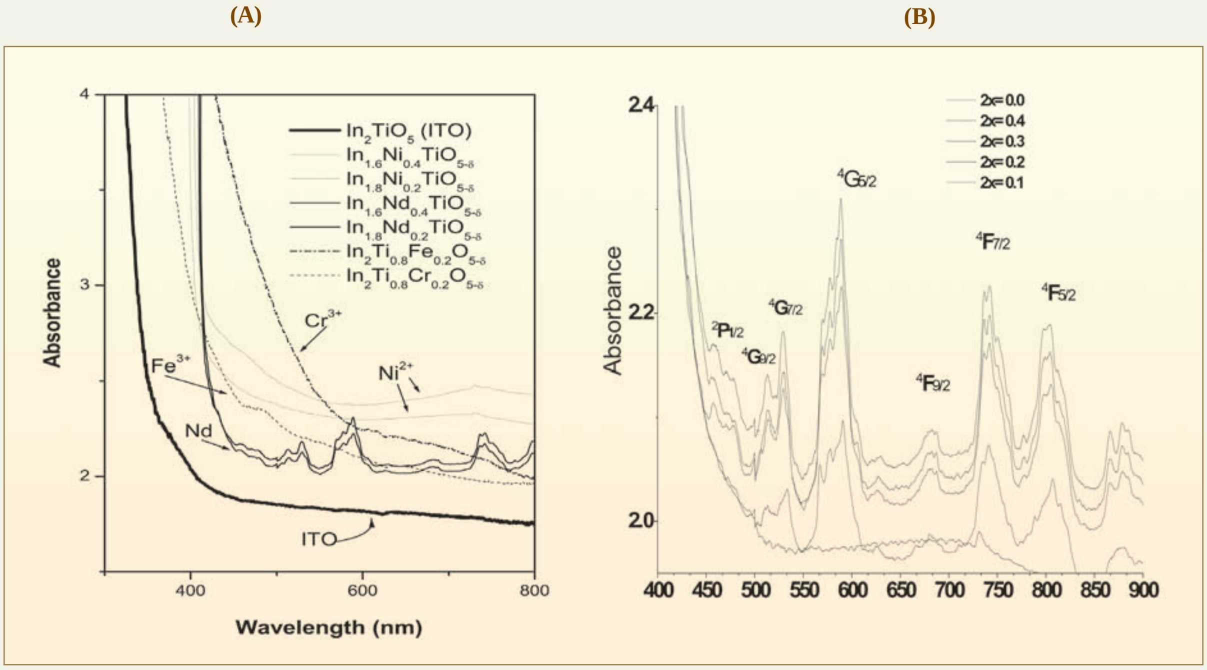

Fig. :2 (a) Effect of different metal ion substitutions at both A and B-sites on Absorption spectra of Indium titanate, viz. of $In_{2(1-x)}A_{2x}TiO_{5-\delta}$ and $In_2Ti_{1-x}B_xO_{5-\delta}$, A = Ni^{2+}, Nd^{3+} and B = Fe^{3+}, Cr^{3+}) samples (b) Dr-UV-Vis spectra of $In_{2(1-x)}Nd_{2x}TiO_{5-\delta}$ as a function of x. Symbols for each absorptions show the excited states of isolated Nd 4f. The ground states are: Nd, $^4I_{9/2}$

Ti 5d (t_{2g}) band. In particular, a much broader absorption in the range 300–400 nm suggests, possible charge-transfer transitions between Nd 4f and other bands. $In_2Ti_{1-x}Fe_xO_{5-\delta}$ samples show that the visible absorption spectra of these compounds, are characteristic of photocatalysts which are able to respond to visible light.

SEM

Fig. 3 shows the SEM micrograph of a typical sample of In_2TiO_5 , where we can see that the particles have clear facet grain boundaries, whereas on the substituted samples, the facets disappear. Also the particle size is in micron range, due to high temperature sintering.

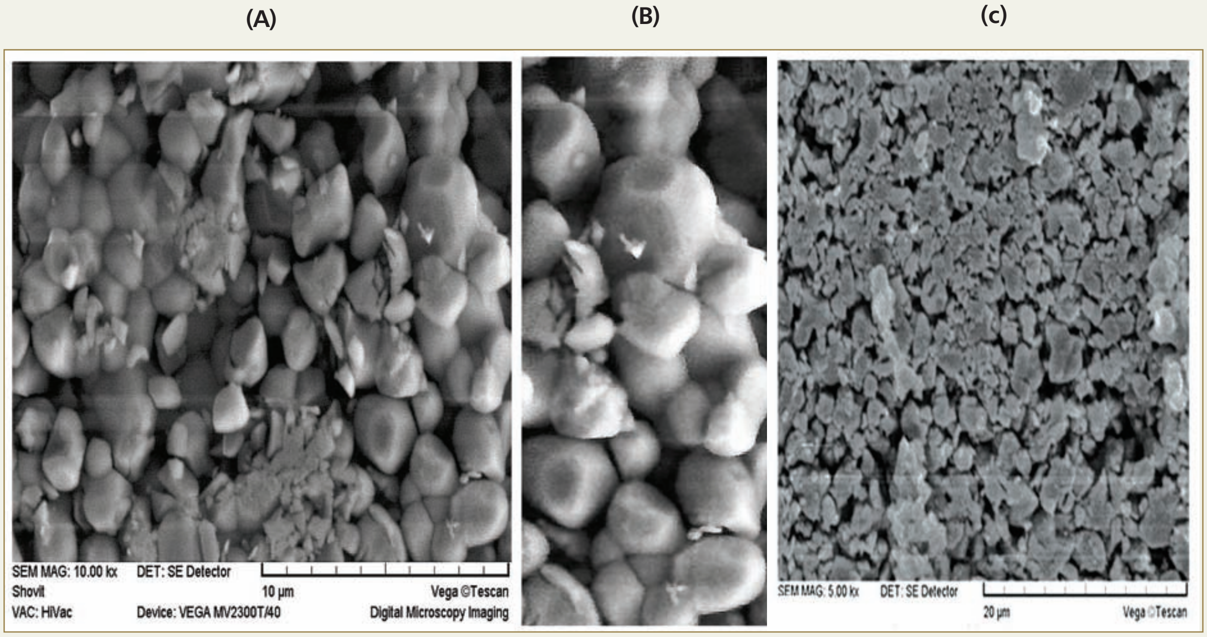

Fig. 3 : SEM image of a) In_2TiO_5 b) enlarged portion showing the facets in surface of In_2TiO_5 c) Nd (0.2) substituted sample

ABOUT THE AUTHORS

Mr. Atindra Mohan Banerjee completed his Master of Science in Chemistry from Calcutta University in 2004. He undergone a one year Orientation Course in Nuclear Science and Engeneering from BARC Training School (OCES - 48 batch). Subsequently he joined the Chemistry Division of BARC, Mumbai in Sept. 2005. He is involved in the development of catalyst for sulphuric acid decomposition reaction in thermochemical cycle for hydrogen generation by water splitting and photocatalytic water splitting. He has 2 publications in International journals and 6 publications in Symposia/conferences. He is a recipient of Best Paper Award conferred during ISMC-2006 for the paper titled " Studies for S-I Thermochemical Cycle for Hydrogen production".

ABOUT THE AUTHORS

Dr. (Ms.) Mrinal R. Pai joined BARC through Training School (40th Batch) after completing her Post graduation in Chemistry from IIT Delhi in 1996. She initiated her research activities in the field of catalysis with development of H_2 mitigation catalyst during year 1999 in Chemistry Division. She was awarded Ph.D degree in Physical Chemistry from Mumbai University in year 2005. Also, she gained experience in synthesizing fine powders of nano-size oxides/mixed oxides with spinels, perovskites and pyrochlore structures and characterizing them by various techniques for their prospective applications in pollution abatement, water splitting by photocatalysis and sulfuric acid decomposition reaction in S-I thermochemical cycle. There are sixteen publications in refereed international journals, several publications in symposium and conferences and invited talks to her credit.

Dr. Shyamala Bharadwaj obtained her B.Sc. Degree from Mumbai University in the year 1976 and joined the Department of Atomic Energy in the year 1977, after graduating from the 20th Batch of BARC Training School. Later she completed her Masters Degree and obtained Ph. D. in Physical Chemistry from Mumbai University. She has been working in the area of high temperature thermodynamics of nuclear as well as other refractory materials for the past 30 years. During the year 2000-2001, she worked as a Guest Scientist at the Juelich Research Centre, Juelich, Germany, where she was involved in the investigations of Solid Oxide Fuel Cell materials. Presently, she is heading the Fuel Cell Materials and Catalysis Section of Chemistry Division, BARC. Her current interests are in the field of Intermediate Temperature Solid Oxide Fuel Cells and generation of hydrogen by water splitting, by thermochemical and photocatalytic methods. She has more than 180 publications to her credit, with more than 75 publications in reputed international journals. She is a Ph.D. Guide of Mumbai University. She was Hon. Treasurer of Indian Thermal Analysis Society (ITAS) during 1996-2000 and is currently the Hon. Secretary of ITAS. She has been bestowed with NETSH-ITAS Award 2006, for her contribution in the field of thermodynamics and thermal analysis.

बीएआरसी न्यूज़लैटर
BARC NEWSLETTER

LASER WELDING OF FULLY AUSTENITIC STAINLESS STEEL (D9) THIN WALLED TUBE WITH 316M AUSTENITIC STAINLESS STEEL ENDPLUG

A. Kulshrestha, P.V. Suresh Varma, A. Gupta, R.B.Bhatt, Md. Afzal, J.P. Panakkal and H.S. Kamath
Advanced Fuel Fabrication Facility

This paper was presented at the 46th National Metallurgist Day and the 62nd Annual Technical Meeting of the Indian Institute of Metals, held at New Delhi, from Nov. 13-16, 2008. It was selected from among 396 papers

ABSTRACT

The fabrication of fuel elements for Prototype Fast Breeder Reactor (PFBR), involves welding of fully austenitic stainless steel thin-walled clad tube and stainless steel 316M end plug. Pulsed TIG technique is generally used, for welding of clad tube and end plug. Laser welding has been introduced for end plug welding at the Advanced Fuel Fabrication Facility, BARC, Tarapur. Laser welding offers some advantages like low heat input, high speed, consistent penetration and bead geometry. In this paper, the effect of various laser welding parameters on penetration and bead geometry has been studied. Experiments were carried out by varying parameters like peak power, energy per pulse, spot overlap, welding speed, defocusing distance and repetition rate and their effect on bead geometry and penetration was determined. The process was modeled using Taguchi method and was validated experimentally. Based on the S/N ratio, the effect of each parameter on penetration and bead geometry was analyzed. The contribution made by each parameter in determining penetration and bead geometry was found using ANOVA. The results of Pulsed Nd-YAG laser welding were compared with Pulsed TIG welding of end plugs. It was found that laser welding gives consistent penetration and bead geometry as compared to pulsed TIG. The welds were characterized and the effect of parameters on microstructure was also studied.

IIntroduction

Fully austenitic stainless of grade D9 alloy has been chosen as the cladding material, for the upcoming Prototype Fast Breeder Reactor. Conventionally GTAW process is being used in India, for the end plug welding of fuel tubes. End plug welding is an autogenous welding process, because of low wall thickness of the clad tube. Even though GTAW was successful so far, it has a few drawbacks. The problems that are encountered in GTAW welding are, difficulty in alignment of the electrode with weld joint, variation in penetration throughout the circumference of the weld and tungsten inclusion of the weld. Laser Beam Welding (LBW) is a potential welding process, that can offer a solution to the above-mentioned problems. Laser heat input for the fusion of the weld is comparatively lower than GTAW welding. So the distortion associated with heat build up is low.

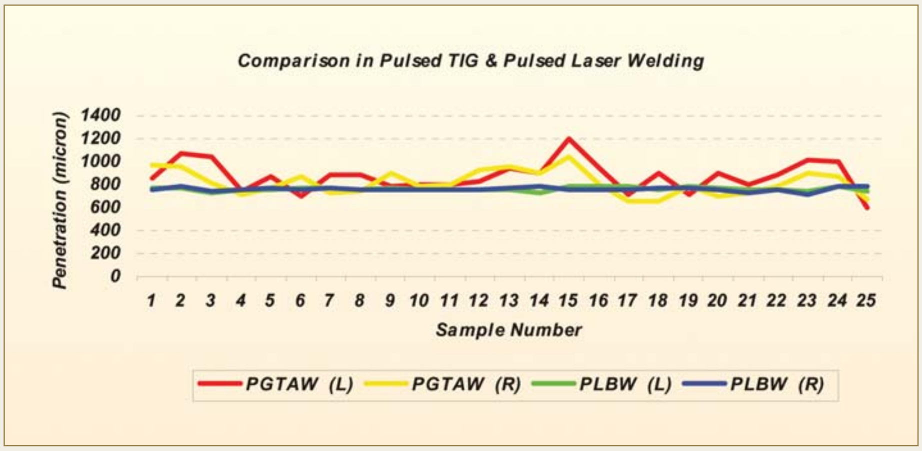

Fig. 1: Penetration in pulsed TIG and pulsed laser welding (for section A & B)

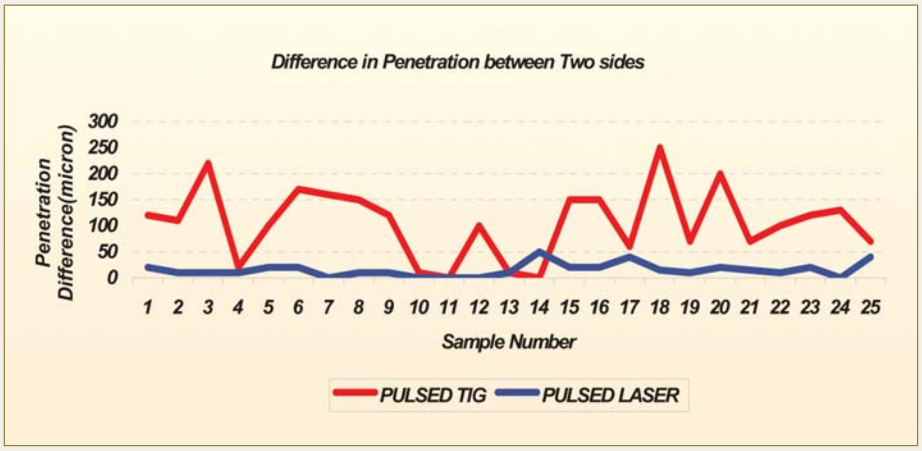

Fig. 2 : Penetration difference between section A & B in pulsed TIG and pulsed laser welding

The depth of penetration for end plug welding using laser welding and TIG welding are compared in Figs. 1 & 2. Optimization of laser welding parameters has been done using Taguchi method. Theoretical approach has been done, to find out the effect of parameters on weld bead geometry.

Pulsed Nd-YAG Laser Welding

Pulsed Nd-YAG laser beam welding involves many variables like peak power, pulse repetition rate, pulse duration, energy per pulse, spot overlap, welding speed, defocusing distance and shielding gas. All these variables affect the bead geometry of the fusion zone, which in turn influence the properties of the weldment. Pulse peak power plays an important role in achieving good weld penetration. At constant duration of pulse, increase in pulse peak power increases the energy input and thus the penetration [1]. Increase in repetition rate will lead to higher heat input and hence better penetration [1]. Defocusing reduces the power density and resulted in widening of the weld at the expense of depth. At constant pulse power, depth of penetration is directly related to pulse duration.But the use of the technique in inappropriate settings, can reduce its effectiveness in welding operation.

Taguchi experimental design

Optimization of process parameters is the key step in the Taguchi method, for achieving high-quality welds. The process control parameters can be optimized for minimum noise, cost and high-performance and quality. It reveals the dominant control factors along with optimal values of each control factor for achieving desired values of dependent parameters. For better root fusion, penetration depth and aspect ratio (depth/width ratio) have to be maximized. So, larger-the-better S/N ratio equation is used as follows:

$$S/N = -10 \, \mathrm{Log10} \left(1/n \ \Sigma \, 1/Y_i^{\,2} \right)$$

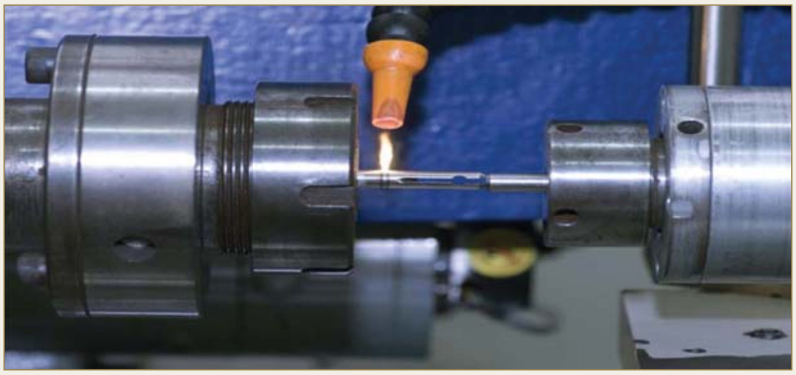

Fig. 3 : Laser welding set-up

Table 1: Chemical composition of the D9 clad tube

C	Cr	Ni	Mn	Si	Mo	P	S	Ti	Fe
0.04	14.53	14.25	1.5	0.59	2.07	0.053	0.005	0.23	Bal.

Table 2: Chemical composition of the 316 M S.S. end plug

C	Cr	Ni	Mn	Si	M	P	S	Fe
0.04	17.2	10.19	1.45	0.58	2.19	0.053	0.015	Bal.

MATERIAL AND EXPERIMENTAL METHOD

A Nd-YAG pulsed laser welding machine with a maximum average power of 500W was employed for the work. The material used was fully austenitic D9 stainless steel tube (OD 6.6 mm and wall thickness 0.45 mm) and SS 316M end plug of O.D. 6.6 mm. The chemical composition of the D9 stainless steel tube and SS 316M end plug is shown in Table 1 and 2 respectively. The tube and the end plug were held in the chuck of a welding lathe as shown in Fig. 3 and rotated below the welding head at the required speed. Autogenous welding beads were made on the joint. The laser beam was delivered by a stationary welding head, held vertically over the weld joint as shown in Fig. 4. The focal length of the focusing optics was kept at 200 mm. Helium gas was used for shielding, blown at the constant rate of 20 lpm at 45° onto the job. For all sets of experiments, the spot size on the surface was 0.4 to 0.6 mm (Fig. 5) as per the defocusing distance chosen and the percentage overlap of bead was kept at 70%.

Optimization of pulsed Laser parameters

The Taguchi method separates factors into two main groups, the control factors and the noise factors. Control factors are those that allow a manufacturer to control during processing and noise factors are difficult to control. In this welding process peak power, travel speed, repetition rate, pulse duration, pulse energy, torch angle, shielding gas type, defocusing distance and the gas nozzle angle were selected as control factors.

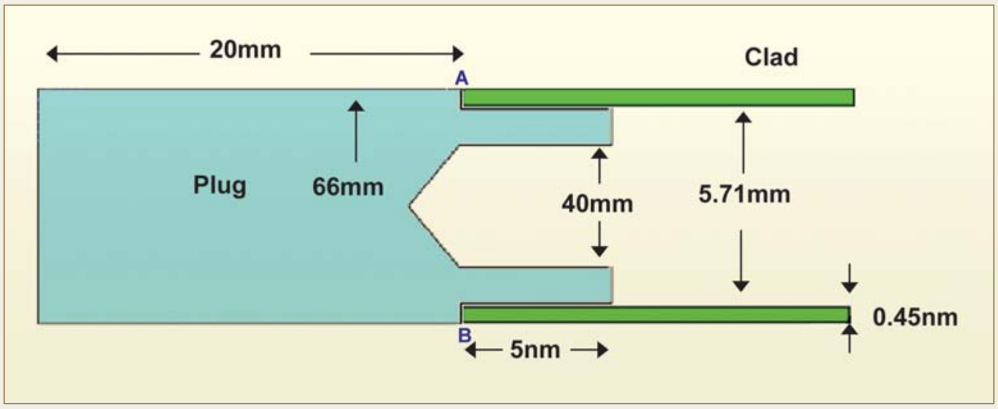

Fig. 4: PFBR end plug weld joint (cut from section A & B)

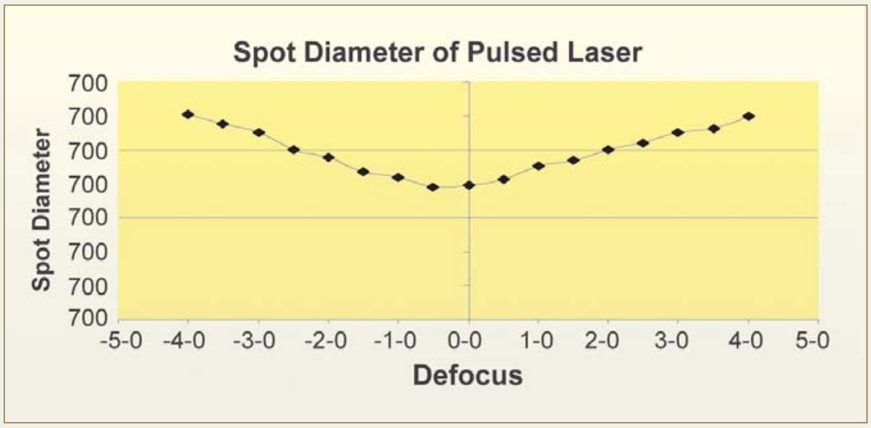

Fig. 5: Spot diameter of the pulsed laser at different defocusing distances

Selection of parameters

In this study, peak power, pulse frequency, pulse duration and defocusing distance were selected at three levels. The values of the welding process parameters at different levels are listed in Table 3. The fundamental principle of robust design, is to improve the quality by minimizing the effects of the causes of variation. Due to the circular geometry, heat buildup is the major cause of variation in penetration and aspect ratio. Hence it is chosen as the noise factor. 50% of the total revolution of tube was designated as level 1 (section A) and 100% as level 2 (section B) as shown in Fig. 4.

Table 3 : Laser welding parameters and their levels

Character	Parameter	Levels		
		1	**2**	**3**
P	Peak Power (W)	900	1000	1100
T	Pulse Duration (msec)	10	15	20
F	Pulse Frequency (Hz)	8	14	20
D	Defocussing Distance (mm)	-1.0	-2.5	-4.0

Selection of orthogonal arrays

Orthogonal array-based matrix experiments are used, to study the effects of control factors and noise factors, to determine the bead quality characteristics for a particular application. In this study, an L9 orthogonal array with 4 columns and 9 rows was used. This array has eight degrees of freedom and it can handle four process parameters with three levels as shown in Table 4. Nine experiments for two noise level settings were carried out and the response of each experiment is investigated as shown in Table 5.

Table 4 : L_9 Taguchi matrix

Expt. No.	Peak Power (P)	Pulse Duration (T)	Pulse Frequency (F)	Defocussing Distance (D)
1	1	1	1	1
2	1	2	2	2
3	1	3	3	3
4	2	1	2	3
5	2	2	3	1
6	2	3	1	2
7	3	1	3	2
8	3	2	1	3
9	3	3	2	1

Table 5 : Response values at noise level 1&2

Expt.No.	Depth of Penetration		Depth/Width Ratio (micron)	
	Noise Levels		Noise Levels	
	1	2	1	2
1	500	520	0.700	0.688
2	700	700	0.921	0.875
3	800	820	0.755	0.745
4	600	600	0.545	0.571
5	1120	1100	1.020	1.0185
6	1000	1000	1.111	1.099
7	780	800	0.918	0.930
8	880	880	0.765	0.800
9	1300	1250	1.273	1.295

Evaluation of optimal conditions by use of signal-to-noise ratios

Taguchi has created a transformation of data to another value, which is a measure of the variation present. This transformation called the S/N ratio, is used in evaluating the quality of product. The S/N ratio measures the level of performance and the effect of noise factors on performance and is an evaluation of the stability of performance of an output characteristic. In this investigation, response considered is penetration depth and the depth/width ratio.

ANalysis Of VAriance (ANOVA)

The purpose of ANOVA is to investigate welding process parameters, which can significantly affect the quality characteristics. This is accomplished by separating the total variability of the S/N ratios, which is measured by the sum of squared deviations from the total mean of the S/N ratio, into contributions by each welding process parameter and the error. The percentage contributions by each of the process parameters is the total sum of the squared deviations and can be used to evaluate the importance of the process parameters change, on quality characteristics. In addition to this the F-test can also be used to determine which welding process parameters have significant effect on the quality characteristics. Usually, the change of the welding process parameter has a significant effect on the quality characteristics, when the F value is large.

Confirmation tests

The final step is to predict and verify the improvement of the quality characteristics, using the optimal level of the process parameters. The predicted S/N ratio using the optimal level of the process parameters can be calculated from the table, considering the process parameters that significantly affect the multiple quality characteristics.

Metallurgical Charactorization

Figs. 6 & 7 depict the various combinations of welding parameters for laser welding in this work. At constant peak power, the effect of other parameters can also be clearly seen in the metallograph.

Results and discussion

The aim of the present study is to reduce the variation and make the weld bead geometry insensitive to the noise factor. So S/N ratio is calculated on 18 cases. The responses considered are depth of penetration and the aspect ratio.

Fig. 6 : Metallograph for Experiment 4 ($P_2T_1F_2D_3$)

Fig. 7 : Metallograph for Experiment 4 ($P_2T_2F_3D_1$)

Effect of Process Parameters on The Depth of Penetration

Table 6 shows the ANOVA table for effect of penetration. The F-test value for all the welding process parameters is greater than the tabulated value ($F_{0.05;\ 2,9} = 4.26$). It shows that all the process parameters are significant. The percentage effects of these parameters are also shown in the table.

For better fusion of the root, the depth of penetration is to be maximized. The average S/N ratios of the parameters are given in Table 7. S/N curves for all these parameters for various levels and the optimal welding conditions are shown in Fig. 8. The predominant parameters that affect the depth of penetration, are also shown in Fig. 9.

Effect of process parameters on the aspect ratio

Table 8 shows the ANOVA table for the aspect ratio i.e. depth / width ratio. The F-test shows that all the process parameters are significant. The percentage effects of these parameters are also shown in the table.

For bead geometry, aspect ratio is to be maximized. The average S/N ratios of the parameters are given in Table 9. S/N curves for all these parameters for various levels and the optimal welding conditions are shown in Fig. 10. The predominant parameters that affect the aspect ratio are shown in Fig. 11.

Table 6 : ANOVA table for depth of penetration

Symbol	Sum of Square	Degree of Freedom	Mean Square	F Statistics	Contribution Percentage
P	1199100.0	2	599550.0	2632.2	28.78
T	1553633.3	2	776816.7	3410.4	37.30
F	456633.3	2	228316.7	1002.4	10.96
D	954233.3	2	477116.7	2094.7	22.91
Error	2050	9	227.8		0.05

Table 7 : S/N Response table for depth of penetration

Level	Average S/N Ratio (db)			
	P	**T**	**F**	**D**
1	56.38	55.86	57.65	59.03
2	58.82	58.90	58.19	58.28
3	59.65	60.09	59.01	57.54
Maximum	59.65	60.09	59.01	*59.33*
Minimum	*56.38*	*55.86*	*57.65*	*57.54*
Difference	*3.27*	*4.53*	*1.36*	*1.49*
Rank	***2***	***1***	***4***	***3***
Optimum Condition	**P3**	**T3**	**F3**	**D1**

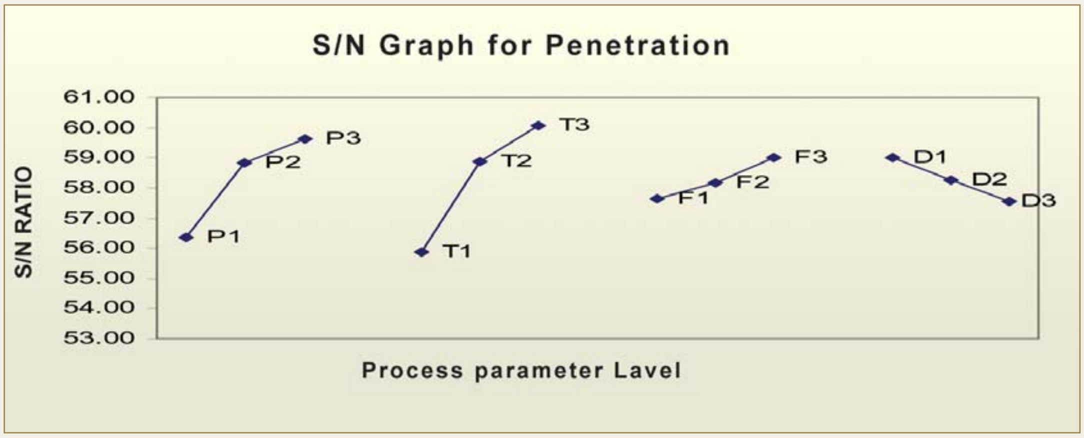

Fig. 8 : S/N curve for penetration

Confirmation test

Initially all the parameters were at level 1 with the S/N ratio of 54.07 db for depth of penetration &

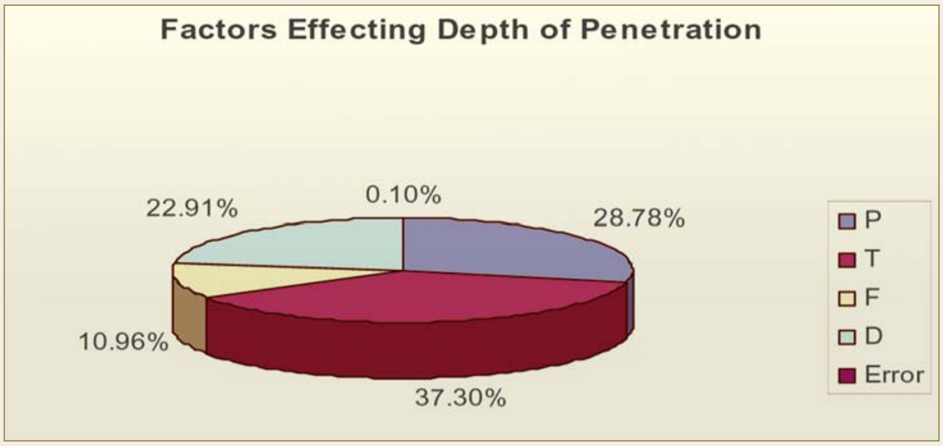

Fig. 9 : Effect of various parameters on depth of penetration

Table 8 : ANOVA table for depth of penetration

Symbol	**Sum of Square**	**Degree of Freedom**	**Mean Square**	**F Statistics**	**Contribution Percentage**
P	0.140	2	0.070	250.77	17.5
T	0.310	2	0.155	553.94	38.7
F	0.009	2	0.004	15.81	1.1
D	0.339	2	0.170	606.47	42.4
Error	0.003	9	0.003		0.3

Table 9 : S/N response table for depth / width ratio

Level	Average S/N Ratio (db)			
	P	**T**	**F**	**D**
1	-2.28	-2.98	-1.48	-0.28
2	-1.35	-1.04	-1.35	-0.33
3	-0.22	0.18	1.01	-3.23
Maximum	-0.22	0.18	-1.01	-0.28
Minimum	*-2.28*	*-2.98*	*-1.48*	*-3.23*
Difference	*2.06*	*3.16*	*0.47*	*2.95*
Rank	***2***	***1***	***4***	***3***
Optimum Condition	**P3**	**T3**	**F3**	**D1**

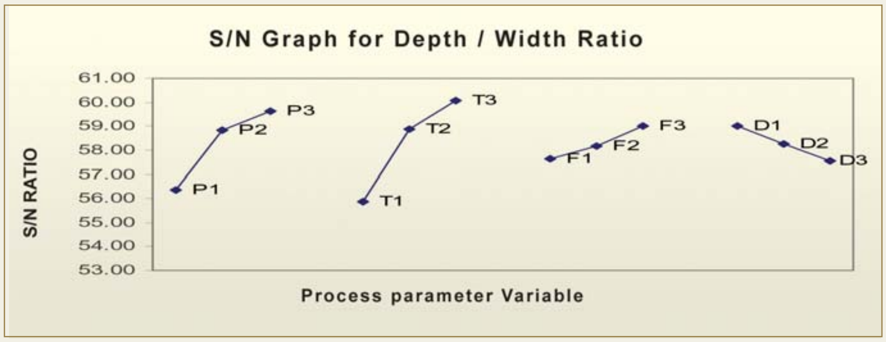

Fig. 10 : S/N curve for depth / width ratio

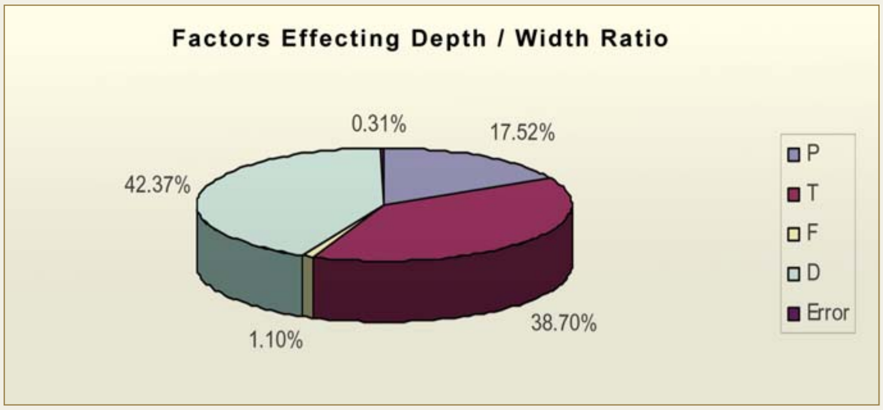

Fig. 11 : Effect of various parameters on depth / width ratio

-3.175 db for the aspect ratio. The optimum setting of process parameters for both are at peak power, pulse duration and frequency at level 3 and defocusing distance at level 1. But in this case, the depth of penetration will be so large, that it can puncture the weld bead. The optimal parameter setting was so chosen, as to give the maximum depth of penetration and the aspect ratio, without any defect like bead concavity and the cracking and reduction in welding setup time accurately. Hence peak power, pulse duration and defocusing distance are set at level 3 and the frequency kept at level 1. The improvement in the S/N ratio was seen as 59.08 db and -2.50 db for depth of penetration and the aspect ratio respectively.

Conclusions

1. All the factors namely peak power, pulse duration, defocusing distance and frequency have significant effect on bead geometry.
2. It was observed that pulse duration and peak power are the most important factors for determining the bead geometry.
3. The pulse duration is the predominating factor for increasing the depth of penetration. The peak power also has an important effect on it.
4. The defocusing distance has the greatest effect on aspect ratio but the affect of pulse duration is also comparable. The effect of peak power is also significant. The effect of frequency here is also the least.
5. The contribution of frequency has the least effect on both.
6. From the confirmation test, bead geometry can very well be predicted by the Taguchi method.
7. Nd-YAG laser welding gives consistent weld penetration in comparison with TIG welding.
7. Nd-YAG laser welding gives consistent weld penetration in comparison with TIG welding.

Acnoledgement

The authors wish to acknowledge the contribution made by our colleagues at AFFF, BARC, Tarapur in carrying out the experiments.

References

1. Effect of Pulsed Nd-YAG Laser Parameters On Penetration And Bead Geometry Of 304 Stainless Steel Welds - Amit Kulshrestha, Amit Gupta, Aniruddha Kumar, R.B.Bhatt, Md. Afzal,J. P.Panakkal and H.S. Kamath, Jan. 2008, IC-08, Chennai.
2. Mathematical Modelling for the prediction of penetration in 304 stainless steel plate using Pulsed GTAW – Amit Kulshrestha, R.B.Bhatt, J.P. Panakkal, H.S.Kamath, 15-17 Dec. 2005, National Welding Seminar – 2005, Bhilai.
3. End plug welding of nuclear fuel elements - AFFF experience - R.B.Bhatt, S.Singh, Aniruddha Kumar, Amit, Arun Kumar, J.P. Panakkal, H.S.Kamath, Dec. 2002, International Conference on Characterization and Quality Control of Nuclear Fuels, Hyderabad.
4. End plug welding of fast reactor fuel elements – R.B.Bhatt, S.Singh, Aniruddha Kumar, Amit, Arun Kumar, J.P. Panakkal ,H.S.Kamath, Jan.2003, National Welding Seminar – 2002, Kolkata.
5. End plug welding of MOX fuel elements at AFFF - R.B.Bhatt, S.Singh, Aniruddha Kumar, Amit, Arun Kumar, J.P. Panakkal, H.S.Kamath, Dec. 2003, Indian Nuclear Society – 2003, Kalpakkam.
6. Welding in fabrication of nuclear fuel elements – Amit, Aniruddha Kumar, S.Singh, R.B.Bhatt, J.P. Panakkal, H.S.Kamath. Jan. 2005, International Welding Conference, Mumbai.

ABOUT THE AUTHOR

Mr. Amit Kulshrestha graduated in Science from Dayalbagh University, Agra in 1988 and also holds the Masters degree in the field of Total Quality Management. He joined the Advanced Fuel Fabrication Facility, BARC, Tarapur in 1988. Since then, he has been involved in the production of different MOX elements. He has been involved in the fabrication of BWR and PHWR MOX fuel assemblies. Currently he is involved in the production of PFBR fuel elements. He played a major role in the installation, commissioning and qualification of Pulsed Nd:YAG laser welding system.

Mr. P.V. Suresh Varma received his B.E.(Metallurgy) from Andhra University in 2004. He graduated from BARC Training School (49th Batch) in 2006. Then he joined the Advanced Fuel Fabrication Facility, BARC, Tarapur. He is involved in the production of PFBR fuel elements. He played a major role in the installation, commissioning, qualification of Pulsed Nd:YAG laser welding system. His area of interest is laser material processing.

ABOUT THE AUTHORS

Mr. Amit Kumar Gupta received his B.Tech. (Mechanical) from AMU in 2005. He graduated from BARC Training School (48th Batch) in 2005 and joined the Advanced Fuel Fabrication Facility, BARC, Tarapur. Since then, he has been working in Fuel Rod Fabrication Group. Currently he is involved in the production of PFBR fuel elements. He is also engaged in installation and commissioning of fabrication line, for the production of fuel elements for AHWR critical facility. He is also working on the development of systems required for MOX fuel fabrication.

Mr. R.B. Bhatt received his B.E.(Metallurgy) from REC, Jaipur in 1988 and acquired M.Tech. degree in the field of Metal Joining from IIT, Chennai in 1991. After graduating from BARC Training School he joined the Advanced Fuel Fabrication Facility, BARC, Tarapur He was associated with development and fabrication of MOX assemblies for BWR and PHWR. Presently he is working as Superintendent, Fuel Rod Fabrication and is involved in the production of PFBR fuel elements. His main areas of interest are systems for nuclear fuel fabrication and welding technology. He is a life member of the Indian Institute of Welding and the Indian Nuclear Society.

Mr. Mohd. Afzal, Plant Superintendent, Advanced Fuel Fabrication Facility, BARC, Tarapur graduated from the 23rd batch of BARC Training School. He was responsible for the installation of new glove box lines for PFBR and AHWR critical facility, automation, maintenance of equipment in GB, bird cages design of equipment and plant operations. His area of expertise is installation and commissioning of fuel fabrication lines and automation systems, GB adaptation of equipment and plant operations.

Dr. Jose P. Panakkal, Head, Advanced Fuel Fabrication Facility, BARC, Tarapur is responsible for the manufacture and quality control of Plutonium based nuclear fuels for various types of reactors (BWRS, PHWRS, PFBR and AHWR Critical Facility). Dr. Panakkal has developed a number of methods for quantitative NDE/C of nuclear fuels and materials. He has published more than 155 papers including 68 in international journals. Dr. Panakkal was certified by the American Society for Nondestructive Testing (ASNT) as Level III in RT, UT and NRT in 1988. He was conferred the National NDT Award in R&D for his contributions to NDE applications in quality control of nuclear fuels, by ISNT in 1994.

Mr. H.S. Kamath graduated in metallurgical engineering from Regional Engineering College, Surathkal in 1969 and joined the Radiometallurgy Division, BARC in 1970 At present he is Director, Nuclear Fuels Group, BARC. Mr. Kamath has been associated with development of plutonium bearing nuclear fuels for the last 36 years which started with the fabrication of fuel for 'PURNIMA'. Mr. Kamath's main area of work is in the development of uranium-plutonium mixed oxide (MOX) fuels, for nuclear power programme. He has made important contributions in laboratory scale as well as industrial scale activities of MOX fuel manufacture for thermal and fast reactors.

RADIOLOGICAL SAFETY ASPECTS DURING OPERATION OF THE ADVANCED VITRIFICATION SYSTEM (AVS), AT TARAPUR

U.V. Deokar, P. Mathew, V.V. Kulkarni and M.D. Deshpande
Health Physics Division

This paper received the Best Paper Award (Oral Presentation) at the 28th IARP National Conference, held in Jodhpur, from Nov. 19-21, 2008

ABSTRACT

Advanced Vitrification System (AVS) is designed for vitrification of High Level Waste (HLW) generated in reprocessing plant operation, by using Joule Heating Ceramic Melter for the first time in India. Glass frits are used for vitrification. Health Physics Unit of WMF, Tarapur was involved in planning, setting up and operation of the radiological surveillance system, since the inception of the AVS facility. This paper summarizes the radiological safety aspects during production of 100 vitrified waste products in AVS. Vitrification of the concentrated High Level Waste started on 11th August, 2006 and completed 100 operations on 2nd Jan., 2008. Around 4.13 million curries (153070 TBq) gross beta activity, was vitrified in 100 canisters.

Key words: Joule Melter, Vitrification, Glass frits, Canister, Overpack, Storage Vault

Introduction

Initially, a Metallic Melter was used in vitrification technology for immobilization of HLW, which uses an induction heating system. It was a batch process with low throughput. Advanced Vitrification System (AVS) is designed for vitrification of High Level Waste by using Joule Heating Ceramic Melter. This is a continuous process with higher capacity. Glass frits are used for vitrification of high level radioactive waste in Joule melter. AVS joule melter furnace is located in Cell-2. High active aqueous wastes are generated from fuel reprocessing plants as first cycle raffinate of the PUREX process. The waste contains fission products and activation products i.e. more than 99.9 % of its inventory generated in the nuclear fuel cycle. This waste stream also contains traces of actinides, Pu, U, etc. To ensure that these long lived radioactive nuclides do not pose any hazard, this waste is to kept isolated from the biosphere, for extended periods of time. The two canisters are packed in an overpack and stored at interim storage facility under air cooling and constant surveillance.

Pre-Operational Health Physics activities

AVS joule melter furnace is located in Cell-2. Cell- 3 housed primary and secondary Evaporator. Prior to cold commissioning of AVS, all Area Gamma Monitors, Continuous Air Monitors are installed. All the installed monitors are connected to a Centralized Radiation Protection Console (CRPC) in control room and in HP shift room, to provide information continuously as well as on demand. Other portable Health physics instruments required for monitoring purpose were procured, calibrated and installed to increase the effectiveness of the monitoring programme. Stack monitor was installed, to monitor particulate activity discharged to environment through stack. Personal contamination monitors were placed in different plant areas, to detect personal contamination. Radiometric testing of walls and embedment of process cells was carried out. Plant areas were segregated into different zones, based on ventilation pattern and access control. Radiation survey and air activity measurement were carried out as a baseline data prior to commissioning.

Surveillance programme during operation of AVS

In the period from 11th August, 2006 to 2nd Jan., 2008, about 211 M^3 of HLW having gross β activity 25 Ci/l was received in AVS for vitrification. The radiological data, collective dose and effluent discharges during AVS operation are given in Table 1 and Table 2 respectively. Health physics surveillance was provided to monitor radiation field, air activity and contamination levels of pump house, waste transfer trench chambers, annulus air sampling system, off gas room housing process, off gas filters & blowers, etc.

HP coverage was given for around 5500 process samples. Sample bottle showed a radiation level of 0.01 to 280 mGy/h.

Fifty Over packs (AVS-1 to AVS-50) each containing two canisters (total gross β activity 153070 TBq and gross Alpha activity 507 TBq) was shifted to SSSF storage vault with HP coverage, for interim storage under air cooling and constant surveillance. Radiation survey of over pack was carriedout, by exposing DRD and TLD for a fixed time. The RL on overpack was estimated in the range of 50-82Gy/h. Transferable β contamination on over pack was 2 -3 Bq/cm^2.

In cell air samples were collected through in cell sampling line, at the time of each 100 pouring operations. The gross beta air activity observed was in the range of 20 - 365 KBq/m^3 and gross alpha 0.005 - 28.46 KBq/m^3 for initial 15 pouring. Later on in cell air sample during pouring showed 900 Bq/M^3 (β), 8.0 Bq/M^3 (α) due to installation of hood containment during pouring.

Monitoring of Melter Off Gas (MOG) Filter: Online Area Gamma Monitor is installed on MOG Filter, which gives continuous radiological status of Filter in Control Room, as well as in Shift HP Room. That helped in changing over the MOG filter before it crosses the limit of radiation level of 2.0mGy/h on shielding.

Monitoring of Exhaust Filter bank: Area Gamma Monitor (AGM) at a distance of 1.5 meter was installed, on duct of respective filter banks. The AGM will monitor the radiation level on duct and which is correlated with respect to the contact radiation level on the filter bank. The factor of 25 is found by exposing TLD and DRD on the contact of filter bank. This on line monitoring of exhaust duct of filters, gives continuous radiological status of filter banks. Thus it facilitated the plant operator to change over to the other filter banks, when radiation field on filter banks exceeds 2.0 mGy/h.

Modifications

Following modifications were carried out by plant management, to reduce personnel exposure, environmental releases and generation of secondary waste.

Installation of washable filter: During each Vitrification operation, there was built up of radiation field on Melter Off Gas (MOG) filter, to

350 - 450 mGy/h. To slow down the built up of radiation field on MOG filter, washable fiber glass filter assembly is installed before MOG filter, which has resulted in reduction of the activity load on MOG. The washing provision of this filter enables to reuse the filter for many times. The washed liquid can be handled as liquid waste in the plant process.

Installation of hood with filter: Due to open pouring in cell atmosphere, the radiation level of exhaust filter bank was increased up to 1 mGy/h. in each pouring operation. Also stack release was increased by 10 times the normal value during pouring operation. An enclosure in the form of hood is provided in the space between drain point of Joule melter and canister. The exhaust of hood was routed through composite filter assembly (PRE & HEPA) to cell exhaust. Hood was maintained under vacuum by blower. The arrangement was used during pouring operation and has given encouraging results. It has reduced stack release activity by 8 times and radiation level on exhaust filter bank by 5 times.

Work contributed for Collective Dose

Fifty MOG (Melter off Gas) filters, Two EOG filter & 8 Hood filters were disposed. Radiation levels on filter casing were in the range of 1.8-4.8 mGy/h. and radiation level on filter cartridge was in the range of 380 - 1020 mGy/h. Exposure incurred was 8.7 % of collective dose.

390 HEPA filters and 100 Pre filters were changed. Radiation level on HEPA filters as 1.7 - 3.6 mGy/h. Radiation level on PRE filters was 1.7 - 10 mGy/h. Air activity in exhaust filter bank room during changing of filters: 1 Bq/ M^3 β & β BDL.Total exposure contribution was 21.2 % of collective dose.

There were few safety-related unusual observations in the beginning, like Air activity releases during interruption of power. There was release of air activity in working areas of the plant, in the range of 2.5 – 9 DAC.h (β), which came down to normal level within 10 minutes due to plant ventilation.

Table 1 : Radiological data of AVS vitrification operation

Waste Receipt (M^3)	Waste concentrated (M^3)	Number of VWPS	Activity vitrified	
			Gross Alpha	Gross Beta
211	68.12	100	507 TBq (13.7 x 10^3 Ci)	153070 TBq (4.13 x 10^6 Ci)

Table 2 : Collective dose and effluent discharges

Collective dose (Per-mSv)	Environmental Releases			
	Stack discharge (particulate) % of annual authorized limit		Liquid Effluent % of annual authorized limit	
	Alpha	Beta	Alpha	Beta
431.4 (2.818 µSv /TBq)	3.27x 10^{-3}	1.176	BDL	2.78

Research and Development Activities

Overpack Monitoring: Two Canisters placed in one Overpack which is having Gross Beta Activity 80 - 100 KCi/Overpack and Gross Alpha Activity = 0.25 - 0.30 KCi/Overpack. One high range (1000 R/h) AGM is installed at 1m distance from the overpack at monitoring location. Radiation field of the overpack at contact was monitored, by exposing TLD and DRD for fixed period of time. Comparing the TLD, DRD and AGM readings, multiplication factor between AGM reading and overpack contact radiation level was worked out. The comparative radiation levels on contact of overpack was estimated by using TLD, DRD and AGM and are given in Table 3.

Table 3 : Comparative Study of radiation levels on Overpack

Overpack No.	Activity in Ci (β) (TBq)	Estimated radiation levels based on TLD in (Gy/h)	Estimated radiation levels based on DRD in (Gy/h)	Estimated radiation levels based on AGM Reading in (Gy/h)
AVS 1	26053	20	18	21
AVS 2	51000	35	33	34
AVS 3	58991	50	45	53
AVS 4	65997	54	50	49
AVS 5	71995	60	54	62
AVS 6	77269	63	57	55
AVS 7	80532	62	57	65
AVS 8	89893	63	58.5	61
AVS 9	89076	70	67.5	65
AVS 10	83330	68	63.5	62

AGM readings obtained were confirmed with TLD, DRD readings and also verified by theoretical tools.

Neutron monitoring of overpack cask: Neutron monitoring of cask containing overpack was carried out by using BF3 proportional counter and also by exposing SSNTD on the contact of the cask. The neutron field observed on cask was 70 to100 μGy/h. However it has not contributed significantly to personnel exposure.

Modified Annulus air sampling system: During the transfer of concentrated liquid, there was spill of liquid from annulus sampling line. The transfer line was abandoned with steam flushing to flush out hold up in the line. Annulus air sampling procedure was revised with free flow air sampling system, through cache pot and HEPA filter assembly.

Free Flow Annulus sampling is an arrangement consisting of cache pot (3Lt capacity), HEPA filter cartridge and vacuum pump, all connected to exhaust blower of Melter off gas system. During sampling, cache pot suction will be linked up to annulus sampling line, by suitable valving operation. An air flow rate of 40 – 60 lpm will be controlled, from free flow side of annulus sampling end, during waste transfer operation. Reading of area gamma monitor installed on cache pot, will be continuously monitored. Also radiation level on filter cartridge will be measured intermittently during transfer operation.

Acknowledgement

Authors are thankful to Mr. H.S. Kushwaha, Director, HS&E Group, Mr. K.A. Pendharkar, Head, Health Physics Division and Mr. Lal Chand, Head, FRSS, Health Physics Division for their guidance and encouragement. Authors also express sincere thanks to Mr. Kanwar Raj, Head, WMD and Mr. Y. Kulkarni, Superintendent WMF, Tarapur, for their valuable suggestions in the course of implementation of radiological procedures during operation of AVS. Authors also wish to acknowledge the valuable contribution of Mssrs. S.Sharma, K.K.Singh, A.R.Khot, Kamlesh and other HP staff of WMF, Tarapur.

ABOUT THE AUTHORS

Mr. U.V. Deokar joined BARC in 1990 after completion of one year Health Physics training course. He did his M.Sc. (by research) degree from Mumbai University in 1997. Initially up to 1995, he was associated with HP training course and internal dose monitoring programme. Presently he is associated with health and safety programme of Waste Management Facility (WMF) Tarapur as operational Health Physicist. He is responsible for radiological safety during operation and maintenance of WMF plants. He has several publications on radiological safety aspects of different operating plants of Waste Management Facilities.

Mr. P. Mathew joined BARC in 1992, after completion of Health Physics training course. He has vast experience in the field of radiological safety aspects and surveillance of waste management. He has worked extensively for remote measurement of radiation field of high level vitrified waste products. Currently he is working in Health Physics unit for the Advanced Vitrification System.

Mr. V.V. Kulkarni joined Health Physics Division, BARC in 1975, after graduation from Bombay University (B.Sc. (Chemistry-Physics)). He worked initially for two years in PP as Health Physics Supervisor with formal training at Modular Laboratories. He was posted to HP unit PREFRE in the year 1977. He gained experience as shift Health Physicist in PREFRE for two years. Later, he was posted to work in Waste Management Facilities, Tarapur. He has vast experience in providing radiological surveillance in Waste management operations involving different categories of solid waste packages and different categories of liquid waste streams. He has successfully completed many challenging jobs in waste management operations having high potential of overexposure. He has many publications on radiological monitoring experiences in Waste Management plants. Currently he is working in the capacity of Plant Health Physicist at WIP, AVS Tarapur.

Mr. M.D. Deshpande joined Health Physics Division 1973 after graduation (B.Sc. (Phy.)) from Shivaji University Kolhapur. After 2 years of initial experience in PP, he was posted at Tarapur in PREFRE. He acquired AMII Chem.E in 1985. At present with 36 years of experience as operational Health Physicist in Nuclear Fuel Recycle facilities, he holds the responsibility of Officer-in-charge of HP Unit BARC Tarapur. He has several publications on Thoron daughters, Pu in air monitoring, inhalation potential in reprocessing plants etc.

DETERMINATION OF ISOTOPIC COMPOSITION OF BORON AS $Rb_2BO_2^+$ BY TIMS

R.M. Rao, A.R. Parab, K. Sasibhushan and S.K. Aggarwal
Fuel Chemistry Division

This paper received the Best Paper Award (1st prize) in the Contributory Paper Session at the 13th ISMAS-WS 2008 held at BARC, Mumbai, during January 27-31, 2008

Introduction

The measurement of precise isotopic composition of boron is very important to nuclear industry, geochemistry, isotope hydrology and paleooceanography. PTIMS where boron is analyzed as polyatomic ions, $Cs_2BO_2^+$ or $Na_2BO_2^+$ and NTIMS where BO_2^- ions are monitored, are the most widely used techniques. Analysis at low masses of 42 and 43 (BO_2^-) or 88 and 89 ($Na_2BO_2^+$) can lead to poor precision, due to high fractionation effects. Attempts have been made to reduce the mass discrimination by using improved loading techniques[*1,2,3*]. However, ion source isotope fractionation which causes variable systematic error, limiting the accuracy of the isotopic ratio cannot be eliminated. Isotopic fractionation has been observed even during analysis of heavy mass ion $Cs_2BO_2^+$ at masses 308 & 309[*4*]. Though Rubidium is not monoisotopic like Sodium or Cesium, analysis of Boron as $Rb_2BO_2^+$ has certain advantages. 1) The mass of the molecular species $Rb_2BO_2^+$ is reasonably high (212-213) resulting in less isotopic fractionation. 2) Unlike $Cs_2BO_2^+$, simultaneous collection of ions is possible 3) There exists a possibility of correcting for isotope fractionation effects, using the known isotopic composition of Rubidium as internal standard. However as Rubidium has two isotopes, a number of species, 36 vs. 12 for $Na_2BO_2^+$ and $Cs_2BO_2^+$ are produced. A detailed theoretical study on the use of $Rb_2BO_2^+$ ions for isotopic analysis of Rubidium and Boron is discussed in [*5*]. A number of studies are reported for formation of $Na_2BO_2^+$, $Cs_2BO_2^+$ for analysis of boron in different samples and $Li_2BO_2^+$ for isotopic analysis of Li and B, but only a few studies have been carried out on the use of $Rb_2BO_2^+$ species [*6,7*]. In most of the cases, the observed ion intensity and isotope ratio of boron depends on Boron-to-alkali metal atom ratio. The loading technique and the reagent used also affects the ion intensity. For example, when isotopic standard of rubidium in the form of Rubidium chloride was used with boric acid, the ion current yield for $Rb_2BO_2^+$ was very low[*6*]. Xaio et al[*7*] reported reaction of rubidium carbonate with boric acid and use of graphite slurry on the tantalum single filament to give ion current of more than 10^{-11} A, for 2 μg boron. This is expected as boric acid which is a weak acid can only react with a reasonably strong base, to produce borate salt and water.

The present work focuses on the experimental methods for generating $Rb_2BO_2^+$ ions and explores the possibility of a correlation between the K-factor(mass discrimination factor) for boron isotope ratios and the observed isotopic composition of rubidium. NIST-SRM-951 which is in the form of boric acid with $^{10}B/^{11}B$ isotopic ratio of 0.2473 ± 0.0002 and Rubidium carbonate with natural isotope abundance of rubidium was used in this work.

Experimental

A state-of-the art, multicollector TIMS with nine adjustable Faraday cups was used for the analysis. Rubidium borate was obtained by reaction of boric acid with rubidium carbonate. Different mixtures of Rb(Natural) and boron(SRM-951) were prepared with boron/rubidium 10 to 0.05. The solutions were loaded as a boronmannitol complex on Ta filament. The filament was coated with about 100μg graphite slurry in 1:1 ethanol solution, on which the sample solution was loaded and dried at 1.6 A for 5 minutes. In the ion source, the filament was slowly heated to 1.6A in ten minutes and after degassing for ten more minutes, the sample filament was further heated to obtain $Rb_2BO_2^+$ ions. In the present experiment, the Faraday cups were adjusted to simultaneously collect ions from m/q 212 to 217. The ions were integrated for 5 seconds in each scan and typically the data was acquired in three blocks of 12 scans each. Two to three acquisitions of the same loaded sample at higher filament current, were also carried out.

Results and Discussion

For 1.5 to 2 μg boron on the filament, intensity of more than 1x 10^{-11} A was obtained, for the ^{11}B for all solutions, except B/Rb-10 and 0.05. The $^{10}B/^{11}B$ ratio of the standard was found to vary from 0.2465 to 0.2470, depending on the filament current during analysis and on the B/Rb atom ratio.

The different species obtained at masses 212 to 217 are given in Table 1 along with their abundances for natural boron and rubidium. Though rubidium borate species upto m/q 221 are produced, $Rb_2B^{16}O_2$ species which constitute the major species are obtained only from m/q 212 to 217.

As can be seen from Table 1, measured ion intensity ratio of the molecular pair at m/q 212/213 ($^{212}I/^{213}I$) gives measured $^{10}B/^{11}B$ atom ratio and the ion intensity ratio of the molecular pair at m/q 215/213, ($^{215}I/^{213}I$) = 2 x ($^{85}Rb/^{87}Rb$ + $^{18}O/^{16}O$), obtained by ignoring the negligible contributions of the molecular ions of very low abundance. Using natural isotopic composition of Rb ($^{85}Rb/^{87}Rb$ = 2.593) and O ($^{18}O/^{16}O$ =0.002), internal normalization technique was initially used, to correct for fractionation. However, no improvement in the precision of $^{10}B/^{11}B$ was observed. This is because, the fractionation factor for a species is influenced by the individual elements constituting the molecular species. Therefore, the fractionation factor K for the molecular species $^{85}Rb_2{}^{11}B^{16}O_2/{}^{85}Rb_2{}^{10}B^{16}O_2$ = $^{11}B/^{10}B$ atom ratio and ($^{85}Rb^{87}Rb^{11}B^{16}O_2$ + $^{85}Rb_2{}^{11}B^{16}O^{18}O$) / $^{85}Rb_2{}^{11}B^{16}O_2$ =($^{85}Rb/^{87}Rb$ + $^{18}O/^{16}O$) atom ratio are different. Thus, *in situ* normalization is not possible. However, a correlation

Table 1: Different molecular species of rubidium borate

S.No.	m/q	Major species	Abundances (nat Rb &nat B)
1	212	$^{85}Rb_2{}^{10}B^{16}O_2$	10.28
2	213	$^{85}Rb_2{}^{11}B^{16}O_2$, $^{85}Rb_2{}^{10}B^{16}O^{17}O$	41.57
3	214	$^{85}Rb^{87}Rb^{10}B^{16}O_2$, $^{85}Rb_2{}^{10}B^{16}O^{18}O$, $^{85}Rb_2{}^{11}B^{16}O^{17}O$	7.99
4	215	$^{85}Rb^{87}Rb^{11}B^{16}O_2$, $^{85}Rb_2{}^{11}B^{16}O^{18}O$, $^{85}Rb^{87}Rb^{10}B^{16}O^{17}O$	32.11
5	216	$^{87}Rb_2{}^{10}B^{16}O_2$, $^{85}Rb_2{}^{87}Rb^{10}B^{18}O^{16}O$, $^{85}Rb^{87}Rb^{11}B^{16}O^{17}O$	1.55
6	217	$^{87}Rb_2{}^{11}B^{16}O_2$, $^{87}Rb_2{}^{10}B^{16}O^{17}O$, $^{85}Rb^{87}Rb^{11}B^{16}O^{18}O$	6.32

between the fractionation pattern of the two monitoring pairs (m/q 213/212 for $^{10}B/^{11}B$) and (m/q 215/213 for $^{85}Rb/^{87}Rb + ^{18}O/^{16}O$) could be achieved. Jason et al [8] had obtained a linear relationship between the measured $^{18}O/^{16}O$ ion intensity ratios and measured $^{11}B/^{10}B$ ion intensity ratios and used the linear relationship to correct for fractionation during BO_2^- analysis. A similar linear relationship was also observed, during $Rb_2BO_2^+$ analysis.

It was observed that larger amounts of Rb on the filament and higher filament current, resulted in higher fractionation for both $^{87}Rb/^{85}Rb$ and $^{10}B/^{11}B$ atom ratios. The data obtained from the analysis of SRM-951 with different B/Rb ratios, was used for obtaining the relationship between the fractionating $^{213}I/^{212}I$ and $^{215}I/^{213}I$. As shown in Figs. 1 and 2, it was observed that both $^{213}I/^{212}I$ (i.e. $^{11}B/^{10}B$) and $^{215}I/^{212}I = {}^{213}I/^{212}I \times {}^{215}I/^{213}I$ {i.e. $^{11}B/^{10}B \times 2 \times (^{87}Rb/^{85}Rb + ^{18}O/^{16}O)$} vary linearly with $^{215}I/^{213}I$. A correlation between the mass discrimination factor, $K = (^{10}B/^{11}B)_{true} / (^{10}B/^{11}B)_{observed}$ and the $^{215}I/^{213}I$ could be obtained, by using isotope reference material SRM-951. Fig. 3 shows the correlation between K and $^{215}I/^{213}I$ and Fig. 4 which

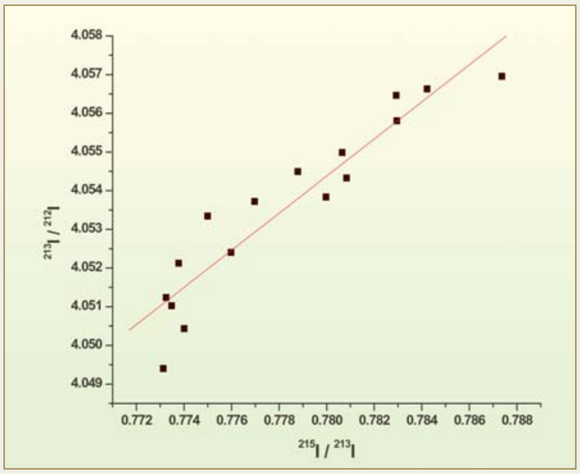

Fig.1: Relationship between the ion intensity ratios $^{213}I/^{212}I$ vs $^{215}I/^{213}I$

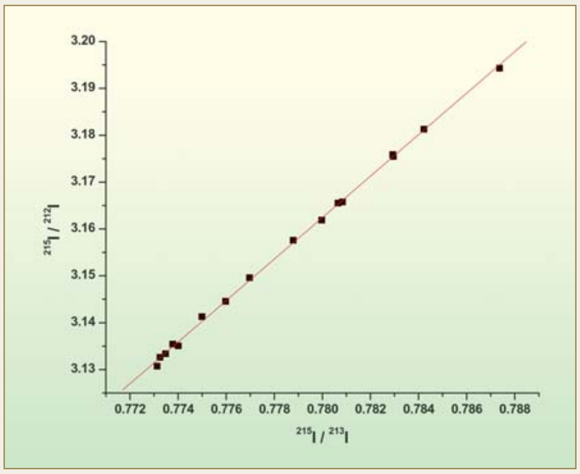

Fig. 2: Relationship between the ion intensity ratios $^{215}I/^{212}I$ vs $^{215}I/^{213}I$

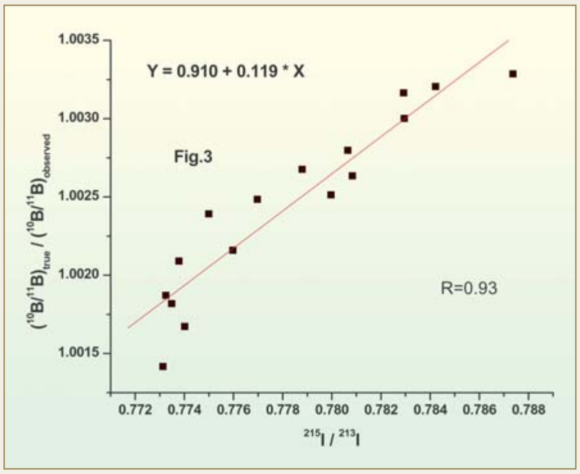

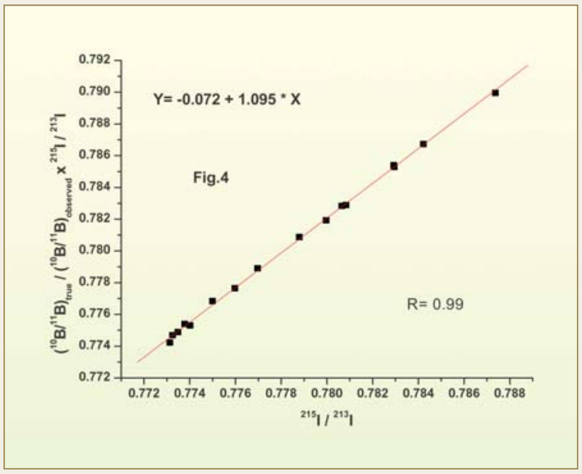

Figs. 3 and 4: Based on the linearity observed in Figs. 1 & 2 showing the linearity of K- factor of boron with the observed $^{215}I/^{213}I$

shows improved regression coefficient, is a plot of K x $^{215}I/^{213}I$ Vs $^{215}I/^{213}I$. The certified value of 0.2473 for $^{10}B/^{11}B$ was used for obtaining the K factor. Using the equation obtained, a correction for fractionation can be carried out, to improve the precision of the analysis. It should be noted that since the same rubidium solution is used in all samples, it is not necessary to obtain the K-factor for $^{87}Rb/^{85}Rb$ + $^{18}O/^{16}O$, thus eliminating the need for isotopic standard of rubidium. The equation obtained from the plot of Fraction Factor for Boron vs $^{215}I/^{213}I$ also makes the calculation for corrected $^{10}B/^{11}B$ atom ratio in unknown samples easy and simple. Also because of high abundance of the molecular ion beam of interest at m/q 212, 213, 214, 215 and negligible abundance of the isobaric species at these masses, the equation $^{213}I/^{212}I = {}^{10}B/^{11}B$ & $^{215}I/^{213}I = 2 \times (^{87}Rb/^{85}Rb + {}^{18}O/^{16}O)$ is easily derived with minimum uncertainity leading to increased reliability of the method [*9*].

Validation of the Correction method

A few irradiated alloy samples analyzed by $Na_2BO_2^+$ method for $^{10}B/^{11}B$ were also analyzed by $Rb_2BO_2^+$ method and correction for fractionation carried out using the linear equation obtained. The observed $^{215}I/^{213}I$ and $^{213}I/^{212}I$ during analyses were used, for obtaining the correction. The correction was carried out for each analysis and not on individual scans. The results are given in Table 2. The Table also gives the data obtained for a natural boric acid sample and boron isotopic standard SRM-951 with different B/Rb atom ratio. Each sample was analyzed at two or more filament currents, with each analysis consisting of 3 blocks with a total of 36 scans. Column 3 of the Table gives the $^{10}B/^{11}B$ ratio obtained for each analysis with the uncertainty given in parenthesis. Column 4 gives the agreement among the different analyses of the same sample loading. As can be seen, the analysis at higher filament current leads to increased isotope fractionation and increases the uncertainity of the isotopic ratio. Column 5 gives observed 2 x ($^{87}Rb/^{85}Rb$ + $^{18}O/^{16}O$) ratio obtained during each analysis with the uncertainity in the ratio given in parenthesis. Column 6 gives the $^{10}B/^{11}B$ ratio obtained through internal normalization

Table 2: $^{10}B/^{11}B$ ratio observed and corrected for fractionation in different samples

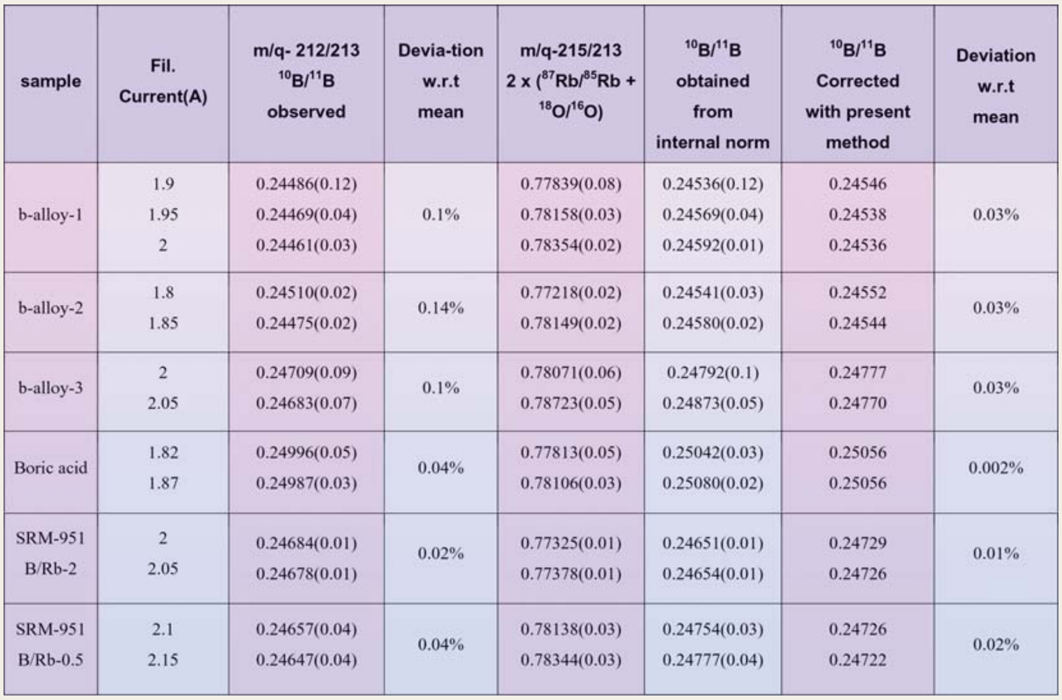

sample	Fil. Current(A)	m/q- 212/213 $^{10}B/^{11}B$ observed	Devia-tion w.r.t mean	m/q-215/213 2 x ($^{87}Rb/^{85}Rb$ + $^{18}O/^{16}O$)	$^{10}B/^{11}B$ obtained from internal norm	$^{10}B/^{11}B$ Corrected with present method	Deviation w.r.t mean
b-alloy-1	1.9	0.24486(0.12)	0.1%	0.77839(0.08)	0.24536(0.12)	0.24546	0.03%
	1.95	0.24469(0.04)		0.78158(0.03)	0.24569(0.04)	0.24538	
	2	0.24461(0.03)		0.78354(0.02)	0.24592(0.01)	0.24536	
b-alloy-2	1.8	0.24510(0.02)	0.14%	0.77218(0.02)	0.24541(0.03)	0.24552	0.03%
	1.85	0.24475(0.02)		0.78149(0.02)	0.24580(0.02)	0.24544	
b-alloy-3	2	0.24709(0.09)	0.1%	0.78071(0.06)	0.24792(0.1)	0.24777	0.03%
	2.05	0.24683(0.07)		0.78723(0.05)	0.24873(0.05)	0.24770	
Boric acid	1.82	0.24996(0.05)	0.04%	0.77813(0.05)	0.25042(0.03)	0.25056	0.002%
	1.87	0.24987(0.03)		0.78106(0.03)	0.25080(0.02)	0.25056	
SRM-951 B/Rb-2	2	0.24684(0.01)	0.02%	0.77325(0.01)	0.24651(0.01)	0.24729	0.01%
	2.05	0.24678(0.01)		0.77378(0.01)	0.24654(0.01)	0.24726	
SRM-951 B/Rb-0.5	2.1	0.24657(0.04)	0.04%	0.78138(0.03)	0.24754(0.03)	0.24726	0.02%
	2.15	0.24647(0.04)		0.78344(0.03)	0.24777(0.04)	0.24722	

using the value of 0.77531 for 2 x (^{87}Rb/^{85}Rb+^{18}O/^{16}O) and the observed value at m/q 215/213. As can be seen, the *in situ* normalization does not result in any improvement in the precision between the different analyses. Column 7 gives the corrected ^{10}B/^{11}B ratio obtained from the linear equation from either Fig. 3 or 4. The correction improves the precision between the analysis by a factor of 2 to 3 as can be seen from columns 4 and 8.

Conclusion

$Rb_2BO_2^+$ method is an attractive viable alternative to $Cs_2BO_2^+$ method as its mass is reasonably high and also suitable for simultaneous collection of different ionic species. In addition to this, the fractionation effects on the isotopic ratio of boron can be corrected, by using the linear relationship between the fractionation factors of boron isotopic ratio and rubidium isotopic ratio.

References

1. N. G. Hemming, G. N. Hamson, *Chemical Geology* 114(1994) 147.
2. S. Eisenhut, K. G. Heumann, A.Vengosh, Fresenius *J. Anal. Chem.* 354(1996) 903.
3. R. M. Rao, A. R. Parab, K.Sasi Bhusan and S. K. Aggarwal, *CP-7, 12th ISMAS-WS* 2007.
4. K. L. Ramakumar, P. S. Khodade, A. R. Parab, S. A. Chitambar, H. C. Jain, *J. Radioanal.Nucl. Chem*. 107 (1985) 215.
5. S. K. Aggarwal & H. C. Jain BARC/1994/E/028.
6. R. Gensho & M. Honda, *Mass Spectroscopy(Japan)* 19 (1971)134.
7. Y. K. Xiao, L. Jin and Hai-Ping Qi, *International J. of Mass Spectrometry and Ion Processes* 107 (1991)205.
8. Jason Jiun-San Shen and Chen-Feng You, *Anal. Chem.* 75(2003) 1972.
9. B. P. Datta, A. R. Parab, P. S. Khodade and H. C. Jain, *International J. of Mass Spectrometry and Ion Processes*, 116(1992)87.

ABOUT THE AUTHORS

Ms. R.M. Rao joined the Mass Spectrometry Section of FCD, BARC in 1984 after completing her M.Sc(Chemistry) from I.I.T, Mumbai. She has been working in the field of Inorganic Mass Spectrometry for precise isotopic analysis and determination of concentration of various elements of importance in Nuclear Technology. She has more than 40 research papers in various journals and symposia. Her other areas of interest are HPLC, Alpha spectrometry and Microwave assisted digestion.

Mr. A. R. Parab is working in the Mass Spectrometry Section of FCD, BARC. His scientific interest is in the area of thermal ionization Mass Spectrometry and alpha spectrometry for precise isotopic analysis of elements which are important in nuclear technology. He has more than 60 research publications in various journals and symposia.

ABOUT THE AUTHORS

Mr. K. Sasibhushan is working in the Mass Spectrometry Section of FCD, BARC since 2006, after graduating in Chemistry from Andhra University. His present nature of work includes Thermal Ionization Mass Spectrometry of U, Pu, Ga, lanthanides and B. He is also working in the field of alpha spectrometry.

Dr. S. K. Aggarwal is Head, Fuel Chemistry Division, BARC since July 2005 and is a Professor of Chemistry at Homi Bhabha National Institute (HBNI). He joined the 16th Batch of BARC Training School in 1972 and received the Homi Bhabha Award. He did his Ph.D. from Mumbai University and his Post-Doctoral training at University of Virginia, USA. Dr. Aggarwal was honoured with the Eminent Mass Spectrometrist Award by the Indian Society for Mass Spectrometry (ISMAS) in 1996 and was recently conferred with the DAE Special Contributions Award, 2006. He is a specialist in the field of atomic mass spectrometry and alpha spectrometry and is interested in various mass spectrometric techniques. His other areas of interest include laser-based analytical techniques, Electrochemistry, X-ray spectroscopy and Separation techniques like HPLC, solvent extraction etc. He has more than 100 publications in reputed international journals and is a recognized Ph.D. guide of Mumbai University and of HBNI.

बीएआरसी न्यूज़लैटर
BARC NEWSLETTER

STUDIES ON THE APPLICATION OF INTERNAL NORMALIZATION IN THE DETERMINATION OF URANIUM ISOTOPIC RATIO USING OXYGEN ISOTOPIC RATIO

S.K. Aggarwal, D. Alamelu, A.R. Parab and K. Sashi Bhushan
Fuel Chemistry Division

This paper was conferred the Best Paper Award (2nd prize) in the Contributory Paper Session at the 13th ISMAS-WS 2008 held at BARC, Mumbai during January 27-31, 2008

Introduction

Thermal Ionization Mass Spectrometry is an internationally recognized mass spectrometric technique, for the determination of isotopic composition and concentration of various elements in a variety of matrices. It is a highly preferred technique, due to its ability to provide data with high precision and accuracy. But it has some limitations due to the inherent time-dependent isotope fractionation, in the ion source. A variety of methodologies have been developed and employed, to account for this isotope fractionation. These are (i) external normalization (ii) internal normalization and (iii) total evaporation and ion current integration. Each of the methods has its inherent advantages as well as limitations.

In this paper, we describe a new methodology of internal normalization, to correct for the isotopic fractionation of U, using UO^+ ions for obtaining isotopic analysis data for U. The methodology is promising for application to U isotopic analysis by TIMS. The suitable conditions for application of this method are also discussed in this paper.

Experimental

Certified reference materials of U namely NIST CRM-005, CRM-010, CRM-050, CRM-200 and CRM-500 were used in this work. About 1 mL of the solutions containing U in the range of 1 to 2 mg was loaded on to high purity tantalum filament, employed as the evaporation filament in the double filament assembly. High purity rhenium was used as the ionization filament. The samples were analyzed in a thermal ionization mass spectrometer, equipped with multiple Faraday cup detection system, under static mode of multi-collection. Instead of the conventionally employed U^+ ions, UO^+ ions were employed for acquiring the isotopic composition data of U.

Results and Discussion

The filament heating conditions for obtaining a stable signal of UO^+ ions, were initially obtained by studying the variation in the ion current, as a function of both evaporation filament current at constant ionization filament current, as well as with that of ionization filament current at constant evaporation filament current. This data is shown in Figs. 1 and 2 respectively. As can be seen, significant signal of UO^+ is obtained at lower ionization filament currents and higher vaporization currents respectively. It should also be noted, that this type of behaviour was only observed when Ta was used as the evaporation filament and not observed in case of rhenium filament. This may be due to the fact, that as the samples are loaded in atmosphere and treated under red hot conditions, significant amount of Ta is also converted as oxide, which provides a stable supply of oxygen for the formation of UO^+ ions during analysis.

Based on these studies, the conditions for analysis of U as UO^+ ions were optimized and employed for the further analysis of all the certified standards of U. U isotopic ratio in the sample $^{235}U/^{238}U$ was obtained, using m/q of 251 and 254 respectively, while that of Oxygen (i.e $^{18}O/^{16}O$) was obtained, using data of m/q 256 and 254 respectively.

The fractionation in U, O was calculated, using the certified ratios for $^{235}U/^{238}U$ and the oxygen isotopic ratio of 0.002096, determined previously in our laboratory. A plot between Oxygen fractionation [$(256/254)_{obs}/(18O/16O)_T$] with respect to the product of U fractionation and Oxygen fractionation [$(256/251)_{obs}/((^{238}U/^{235}U)_{cert}(18O/16O)_T$] is shown in Fig. 3. As can be seen, the correlation between O K-Factor with the product of K-factors for U & O is linear for the conditions of analysis applied in this study. Knowing the K-factor for oxygen in the sample (obtained from m/q ratio 256/254), one can obtain the combined fractionation of both U & O which can then be applied for correcting the K-factor for U (in the ratio 256/251).

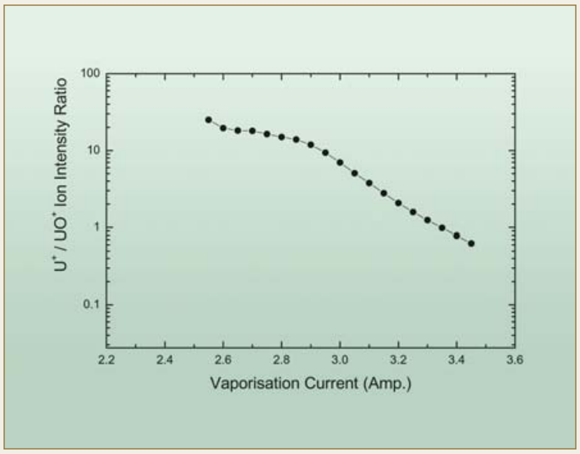

Fig.1: Variation in the ion intensity ratio of U^+/UO^+ as a function of vaporization filament current at constant ionization filament current

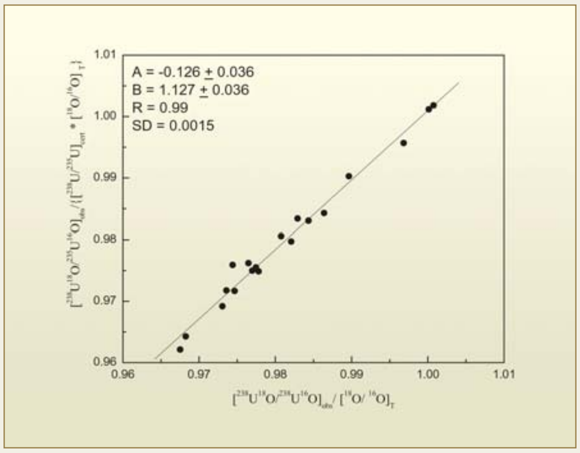

Fig. 3: Correlation between fractionation of O and the product of fractionation of U & O

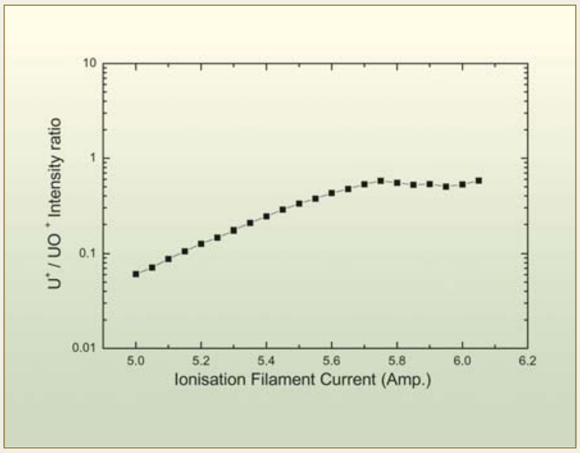

Fig. 2: Variation in the ion intensity ratio of U^+/UO^+ as a function of ionization filament current at constant vaporization filament current

Another correlation with respect to O fractionation/ mass unit (i.e. 2) vs. UO fractionation per mass unit (i.e 5) was also tried, using this data. This is shown in Fig. 4. This also gave a linear relation and can also be applied for correcting the isotope fractionation in U. Knowing the K-factor/mass unit for oxygen in the sample (obtained from m/q ratio 256/254), one can obtain the K-factor for UO which can then be applied for correcting the K-factor for UO (in the ratio 254/251). The precision in U isotopic analysis obtained from 256/251 ratio would be poorer, since ^{18}O is the less abundant isotope, while the second correlation would give a better precision on the isotopic ratio of

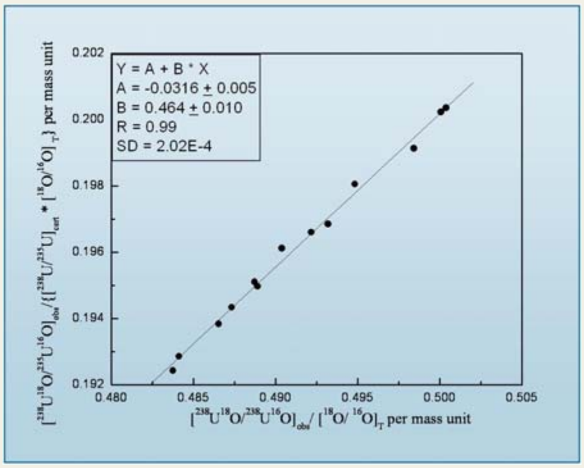

Fig. 4: O fractionation per mass unit vs. UO fractionation per mass unit

U in addition to correcting for isotope fractionation. These correlations were then applied for a number of independent U analyses (of certified standards). Both the correlations were found to correct for fractionation of U in the analysis significantly. In some of the analyses, it was found that this method was not applicable. In these analyses, it was also found that the O ratio measured from 256/254 was not stable or was decreasing from one block to another. It was also observed, that the fractionation correction by this internal normalization improved the results whenever the oxygen isotopic ratio between individual blocks was stable or showed an increasing trend and yielded poorer results, whenever the oxygen isotopic ratio measured between individual blocks was not constant and showed decreasing trend. This can be interpreted as while there was increasing trend, significant amount of oxygen compound between Ta and U was present on the filament for analysis, which provided a positive fractionation, while in the other case, the fractionation trend is negative for oxygen indicating the non-availability of oxygen supply from the intermetallic (U-Ta) Oxide compound, formed on the surface of the filament. This variation is possible since the loading of the sample is done manually and slight variations from loading (ie heating conditions employed for drying the sample) is probable.

While the results of this study are interesting, for regular application in case of analysis of actual samples, the conditions of analysis may tend to vary which would reduce the confidence in the application of this methodology. The intermetallic oxide compound formed on the filament has to be characterized by suitable means, for obtaining a suitable condition for loading can be optimized, for increasing the confidence on application of this methodology on a regular basis.

Acknowledgements

The authors are thankful to Dr. V. Venugopal, Director, Radiochemistry and Isotope Group, for his interest and support.

About the Authors

Dr. S. K. Aggarwal is Head of the Fuel Chemistry Division, BARC since July 2005 and is a Professor of Chemistry at Homi Bhabha National Institute (HBNI). He joined the 16th Batch of BARC Training School in 1972 and received the Homi Bhabha Award. He did his Ph.D. from Mumbai University and had his Post-Doctoral training at University of Virginia, USA. Dr. Aggarwal was honoured with the Eminent Mass Spectrometrist Award by the Indian Society for Mass Spectrometry (ISMAS) in 1996 and was recently conferred with the DAE Special Contributions award 2006. He is a specialist in the field of atomic mass spectrometry and alpha spectrometry and is interested in various mass spectrometric techniques. His other areas of interest include laser-based analytical techniques, Electrochemistry, X-ray spectroscopy and Separation techniques like HPLC, solvent extraction etc. He has more than 100 publications in reputed international journals and is a recognized Ph.D. Guide of the Mumbai University and of HBNI.

Dr. (Ms) D. Alamelu obtained her M.Sc. Degree in Physics from Annamalai University and Ph.D. Degree in Chemistry from Mumbai University. After graduating from 38th Batch of Training School, BARC, she joined Mass Spectrometry Section of the Fuel Chemistry Division in 1995. Initially, she was involved in the indigenous development of Time of Flight Mass Spectrometer. Her other areas of interest include thermal ionization mass spectrometry, alpha spectrometry and Laser Induced Breakdown Spectroscopy (LIBS).

Mr. A. R. Parab is working in the Mass Spectrometry Section of FCD, BARC. His scientific interest is in the area of thermal ionization Mass Spectrometry and alpha spectrometry for precise isotopic analysis of elements which are important in nuclear technology. He has more than 60 research publications in various journals and symposia.

Mr. K. Sashi Bhushan is working in the Mass Spectrometry Section of FCD, BARC since 2006, after graduating in Chemistry from Andhra University. His present nature of work includes Thermal Ionization Mass Spectrometry of U, Pu, Ga, Lanthanides and B. He is also working in the field of alpha spectrometry.

DEVELOPMENT OF CARBON PASTE ELECTRODE: APPLICATION TO THE DETERMINATION OF HEAVY METALS USING VOLTAMMETRIC METHODS

A.K. Satpati, S. Sahoo and P.V. Ravindran
Analytical Chemistry Division

This paper received the Third Best Paper Award in a Symposium "Discussion Meet on Electroanalytical Techniques and their Applications" (DMELANTE-2008) held at Munnar, Kerala, during Feb. 25-28, 2008

ABSTRACT

Carbon paste electrode (CPE) was developed from spectroscopic grade graphite powder, after suitable modifications. The appropriate contents of the organic binder and wax were optimized, for better response of the electrode. Electrochemical Impedance Spectroscopy was carried out, to derive the information about the resistive-capacitive behaviour of the electrochemical interface, formed between carbon paste electrode and aqueous solution. Potential of zero charge (PZC) of the electrode-electrolyte interface, obtained was –0.20 V (vs SCE) in 0.1 M HCl solution. Morphology of the electrode surface was examined. It is observed that wax impregnated carbon paste electrode, developed in the present case, gave low background current and the paste was stable for three months and easily renewable. The electrode is stable in the potential window of -1.2V to 0.8V in 0.1M HCl solution. Renewing of the surface and obtaining a stable background, is an important issue for the determination of Hg, using solid electrodes. Use of carbon paste electrode, avoids the renewability problem and also provides excellent sensitivity. A method has been developed, by optimizing the electrochemical parameters, for the determination of Hg at ultra-trace levels. Effect of the deposition time, deposition potential and also the supporting electrolyte has been studied. The deposition potential in the present case was chosen to be –0.8V (SCE) and a well-defined Hg oxidation peak is observed at 0.125 V (SCE). The electrode also performed well, when used for simultaneous determination of heavy metals like Zn, Cd, Pb, Cu in aqueous solutions. The method has been used for determination of heavy metals in various water samples and aurvedic medicines.

Introduction

Chemically Modified Electrodes (CMEs) are of interest, because they can exert more direct control over the chemical nature of an electrode. There are IUPAC definitions and terminology, and also preparation methods of CME, which have been described and classified in a recent report [1]. Numerous important applications of CMEs are - solar energy conversion and storage, selective electro-organic synthesis, molecular electronics, electrochromic display devices, corrosion protection, and electroanalysis [1]. Hanging mercuric drop electrode (HMDE) is widely used in electrochemical stripping analysis, due to readily renewable, reproducible surface, high over potential for hydrogen evolution and its ability to dissolve many of the metals [2,3]. But in recent times, use of metallic mercury as an electrode is a debatable issue, because of the toxicity of this liquid metal [4-6]. Carbon paste is an excellent alternate material to Hg electrode, for the determination of heavy metals in trace levels [7, 8]. In the present study, carbon paste electrode was developed for its use in various electrochemical applications, as the working electrode. The interfacial behaviour of the electrode was observed using electrochemical impedance spectroscopy. The method for the determination of Hg at ultra trace level was also developed, in the present study. The electrode was also used to check its performance for the determination of Zn, Cd, Pb and Cu simultaneously.

Instrumentation and Chemicals

The electrochemical experiments were carried out using an Eco-Chemie (The Netherlands) make electrochemical system Autolab PGSTAT 100 running with GPES (General Purpose Electrochemical System) version 4.8, software. Voltammetric curves were recorded at room temperature (25^0 C) in a three-electrode cell set-up. The working electrode was wax impregnated carbon paste electrode, with 2mm diameter, saturated calomel (SCE) was used as a reference electrode and platinum wire as the counter electrode. Spectroscopic grade graphite powder was used, for the preparation of carbon paste electrode. All acids and general chemicals used in the present study, are of analytical-reagent grade. Nano pure water was used in all the experiments and also for the washing of the electrochemical cell set up. All the electrochemical potentials reported, measured and applied in the present study, are with respect to the saturated calomel as reference electrode.

Results and Discussion

Spectroscopic grade carbon powder was heated at 400^0 C for 4 hrs in inert atmosphere, taking 0.5 g of the powder in a quartz boat. After heating, the powder was transferred to a beaker, containing high purity paraffin dissolved in n-hexane. The mixture was kept under the fume hood pressure and the n-hexane was

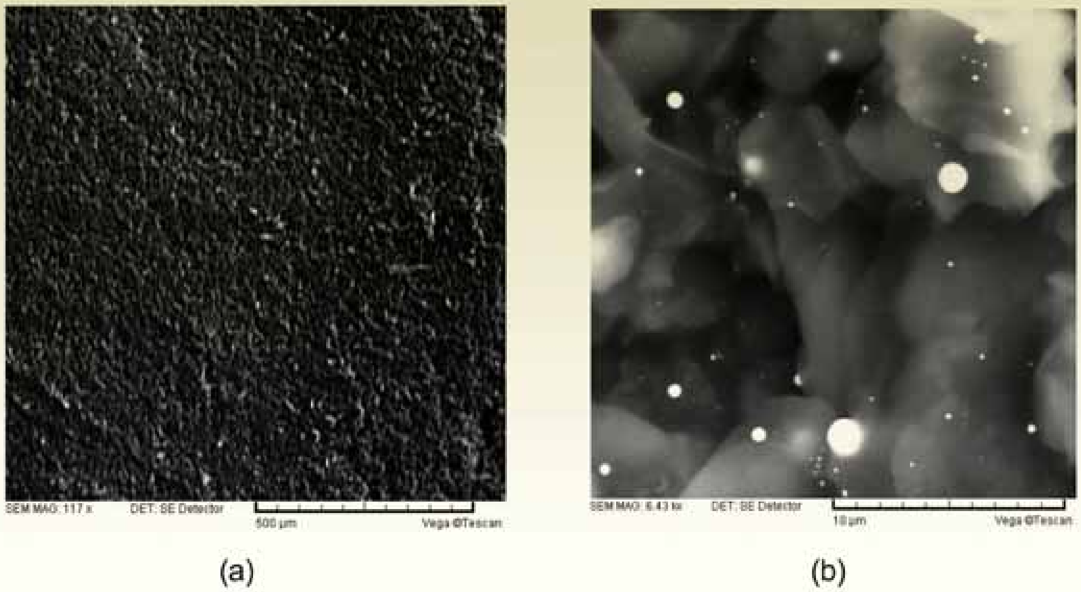

Fig.1: SEM micrograph of bare wax impregnated carbon paste (a) and the Hg thin film modified carbon paste (b) surface.

allowed to evaporate, at the end the mixture and was kept under hot air blower for complete removal on the n-hexane. Heating removes the adsorbed gases from the surface of the carbon paste and upon paraffin impregnation, the re-adsorption of gases is minimized. In this study ~1.5 % (weight %) of paraffin wax was added to the carbon powder. After paraffin impregnation, the required quantity of silicone oil was added as the binder (25% of the mass of modifier and carbon powder) and ground well, to get a homogeneous paste. The carbon paste was filled inside a glass tube with 2 mm diameter at the bottom end; the connection from the carbon paste to the electrode connector of the instrument was made, using a platinum wire. The SEM image of the bare carbon paste electrode and the Hg thin film coated carbon paste electrode is shown in Fig. 1. The Hg droplets are seen in the Hg film coated carbon paste electrode. These Hg droplets pre-concentrate the metal ions, during the deposition process. The deposited metal ions, using the produce sharp peaks while diffusing out from the droplets. Electrochemical response of the carbon paste electrode has been checked, by using electrochemical impedance measurements. Very well defined capacitive and resistive behaviour was obtained, with respect to the change in the applied potential, as seen from Figs. 2 and 3. The capacitance showed minima at around -0.20 V in 0.1 M HCl solution. The lowest capacitance value at around –0.20 V signifies the interface at zero charging conditions of the double layer. Therefore, a potential more negative to this potential, will attract the positively charged cations and at the application of suitable deposition, the metal ions could be deposited at the electrode surface. The charge transfer resistance was also found to follow a similar trend as that of the capacitance (Fig. 3) and the maxima of that plot are also seen at around –0.16 V. Therefore the capacitive and the resistive measurements using this carbon paste electrode, correspond well with respect to the change in the applied potential and there is no specific interaction due to adsorption, which was seen at the observed potential window. With increase in the binder and wax, concentration stability of the electrode material increases, but the sensitivity of the electrochemical response decreases drastically. Voltammetric stripping plots for Hg showing very high sensitivity of Hg determination using carbon paste electrode is shown in Fig. 4. Very good electrochemical response has been observed even at 16 ppt of Hg concentration in 0.1 M ($NaNO_3$ + HCl) solution. The mercury thin film coated carbon paste electrode was tested for differential pulse anodic stripping voltammetric determination of Zn, Cd, Pb and Cu. All the stripping peaks were clearly seen in the stripping voltammogramme (Fig. 5).

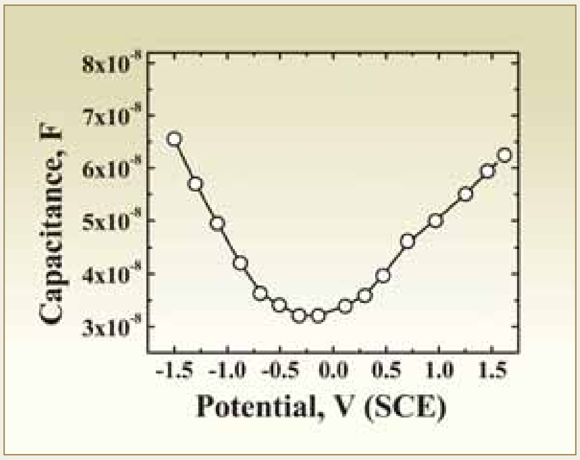

Fig. 2: Change in capacitance with the change in the applied potential, V vs SCE.

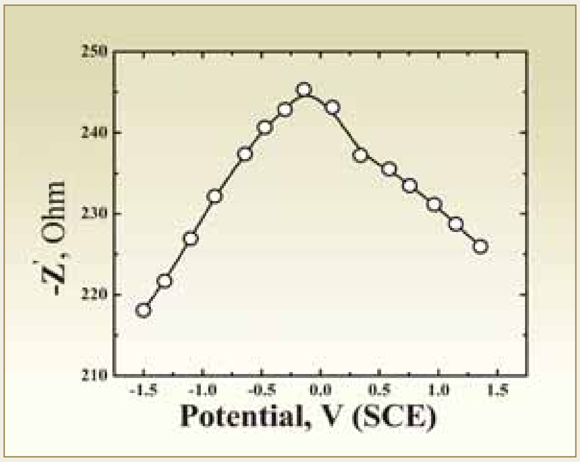

Fig. 3: Plot of the change in the real impedance with the change in the applied potential V vs SCE.

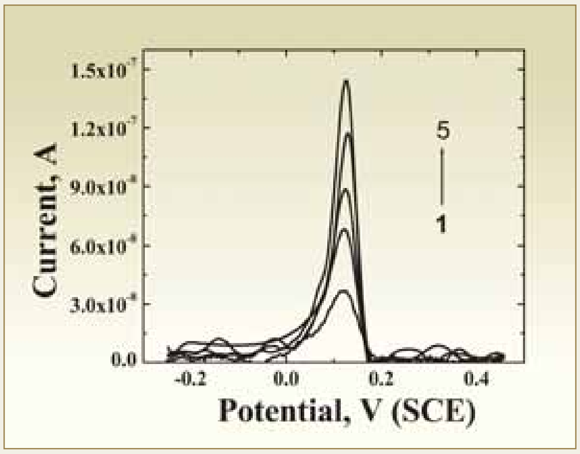

Fig. 4: Calibration plot of Hg in 0.1 M ($NaNO_3$ + HCl) solution, every time 16 ppt of Hg was added.

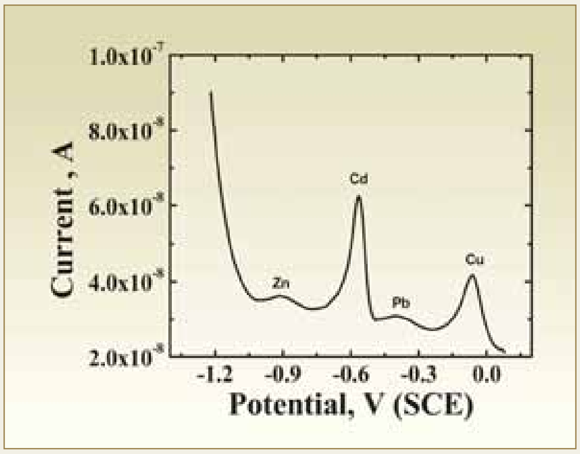

Fig. 5: Voltametric response of the Hg thin film coated carbon paste electrode for the stripping peak of Cd (10 ppb) and Cu (5 ppb) in 0.1M HCl as the supporting electrolyte solution. Signature due to Zn and Pb present in blank was also seen.

Conclusion

Parameters for the preparation of the carbon paste electrode have been optimized. Electrochemical behavior of mercury film supported on wax impregnated carbon paste electrode, has been studied. The carbon paste electrode developed, was found to be an excellent material for determination of heavy metals.

References

1. W. Kutner, J. Wang, Mauricelher, R. P. Buck, *Pure & Appl. Chem*., 70 (1998) 1301.
2. F. Qneirolo, P. Valenta, *Anal. Bioanal. Chem*., (Historical Archive). 328 (1987) 93.
3. C. F. Bobes, M. T. Fernandez-Abedul, A. Costa-Garcia, *Electroanalysis*, 10 (1998) 701.
4. Mikkelsen, and K.H. Schroder, *Electro analysis*., 15 (2003) 679.
5. O. L. Bagel, G. Girault, H. H. Brack, D. Loyall, U. H. Schäfer, *Electro analysis.*, 13 (2001) 100.
6. J. M. Zen, C. C. Yang, A. S. Kumar, *Anal. Chim. Acta*. 464 (2002) 229.
7. I. K. Tonle, E. Ngameni, A. Walcarius, *Sensors and Actuators* B 110 (2005) 195.
8. E. Shams, R. Torabi, *Sensors and Actuators* B 117 (2006) 86.

ABOUT THE AUTHORS

Dr. A.K. Satpati joined the Analytical Chemistry Division in September 2000 after completion of one year training from 43rd batch of OCES, Chemistry discipline. His research interest is studying the electrochemical property of modified electrodes, electrochemical aspects of corrosion of important metals and alloys and the dynamics of electron transfer processes in homogeneous and heterogeneous media. He has optimized the parameters for the preparation of carbon paste electrode, which is being modified for high sensitive and selective determination of metal ions, in complex matrices. He is working in the modification of carbon paste, glassy carbon gold etc. electrodes, using electropolymerization and self assembly techniques, which are being characterized for their possible use as the working electrode material.

Mr. Srikant Sahoo joined the Analytical Chemistry Division in 2006, after completion of CAT-1 training during 2005-2006. He has expertise in the voltammetric determination of metal ions at a wide concentration ranges, He is involved in the development of analytical methodologies, for highly selective and sensitive determination of metal ions and organic molecules, using modified carbon paste, Gold, Glassy carbon electrodes.

Dr. P.V. Ravindran is from the 13th Batch of BARC Training School. His recent research interest is in the study of various aspects of thermal and electrochemical processes, for studying the decomposition property of simulated nuclear waste material and development of electroanalytical methodologies. Assessment of high temperature reactions and intermediate compound formation in binary mixtures of uranyl nitrate hexahydrate with (1) sodium nitrate, (2) rubidium nitrate, (3) strontium nitrate, (4) nickel nitrate hexahydrate and (5) barium nitrate. These studies showed evidence of hydrolysis and polymerization of nitrato complexes in the systems investigated. Some new nitrato complexes have been identified, through a combination of thermal, X-ray diffraction and infra-red spectral measurements. He is a registered PhD guide of the University of Mumbai.

TIME RESOLVED FLUORESCENCE STUDIES ON INTERACTION OF Eu(III) WITH N,N,N',N'-TETRAOCTYL DIGLYCOLAMIDE

P.N. Pathak, S.A. Ansari, S.V. Godbole, A.R. Dhobale and V.K. Manchanda
Radiochemistry Division

This paper was awarded the Best Paper Award
at SESTEC-2008 Symposium, held at University of Delhi, Delhi during
March 12-14, 2008

ABSTRACT

Complexation of Eu(III) with *N,N,N',N'*-tetraoctyl diglycolamide (TODGA) has been studied by Time Resolved Fluorescence Spectroscopy (TRFS). Measurements have been performed at varying metal-to-ligand ratio in ethanol/water mixture. Investigation of TRFS spectra suggested the exclusive formation of 1:3 complex between Eu(III) and TODGA. The luminescence decay curves have been used for the calculation of conditional stability constant of the $[Eu(TODGA)_3]^{3+}$ complex.

Introduction

N,N,N',N'-tetraoctyl diglycolamide (TODGA) is one of the most promising extractants known for actinide partitioning from high-level nuclear waste [1,2]. It is suggested that TODGA coordinates with metal ions in a tridentate fashion, involving two oxygen atoms from carbonyl groups and one from the etherial group, leading to the formation of a cyclic ring [3]. The stoichiometry of the species formed varied, however, with the nature of the diluent used. Whereas for nonpolar diluents like dodecane and toluene, four TODGA molecules were present in the extracted species of Am(III) from nitric acid medium; the extracted species in the polar medium like octanol and 1,2 dichloroethane involved only two TODGA molecules. According to EXAFS study, the Nd(III)-diglycolamide complexes in alcohol medium are composed of two ligand molecules bonded in tridentate fashion with some water molecules in the inner coordination sphere [3]. SANS studies also indicated that the stoichiometry of the extracted species was dependent on the nature of diluent [4]. This led us to investigate the complexation behaviour of TODGA with trivalent metal ion like Eu(III), using Time Resolved Fluorescence Spectroscopic (TRFS) technique.

In the present work, an attempt was made to use TRFS data of Eu(III)-TODGA complex in ethanol/water mixture, for the determination of conditional stability constant of the complex.

Experimental

Stock solutions of TODGA were prepared in spectroscopic grade ethanol. Stock solution of Eu(III) ($5x10^{-3}$ M) was prepared, by dissolving $Eu(NO_3)_3 \cdot 6H_2O$ (spectroscopic grade, Alpha Biochem) at 0.05 M HNO_3. Supra pure nitric acid and HPLC grade alcohols were obtained from Merck. Deionized water from a milli-Q purification system (Millipore) of resistivity

MW cm was used for all dilutions. Solutions for TRFS measurements were prepared by mixing precise volumes of ligand and Eu(III) stock solutions, to give metal-to-ligand ratios (M/L) in the range of 0.1 to 5. Sample solutions were made with appropriate amount of EtOH/H_2O mixtures. Final concentration of Eu(III) was 10^{-4}M at pH 3 (HNO_3).

TRFS measurements were carried out with Edinburgh F-900 fluorescence spectrometer, equipped with Xenon lamp and 375nm diode laser as excitation sources. The excitation wavelength was fixed at 230nm with xenon lamp, while emission spectrum was recorded in the range of 575 to 625 nm. The pulse repetition rate was kept constant at 10Hz for life time measurements. Fluorescence decay curves were fitted into the exponential function, to obtain the lifetime of excited states.

Results and Discussion

Preliminary experiments were done to homogenous solution of $Eu(NO_3)_3$ and TODGA in ethanol/water mixture by measuring the life time of $^5D_0$ level of the aquo Eu(III) ion (110±10μs), which corresponds to nine water molecules in the inner coordination sphere [5]. Table 1 shows the variation in the lifetime of $^5D_0$ level of Eu(III) ion with the composition of medium. It is evident, that the lifetime of $^5D_0$ level of Eu(III) ion is not affected up to 60% ethanol + 40% water mixture. Negligible variation in the lifetime suggested, that ethanol molecules are absent in the inner coordination sphere of Eu(III) ion. However, there was variation in the relative peak intensities as reported in literature. The composition (60% ethanol + 40% water) was found suitable for sample preparations with wide ligand-to-metal concentration ratios. The lifetime of $^5D_0$ Eu(III) emitting level, depends on the vibration modes of OH bond. Colette et al, [6] obtained a correlation between primary hydration number of Eu(III) (N_{H2O}) and the lifetime (t) of its $^5D_0$ emitting level (in millisec) for methanol/water mixtures as follows [6]:

$$N_{(H2O)} \pm 0.5 = (1.06 / t) - 0.19 \qquad (1)$$

Fig.1 shows the luminescence spectra of Eu(III)-TODGA complexes in different ligand-to-metal proportions with characteristic peaks at 590, 616, and 690 nm corresponding to the de-excitation of $^5D_0$ level to $^7F_1$, $^7F_2$ and $^7F_4$ levels, respectively. Equation (1) was used for the determination of hydration number of Eu(III) in water-ethanol medium, with an uncertainty of ±0.5.

Table 1. Lifetime data of $^5D_0$ level of Eu(III) ion in different media; [Eu(III)] = 1 x 10^{-3} M; [HNO_3] = 1 x 10^{-3} M

Medium	Lifetime (τ), ms
Aq. Eu(III)	0.114
10% Ethanol + 90% Water	0.114
25% Ethanol + 75% Water	0.115
50% Ethanol + 50% Water	0.116
60% Ethanol + 40% Water	0.117
75% Ethanol + 25% Water	0.132
100% Ethanol	0.303

The emission intensity ratio of 590nm / 616nm decreased with increased L/M ratio. The intensity of 590nm peak does not change significantly as compared to that of 616nm. This can be attributed to the fact, that $^5D_0$ to $^7F_2$ transition is hypersensitive to complexation, due to the electric dipole nature of the transition, while $^5D_0$ to $^7F_1$ transition has magnetic dipole character.

The data fitting of decay plots of $^5D_0$ level at varying ligand-to-metal ratios (0.1 to 5), showed two components, which were correlated with the lifetime/ hydration number of Eu(III) ions in 60% ethanol + 40% water mixture. Based on the lifetime measurements, these two components were identified as (i) the uncomplexed fraction of Eu(III) with the lifetime of aquo ion (0.11 ms), and (ii) the complexed fraction of Eu(III) with enhanced lifetime (1.3±0.1

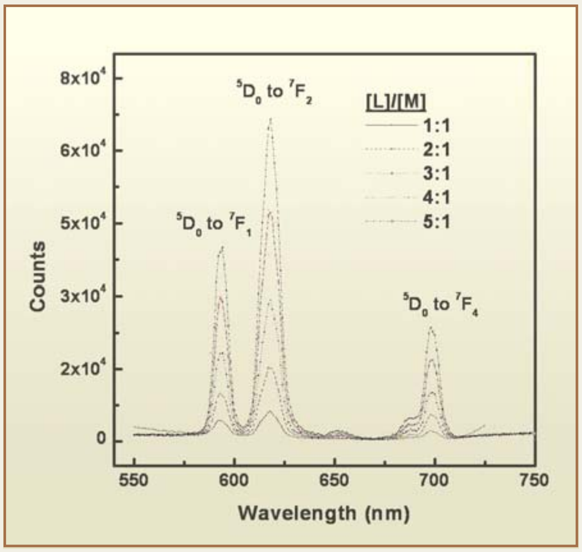

Fig. 1: Eu(III)-TODGA fluorescence spectra; [Eu(III)] = 1 x 10 $^{-4}$ M; [HNO$_3$] = 1 x 10 $^{-3}$ M; Medium = Ethanol / Water (v/v): 3:2

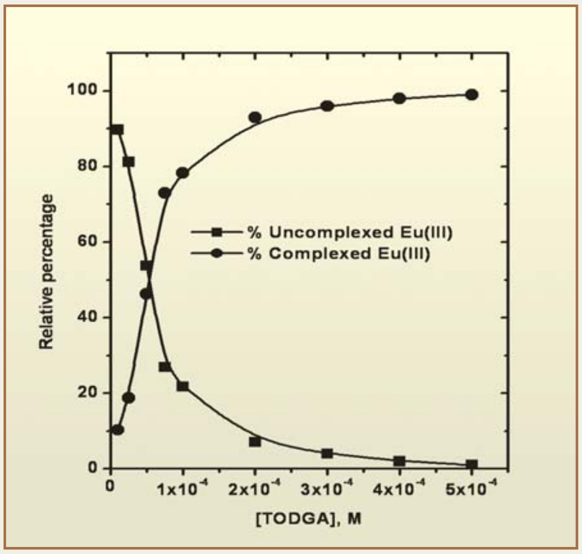

Fig. 2: Relative composition of the species for Eu(III)-TODGA system;
[Eu(III)] = 1.0 x 10 $^{-4}$ M; [HNO$_3$] = 1.0 x 10 $^{-3}$ M; Medium = Ethanol/Water (v/v): 3:2

ms). The lifetime data for second component when fitted in equation (1) showed the absence of water molecules in the complexed fraction. As TODGA is expected to be a tridentate ligand, therefore, each molecule entering the primary co-ordination sphere of Eu(III) is likely to replace the three H_2O molecules. This suggests that the species present under such conditions can be considered as $[Eu(TODGA)_3]^{3+}$. The data fitting of lifetime measurements led us to calculate the relative proportions of the free Eu(III) ion, and that in the complex form (Fig. 2).

Using this data, the equilibrium concentrations of free and complexed metal ion, and that of the free TODGA concentration can be obtained. The conditional stability constant ($\log b_3$) of the complex ($Eu(TODGA)_3^{3+}$ type) can be calculated as follows:

$$Eu^{3+} + 3TODGA \; ! \; Eu(TODGA)_3^{3+} \tag{2}$$

$$b_3 = [Eu(TODGA)_3^{3+}]/[Eu^{3+}]_{free} \{TODGA\}^3_{free} \tag{3}$$

The concentrations of complexed metal ions can be obtained as, $[Eu(TODGA)_3^{3+}] = C_{Eu} - [Eu^{3+}]_{free}$, where C_{Eu} refers to the total europium concentration. Similarly, $[TODGA]_{free} = [TODGA]_{total} - [TODGA]_{comp}$. The $\log b_3$ for the $[Eu(TODGA)_3]^{3+}$ complex was calculated as 14.3±1.6..

References

1. Y. Sasaki, Y. Sugo, S. Suzuki and S. Tachimori, *Solv. Extr. Ion Exch*., 19 (2001) 91.
2. S.A. Ansari, P.N. Pathak, M. Husain, A.K. Prasad, V.S. Parmar and V.K. Manchanda, *Solv. Extr. Ion Exch*., 23 (2005) 463.
3. H. Narita, T. Yaita and S. Tachimori, *Society of Chemical Industry*, London, 2001, Vol. 1, P. 693-696.
4. M.P. Jensen, T. Yaita and R. Chiarizia, *Langmuir*, 23 (2007) 4765.
5. G.R. Choppin and D.R. Peterman, *Coord. Chem. Rev.*, 174 (1998) 283.
6. S. Colette, B. Amekraz, C. Madic, L. Berthon, G. Cote and C. Moulin, *Inorg. Chem*., 43 (2004) 6745.

ABOUT THE AUTHORS

Dr. P.N. Pathak joined the Radiochemistry Division, BARC in 1995. His research interests include separation of actinides and fission products, using new extractants and supercritical fluid extraction. He has also carried out extensive research work on actinide speciation in aquatic environment. He is a Ph.D. guide in Chemistry for HBNI. Dr. Pathak has to his credit over 60 publications in reputed international journals.

Dr. S.A. Ansari did his Ph.D. under BARC-Mumbai University Programme in 2008 and subsequently joined the Radiochemistry Division of BARC as KS Krishnan Research Associate. He has been instrumental in design and development of extractants, for the separation of actinide and fission elements, from nuclear waste. He has gained expertise in membrane separation processes including hollow fibre liquid membrane technology. He has more than 20 publications in reputed international journals.

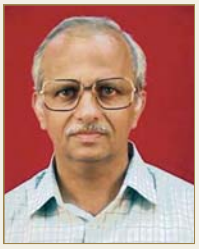

Dr. S.V. Godbole is working as a senior scientific officer in Radiochemistry Division, BARC. He joined BARC in 1975 and since then has worked extensively in the areas of Spectroscopic investigations of lanthanides and actinides, and analytical spectroscopy of nuclear materials. He is also a recognized Ph.D. guide of the University of Mumbai and of HBNI. He has to his credit over 50 publications in reputed international journals.

Dr. A.R. Dhobale joined the Radiochemistry Division, BARC in 1976. He was awarded Ph.D. from Mumbai University and carried out Post Doctoral research studies at the National Taiwan University, Taipei. His fields of interest are analytical spectroscopy of nuclear materials, photoacoustic and fluorescence spectroscopy.

Dr. V.K. Manchanda is Head, Radiochemistry Division, BARC. His research interests include; thermodynamics and kinetics of complexes of macrocyclic ligands with lanthanides and actinides, design and synthesis of novel extractants of actinides, chemical quality control of Pu based fuels and speciation of actinides in aquatic environment. He is a Ph.D. guide in Chemistry of University of Mumbai and of HBNI. He has about 190 publications in international journals. He is currently on the Advisory Board of "*Radiochimica Acta*", and of "*Solvent Extraction and Ion Exchange*". He is the President of IANCAS and is the Founder President of the Association of Separation Scientists and Technologists (ASSAT).

SEPARATION OF Am(III) FROM SHLW USING A HOLLOW FIBER SUPPORTED LIQUID MEMBRANE CONTAINING TODGA AS THE CARRIER

S.A. Ansari, D.R. Raut, P.K. Mohapatra and V.K. Manchanda
Radiochemistry Division

This paper received the "Best Paper Award" at the 3rd Symposium on Emerging Trend in Separation Science and Technology (SESTEC-2008) held at University of Delhi, Delhi, from March 12-14, 2008

ABSTRACT

Facilitated transport of Am(III) from nitrate medium has been investigated, using a hollow fibre supported liquid membrane, impregnated with N,N,N2,N2-tetraoctyl diglycolamide (TODGA) as the carrier. The influence of feed acidity / strippant acidity composition, on the permeability of Am(III) was studied. Quantitative transport of Am(III) was observed in about 45 minutes from a feed solution containing 1g/L Nd(III) at 3.5M HNO_3. Similarly, quantitative transport of Am(III) was observed in about 30 minutes, from PHWR-High Level Waste containing ~0.6g/L total lanthanides.

Introduction

N,N,N′,N′-tetraoctyl diglycolamide (TODGA) has been extensively studied, for solvent extraction of actinides / lanthanides [1,2]. Our earlier studies included carrier mediated transport of actinides and fission products from nitric acid solution across the SLM, containing TODGA/*n*-dodecane as the carrier. A detailed study was undertaken, to maximize metal ion (trivalent lanthanide and actinide ions) mass transfer, by optimizing various parameters such as the nature of strippant, carrier concentration, feed acidity etc. In the present paper, an attempt has been made for the first time, to investigate the applicability of TODGA-SLM technique on large scale separation of lanthanides / actinides, employing a Hollow Fibre Supported Liquid Membrane (HFSLM).

Although SLM technique has been widely studied for the separation and concentration of a variety of compounds, it has limitation of low stability and low transport rate, when used as flat sheet SLM (FSSLM). Whereas the instability of SLM arises due to the loss of the carrier / or solvent from the support, the low transport of metal ions is due to the small surface area encountered in FSSLM. It has been observed, that changing the configuration from flat sheet to tubular hollow fibres (HFSLM), improves the lifetime of the liquid membrane as well as the transport flux [3]. The HFSLM has major advantages over flat sheet SLM due to very large surface area and also due to the fact, that the eroded liquid membranes can be easily regenerated, by passing the ligand solution through the module [4]. The main objective of the present work was to develop a HFSLM system, for the separation of actinides and lanthanides from PHWR-SHLW, using TODGA as the carrier.

Experimental

TODGA and DHOA were synthesized indigenously. All the chemicals used were of analytical reagent grade. SHLW was procured from the Waste Management Division, BARC, Mumbai. India. The composition of the SHLW is given in Table 1 which corresponded to a typical PHWR waste of ~ 6500 MWD/T burn up (after 3 years of cooling and ~ 800 litres of the waste).

A 28.25cm long module with 6.65cm diameter was employed in the present study. The total effective surface area was 1.4 square meters with ~10,000 fibers. The HFSLM was prepared by pumping the ligand solution through the lumen side of module, at a pressure of 3Psi in recycling mode, till it is ejected from the shell side. After complete soaking, the excess ligand solution was washed out with distilled water, prior to the introduction of the feed and strip solutions. The feed solution was passed through the lumen side, while strip solution was passed through the shell side of the module, in all the experiments. The flow rates of the feed and strip solutions were maintained constant at 200mL/min, with the help of gear pumps equipped with precise flow controller.

Results and Discussion

The long term stability of the HFSLM is important from the standpoint of its industrial application. For such stability test, the module was impregnated with the carrier solution and the system was run continuously in several successive cycles, for the transport of Nd(III) from a solution containing 1g/L Nd at 3.5M HNO_3. The permeability of Nd(III) was measured for 45min and after this period of time, the depleted feed and enriched strip solutions were withdrawn and replaced with fresh solution. From the data reported in Fig. 1, it can be observed, that the Nd(III) transport was consistent within the error limit in all the ten runs. According to Pearson et al [5], probable causes of membrane instability could be (a) loss of

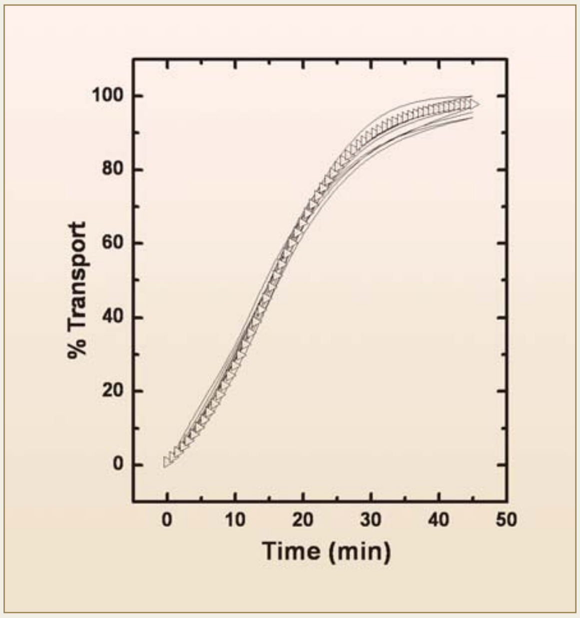

Fig. 1: Successive transport experiments for Nd(III) to evaluate the stability of HFSLM; Carrier: 0.1M TODGA + 0.5M DHOA in NPH; Feed: 1g/L Nd at 3.5 M HNO_3; Strippant: Distilled water; Temperature: 25°C

Table 1: Composition of a typical PHWR-SHLW used in the present study; Acidity: 3 M HNO_3

Element	Conc., g/L	Element	Conc., g/L
Fe	0.72	Ba	0.06
Cr	0.12	La	0.18
Ni	0.11	Ce	0.06
Na	5.50	Pr	0.09
K	0.22	Nd	0.12
Mn	0.43	Sm	0.086
Cs	0.32	Y	0.06
Sr	0.03	Zr	0.004
U	6.34	Mo	0.14

extractant by solubility in adjacent aqueous solution, (b) progressive wettabilty of the support pores induced by lowering of the organic-water interfacial tension which results from the surface active nature of the carrier molecules and (c) the differential pressures existing between the inside and outside of HFSLM. Danesi et al [3,6], reported that the loss of carrier from the pores are more significant when carrier molecules are very strong surfactants such as alkyl / aryl sulphonic acids and long chain quaternary ammonium salts. On the other hand, no significant loss was observed when weaker surface active carriers such as CMPO, TOPO and long chain amines were used. They reported, that the HFSLM was quite stable for 60 days with polypropylene hollow fibre SLM containing tridodecylamine in *n*-dodecane as the carrier, when outside and inside hydraulic pressures were balanced. In the present work, TODGA being a weaker surface active carrier, a similar stability of HFSLM is envisaged, though our study was restricted to only 72 hrs of continuous operation.

Since, HLW contains lanthanides at several times higher concentration than the minor actinides, it was of interest to investigate the effect of rare earth metal concentration on the transport of Am(III). By taking Nd(III) as the representative element of lanthanides, the transport of Am(III) was investigated in the presence of 1g/L Nd(III) and the results are shown in Fig. 2. It was evident, that the quantitative transport of Am(III) was achievable in 45min of operation. Similarly, the quantitative transport of Am(III) was achieved in 30min under SHLW conditions (Fig. 2). Faster transport of Am(III) from SHLW as compared to pure Nd solution was ascribed to lower concentration of lanthanides (~0.6g/L) and salting out effect due to the presence of large concentration of metal salts.Present observation suggests, that HFSLM offers a promising alternative approach for actinide partitioning, using TODGA as the carrier. The basic phenomena which occur at SLMs separation processes, are sufficiently well understood, to permit the scale-up of laboratory units to commercial scale. However, studies need to be undertaken for the radiation stability of the HF modules before applying the system to the actual HLW.

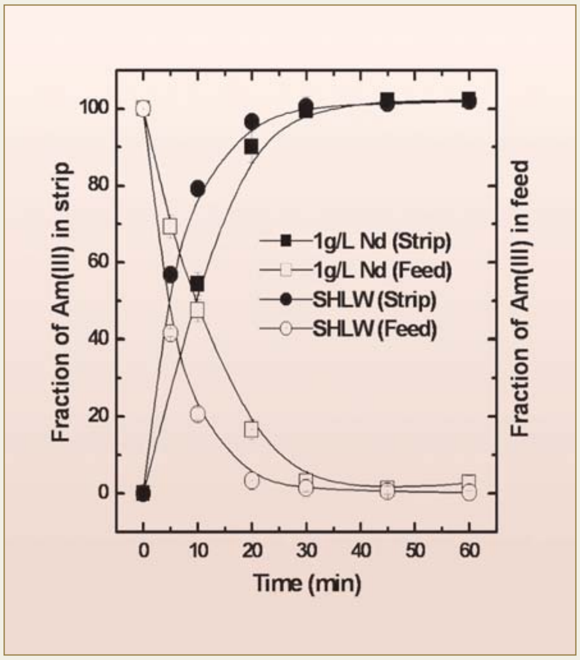

Fig. 2: Transport of Am(III) by HFSLM; Carrier: 0.1M TODGA + 0.5M DHOA in NPH; Feed: 1g/L Nd at 3.5M HNO_3 / SHLW spiked with ^{241}Am tracer; Strippant: Distilled water; Temperature: 25°C

References

1. Y. Sasaki, Y. Sugo, S. Suzuki and S. Tachimori, *Solv. Extr. Ion Exch*., 19 (2001) 91.
2. S.A. Ansari, P.N. Pathak, M. Husain, A.K. Prasad, V.S. Parmar and V.K. Manchanda, *Solv. Extr. Ion Exch*., 23 (2005) 463.
3. P.R. Danesi and P.G. Rickert, *Solv. Extr. Ion Exch*., 4 (1986) 149.
4. C. Fontas, C. Palet, V. Salvado and M. Hidalgo, *J. Membr. Sci*., 178 (2000) 131.
5. D. Pearson, Ion Exchange Membranes, D.S. Flett (Ed.), *Society of Chemical Industry, London* (1983), P. 55-73.
6. P.R. Danesi, *Sep. Sci. Technol*., 19 (1985) 857.

ABOUT THE AUTHORS

Dr. S.A. Ansari did his Ph.D. under BARC-Mumbai University Programme in 2008 and subsequently joined the Radiochemistry Division of BARC as KS Krishnan Research Associate. He has been instrumental in design and development of extractants, for the separation of actinide and fission elements, from nuclear waste. He has gained expertise in membrane separation processes including hollow fibre liquid membrane technology. He has more than 20 publications in reputed international journals.

Dr. P. K. Mohapatra joined the Radiochemistry Division, BARC in 1987 after graduating from the 30th batch of BARC Training School. His research interests include separation of actinides and fission products using liquid membranes. He has developed hollow fiber liquid membrane separation method, for the recovery of actinides and fission products from radioactive waste samples. Dr. Mohapatra has to his credit about 100 publications in reputed international journals.

Dr. V.K. Manchanda has research interests in the areas of separation science of actinides, actinides' speciation, CQC of plutonium-based fuels, complexation of actinides and fission products with macrocyclic ligands. He has more than 190 publications in reputed international journals to his credit. He is the past President of IANCAS and founder president of ASSET. He is on the Advisory Board of international journals such as *Radiochimica Acta* and *Solvent Extraction & Ion Exchange*. He currently heads the Radiochemistry Division, BARC.

PREDICTION OF FIRING TIME OF MAGNESIO THERMIC REDUCTION (MTR) REACTION AND STUDY OF RELATIVE IMPORTANCE OF THE DEPENDENT PARAMETERS USING ARTIFICIAL NEURAL NETWORK

S. Manna, S. Chowdhury, S. K. Satpati and S. B. Roy
Uranium Extraction Division

This paper received the Kuloor Memorial Award for the Best Technical Paper published in the Journal *"Indian Chemical Engineer"* in its issues for 2007 and also the NRC Award for the 2nd Best Paper in *"Indian Chemical Engineer"* in 2007

ABSTRACT

In uranium metal production process, uranium ingot is generally produced by Magnesio Thermic Reduction (MTR) of uranium tetra fluoride. This highly exothermic reaction is carried out in a closed vessel, called 'bomb reactor', lined with MgF_2. Initiation of this instantaneous reaction is indicated by sudden temperature shoot up of the reaction mixture and it is called firing. It is observed that the time required to initiate the reaction (firing time), depends on various parameters of the reactants and the lining material along with operating parameters. But no correlation is available to correlate the firing time as a function of all these parameters together. Artificial neural network is used here to predict firing time, based on these parameters using BIKAS software and exclusive studies were carried out here, to study the relative importance of the parameters on firing time.

Key words: Artificial Neural Network, Magnesio Thermic Reduction and Firing time.

Introduction

Uranium production processes are categorized in four groups: 1) reduction of uranium halides with metals, 2) reduction of uranium oxides with metal and carbon 3) electrolytic reduction and 4) disproportionate or thermal decomposition of uranium halides [1].

The reduction of uranium tetrafluoride by magnesium, is one of the main industrial methods for producing commercially pure uranium ingot. The main reaction:

$UF_4 + 2Mg = 2MgF_2 + U, \Delta H_{298} = -83.5$ Kcal/ gm atom of U.

The hot metal product is chemically very reactive and therefore must be contained in an inert reaction vessel. Furthermore, the peak temperature attained is well above the boiling temperature of magnesium and therefore the reaction must be carried out in a closed vessel. The reaction vessel, called a bomb reactor, commonly used is a flanged steel bomb lined with either electrically fused dolomitic lime or recycled magnesium fluoride slag liner. These lining materials are poor conductors. They are used to protect the reactor from the high heat of reaction. Initiation of this instantaneous reaction is indicated by sudden temperature shoot up of the reaction mixture and the reaction is over within a few seconds. The time taken for spontaneous initiation of the reaction or the ignition is defined as the firing time. Very high temperature is generated due to high heat of reaction. Under adiabatic conditions, the maximum temperatures that can be generated in the bomb reactor at various ignition temperatures (firing temperatures) have been reported [1,2]. For very good metal (Uranium) and slag separation, both the reaction products should be in molten condition for sufficient time. If the reaction is started at any temperatures below 175°C, complete fusion of the slag cannot occur. To avoid this problem, reactor is preheated following a predefined schedule. Firing temperature depends on preheating time, which is known as firing time [1]. An optimum firing time is important for maintaining product recovery, safe operation and proper energy utilization. Based on importance of firing time and its uncertainty of prediction due to wide variation, prediction of firing time is very much needed for the plant.

During preheating, many side reactions occur inside the bomb reactor. These reactions have effect on the reduction process and indirectly on the firing time. It is observed from plant experiences, that firing time depends on 12 parameters of reactants and lining materials:1) moisture content in UF_4, 2) free acid content in UF_4 3) UO_2F_2 content in UF_4, 4) AOI (ammonium oxalate insoluble) in UF_4, 5) tap-density of the UF_4, 6) moisture in lining material (MgF_2) 7) uranium in lining material, 8) iron content in lining material, 9) LOI (Loss Of Ignition) in lining material, 10) tap-density of lining material, 11) Mg particle size and 12) MgO content in Mg. Overall parametric effect is not well established yet. These parameters are so interrelated, inherently non linear and transient, that it is impossible to correlate them by a theoretical equation.

Mathematical modeling or white box model is also difficult. As an easier alternative, the plant data can be used to find out a black box model or an empirical correlation describing the system. For the success of this method, proper mathematical function has to be assumed to correlate the parameters. Improper assumption may end as wrong representation of the system. In Artificial Neural Network (ANN) modeling, there is no need to understand the physics of the system. This is the advantage of using ANN. Theoretically ANN, with three layers can approximate any non-linear function with arbitrary accuracy [3] and this feature makes the neural network a promising nonlinear modeling tool. As a tool of modeling, neural networks have been used by Raha (2005) [4] for management of waste water treatment plan, Sharma et al (1999) [5] for vapor-liquid equilibrium prediction, Qiang Xiong (2002) [3] for chemical process control, Singh et al (2004) [6] for modeling of head power characteristics of pump-mixer and Parisi (2001) [7] for steady state modeling of heterogeneous gas solid reactors.

An attempt has been taken here to predict the firing time based on these parameters and to study the relative importance of these parameters on the firing time by artificial neural network, using the software BIKAS.

Chemistry of Magnesio thermic reduction reaction

All input materials, UF_4, lining material and magnesium play a major role in the performance of magnesio-thermic reduction reaction hence on firing time. Green salt (UF_4) composition is a well recognized variable in the reduction of UF_4 and has a significant effect on firing time, bomb yields and uranium metal quality. UF_4, produced by hydrofluorination of UO_2, normally contains small amount of uranyl fluoride (UO_2F_2), known as water soluble content and mixed oxides, known as AOI (ammonium oxalate insoluble), moisture and little bit of free acid (HF). During pre heating stage, moisture hydrolyses UF_4 and generates UO_2. UO_2 does not get dissolved in the slag and as a result reduces the fluidity of the slag and metal and slag separation. HF reacts with magnesium and forms refractory MgF_2 film on magnesium, which hinders the vaporization of the magnesium chips and the triggering of the reaction, is delayed i.e. firing time increases. Hydrogen generated by this side reaction reacts with UO_2F_2, to produce harmful HF again. Moisture in the UF_4 reacts with magnesium, forms magnesium oxide film on the surface of the chips and hydrogen is evolved. Magnesium oxide is a refractory material and affects the reaction in the same way as MgF_2. HF in the UF_4 reacts with MgO to form moisture in a similar fashion and this vicious cycle goes on. The net effect of all the above side reactions is delay in firing or increase in the firing time. UO_2F_2 in UF_4 plays a major role in the reduction reaction. UO_2F_2 when heated in the presence of moisture, hydrolyses to UO_3 and HF. UO_3 remains unreduced during the Magnesio Thermic Reduction and naturally bomb yield decreases and HF causes similar problems. AOI content of the green salt is a mixture of all the un-hydro-fluorinated oxides. These oxides neither get reduced during the course of the reaction nor they get dissolved in the slag and as a result, reduce the fluidity of the slag and metal and slag separation. It has been observed that the effects of UO_2F_2 and AOI are lesser than moisture and free acid content in UF_4. Compactness of the reaction mixture depends on the tap density of UF_4. The more the compactness, faster the heat transfers to reactant mixture and less the firing time.

$$UF_4 + 2H_2O = UO_2 + 2HF \qquad (1)$$

$$Mg + 2HF = MgF_2 + H_2 \qquad (2)$$

$$UO_2F_2 + H_2 = UO_2 + 2HF \qquad (3)$$

$$UO_2F_2 + H_2O = UO_3 + 2HF \qquad (4)$$

Lining material is used to protect the freshly reduced molten uranium metal from coming in contact with the material of construction of the reaction vessel. A good quality lining should act as a good heat conductor in the preheating stage, despite being a bad conductor of heat. Faster the heat transfer rate, lower the firing time. On the contrary, it should act as a heat insulator immediately after the reaction i.e. it should contain the heat generated during the reduction, thereby holding the molten mass for a sufficiently long time, to effect a good metal slag separation. But moisture present in the lining material affects the firing time as does the moisture present in UF_4. Presence of iron and uranium increase the conductivity of the lining material.

Since the Magnesio Thermic Reduction reaction is in all probability initiated by the reaction of the magnesium vapour and UF_4, the size of the magnesium particle and MgO content in magnesium are very important parameters for the initiation of the reaction, hence in firing time [1].

Artificial Neural Network

An artificial neural network is defined as a data processing system, consisting of a large number of highly interconnected processing elements (artificial neurons) in an architecture inspired by the structure of cerebral cortex of the brain [8]. An artificial neuron is developed, to mimic the characteristics and functions of a biological neuron. Analogous to a biological neuron, an artificial neuron receives much input representing the output of the other neurons. Each input is multiplied by the corresponding weights analogous to synaptic strength. All these weighed inputs are then summed up and passed through an activation function, to determine the neuron output. A simplified artificial neural model is shown in Fig. 1.

$$U = W_1 I_1 + W_2 I_2 + W_1 I_1 + \dots\dots + W_0 I_0$$

$$= \sum_{i=0}^{n} W_i I_i$$

$$O = f\,(U),$$

More complex neural networks are available as software packages.

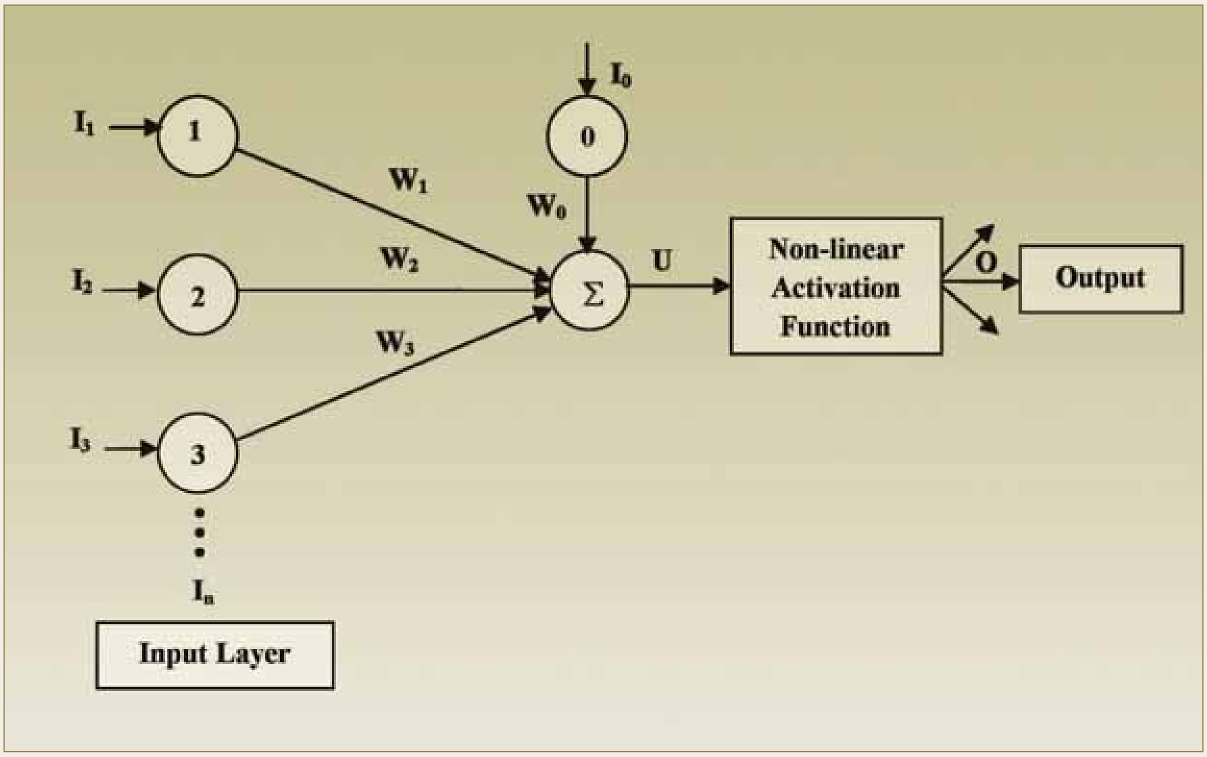

Fig. 1: A simplified artificial neural model

Present Work

In the present work, artificial neural network has been used, based on data obtained from the Uranium Metal Plant of BARC using the software BIKAS (BARC IIT Kanpur ANN Software). The work can be classified into four categories- 1) selection of proper training, testing and prediction file, 2) selection of proper network and 3) prediction of firing time based on proper network & 4) study of relative importance based on proper network. Interfacing of plant data with BIKAS software is shown in block diagram (Fig. 2).

1) Selection of proper training file: Once a network has been structured for a particular application, that network is to be trained. As artificial neuron is developed to mimic characteristics, it is a very good interpolator but not a good extrapolator. So selection of proper training and testing files is important to make the ANN efficient. There are 12 input parameters on which one out parameter (firing time) is dependent. The training file has been chosen such that, training data file covers the full range of values for each parameter.

2) Selection of proper network: In the present case, feed forward multilayer network with supervised learning method is used. A nonlinear function has been chosen as activation function, to emulate the nonlinear behaviour of the conduction current mechanism, in a biological neuron. Neurons with sigmoidal functions bear a greater resemblance to biological neurons than with other activation functions. It is also seen that for sigmoidal functions, the output of a neuron varies continuously but not linearly with the input [9]. As firing time (output in the present case) is never negative, unipolar sigmoidal function is taken as activation function. Different networks are useful for different kinds of applications. There are no general rules to select proper network for different applications. Efficiency of different networks has been checked here, to select proper network. Average error

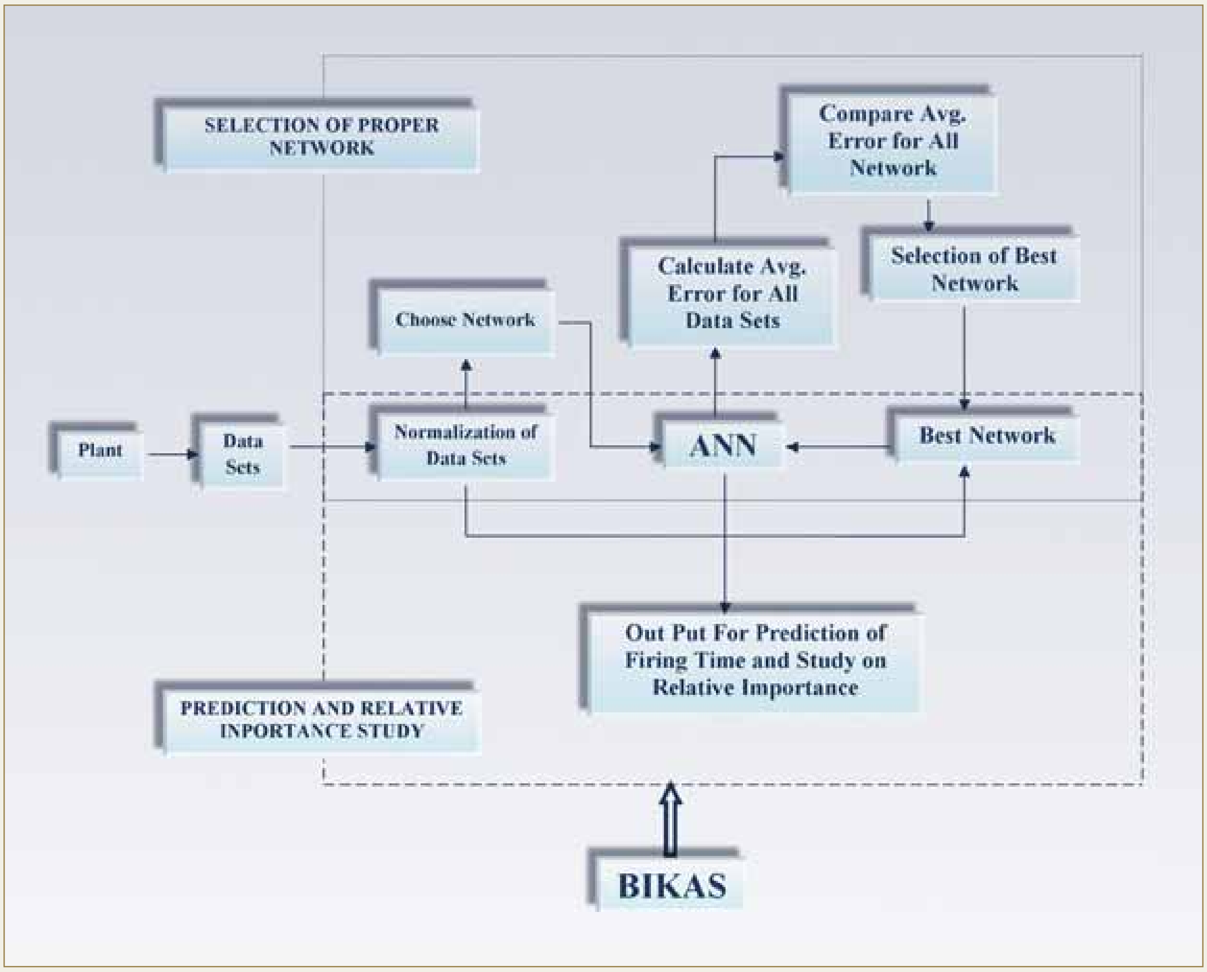

Fig. 2: Block diagram showing interfacing between plant data and BIKAS

of testing is considered as indication of efficiency of the networks, more the average error, lesser the efficiency. Details of different networks with tuning parameters have been presented here.

a) Back propagation with momentum: Back propagation is a systematic method of training multilayer artificial neural networks. Back propagation was developed by Rumelhart, Hinton and Wilham in 1985. They [10] presented a clear and concise description of the back propagation algorithm. Parker [11] has also supported Rumelhart's views.

Proper selection of tuning parameters such as number of hidden layers and number of neurons in the each hidden layer, momentum factor and learning rate are required, for efficient learning and designing of a stable network.

i) *Effect of Number of hidden layers and number of neurons in each hidden layer:* There is no general criterion about deciding the number of the hidden layers and number of nodes (neurons) in the hidden layer. It is checked based on trial and error method. Different case studies have been carried out in the present work (Table 1).

It has been observed (Table 1) that average testing error is obtained when number of hidden layers is 2 and number of neurons in first and second hidden layers are 6 and 3 respectively.

Table 1: Effect of different networks of back propagation (with momentum)

Case No.	Number of hidden layer and number of neurons in each hidden layer	Average error (%)
1	No. of hidden layer: 1 No. of nodes in the hidden layer 1: 11	21.45
2	No. of hidden layer: 1 No. of nodes in the hidden layer 1: 6	19.93
3	No. of hidden layer: 1 No. of nodes in the hidden layer 1: 24	26.36
4	No. of hidden layer: 2 No. of nodes in the hidden layer 1: 12 No. of nodes in the hidden layer 2: 12	29.33
5	No. of hidden layer: 2 No. of nodes in the hidden layer 1: 6 No. of nodes in the hidden layer 2: 6	18.10
6	No. of hidden layer: 2 No. of nodes in the hidden layer 1: 8 No. of nodes in the hidden layer 2: 4	20.56
7	No. of hidden layer: 2 No. of nodes in the hidden layer 1: 24 No. of nodes in the hidden layer 2: 12	23.60
8	No. of hidden layer: 2 No. of nodes in the hidden layer 1: 6 No. of nodes in the hidden layer 2: 3	16.33
9	No. of hidden layer: 2 No. of nodes in the hidden layer 1: 24 No. of nodes in the hidden layer 2: 6	24.05
10	No. of hidden layer: 2 No. of nodes in the hidden layer 1:16 No. of nodes in the hidden layer 2: 8	28.87
11	No. of hidden layer: 3 No. of nodes in the hidden layer 1: 8 No. of nodes in the hidden layer 2: 6 No. of nodes in the hidden layer 3: 4	19.06
12	No. of hidden layer: 3 No. of nodes in the hidden layer 1: 12 No. of nodes in the hidden layer 2: 8 No. of nodes in the hidden layer 3: 4	23.06
13	No. of hidden layer: 3 No. of nodes in the hidden layer 1: 24 No. of nodes in the hidden layer 2: 12 No. of nodes in the hidden layer 3: 6	27.53

ii) *Effect of momentum factor:* Rate of convergence can be improved by adding some inertial or momentum to the gradient expression. This has been accomplished by adding a fraction of the previous weight change to the current weight change. The addition of such a term, helps to smooth out the descent path, by preventing extreme changes in the gradients due to local anomalies. A commonly used update rule by [10] introduces such a momentum term.

$$[\Delta W]^{t+1} = -\eta \frac{\partial E}{\partial W} + \alpha [\Delta W]^{t}$$

Where α is momentum factor, W= Weight t= No. of iteration, E = error.

The value of α should be positive but less than 1. Typical values lies in the range of 0.5-0.9 [9]. Effect of momentum factor is shown in (Fig. 3) for same number of iterations, same learning rate and same activation function.

It has been observed that the network is best when 0.8 is the momentum factor.

iii) *Effect of learning rate:* Learning rate coefficient determines the size of the weight adjustments made at each iteration and hence influences the rate of convergence. If the learning rate coefficient is too large, the search path will oscillate and network may not be able to make the fine discriminations possible with that system more slowly. On the other hand if learning rate is too small, the descent will progress in small steps significantly increasing the time to converge. Learning rate cannot be negative because this would cause the change of weight vector to move away from ideal weight vector position [9]. If it is zero, no learning takes place and hence, the learning coefficient must be positive. If learning coefficient is equal to 2 the network is unstable and if it is greater than 1, the weight vector will overshoot from its ideal position and oscillate [9]. Hence, the learning rate must be between zero and one. Effect of different learning rates based on presented problem is tested for same number of iterations, same momentum factor and same activation function in the present work (Fig. 4).

It has been observed that networked trained best, when value of learning rate was 0.6.

So it is concluded that back propagation network with unipolar sigmoidal activation function give best result when momentum factor is 0.8, learning rate is 0.6 and there are 2 hidden layers and 6 and 3 neurons in the 1st and 2nd hidden layers respectively.

b) *Quick propagation network:* Back prop works by calculating the partial first derivative of the overall error with respect to each weight. This gives the gradient of the error surface. Once this gradient is known, this gradient is descended down until a minimum error is found. But the gradient is only known at this one point at any time and so an infinite number of small steps need to be taken. This is why the back propagation algorithm takes too long. Quick propagation speeds things up by taking large steps down the gradient, by keeping a copy of the previous change in overall error with respect to the weight, the difference between the previous weight and the present weight and the present derivative of error with respect to the weight. It is also assumed, that the change in the slope of the error curve is only going to be affected by the weight whose next step is being calculated, and the error curve would be similar to a parabola.

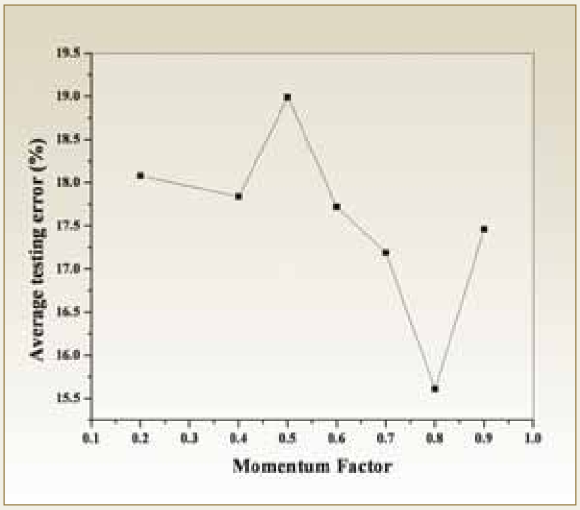

Fig. 3: Effect of momentum factor on the average testing error

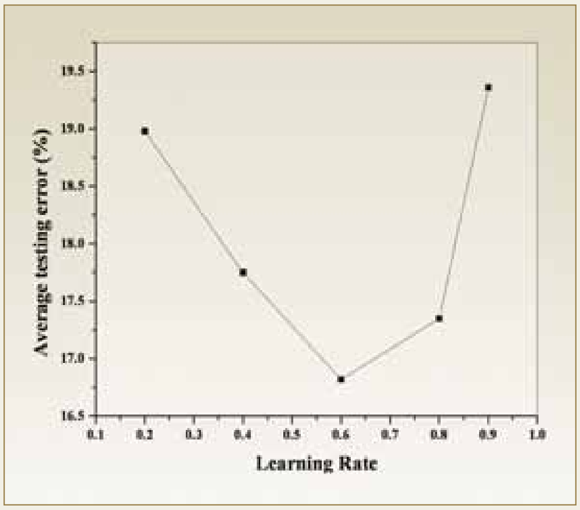

Fig. 4: Effect of learning rate on the average testing error

C) *Delta-bar-Delta (batch mode)*: Delta-Bar-Delta is a heuristic algorithm for modifying the learning rate as training progresses. One of the salient features of the delta-bar-delta algorithm is that, each weight has its own learning rate. There are two factors associated with the learning rate: The learning-rate increment factor η^+, and the learning-rate decrement factor η^-. The typical values for η^+ and η^- are 0.1 and 0.5 respectively.

D) *Resilient Back Propagation*: It is a local adaptive learning scheme, performing supervised batch learning in multi-layer perceptrons. The basic principle is to eliminate the harmful influence of the size of the partial derivative on the weight step. As a consequence, only the derivative is considered to indicate the direction of the weight update.

E) *Self Scaled Conjugate Gradient Algorithm*: The steepest descent algorithm based on first order scheme having several shortcomings such as: the convergence tends to be extremely slow and convergence to global minimum is not guaranteed. To combat above shortcoming, second order gradient technique, Self Scaled Conjugate Algorithm has been used. In this method, the error gradient information has been used at two time consecutive steps to improve the convergence speed. Dr. Manoranjan Sinha, from IIT Kanpur, developed it in 2000.

The comparisons of efficiency of different learning rules for same number of iterations are summarized in Table 2.

Table 2: Effect of different Learning Rules

Learning rule	Average error
Back Propagation with Momentum	16.33%
Quick Propagation	17.42%
Delta Bar Delta	17.30%
Resilient Back Propagation	16.68%
Self Scaled Conjugate Gradient Algorithm	19.56%

It has been concluded that Back Propagation with momentum is the best learning rule for present system. It has also been concluded, that artificial neural network with two hidden layer and 6 and 3 neurons in the 1st and 2nd hidden layers is the best network with Back Propagation with Momentum learning rule with 0.8 momentum factor and 0.6 learning rule and unipolar sigmoidal activation function.

Prediction of firing time based on proper network

Firing times have been predicted from not-trained and not-tested input data sets (prediction file) using best artificial network for this job. Results have been shown in Table 3. It has been observed that prediction of the firing times using artificial neural network based on 12 parameters is within tolerance limit.

Firing time more than 28 hrs leads to unsafe condition, which attracts administrative control of different authorities. To avoid this situation, results of this study (prediction of firing time) can be useful tools for managing the input parameters, to get firing time within desired range. Prediction of firing time eliminates the uncertainty of firing and is helpful for plant operation. It has been observed from plant experience that optimal recovery and maximum efficiency of the MTR process are obtained, when firing

Table 3: Prediction of firing time using BIKAS software

Sr. No.	Actual firing time (hr)	Predicted firing time (hr)	% Error
1	17.92	20.31	13.33
2	16.25	18.21	12.06
3	20.25	20.07	0.89
4	28.25	25.79	8.70
5	22.50	22.03	2.09
6	18.00	20.27	12.61

time is in the range of 16-30 hrs. This range can be maintained using this software.

Study of relative importance based on best network

It has been experienced that firing time depends on the twelve properties of the reactants and lining material, if other process parameters remain unchanged. But relative importance of these parameters is not studied yet. As reaction occurs at high temperature, lots of inter-related side reactions take place and it is quite impossible to theoretically correlate these parameters. An effort has been taken here to study the relative importance of these parameters by artificial neural network using BIKAS software.

After selecting best network (as mentioned earlier), the best network has been tested with test data sets (test file). Among these, only best test data set (consisting of 12 input and one output data) has been used, for relative study of these parameters. The error between calculated and desired firing time is only 0.05% in case of best test data set. One parameter of the best test data set (consists of 12 input parameters and one output parameter) has been increased by 10 % taking care that, that value of the test data set should not go beyond the range of the training data sets. The best network then tested with changed test data set and deviation in calculated firing time with respect to best-calculated firing time was noted. The same test was carried out twelve times for twelve input parameters. Deviation of firing time with defined deviation of only one parameter has been studied and more the deviation of firing time, more the importance of the parameter. These parameters are nonlinear and so interrelated, that it is not possible to give a fixed ranking based on the relative importance of these parameters. It has been finally concluded, that firing time mainly depends on tap density of UF_4, moisture and free acid in UF_4, particle size of magnesium and MgO content in magnesium. Almost similar result was also observed from plant experience during operation.

Conclusions

Initiation of the Magnesio Thermic Reduction of UF_4, carried out in a closed vessel called bomb reactor, is realized by sudden shoot up of the core temperature and it is called firing. Based on the importance of firing time and its uncertainty of prediction due to wide parametric variation, an attempt has been made here to predict firing time, using available operational data. Firing time depends on twelve properties of reactants and lining materials. There is no correlation available among these variables. Prediction of Firing Time and study on relative importance of the parameters has been carried out here, using software BIKAS based on Artificial Neural Network. Back Propagation with 0.8 momentum factor and 0.6 learning rate is found to be the best network for the present problem. The software is able to predict the firing time with acceptable error using properly selected network. Tap density of UF_4, moisture and free acid in UF_4, particle size of magnesium and MgO content in magnesium are the most important parameters for determination of firing time. As ANN works based on input and output data sets and selection of proper network has been done by trial and error method, more rigorous tuning of all parameters with more data sets may provide better results.

Acknowledgements

The authors are very much grateful to Dr. A. K. Suri, Director, Materials Group, BARC, for providing us an opportunity to do this work. The authors acknowledge the kind co-operation of Mr. N. Hadap and Ms. M. Singha of UED, BARC.

Nomenclature

E = Error
f = Transfer function.
I = Input parameters to neural network.
I_0 = Threshold input parameter.
t = Number of iteration.
O = Out put from neural network.
U = Summation function.

W = Weight.
W_0 = Thresholds value.

Greek Letters:

α = Momentum factor
η = Learning rate
η^+ = Learning rate increment factor
η^- = Learning rate decrement factor

References

1. C. D. Harrington and A. E. Euchle, Uranium production Technology, D. Van Nostrand Company, Inc. Princeton.
2. N. P.Galkin and B. N. Sudarikov, Technology of Uranium, Israel Program for Scientific Translation, Israel.
3. Qiang Xiong and Arthur Jutan, *Chemical Engineering Science*, 57,1027-1039, (2002).
4. Debashis Raha, *Indian Chemical Engineer,* Section B, 47, 182-188, (2005).
5. R. Sharma, D. Singhal, R. Ghosh and A Dwivedi, *Computers and Chemical Engineering*, 23,385-390, (1999).
6. K. K. Singh, K. T. Shenoy. A. K. Mahendra and S. K. Ghosh, *Chemical Engineering Science*, 59,2937-2945, (2004).
7. D. R. Parisi and M. A. Laborde, *Computers and Chemical Engineering*, 25,1241-1250, (2001).
8. Tsoukalas Lefteri, H. and A. Uhrig Robert, Fuzzy and Neural Approaches in Engineering, John Wiley and Sons, Inc (1997).
9. S. Rajasekaran and G.A. Vijayalakshmi Pai, Neural networks, Fuzzy Logics, and generic Algorithms, Prentice Hall of India Pvt Ltd, (2004).
10. Rumelhart, D. E., G. E. Hinton and R. J. Williams, *Parallel Distributed Processing*, 1,318, (1986).
11. Parker, D. B. Learning Logic, Invention Report S 81-84, File 1, Office of Technology, Stanford University, Stanford, CA.

ABOUT THE AUTHORS

Mr. S. Manna of Uranium Extraction Division, BARC Mumbai, obtained B. Tech. in Chemical engineering from Haldia Institute of Technology and M. Tech in Chemical Engineering from IIT Kharagpur. He has joined BARC through DGFS 02 batch and ranked 1st in Chemical Engineering during orientation course in training school. He is involved in Fluoride Effluent Treatment Plant project and Nitrate Effluent Treatment Plant project. He is associated with different developmental studies for betterment of the processes. He has five national and international conference/ journal papers to his credit.

ABOUT THE AUTHORS

Mr. S. Chowdhury obtained his B.E. (Metallurgy) from Bengal Engineering College, Calcutta University in 1994 and thereafter moved to IT-BHU for M. Tech. Subsequently, he joined BARC training school (39th batch) in 1995. He is engaged in uranium metal production and associated developmental activities since 1996. He obtained his M. Tech. degree in the year 2002. He has authored a few journal and conference papers.

Mr. S. K. Satpati of Uranium Extraction Division, BARC obtained B. Tech. (Chemical Engineering) from Calcutta University and M. Tech. (Chemical Engineering) from IIT Kharagpur and joined BARC through 36th Batch of Training School. Since 1993 he has been carrying out activities related to uranium metal ingot production of different sizes and carrying with different input uranium materials. He is also involved in R & D activities in the field of process development, design and application relevant to uranium, material processing and production. He has 21 international and national conference / journal papers to his credit.

Dr. (Ms) S.B. Roy a Chemical Engineer from Calcutta University, joined the Uranium Extraction Division in 1982, after successful completion of the 25th batch of BARC Training School. Ever since she has been engaged in regular production, related R&D and project engineering activities in the field of research reactor grade uranium metal production. She obtained her Ph.D. degree in Chemical Engineering from IIT, Mumbai in 2001. Presently, she is heading the Uranium Extraction Division, BARC and is a member of various safety committees for processing and production of uranium compounds. She is a Professor of the Homi Bhabha National Institute and was conferred the DAE Scientific and Technical Excellence Award for the year 2006.

ELECTROWINNING OF COBALT FROM SULPHATE SOLUTIONS

I.G. Sharma, P. Alex, A.C. Bidaye and A.K. Suri
Materials Processing Division

This paper was awarded the IIME-Best Published Paper in the journal *Extractive Metallurgy*, during the year 2005

ABSTRACT

This paper reports an account of study, conducted on optimization of the process parameters, for electro-winning of cobalt from cobalt sulphate solution. Effect of parameters such as bath composition, temperature, current density, agitation etc. on the voltage requirement, current efficiency and power efficiency of cobalt electro-deposition was explored. A maximum current efficiency of 97% was attained with an electrolyte composition of 60 g / L Co, 15 g / L Na_2SO_4, at a temperature of 60°C, a pH of 4.0 and a cathode current density of 400 A / m^2. The energy consumption was 3.0 kWh / kg of Co deposited. The optimum conditions so established were test examined for recovery of cobalt values from leach liquors, generated on processing of Alnico magnet scrap, cemented carbide tool scrap and spent hydrogenation catalyst. The cathode current efficiency ranged from 86 to 94 %, due to lower concentration (25 to 40 g/L) of cobalt in the processed leach liquor.

Keywords : Electro-winning, Cobalt, Secondary resources.

Introduction

Cobalt is a strategic metal finding use in diverse commercial, industrial, medical and military applications. As a metal, its largest use is in superalloys for critical applications in defense and industry. Other uses include additions in HSLA steels, cemented carbide tools, magnetic alloys, battery electrodes, preparation of Co^{60} radiation sources, body implants and in electroplating. Non metallic uses include those in ceramics, catalysts, paint pigments, steel belted radials, etc.

Cobalt occurs in nature in a widespread but dispersed form, almost exclusively in admixtures with ores of other metals. It is essentially extracted as a byproduct of Cu, Ni and Zn processing and as such cannot adjust to demand fluctuations. Recovery of Co from secondary resources is increasing, but the associated technology is hardly documented for proprietary and commercial reasons. About 70% of the world's total cobalt production is obtained from pure cobalt sulphate solutions through hydrometallurgical routes (Pradhan et al, 2001). Generally, in the recovery of Co from these sources, solvent extraction followed by electro-winning, is finding increasing application.

India has a cobalt production of 140 tonnes / annum; the balance requirement is met through imports. Several Indian laboratories have developed flow-sheets to effectively deal with selected secondary sources for recovering cobalt values (Tangri and Suri, 1999; Das, recovering cobalt values (Tangri and Suri, 1999; Das, 1998; Alex et al, 2001; Alex et al, 2004; Sadanandam et al, 2002, Tripathy et al, 2001). Extensive work has also been carried out in our laboratory at MPD, BARC, to develop flow-sheets for various indigenous sources such as Alnico magnet scrap (Alex et al, 2001), cemented carbide tool bits (Alex et al, 2004), spent catalyst (Sadanandam et al, 2002), etc. While the earlier work was concerned with bringing the metal values into solution, the present programme on electro-winning was undertaken to complete the flow-sheet.

During the electrolysis of $CoSO_4$ solution, the predominant reactions at the electrodes are as follows

At the cathode

i) $$Co^{2+} + 2e^- \rightarrow Co \qquad (1)$$

ii) $$2H^+ + 2e^- \rightarrow H_2 \qquad (2)$$

At the anode

i) $$2H_2O \rightarrow O_2 + 4H^+ + 4e^- \qquad (3)$$

The reduction of H^+ ions at the cathode, results in a rise in pH while the generation of H^+ ions at the anode, results in a decrease of pH. If the anolyte and catholyte are allowed to mix, then in normal Co electro-winning where current efficiency for Co deposition is in the range of 90%, the pH of the electrolyte will drop. Similarly, the Co strength of the electrolyte will also deplete. If the above three reactions are the only reactions taking place, then the drop in pH is proportional to the Co ion depletion. Therefore, if $Co(OH)_2$ is added to this solution, then, when the pH of the solution is restored, the Co strength of the solution will also be restored. Thus, restoring the pH is an effective method of regenerating the bath with respect to both the pH and the Co concentration.

However, other reactions do take place at the electrodes, prominent amongst these being (Lakshminarayan et al, 1996)

$$Co^{2+} \rightarrow Co^{3+} + e^- \qquad (4)$$

Most of the Co^{3+} ions deposit at the anode as a black oxide / hydroxide powder. The probability of a small fraction reaching the cathode cannot be ruled out. The presence of multivalent ions in the electrolyte affect the nature of the deposit. However, in the purified solutions used in this investigation, the activity of other ions was very low and their discharge at the electrodes could be neglected. Similarly, reaction (4) could also be neglected because the Co oxide deposited at the anode was only a small fraction of the Co deposited at the cathode.

This paper presents detailed studies on optimization of electrolysis parameters. Experiments were carried out on pure synthetic cobalt sulphate solutions to establish the optimum conditions for electrolysis. These conditions were then used on solutions, derived from leaching of secondary resources. It was aimed to prepare a cobalt plate of 1 mm thickness, to enable subsequent processing to a slug of 1m dia and 1 mm height, for conversion to Co^{60} isotopes.

Experimental

Materials

The synthetic electrolyte solutions were prepared by dissolving analytical grade cobalt sulphate and sodium sulphate in distilled water. Analytical grade sodium hydroxide was used, to prepare cobalt hydroxide slurry from cobalt sulphate solution. The purified leach liquors were prepared, by processing secondary resources of cobalt such as alnico scrap, cemented carbide tool bits and spent catalyst, the solutions were also subjected to electro-winning studies.

Equipment

Electro-winning experiments were conducted using a Pyrex glass laboratory cell. This cell, having a volume of 500 mL, consisted of an inlet for pH adjusted cobalt solution (regenerated electrolyte feed) and an outlet, from where the spent acidic electrolyte overflowed into the regeneration tank. Cobalt hydroxide slurry was pumped at a fixed rate into the regeneration tank to replenish the depleted electrolyte with cobalt and adjust the pH to the desired level. The regenerated electrolyte was next transferred to a buffer tank, from where it was fed back to the electro-winning cell at a metered rate. This procedure ensured that the bath composition, particularly the bath pH, was maintained constant throughout the experiment, unlike in some of the earlier studies (Das and Subbaiah, 1984). The temperature of the system was maintained by using a thermostat. The cathodes used were rectangular stainless steel /aluminium sheets of fixed dimensions. A thin layer of lacquer was applied on one side of the cathode. The anode was a Pb-8% Sb plate, placed at a constant distance of 30 mm from the cathode. A regulated DC power supply was used, for obtaining a constant current density during electrolysis. For measuring cell voltage and current, precision voltmeter and ammeter were incorporated in the circuit. The bath pH was measured continuously using a pH meter. For stirring of the electrolyte and keeping the cobalt hydroxide slurry in suspension, magnetic stirrers were used, while pumping of the electrolyte was done through metered peristaltic pumps.

Procedure

A solution of cobalt sulphate and sodium sulphate of known strength was filled in both electrolytic and regeneration tanks. Both the anode and the un-lacquered face of the cathode were polished with fine silicon carbide paper, rinsed with distilled water and acetone. Voltage was applied across the electrodes to achieve the desired current density. After electrolysis, the cathode was removed, washed thoroughly with distilled water, dried in an oven and the deposited plate was scraped off carefully from the cathode surface and weighed. From the weight gain, current efficiency was calculated. The thin powder coating at the anode was also scraped off and analyzed. The effect of the following parameters on the current efficiency, power efficiency and quality of deposit were studied : Co^{2+} concentration, Na_2SO_4 concentration, cathode current density, bath temperature, pH.

All the electro-deposition tests were conducted for a minimum period of 3 hours in pure cobalt sulphate solutions. This was followed by electrolysis of purified leach liquors obtained from various secondary sources.

Results and Discussion

Effect of Co^{2+} Concentration : Electrolysis was conducted by varying the cobalt concentration from 20g / L to 70g / L in the presence of 15 g / L of sodium sulphate, at a temperature of 60° C, pH 4 and a current density of 400 A/m^2. The results, summarized in Fig. 1 show, that the current efficiency increases with increase in cobalt concentration in the electrolyte. It was also observed that a low concentration of cobalt results in brittle and stressed deposits, which get easily detached from the SS cathode during electrolysis. All this is obviously due to the more abundant availability of cobalt ions, vis-a-vis hydrogen ions, at the higher cobalt concentrations, while at lower

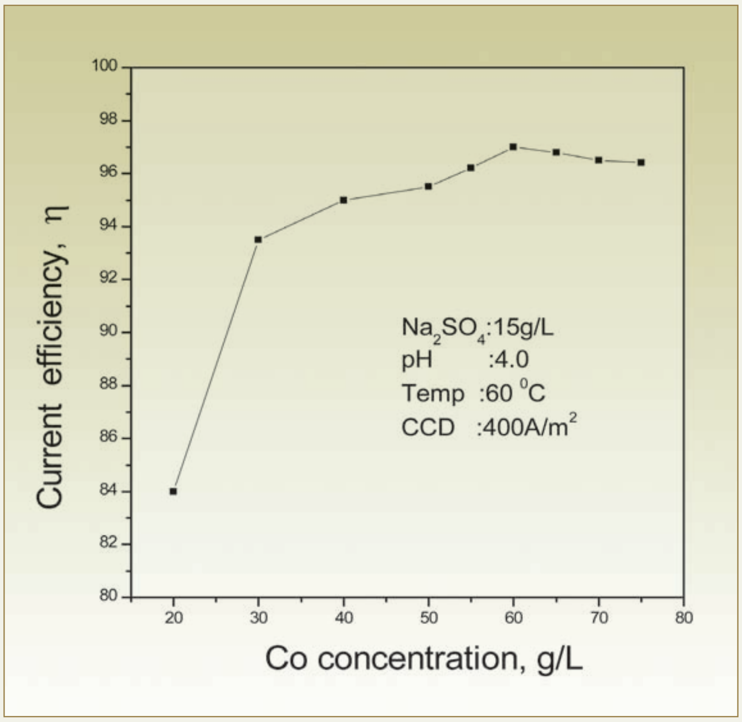

Fig. 1: Effect of Co concentration on the current efficiency

cobalt concentrations, relatively higher hydrogen evolution, and its consequent incorporation into the deposit, results not only in lower current efficiencies, but also in stressed and brittle plates. Since no additional benefit is derived in going beyond 60 g / L, this value was chosen as the optimum Co concentration.

The energy required to deposit cobalt also drops as the Co concentration increases, as can be seen from Fig. 2. This is an obvious consequence of the lower voltage requirement (due to higher conductivity at the higher Co concentration) and the increased current efficiency.

Na_2SO_4 Concentration: The incorporation of alkaline sulphate into the electrolyte, increases the conductivity of the solution. Experiments were performed by the addition of different alkaline sulphates such as potassium, sodium, ammonium and magnesium. Of these, a small amount of sodium sulphate addition resulted in adherent and good quality deposit. The effect of sodium sulphate concentration on the current efficiency is depicted in Fig. 3. As can be seen, the current efficiency increases with Na_2SO_4 addition up to 15 g / L, beyond which there is no benefit. The increase can be explained using Fig. 4, which depicts the voltage required to obtain the desired current density. The decreased voltage results in lower H_2 evolution and higher efficiency for Co recovery. Beyond 15 g / L Na_2SO_4, there is no drop in voltage and no change in current efficiency. The lowering in the applied voltage and the increased current efficiency also results in lower energy requirement as can be seen in the figure.

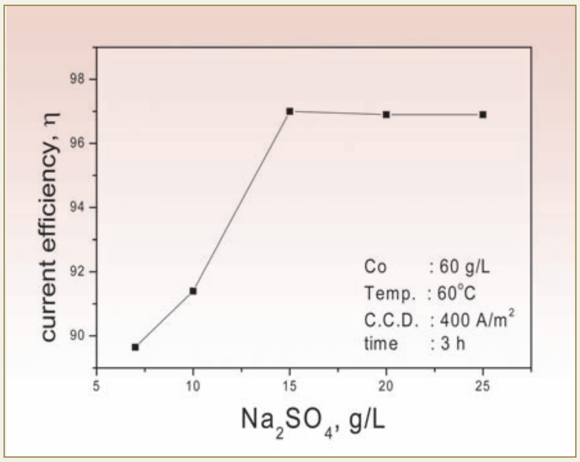

Fig. 3: Effect of sodium sulphate concentration on the current efficiency

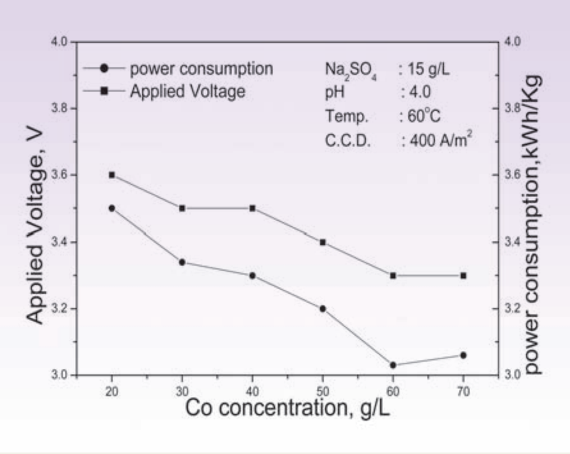

Fig.2: Effect of Co concentration on the applied voltage and power consumption

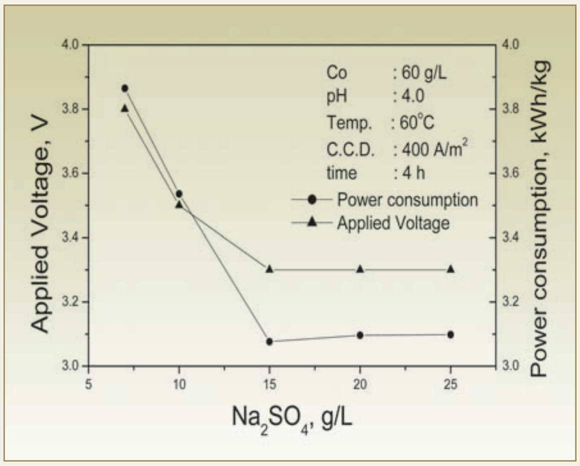

Fig. 4: Effect of sodium sulphate concentration on the applied voltage and power consumption

Temperature: Fig. 5 gives the effect of temperature on the current efficiency, at a current density of 400 Amp / m^2, pH3 and using an electrolyte composition of 60g / L cobalt and 15g / L of sodium sulphate. By increasing the temperature from 27 to 70°C, it was observed that the current efficiency increased and power consumption decreased. The deposit formed at temperatures up to 50°C was non-uniform and non-adherent, however, higher temperatures improved both quality and adherence.

The higher current efficiency is obviously due to increased ionic mobilities at higher temperatures. This is reflected in Fig. 6 which shows that the voltage required to obtain the desired current density decreases with temperature. The rapid availability of Co ions at the cathode can also result in less stressed, better quality deposits. Other factors that can affect quality of the deposit are as follows (Trevor, 2003) : cobalt exists in both α and β forms, the α form is hexagonal close packed and is not usually deposited in an electrochemical cell, the β form is face centered and is the preferred form. If deposited at higher temperatures, it is claimed that the deposit will be β and at lower temperatures will be a mixture of both α and β (Nakahara,1980;Goddard, 1963) will obviously cause a stress in the deposit, which results in detachment of the deposit. Another problem with cobalt is that, besides Co^{2+} it also exists as Co^{3+} in the electrolyte, the latter being generated at the anode. The Co_2O_3 powder collected at the anode and analyzed by oxidation- reduction reaction of ferrous sulphate solutions (Lakshminarayan, 1996) confirmed this. Though, the effects of Co^{3+} in the electrolyte are unclear, the presence of multivalent cations in the electrolyte results in lower efficiency and dendritic nature of the deposit. Hence a temperature of 60°C was selected, for obtaining cobalt plates of good morphology. The power consumption also stabilizes at around this temperature, as can be seen in Fig. 6.

pH: Fig. 7 depicts the influence of pH of the electrolyte on Co electro-deposition. The current efficiency rises sharply as the pH rises to around 3; beyond that it stabilizes. At lower pH, the higher H^+ ion concentration results in substantial H_2

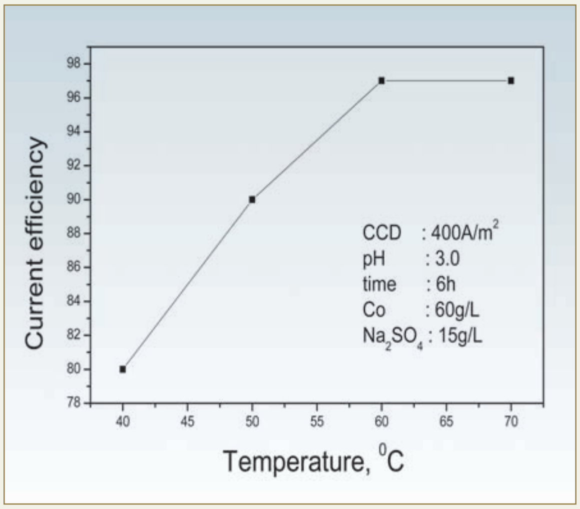

Fig. 5: Effect of temperature on the current efficiency

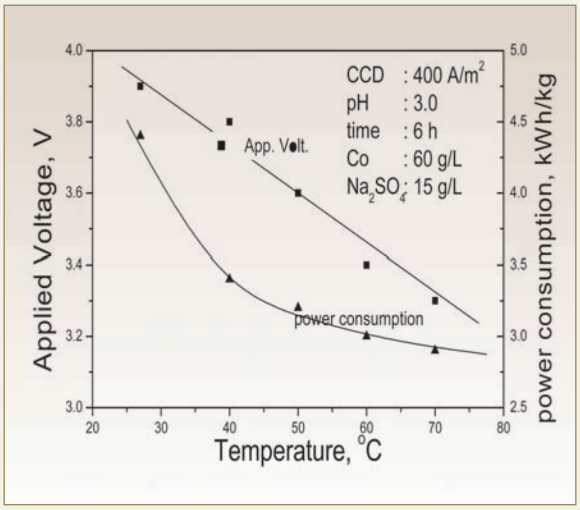

Fig. 6: Effect of temperature on the applied voltage and power consumption

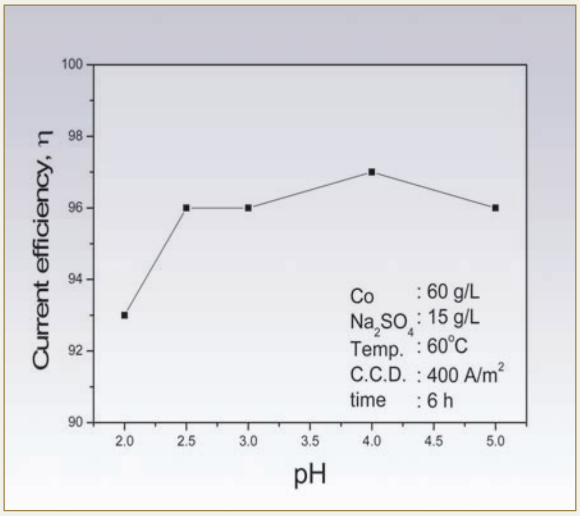

Fig. 7: Effect of pH variation

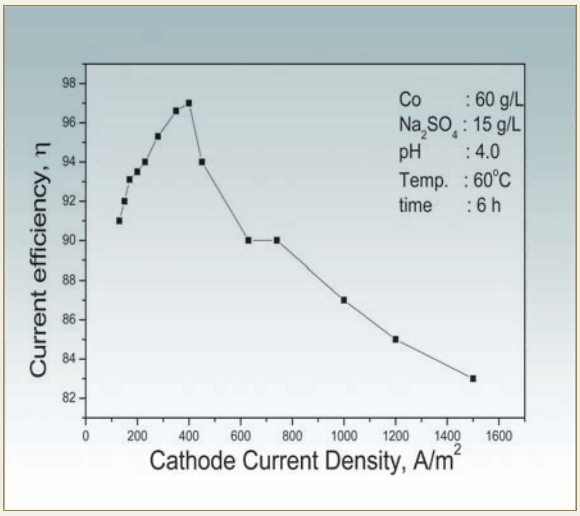

Fig. 8: Effect of Cathode current density on the current efficiency

gas evolution, resulting in reduced current efficiency and also poor quality deposits that get detached from the substrate during electrolysis. At pH greater than 5, the small amount of H^+ discharge (and H_2 gas evolution) at the cathode, results in increased pH in the catholyte and initiates $Co(OH)_2$ precipitation. This hydroxide gets incorporated in the electro-deposit, resulting in very poor quality plates. It can be said that below pH 2.5, the current efficiency drops. Hence a pH range of 3 to 4 appears to be reasonably satisfactory from the current efficiency point of view.

Cathode Current Density: The effect of Cathode Current Density (CCD) on the current efficiency is depicted in Fig. 8. As can be seen, the current efficiency went through a maximum at 400 A / m^2, above which it declined steadily, while applied voltage increases with CCD as seen from Fig. 9. Similar results have been reported by Das et al (Das et al, 1984). The quality of the deposit also changed with the CCD. The deposit was patchy and non-adherent at low CCD. As the CCD increased, the cobalt coverage of the cathode increased and the deposit was more adherent. Beyond 400 A / m^2, the efficiency decreased because to increase the CCD it was necessary to increase the cathodic voltage which resulted in greater H_2 evolution. As the CCD increased, the deposit at the edges became increasingly powdery and dendritic growth was becoming prominent at the edges mainly because of two reasons. First, due to current concentration at the edges and secondly due to the more abundant availability of Co ions at the edges, from all sides unlike at the centre of the cathode. This generally leads to very thick growth at the edges and in extreme conditions to powdery, dendritic growth. Stirring alters the condition to yield a more uniform deposit all over. Stirring of the electrolyte during electrolysis mixes the acidic anolyte with the bulk electrolyte and increases mass transfer of Co^{2+} ions to the cathode. In one experimental run at 1500 A / m^2 for a duration of 3 h, stirring during the electrolysis decreased the current efficiency from 83% to 76%. But the dendritic growth at the edges came down very substantially. Fig 9 depicts the effect of applied voltage on current density, showing an increase in voltage requirement with current density.

Initial electro-winning trials at low current density (< 200 A / m^2) on SS substrate, resulted in patchy and non-adherent deposits. Roughening the cathode surface with 80 mesh paper and / or electro-etching the surface just prior to plating, generally proved beneficial for the deposit quality. While deposit quality improved at higher CCD, the plates continued to be

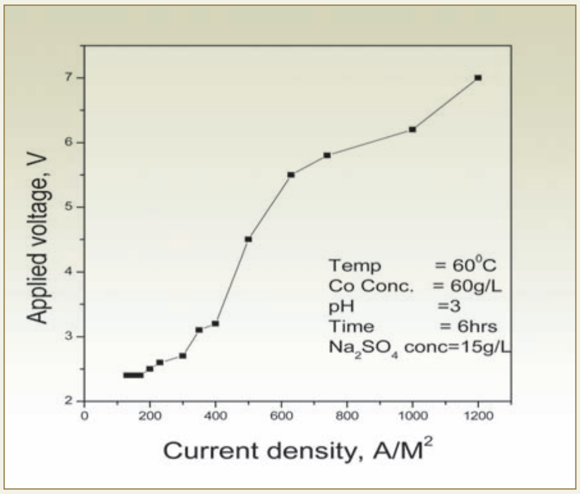

Fig. 9: Effect of applied voltage on current density

highly stressed with the edges bending towards the anode, if they got detached during electro-winning. Residual stress values were measured at different locations of the plate, using XRD (Kushner,1962; Prevey,1986), and ranged from 300 to 600 MPa and were tensile in nature. The best results were however obtained with Al substrates that had been polished with 80 mesh paper. The electrodeposited Co plates were adherent and flat.

Based on these studies, the optimum conditions for electro-deposition of cobalt from a sulphate solution were fixed as follows : Co 60 g / L, Na_2SO_4 15 g / L, temperature = 60°C, pH = 3 to 4, CCD = 400 A / m^2. These conditions were directly applied for the electro- deposition of cobalt from various secondary resources to prepare cobalt metal sheets.

1. Alnico scrap : Alnico scrap used in this investigation was analyzed and contained 8.5-10 % Ni, 11-12 % Co, 32-50 % Fe, 10-11 % Al and balance SiO_2. After processing the scrap through a hydrometallurgical route (including $CuCl_2$ leaching) a leach liquor containing 18-20 g / L (Ni + Co), 7-8 g/L Cu and 0.1 g / L Fe was obtained. On further processing through solvent extraction, a purified $CoSO_4$ solution (99.99 %) containing 30-35 g / L Co was generated.
2. Cemented Carbide Sludge: The average composition of a typical cemented carbide sludge was found to be 37 % Co, 10 % Ta, 0.78 % Nb, 5 % Ti and 12.37 % W. Processing of the sludge involved fusion with soda ash in the presence of sodium nitrate followed by acid leaching. The leach liquor analyzed 25-30 g / L Co with less than 1 % Fe. A solvent extraction step resulted in a 99.99% pure solution of strength 35-40 g / L.
3. Spent ammonia cracker catalyst: The typical analysis of the spent catalyst revealed 36.5 % Al_2O_3, 31.5 % Fe_2O_3, 29.5 % CoO, 0.27 % NiO, 0.70 % K_2O and balance binder. After crushing and grinding, the catalyst was leached with H_2SO_4 and HNO_3 was added for oxidation. After precipitation and two solvent extraction steps, a 99.99 % solution of strength 25 g / L was obtained.

The Co solution from each of the above secondary sources was first purified from organic solvents, by adsorption on activated charcoal and then subjected to electrowinning without upgrading, with respect to cobalt concentration under the optimum conditions established for the synthetic solutions. A good quality plate was obtained in each case. The current efficiencies were however lower, ranging from 86 % to 94 %, because of the lower Co concentration values.

Table 1: Chemical analysis of electrodeposited Co plate

Element	Weight %	
	At pH 3	At pH 4
Co	99.95	99.94
Ni	0.043	0.023
Fe	0.01	0.009
Mg	0.003	0.009
Cu	0.003	0.009

Table 1 gives the typical analysis of one such plate recovered from the solvent exchanged purified liquor obtained after processing the above mentioned secondary sources.

Conclusions

The optimum conditions for the electro-deposition were found to be as follows: Co concentration = 60 g / L, Na_2SO_4 concentration = 15 g / L, temperature = 60°C, pH = 3 to 4, CCD = 400 A / m^2. Under these conditions the current efficiency was 97% while the energy efficiency was 3.0 kWh / kg of Co deposited.

The feasibility for recovering Co metal values from a variety of secondary sources like Alnico scrap, Carbide sludge, heavy water spent catalyst, etc. by leaching, solvent extraction and electro-deposition has been established.

Acknowledgements

The authors wish to thank Mr. S.K. Tangri, Head, Solvent Extraction Section, MPD, BARC, for providing the purified liquors and Mr. P.K. Maity for conducting some of the work as part of his training project.

References

Alex P. Mishra P. and Suri A.K., 2001. Studies on Processing of an Alnico Scrap. *Mineral Proc. Ext. Met. Rev*. 22, 547-567.

Alex P., Bhave V.S., Hubli R.C. and Suri A.K., 2004. Processing of Cobalt bearing Hard Metal Waste. *Metal, Minerals and Processes*, 16, 79-84.

Das R.P., 1998. Recovering Cobalt from Secondary Sources in India. *JOM* 98, 51-52.

Das S.C. and Subbaiah, 1984. Electrowinning of Cobalt I. Winning from pure Cobalt Sulphate bath. *Hydrometallurgy* 12, 317-333.

Lakshminarayanan G.R., Chen E.S., Sadak J.C. and Sautter F.K., 1996. Electrodeposition of Cobalt using an Insoluble Anode. *J. Elecrochem. Soc*. 123 (No. 11 Nov.), 1612-1616.

Pradhan N. Singh P. Tripathi B.C. and Das S.C., 2001. Electrowinning of cobalt from acidic sulphate solutions-Effect of chloride ions. *Minerals Engg*. 14 (No 7), 775-783.

Sadanandam R., Menon N.K., Rane M.V., Sharma A.K. Fonseca M.F. Tangri S.K. and Suri A.K., 2002. Recovery of high purity Cobalt Oxalate from Spent Ammonia Cracker Catalyst. *Proc. Intl. Sem. on Mineral Processing Technology* MPT-2002, Bangalore, India, 366-370.

Tangri S.K. and Suri A.K., 1999. Solvent Extraction of Metals from Ocean Nodules Leach Liquor. Metals, *Minerals and Processes* 11 (No. 2), 145-150.

Trevor C., 2003. Reducing the Stress in Cobalt Alloy Plating. Available at http://www.finishing.com/204/83.shtml.

Nakahara, S and Mahajan S, 1980, The influence of solution pH on micro structure of electrodeposited cobalt, *Journal Electrochem. Soc*., 127,283-8.

Goddard J. and Wright J. G, 1964, The effect of solution pH and applied magnetic field on the electrodeposition of thin single- crystal films of cobalt, *British journal of applied physics*,15, 807-814.

Tripathy B.C., Singh P. and Muir D.M., 2001. Effect of Manganese(II) and Boric Acid on the Electrowinning of Cobalt from Acidic Sulphate Solutions. *Metallurgical and Materials Trans.B 32B* (June), 395-399.

Kushner J.B. , 1962 Stresses in electrodeposited metals, *Metal Progress*, 81, (2), 88-93.

Prevey P.S, X-ray diffraction residual stress techniques, 1986, Metals Handbook 9th edition, vol -10, 380-392.

ABOUT THE AUTHORS

Dr. I. G. Sharma, Head, Materials Processing Division, is a Metallurgist from the 15 th batch of Training School. His major contributions are in the field of (a) process metallurgy of reactive, refractive metals (b) development of refractory metal alloys (c) powder metallurgy (d) ultra purification of metals (e) processing of secondary resources (f) molten salt and aqueous electrolysis (g) protective coatings (h) extractive metallurgy of cobalt. He has more than 80 technical publications in national and International journals to his credit.

Dr. Pamela Alex joined the Metallurgy Division in the year 1979 and obtained PhD in Chemistry from Mumbai University in 1991. Her research areas include extractive metallurgy of rare and strategic metals, secondary resource processing, electrochemical processes for bulk as well as nano powders, electro-less coating and preparation of refractive metal alloys. She has successfully transferred technology for recovery of metal values from hard metal scrap with special reference to cobalt.

Dr. A.C. Bidaye joined the Extractive Metallurgy Section of the erstwhile Metallurgy Division in 1978 after graduating from the 21st batch of the Training School. He has worked on pyro- and electro- metallurgical techniques for preparing metals and alloys of some of the rare and refractory metals and also on the processing of secondary resources. He is currently Heading the Surface Engineering Section of Materials Processing Division.

Dr. A.K. Suri, Director, Materials Group has made major contributions in the areas of Chemical Process Metallurgy, Materials Synthesis and Advanced Materials & Processes. Dr. Suri has been instrumental in the development of processes leading to the setting up of production scale facilities for strategic materials critical to the nuclear programme. Besides being conferred with several prestigious awards for his contributions during his illustrious career, he received the G.D. Birla award (2007) for the development of a new route for the processing of an indigenous uranium resource.

CONCENTRATION-DEPENDENT ANTIOXIDANT/ PRO-OXIDANT ACTIVITY OF CURCUMIN IN HUMAN RED BLOOD CELLS (RBCS)

A. Banerjee, A. Kunwar and K.I. Priyadarsini
Radiation & Photochemistry Division

This paper was adjudged as one of the Best Posters at the "International Conference on Free Radicals & Natural Products in Health -2008" held at Jaipur, India during February 14-16, 2008.

ABSTRACT

The antioxidant / pro-oxidant properties of curcumin have been studied by evaluating its ability to protect RBCs from AAPH (2,2'-azobis(2-amidinopropane) hydrochloride) induced oxidative damage. Lipid peroxidation, hemolysis and K^+ ion loss in RBCs were assessed respectively by formation of ThioBarbituric Acid Reactive Substances (TBARS), absorbance of haemoglobin at 540 nm and flame photometry. The treatment of RBCs with curcumin showed concentration-dependent decrease in level of TBARS and haemolysis. However in contrast to the above mentioned effects, curcumin in a similar concentration range, did not prevent release of intracellular K^+ ions during the process of haemolysis, rather curcumin itself induced it's release even in the absence of haemolysis. The ability of curcumin to prevent oxidation of intracellular GSH due to hemolysis showed mixed results. At low concentrations of curcumin (<10 µM) it prevented GSH depletion and at higher concentrations, the GSH levels decreased gradually. These results indicate that curcumin while acting as an antioxidant, also exhibits pro-oxidant activity at high concentrations.

Introduction

Curcumin (diferuloylmethane), a dietary pigment responsible for the yellow colour of turmeric, has been used in traditional medicine. Extensive research within the past one decade has confirmed that curcumin possesses antioxidant activity and mediates anti-inflammatory effects [1,2]. Curcumin has been shown to inhibit lipid peroxidation and effectively scavenge superoxide and peroxyl radicals [3]. It also shows anti-tumour activity, by suppressing the proliferation of a wide variety of tumour cells [4]. In contrast to these studies, some reports suggest that curcumin induces production of Reactive Oxygen Species (ROS) and leads to apoptosis in proliferating cells [5]. Taken together, these contrasting reports suggest that curcumin exhibits both antioxidant and pro-oxidant activities depending on cell type. Therefore in this present work, we have investigated the differential antioxidant/pro-oxidant behaviour of curcumin, by following its ability to protect human RBCs from free radical-induced damages. RBCs are enucleated cells, containing poly-unsaturated fatty acids in their cell membrane [6]. The major protein component found within these RBCs is the red pigment haemoglobin (Hb) [6]. RBCs are fragile cells and are highly susceptible to free radical-induced damage of cell membrane (lipid peroxidation) leading to leakage of Hb (haemolysis) from within. K^+ ions present within the cell, which maintain the osmotic balance, are prone to leakage following haemolysis [6]. Therefore, oxidative haemolysis of RBCs and its protection by compounds, act as a good model system to screen the test compounds for their antioxidant/pro-oxidant behaviour [6]. Haemolysis, was initiated by the peroxyl radicals generated by thermal decomposition of an azo compound 2,2'-Azobis (2-Amidino Propane) Hydrochloride (AAPH) in the presence of oxygen. Since ROS can influence the glutathione (GSH) concentration in cells, GSH levels were also monitored following haemolysis.

Materials and Method

Curcumin,2,2'-Azobis(2-AmidinoPropane) Hydrochloride (AAPH), and 5,5'-DiThiobis-2-NitroBenzoic acid (DTNB) were of the best purity available and obtained from commercial sources. All the other chemicals were of analytical grade. Blood samples were obtained by venipuncture from healthy volunteers, with strict adherence to the ethical guidelines laid down by the institutional animal ethics committee and RBCs were isolated. Haemolysis of RBCs was initiated by mixing RBCs suspension in Phosphate Saline Buffer (PBS) with AAPH solution (final concentration 50 mM) and incubating the mixture at 37 ^{o}C for 3 hours. The lipid peroxidation, haemolysis and K^+ ion loss in RBCs as a consequence of haemolysis were assessed respectively by formation of ThioBarbituric Acid Reactive Substances (TBARS), absorbance of haemoglobin at 532 nm and flame photometry [7]. The concentration of GSH in RBCs was determined using 5,5'-DiThiobis-2-Nitro Benzoic acid (DTNB) reagent [7]. In order to test the effects of curcumin on the above processes, RBCs were pre-incubated with varying concentrations of curcumin at 37^{o}C for 30 min, washed twice with cold PBS and then subjected to AAPH-induced haemolysis. The IC_{50} value i.e. the concentration of curcumin required to inhibit hemolysis or lipid peroxidation by 50%, was determined by plotting the percent haemolysis or TBARS levels respectively, as a function of curcumin concentration and from the plot, the concentration of curcumin required to reduce the activity by 50% was identified. Each experiment was done in triplicate and results are presented as means ± SEM, n = 3.

Results

(i) Inhibition of AAPH-induced haemolysis and lipid peroxidation in human RBCs by curcumin

In the absence of AAPH, RBCs were stable and the haemolysis was negligible. When aqueous suspension of RBCs was incubated with AAPH, about 53% of haemolysis was observed. Fig. 1 shows variation in % haemolysis in RBCs, pre-incubated with increasing concentrations of curcumin (5-50 μM) for 30 minutes at 37^{o}C and then subjected to AAPH-induced haemolysis. It is evident from Fig. 1, that the percent haemolysis gradually decreased with increasing concentration of curcumin, from which the IC_{50} value, was found to be 43 ± 5 µM. Inset of Fig.1 shows variation in TBARS level in RBCs, after being subjected to AAPH-induced damage, in the presence and absence of different concentrations of curcumin. The level of TBARS was significantly increased after incubation of RBCs with AAPH as compared to the control sample. In the presence of curcumin, there was gradual decrease in TBARS formation and this inhibition increased with increasing curcumin concentration from 5 to 40 μM, from which the IC_{50} value, was found to be 23.2 ± 2.5 µM. The percent haemolysis in RBCs, incubated with curcumin (5-50 μM), in the absence of AAPH was almost identical to that of control sample, indicating that curcumin itself could not induce haemolysis. The incubation of RBCs with curcumin in the absence of AAPH did not show any significant change in the level of TBARS as compared to control sample.

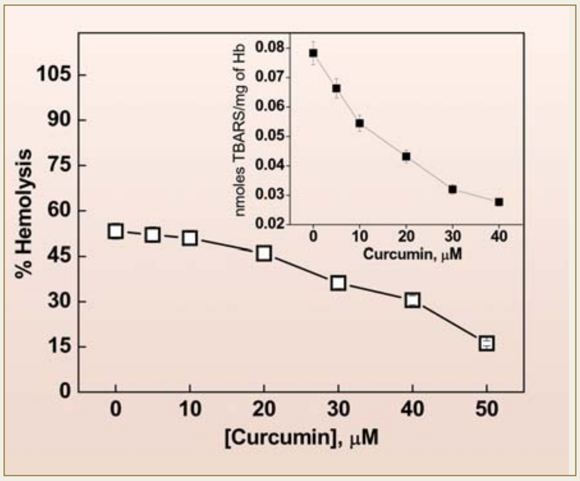

Fig. 1: Percent haemolysis in human RBCs pre-incubated with different concentrations of curcumin and subjected to haemolysis by AAPH for 3 hours. Inset shows variation in TBARS in the same system.

(ii) Inhibition of AAPH induced K^+ ion leakage in human RBCs by curcumin.

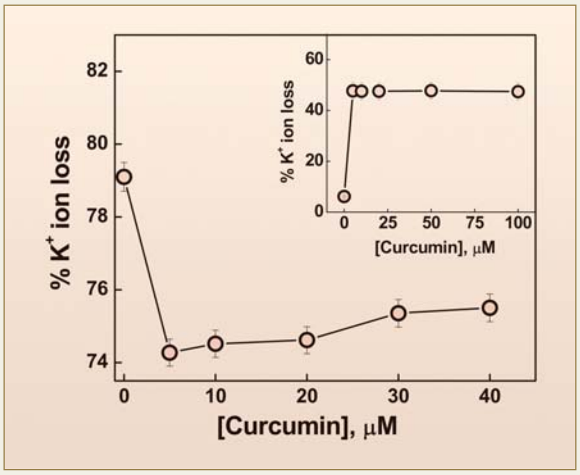

Fig. 2: Variation in percent K^+ ion loss in human RBCs incubated with AAPH for 3 hours in presence of different concentrations of curcumin. Inset shows variation in percent K^+ ion loss in human RBCs incubated with different concentrations of curcumin.

In the absence of AAPH, the RBCs were stable and the K^+ ion leakage was negligible. When aqueous suspension of RBCs was incubated with AAPH, about 79% of K^+ ion leakage was observed. Fig. 2 shows the variation in % K^+ ion leakage from RBCs pre-incubated with increasing concentrations of curcumin (5-40 μM) for 30 minutes at 37^0C and then subjected to AAPH -induced haemolysis. It is evident from Fig. 2 that the percent K^+ ion leakage is lower in curcumin pretreated samples as compared to control sample, however in each case, the K^+ ion leakage increased with increasing concentration of curcumin. Inset of Fig. 2 shows variation in percent K^+ ion loss in RBCs after incubation with different concentrations of curcumin (5 to 100 μM) for 3 hours in the absence of AAPH. From the figure it is clear that the percent K^+ ion loss is significantly higher in curcumin treated samples, as compared to the control sample. The percent K^+ ion loss was almost identical; nearly 47% at all the concentrations of curcumin (5 to 100 μM) tested in the present study.

(iii) Effect of curcumin on GSH levels in RBCs after hemolysis

Fig. 3 shows change in GSH levels in RBCs after treatment with AAPH and also in the presence of increasing concentration of curcumin (5 to 40 mM). The normal basal level of GSH in RBCs was found to be 2.74 ± 0.05 nmoles/mg of haemoglobin and after incubation with AAPH, the GSH level reduced to about 1.82 ± 0.03 nmoles/mg of haemoglobin. Addition of curcumin to this reaction system, prevented the reduction in GSH content in a concentration-dependent manner up to 10 mM. However at higher concentrations of curcumin treatment, GSH content reduced in a concentration-dependent manner.

Inset of Fig. 3 shows variation in glutathione level in RBCs, after incubation with different concentrations of curcumin (5 to 40 μM) for 3 hours in the absence of AAPH. From the figure it is clear, that the level of glutathione in curcumin treated RBCs was almost constant up to treatment concentration of 10 μM, however beyond that, a concentration-dependent decrease in level of glutathione was observed.

Discussion

Haemolysis of human RBCs is a very good model for studying free radical-induced oxidative damage to membranes and to evaluate the antioxidant activity of new compounds [6]. Therefore, to evaluate the antioxidant activity of curcumin, lipid peroxidation of the membrane fatty acids, loss of haemoglobin and release of intracellular K$^+$ ions have been estimated in human RBCs treated with AAPH. The results obtained from these studies indicate, that curcumin protects RBCs from AAPH-induced lipid peroxidation and thereby prevents haemolysis.

Like in lipid peroxidation and haemolysis assays, curcumin did not show progressive inhibition of K$^+$ ion loss and GSH depletion under AAPH-treated condition, thus making us unable to estimate their IC$_{50}$ values. Curcumin treated samples showed lower percent of K$^+$ ion loss as compared to AAPH-treated samples. However among them, the percent K$^+$ ion loss was increasing with increasing concentrations of curcumin. Therefore, to know whether curcumin itself has any effect on K$^+$ ion loss, we looked at the loss of K$^+$ ion only in curcumin treated samples. The results clearly suggest, that curcumin at concentration as low as 5 mM drastically increased the loss of K+ ions (47%) from RBCs. With increasing curcumin concentration, the percent of K$^+$ ion loss remained almost the same, suggesting the saturation effect of curcumin on K$^+$ ion loss. The ability of curcumin to induce the K$^+$ ion loss may be because of its effect on Na$^+$/K$^+$ ion channels present on RBCs membranes. This indicates that curcumin may not be acting as a simple antioxidant, but probably has a pro-oxidant effect.

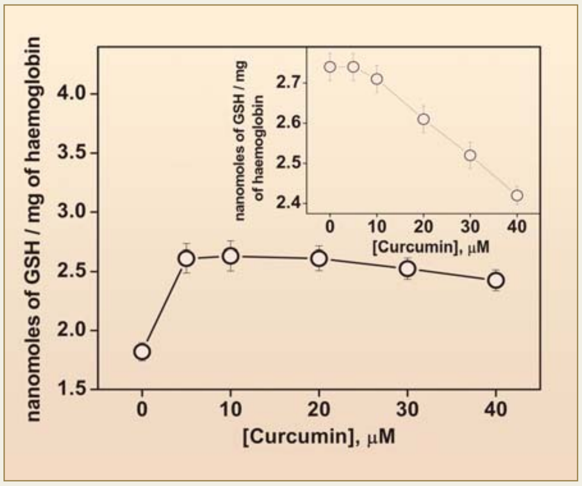

Fig. 3: Variation in GSH levels in human RBCs incubated with AAPH for 3 hours in the presence of curcumin. Inset shows variation in GSH levels in human RBCs incubated with different concentrations of curcumin without AAPH.

GSH, a tripeptide containing cysteine, is the most abundant thiol present in mammalian cells [7]. During oxidative stress, the cellular pool of GSH is depleted. Exogenously applied antioxidants protect GSH levels in cells by preventing them from being consumed in reaction with free radicals. Our results indicate that the GSH levels come down significantly in RBCs after AAPH incubation, but treatment with curcumin in the concentration range from 5 to 10 μM prevents decrease in GSH level. However, further increase in concentration of curcumin, showed decrease in GSH level, in a concentration-dependent manner. Some reports suggest, that curcumin reacts with free radicals and generates less reactive phenoxyl radical [8]. Therefore, the observed decrease in reduced GSH level in curcumin (>10 mM) pretreated samples, after exposure to AAPH, could also be due to the excess accumulation of phenoxyl radicals and thereby oxidation of cellular reduced GSH pool to GSSG. Hence, this observation suggests pro-oxidant behaviour of curcumin at higher concentrations of treatment. In conclusion, curcumin shows both antioxidant and pro-oxidant activity in RBCs haemolysis model and at high curcumin concentration, it is the later which predominates over the former.

Acknowledgements

The authors are thankful to Dr. S. K. Sarkar and Dr. T. Mukherjee, for constant encouragement and support.

References

1. R. A. Sharma, A. J. Gescher, W. P. Steward, *Eur. J. Cancer* 41 (2005) 1955-1968.
2. S. Shishodia, G. Sethi, B. B. Aggarwal, Ann. N. Y. *Acad. Sci.* 1056 (2005) 206-217.
3. K.I. Priyadarsini, Free Radic. *Biol. Med.* 23 (1997) 838-844.
4. B. B. Aggarwal, A. Kumar, A. C. Bharti, *Anticancer Res.* 23 (2003) 363-398.
5. S. Bhaumik, R. Anjum, N. Rangaraj, B.V. Pardhasaradhi, A. Khar, *FEBS Lett*. 456 (1999) 311-314.
6. E. Niki, E. Komuro, M. Takahashi, S. Urano, E. Ito, K. Terao, *J. Biol. Chem*. 263 (1988) 19809-19814.
7. A. Kunwar, B. Mishra, A. Barik, L.B. Kumbhare, R. Pandey, V.K. Jain, K.I Priyadarsini, Chem. Res. *Toxicol*. 20 (2007) 1482–1487.
8. G. Galati, O. Sabzevari, J.X. Wilson, P.J. O'Brien, *Toxicology* 177 (2002) 91–104.

ABOUT THE AUTHORS

Mr. Arnab Banerjee obtained M. Sc. degree in Biotechnology from Kumararani Meena Muthiah College of Arts and Science, Department of Biotechnology, Madras University, Chennai. He completed dissertation work for partial fulfillment of his M.Sc. programme at the Radiation and Photochemistry Division, BARC during May 2007 to July 2007.

Mr. Amit Kunwar obtained M. Sc. degree in Biotechnology from the Centre For Plant Molecular Biology, Tamil Nadu Agricultural University in 2003. After graduating from BARC Training School in 2005 (48th Batch, Bioscience discipline), he joined the Radiation & Photochemistry Division, BARC. Since then he is involved in free radical cellular biochemistry and evaluation of synthetic as well as natural molecules for their anti-oxidant and pro-oxidant activity, employing spectroscopic and biochemical techniques.

Dr (Ms.) K. Indira Priyadarsini joined BARC in 1983. She is currently working on the elucidation of mechanisms of antioxidant action involving organoselenium compounds, natural products and herbal extracts with potential application as radioprotectors, employing spectroscopic methods, electron pulse radiolysis and biochemical studies. Dr Priyadarsini has co-authored more than 135 papers in peer reviewed international journals on radiation chemistry, photochemistry, biophysics and radiation biology. She has been elected as the Fellow of the National Academy of Sciences, India and is the recipient of the Homi Bhabha Science & Technology Award.

TO IDENTIFY THE ACTIVE PRINCIPLE OF FORMULATED ANTI DIABETIC DRUG SYNDREX® WITH STRONG ANTIOXIDANT POTENTIAL

S.S. Khole and S. Ghaskadbi
Department of Zoology, University of Pune, Pune
and
T.P.A. Devasagayam
Radiation Biology and Health Sciences Division

This paper won the Best Poster Award at the International Conference on "Free Radicals and Natural Products in Health" organized by the Society for Free Radical Research-India at Jaipur, India, during 14-16, February 2008.

ABSTRACT

Diabetes mellitus is a complex chronic disease characterized by hyperglycemia, which *via* several mechanisms leads to an increase in production of ROS (Reactive Oxygen Species) and oxidative stress. Additionally, impaired synthesis of naturally occurring antioxidants under diabetic condition also results in increased oxidative injury to biological molecules. Oxidative stress has been shown to be responsible for development of diabetic complications. Hence antioxidant supplementation along with a drug to control hyperglycemia would be a helpful therapy to combat diabetes. Therefore many products of herbal origin are being tested for both their antidiabetic and antioxidant properties. Syndrex® manufactured by Plethico Laboratories, Indore, is a formulated antidiabetic drug, which contains powder of germinated fenugreek seeds. The antioxidant potential of this drug was already demonstrated in our laboratory and among the different soxhlet fractions checked, the methanolic fraction was found to possess the highest antioxidant activity (Dixit et al, 2008). The aim of the present study is to sub fractionate the soxhlet methanolic fraction of Syndrex® and to purify the compounds with high antioxidant activity. Sub-fractionation of methanolic extract by silica gel column chromatography followed by flash column chromatography lead to elution of eight fractions, which were then assessed for their antioxidant potential using various *in vitro* standard biochemical assays and by pulse radiolysis. Among the eight fractions obtained, fraction one, two and three showed high antioxidant activity in all the biochemical assays corresponding to different levels of protection. Fraction 1 gave 91% protection against DPPH (2,2'-Diphenyl-1-picrylhydrazyl) radicals and 82% protection against deoxyribose degradation. Fraction 1, 2 and 3 also conferred protection to lipids and proteins against oxidative damage, using rat liver mitochondria as model systems. Pulse radiolysis study revealed the ability of fraction 1 to scavenge $ABTS^{\bullet -}$ (2,2'- azinobis (3-ethylbenzothiazolin-6-sulphonic acid)) and $CO_3^{\bullet -}$ radicals with a value of 27 μg/ml AEAC (ascorbic acid equivalent antioxidant capacity) and 4.7 μg/ml AEAC. HPLC analysis of fractions 1, 2 and 3 revealed peaks corresponding to the purity of each fraction. Thus we have succeeded in standardizing methods, for resolving the soxhlet methanolic fraction of Syndrex® into subfractions exhibiting high antioxidant activity.

Introduction

Diabetes is a metabolic disorder characterized by hyperglycemia. Persistent hyperglycemia is accompanied by increase in free radicals generated due to auto-oxidation of glucose, AGE (Advanced Glycation Endproducts) formation and their binding to respective receptors, increased substrate flux through the polyol pathway and stimulation of eicosanoid metabolism (De Vriese et al, 2001). Additionally hyperglycemia leads to generation of excess ROS (Reactive Oxygen Species) *via* oxidative phosphorylation, thereby inducing oxidative stress that a plays a key role in the development of diabetic complications such as nephropathy, retinopathy and neuropathy (Valko et al, 2007). In addition to the increased generation of free radicals in diabetes, impaired generation of naturally occurring antioxidants also results in increased oxidative injury, by failure of protective mechanisms. Antioxidant defense system appears to be compromised in diabetic patients (Glugliano et al, 1996). Recent findings suggest that the same pathways used in the activation of GDIS (Glucose Dependent Insulin Secretion) can dramatically enhance ROS production and manifestations of oxidative stress and possibly apoptosis (Leonid et al, 2004). Thus free radicals play a significant role in the pathogenesis of chronic diabetic complications (Segal , 2004).

Many dietary components and their individual constituents have antioxidant properties and are capable of interacting with reactive molecules. One of the most potent groups possessing antioxidant properties includes polyphenols and flavonoids. These components are known to be present in seeds of fenugreek (*Trigonella foenum-graecum*) which is widely used as a spice and a rich source of fibre. Its sub-fractions are known to have hypoglycemic effects in different model systems (Srinivasan, 2006). Additionally, fenugreek seed extract was known to stimulate hypoglycemic effect by activation of an insulin signaling pathway (Vijaykumar et al, 2005). Supplementation of this seed in diet, enhances the antioxidant potential in control and diabetic rats (Anuradha and Ravikumar, 2001). The polyphenol rich extract of fenugreek seeds is shown to protect erythrocytes from oxidative damage demonstrating the potent antioxidant activities of this seed (Kaviarasan et al, 2004).

The present study was done to evaluate the antioxidant potential of one such anti-diabetic drug Syndrexâ. Syndrex® is manufactured by Plethico laboratories, Indore, India. It contains powder of germinated fenugreek seeds. We have shown that germinated fenugreek seed extracts, exhibit high *in vitro* antioxidant potential (Dixit et al, 2005). Previous studies of this drug in our laboratory have shown, that the soxhlet methanolic extract of this drug has high *in vitro* antioxidant properties. Besides the whole drug extract has shown to improve the functionality and viability of pancreatic islet *in vitro* (Dixit et al, 2008). Additionally, *in vivo* studies of this drug also showed that pre-treatment of this drug, prevented STZ induced diabetes in mice (Dixit et al., Communicated). As the soxhlet methanolic extract of Syndrex® exhibited high antioxidant potential, we have tried to sub-fractionate the methanolic extract and identify pure compounds responsible for conferring high antioxidant activity.

Materials and Methods

Chemicals

Chemicals were either from one of the following companies: Sisco Research Laboratories (Mumbai-India), British Drug House (Mumbai-India), Hi-media (Mumbai-India), Sigma-Aldrich (U.S.A) and Merck (Mumbai-India).

Preparation of extract

Syndrex® tablets were purchased from local market, finely powdered and subjected to sequential extraction using solvents in increasing order of polarity such as petroleum ether, chloroform and methanol. The powder was extracted with each solvent for 8-10 hrs to remove soluble matter. The methanolic extract obtained was used for further fractionation.

Chromatographic Procedures

Thin Layer Chromatography

TLC plates precoated with silica plates (Silica gel G) were used, to separate constituents of methanolic extracts. Methanolic extract was spotted on the TLC plates and air-dried. Several solvents were used for developing the plates. The solvent that gave best separation was chloroform : ethylacetate : methanol :water (1:8:1.5:0.8, v/v/v). Bands were noted by UV (254nm) and the TLC plate was captured using gel documentation system.

Column Chromatography

The methanolic extract was fractionated using silica gel (200-400 mesh size) as stationary phase and eluted following a stepwise gradient of chloroform, ethyl acetate, methanol and water in order of increasing polarity and in varying concentrations. Fractions were collected and TLC plate was developed using chloroform: ethyl acetate: methanol: water (1:8:1.5:0.8), observed under UV (254 nm) and captured using gel documentation system.

Flash Chromatography

Methanolic extract was separated using silica gel (200-400 mesh size) as stationary phase and chloroform: ethyl acetate: methanol: water (1:8:1.5:0.8) as mobile phase and under pressure. Fractions were collected, resolved on TLC plates and observed under UV (254 nm).

High Performance Liquid Chromatography

Reverse phase chromatographic separation of fractions of methanolic extract was carried out, by using C18 as the station phase and water (solvent A) and acetonitrile (solvent B) as the mobile phase with the following gradient programme:

Time	A (%)	B (%)
0	100	0
6	90	10
12	70	30
18	30	70
24	20	80
30	100	0

and a flow-rate of 1 ml/min. Chromatographic peaks were identified at 280 nm.

In vitro antioxidant assays

DPPH radical scavenging assay

Determination of scavenging effects on 2,2'-Diphenyl-1-picrylhydrazyl (DPPH) radical was carried out with different fractions of soxhlet methanolic extract. In this assay, a commercially available and stable free radical (DPPH$^{\cdot}$) which is soluble in methanol was used. DPPH$^{\cdot}$ has a strong absorption band at 517 nm, which disappears on reduction by an antioxidant (Aquino et al, 2001). The calibration curve was plotted with %DPPH$^{\cdot}_{\text{SCAVENGED}}$ versus concentration of the standard antioxidant ascorbic. The results were expressed as ascorbic acid equivalent antioxidant capacity (TEAC).

ABTS radical scavenging assay

In this assay, 2,2'- azinobis (3-ethylbenzothiazolin-6-sulphonic acid) (ABTS) (7 mM) was allowed to react with potassium persulphate (2.5 mM) for a duration of more than 16 hrs in dark, at room temperature (Lee et al, 2006). This leads to incomplete oxidation of ABTS by persulphate to form ABTS radical. The fractions were then allowed to react with this solution and were checked for their ability to reduce the free radical, by a decrease in absorbance at 734 nm.

Ferric Reducing Antioxidant Power (FRAP)

The ferric reducing ability of the fractions was assayed using the FRAP assay. In this assay, the ability of the fractions to reduce the ferric-tripyridyltrazine (Fe^{3+}-TPTZ) to ferrous form was checked. The ferrous form gives intense blue colour, which is monitored spectrophotometrically at 595 nm (Pulido et al, 2000). The results are expressed as ascorbic acid equivalent antioxidant capacity.

2-Deoxy-D-ribose degradation assay

The ability of the fractions to scavenge hydroxyl radical ($^{\cdot}OH$) was conducted in Fe^{3+}–EDTA–H_2O_2–deoxyribose system. In this assay $^{\cdot}OH$ are formed by the Fenton reaction which leads to oxidation of 2-deoxyribose (Halliwell et al, 1987). The oxidation products when heated with thiobarbituric acid (TBA) under acidic conditions, yield a pink chromogen with the maximum absorbance at 532 nm. Results are expressed as percent inhibition of hydroxyl radical formation.

Isolation of rat liver mitochondria

Three months old female Wistar rats (weighing about 250 ± 20 g) were used, for the, preparation of mitochondria (Devasagayam et al, 1996). In brief, rat livers were homogenized and the homogenate was centrifuged. The resultant supernatant was centrifuged at 10,000 x g for 10 min to sediment mitochondria. This pellet was washed thrice with 5 mM potassium phosphate buffer, pH 7.4, to remove sucrose. Protein was estimated and pellets were suspended in the above buffer at the concentration of 10 mg protein/ml. Mitochondria at a final concentration of 0.25 mg/ml were treated with ascorbate-Fe^{2+} to generate hydroxyl like radical and to induce oxidative stress (Devasagayam et al, 1983).

Lipid Peroxidation

After exposure of mitochondria to oxidative stress, the products of lipid peroxidation were measured as lipid hydroperoxides (LOOH) and thiobarbituric reactive substances (TBARS). Lipid hydroperoxides were measured using FOX II (Ferric oxidation in xylenol orange) method (Nourooz-Zadeh et al, 1996). FOX II contains 90% methanol which facilitates solubilization of lipids. Oxidation of ferric in xylenol orange due to lipid hydroperoxides, results in change in colour from orange to blue which is read at 560 nm. Concentration of LOOH is then calculated with the help of standard graph using H_2O_2. One of the end products of lipid peroxidation is Malonaldehyde (MDA) and other aldehydes. These aldehydic products were measured spectrophotometrically using TBA reagent which reacts with aldehydes to give a pink coloured product, which is read at 532 nm (Devasagayam et al, 1983; Pushpendran et al, 1998). The standard was prepared by acid hydrolysis of tetramethoxypropane.

Protein sulphydryl depletion assay

Depletion in protein sulphydryls were quantitated using Ellman's reagent (5, 5 –dithiobis-(2- nitrobenzoic acid and expressed as nmoles protein sulphydryls/mg protein (Santos et al, 1998).

Pulse radiolysis

The ability of the fractions to scavenge $ABTS^{\cdot -}$ and $CO_3^{\cdot -}$ radicals were determined by pulse radiolysis. $ABTS^{\cdot -}$ radical was produced by the reaction of radiolytically generated azide radicals with $ABTS^{\cdot -}$. $CO_3^{\cdot -}$ radicals were generated using reaction mixture containing 0.05 M $NaHCO_3$ and 0.05 M Na_2CO_3 saturated with N_2O. In the presence of the extract, the decay of $ABTS^{\cdot -}$ and $CO_3^{\cdot -}$ are correlated with the concentration of ascorbic acid equivalents (Dixit et al, 2005). Pulse radiolysis experiments were carried out at the National Centre for Free Radical Research, University of Pune.

Results

Thin Layer Chromatography

Thin layer chromatography of methanolic extract developed using chloroform: ethyl acetate: methanol: water (10:80:15:8) yielded 3 bands with R_f value of 0.6, 0.5 and 0.4 (Fig.1). Excellent resolution of the methanolic extract was obtained in this system.

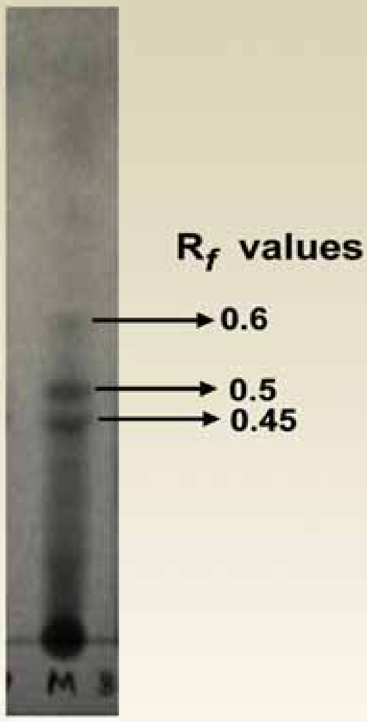

TLC profile of soxhlet methanolic fraction of Syndrex was resolved using chloroform: ethyl acetate: methanol: water (10:80:15: 8)

Fig. 1: Thin layer chromatography of soxhlet methanolic extract of Syndrex

Column Chromatography

Column chromatography of methanolic extract using glass column packed with silica gel and eluted with chloroform following stepwise gradient of ethyl acetate, methanol and water, yielded 200 fractions of 1 ml each. These fractions were analyzed using TLC, fractions showing similar R_f values on TLC plates were pooled to yield a total of 34 fractions. These fractions were evaluated for their antioxidant potential using *in vitro* antioxidant assays.

In vitro antioxidant assays of column chromatography fractions

The fractions were assayed for their antioxidant potential by various *in vitro* antioxidant assays, which corresponded to action of antioxidants at different levels. The DPPH$^{\bullet}$ and ABTS radical scavenging assay corresponds to scavenging ability, while the FRAP assay corresponds to the reducing ability of the fractions. As can be seen in Figs. 2a and 2b, 0.1% of fractions 10, 11, 12, 14, 18, 21 and 24 exhibited high DPPH as well as ABTS radical scavenging activity. The ferric complex reducing ability of the fractions is shown in Fig. 2c. 0.1% of fractions 10, 11, 12, 14, 18, 21 and 24 exhibited highest reducing ability. The TLC profile of fractions 10, 11, 12, 14, 18, 21 and 24 is shown in Fig. 2d. These fractions contained a mixture of components. Therefore to facilitate better separation of the components, soxhlet methanolic extract was subjected to flash chromatography.

Flash Chromatography

Fractionation of soxhlet methanolic extract of Syndrex using flash chromatography yielded eight fractions. The TLC profile of these fractions is shown in Fig. 3. These eight fractions contained different components in varying concentrations, thus exhibiting better separation of the methanolic extract. These 8 fractions were then subjected to various *in vitro* antioxidant assays.

In vitro antioxidant assays of flash chromatography fractions

Among the 8 fractions tested 0.01% of fractions 1, 2 and 3 exhibited high DPPH and ABTS radical scavenging activity as well as were effective in reducing the ferric complex in the FRAP assay (Figs. 4a, 4b and 4c). Among the three fractions, 0.01% of fraction 1 scavenged 91% of DPPH radicals and 68% of ABTS radicals, whereas in the FRAP assay 0.01% of fractions 3 showed highest AEAC of 0.402. The inhibition of deoxyribose degradation capacity is shown in Fig. 4d. Nearly all the fractions tested exhibited this ability with 0.01% fraction 1 showing 82% inhibition.

The ability of these fractions to prevent oxidative damage to mitochondrial lipids induced by ascorbate-Fe^{2+} system was checked in terms of TBARS

Fig. 2: *In vitro* antioxidant assays

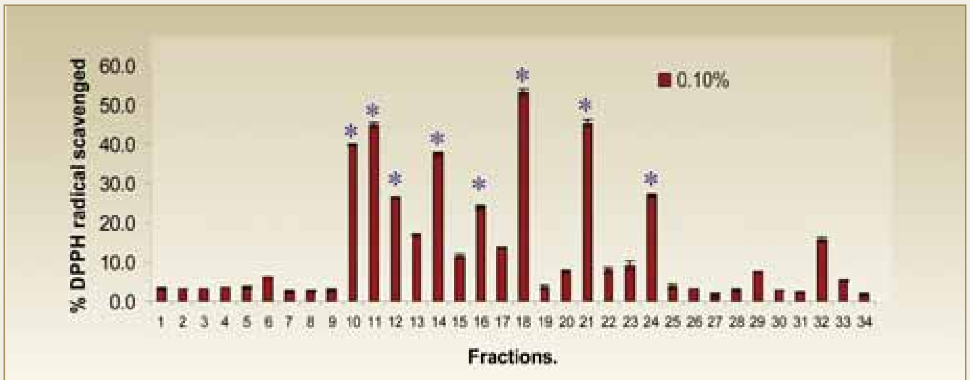

Data expressed as mean ±S.D from three individual experiments

Fig. 2a: Radical scavenging activity of fractions as measured by DPPH assay

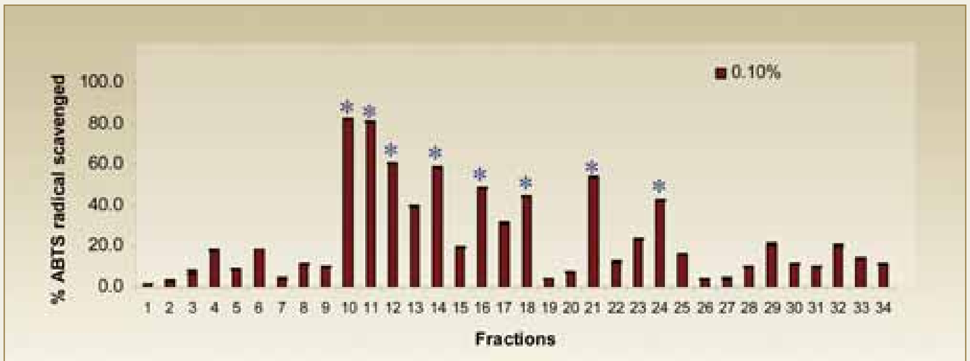

Data expressed as mean ±S.D from three individual experiments

Fig. 2b: Radical scavenging activity of fractions as measured by ABTS assay

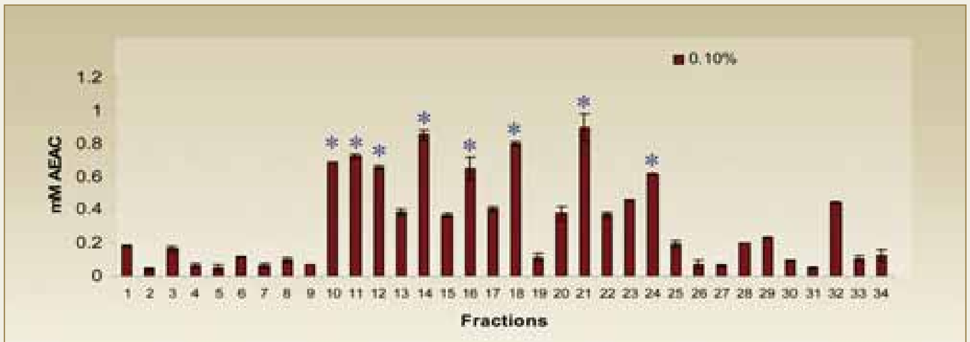

Antioxidant activity of fractions as measured by FRAP. AEAC: Ascorbic acid equivalent antioxidant capacity. Data expressed as mean ±S.D from three individual experiments

Fig. 2c: Ferric complex reducing ability of fractions by FRAP assay

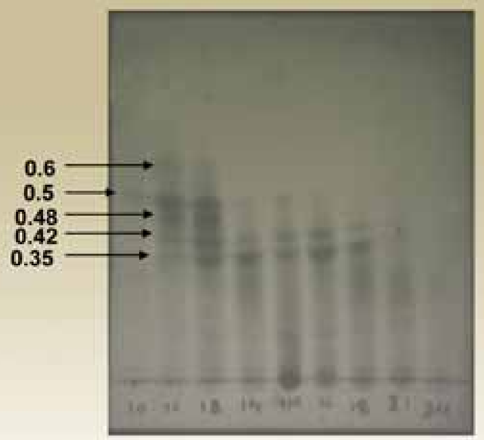

TLC profile of fractions 10, 11, 12, 14, 16, 18, 21 and 24 obtained from column chromatography and exhibiting high antioxidant activity as measured by DPPH, ABTS and FRAP assay. M: Soxhlet methanolic extract of Syndrex.

Fig. 2d: Thin Layer chromatography of fractions showing high antioxidant activity

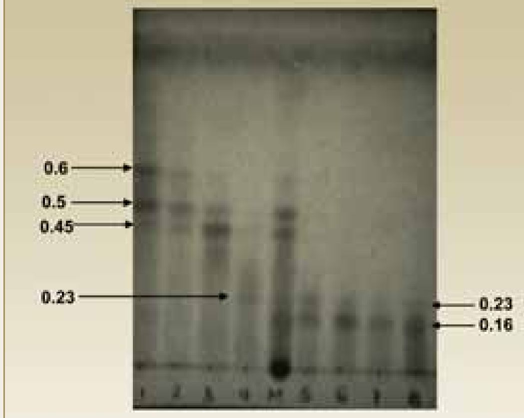

TLC profile of eight fractions obtained from flash chromatography and developed using chloroform: ethyl acetate: methanol: water (1:8:1.5:0.8).

Fig. 3: Thin layer chromatography of fractions obtained from flash chromatography

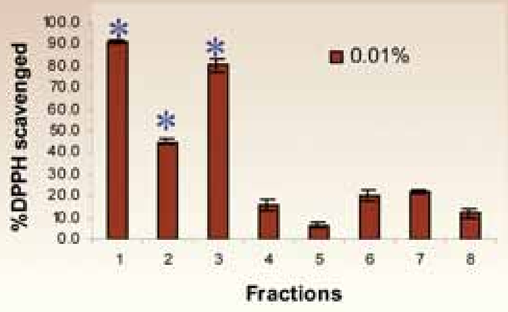

Fig. 4a: DPPH radical scavenging assay

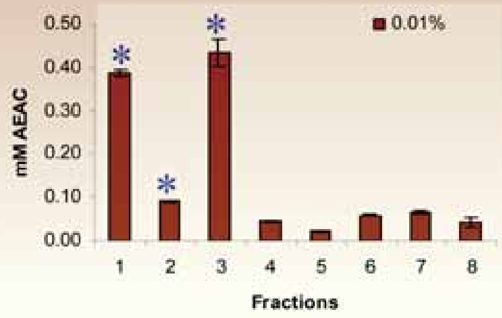

Fig. 4b: FRAP assay

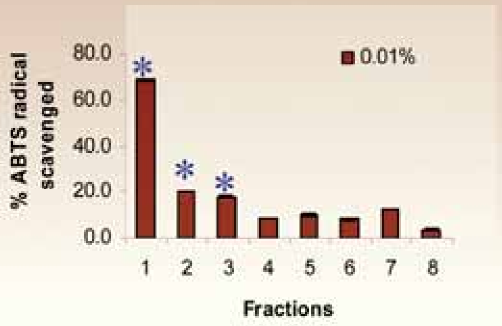

Fig. 4c: ABTS radical scavenging assay

and lipid hydroperoxides formed. 0.1% of fraction 1 inhibited formation of TBARS as well as lipid LOOH (Figs. 5a and 5b). Similarly 0.01% of fraction 1 prevented depletion in protein sulphydryls in mitochondria, in response to oxidative damage (Fig. 5c). Therefore as fractions 1, 2 and 3 exhibited high antioxidant activity, the radical scavenging activity was quantified using pulse radiolysis. Decay of ABTS$^{\cdot-}$

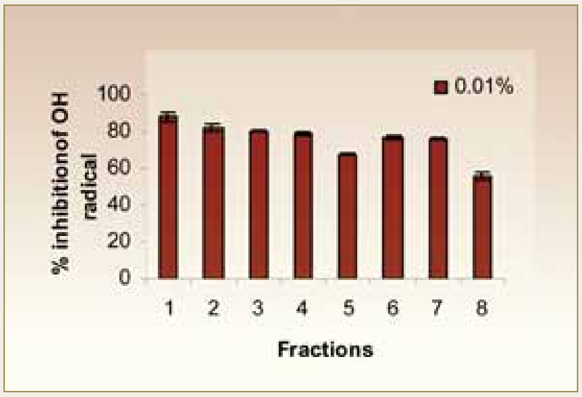

Fig. 4d: Deoxyribose degradation assay

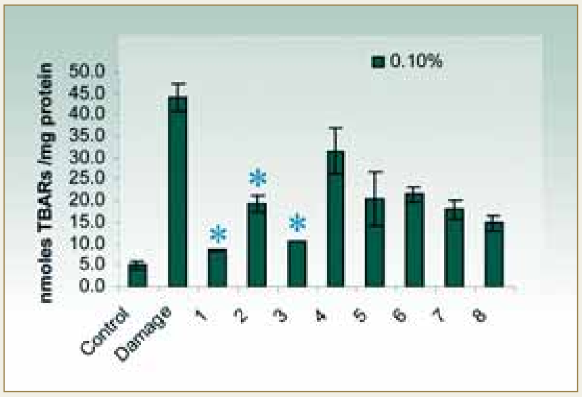

Fig. 5a: Thio B-Arbituric Reactive Substances (TBARS) assay

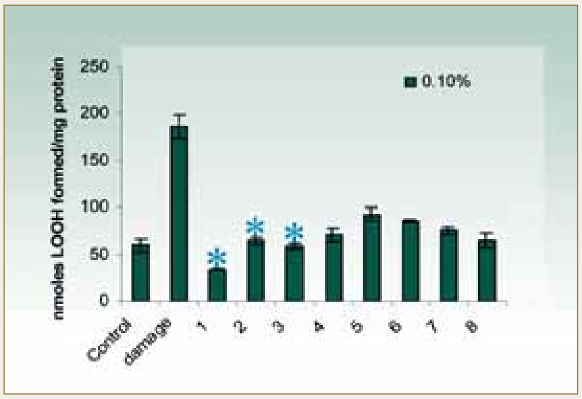

Fig.5b: Lipid hydroperoxide assay

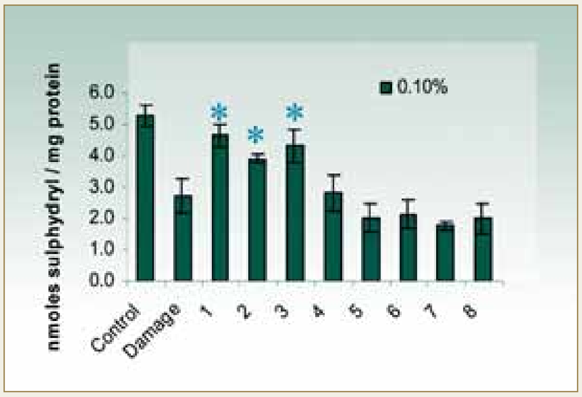

Fig. 5c: Protein sulphydryl depletion assay

and $CO_3^{\cdot-}$ radical was monitored in presence of ascorbic acid and the linear plot of pseudo-first order rate constant (K_{abs}) versus ascorbic acid concentration was used, to calibrate the standard curve for estimation of ascorbate equivalents in the extracts. The pseudo-first order rate constants for the decay of $ABTS^{\cdot-}$ and $CO_3^{\cdot-}$ were determined for the known concentrations of extracts and from the calibration curve, the ascorbate equivalents present in different extracts were determined. Fig. 6a shows the $ABTS^{\cdot-}$ and Fig. 6b shows $CO_3^{\cdot-}$ radical scavenging activity by fraction 1, 2 and 3 respectively. Maximum $ABTS^{\cdot-}$ radical scavenging activity was exhibited by 1% of fraction 1 with a value of 27 μg/ml of AEAC and maximum $CO_3^{\cdot-}$ radical scavenging activity was exhibited by 1% methanolic soxhlet extract with a value of 4.4 μg/ml of AEAC.

High Performance Liquid Chromatography

HPLC analysis of fraction 1 using 0-80% acetonitrile revealed three peaks having different retention times (Fig. 7a). The chromatograms for fractions 2 and 3 (Figs. 7b & 7c) showed peaks corresponding to the TLC profile of the fractions. The area under curve for the obtained peaks co-related to the visible concentrations of these fractions as seen in their respective TLC profiles.

Discussion and Conclusion

Hyperglycemia causes auto-oxidation of glucose, glycation of proteins and activation of polyol metabolism. These changes accelerate generation of ROS and increases oxidative chemical modification of lipids, DNA and proteins in various tissues. Oxidative stress plays an important role in the development of complications in diabetes such as lens cataracts, nephropathy and neuropathy (Valko et al, 2007).

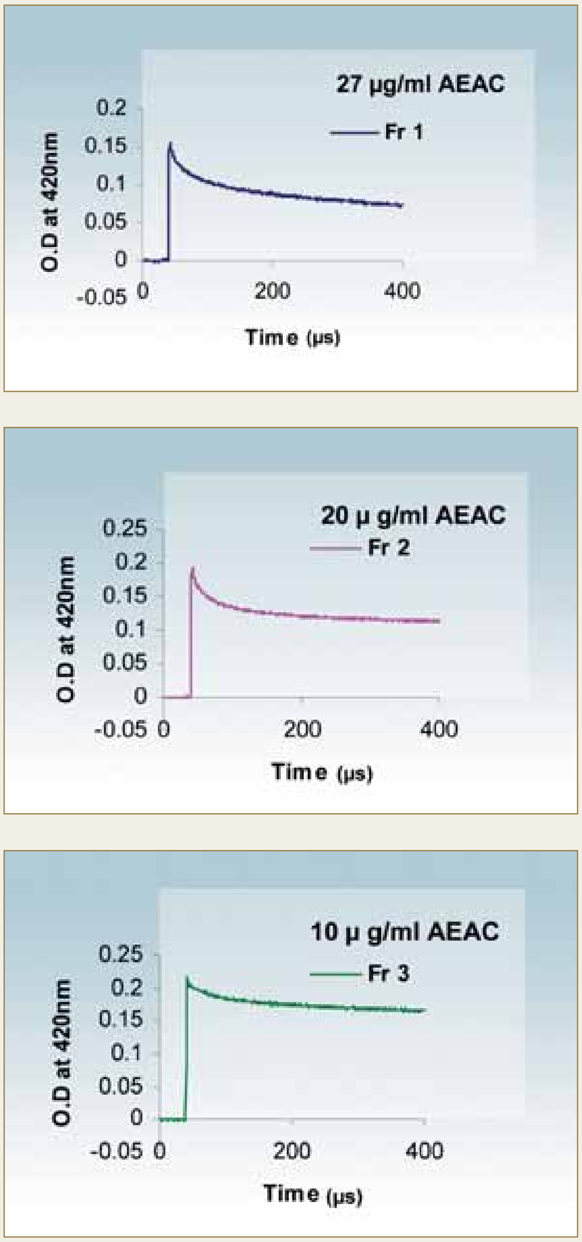

Fig. 6a: Pulse radiolysis study of fractions using $ABTS^{\bullet-}$ radical scavenging by fraction 1, 2 and 3 by pulse radiolysis

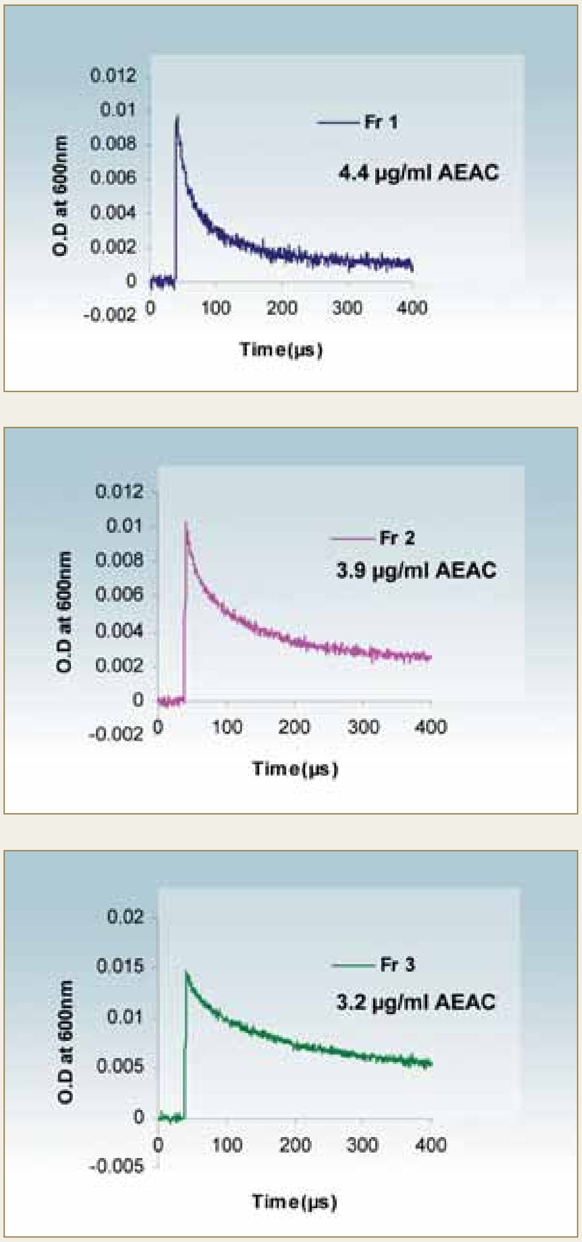

Fig. 6b: Pulse radiolysis study of fractions using $CO^{3\bullet-}$ radical scavenging by fraction 1, 2 and 3 by pulse radiolysis

Therefore supplementation with antioxidants to diabetic patients would help in reducing the oxidative load. At present, the treatment of diabetes mainly involves a sustained reduction in hyperglycaemia by the use of biguanides, thiazolidinediones, sulphonyl ureas, D-phenylalanine derivatives, meglitinides and α-glucosidase inhibitors in addition to insulin. However, due to unwanted side effects, the efficacies of these compounds are debatable and thus there is a demand for new compounds for the treatment of diabetes. Hence, plants have been suggested as a rich and unexplored source of potentially useful antidiabetic as well as antioxidative drugs (Saxena et al, 2004).

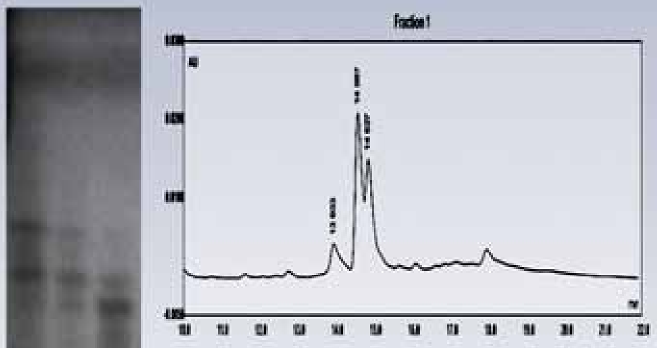

a) Chromatogram of fraction 1 detected at 280nm for 20 minutes. TLC profile of fraction one developed in chloroform: ethyl acetate: methanol: water (10:80:15:8)

Fig. 7a: HPLC analysis of fractions from flash chromatography

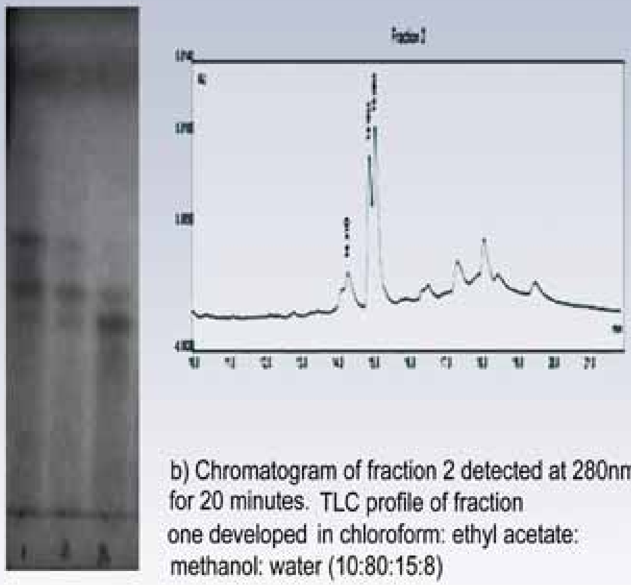

b) Chromatogram of fraction 2 detected at 280nm for 20 minutes. TLC profile of fraction one developed in chloroform: ethyl acetate: methanol: water (10:80:15:8)

Fig. 7b: HPLC analysis of fractions from flash chromatography

Fenugreek is one of the oldest herbs known to have beneficial therapeutic effects. Seeds of fenugreek have been shown to have multiple benefits in patients with diabetes such as reduction in blood sugar and its complications (Madar et al, 1998; Preet et al, 2006). Many earlier studies whether using whole seeds (Shani et al, 1974) or extracts (Ribes et al, 1989) showed that fenugreek seeds decreased fasting blood sugar levels in animals. Additionally fenugreek seeds also possess antioxidant activity, which can be attributed to the presence of various polyphenols. (Dixit et al, 2005) have shown that among the various extracts tested the soxhlet methanolic extract of germinated fenugreek seeds exhibited strong antioxidant activity. Evaluation of antioxidant activity of antidiabetic drug Syndrex, which contains powder of germinated fenugreek seeds, revealed that the soxhlet methanolic extract possessed strong antioxidant activity. Additionally this extract contained highest amount of flavonoids and polyphenols. This prompted us to further sub-fractionate the extract and identify the active principle conferring high *in vitro* antioxidant activity.

To resolve the soxhlet methanolic fraction, various chromatographic procedures were used. The extract was first separated onto a thin layer of silica gel using a combination of polar and non-polar solvents. Among the various combinations tried, 3 bands of R_f value 0.6, 0.5 and 0.45 were obtained in a solvent system comprising of chloroform: ethyl acetate: methanol: water in

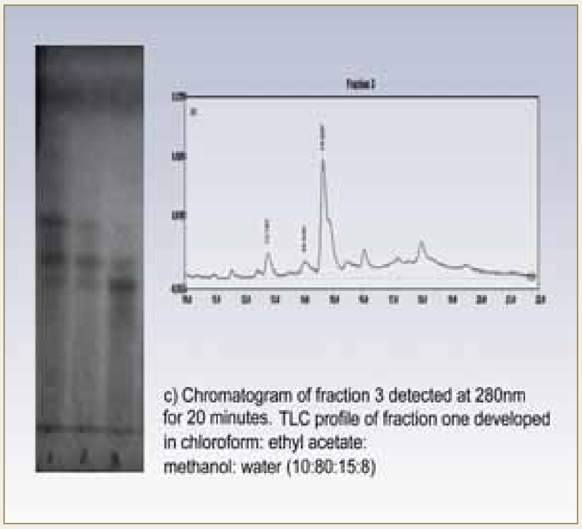
c) Chromatogram of fraction 3 detected at 280nm for 20 minutes. TLC profile of fraction one developed in chloroform: ethyl acetate: methanol: water (10:80:15:8)

Fig. 7c: HPLC analysis of fractions from flash chromatography

a ratio of 10: 80: 15: 8. As the thin layer plates were UV active, bands were observed under UV at 254 nm. To obtain the fractions in large amount so as to enable their characterization, silica gel column chromatography was used. The soxhlet methanolic fraction was eluted sequentially, following a step-wise gradient starting from chloroform and ending with water. These gradual elutions lead to 34 fractions, each containing mixture of different compounds. To evaluate the active antioxidant fractions, all the fractions were assayed for their antioxidant activity at different levels of antioxidant action. Free radical scavenging capacities of these fractions were measured by standard assays like DPPH and ABTS (Figs. 3a and b). The ferric reducing capacities were also determined, ascorbic acid equivalent antioxidant activities were calculated (Fig. 3c). Among the 34 fractions evaluated only 8 fractions possessed fairly high antioxidative scores. TLC analysis of these fractions revealed that these contain a mixture of two or more compounds (Fig. 3d). Thus to obtain better separation, soxhlet methanolic extract was separated under pressure using flash chromatography.

Flash chromatography makes use of pressure to facilitate better separation of components of a mixture. 8 fractions eluted using chloroform: ethyl acetate: methanol: water (10: 80: 15: 8) containing different amounts of compounds were obtained (Fig. 3). To further narrow down the search for active antioxidant principle, the 8 fractions were tested for their antioxidant ability. Low concentration (0.01%) of fractions 1, 2 and 3 showed differential radical scavenging and ferric reducing activities. Besides checking the direct radical scavenging activity, antioxidant activity can be evaluated by checking the ability of the compounds to inhibit the damage caused by free radicals. Various human diseases, such as heart aliments, diabetes, cancer and Alzheimer's disease are known to be either consequence or cause of ROS production. The major consequence of ROS production is damage to membrane lipids by formation of lipid peroxides, which via chain reaction enhances membrane damage (Hirokazu, 2007). One of major sites of free radical production in the cell, is mitochondria. Therefore the ability of the fractions to prevent oxidative damage to membrane lipids was checked by measuring the aldehydic products (in terms of TBARS) and lipid hydroperoxides (LOOH) formed. Oxidative damage to rat liver mitochondria was induced by ascorbate-Fe^{2+} system that generates OH-radical like species on incubation at physiological temperature of 37°C. Fraction 1 was the best at preventing ascorbate-Fe^{2+} induced damaged to lipids as well as proteins in rat liver mitochondria. Pulse radiolysis reveals the ability of antioxidants to scavenge secondary radicals such as $ABTS^{\bullet -}$ and $CO_3^{\bullet -}$. Fraction 1 efficiently scavenged the generated secondary radicals exhibiting the possible mechanism of its action. Thus fraction 1 exhibited high antioxidant activity in all the assays performed. TLC profile of fraction 1 showed that it is a mixture of 3 compounds in different amounts. The observed antioxidant activity of fraction 1 could be due to the additive effect of the compounds present in the fraction. HPLC analysis of fraction 1, 2 and 3 revealed presence of peaks at retention time from 14-15 minutes, suggesting that the different fractions contain overlapping compounds. Chromatogram of fraction 1 showed three different peaks with different area under curve, which correlated with the differential amount of bands seen in the TLC profile of fraction 1(Fig. 7a). Similar analysis was observed for fraction 2 and 3. All of these fractions eluted in 30% acetonitrile, suggesting the polar nature of the compounds in the fractions.

The above antioxidant activity and functional analysis of fractions indicate the likely presence of polyphenolic compounds in these fractions. Polyphenolic compounds are well known to play an important role in antioxidant activity. Naturally occurring polyphenols are known to have numerous biological activities and found to be potential candidates for use as drugs, in diseases like heart aliments, ulcer, diabetes and neuronal disorders. From a chemical point of view, polyphenols can react with one-electron oxidants which prevent free radical formation in biological systems. Such single electron oxidation products are considered to be key steps of polyphenols while acting as drugs (Hadique and Baruah, 2002).

Our results thus suggest, that we were successful in standardizing the method for sub-fractionating the soxhlet methanolic extract. The obtained fractions revealed antioxidant activity comparable to that of known antioxidant such as ascorbic acid. Further studies such as purification of the fractions, characterization of the functional groups and identification of the pure compounds from the fractions would help us to give insights in the structure activity relationship of the compounds. Additionally *in vivo* studies would help to further understanding the mechanism of action of the purified compounds.

References

1. Anuradha CV, Ravikumar P. Restoration of tissue antioxidants by fenugreek seeds (*Trigonella foenum-graecum*) in alloxan-diabetic rats. *Indian J Physiol Pharmacol*. 2001: 45: 408–420.
2. Aquino R, Morelli S, Lauro MR, Abdo S, Saija A, Tomaino A. Phenolic constituents and antioxidant activity of an extract of *Anthurium versicolor* leaves. *J. Natl. Prod*. 2001: 64: 1019-1023.
3. De Vriese An S, Verbeuren TJ, Voorde Van de J, Lameire NH, Vanhoutte PM. Endothelial dysfunction in Diabetes. *Br J Pharmacol*. 2001; 130:963-974.
4. Devasayagayam TPA, Pushpendran CK, Eapen J. Differences in lipid peroxidation in rat liver rough and smooth microsomes. Biochim. *Biophys. Acta.* 1983: 750: 91-97.
5. Devasagayam TPA, Kamat JP, Mohan H, Kesavan PC. Caffenine as an antioxidant: Inhibition of lipid peroxidation induced by reactive oxygen species in rat liver microsomes. Biochim. *Biophys. Acta*. 1996: 1282: 63-70.
6. Dixit P, Ghaskadbi S, Mohan H, Devasagayam TPA. Antioxidant properties of germinated fenugreek seeds. *Phytother. Res*. 2005: 19: 977-983.
7. Dixit PP, Devasagayam TPA, Ghaskadbi SS. Formulated antidiabetic preparation Syndrex® has a strong antioxidant potential. *Eur. J. Pharmacol*. 2008; 581: 216-225.
8. Dixit PP, Misar A, Mujumdar AM, Ghaskadbi SS. Pre-treatment of Syndrex® protects mice from 18. Preet A, Siddiqui MR, Taha A, Badhai J, Hussain ME, Yadava PK, Baquer NZ. Long-term effect of *Trigonella foenum-graceum* and its combination with sodium orthovandate in preventing histopthological and biochemical abnormalities in diabetic rat ocular tissues. *Mol. Cell Biochem*. 2006: 289: 137-47.
19. Pulido R, Bravo L, Saura-Calixto F. Antioxidant activity of dietary polyphenols as determined by a modified Ferric Reducing Antioxidant Power assay. *J. Agri Food Chem*. 2000: 46: 3396-3402.
20. Pushpendran CK, Subramaniam M, Devasagayam TPA, Singh BB. Study on lipid peroxidation potential in different tissues induced by ascorbate-Fe^{2+}: Possible factors involved in differential susceptibility. *Mol. Cell. Biochem.* 1998: 178: 197-202.

21. Ribes G, Sauvaire Y, Costa CD, Baccou JC, Loubatieres-Mariani. Anti-diabetic effects of sub-fraction from fenugreek seeds in diabetic dogs. *Proc. Soc. Exp. Biol. Med*. 1989: 182: 159-66.

22. Santos AC, Vyemyra SA, Lopes JLC, Bazon JN, Mingotto FE. Effect of naturally occurring flavonoids on lipid peroxidation and membrane permeability transition in mitochondria. *Free Rad. Med. Biol*. 1998: 24: 1455-1461.

23. Saxena A and Vikram NK. Role of selected Indian plants in management of type 2 diabetes. *J. Altern. Complement. Med*. 2004: 10: 369-378.

24. Segal KR. Type 2 diabetes and disease management: exploring the connections. *Diab Manag*. 2004: 7(Suppl): s11-s22.

25. Shani J, Schmied G, Joseph B, Abronson Z, Sneman FG. Hypoglycemic effects of *Trigonella foenum*-graecum and *Lupinus termis* (Leguminosae) seed and their major alkaloids in alloxan-diabetic and normal rats. *Arch. Int. Pharmacodyn. Ther*. 1974: 210: 27-37.

26. Srinivasan K. Fenugreek (*Trigonella foenum – graecum L.*): A review of health beneficial physiological effects. *Food Reviews International*. 2006: 22: 203 – 224.

27. Valko M, Dieter Leibfritz JM, Mark TD Cronin, Milan Mazur and Joshua Telser. Free radicals and antioxidants in normal physiological functions and human disease. *Int. J.Biochem. Cell Biol.* 2007: 39: 44-84.

28. Vijaykumar MK, Singh S, Chhipa RR, Bhat MK. The hypoglycemic activity of fenugreek extract is mediated through the stimulation of an insulin signaling pathway. *Br. J. Pharmacol.* 2005: 146: 41-48.

ABOUT THE AUTHOR

Dr. T.P.A. Devasagayam joined BARC in 1975, from BARC Training School in Biology and Radiobiology, subsequent to his completion of Masters in Zoology from the American College, Madurai. At present he is Scientific Officer (H) and Head, Radiation Biochemistry Section in the Radiation Biology and Health Division of BARC. His major area of research relates to the role of free radicals in human health and radiation biology and potential uses of natural antioxidants. He has done his post-doctoral research in Germany and USA. He has over 130 publications in refereed journals with over 1500 citations. He has played a central role in the organization and development of the Society for Free Radical Research-India (SFRR-India). He was the first Secretary-General of SFRR-India and currently holds the position of President. He is also the current President of SFRR-Asia.

INFLUENCE OF H_2O_2 ON PHYSICO-CHEMICAL PROPERTIES: A CASE STUDY ON DOPED CERIA SYSTEM

B. P. Mandal, V. Grover, M. R. Pai and A. K. Tyagi
Chemistry Division

This paper was awarded one of the Best Posters Award at the 2nd DAE-BRNS International Symposium on Material Chemistry, held at BARC during Dec. 2-6, 2008

ABSTRACT

Effect of H_2O_2 on synthesis and powder properties like surface area, agglomerate size etc. of nanocrystalline $Ce_{0.8}M_{0.2}O_{1.90}$ (M: Sm, Gd) has been explored, by treating cerium nitrate and rare-earth nitrate with NaOH in the presence/absence of H_2O_2. The resultant products have been characterized by several techniques. The presence of H_2O_2 is found to have a profound effect on powder properties like surface area, particle size etc. A mechanism has been proposed, to explain the observed superior powder properties of the samples. It has also been shown, that the samples prepared in the presence of H_2O_2, can lower the conversion temperature of CO to CO_2, proving them as better catalysts. Interestingly, temperature programmed reduction studies on Sm^{3+} doped samples revealed, that the doping in conjunction with the use of H_2O_2, leads to enhanced reduction properties of the samples over multiple cycles.

Introduction

Ceria (CeO_2) is an important oxide, that has been attracting ever-growing attention, due to its varied applications in fuel cells, oxygen gas sensors, polishing agent, in oxygen permeation membrane system and as a catalyst in different technologically important processes. Ceria is an essential component of Three-Way Catalyst (TWC), which is being used for environment cleaning purpose, as well as in different emerging fields of catalysis like oxidation of hydrocarbons, removal of total organic carbon from waste, automobile exhaust gas conversion and even in deNO_x reaction. The possibility of transformation from Ce^{3+} ! Ce^{4+} aids in accepting or removing oxygen from ceria. At high temperatures, not only the surface area of CeO_2 reduces drastically, but it also loses its redox properties and oxygen storage capacity. It has been observed, that ceria with suitable dopants (specially rare-earth oxide) improves its stability towards sintering as well as the catalytic activity of the resulting catalysts. On substitution of trivalent rare-earth element, the oxygen vacancies increase, which in turn improve the oxygen mobility and also improves the oxygen storage capacity.

It has been observed that CeO_2 in nanocrystalline form is further more important since nanocrystalline CeO_2 exhibits superior optical and electrical properties to bulk CeO_2. It is also found that catalyst shows better catalytic action in its nano-form.

The present study aims at synthesizing and characterizing the nominal compositions $Ce_{0.8}Sm_{0.2}O_{1.90}$ and $Ce_{0.8}Gd_{0.2}O_{1.90}$ and to investigate the effect of the presence of H_2O_2 on synthesis and various physico-chemical properties of doped ceria nano-powders. A plausible mechanism for formation of nano particle has been proposed, for the samples prepared in the presence of H_2O_2. The study also investigates the effect of particle size and surface area and doping on CO oxidation to CO_2. In addition to this, the reduction properties of Sm^{3+} doped ceria have only been studied because of their better powder properties than that of Gd^{3+} doped ceria.

Experimental

The samples were synthesized by sol-gel route. Four sets of samples were prepared wherein two sets consisted of $Ce_{0.8}M_{0.2}O_{1.90}$ (M:Gd^{3+}, Sm^{3+}) without H_2O_2 and the two other sets consisted of $Ce_{0.8}M_{0.2}O_{1.90}$ (M:Gd^{3+}, Sm^{3+}) with H_2O_2. Thereafter, 1M NaOH was added drop wise, till the pH reached 10.0. Henceforth, the samples will be referred to as GDC1 for gadolinia-doped ceria and SDC1 for samaria doped ceria. The samples prepared in the absence of H_2O_2 have been referred to as GDC2 and SDC2, respectively.

XRD patterns were recorded on as-prepared and calcined samples on a Philips X-ray diffractometer (Model PW 1710). Thermo gravimetric analysis was performed using model STA 409, M/s. Netzsch Geratebau. TEM data was recorded on the samples, to determine the microstructure and particle size of the samples. The extent and nature of agglomeration was studied by a particle size analyzer (Horiba, Model LA-500 (Japan)). The Raman spectra were recorded using a 532nm line from a solid state Nd:YAG laser. X-ray photoelectron spectroscopic studies were done, using VG Microtech hemispherical electron spectrometer, with a dual anode power supply (Model 8025).

To determine the redox properties of the material TPR-TPO studies have been carried out with Thermoquest TPDRO instruments, Italy. The catalytic activity was evaluated by a gas chromatograph.

Results and Discussion

The samples were characterized by powder-XRD for phase identification. The XRD patterns are shown in Fig. 1. The XRD peaks of the uncalcined samples are broad, which indicates that the particle sizes are in nano regime. The analysis of XRD patterns of calcined samples revealed the doped samples to be fluorite-type (F-type), with structure similar to pure ceria. Also, it is clearly visible from Fig.1, that the diffraction peaks of SDC1 and GDC1 are broader than that of SDC2 and GDC2 which implies that, the samples prepared in presence of H_2O_2 have smaller crystallite size, than the samples prepared in absence of H_2O_2. Thus, H_2O_2 affects the particle size of the nanoparticles.

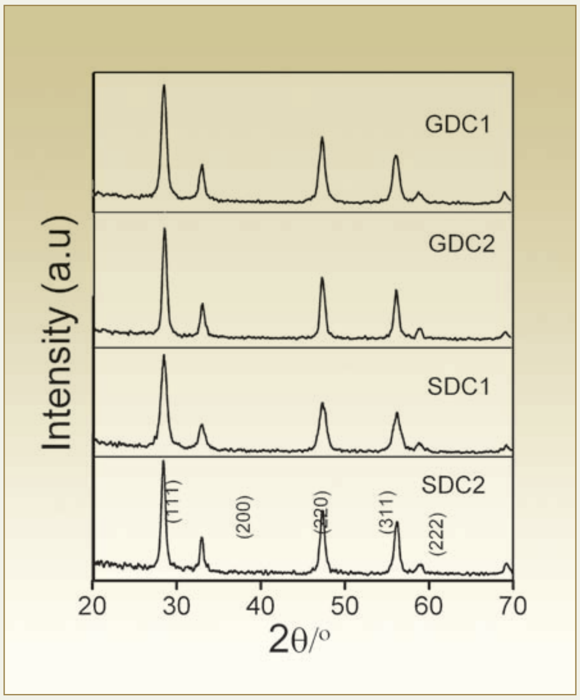

Fig. 1: XRD pattern of calcined (a) SDC2 (b) SDC1 (c) GDC2 (d) GDC1

The surface areas of these samples were measured by BET technique. It was revealed that the surface area for GDC1 and SDC1 samples are comparatively higher than those of GDC2 and SDC2 i.e. use of H_2O_2 yields the products with higher surface area and smaller particle size.

In order to observe the extent and nature of agglomeration, the powders were studied by particle size analyzer, based on light scattering and the particle size distribution of the powder was measured before and after ultrasonic treatment. After ultrasonication, all the samples showed fragmentation into smaller agglomerates, but interestingly agglomerates of GDC1 and SDC1 broke into much smaller sizes and that too in a shorter time as compared to GDC2 and SDC2. This further indicates that the agglomerates obtained from samples prepared in the presence of H_2O_2 are softer than those prepared without H_2O_2.

Raman spectra of the as prepared and calcined samples are shown in the Fig. 2(a-b). Pure bulk CeO_2 shows sharp Raman peak at 465cm^{-1} (F_{2g}). This is the symmetric breathing mode of O^{2-} ion, around each cation. The peaks observed here are assigned to the F_{2g} mode, due to symmetrical stretching of the Ce-O vibrational unit in 8 fold coordination. The F_{2g} peak of GDC1 and SDC1 samples appear at lower wavelength, which is attributed to smaller particles present in these samples, as compared to the samples prepared without H_2O_2. Another interesting observation is that, the calcined samples do not show any red shift and the peaks are relatively sharp which can be attributed to comparatively higher crystallite size.

An interesting observation is the manifestation of a peak at 835cm^{-1} for the uncalcined samples prepared in the presence of H_2O_2 (SDC1 and GDC1). This peak is due to O-O stretching mode of peroxo (O_2^{2-}) linkage.

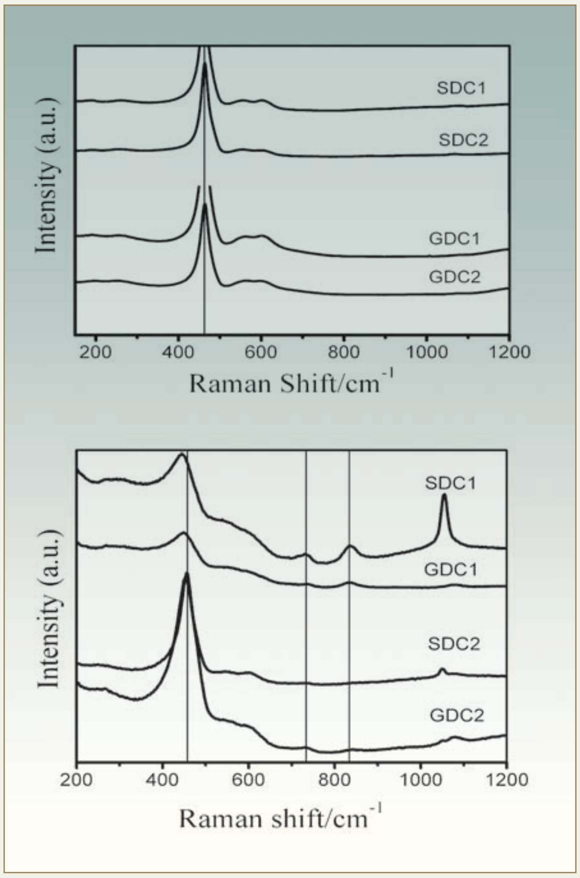

Fig. 2 : Raman Spectra of (a) as prepared samples (b) calcined samples.

The mechanism of formation of lower particle size, can also be understood from Raman spectroscopy. The samples prepared in the absence of H_2O_2 form hydroxide precipitate, by reaction of metal ions and OH^- ion. During condensation, the precipitate eliminates H_2O and form M-O-M (M= metal ion) network. The samples prepared in the presence of H_2O_2 form peroxo linkage, which hinder the formation of infinite network. Again upon calcination, this O-O linkages also break down, which ultimately lead to lower particle size and higher surface area. Correspondingly, this results in the disappearance of the peak at 830cm^{-1} from the Raman spectrum of both the compositions upon calcinations.

The transmission electron microscopy studies have been performed on the samples prepared in the presence of H_2O_2 and without H_2O_2. Comparatively narrower particle size distribution is observed, for the samples prepared in the presence of H_2O_2 (5-10nm) than the sample prepared without H_2O_2 (10-18nm) (Figure not shown). Thus, there is a reasonably good agreement between the average particle size obtained from XRD peak broadening and TEM studies.

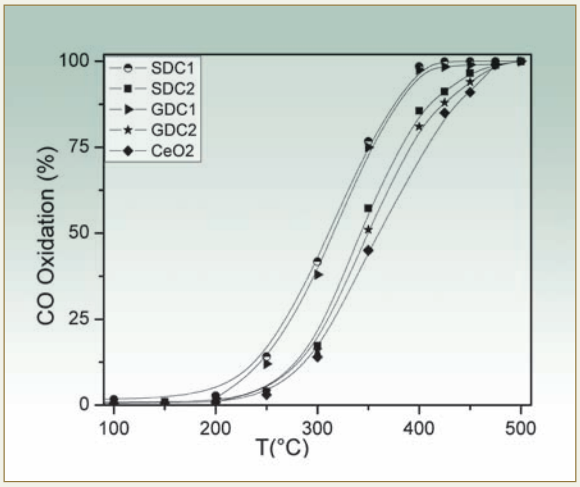

Fig. 3 : CO oxidation with O_2 by different catalysts SDC1, GDC1, SDC2, GDC2 and pure CeO_2.

To study the efficiency of these nanopowders as catalyst, as well as to investigate the effect of H_2O_2 on the same, all the samples were investigated for their catalytic activity. The catalytic property of pure CeO_2 prepared by same route was also studied under similar conditions, for better comparison. Fig. 3 presents the catalytic activity of CeO_2, GDC2, SDC2, GDC1 and SDC1 nanopowders for $CO+O_2$ reaction as a function of temperature. Substituted samples have been found to show better activity, as compared to the unsubstituted sample. Even though the onset of conversion of CO to CO_2 could be observed in unsubstituted ceria at room temperature itself, 100% conversion was achieved only at ~500°C, suggesting a sluggish rise in activity with increase in temperature. For the doped sample prepared in absence of H_2O_2, the 100% conversion temperature was 475°C whereas for the same composition prepared in the presence of H_2O_2, the 100% conversion temperature dropped to 395°C which is a marked improvement from 500°C. This observation reveals, that substitution as well as addition of hydrogen peroxide have profound effects on conversion temperature and subsequently on the catalytic activity. The decreasing order of catalytic activity as evident from Fig. 3 is: SDC1~GDC1 > SDC2~GDC2 > CeO_2. The catalytic activity of ceria is attributed to factors like lattice ion mobility and the possibility of readily changing between Ce^{3+} and Ce^{4+}, together with the high oxidizing power of the Ce^{4+} cation. The presence of a trivalent rare earth ion introduces oxygen ion vacancies, which further increases the mobility. Now, the higher catalytic activity of SDC1 (and GDC1) as compared to SDC2 (and GDC2) could be attributed to the higher surface area and lower particle size of the former as compared to the latter. In the samples having higher surface area and lower particle size, the activation barrier is easily overcome and subsequently higher conversions are observed at relatively lower temperature.

In order to study the reduction behaviour of the doped ceria samples, temperature programmed reduction studies were performed. Fig. 4 (a-e) presents the typical first temperature programmed reduction cycles of CeO_2 as well as $Ce_{0.8}M_{0.2}O_{1.9}$ (where M = Gd^{3+}/Sm^{3+}) samples. Here, all $Ce_{0.8}M_{0.2}O_{1.9}$ samples have only Ce^{4+} as the reducible cation. In the present study, the TPR profile of nano-sized CeO_2 (prepared by same

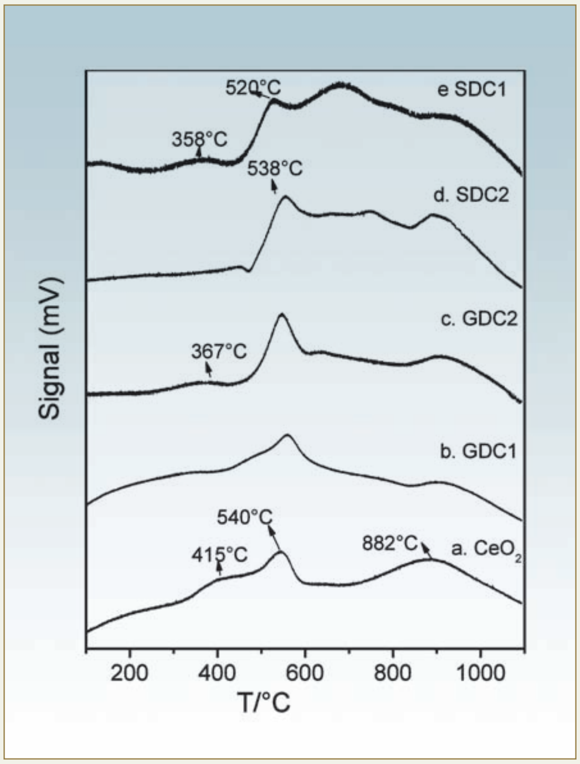

Fig. 4 : Temperature programmed reduction profiles (a) CeO_2, (b) GDC2 (c) GDC1 (d) SDC2 (e) SDC1.

route) exhibits the two peaks having nearly the same intensity. The peak at low temperature, in general, is attributed to the reduction of Ce^{4+} to Ce^{3+} species present at surface, whereas peak at temperature >1073°C is normally observed due to bulk reduction of Ce^{4+} to Ce^{3+} metal ions. The relative intensity of these two peaks will depend upon the ratio of reducible cations present on the surface and bulk in the sample. It can be inferred from the figure, that the sample has a significant amount of reducible surface cations. The sample synthesized by solid state reaction requires reduction temperature above >1273°C. Hence, here the lower particle size has facilitated the reduction at much lower temperature and this is supposed to have direct impact on its catalytic properties. Multiple TPR cycles were recorded, to monitor the reproducibility of these samples, towards their redox behaviour. Sm^{3+} incorporation in ceria enhances its reproducibility. The multinodal profile observed in the first cycle of SDC1 sample is consistently present in all the subsequent TPR cycles. The ease in reducibility of SDC1 sample and its improved reproducibility, could be attributed to generation of microstructural defects and anionic vacancies in lattice of ceria, as a result of Sm^{3+} substitution albeit non-reducible cation.

Conclusions

Nanocrystalline $Ce_{0.8}M_{0.2}O_{1.90}$ (M: Sm, Gd) were prepared in the presence and absence of H_2O_2 to investigate the role of H_2O_2 on its physico-chemical properties. Hydrogen peroxide introduces peroxo linkages, which greatly influence the powder properties of the samples. The formation of ceria solid solution nanoparticles, proceeds via condensation reaction, between the neighbouring –OH groups of $M(OH)_n$ forming -O-M-O- (M: Ce, Sm/Gd) networks. The peroxo species would disrupt this 3-D network and would lead to the following (i) formation of smaller crystallite sizes as shown by XRD and TEM (ii) Higher surface area due to the rapid elimination of peroxo species as shown by BET measurements and Raman spectroscopy (iii) Smaller agglomerate sizes as shown by DLS studies. Moreover, the Sm and Gd doped samples prepared in the presence of H_2O_2 showed marked improvement in catalytic properties. TPR studies reveal the enhancement in the reduction properties of samaria doped samples as well as reproducible behaviour on performing multiple TPR cycles as compared to unsubstituted ceria.

References

1. S. J. Park, J. M. Vohs, R. J. Gorte, *Nature*, 265, 404, (2000).
2. E. P. Murray, T. Tsai, A. Barnett, *Nature*, 400, 649 (1999).
3. S. Imamura, I. Fukuda, S. Ishida, *Ind. Eng. Chem Res.* 27, 718(1988).
4. G. Colon, J. A. Navio, R. Monaci, I. Ferino, *Phys. Chem. Chem. Phys.* 2, 4453, (2000).
5. K. Krishna, A. Bueno-Lopez, M. Makkee, J.A. Moulijn, *Appl Catal B* 75,189(2007).
6. B. P. Mandal, V. Grover, A. K. Tyagi, *Mater. Sci. and Eng. A*, 430 120 (2006).
7. T. Moeller, in The Chemistry of Lanthanides, Pergamon Press, Oxford, 1973.
8. B P Mandal, V Grover, M Roy, and A K Tyagi, *J. Am. Ceram. Soc.,* 90, 2961 (2007).
9. B P Mandal, M Roy, V Grover, A K Tyagi, *J. App. Phys.* 103, (2008).
10. J. Guzman, S Carrettin, A. Corma, *J. Am. Chem. Soc.* 17, 3286 (2005).

ABOUT THE AUTHORS

Mr. Balaji P. Mandal joined the Chemistry Division, BARC from 47th batch of Training School. His research interests are in the field of synthesis and structural elucidation of inorganic materials based on mixed oxides and fluorides. He has prepared several new ionic conductors as guided by structure-property correlation.

Dr. (Ms.) Vinita Grover Gupta joined the Chemistry Division, BARC from 44th batch of Training School. She was awarded Ph.D. degree (Chemistry) in 2006 by Mumbai University in recognition of her work on Inert Matrix Fuels. Recently, she has initiated research on optical materials in fluoride systems. She is a winner of IUPAC Young Chemist Award.

Dr. (Ms.) Mrinal R. Pai joined BARC from 40th batch of Training School. Initially she worked on development of H_2 mitigation catalyst. Current she is working on water splitting by photocatalysis and sulfuric acid decomposition reaction in I-S thermochemical cycle. She was awarded Ph.D. degree (Chemistry) from Mumbai University in 2005. She is a recipient of TA instruments ITAS- Young Scientist Award -2008.

Dr. A.K. Tyagi, presently Head, Solid State Chemistry Section, joined the Chemistry Division, from 29th batch of Training School. Since then he has been working in the field of Chemistry of wide ranging materials. He is a recipient of several prestigious awards. He is a recognized Ph.D. guide of Mumbai University and of Homi Bhabha National Institute (HBNI).

T HELPER CELL DIFFERENTIATION (TH1/TH2) DURING RECOVERY FROM RADIATION-INDUCED LYMPHOPENIA AND ITS MODULATION BY CHLOROPHYLLIN

D. Sharma, S.K. Sandur, R. Raghu and K. B. Sainis
Radiation Biology & Health Sciences Division

This paper was given the Best Poster Award at "The Society for Free Radical Research (SFRR) - India Satellite Meeting 2008, held at All India Institute of Medical Sciences (AIIMS), New Delhi, during Feb. 11-12, 2008

ABSTRACT

Acute radiation (dose >2Gy) is known to cause lymphopenia in exposed animals. This state can be overcome by administration of syngenic lymphocytes. T cells undergo Homeostasis Driven Proliferation (HDP), in response to lymphopenia, to fill the empty lymphoid space and acquire a memory phenotype, without becoming effector cells. However, the consequences of HDP on Th1 /Th2 differentiation, have not been carefully examined. The effects of an antioxidant, chlorophyllin on HDP of CD4+ T cells and their Th1 / Th2 differentiation were evaluated. The CD4+ T cells divided in response to lymphopenia, in the T cell zones in spleens of syngenic mice. The cells recovered from lymphopenic mice, 4 days after injection, secreted significantly higher levels of Th1 cytokine IFN-γ and Th2 cytokine IL-4 as compared to that in cells isolated from control mice. However, the cells recovered from mice 19 days and 100 days after injection, secreted significantly higher levels of Th17 cytokine IL-6, but lower levels of IL-4. Chlorophyllin inhibited HDP of CD4+ T cells *in vivo* and IL-6 production *in vitro*. The present results show, that following transient lymphopenia, Th1 differentiation dominates during initial recovery period, as compared to Th2 differentiation.

Introduction

Exposure to ionizing radiations (in excess of 200cGy), can induce significant hematopoietic damage, leading to transient lymphopenia and leucopenia. Chemotherapy, viral infections (HIV) and several genetic disorders can also result in lymphopenia. In lymphopenic, conditions, T cells expand to establish homeostasis, by a process dependent on self-peptide Major Histocompatibility Complex (MHC) recognition and the availability of proliferation and survival-promoting cytokines (Surh and Sprent, 2000). Although physiologically normal, chronic recurrence of this process might lead to selection of high-affinity self-reactive T-cell clones and autoimmune disease in susceptible individuals (La Gruta et al, 2000; Theofilopoulos et al, 2001; King et al, 2004; Marleau et al, 2005). CD4+ T cells help in generation of effective humoral and cell-mediated immune responses, against intracellular as well as extracellular pathogens. Thus, understanding the mechanisms involved in Homeostasis Driven Proliferation (HDP) of T cells and its modulation, would find several clinical applications. In recent times, antioxidants have been looked upon as versatile modulators of several biological responses, that involve oxidative stress. Many of these antioxidants have been reported to modulate immune responses. The antioxidants like Mn(III) tetrakis (5,10,15,20- benzoic acid) porphyrin (MnTBAP), glutathione and N-acetyl cysteine, have been shown to inhibit activation induced cell death, by upregulation of antiapoptotic genes lymphocytes (Voehringer, 1999; Hildeman et al, 2003; Rosati et al, 2004).

Chlorophyllin is a water-soluble mixture of sodium-copper salts of green plant pigment, chlorophyll. CHL is widely marketed for a variety of dietary and medicinal uses (Young and Bergei, 1980). Its chemopreventive, antimutagenic and anticarcinogenic properties, are well reported (Egner et al, 2001; 2003). Chlorophyllin exhibited protection against radiation and chemical-induced cytogenetic damage. It was found to inhibit radiation-induced single strand breaks in plasmid pBR322 DNA (Santosh Kumar et al, 1999). Apart from this, it has direct radical scavenging ability as shown by electron spin resonance spectroscopy (Santosh Kumar et al, 2001). In cellular and animal models CHL acted as an antioxidant (Santosh Kumar et al, 2004) and augmented immune responses mediated by macrophages, B cells and T cells (Sharma et al, 2007a and b). More importantly, CHL has been successfully used as a cancer chemopreventive agent in human population, residing in certain parts of China, who are at high risk of aflatoxin B1 (a hepatocarcinogen) exposure (Egner et al, 2001; Egner et al, 2003).

In the present study, the cytokine profile of T cells recovered from reconstituted lymphopenic mice was investigated. The effects of chlorophyllin on T cell proliferation, gene expression, cytokine secretion and homeostasis driven proliferation of purified CD4+ T cells in lymphopenic mice, were also investigated.

Methods

Eight to ten week old inbred BALB/c mice were used. The guidelines issued by the Institutional Animal Ethics Committee of BARC, Government of India, regarding the maintenance and euthanasia of small animals, were strictly followed. For induction of lymphopenia, animals were placed in ventilated perspex boxes and exposed to 600 cGy whole body γ-radiation in a Gamma Cell-220 Irradiator (AECL, Canada). CD4+ T cells were sorted from spleen cells using magnetic cell sorter and were treeated with chlorophyllin (100μM). The lymphopenic animals were reconstituted with carboxy fluoresceindiacetate succinimidyl ester (CFSE) labeled autologous CD4+T cells and were sacrificed 4 days or 19 days after injection. Proliferation of donor cells was monitored from CFSE dye dilution, using a flowcytometer. Cytokine production was monitored by Enzyme Linked Immuno Sorbent Assay (ELISA). Donor cells were visualized in the host spleen by immunofluorescence mircroscopy. Gene expression was studied by semiquantitative Reverse Transcriptional-Polymerase Chain Reaction (RT-PCR) using actin-β gene expression as internal control (Sharma et al, 2007b).

Results

HDP of CD4+ T cells occurs in lymphopenic mice

Fig. 1a shows the homeostasis driven proliferation of CFSE labeled donor CD4+ T cells, in the spleen of lymphopenic host. The bars in Fig. 1b, show the percentage of undivided donor cells and cells which had undergone one, two or three cell divisions, 96 h after reconstitution. About 50% of the normal CD4+ T cells injected into lymphopenic mice, had undergone one or more cell divisions.

Spatial distribution of CD4+ T cells undergoing HDP.

To decipher the specific anatomical locations that permit empty space sensing leading to HDP, the CFSE labeled CD4+ T cells were injected intravenously or intraperitoneally into lymphopenic or normal mice. Lymphocytes were recovered from the host spleen, lymph nodes or peritoneal fluid, 96 h after injection.

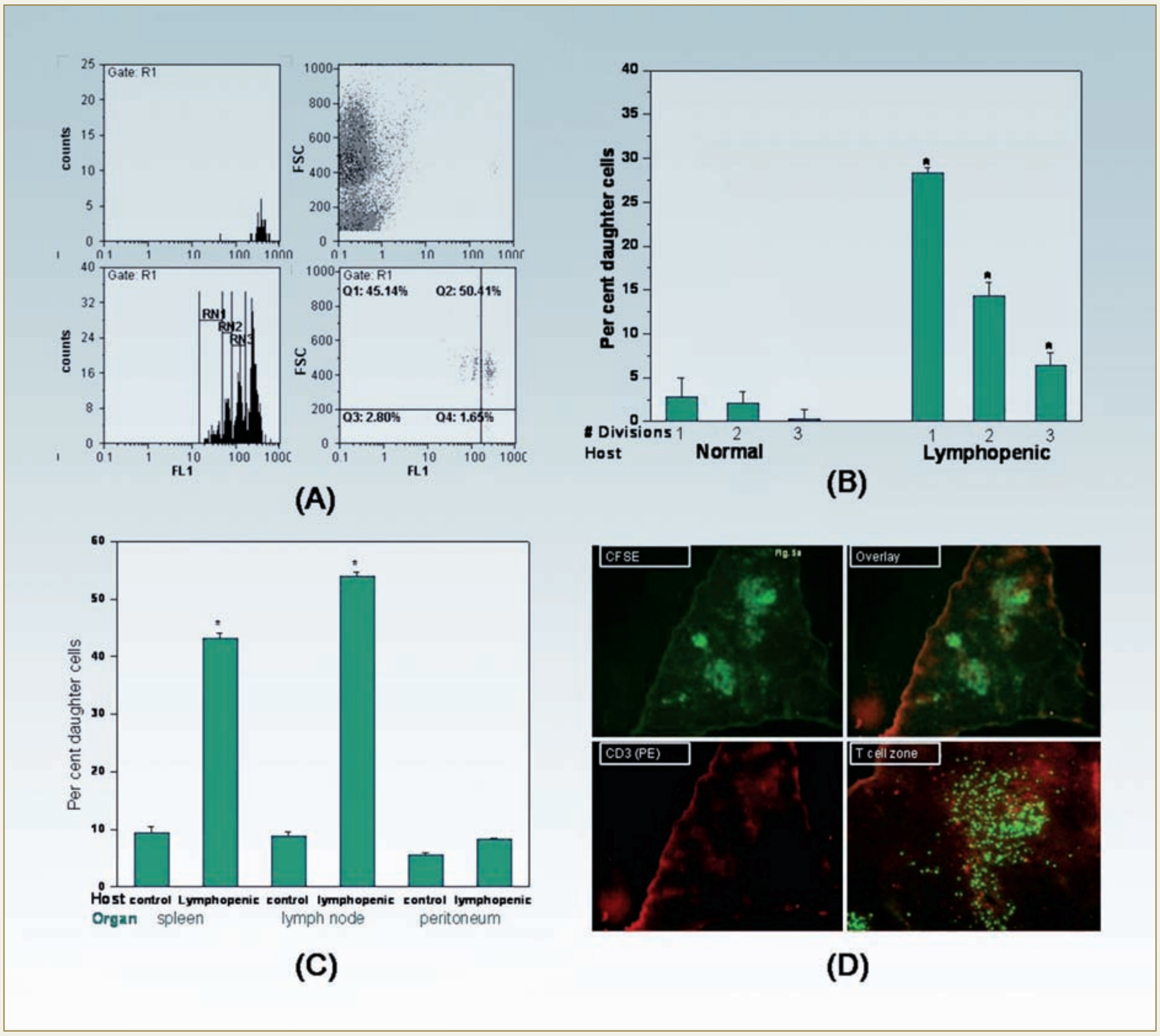

Fig. 1: Homeostasis driven proliferation (HDP) of CD4+ T cells in vivo. CD4+ T cells were purified from total splenic lymphocytes, stained with CFSE and 1.5×10^{6} cells were injected i.p. or i.v. into tail vain of normal or lymphopenic mice. Lymphocytes were recovered from spleen, lymph nodes or peritoneum of the host mice 96 h after reconstitution and 50,000 cells were acquired in flowcytometer. Percent daughter cells were calculated from decrease in mean fluorescence intensity. (A) Representative flowcytometric histograms and dot plots of CFSE labeled cells representing HDP of CD4+ T cells only in spleen of lymphopenic mice and not in normal mice. (B) The bars represent frequency of daughter cells in different division cycles in each treatment group. (C) The bars represent per cent daughter cells in the donor cell population isolated from different anatomical sites of the host. Data points represent mean ± S.E.M. from four mice and three such experiments were carried out. *$p < 0.01$, as compared to cells injected in normal mice. (D) T cells undergoing HDP make T cell zones in spleen of a lymphopenic mouse: Spleens from the host were harvested 96 hr after injection and frozen in liquid nitrogen. Transverse sections (20mM) of fresh frozen spleen were mounted on glass slides and stained with PE conjugated CD3 antibody and observed under fluorescence microscope. Overlaid pictures show homing of the CFSE+ cells to the T cell zones of the host. Sections from two spleens are shown.

A significant increase in the fraction of donor derived daughter cells, was seen in the spleen and lymph nodes of lymphopenic mice, as compared to that from normal mice. On the contrary, there was no increase in the fraction of daughter cells in the peritoneal cavity of lymphopenic mice (Fig. 1C), indicating that, T cells divided only in the secondary lymphoid organs of lymphopenic mice. To further find out the spatial distribution of donor CD4+ T cells undergoing HDP within the host spleen, transverse sections were stained with phycoerythrin (PE)-conjugated anti-CD3 antibody. T cell zones focally and avidly staining with CD3 antibody, were visible in the spleen obtained from normal mice (Fig. 1D). The donor derived CFSE-labeled T cells, were distributed into these specific T cell zones, in the host spleen (Fig.1D)

Cytokine production after HDP of CD4+ T cells in lymphopenic mice

Lymphopenic BALB/c mice or Swiss mice were reconstituted with autologous lymphocytes, isolated from age and sex matched donors and were sacrificed 4, 19 or 100 days after injection. The con A induced IL- 2 production in cells, from lymphopenic mice 4 and 19 days after reconstitution, was significantly lower than that in con A treated lymphocytes, from age and sex-matched normal mice (Fig. 2A).However, IL-2 levels were significantly higher at 19 days as compared to 4 days after adoptive transfer. On the contrary, the IL-2 production in lymphocytes isolated from lymphopenic mice 100 days after adoptive transfer, was similar to that in lymphocytes from normal mice (Fig. 2A). At 100 days, spleen size in mice recovering from lymphopenia was similar to that in normal mice, indicating a complete recovery.

The con A induced IL-4 production in normal mice increased steadily with age, indicating a progressive increase in Th2 bias in BALB/c mice. However, cells taken from lymphopenic mice 4 days after reconstitution and stimulated with con A, produced significantly higher IL-4 than that in lymphocytes from normal mice. Interestingly, the IL-4 level decreased 19 and 100 days after reconstitution, as compared to that in cells from normal mice (Fig. 2B).

The con A induced IL-6 production in lymphopenic mice, 4 days after reconstitution, was significantly lower than that in lymphocytes from normal mice (Fig. 2C). On the contrary, the IL-6 levels in lymphocytes from lymphopenic mice 19 and 100 days after reconstitution, were significantly elevated as compared to that in cells from normal mice (Fig. 2C). These results indicated a clear augmentation of IL-6 production during recovery from lymphopenia. The con A-induced IFN-γ production in lymphopenic mice, 4 days after reconstitution, was significantly higher than that in lymphocytes from normal mice (Fig. 2D). The IFN-γ levels in lymphocytes from lymphopenic mice 19 days after reconstitution, were lower than that in cells from normal mice. On the contrary, the IFN-γ production at 100 days after injection was again higher than that in lymphocytes from normal mice. BALB/c mice are known to have a genetic Th2 bias. This was also reflected by an increase in con A-induced IL-4 production, with increased age in the present studies (Fig. 2B). Until recently, it was believed that IL-6 is produced by Th2 cells (Szabo et al, 2003). Thus the increased IL-6 production in lymphocytes, during recovery from lymphopenia, could be attributed to genetic Th2 bias in BALB/c mice. However, now it is established that IL-6 is produced primarily by Th17 cells (Weaver et al, 2007). These experiments were repeated using Swiss mice. The variation in levels of IL-2, IL-4 and IFN-γ during recovery from lymphopenia in Swiss mice, was similar to that observed in BALB/c mice (Data not shown). Interestingly, con A-induced IL-6 production in lymphocytes, from lymphopenic swiss mice, was higher even on day 4 after reconstitution (Fig. 2E).

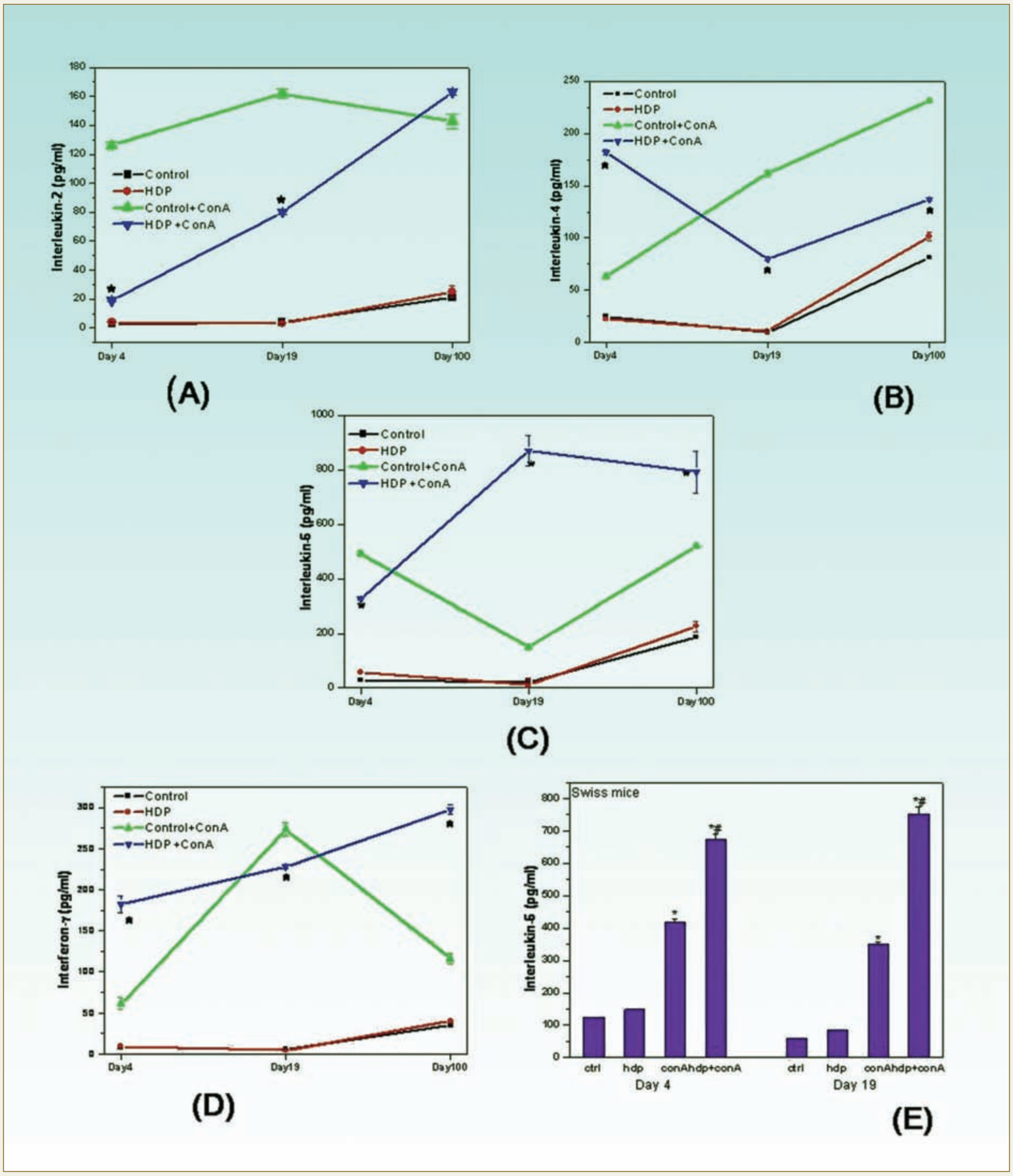

Fig. 2: Changes in cytokine production by lymphocytes during recovery from lymphopenia. Lymphopenic mice were reconstituted with autologous CD4+ T cells and sacrificed 4, 19 and 100 days after adoptive transfer. The splenic lymphocytes from mice recovering from lymphopenia and age/sex matched normal mice were cultured in presence of con A (10μg/ml) at 37^{0}C in CM in a 95% air/5% CO_2 atmosphere for 24 h. The levels of (A) IL-2, (B) IL-4, (C) IL-6 and (D) IFN-γ in the culture supernatants of cells obtained from BALB/c mice and (E) the levels of IL-6 in the culture supernatants of cells obtained from Swiss mice were estimated by ELISA. #p < 0.01, as compared to that in con A stimulated cells from normal mice

Effect of CHL on con A induced proliferation and IL-6 production in T cells in vitro and HDP of CD4+ T cells in vivo

The effect of CHL on con A-induced proliferation of splenic T lymphocytes of BALB/c mice, as assessed by CFSE dye dilution, is shown in Fig. 3A. The bars represent percentage of daughter cells obtained after more than four divisions during 72 h culture. Chlorophyllin up to 10μM did not inhibit con A induced proliferation of T cells. At higher concentrations of CHL, a significant decrease in the percentage of daughter cells was observed. At 100μM, almost complete inhibition of proliferation was seen (Fig. 3A). CHL also significantly inhibited mitogen induced IL-6 production in T cells (Fig. 3B). The HDP of CFSE labeled CD4+ T cells treated with CHL (100μM) and injected into syngenic lymphopenic mice, was significantly inhibited as compared to that of untreated CD4+ T cells, injected into syngenic lymphopenic mice (Fig. 3C and 3D).

Chlorophyllin enhanced the expression of apoptosis-related genes bcl-2 and bcl-xL in lymphocytes

Since CHL inhibited T cell proliferation *in vitro* as well as *in vivo* without inducing cell death, the expression of antiapoptotic genes bcl-2 and bcl-xL was studied in splenic lymphocytes, from normal and CHL-treated mice 72 hr after injection. Fig. 4 shows the expression of antiapoptotic genes bcl-2 and bcl-xL in lymphocytes, as examined by semi-quantitative RT-PCR using β-actin as an internal control (Fig. 4A and B). The bands appearing at 409, 550 and 556 bp on the agarose gel correspond to β-actin, bcl-2 and bcl-xL mRNA, respectively. The expression of bcl-2 gene was significantly higher in cells from CHL-treated mice as compared to that in cells from medium treated mice (Fig. 4C). The bcl-xL mRNA was not detectable in the cells from medium treated mice. However, it appeared in the cells obtained from CHL treated mice (Fig. 4C).

Discussion

Several studies in humans and rodents indicated that lymphopenia might be associated with autoimmune manifestations. In humans, lymphopenia accompanies insulin-dependent diabetes mellitus (IDDM), rheumatoid arthritis, Sjogren's syndrome and systemic lupus erethematosus. Signs of autoimmunity are also frequently observed in HIV-infected patients (Reviewed in Krupica-Jr et al, 2006). In rodent models, examples of lymphopenia-associated autoimmunity include, systemic autoimmunity after neonatal thymectomy, discontinuation of cyclosporine treatment, total lymphoid irradiation or infection with mouse T lymphotropic virus. Accelerated onset of diabetes in nonobese diabetic (NOD) mice, thymectomized at weaning or neonatally injected with cyclosporine, has also been observed (Dardenne et al, 1989; Bucy et al, 1993; Lafaille et al, 1994; Sai et al, 1994). Thus, there is need to identify modulators which can specifically block HDP of T cells.

In the present report, we describe the spatial characteristics and cytokine production, during HDP of CD4+ T cells. HDP was found to occur in the spleen as well as lymph nodes of the lymphopenic mice, but not in peritoneum (Fig. 1). Several reports have shown the importance of lymphocyte trafficking through and homing to draining lymph nodes for antigen driven proliferation, using intravital microscopy (Mempel et al, 2004; Henrickson et al, 2008). Since peritoneal fluid is not directly connected to blood circulation, the factors sensing empty lymphoid space may not be accessible to the peritoneum resident lymphocytes. Antigen driven proliferation (ADP) is generally more robust in the draining lymph nodes and is localized to T cell zones (Mempel et al, 2004; Henrickson et al, 2008). Our results showed that HDP took place in lymph nodes as well as spleen and was localized to T cell zones in the later (Fig. 2) suggesting that HDP and ADP share common spatial requirements.

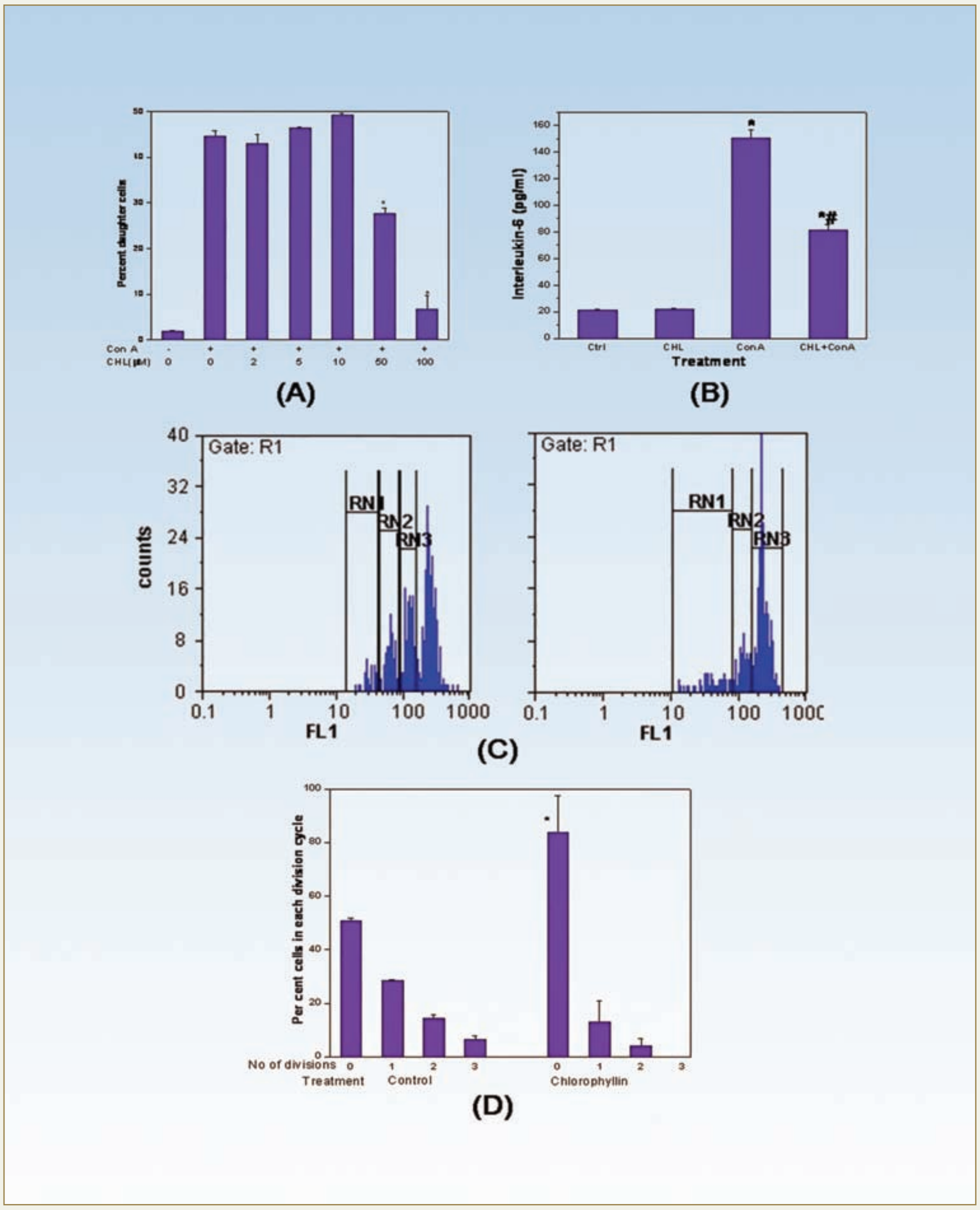

Fig. 3: Effect of CHL on con A induced proliferation: (A) CFSE labeled spleen cells were stimulated with the mitogen in presence of various concentrations of CHL at 37^0C in RPMI 1640 medium supplemented with 10% FCS in a 95% air/5% CO_2 atmosphere for 72 h and 20,000 cells were acquired in flowcytometer. Percent daughter cells were calculated from decrease in mean fluorescence intensity using Cellquest® software. Each bar represents percentage of daughter cells after more than four divisions. (B) Concentration of Interleukin-6 in the culture supernatant of lymphocytes stimulated with con A for 24 hr as estimated by ELISA. (C) Effect of CHL on homeostasis driven proliferation of CD4+ T cells in lymphopenic mice in vivo. CD4+ T cells were purified from total splenic lymphocytes, stained with CFSE and cultured in presence of CHL (100mM) at 37^0C in CM in a 95% air/5% CO_2 atmosphere for 24 h. Cells were washed once with RPMI to remove unbound drug1.5×10^6 cells were injected i.v. into tail vain of lymphopenic mice. Lymphocytes were recovered from spleen of the host mice 96 h after reconstitution and 50,000 cells were acquired in a flowcytometer. Percent daughter cells were calculated from decrease in mean fluorescence intensity. (D) The bars represent frequency of daughter cells in different division cycles in each treatment group. Each bar represents mean±S.E.M. from three replicates and two such experiments were carried out. *$p < 0.01$, as compared to untreated control.

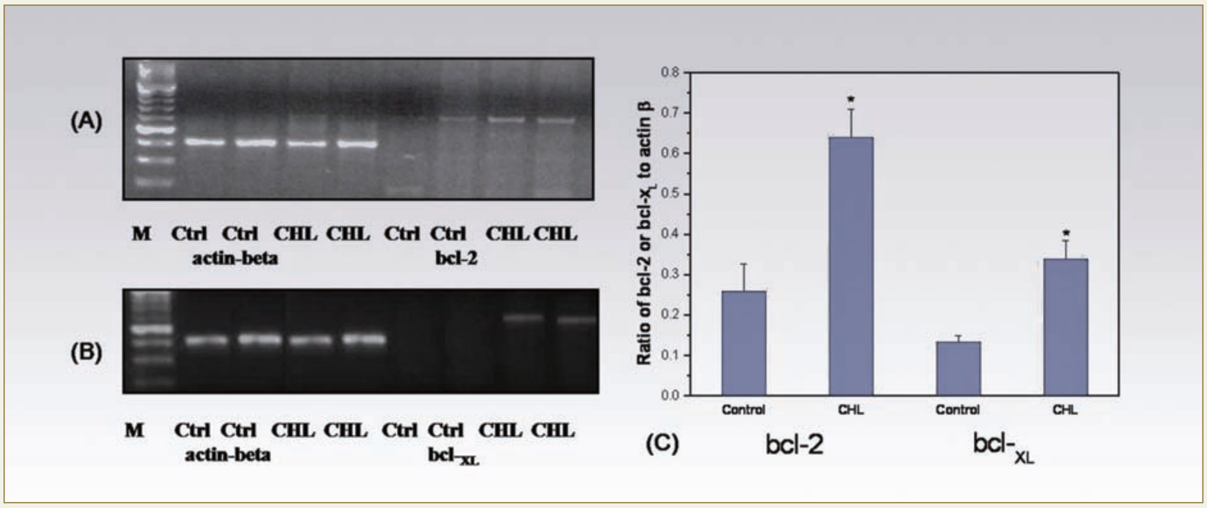

Fig. 4: Upregulation of bcl-2 and bcl-xL expression in lymphocytes of CHL treated mice. RT-PCR analysis of (A) bcl-2 and (B) bcl-x_L was carried out using lymphocytes isolated from medium and CHL (200 μg/gbw, 72 h) treated mice. Total RNA from 0.5×10^6 cells was reverse transcribed and PCR amplified with specific primers. PCR products were resolved on 2% agarose gels containing ethidium bromide. β-Actin gene expression in each group was used as an internal control. (C) Ratio of intensities of bcl-2 or bcl-xL band to that of respective β-actin band as quantified from gel pictures. Each value represents mean±S.E.M. from triplicates and two such experiments were carried out. *$p < 0.01$, as compared to medium treated mice

Mitogen-induced cytokine production in T cells, recovered from reconstituted lymphopenic mice, showed a pro-inflammatory pattern as compared to that in cells from normal mice. IL-2 and IFN-γ production, showed steady increase during recovery from lymphopenia, indicating that their levels may be used as reliable markers, to assess recovery from lymphopenia (Fig. 2A and D). Sanchez-Guajardo et al (Sanchez-Guajardo et al., 2005) had shown that CD4+ Th2 cells from Stat4"/" mice divided slower than CD4+ Th1 cells from Stat6"/" mice. The present results using polyclonal CD4+ T cells showed a similar trend with increased IFN-γ production with time (Fig. 2D). However, a decrease in con A-induced IL-4 production in lymphocytes 19 and 100 days after reconstitution, indicated that, recovery from lymphopenia was possibly associated with decreased Th2 differentiation in mice.

Most strikingly, mitogen induced IL-6 production was significantly higher in lymphocytes, taken from lymphopenic BALB/c mice 19 and 100 days after reconstitution as compared to that in cells from age/sex matched normal mice (Fig. 5C). Recent evidence shows, that IL-6 is produced primarily from TH17 cells (Langrish et al, 2005; Weaver et al, 2007). The decrease in a Th2 cytokine and a concurrent increase in a Th17 cytokine during recovery from lymphopenia, may be an underlying cause for increased chances of autoimmunity in patients recovering from lymphopenia (Theofilopoulos et al, 2001; Baccala and Theofilopoulos, 2005; Calzascia et al, 2008). Chlorophyllin, a dietary antioxidant completely inhibited mitogen driven proliferation as well as HDP of T cells *in vitro* and *in vivo*. This inhibition of T cell proliferation was due to increased expression of antiapoptotic genes bcl-2 and bcl-xL in lymphocytes resulting in cell cycle arrest.

In summary, the present work describes spatial distribution and cytokine production by CD4+ T cells in lymphopenic environment. To our knowledge, this is the first report describing an elevated production of IL-6 in T cells taken from mice, recovering from lymphopenia. Further, for the first time, inhibitory action of an antioxidant on lymphopenia driven proliferation was shown (Sharma et al, 2007). Any possibility of a therapeutic application of CHL, for prevention of autoimmune disorders, needs to be verified by careful experimental examination of signaling events, blocked by CHL.

Acknowledgements

We thank Prof. Shobhona Sharma, Tata Institute of Fundamental Research, Mumbai for her help in flow cytometry and we thank Mr. Rahul Checker for his help. We also acknowledge Mr.. K.S. Munankar, Mr. N. Sidnalkar and Mr. D. Kathole for technical assistance.

References

1. C. D. Surh, J. Sprent, *J Exp Med* 192, F9 (Aug 21, 2000).
2. N. L. La Gruta, I. R. Driel, P. A. Gleeson, *Eur J Immunol* 30, 3380 (Dec, 2000).
3. A. N. Theofilopoulos, W. Dummer, D. H. Kono, *J Clin Invest* 108, 335 (Aug, 2001).
4. C. King, A. Ilic, K. Koelsch, N. Sarvetnick, *Cell* 117, 265 (Apr 16, 2004).
5. A. M. Marleau, N. Sarvetnick, *J Leukoc Biol* 78, 575 (Sep, 2005).
6. D. A. Hildeman *et al.*, *Proc Natl Acad Sci U S A* 100, 15035 (Dec 9, 2003).
7. D. W. Voehringer, *Free Radic Biol Med* 27, 945 (Nov, 1999).
8. E. Rosati *et al.*, *J Leukoc Biol* 76, 152 (Jul, 2004).
9. R. W. Young, J. S. Beregi, Jr., *J Am Geriatr Soc* 28, 46 (Jan, 1980).
10. P. A. Egner *et al.*, *Proc Natl Acad Sci U S A* 98, 14601 (Dec 4, 2001).
11. P. A. Egner, A. Munoz, T. W. Kensler, *Mutat Res* 523-524, 209 (Feb-Mar, 2003).
12. S. S. Kumar, R. C. Chaubey, T. P. Devasagayam, K. I. Priyadarsini, P. S. Chauhan, *Mutat Res* 425, 71 (Mar 10, 1999).
13. S. S. Kumar, T. P. Devasagayam, B. Bhushan, N. C. Verma, *Free Radic Res* 35, 563 (Nov, 2001).
14. S. S. Kumar, B. Shankar, K. B. Sainis, *Biochim Biophys Acta* 1672, 100 (May 3, 2004).
15. D. Sharma, S. S. Kumar, R. Raghu, S. Khanam, K. B. Sainis, *Mol Immunol* 44, 2831 (Apr, 2007).
16. D. Sharma, S. S. Kumar, K. B. Sainis, *Mol Immunol* 44, 347 (Jan, 2007).
17. S. J. Szabo, B. M. Sullivan, S. L. Peng, L. H. Glimcher, *Annu Rev Immunol* 21, 713 (2003).
18. C. T. Weaver, R. D. Hatton, P. R. Mangan, L. E. Harrington, *Annu Rev Immunol* 25, 821 (2007).
19. T. Krupica, Jr., T. J. Fry, C. L. Mackall, *Clin Immunol* 120, 121 (Aug, 2006).
20. M. Dardenne, F. Lepault, A. Bendelac, J. F. Bach, *Eur J Immunol* 19, 889 (May, 1989).
21. R. P. Bucy, X. Y. Xu, J. Li, G. Huang, *J Immunol* 151, 1039 (Jul 15, 1993).
22. J. J. Lafaille, K. Nagashima, M. Katsuki, S. Tonegawa, *Cell* 78, 399 (Aug 12, 1994).
23. P. Sai, O. Senecat, L. Martignat, E. Gouin, *Clin Exp Immunol* 97, 138 (Jul, 1994).
24. T. R. Mempel, M. L. Scimone, J. R. Mora, U. H. von Andrian, *Curr Opin Immunol* 16, 406 (Aug, 2004).
25. S. E. Henrickson *et al.*, *Sci Signal* 1, pt2 (2008).
26. V. Sanchez-Guajardo, J. A. Borghans, M. E. Marquez, S. Garcia, A. A. Freitas, *J Immunol* 174, 1178 (Feb 1, 2005).
27. C. L. Langrish *et al.*, *J Exp Med* 201, 233 (Jan 17, 2005).
28. R. Baccala, A. N. Theofilopoulos, *Trends Immunol* 26, 5 (Jan, 2005).
29. T. Calzascia *et al.*, *Proc Natl Acad Sci U S A* 105, 2999 (Feb 26, 2008).

ABOUT THE AUTHORS

Dr. Deepak Sharma, joined BARC after securing First Rank from the 44th batch of BARC Training School. He received the Homi Bhabha Award and medal in 2001. He is presently working in the Radiation Biology & Health Sciences Division of BARC. He has demonstrated the signaling requirements for mitogen driven proliferation vis-à-vis homeostasis driven proliferation of CD4+T cells. He also showed the redundant role of PI3kinase, mTOR and PKCq during homeostatic proliferation, but an essential role of NF-kB and AKT. Further Dr. Sharma showed that chlorophyllin a water-soluble analog of green plant pigment chlorophyll, inhibited homeostatsis driven-proliferation of CD4+T cells. He was recently awarded PhD in Applied Biology by University of Mumbai. His research interests include radioprotection and immunomodulation by phytochemicals.

Dr. Santosh Kumar Sandur, joined BARC after graduating from the 38th batch of BARC Training School. He is presently working in the Radiation Biology & Health Sciences Division of BARC. He was conferred the DAE Young Scientist Award for the year 2007, for his outstanding contributions related to radioprotective actions of antioxidants of natural origin and their antitumour activities. He demonstrated the efficacy of chlorophyllin (CHL) in ameliorating radiation-induced alterations, in cell free and cellular systems, *in vitro* as well as *in vivo*. In addition to this administration of CHL to animals augmented both innate as well as adaptive immune responses and prevented programmed cell death in lymphocytes, by upregulation of antiapoptotic genes *bcl-2* and *bcl-*$_{XL}$. He has shown the novel mechanism of antitumour and anti-inflammatory effects of curcuminoids.

Dr. K. B. Sainis, Director, Bio-Medical Group, BARC, joined BARC after securing First rank from the 15th batch of BARC Training School (Biology-Radiobiology). He is the recipient of the Homi Bhabha Award, INSA Young Scientist Award, Shanti Swarup Bhatnagar Award and INS Senior Scientist Award. He is a PhD guide in Applied Biology (University of Mumbai) and Life Sciences (Homi Bhabha National Institute). He has about 80 publications in international and national journals to his credit. His research interests include biological effects of low-dose radiation, immunomodulation by plant derived natural products, tumour immunology and radiation biology. He oversees the research and development programmes of six divisions of Bio-medical Group and delivery of health care to more than 80,000 beneficiaries of CHSS. He represents India at United Nations Scientific Committee on Effects of Atomic Radiation (UNSCEAR). He is also a member of the Standing Advisory Group on Nuclear Apllications (SAGNA), IAEA and Shanti Swarup Bhatnagar Award selection committee.

REVERSIBLE PROTEIN PHOSPHORYLATION CONTROLS THE NUCLEOLYTIC DNA DEGRADATION IN A RADIORESISTANT BACTERIUM, DEINOCOCCUS RADIODURANS

V. A. Kamble and H. S. Misra
Molecular Biology Division

This paper was awarded the B. S. Narasinga Rao Best Poster Award at the Scientific Session of "Cell Signaling and Apoptosis" during the "77th Annual Meeting of the Society of Biological Chemists (India) (SBC (I)) and Symposium on "Impact of Basic and Translational Research on Medicine, Agriculture and Industry", held at the Department of Biotechnology, Indian Institute of Biotechnology, Chennai, during December 18-20, 2008

ABSTRACT

Deinococcus radiodurans R1 exhibits the extraordinary ability, to reassemble the nearly 3000 single strand breaks and 200 DNA double strand breaks, produced from 6.5kGy γ radiation and desiccation with less 5% humidity. This bacterium has nearly similar DNA recombination and DNA repair complements of a radiation-sensitive bacterium, *Escherichia coli*, except the absence of RecBC recombination pathway proteins. However, the unique mechanism of fragmented genome protection from nucleolytic degradation, possibly makes this bacterium outperform other organisms. The molecular mechanism of DNA protection from nuclease attack is not clearly understood. This study reports novel findings, suggesting the high-energy attenuation of nuclease activity in *Deinococcus*, a unique process that controls nucleolytic degradation of DNA, during post irradiation recovery of γ irradiated cells. Cell free extracts of γ irradiated *D. radiodurans* exhibit less nucleolytic degradation of double stranded DNA than *E. coli*. However, unlike *E. coli*, which showed ATP-dependent stimulation of nuclease function, deinococcal nuclease activity was reduced by addition of exogenous ATP. The nuclease activity was constitutive, but the ATP responsive inhibitory function was sensitive to chloramphenicol and was γ-radiation inducible. Inhibitors of protein kinase A activity prevent ATP-dependent inhibition of nuclease activity. The nuclease inhibition was alleviated by dephosphorylation, which upon incubation with ATP in the presence of phosphatase inhibitor, could be resumed. This suggested that the nuclease function is regulated by reversible protein phosphorylation. We suggest, that the ability to control nuclease activity during post-irradiation, provides *D. radiodurans* with an advantage over less DNA damage-tolerant species. DNA degradation proceeds until the substrates necessary for strand annealing are generated, after which the potentially lethal nuclease activity can be shut off, preventing excessive DNA degradation.

Introduction

Protein phosphorylation constitutes an important regulatory network that controls the cellular functions including cell division, cellular differentiation and signal transduction in all organisms. At the molecular level, this regulates metabolic functions such as enzyme activity modulation, protein trafficking, protein–protein and DNA–protein interactions and recycling of the proteins. By reversible protein phosphorylation, the functions of proteins can be rapidly modulated, without necessity of new protein synthesis or degradation. This phenomenon is regulated by the relative abundance of stress responsive protein kinases and phosphatases in the cells. The significance of reversible protein phosphorylation is amply illustrated by the involvement of DNA damage induced signal transduction and protein kinase C mediated signaling mechanism in cell cycle regulation, following DNA damage in eukaryotes (1). The existence of such mechanisms and their implications in DNA strand break repair and bacterial growth, would be worth investigating in bacteria, tolerant to DNA damage.

Deinococcus radiodurans R1 (DEIRA) is characterized for its extraordinary radioresistance contributed primarily by an efficient DNA Strand Break (DSB) repair and a strong oxidative stress tolerance mechanism (2). DEIRA exposed to DNA damage showed a rapid and kinetic change in gene expression profile and a rapid protein turnover (3). DEIRA shows a biphasic DSB repair mechanism. Phase I is characterized as the reassembling of shattered genomes into larger size molecules by Extended Synthesis-Dependent Strand Annealing (ESDSA) followed by slow events of homologous recombination. During this period, the shattered genome is protected from nucleolytic degradation by end capping proteins and presumably processed for further steps in DNA repair, by a still unknown mechanism. However, the DSB repair kinetics monitored on Pulsed Field Gel Electrophoresis (PFGE) and by [^{3}H] labeled genomic DNA stability *in vivo* (4) shows a rapid increase in DNA degradation upon γ irradiation, which gets arrested within 30 min of PIR. Although, the DNA damage induced change in gene expression and protein turnover have been reported in DEIRA, the mechanism that links DNA damage response to these critical processes is not known. In this study, we report the gamma radiation inducible change in the levels of signaling molecules in *Deinococcus radiodurans* and demonstrated that the cells exhibiting higher levels of signaling molecules, also showed reversible modulation of nucleolytic functions. The role of DNA damage inducible protein kinase A activity in regulation of nucleolytic functions during post irradiation recovery of *Deinococcus radiodurans* was demonstrated.

Methodology

Gamma irradiation and cell free extract preparation

DEIRA was maintained in the laboratory as described earlier (5). Exponentially growing cells were irradiated with 6kGy γ-radiation, aliquots were collected at 1 h intervals and cells were washed with butanol saturated 100 mM phosphate buffer (pH 7.0). The pellet was suspended in lysis buffer (20mM Tris-HCl pH 7.6, 1mM $MgCl_2$ 1mM DTT and 1mM PMSF) containing 200μg/ml of lysozyme and incubated at 37^0C for 20 min. To this, 1 % Triton X-100 was added and incubated further for 30 min at room temperature. Cell suspension was sonicated with 4μm tip at 50% duty cycles and 30sec pulse with intermittent cooling on ice for 4 min. Protein content was estimated by Bradford dye binding method. Cell free extract was maintained in 10% glycerol at 4^oC and subsequently used for activity assays.

Nucleotide binding proteins purification

Cell free extract was prepared from DEIRA cells collected 0, 1, 2, 3 and 4 h post-irradiation, by centrifugation at 15000 rpm for 30 min. Extracts were diluted with ten volumes of column binding buffer (10mM sodium phosphate buffer, pH7.0, 50mM NaCl, 1mM EDTA, pH 8.0, 1mM DTT, 1mM PMSF).

Nucleotide binding proteins were affinity purified using heparin-sepharose affinity chromatography, as described in the manufacturer's protocol (GE Healthcare, Sweden). Cell free extracts were passed through the Hi-Trap heparin column, pre-equilibrated with column binding buffer. The column was washed with binding buffer, until the proteins stopped coming from the column. The bound proteins were eluted with 500mM NaCl in binding buffer. The 500ml fractionswere collected and analyzed on SDS-PAGE. Protein concentration was determined by dye binding method. The effect of ATP on nuclease activity was monitored as described earlier (6). The fraction showing nuclease activity and its inhibition with ATP was further purified, using ion exchange chromatography. Each fraction was tested for separation of nuclease activity from ATP responsive fractions.

Enzymes activity measurement

The nuclease activity was measured as described by Kota and Misra (2008) (6). The 500 ng heparin purified proteins were incubated with 200 ng of 1 kb PCR product from DEIRA genome, in a buffer (10 mM Tris-HCl, pH7.5, 3mM $MgCl_2$, 15 mM KCl and 2% glycerol) for 20 min at 37°C. For ATP and calf intestinal phosphatase (AP) treatment, the proteins were preincubated with these agents for 30 min at 37°C. For phosphatase and protein kinase inhibitors treatment, the samples were treated with 10 mM sodium fluoride and different concentrations of protein kinase inhibitors respectively, for 20 min. Treated samples were incubated with dsDNA substrate for 20 min at 37°C and reaction products were analyzed on 1% agarose gel.

Protein kinase activity was measured as described earlier (7). In brief, the cell free extract was prepared from cells treated with gamma radiation and equal amount of proteins were incubated with 50 mCi $[^{32}P]$ γ ATP (2500Ci /mmol) for 1 h at 37°C. To this, the DNAse (50mg/ml) and RNAse (50mg/ml) were added and further incubated for 1 h. The mixture was passed through G-25 microspin columns (GE Healthcare) to remove the unincorporated radionucleotides and smaller non-proteinaceous phospho-contaminants. Incorporation of $[^{32}P]$ was measured by scintillation counting and counts per mg protein were presented. The acid and alkaline phosphatases were assayed in 100 mM acetate buffer (pH 5.0) or 50 mM Tris-HCl buffer (pH 9.0) respectively, using disodium salt of p-nitrophenyl phosphate as a substrate. The phosphatase activity was expressed as nanomoles para-nitrophenol formed per min per mg of proteins. Similarly, the total PhosphoDiesterase (PDE) activity was measured in a reaction mixture containing 1 mM bis(p-nitrophenyl) phosphate substrate in 50 mM sodium acetate, pH 5.0 for 30 at 30°C. The adenylyl cyclase (AC) activity was measured using a modified protocol described earlier (8). In brief, the a $[^{32}P]$-ATP was replaced with 500mM ATP and the cAMP was omitted from the standard reaction mixture. The other modifications were the use of caffeine in place of isobutylmethylxanthine and the estimation of cAMP by HPLC as described below.

Nucleotide extraction and estimation by HPLC analysis

The quantitative determination of purine nucleotides including ATP and cyclic AMP was carried out using the protocols similar to those described by Giannattasio et al 2003 (9), in their studies of cerebellar granule cells, but with modifications appropriate for use in DEIRA. These cells were washed with 70% ethanol and incubated with lysozyme (5mg / ml) for 30 min on ice. Treated cells were collected by centrifugation at 5000 x g at 4°C. Cell pellets were suspended in ice-cold 0.5 M perchloric acid. The suspension was mixed vigorously by shaking and incubated in ice-bath for 20 min. The acid extract was centrifuged (20,000 x g for 15 min at 4°C), to remove insoluble macromolecules. The supernatant was neutralized with equal volume of mixture, containing 4 / 5 volumes 0.5 M KOH plus 1 / 5 volume of 0.1 M KH2PO4, pH 7.5 and left for 30 min on ice. The potassium perchlorate precipitate was finally removed by centrifugation (20000 x g for 15 min at 4°C) and neutralized supernatant was stored at –20°C until used for HPLC analysis. The retention times of individual peaks and spiking with pure nucleotides were used, for the identification of respective nucleotides. The peak area was calculated per mg of protein for comparative studies.

Results and Discussion

Differential effect of ATP on nuclease activity of bacteria with contrasting response to γ radiation

Cell free extracts of g irradiated *Deinococcus radiodurans* (DEIRA) and *E. coli* were incubated with linear double stranded DNA, in the presence and absence of ATP, in solution. *E. coli* proteins showed relatively higher rate of DNA degradation as compared to DEIRA and showed several fold stimulation of nuclease activity with ATP. On the contrary, DEIRA showed less nuclease activity (Fig. 1A), which was inhibited with ATP. The ATP stimulation of nuclease activity in wild type *E. coli* has been attributed mainly to RecBCD complex (Exo V) (10). Lack of ATP stimulation of dsDNA exonuclease activity in DEIRA, cannot be solely accounted to the absence of only RecBC enzymes, because DEIRA cells expressing RecBC from *E. coli* did not show ATP stimulation of exonuclease activity (Fig. 1B) (4). This suggested that the DEIRA confers unique regulation of nucleolytic function by ATP and the nuclease composition in these two bacteria, showing contrasting radiation response, was different. The ATP attenuation of nuclease activity in DEIRA was subsequently shown to be mediated by protein kinase function and not as a metal ion chelator.

Nuclease activity was regulated by DNA damage induced reversible protein phosphorylation

The nucleotide-binding proteins of DEIRA cells recovering from high-density DNA strand breaks were purified by Heparin-Sepharose affinity chromatography (Fig. 2). Fractions were tested for nuclease activity on dsDNA substrate. Results showed, that the nuclease activity present in both unirradiated (UI) and γ irradiated cells at zero PIR, was completely inhibited at 1h and 2h PIR (Fig. 3a). Interestingly, the nuclease activity reappeared in 3h and 4h PIR samples. In all these samples, except the unirradiated (UR) control, the nuclease activity was inhibited by 2 mM ATP (Fig. 3b). The nuclease activity inhibition in PIR1 and PIR2 samples was revoked by dephosphorylation with alkaline phosphatase (AP), *in vitro* (Fig. 3c). These results suggested the possible involvement of protein

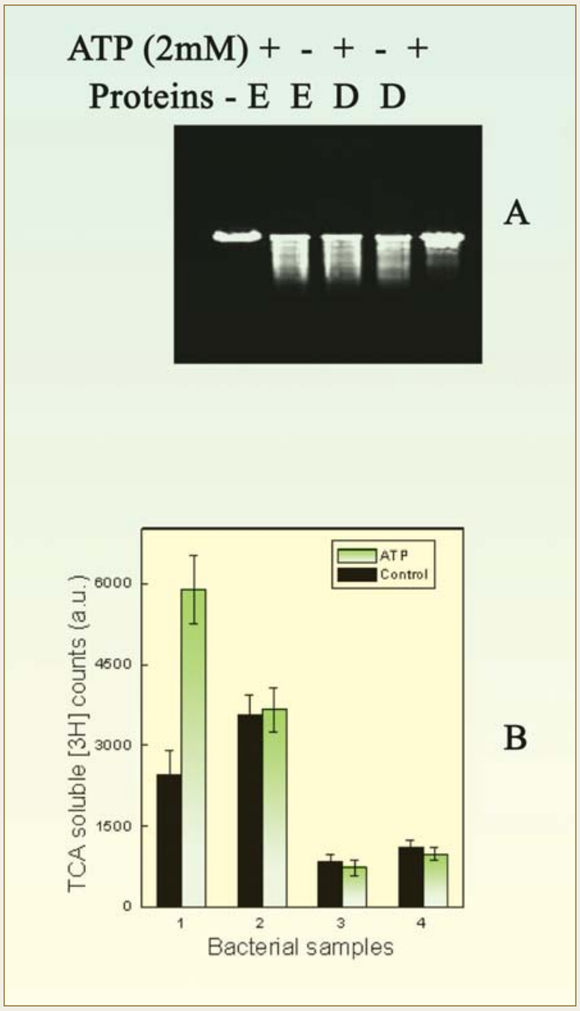

Fig. 1: Effect of ATP on nuclease activity of cell free extract from *E. coli* and *Deinococcus.* Cell free extract was prepared from stationary phase cells of *E. coli* (E) and DEIRA (D). The 200ng proteins were pre-incubated with 2mM ATP before DNA substrate (S) was added and further incubated for 30 min at 37^{o}C. Products were analyzed on 1% agarose gel (A). Nuclease activity of cell free extract from wild type (1) and *recD* mutant (2) of *E. coli* and DEIRA control (3) and RecBC expressing DEIRA (4) was also checked on [3H] labeled genomic DNA of DEIRA in the presence and absence of ATP (B).

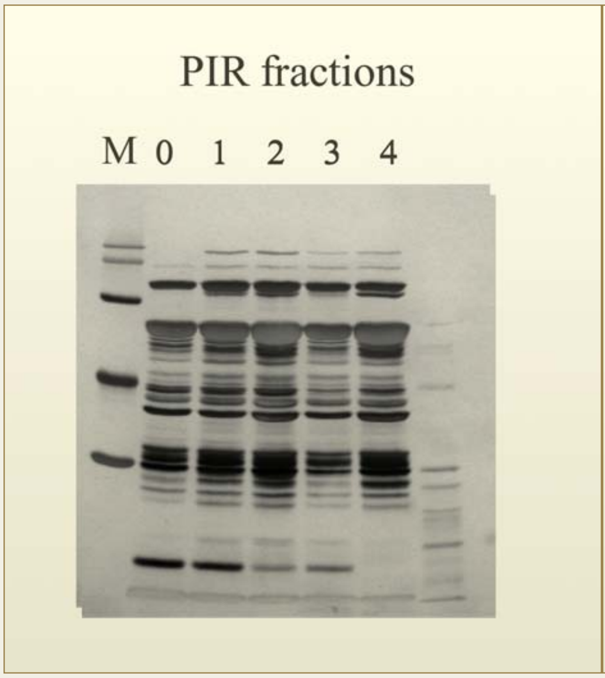

Fig. 2: SDS-PAGE analysis of total nucleotide binding proteins purified by Heparin affinity chromatography.The gamma irradiated cells were allowed to grow and samples were collected at 0,1,2,3 and 4 h of post irradiation recovery and proteins were puriifed.

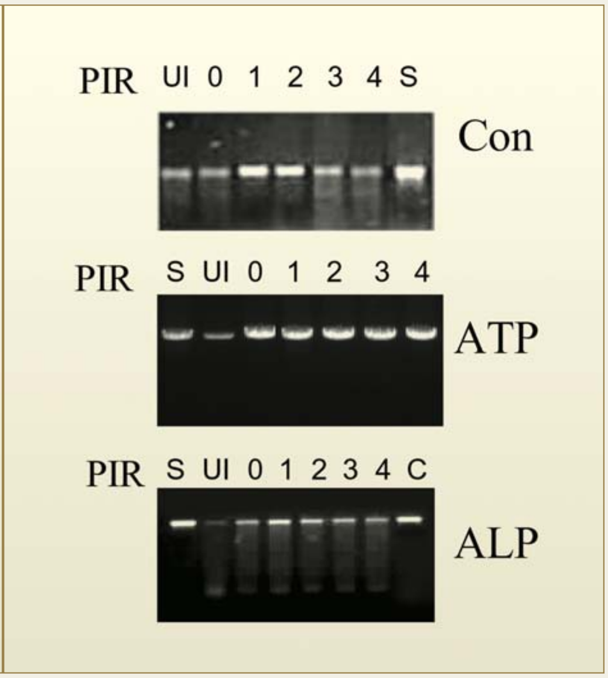

Fig. 3: Regulation of nucleolytic functions during PIR of DEIRA. Heparin binding proteins were purified from cells collected at different time intervals (0,1,2,3,4 h) of post irradiation recovery and unirradiated control (UI). These proteins were assayed for their nucleolytic activity (A) in the presence of ATP (B) and alkaline phosphatase (C) treatment. Reaction products were analyzed on 1% agarose gel.

phosphorylation in ATP-attenuation of nuclease function. Further, when dephosphorylated samples were incubated with ATP in the presence of 10 mM sodium fluoride, a phosphatase inhibitor; the nucleolytic activity was inhibited in all PIR fractions, but not in UI control (Fig. 4). The 1h PIR dephosphorylated sample was incubated with ATP in the presence of phosphatase, protein kinase A (H89) and protein kinase C (staurosporine) inhibitors and the ATP effect on nuclease activity was measured. Both H89 and high concentration of staurosporine, inhibit protein kinase A (PKA) activity also inhibited ATP effect on nuclease activity (Fig. 5). It suggested that PKA-type kinase might be involved in the post-translational regulation of nucleolytic functions. These results indicated that the DNA damage induces ATP responsive function and the nucleolytic activity was modulated by reversible protein phosphorylation, in DEIRA.

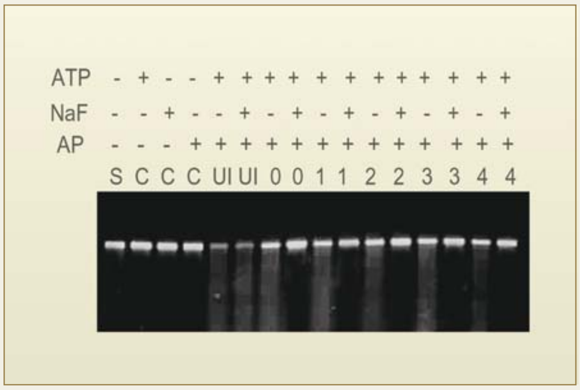

Fig. 4: Reversible protein phosphorylation regulates nucleolytic functions during PIR of DEIRA. Heparin purified proteins were dephosphorylated with alkaline phosphatase and incubated with ATP in the presence and absence of sodium fluoride, an inhibitor of phosphatase activity, for nuclease assay

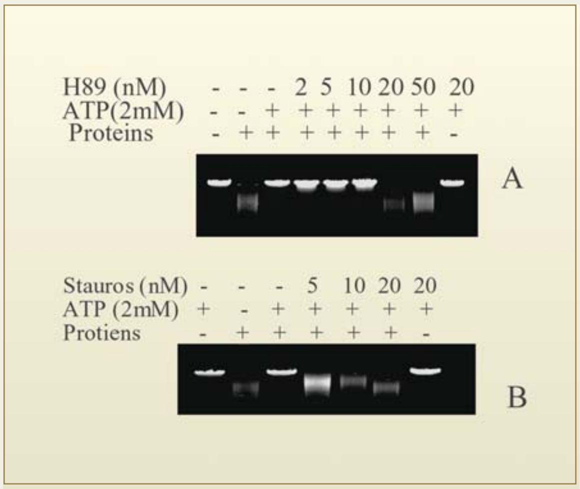

Fig. 5: ATP effect is manifested by protein kinase A. The dephosphorylated 1h PIR sample was incubated with 2mM ATP with an increasing concentration of H89 (B) and staurosporine (stauros) (C) and their effect on nuclease activity was assayed

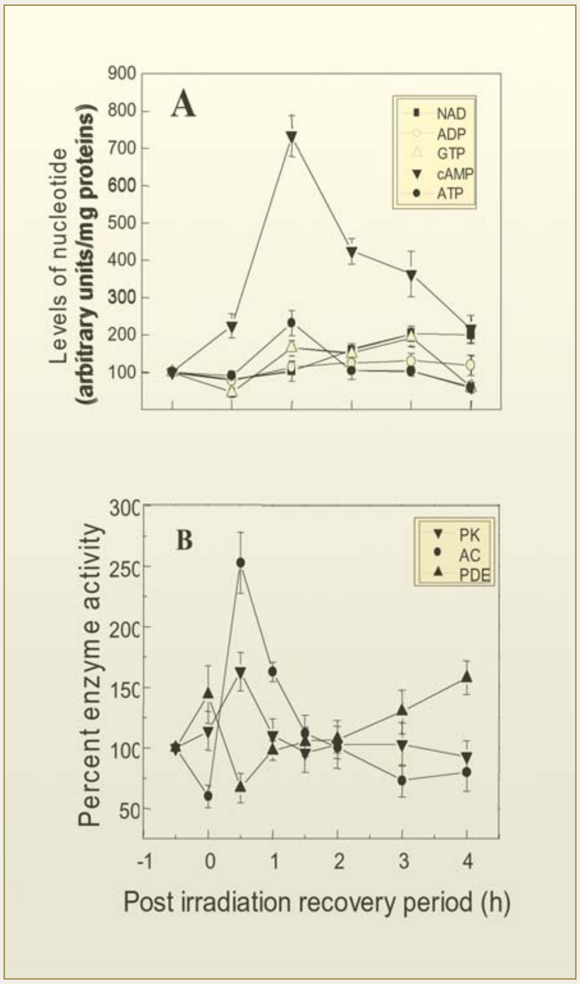

Fig. 6: Effect of DNA damage on the levels of signaling molecules. Total nucleotides were extracted with perchloric acids from unirradiated (UI) and γ irradiated cells collected at 0, 1, 2, 3 and 4 h of PIR and their levels were determined as described in materials and methods (A). The cell free extracts of unirradiated (UI) and γ irradiated cells collected at 0, 0.5, 1, 1.5, 2, 3 and 4 h of PIR, were used for monitoring the total protein kinase (PK), adenylyl cyclase (AC) and phosphodiesterase (PDE) (B). The activity of all the enzymes was measured as amount of products formed / unit time / mg total proteins. One hundred percent activity of PK, AC and PDE, corresponds to 1546600 CPM [^{32}P] / mg protein, 9.80 nmoles / min / mg protein and 6.30 mmoles / min/ mg proteins, respectively.

DNA damage induces signaling molecules in DEIRA

The change in the levels of secondary messengers like cAMP, cGMP, Ionositol phosphates, Ca2+ etc. and their correspondingly regulated signaling enzymes like adenylyl cyclase (AC), phosphodiesterases (PDEs), and protein kinases, have been considered as indicators of signal transduction mechanism, in response to a specific stress. We studied the effect of radiation-induced DNA damage on the levels of some of these molecules. We observed that the levels of cAMP, ATP change in DEIRA cells, recovering from very high dose of gamma radiation treatment (Fig. 6A). These cells showed differential expression of AC and PDEs. The enzyme system regulates the relative abundance of cAMP and ATP in biological system (Fig. 6B). The functional significance that these signaling molecules change on the regulation of protein kinases, in response to gamma irradiation, could be hypothesized. Recently, the involvement of protein phosphorylation in bacterial radiation resistance and DSB repair has gained considerable importance with the demonstration (7), that DEIRA cells lacking pyrroloquinoline-quinone, an inducer of protein kinase activity, exhibit relatively low protein kinase activity, impairment in DSB repair function and subsequently very low tolerance to γ radiation. A multiprotein complex isolated from DEIRA shows (6) the possible interaction of DNA repair proteins with protein kinase and phosphoproteins. The involvement of ATP in regulation of the metabolically opposite functions of DNA metabolism has been demonstrated. A periplasmic protein kinase activity, required for radiation resistance and DSB repair, has been detected in *Escherichia coli* (11). The phosphorylation of the single stranded DNA binding protein (SSB) and the differential binding to different types of DNA substrates as a function of protein phosphorylation, have been shown in *Bacillus subtilis* (12).

The signal transduction mechanism in response to nutritional stress and other abiotic stresses except DNA damage, has been shown in bacteria. In this study, we highlight, for the first time, the presence of gamma radiation-induced signaling mechanism, in the bacterium, *Deinococcus radiodurans*. We demonstrate that the DNA damage-induced synthesis of cAMP and ATP, was possibly manifested, by upregulation of adenylyl cyclase and downregulation of phosphodiesterase activity during PIR. The presence of different ACs and their involvement in bacterial signal transduction, has been well established. Although, the mechanism by which cAMP regulates DNA damage response is not clear, it presumably acts as an inducer of protein kinase activity and as a signaling molecule in signal transduction processes in bacteria, similar to that reported in eukaryotes. Similarly, the effect of DNA damage and oxidative stress on the AC and 2′, 3′cyclic PDE activity has not been reported, but the regulation of PDE and AC activities by a membrane receptor relaxin-mediated tyrosine phosphorylation, is known in mammalian cells. Since, cAMP is a known activator of MAP kinases and other soluble as well as membrane- bound protein kinases in eukaryotes, it is likely that the higher levels of cAMP and AC activity in 1h and 2h PIR samples, regulate protein phosphorylation by similar mechanisms. Our results show that (i) the levels of cAMP and ATP change in response to DNA damage and that was possibly manifested by differential regulation of AC and PDE enzymes upon γ irradiation and (ii) the involvement of DNA damage inducible protein kinase mediated ATP attenuation of nucleolytic activity during PIR. This is consistent with the activation of protein kinase by DNA damage in eukaryotes. Thus, there exists a DNA strand break-induced signaling mechanism in an extremophile, *Deinococcus radiodurans*, which is known to have acquired the genetic elements possibly contributing to some of its phenotypes, from higher organisms through horizontal gene transfer. And the possibility that this super bug has acquired the DNA damage induced signaling pathway from other organisms during evolution cannot be ruled out and will be studied independently.

Acknowledgement

Authors are grateful to Dr. S. K. Apte, BARC, Mumbai, for his constant support and critical comments during the progress of this work. Mr. Ashish Srivastava, NABTD, for his assistance in HPLC analysis of purine nucleotides.

References

1. A. Sancar, et al, *Ann. Rev. Biochem*. 73 (2004) 39-85.
2. A. M. Blasius et al, *Crit. Rev. Biochem. Mol. Biol*. 43 (2008) 221-238.
3. B. Joshi et al, *Biochem. Biophys*, *Res. Commun*. 320 (2004)1112-1117.
4. N. P. Khairnar, V. A. Kamble, and H. S. Misra, *DNA Repair*, 7 (2008) 40-47.
5. S. Kota, and H. S. Misra, *Appl. Microbiol. Biotechnol*. 72 (2006) 790-796.
6. S. Kota, and H. S. Misra. *Biochem*. *Cell Biol*. 86 (2008) 448-458.
7. Y. S. Rajpurohit, R. Gopalakrishnan, and H. S. Misra, *J. Bacteriol*. 190 (2008) 3948-3954.
8. S.R. Post et al, *Methods Mol. Biol*. 126 (2000) 363-374.

9. S. Giannattasio et al, *Brain Res. Protocols* 10 (2003)168-174.
10. A. Kuzminov, *Microbiol. Mol. Biol. Rev*. 63 (1999) 751-813.
11. N. P. Khairnar et al, *Mol. Microbiol*. 65 (2007) 294-304.
12. I. Mijakovic et al, *Nucleic Acids Res*. 34 (2006) 1588-1596.

ABOUT THE AUTHOR

Dr. Hari S. Misra is Head, Molecular Genetics Section, Molecular Biology Division, BARC. Dr. Misra's areas of interest are bacterial response to abiotic stresses and genetic modification of plants for crop improvement. Dr. Misra's group is currently working on elucidating the molecular mechanisms, underlying the cellular response to DNA damage and oxidative stresses, by employing advanced molecular biology tools. His group reports for the first time, the involvement of a signal transduction component in DNA strand break repair in bacteria and regulation of nucleolytic functions in *Deinococcus* cells, recovering from very high dose gamma radiation treatment. Dr. Misra is the recipient of INS Medal 2004 and an elected Fellow of Maharashtra Academy of Sciences, 2003.

DETECTION OF PROMOTER METHYLATION PROFILES OF MULTIPLE CANCER RELATED GENES IN THYROID CARCINOMA

A.A. Damle, A.H. Shikari, A.A. Narkar
Radiation Medicine Centre, Bio-Medical Group

This paper received the Best Poster Award at the DAE-BRNS 4th Life Science Symposium on Recent Advances in Immunomodulation in Stress and Cancer, held at BARC Guest House and Traning School Hostel Auditorium, from Dec. 22-24, 2008.

Introduction

Thyroid tumours are the most commonly encountered neoplasms in the endocrine system, and the vast majority are epithelial thyroid cancers, mainly Papillary and Follicular Thyroid Cancers (PTCs and FTCs) accounting for 95% of all thyroid malignancies. When diagnosed early, these cancers are generally curable. Fine Needle Aspiration (FNA) cytology is currently the best diagnostic tool, in the differential diagnosis of a thyroid nodule. Whereas this cytological assessment is diagnostic in a majority of the patients, approximately 15–20% of patients have insufficient biopsies and indeterminate cytological findings (1). Complete thyroidectomy is required in the surgical treatment of a malignant nodule, whereas partial thyroidectomy or observation is preferred for most benign nodules. Consequently, a majority of patients with cytologically indeterminate thyroid nodules who undergo total thyroidectomy do so, without a definitive diagnosis of malignancy and have to endure unnecessary discomfort. Therefore, an alternative unequivocal diagnostic approach, using an accurate blood test, would be an attractive option for evaluating thyroid nodule patients.

Thyroid cancer frequently recurs in 20-40% of patients, causing significant morbidity and even mortality, particularly when extensive metastasis has occurred (2). Therefore, after the initial treatment, it is critical to monitor patients for cancer recurrence, a process that currently depends on serum thyroglobulin (s-Tg) measurement, radioiodine scans and other imaging modalities (3). However, the utility of s-Tg test is limited by autoantibody interference in 25% of patients (4) and previous studies have also examined the potential value of alternative circulating molecular tumour markers, such as m-RNAs for Tg, TPO and TSH-R (5,6). However, there are conflicting results over the clinical use of such markers (7). The sensitivity of s-Tg measurement and radioiodine scans is low, when the patient is on thyroid hormone replacement therapy. To increase the sensitivity of these assays, the patient has to be off thyroxine for 4 - 6 weeks. This makes the patient hypothyroid and also results in stimulation of metastatic tissue. These problems in thyroid cancer treatment have long been the focus of studies with the goal to find novel and effective diagnostic and prognostic markers.

Reports that tumours shed nucleic acids, which are epigenetically modified has opened new areas in diagnosis and follow-up of cancer. Thus, circulating methylated DNA may potentially be a novel diagnostic marker for thyroid cancer. DNA methylation is a process that entails the addition of a methyl group to the fifth carbon position of the cytosine residue in a CpG dinucleotide by DNA methyltransferase (DNMT) enzymes (Fig. 1) and usually occurs in CpG islands, located in the 5′-flanking promoter regions of genes. Promoter methylation is one of the most common epigenetic alterations in tumourigenesis. A specific epigenetic modification of DNA promoter methylation induced gene silencing (Fig. 2) has been described in a large number of cancers and involves an increasing number of tumour suppressors. There is evidence that aberrant hypermethylation of genomic DNA is associated and may be in part responsible for transcriptional silencing during carcinogenesis (8). Gene silencing due to aberrant hypermethylation is a common epigenetic event in cancer progression (9,10) and tumour-specific patterns of hypermethylation can be detected by sensitive DNA-based assays, such as the methylation-specific PCR (MSP) on very limited clinical material (11), thereby presenting a uniquely attractive target for the development of a thyroid cancer-specific diagnostic assay.

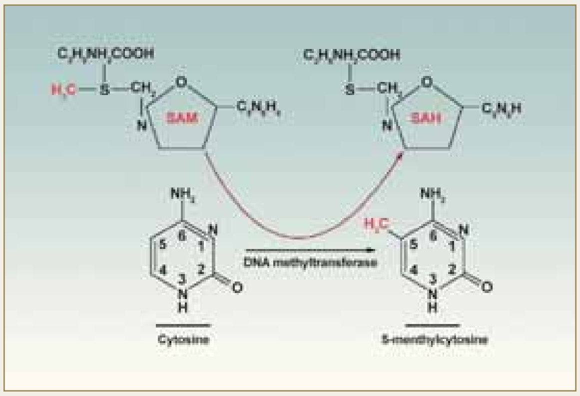

Fig.1: DNA methylation catalyzed by DNA Methyl Transferase (DNMT)

Aberrant gene methylation is common in human cancers, such as the genes for RASSF1A (12), calcitonin (CALCA) (13), thyroid-stimulating hormone receptor

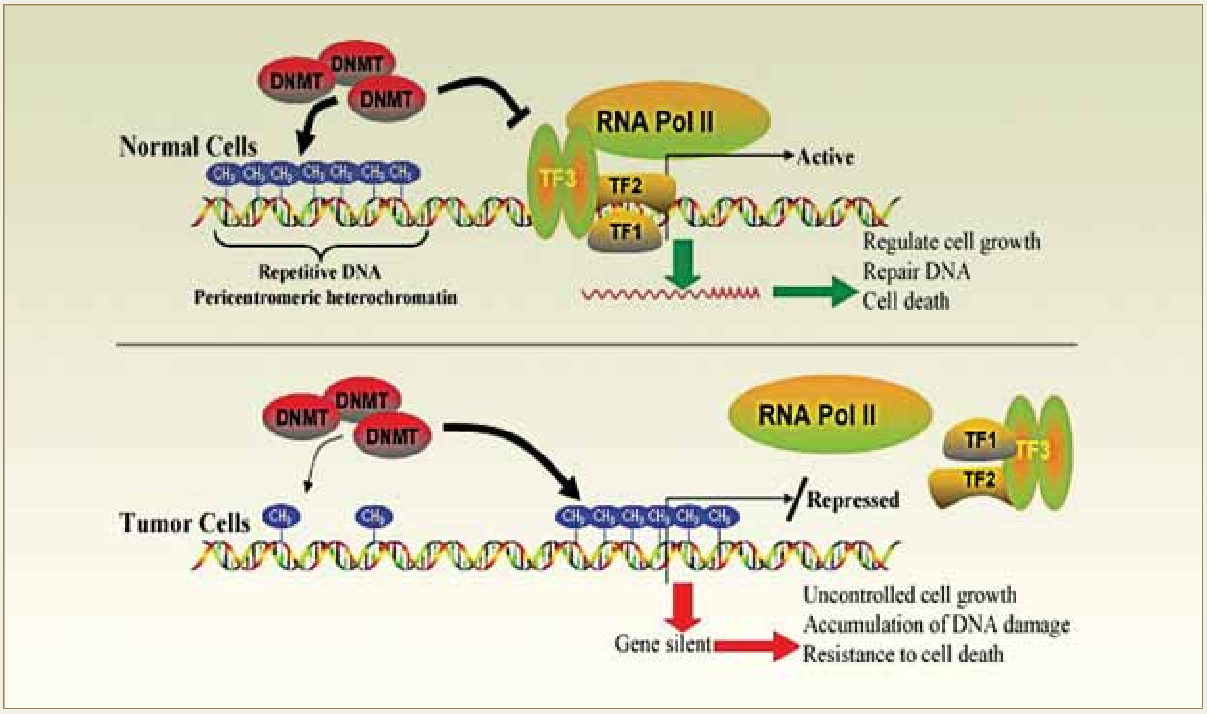

Fig. 2 : Gene silencing in Cancer caused by DNA methylation

(TSH-R) (14), E-cadherin (CDH1) (15), tissue inhibitor of metalloproteinase 3 (TIMP3) (16), death-associated protein kinase (DAPK) (17), and retinoic acid receptor â2 (RAR â2) (18) in various human cancers, including thyroid cancer. We investigated the promoter methylation status of the RASSF1A, CALCA, TSH-R, TIMP3, DAPK, RARâ2 and CDH1 gene in thyroid carcinoma. Many of these genes are tumour suppressor genes and are involved in cell cycle regulation, apoptosis, cell adherence, etc. and their epigenetic silencing is believed to play an important role in tumourigenesis. The gene targets along with their location, size and functions are depicted in Table 1. In this study, we investigated the usefulness of blood DNA methylation as a novel diagnostic marker for thyroid carcinoma.

Methods

Sample collection and processing

A total of 25 samples were used for this study, which included healthy individuals (n=5) and thyroid cancer patients (n=20). Histopathological classification of these patients was as follows: Hurthle cell carcinoma (n=1), anaplastic thyroid carcinoma (ATC, n=1), papillary thyroid carcinoma (PTC, n=4), follicular variant of PTC (FVPTC, n=9), follicular variant of poorly differentiated PTC (FVPDPTC, n=4); follicular thyroid carcinoma (FTC, n=3) and poorly differentiated FTC (PDFTC, n=1). Blood was collected by venipuncture in heparinized vacutainers and leukocyte separation was done using Histopaque (Sigma-Aldrich, USA).

Thyroid cancer cell lines

Human thyroid carcinoma cell lines: NPA (papillary), FRO (anaplastic), ARO (anaplastic) and WRO (follicular) were used for the study. Each of these cell lines were cultured in IMDM (GIBCO) supplemented with 10% sterile FBS (GIBCO), sodium carbonate ($NaHCO_3$), glutamine, β-2-mercaptoethanol (β-2-ME) and antibiotics in a 37°C humidified incubator with 5% CO_2. Cells were routinely sub-cultured every 3-4 days

Table 1 : Gene targets for methylation specific PCR

GENE	LOCATION	FUNCTION	SIZE
RASSF1A – Ras Association Domain Family 1A	3p21.3	Tumour suppressor gene, involvement in apoptotic signaling	74bp
CALCA – Calcitonin	11p15.2 - p15.1	Reduces serum calcium, involved in regulation of G1/S transition in cell cycle	100bp
TSH-R – Thyroid Stimulating Hormone Receptor	14q31	Stimulates several key steps in thyrocyte concentration of iodine	121bp
TIMP-3 – Tissue inhibitor of metalloproteinase 3	22q12.3	Inhibits the activity of MMPs; suppresses tumour growth, invasion & metastasis	92bp
DAPK – Death *associated Protein* Kinase	9q34.1	Positive mediator of IFN-γ-induced programmed cell death.	97bp
RARβ2 – Retinoic acid receptor β2	3p24.2	Induces growth arrest & apoptosis	91bp
CDH1 – E-cadherin type 1	16q22.1	Involved in adhesion between epithelial cells	69bp

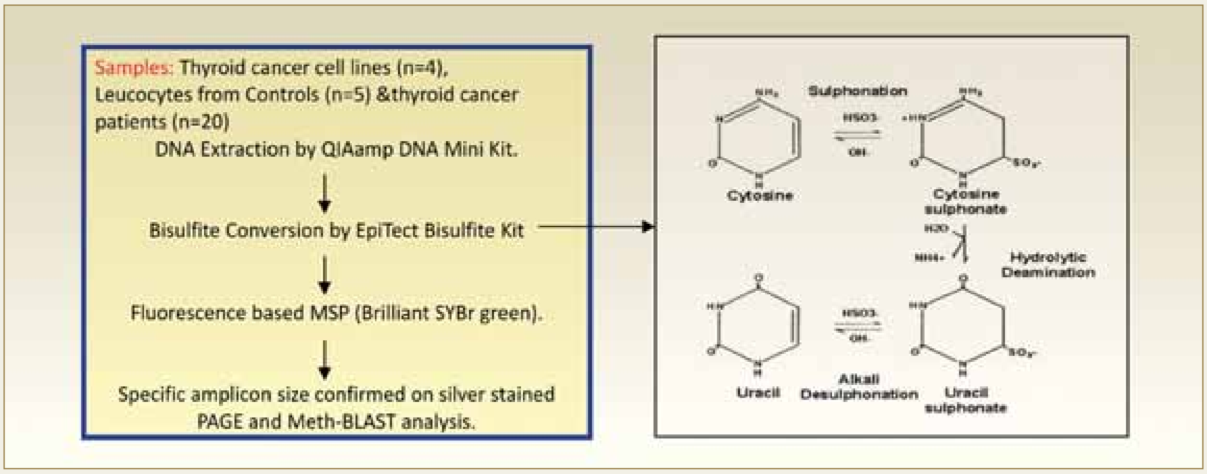

Fig. 3 : Flow chart of MSP and Bisulfite conversion of unmethylated Cytosines to Uracils

using trypsin-EDTA and harvested at 80% confluency.

DNA extraction and Sodium bisulfite treatment

DNA was extracted from separated leukocytes and thyroid cancer cell lines by QIAamp DNA Mini kit (Qiagen, USA), 1 μg of extracted genomic DNA was bisulfite converted using the EpiTect Bisulfite Kit (Qiagen, USA) as per manufacturer instructions and further used in methylation specific PCR (MSP) as shown in Fig. 3.

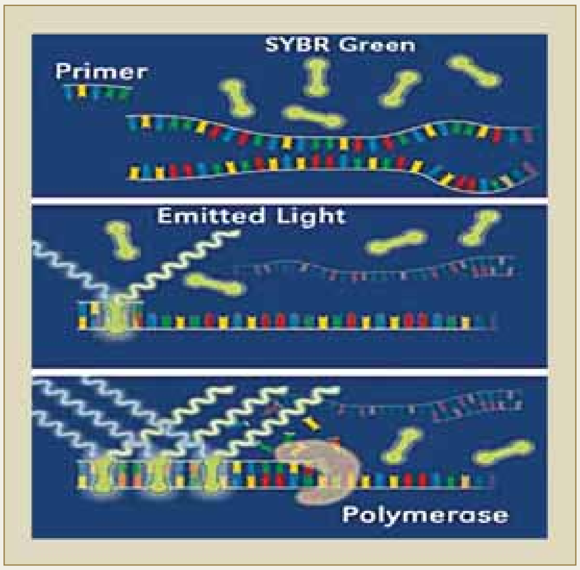

Fig. 4 : SYBr Green based PCR

Real-time methylation-specific PCR

Bisulfite-modified DNA was used as the template for fluorescence (Brilliant SYBR Green) based MSP (Fig.4). Briefly, oligonucleotide primers were designed to specifically amplify the bisulfite-converted DNA of the gene of interest. The primers used were as previously described (14,19,20) and the sequences are summarized in Table 2. Primers were synthesized by Operon Biotechnologies (Germany) and the Board of Radiation and Isotope Technology (BRIT), Mumbai, India.

Fluorogenic PCRs were carried out in a reaction volume of 25μl in an MXPro3000 Real-Time PCR machine (Stratagene, USA).The reaction mixture contained 5μl of bisulfite converted DNA, 400nM of forward and reverse primers and 2X Brilliant SYBr Green PCR mixture (Stratagene, USA). The thermal profile of amplification was: 95 °C for 10 min; followed by 40 cycles at 95 °C for 30 sec, 60 °C for 1 min and 72 °C for 1 min. The dissociation curves were obtained at the following setting: 1 cycle at 95 °C for 1 min, 60 °C for 30 sec and 72 °C for 30 sec. Each setup consisted of patient samples as well as positive and negative controls. Leukocytes from a healthy individual were methylated *in vitro* with excess M.SssI methyltransferase (New England Biolabs Inc., USA) to generate completely methylated DNA. The *in vitro* methylated DNA along with the CpG Methylated Hela

Table 2 : Primer sequences used for MSP

Gene	Forward primer sequence (5' - 3')	Reverse primer sequence (5' - 3')
RASSF1A	GCGTTGAAGTCGGGGTTC	CCCGTACTTCGCTAACTTTAAACG
CALCA	GTTTTGGAAGTATGAGGGTGACG	TTCCCGCCGCTATAAATCG
TSH-R	GGTGTAGAGTTGAGAATGAGGTGATTTC	GCCCAAATCCCTAAACAAATCG
TIMP3	GCGTCGGAGGTTAAGGTTGTT	CTCTCCAAAATTACCGTACGCG
RARâ2	GGGATTAGAATTTTTTATGCGAGTTGT	TACCCCGACGATACCCAAAC
DAPK	GGATAGTCGGATCGAGTTAACGTC	CCCTCCCAAACGCCGA
CDH1	AATTTTAGGTTAGAGGGTTATCGCGT	TCCCCAAAACGAAACTAACGAC

Genomic DNA (New England Biolabs Inc.,USA) was used as positive controls in each reaction setup. The final PCR products were resolved on an 8% non-denaturing polyacrylamide gel and visualized by silver staining.

Results

Real-time MSP

We tested promoter methylation by MSP on the seven genes: RASSF1A, CALCA, TSH-R, DAPK, TIMP3, RARâ2 and CDH1 in DNA isolated from the four thyroid cancer cell lines (NPA, FRO, ARO and WRO). Based on the results analyzed in thyroid cancer cell lines, we performed an MSP analysis of the RASSF1A, CALCA and TSH-R CpG islands in DNA isolated from leukocytes from healthy controls (n=5) and thyroid cancer patients (n=20) with different histological sub-types.

Gene methylation in thyroid cancer cell lines

All the thyroid cancer cell lines – NPA, FRO, ARO and WRO, showed methylation of the promoter CpG island by MSP for RASSF1A and CALCA. TSH-R and TIMP-3 genes were not methylated in WRO and NPA cell lines. DAPK and RARâ2 showed the lowest frequencies in methylation and were found to be methylated only in NPA and FRO respectively. Methylation was undetectable for CDH1 in all the thyroid cancer cell lines analyzed (Table 3, Fig. 5 and Fig. 6).

Gene methylation in controls and thyroid cancer patients

We performed an MSP analysis of the RASSF1A, CALCA and TSH-R CpG islands in healthy subjects and thyroid carcinoma patients. The amplification plots and dissociation curves followed by the PAGE analysis of the specific amplicons are depicted in Fig. 6. The results of the MSP for the three targets are summarized in Table 4.

The overall methylation frequency of the RASSF1A and CALCA gene was 40% (8/20) and that of TSH-R was 50% (10/20) in thyroid carcinomas. RASSF1A and CALCA methylation was detected in 40% (2/5) normal thyroid controls, 66% (6/9) FVPTC, 33% (1/3) FTC and in the only case of Hurthle cell carcinoma studied. In ATC, PTC and the poorly differentiated variants of FTC and PTC, no gene methylation was observed except that of TSH-R in ATC. The methylation frequency of TSH-R detected in controls was 60% (3/5) FTC was 33% (1/3) and 77% (7/9) in FVPTC. The only Hurthle cell carcinoma case analyzed was also found to be methylated for the TSH-R target gene.

Table 3 : Summary of the methylation analysis in cell lines

GENE	NPA	FRO	ARO	WRO
RASSF1A	+	+	+	+
CALCA	+	+	+	+
TSH-R	+	+	+	-
TIMP-3	-	+	+	+
DAPK	+	-	-	-
RARâ2	-	+	-	-
CDH1	-	-	-	-

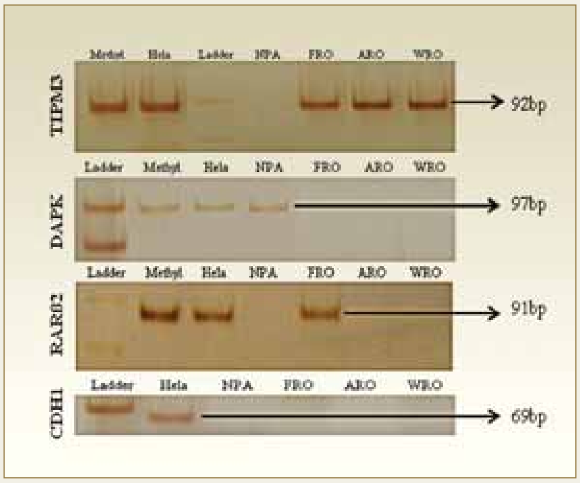

Fig. 5 : Gene methylation in Thyroid Cancer cell lines: analysis of MSP products by PAGE

The RASSF1A and CALCA MSPs generated a 74 bp and 100bp methylation-specific products with melting temperatures (T_m) of 77.5 °C and 73.7 °C respectively. The TSH-R specific primers generated a 121 bp methylation-specific product and its melting temperature was (T_m) is 77.2 °C.

Discussion

Gene methylation studies were carried out in thyroid cancer cell lines and peripheral blood samples of controls and thyroid cancer patients with different histologies.

Out of the 20 thyroid cancer patients, 8 (40%) were positive for both RASSF1A and CALCA MSP and 10 (50%) were positive for TSH-R MSP. Interestingly out of the 5 healthy controls, 2 (40%) were positive for both RASSF1A and CALCA MSP whereas 3 (60%) were positive for TSH-R MSP. Presence of methylation in healthy controls probably suggests that basal level methylation does exist in some percent of healthy controls. However, in order to have a much clear picture, it would be necessary to analyze more number of healthy controls. Further, it was seen that control samples which were methylation positive, generated a small dissociation peak and also generated very faint bands on PAGE analysis.

It was also observed that the controls and patients which harboured RASSF1A methylation were also the ones to test positive for CALCA and TSH-R methylation by MSP. If one of these genes showed methylation, then the other two genes were also methylated. This can be attributed to the fact, that methylation associated gene silencing, affects a broad spectrum of genes. Thus methylation and transcriptional silencing of one of these genes may in turn lead to silencing of the other (11).

The only undifferentiated sample type i.e. ATC analyzed was found to be methylated for TSH-R and not for RASSF1A and CALCA. ATCs are known for their poor inability to concentrate iodine. The thyroid cells get activated when TSH binds to the TSH-receptor. The reduced expression of TSH-R resulting in lower stimulation by TSH could be one of the reasons for the decreased uptake of iodine. This in turn can be attributed to the methylation and silencing of TSH-R gene.

Further, our study in thyroid cancer patients demonstrates that RASSF1A, CALCA and TSH-R methylation is more prevalent in FTC and FVPTC and not in PTC. This probably suggests that RASSF1A, CALCA and TSH-R may not be playing a significant role in carcinogenesis of PTC. However, the papillary cancer cell line - NPA demonstrated methylation for RASSF1A, CALCA and TSH-R. The stage

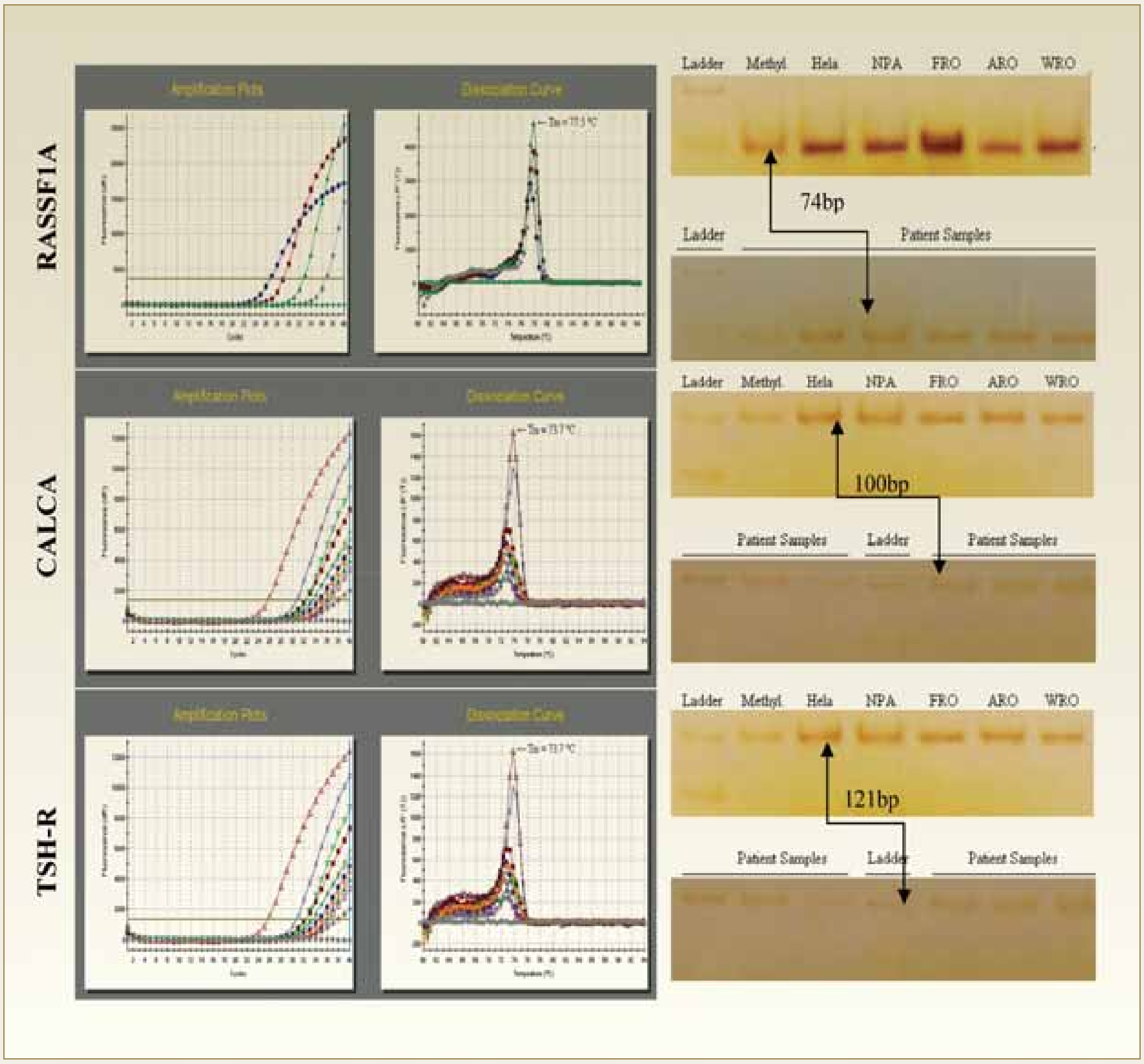

Fig. 6 : Gene methylation in Control & Thyroid Cancer patients: amplification plots, dissociation curves and PAGE analysis

of differentiation may be varied in the analyzed cell lines and the PTC patients and could be one of the reasons for such an observation.

In the present findings on the four thyroid cancer cell lines (NPA, FRO, ARO and WRO) it was demonstrated that all the four cell lines were methylated for RASSF1A and CALCA. Only WRO was not found to be methylated for TSH-R, whereas NPA was the only one not methylated for TIMP3. However, only NPA was found to harbour DAPK methylation whereas FRO was also the only one to test positive for RARâ2 methylation. Lastly, no methylation, was detected for CDH1 in the four cancer cell lines analyzed. The differential methylation patterns obtained in thyroid cancer cell lines, could be attributed to their variable histological types and the presence of different pathways responsible for thyroid cancer tumourigenesis.

Table 4 : Summary of methylation analysis in healthy controls and patient samples

CASE	RASSF1A	CALCA	TSH-R
Controls (n=5)	2/5 (40%)	2/5 (40%)	3/5 (60%)
Thyroid Cancer (TC)Patients (n=20)			
Hurtle Cell TC	1/1 (100%)	1/1 (100%)	1/1 (100%)
Anaplastic TC	0/1 (0%)	0/1 (0%)	1/1 (100%)
Papillary TC	0/4 (0%)	0/4 (0%)	0/4 (0%)
Foll.Variant of PTC	6/9 (66%)	6/9 (66%)	7/9 (77%)
FVPoorly Diff. PTC	0/1 (0%)	0/1 (0%)	0/1 (0%)
Follicular TC	1/3 (33%)	1/3 (33%)	1/3 (33%)
Poorly Diff. FTC	0/1 (0%)	0/1 (0%)	0/1 (0%)

Conclusion

Our results indicate, that abnormal promoter hypermethylation of cancer-related/tumour suppressor genes is readily detectable in the DNA, extracted from the peripheral blood of thyroid cancer patients using MSP analysis. By using the right combination of target genes, MSP may detect aberrant methylated DNA across a broad spectrum of neoplasms and may be a valuable molecular marker of thyroid carcinoma.

References

1. Kim N. and Lavertu P. Evaluation of a thyroid nodule. *Otolaryngol Clin N Am* 36: 17–33 (2003).
2. Sherman S.I. Thyroid carcinoma. *Lancet* 361: 501–511 (2003).
3. Toubert M.E. Follow-up of thyroid cancer patients with "poor prognosis." *Ann Endocrinol* (Paris) 64: 68–71 (2003)
4. Spencer C.A. Challenges of serum thyroglobulin (Tg) measurement in the presence of TG autoantibodies. *J Clin Endocrinol Metab* 89: 3702-3704 (2004).
5. Ditkoff B.A., Marvin M.R., Yemul S., Shi Y.J., Chabot J., Feind C., Lo Gerfo P.L. Detection of circulating thyroid cells in peripheral blood. *Surgery* **120**: 959–965 (1996).
6. Barzon L., Boscaro M., Pacenti M., Taccaliti A., Palu G. Evaluation of circulating Thyroid specific transcripts as markers of thyroid cancer relapse. *Int. J. Cancer* **110**: 914-20 (2004).
7. Eszlinger K., Neumann S., Otto L., Pashke R. Thyroglobulin mRNA quantification in the peripheral blood is not a reliable marker for the follow up of patients with differentiated Thyroid Carcinoma. *J. Endocrinol.* **147**: 575-582 (2002).
8. Herman J.G., Baylin S.B. Gene silencing in cancer in association with promoter hypermethylation. *New Engl J Med* **349**: 2042–2054 (2003).
9. Jones P.A. and Baylin S.B. The fundamental role of epigenetic events in cancer. *Nature Rev Genetics*. **3**: 415-428 (2002).
10. Baylin S.B., Herman J.G., Graff J.R.,Vertino P.M., issa J.P. Alterations in DNA methylation: a fundamental aspect of neoplasia. *Adv. Cancer Res.* **72**: 141-196 (1998).
11. Hoque M.O., Rosenbaum E., Westra W.H., Xing M., Ladenson P., Zeiger M.A., Sidransky D., Umbricht C.B. Quantitative assessment of promoter methylation profiles in thyroid neoplasms. *J. Cli. Endocrinol. Metab.* **90**: 4011–4018 (2005).
12. Schagdarsurengin U., Gimm O., Hoang-Vu C., Dralle H., Pfeifer G.P., Dammann R. Frequent epigenetic silencing of the CpG island promoter of RASSF1A in thyroid carcinoma. *Cancer Res.* **62**: 3698–3701 (2002).
13. de Bustros A., Nelkin B.D., Silverman A., Ehrlich G., Poiesz B., Baylin S.B. The short arm of chromosome 11 is a "hot spot" for

hypermethylation in human neoplasia. *Proc Natl Acad Sci USA,* **85**: 5693–5697 (1988).

14. Xing M., Usadel H., Cohen Y., Tokumaru Y., Guo Z., Westra W.B., Tong B.C., Talline G., Udelsman R., Califano J.A., Ladenson P.W. and Sidransky D. Methylation of the Thyroid-stimulating Hormone Receptor Gene in Epithelial Thyroid Tumours: A Marker of Malignancy and a Cause of Gene Silencing. *Cancer Res.* **63**: 2316–2321 (2003).
15. Kanai Y., Ushijima S., Hui A.M., Ochiai A., Tsuda H., Sakamoto M. and Hirohashi S. The E-cadherin gene is silenced by CpG methylation in human hepatocellular carcinomas. *Int. J. Cancer* **71**: 355–359 (1997).
16. Bachman K.E., Herman J.G., Corn P.G., Merlo A., Costello J.F., Cavenee W.K., Baylin S.B., and Graff J.R. Methylation-associated Silencing of the Tissue Inhibitor of Metalloproteinase-3 Gene Suggests a Suppressor Role in Kidney, Brain, and Other Human Cancers. *Cancer Res.* **59**: 798–802 (1999).
17. Katzenellenbogen R.A., Baylin S.B. and Herman J.G. Hypermethylation of the DAP Kinase CpG island is a common alteration in B-cell malignancies. *Blood* **93**: 4347–4353 (1999).
18. Hayashi K, Yokozaki H, Goodison S, et al. Inactivation of retinoic acid receptor beta by promoter CpG hypermethylation in gastric cancer. *Differentiation.* **68**: 13–21 (2001).
19. Xing M., Cohen Y., Mambo E., Tallini G., Udelsman R., Ladenson P.W., Sidransky D. Early occurrence of RASSF1A hypermethylation and its mutual exclusion with BRAF mutation in thyroid tumourigenesis. *Cancer Res* **64**: 1664-1668 (2004).
20. Hu S., Ewertz M., Tufano R.P., Brait M., Carvalho A.L., Liu D., Tufaro A.P., Basaria S., Cooper D.S., Sidransky D., Ladenson P.W. and Xing M. Detection of Serum Deoxyribonucleic Acid Methylation Markers: A Novel Diagnostic Tool for Thyroid Cancer. *J. of Clin. Endocrinol. & Metabolism* **91**: 98–104 (2006).

ABOUT THE AUTHORS

Dr. Archana A. Damle received her M.Sc. Degree in Microbiology from Mumbai University in 1987. She joined Radiation Medicine Centre, BARC in 1990 and subsequently received her Ph.D in Biochemistry. Her expertise includes production of monoclonal antibodies for various applications in diagnostic immunoassays. Her major area of research is Thyroid cancer with focus on immuno and molecular diagnostics for development of state-of-the-art techniques for management of patients of thyroid carcinoma.

Dr. Archana A. Narkar joined Radiation Medicine Centre, BARC in 1973. She obtained her M.Sc. and Ph.D. in Biochemistry at RMC and is the Head of Hybridoma and Thyroid Tissue Culture Programme. She was responsible for establishing the Hybridoma Lab at RMC which is actively involved in production of monoclonal antibodies for clinical applications. She is an expert on thyroid cancer and her present interest includes understanding the mechanism of thyroid tumorigenesis, the epigenetic and genetic aspects and use of various molecular targets for diagnosis and prognosis of thyroid carcinoma.

ROLE OF SPECIFIC SIGNALLING MOLECULES DURING PROLIFERATION OF CD4+ T CELLS IN RESPONSE TO DIFFERENT STIMULI

D. Sharma, S.K. Sandur, R. Checker,
R. Raghu and K.B. Sainis
Radiation Biology & Health Sciences Division
and
S. Khanam
Tata Institute of Fundamental Research, Mumbai

This paper received the Best Poster Award at the 4th DAE-BRNS Life Sciences Symposium 2008 (LSS-2008) held at BARC, Mumbai, during Dec. 22-24, 2008

ABSTRACT

CD4+ helper T cells, are known to divide in response to diverse stimuli, including mitogens and lymphopenia. Our earlier studies had shown that PI3kinase and mTOR were redundant for Homeostasis Driven Proliferation (HDP), but not for Mitogen Driven Proliferation (MDP). Experiments were carried out to study the gene expression pattern in CD4+ T cells, after Mitogen Driven Proliferation (MDP) and HDP. Spleen cells were isolated from BALB/c mice and CD4+ T cells were sorted, using antibody coated magnetic beads and were injected into syngenic lymphopenic mice. The cells were recovered from the host, after 4-19 days of injection. In another set, lymphocytes were stimulated with concanavalin A for 24 hr and CD4+ T cells were separated. These cells were used for RNA amplification and hybridization. Gene expression analysis was carried out, using Ocichip (Ocimum Biosolutions, Hyderabad). Cytokine production was studied by ELISA. Out of a total of 28,800 genes, 91 genes were found to be highly upregulated in CD4+ T cells during HDP and MDP. Eight genes were specifically highly upregulated during HDP, but not during MDP. Only one gene was upregulated during MDP and not during HDP. A total of 38 genes were suppressed (>4 fold decrease) in CD4+ T cells during HDP or MDP. These results indicated, that certain common pathways were involved in HDP and MDP of CD4+ T cells. However, a few pathways were specific to either MDP or HDP. Studies using signaling inhibitors confirmed, that NF-kappaB -dependent pathways were involved in HDP as well as MDP. However, protein kinase C, PI3Kinase, mTOR and MEK dependent pathways were specifically required, for MDP and not for HDP. Further, CD4+ T cells produced different levels of Th1, Th2 or Th17 cytokines, following MDP and HDP.

Introduction

T cells undergo Homeostasis Driven Proliferation (HDP) under lymphopenic conditions, suggesting that they can sense the 'empty lymphoid space' surrounding them, but the mechanisms that regulate this proliferation are not fully understood (Rocha et al, 1983). Interactions of T Cell Receptor (TCR) with self Major Histocompatibility Complex (MHC) are required for prolonged survival of T cells (Kirberg et al, 1997; Tanchot et al, 1997). The same ligand receptor interactions have been shown to induce HDP of T lymphocytes during lymphopenic conditions (Khaled and Durum, 2002; Moses et al, 2003). It has also been surmised, that HDP of T cells can be initiated by ow affinity self peptides, similar to those involved in positive selection of T cells in thymus (Ernst et al, 1999; Goldrath and Bevan, 1999; Surh and Sprent, 2000). Such an expansion could, in theory, promote selective proliferation of potentially self-reactive clones, leading to autoimmunity (Theofilopoulos et al, 2001).

Total body irradiation, chemotherapy or HIV infection, can lead to severe depletion of lymphocytes (lymphopenia). Little is known about the TCR signaling events, that result in proliferation during lymphopenia. Studies with lck and fyn knockout mice have suggested, that HDP of T cells may be driven by weak or partial agonist signals, that depend on lck activity (Rocha et al, 1983; Seddon et al, 2000). However, the role of NF-kB, protein kinase C (PKC), mitogen-activated kinase kinase (MAPKK or MEK) and other signaling molecules during HDP of CD4+ T cells and the differentiation of naïve CD4+ T cells into different effector populations (Th1, Th2, Th17, T follicular helper and Treg), during HDP, remain to be investigated. This knowledge will facilitate the search for modulators of signaling interactions and for prevention of autoimmune diseases following HDP (Baccala et al, 2005).

In the present study, we examined the role of NF-kB, MEK, mTOR, PI3kinase and PKC during survival and HDP of CD4+ T cells in lymphopenic mice. The cytokine profile of T cells recovered from reconstituted lymphopenic mice and their modulation by pharmacological inhibitors and plumbagin, were also investigated.

Methods

Eight to ten week-old, inbred BALB/c mice and Swiss albino mice, weighing approximately 20-25g were used. The guidelines issued by the Institutional Animal Ethics Committee of BARC, Government of India regarding the maintenance and euthanasia of small animals, were strictly followed. Animals were placed in ventilated perspex boxes and exposed to 600 cGy whole body γ-radiation in a Gamma Cell-220 Irradiator (AECL, Canada). Lymphopenia induction was confirmed, by counting the number of total splenic lymphocytes, 48-96 h after irradiation (Sharma et al, 2007 a). CD4+ T cells were sorted from spleen cells, using magnetic cell sorter and were treated with different drugs (PI3Kinase inhibitor-Ly294002, MEK/ERK inhibitor-PD98059, mTOR inhibitor-rapamycin, NFkB inhibitor-plumbagin or protein kinase C inhibitor-Go6983 or control). The lymphopenic animals were reconstituted with CFSE labeled autologous CD4+T cells and were sacrificed 4 days or 19 days after injection. Proliferation of donor cells was monitored from carboxy fluoresceindiacetate succinimidyl ester (CFSE) dye dilution, using a flow cytometer. Gene expression analysis was carried out, using RNA amplification, labeling and hybridization (Ocimum Biosolutions, Hyderabad). Protein expression was studied by western blotting. Cytokine production was monitored by ELISA (Sharma et al 2007 a and b).

Results

Gene expression pattern in CD4+ T cells during HDP and MDP

Out of a total of 28,800 genes, 91 genes were found to be highly upregulated in CD4+ T cells during HDP or MDP. These genes included those coding for mitochondrial enzymes, transcription factors, ribonucleoproteins, proteins involved in chromatin remodeling, potassium-gated channel, MAP kinases, ribosomal subunits and proteasomal components.

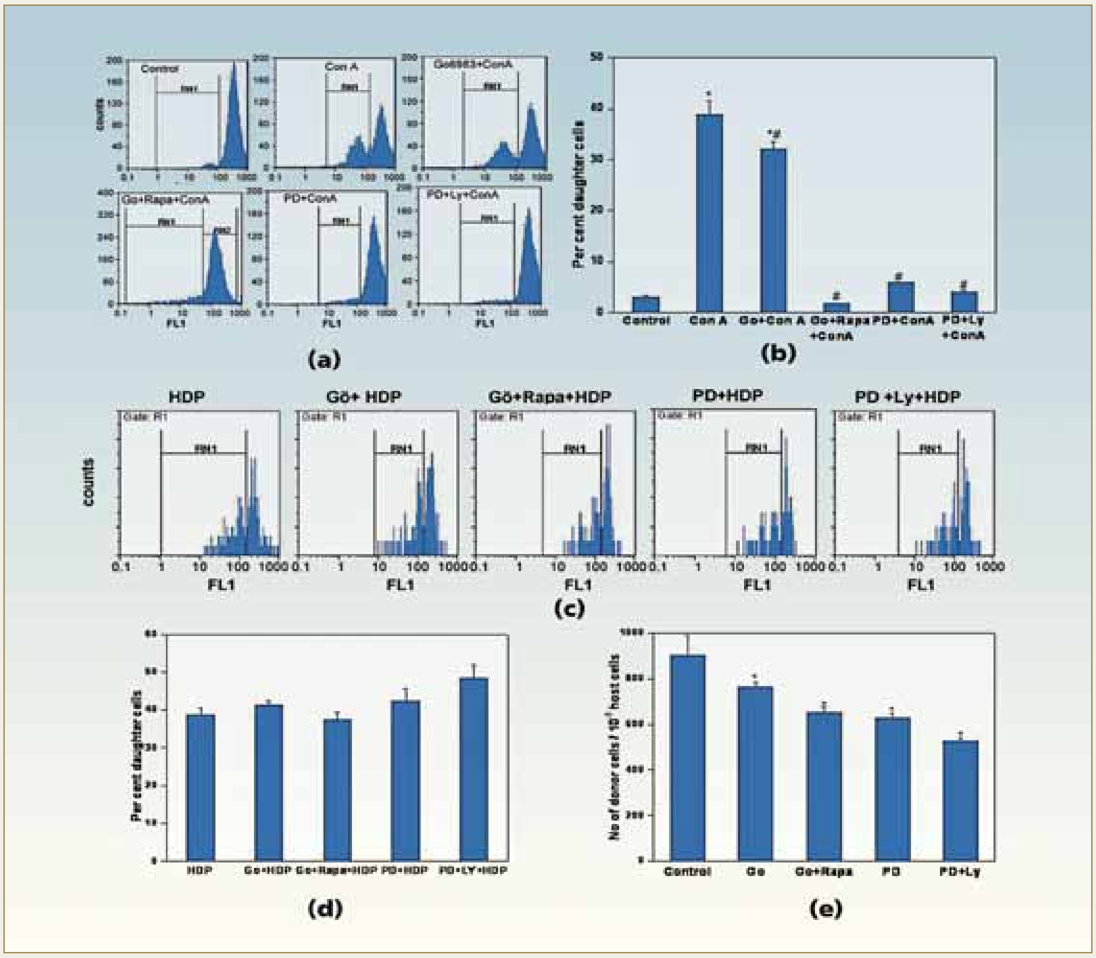

Fig. 1: Differential modulation of MDP and HDP of T cells by MEK inhibitor PD98059 or PKC inhibitor Gö6983 or their combination with rapamycin and PI3kinase inhibitor Ly294002. Splenic lymphocytes were stained with CFSE and treated with PD98059 (50μM) or Gö6983 (25 nM) or PD98059 (50μM)+ Ly294002 (20μM) or Gö6983 (25 nM) + rapamycin (10 nM) and were stimulated with con A (10μg/ml) at 37^0C in CM in a 95% air/5% CO_2 atmosphere for 72 h. In each group 20,000 cells were acquired in flowcytometer. (A) Representative flowcytometric histograms showing proliferation of T cells. (B) Purified CD4+ T cells were stained with CFSE and cultured in presence of PD98059 or Gö6983 or PD98059 + Ly294002 or Gö6983 + rapamycin overnight and 2×10^6 cells were injected i.v. into lymphopenic mice. Lymphocytes were recovered from spleen of the host mice 96 h after injection and 50,000 cells were acquired in flowcytometer. Representative flowcytometric histograms show proliferation of CFSE+ CD4+ T cells. (C) Percent daughter cells in response to con A in each treatment group. (D) The bars represent percentage of donor derived daughter cells in the spleen of lymphopenic host. (E) Frequency of donor cells in the host spleen. Data points represent mean±S.E.M. from three replicates in vitro and four mice in vivo and two such experiments were carried out. *p < 0.01 as compared to con A treated cells (MDP). *p < 0.01 as compared to untreated cells injected into lymphopenic mice.

Eight genes were highly upregulated specifically during HDP, but not during MDP. Only one gene (SMAD specific E3 ubiquitin protein ligase 1) was up-regulated only during MDP and not during HDP. A total of 38 genes were suppressed (>4 fold decrease) in CD4+ T cells, during HDP or MDP. These results indicated that certain common pathways were involved in HDP and MDP of CD4+ T cells. However, a few pathways were specific to either MDP or HDP.

Role of PI3kinase, AKT/mTOR, MAPkinase and PKC signaling pathways in MDP and HDP of T cells

Treatment of CD4+T cells with PD98059 or Gö6983 or a combination of Gö6983 + rapamycin or PD98059 + Ly294002, significantly inhibited the mitogen induced proliferation *in vitro* (Fig. 1A and B). However, the CFSE labeled donor CD4+ T cells treated with above inhibitors, showed HDP comparable to that of untreated CD4+ T cells in lymphopenic mice (Fig. 1C and D). The frequency of donor cells was significantly reduced in the mice reconstituted with CD4+ T cells treated with the inhibitors, which could be due to decrease in survival (Fig. 1E).

Modulation of cytokine production by pharmacological inhibitors

Fig. 2 shows the effects of Gö6983 or PD98059 and their combinations with Ly294002 or rapamycin on con A-induced cytokine production in lymphocytes.

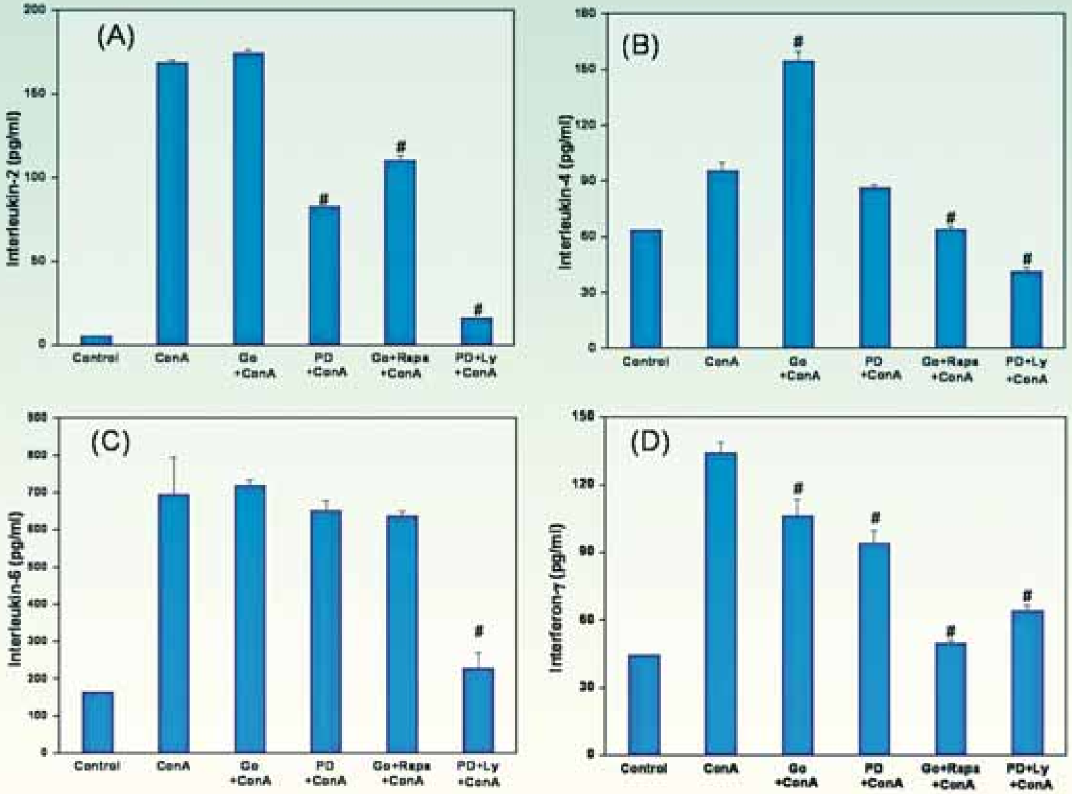

Fig. 2: Modulation of cytokine production by Gö6983, PD98059, Ly294002, rapamycin and plumbagin in con A stimulated lymphocytes: Lymphocytes from BALB/c mice were treated with Go6982 (25 nM) or PD98059 (50µM) or a combination of (Gö6983, 25nM+ Rapamycin 10 nM) or (PD98059, 50µM+ Ly294002, 20µM). Another set of lymphocytes was treated with plumbagin (5mM) in RPMI medium free from 2-mercaptoethanol and 2×10^6 cells were stimulated with con A (10µg/ml) at 37^0C in CM in a 95% air/5% CO_2 atmosphere for 24 h. Unstimulated cells were used as control. The levels of (A) IL-2, (B) IL-4, (C and E) IL-6 and (D) IFN-γ in the culture supernatant were estimated by ELISA. *p < 0.01, as compared to that in con A treated cells.

The lymphocytes treated with con A showed a significantly higher production of IL-2, IL-4, IL-6 and IFN-γ cytokines, as compared to that by unstimulated cells. Gö6983 significantly inhibited con A induced IFN-γ production, without inhibiting IL-2, IL-4 and IL-6 production (Fig. 2A–D). The combination of Gö6983 + rapamycin, significantly inhibited the production of IL-2, IL-4 and IFN-γ but not IL-6. PD98059 significantly inhibited IL-2 and IFN-γ production without inhibiting IL-4 and IL-6 production in con A stimulated lymphocytes (Fig. 2A–D). Interestingly, the cells treated with a combination of PD98059 + Ly294002 showed a significant inhibition of production of all the four cytokines (Fig. 2A–D).

Involvement of NF-kB and signaling mediators in lymphocytes during HDP

Fig. 3A shows degradation of IkB-α and activation of AKT and JNK in CD4+ T lymphocytes, isolated from lymphopenic mice 19 days after reconstitution. Actin-β levels were used as internal control. This suggested that NF-kB, AKT and JNK were activated during HDP of CD4+ T cells.

Plumbagin inhibited MDP, cytokine production and HDP of CD4+ T cells

Fig. 3B shows the effect of plumbagin treatment (5mM, 4 h *in vitro*) on HDP of CD4+ T cells, in autologous lymphopenic hosts. The histograms and dot-plots show donor derived CFSE+ CD4+ T cells in the host spleen, 96 h after reconstitution (Fig. 3B). The frequency of plumbagin treated donor CD4+ T cells was 94% lower, as compared to that of untreated CD4+ T cells injected into the lymphopenic mice (Fig. 3C). Thus plumbagin-treated cells failed to survive or divide under lymphopenic conditions. Similarly, plumbagin completely inhibited mitogen-induced proliferation (Fig.3D) and cytokine production in T cells (Fig.3E) *in vitro*.

Discussion

Many common insults to the immune system may result in transient lymphopenia in vertebrate organisms, and are typically followed by uneventful immune reconstitution. However, in some clinical settings, the drive to re-establish the T cell population size, may compromise the diversity of the T Cell Receptor (TCR) repertoire and allow emergence of autoreactive clones, which in turn may lead to immunodeficiency and autoimmunity respectively (La Gruta et al, 2000; Theofilopoulos et al, 2001; Marleau and Sarvetnick, 2005). Thus, understanding the mechanisms that regulate T cell proliferation under lymphopenic conditions, has important clinical applications.

In the present study, MDP was compared with HDP of purified CD4+ T cells in irradiated lymphopenic mice. A majority of the genes upregulated during MDP as well as HDP of CD4+ T cells, were involved in cellular metabolism, nucleotide synthesis, respiration, DNA replication, cell cycle and survival. Interestingly, E3ubiquitin ligase, which has been shown to be responsible for anergy induction in T cells (Mueller, 2004) was upregulated only during MDP and not during HDP of CD4+ T cells. The lower levels of E3Ubiquitin ligase would compromise peripheral self tolerance, in a lymphopenic environment. Thus, lymphopenic environment may allow proliferation of self reactive clones without induction of anergy.

The present study confirmed that a broad spectrum PKC inhibitor, Gö6983, partially but significantly blocked the MDP of activated T cells *in vitro* (Hermann-Kleiter et al, 2006). Treatment of CD4+ T cells with Gö6983 or MEK inhibitor PD98059 or a combination of Gö6983 plus rapamycin or PD98059 plus Ly294002 did not affect their HDP. The decreased frequency of inhibitor(s)-treated donor cells, in the spleen of reconstituted lymphopenic mice, indicated a possible role for PKC and MEK in survival of CD4+ T cells in lymphopenic mice (Fig. 1A-D) (Kirberg et al, 1997;

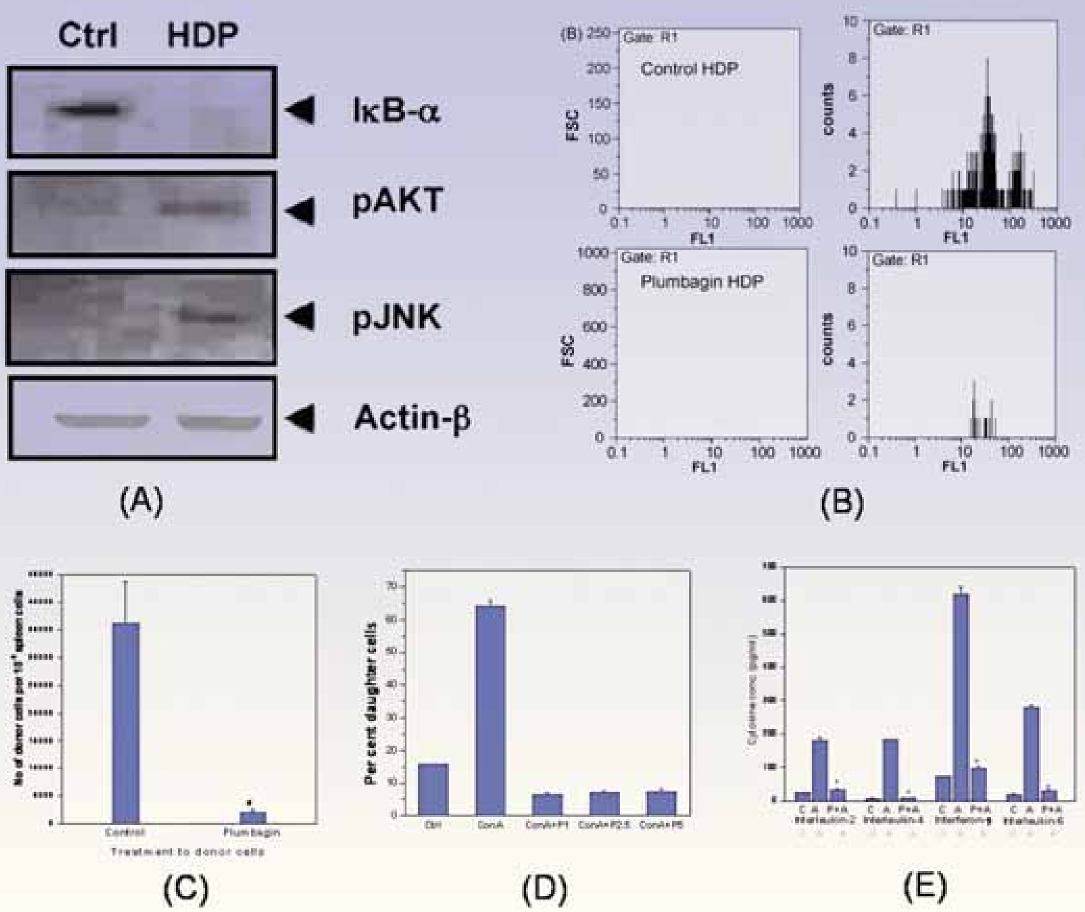

Fig. 3: Activation of NF-kB during HDP of CD4+ T cells and modulation by plumbagin (A) Purified CD4+ T cells were injected i.v. into lymphopenic mice and were recovered from host spleen 4 days after injection. CD4+ T cells were magnetically sorted and used for analysis of IkB-α, phospho AKT, phospho JNK and actin-β using western blotting. (B) Purified CD4+ T cells were stained with CFSE and cultured in presence of plumbagin (5µM) for 4 h and 2×10^6 cells were injected i.v. into lymphopenic mice. Lymphocytes were recovered from spleen of the host mice 96 h after injection and 50,000 cells were acquired in flowcytometer. Representative flowcytometric histograms and dot plots show proliferation of CFSE+ CD4+ T cells. (C) The bars represent frequency of donor cells in the host spleen. Data points represent mean±S.E.M. from three replicates in vitro and four mice in vivo and two such experiments were carried out. $*p < 0.01$, as compared to that in untreated cells injected into lymphopenic mice. (D) CFSE labeled lymphocytes were treated with plumbagin (1 to 5mM, 4 h) and stimulated with con A (10µg/ml) at 37 °C in complete medium for 72 h. Each bar represents percentage of daughter cells in each treatment group. $*p<0.01$, as compared to vehicle treated cells and $*p<0.01$, as compared to con A stimulated cells. (E) Effect of plumbagin on con A induced cytokine production in vitro. Lymphocytes were pre-treated with plumbagin (5mM) for 4 h before stimulation with con A (10 ìg/ml) for 24 h at 37 °C in complete medium. The concentration of cytokines in the supernatant was estimated using ELISA. Each bar represents concentration of cytokines (IL-2, IL-4, IL-6 and IFN-γ). Data points represent mean±S.E.M. from three replicates and three such independent experiments were carried out. $*p<0.01$, as compared to vehicle treated cells and $\#p<0.01$, as compared to con A stimulated cells.

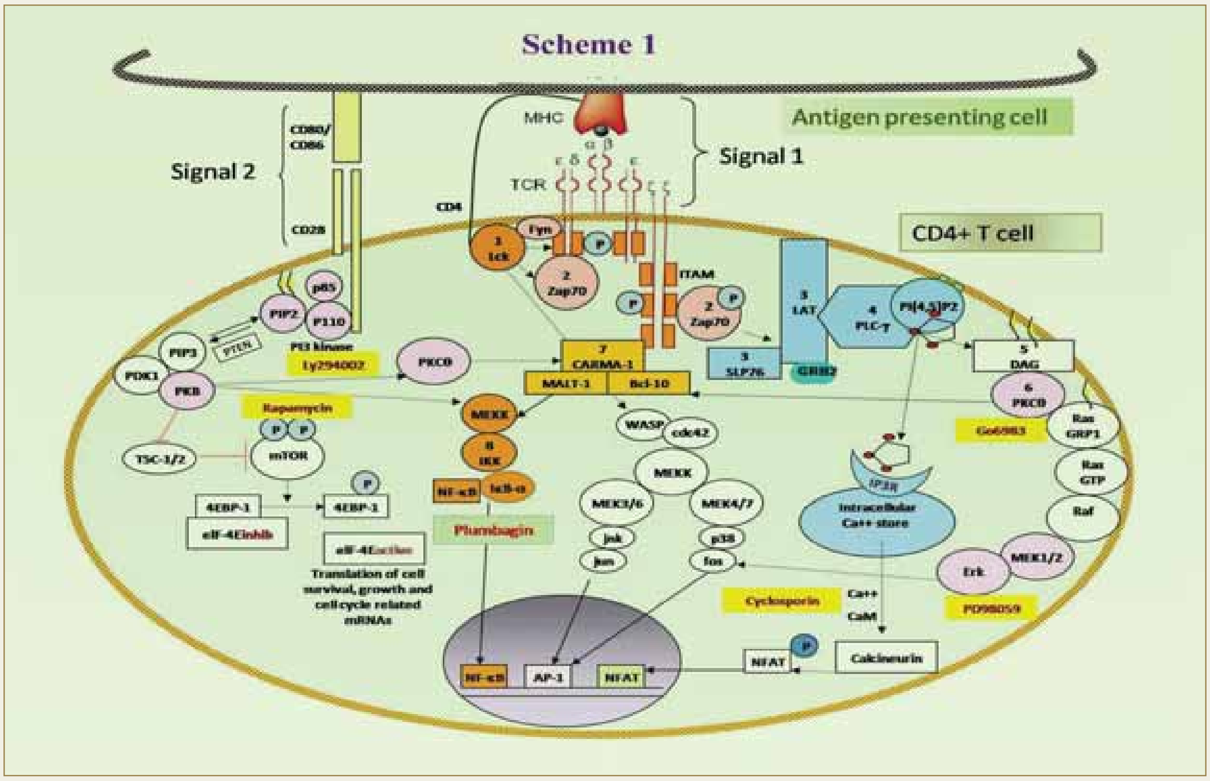

Scheme 1

Pages et al, 1999). Interestingly, the protein kinases AKT and JNK as well as proinflammatory transcription factor NF-kB were activated in CD4+ T cells isolated from reconstituted lymphopenic mice (Fig. 3A). These proteins have also been shown to be activated, during MDP of T cells (Baier et al, 1993; Agrawal et al, 2006). An essential role of NF-kB for survival and HDP of CD4+ T cells was confirmed by the results, showing severely impeded frequency of plumbagin treated CFSE labeled CD4+ donor T cells in the spleen of reconstituted lymphopenic mice (Fig. 3C). Plumbagin has been shown to inhibit NF-kB activation, by prevention of IkB-α degradation as well as by suppression of direct DNA binding ability of NF-kB (Sandur et al, 2006).We had shown that plumbagin blocks LPS induced B cell proliferation by inhibition of NF-kB activation (Rashmi et al, 2009).

We recently showed that mitogen induced cytokine production in T cells, recovered from reconstituted lymphopenic mice, involved an increase in production of pro-inflammatory cytokines, as compared to that in cells from normal mice. Hence, different pharmacological inhibitors were assessed for their ability to block IL-6 production in T cells. Gö6983 or PD98059 or Gö6983 plus rapamycin failed to inhibit IL-6 production, but affected IL-2, IL-4 and IFN-γ production to different extents (Fig. 2). Interestingly, plumbagin alone completely inhibited IL-6 production (Fig. 3E).

In summary, the present report describes the gene expression and signaling requirements for HDP of CD4+ T cells in lymphopenic environment. The pathways shown in Scheme 1 are involved and required during MDP of T cells. Of these pathways, only those shown in red colour were found to be required for HDP of CD4+ T cells *in vivo.* The inhibitors highlighted with yellow color inhibited MDP of T cells. Interestingly, plumbagin (highlighted in green) inhibited both MDP as well as HDP of CD4+ T cells. For the first time, a role for NF-kB during survival and HDP of CD4+ T cells was highlighted. The mechanistic basis for a possible use of plumbagin, in inhibiting onset and progression of autoimmunity, was also indicated.

Acknowledgements

Authors would like to acknowledge Prof. Shobhona Sharma and Dr. Sulabha Pathak, TIFR Mumbai for their help in flowcytometry. We thank Prof. Vidita Vaidya and Dr. Shankar Jha, TIFR, Mumbai for facilitating immunofluorescence experiments. We also thank Mr. Narendra Sidnalkar, Mr. Kashinath Munankar and Mr. Deepak Kathole for their technical assistance.

References

1. B. Rocha, A. A. Freitas, A. A. Coutinho, *J Immunol* 131, 2158 (1983).
2. J. Kirberg, A. Berns, H. von Boehmer, *J Exp Med* 186, 1269 (1997).
3. C. Tanchot, F. A. Lemonnier, B. Perarnau, A. A. Freitas, B. Rocha, *Science* 276, 2057 (1997).
4. A. R. Khaled, S. K. Durum, *Biotechniques* Suppl, 40 (2002).
5. C. T. Moses, K. M. Thorstenson, S. C. Jameson, A. Khoruts, *Proc Natl Acad Sci U S A* 100, 1185 (2003).
6. B. Ernst, D. S. Lee, J. M. Chang, J. Sprent, C. D. Surh, *Immunity* 11, 173 (1999).
7. A. W. Goldrath, M. J. Bevan, *Immunity* 11, 183 (1999).
8. C. D. Surh, J. Sprent, *J Exp Med* 192, F9 (2000).
9. A. N. Theofilopoulos, W. Dummer, D. H. Kono, *J Clin Invest* 108, 335 (2001).
10. B. Seddon, G. Legname, P. Tomlinson, R. Zamoyska, *Science* 290, 127 (2000).
11. R. Baccala, R. Gonzalez-Quintial, W. Dummer, A. N. Theofilopoulos, *Springer Semin Immunopathol* 27, 75 (2005).
12. D. Sharma, S. S. Kumar, R. Raghu, S. Khanam, K. B. Sainis, *Mol Immunol* 44, 2831 (2007).
13. D. Sharma, S. S. Kumar, K. B. Sainis, *Mol Immunol* 44, 347 (2007).
14. N. L. La Gruta, I. R. Driel, P. A. Gleeson, *Eur J Immunol* 30, 3380 (2000).
15. A. M. Marleau, N. Sarvetnick, *J Leukoc Biol* 78, 575 (2005).
16. D. Mueller, *Nat Immunol* 5, 883 (2004).
17. N. Hermann-Kleiter *et al.*, *Blood* 107, 4841 (2006).
18. G. Pages *et al.*, *Science* 286, 1374 (1999).
19. G. Baier *et al.*, *J Biol Chem* 268, 4997 (1993).
20. A. Agrawal, S. Dillon, T. L. Denning, B. Pulendran, *J Immunol* 176, 5788 (2006).
21. S. K. Sandur, H. Ichikawa, G. Sethi, K. S. Ahn, B. B. Aggarwal, *J Biol Chem* 281, 17023 (2006).
22. R. Rashmi, D. Sharma, R. Ramakrishnan, S. Khanam, GJ Chintalwar, KB Sainis, *Immunol Lett.* 123, 60 (2009).

ABOUT THE AUTHORS

Dr. Deepak Sharma, joined BARC after securing First rank from the 44th batch of BARC Training School. He received the Homi Bhabha Award and medal in 2001. He is presently working in the Radiation Biology & Health Sciences Division of BARC. He has demonstrated the signaling requirements for mitogen-driven proliferation vis-à-vis homeostasis driven proliferation of CD4+T cells. He also showed the redundant role of PI3kinase, mTOR and PKCq during homeostatic proliferation, but an essential role of NF-kB and AKT. Further Dr. Sharma showed that chlorophyllin, a water-soluble analog of green plant pigment chlorophyll inhibited homeostatsis driven proliferation of CD4+T cells. He was recently awarded PhD in Applied Biology by the University of Mumbai. His research interests include radioprotection and immunomodulation by phytochemicals.

ABOUT THE AUTHORS

Dr. Santosh Kumar Sandur, joined BARC after graduating from the 38th batch of BARC Training School. He is presently working in the Radiation Biology & Health Sciences Division of BARC. He was conferred the DAE Young Scientist Award for the year 2007, for his outstanding contributions related to radioprotective actions of antioxidants of natural origin and their antitumour activities. He demonstrated the efficacy of chlorophyllin (CHL) in ameliorating radiation-induced alterations in cell-free and cellular systems *in vitro* as well as *in vivo*. In addition administration of CHL to animals augmented both innate as well as adaptive immune responses and prevented programmed cell death in lymphocytes by upregulation of antiapoptotic genes *bcl-2* and *bcl-*$_{XL}$. He has shown the novel mechanism of antitumour and anti-inflammatory effects of curcuminoids.

Mr. Rahul Checker joined the Radiation Biology & Health Sciences Division of BARC, after securing First rank in Bioscience discipline from the 49th batch of BARC Training School. He received Homi Bhabha Award and medal in 2006. He is working on immunomodulatory activities of phytochemicals. He demonstrated the immunosuppressive effect of a plant derived naphthoquinone, plumbagin, *in vitro* and *in vivo*. He elucidated that plumbagin mediated immunosuppression was through inhibition of prosurvival transcription factor NF-kB in activated T cells. Further *in vivo* efficacy of plumbagin was shown in mouse model of graft-versus-host disease.

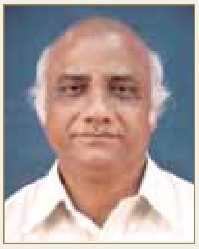

Dr. K. B. Sainis, Director, Bio-Medical Group, BARC, joined BARC after securing first rank from the 15th batch of BARC Training School (Biology-Radiobiology). He is the recipient of the Homi Bhabha Award, INSA Young Scientist Award, Shanti Swarup Bhatnagar Award and INS Senior Scientist Award. He is a PhD guide in Applied Biology (University of Mumbai) and Life Sciences (Homi Bhabha National Institute). He has about 80 publications in international and national journals to his credit. His research interests include biological effects of low-dose radiation, immunomodulation by plant derived natural products, tumour immunology and radiation biology. He oversees the research and development programmes of six divisions of Bio-Medical Group and delivery of health care to more than 80,000 beneficiaries of CHSS. He represents India at the United Nations Scientific Committee on Effects of Atomic Radiation (UNSCEAR). He is also a member of the Standing Advisory Group on Nuclear Apllications (SAGNA), IAEA and Shanti Swarup Bhatnagar Award selection committee.

SHELF STABLE INTERMEDIATE MOISTURE PINEAPPLE (ANANAS COMOSUS) SLICES USING HURDLE TECHNOLOGY

S. Saxena, B. B. Mishra, R. Chander and A. Sharma
Food Technology Division

This paper was conferred the Best Poster Award at the 19th Indian Convention of Food Scientists and Technologists on Health Foods (ICFOST- 2007) held at IIT, Kharagpur, during Dec. 31, 2007 - Jan. 2, 2008 - 09

ABSTRACT

A process has been developed to prepare shelf stable Ready-To-Eat (RTE) intermediate moisture pineapple (*Ananas comosus*) slices, using hurdle technology. The combination of hurdles including osmotic dehydration, infrared drying and gamma radiation dose of 1 kGy, successfully reduced the microbial load to below detectable limit. The shelf life of the intermediate moisture pineapple slices was found to be 40 days at ambient temperature (26 ± 2 °C). The untreated control samples spoiled within 6 days. The RTE intermediate moisture pineapple slices were found to have good texture, colour and sensory acceptability, during this 40 days storage.

Keywords: Pineapple; Hurdle technology; Osmotic dehydration; Infrared drying; Gamma radiation

Introduction

Pineapple (*Ananas comosus*) is one of the most popular tropical fruits. The fruit is known for its nutritive and health promoting properties. It is commonly used as table fruit or in desserts. The shelf life of ripe pineapple is short and limited to 4-6 days (Hajare *et al*, 2006). Fresh pineapple contains thick, thorny inedible peel and a large crown, which consumes storage space and also results in higher transportation costs (Fernandes et al, 2006). Therefore, value addition by processing to a RTE product, is an attractive alternative. Pineapple slices dipped in sugar syrup and canned are normally used around the world (Mortan, 1987). The canned pineapple is shelf stable but it is not liked by some consumers, due to its high level of sweetness.

The shelf life of peeled, sliced and polyethylene packed pineapple sold in market is 4-6 days, when stored at room temperature, whereas, pineapple slices when kept at 8-10 °C, do not stay more than 8-10 days. Therefore, many alternate approaches were followed for pineapple preservation. The blanching treatment for microbial reduction and browning inhibition, affects freshness and taste. Cut pineapple undergoes enzymatic browning which can be inhibited by dipping in potassium metabisulfite solution (Adams & Moss, 2000). In osmotic dehydration, water is partially removed from the product by dipping in hypertonic sugar syrup (Pokharkar et al, 1997; Corzo & Gomes, 2004).The dipping in sugar solution reduces water activity (a_w) to about 0.9 which is not enough for preventing bacterial, yeast and mold growth, these being involved in spoilage. Infrared drying offers a number of advantages including drying uniformity, reduced drying time, energy efficiency and high quality finished products (Afzal & Abe, 1998; Zhu et al, 2002). Due to limitations of individual preservation methods, a combination of these hurdles was used for maximizing pineapple shelf life. The intermediate moisture pineapple products are becoming popular, because these are shelf stable, retain nutritional value, are convenient to use and incur less transportation and storage costs (Leistner, 1992; Thakur & Singh, 1995). Radiation processing, a cold process, is being used as a preservation method for food commodities and is increasingly attaining new applications (Urbain, 1986; Diehl, 1990). This is one of the very effective alternatives for ensuring microbial quality and safety of minimally processed fruits and vegetables and is also recommended for processed pineapple (Shashidhar et al, 2007).

The objective of the present study was to prepare shelf-stable, ready-to-eat and safe intermediate moisture pineapple slices, using a combination of different hurdles.

Materials and Methods

Chemicals

Luria-Bertani agar (LBA), potato dextrose agar (PDA), Baird-Parker agar (BPA), violet red bile agar (VRBA), and egg-yolk tellurite emulsion were purchased from Himedia Laboratories, India. High density polyethylene packages (HDPE) of film thickness, 500 gauge and sucrose were obtained from a local market. Potassium metabisulfite and sodium chloride (NaCl) were purchased from S. D. Fine-Chem. Ltd., India.

Gamma radiation treatment

Gamma radiation treatment was carried out in a cobalt-60 Gamma Chamber-5000 (GC-5000, BRIT; dose rate 7.65 kGy/h) at Food Technology Division, BARC. The packed samples were treated at different doses of gamma radiation (250 Gy, 500 Gy and 1 kGy) at ambient temperature. Non-irradiated samples were used as control. After radiation treatment, the samples were stored at ambient temperature (26 ± 2°C) and relative humidity (56 ± 3 % RH). The radiation dosimetry was carried out by placing Fricke dosimeters.

Pineapple processing

Pineapples (six) procured from a local market were cleaned with water, crowns removed and peeled manually. The fruits were then transversely cut into 8 slices, each approximately of 1 cm thickness. The slices were dipped in potassium metabisulfite solution (0.25%) for 2 h, followed by immersion in sugar (sucrose) solution (70%, 16 h). The slices were taken out of the sugar solution, drained on a two layered muslin cloth and dried in infrared (IR) dryer (Sakav, Shirsat Electronics, Mumbai) at 80 °C/1 h to bring the a_w to 0.82. The slices were then packed in high density polyethylene bags, sealed, radiation-treated and stored at ambient temperature (26 ± 2 °C). Such processed pineapple slices named in this paper as Intermediate Moisture (IM) pineapple slices were periodically examined and subjected to the following analyses, up to a period of 40 days of storage.

Microbiological analysis

Total Bacterial Count (TBC) and Yeast and Mold Count (YMC) were determined as described by ICMSF (2002). Individual pineapple slices (25g) were aseptically homogenized for 2 min in stomacher bags with 75 ml sterile saline water solution (0.85% NaCl) using Stomacher Blender (Stomacher Lab Blender, model 400, Seward, U.K.). Serial dilutions were made in sterile saline and spread plated in duplicate. Media employed were plate count agar, potato dextrose agar for determination of TBC and YMC, respectively. The microbial analyses of pineapple slices were undertaken periodically during storage.

Water activity (a_w) measurement

A small piece of pineapple slice weighing approximately 2 g was used, for determination of water activity using a water activity meter (AqualabCX2T, Decagon Devices, USA). The measurement was taken with samples drawn from four slices and the average value was expressed as water activity of the product.

Moisture content

To determine the moisture content, weighed pineapple slices were kept in a hot air oven (Metlab Scientific Instruments, India) at 100^0C, till the weight remained constant. The percentage decrease in weight was expressed as moisture content (AOAC, 1995). The measurement was replicated with the samples drawn from four different slices and the average was taken as moisture content of the product.

Colour measurement

Colour of the central region of pineapple samples was measured by reflectance measurement, using a Minolta CM-3600D Spectrophotometer (Konica Minolta Sensing, Inc., Osaka, Japan). The reflectance of whole visible spectrum (360 to 780 nm) was recorded at wave length intervals of 10 nm. D_{65} lamp was used as reference light source and the detector was fixed at an angle of 10^o with respect to the light source (Hajare et al 2006). The colour parameters L^* (Lightness), a^* (Redness), b^* (Yellowness) were analyzed with using JAYPAK 4808 software (Quality Control System, Version1.2).

Texture analysis

Texture was analyzed using a Texture Analyser (TA.HD plus, Stable MicroSystems, Godalming, Surrey, UK) with a P/2N needle probe. The probe speed and penetration depth were 0.5 mm/s and 5 mm, respectively. The hold time was 0.01 s and the trigger force was set at 10 g force. The probe travel distance was optimized for 5 mm. Texture was expressed in the unit of gram resistance force (g) measuring resistance offered by the sample to the penetrating needle probe (Hajare, Saroj, Dhokane, Shashidhar & Bandekar, 2007). The instrument was calibrated before each use. In sliced pineapple, tissue firmness varies from centre to periphery and hence, texture was measured at various points starting from the central pith region to the peripheral region of the edible portion.

Sensory evaluation

A preliminary sensory testing was performed by an experienced panel familiar with pineapple fruit characteristics. This panel comprised of 15-20 researchers from different sections of Food Technology Division, BARC. This testing was done in a Taste Panel Laboratory in individually partitioned compartments, under a controlled-environment (Meilgaard, Civille & Carr, 1999). Sensory analysis was carried out on radiation- treated and non-treated processed samples along storage. Panelists were previously briefed and trained to distinguish different pineapple samples and score their respective quality attributes including appearance, colour, texture, odour, taste and overall acceptability. A 7-point hedonic scale (1-very poor, 2-poor, 3-fair, 4-satisfactory, 5-good, 6-very good, and 7-excellent) was used, for grading the samples during evaluation.

Statistical analysis

All the above detailed experiments were repeated in three different batches. In each batch, 3-4 replicates were taken for every tested parameter. The data obtained was expressed in terms of Mean and Standard Deviations (SD). The mean values were compared using one-way ANOVA (ANalysis Of VAriance) test for significance of their difference ($P < 0.05$). The data was analyzed using the Origin 6.1 software version v6.1052 (B232) (OriginLab Corp., Northhampton, Mass., USA).

Results and Discussion

Effect of pineapple processing

The potassium metabisulfite dip, minimized pineapple slices browning which was visible. Browning occurs in cut pineapple due to polyphenol oxidase (PPO) action. This enzyme is located in plastids and cytoplasm inside the cell and phenolic substrates are located in vacuole. Due to cutting, the subcellular compartmentation in pineapple slice is lost. The enzyme and substrate come in contact with each other and in the presence of oxygen, the reaction results in the formation of quinones, which auto polymerize to form brown melanin-like pigments (Vamos-Vigyazo,1981). Potassium metabisulfite water solution releases SO_2 which inactivates the PPO enzyme (Madero & Finne, 1982). The osmotic dehydration alone reduced a_w of pineapple slices from 0.97 to 0.9. The a_w below 0.82 was achieved only after infrared drying.

The a_w and moisture content of the IM pineapple slices were about 0.82 and 37%, respectively and the change was found to be insignificant ($P < 0.05$) during 40 days of storage. The HDPE packaging retained the product moisture content. Polyethylene is known to have good moisture barrier properties (Basantia, Arora, Seth & Singh, 2000). It has been observed that the thickness of the pineapple slices is crucial for uniform drying by infrared. The slices with thickness greater than 1 cm showed uneven drying and took longer time to dry to the desired level. In such slices, a_w could not be maintained below 0.82 during storage, due to improper drying.

Microbiological analysis

The mean values of total bacterial count and yeast and mold count in fresh pineapple slices, were found to be in the range of 10^2 to 10^3 cfu/g. There was an increase in TBC, YMC of freshly cut pineapple slices after 6 days at ambient storage temperature. The difference in microbial load between potassium metabisulfite dipped and freshly cut slices on day 1 of storage was found to be insignificant ($P < 0.05$), whereas, osmotic dehydration was found to decrease the bacterial load. Moreover, the increase in bacterial load and YMC of osmotically dehydrated slices during 6 days of storage was insignificant ($P < 0.05$). The combination of osmotic dehydration with infrared drying, decreased TBC and YMC which remained constant up to 6 days of storage (Table 1). Most bacteria fail to grow at a_w of less than 0.82 (Ledward, 1981). Intermediate moisture products in which a_w is reduced to inhibit microbial growth, can be stored for extended periods under ambient conditions (Ledward, 1981). However, reduction of a_w alone could not bring counts below the detection limit and so, mold growth was observed in samples during storage

Table 1: Microbiological analysis of pineapple slices during storage at ambient temperature (26 ± 2°C)[a].

Treatment	Total Bacterial Count		Yeast and Mold Count	
	Day 1	Day 6	Day 1	Day 6
Freshly cut	3.0^{b}	5.5^{c}	2.7^{b}	5.6^{c}
Potassium metabisulfite dip	2.9^{b}	6.2^{c}	3^{b}	6.1^{c}
Osmotic dehydration	2.1^{d}	2.4^{d}	2.2^{d}	2.4^{d}
Osmotic dehydration and infrared drying	2.0^{e}	2.1^{e}	2.0^{e}	2.2^{e}
Potassium metabisulfite dip, osmotic dehydration, and infrared drying	2.0^{e}	2.1^{e}	2.0^{e}	2.1^{e}

[a] *The data was expressed as logarithm of colony forming unit (cfu/g) and represents the mean of at least 12 slices per treatment. The mean values with different superscript (b, c, d, e) are significantly different ($P < 0.05$) as analyzed by one way ANalysis Of VAriance (ANOVA)*

Table 2: Microbiological analysis of radiation-treated intermediate moisture pineapple slices during storage at ambient temperature (26 ± 2^0C)[a].

Radiation dose (Gy)	Total Bacterial Count			Yeast and Mold Count		
	Day1	Day20	Day40	Day 1	Day 20	Day 40
0	2.0	2.1	-	2.0	2.1	-
250	1.8	1.9	-	1.3	1.4	-
500	1.3	1.3	1.3	1.6	1.5	1.3
1000	*	*	*	*	*	*

Symbol (*) denotes non detectable microbial load and symbol (-) denotes visible mold growth. [a] The data was expressed as logarithm of colony forming unit (cfu/g) and represents the mean of at least 12 slices per treatment.

(Table 2). Molds can grow even at a low a_w of 0.6 (Jay, 1991). When radiation treatment was included among the employed hurdle technologies, counts fell below the detection limits (less than 20 cfu/g). Ionizing radiation can penetrate to inactivate microorganisms that may have gained entry in the tissue (Thakur & Singh,1995). A combination of gamma irradiation at 1 kGy, potassium metabisulfite treatment, osmotic dehydration and infrared drying was found to be effective, in eliminating microbial load below the detection limit (less than 20 cfu/g) up to 40 days at ambient temperature storage (Table 2).

Colour analysis

Pineapple browning is associated with decrease in L* (Lightness), b* (Yellowness) and increase in a* (Redness) value. The potassium metabisulfite treatment maintains colour as it inhibits browning, but storage for five days deteriorated the colour of the slices with significant ($P < 0.05$) decrease in L* and b* values. In osmotically dehydrated and infrared dried samples without potassium metabisulfite dip, the L* value decreased and a* value increased after 5 days of storage along with minor changes in b* value, which indicated intense browning. Thus potassium metabisulfite dip is unavoidable for browning control. The combination of potassium metabisulfite dip, osmotic dehydration and infrared drying caused initial changes in L*, a*, b* values as compared to those of freshly cut pineapple, but they stabilized during subsequent storage (Table 3). There was a minor decrease in L*and b* values and a minor increase in a* value, which were insignificant ($p< 0.05$), at the end of storage time in every sample (data not shown).

Texture analysis

Pineapple slices texture decreased in every sample during storage, many times significantly. The cutting process resulted in tissue disruption and membrane breakdown leading to the release of hydrolytic enzymes. Enzymatic degradation of cellulose, hemicellulose and pectin led to texture losses during storage (Myung 2006). This effect, being pronounced in freshly cut samples in the present study, was not reduced by the potassium metabisulfite dip or its combination with osmotic dehydration. Similar effects of such pre-treatments have also been reported by Karim et al (2008) for air dehydrated pineapple slices. Infrared drying was found to restore texture which remained stable up to 6 days of storage (Table 4). Drying by infrared radiation has also been reported earlier, to stabilize the texture of sugar-infused IM blueberries during storage (Shi et al, 2008). This texture retention could be due to sugar infusion into the intercellular spaces (Stojanovic & Silva, 2006). The combination of potassium metabisulfite dip, osmotic dehydration and infrared drying treatments, were fairly successful in maintaining texture values up to 6 days of storage.

The change in texture due to radiation treatment was found to be insignificant ($P < 0.05$) till 40 days of storage (data not shown). As earlier reported, a radiation dose of 2 kGy did not affect the texture of minimally processed pineapple slices when stored at 10^0C for 12 days (Hajare et al 2006). López-Malo and Palou (2008) also reported the insignificant effect of combined preservation methods such as blanching and osmotic dehydration, on texture of pineapple slices.

Table 3: Colour analysis of pineapple slices during storage at ambient temperature (26 ± 2 °C)^{a}.

Treatment	Colour during storage					
	L* (Lightness)		a* (Redness)		b* (Yellowness)	
	Day 1 ^{b}	Day 5 ^{b}	Day 1	Day 5	Day 1 ^{b}	Day 5 ^{b}
Freshly cut	70 ± 2	58 ± 3	1.0^{c} ± 0.4	4.7^{c} ±0.7	31 ± 8	23 ± 2
Potassium metabisulfitedip	72 ± 2	59 ± 3	1.1 ± 0.3	1.4 ± 0.2	30 ± 6	19 ± 2
Potassium metabisulfite dip and osmotic dehydration	72 ± 2	64 ± 2	1.1^{c} ± 0.4	2.4^{c} ± 1.0	30 ± 1	25 ± 3
Osmotic dehydration and infrared drying	70 ± 2	54 ± 5	2.8^{c} ± 0.6	9.8^{c} ± 2.2	37 ± 2	27 ± 4
Potassium metabisulfite dip, osmotic dehydration, and infrared drying	74 ± 3	68 ± 1	3.7 ± 1.2	4.6 ± 1.6	38 ± 4	34 ± 4

[a] The data represents mean ± SD of at least 9 slices per treatment. The corresponding mean values for day 1 and day 5 across columns superscripted as b are significantly different ($P < 0.05$). The mean a values for day 1 and day 5 along the rows are significantly different ($P < 0.05$) as analyzed by one way ANalysis Of VAriance (ANOVA).*

Sensory evaluation

Panelists gave overall scores ranging between 4 (satisfactory) and 5 (good) for the IM pineapple slices, with no statistical significant differences due to storage days or radiation doses. The scores for colour were better than texture, aroma, taste and overall acceptability. For many of these parameters a minor, though not significant, decrease in average scores was observed during storage (Table 5). These findings are in agreement with those of Hajare et al (2006), who also reported no significant effect of 2 kGy radiation dose, on sensory parameters of minimally processed pineapple slices, when stored at 10 ^{0}C for 12 days.

Table 4: Texture analysis of pineapple slices during storage at ambient temperature (26 ± 2 °C)$^{a\,d}$.

Treatment	Day 1	Day 6
Freshly cut	185^{b} ± 26	111^{b} ± 30
Potassium metabisulfite dip	175^{b} ± 22	113^{b} ± 34
Potassium metabisulfite dip and osmotic dehydration	125^{b} ± 17	106^{b} ± 17
Osmotic dehydration and infrared drying	138 ± 23	137 ± 26
Potassium metabisulfite dip, osmotic dehydration, and infrared drying	125 ± 36	113 ± 37

[a] The data represents mean ± SD of measurements of at least 12 slices.

[b] The corresponding mean values for day 1 and day 6 across columns in each zone are significantly different ($P < 0.05$) as analyzed by one way ANalysis Of VAariance (ANOVA).

[d] The texture was expressed in the unit of gram resistance force (g) measuring resistance offered by the sample to the penetrating needle probe.

Conclusion

The combination of hurdles including potassium metabisulfite dip, osmotic dehydration, infrared drying, HDPE packaging and a radiation dose of 1 kGy was found to be effective in extending the shelf life of pineapple slices up to 40 days under ambient storage temperature, whereas the control non-treated slices spoiled within 6 days. The potassium metabisulfite dip was indispensable for browning inhibition. Osmotic dehydration and infrared drying reduced a_w, which prevented microbial growth. A radiation dose of 1 kGy was found to be effective in eliminating the residual microbial load on these pineapple samples, thus ensuring microbial safety of the product sensorily accepted throughout storage.

Table 5: Effect of radiation on sensory characteristics of intermediate moisture pineapple slices during storage at ambient temperature (26 ± 2 °C)[a b].

Radiation Dose (Gy)	Days of Storage	Colour	Texture	Aroma	Taste	Overall acceptability
0	1	5.0 ± 0.9	4.8 ± 0.7	4.7 ± 0.6	5.1 ± 0.7	5.0 ± 0.7
	20	4.9 ± 0.9	4.6 ± 0.8	4.5 ± 0.7	3.8 ± 1.0	4.5 ± 0.8
	40	4.6 ± 0.9	4.4 ± 0.8	4.1 ± 0.7	3.9 ± 0.8	4.3 ± 0.9
500	1	5.3 ± 0.7	4.6 ± 0.7	4.6 ± 0.6	4.5 ± 0.7	4.6 ± 0.6
	20	5.0 ± 0.9	4.3 ± 0.5	4.3 ± 0.6	4.6 ± 0.6	4.6 ± 0.6
	40	4.8 ± 0.9	4.2 ± 1.2	4.0 ± 0.8	4.6 ± 0.9	4.5 ± 0.9
1000	1	5.2 ± 1.2	4.0 ± 1.2	4.0 ± 1.2	4.0 ± 1.0	4.1 ± 1.2
	20	4.6 ± 0.5	4.4 ± 0.8	4.5 ± 1.0	4.9 ± 0.7	4.6 ± 0.6
	40	4.6 ± 0.7	3.9 ± 1.0	4.0 ± 0.7	4.4 ± 0.9	4.1 ± 1.0

[a] *The data represents mean ± SD of sensory scores of 12 slices. The mean values in a column are not significantly different ($P < 0.05$) as analyzed by one way ANalysis Of Variance (ANOVA).* [b] *Data in the table denote the scoring in a 7-point hedonic scale (1-very poor, 2-poor, 3-fair, 4-satisfactory, 5-good, 6-very good, and 7-excellent*

References

1. Adams, M., & Moss, M. (2000). *Food microbiology* (pp. 349). Cambridge: Royal Society of Chemistry.
2. Afzal, T. M., & Abe, T. (1998). Diffusion in potato during far infrared radiation drying. *Journal of Food Engineering,* 37, 353-365.
3. AOAC (1995). In official methods of analysis. Association of Official Analytical Chemists, Washinton DC, USA.
4. Basantia, N. C., Arora, S., Seth, R., & Singh, A. (2000). Milk proteins in the preparation of edible coatings. *Indian Food Industry*, 19, 36-47.
5. Corzo, O., & Gomes, E. R. (2004). Optimization of osmotic dehydration of cantaloupe using desired function methodology. *Journal of Food Engineering*, 64, 213-19.
6. Diehl, J. F. (1990). Safety of irradiated foods (pp. 217). New York: Marcel Dekker Inc.
7. Fernandes, F. A. N., Rodrigues, S., Gaspareto, O. C. P., & Oliveira, E. L. (2006). Optimization of osmotic dehydration of bananas followed by air-drying. *Journal of Food Engineering*, 77, 188-193.
8. Hajare, S., Dhokane, V., Shashidhar, R., Saroj, S. D., Sharma, A., & Bandekar, J. R. (2006). Radiation processing of minimally processed pineapple (*Ananas comosus* Merr.) : Effect on nutritional and sensory quality. *Journal of Food Science*,71(6), 501-505
9. Hajare, S. N., Saroj, S. D., Dhokane, V. S., Shashidhar, R., & Bandekar, J.R. (2007). Effect of radiation processing on nutritional and sensory quality of minimally processed green gram and garden pea sprouts. *Radiation Physics and Chemistry,* 76, 1642-1649.
10. ICMSF (International Commission for the Microbiological Specifications of Foods). (2002). Microorganisms in Foods 6: Microbial Ecology of Food Commodities (pp. 326-353). New York: Kluwer Academic/Plenum Publishers.
11. Jay, J.M. (1991). Intrinsic and extrinsic parameters of foods that affect microbial growth In Modern Food Microbiology. (pp. 45) New York: Chapman & Hall.
12. Karim, O. R., Awanorin, S. O., & Sanni, L. O.(2008). Effect of pre-treatments on quality attributes of air-dried pineapple slices. *Journal of Food Technology*, 6(4), 155-165.
13. Ledward, D.A. (1981). Intermediate moisture meats. In R.A. Lawrie (Ed.), Developments in meat science, vol. 2 (pp. 159-194). England: Applied Sciences Publisher Ltd.

14. Leistner, L. (1992). Food preservation by combined methods. *Food Res. International*, 25, 151–158.
15. López-malo, A. & Palou, E. (2008). Storage stability of pineapple slices preserved by combined methods. *International Journal of Food Science and Technology*, 43, 289-295.
16. Madero, C.F. & Finne, G. (1982). Properties of phenoloxidase isolated from gulf shrimp. Proceedings of the Seventh Annual Tropical and Subtropical Fisheries Technological Conference of the Americas, (pp. 328-339). New Orleans: LA.
17. Meilgaard, M., Civille, G. V., & Carr, B.T. (1999). Sensory evaluation techniques. 3rd ed. FL : CRC Press.
18. Mortan, J. F. (1987). Pineapple. In: J. F. Mortan. Fruits of warm climates (pp.18-28). Miami: Florida Flair Books.
19. Myung, K., Hamilton-Kemp, T. R., & Archbold, D. D. (2006). Biosynthesis of *trans*-2-hexenal in response to wounding in strawberry fruit. *Journal of Agricultural & Food Chemistry,* 54, 1442–1448.
20. Pokharkar, S. M., Prasad, S., & Das, H. (1997). A model for osmotic concentration of banana slices. *Journal of Food Science and Technology,* 34, 230-232.
21. Shashidhar, R., Dhokane, V., Hajare, S., Sharma, A., & Bandekar, J. R. (2007). Effectiveness of radiation processing for elimination of *Salmonella* Typhimurium from minimally processed pineapple (*Ananas comosus* Merr.). *Journal of Food Science,* 72(3), 98-101.
22. Shi, J., Pan, Z., McHugh, T.H., Wood, D., Hirschberg, E., & Olson, D. (2008). Drying and quality characteristics of fresh and sugar-infused blueberries dried with infrared radiation heating. *LWT Food Science and Technology*, 41, 1962-1972.
23. Stojanovic, J., & Silva, J.L. (2006). Influence of osmoconcentration, continuous high-frequency ultrasound and dehydration on properties and microstructure of rabbiteye blueberries. *Drying Technology*, 24,165-171.
24. Thakur, B. R. & Singh, R. K. (1995). Combination processes in food irradiation. Trends in Food Science & Technology, 6, 7-11.
25. Urbain, W. M. (1986). Food irradiation (pp. 351). London: Academic press Inc.
26. Vamos-Vigyazo L. (1981). Polyphenol oxidase and peroxidase in fruits and vegetables. *CRC Crit Rev Food Sci Nutr,* 15, 49-127.
27. Zhu, K., Zou, J., Chu, Z., & Li, X. (2002). Heat and mass transfer of seed drying in a two pass infrared radiation vibrated bed. *Heat Transfer-Asian Research,* 31(2), 141-147.

ABOUT THE AUTHORS

Mr. Sudhanshu Saxena did his M.Sc. in Biotechnology from Madurai Kamaraj University, Madurai in the year 2003. After graduating from the 47th batch of Training School, he joined the Food Technology Division. His research interest includes radiation preservation of food products and development of shelf stable fruits.

Mr. B. B. Mishra did his M.Sc. in Botany from Ravenshaw College, Utkal Univesity, Orissa in the year 1999. After graduating from the 44th batch of Training School, he joined the Food Technology Division. His research interest includes radiation preservation of foods of plant origin, development of shelf stable fruit products and inhibition of polyphenol oxidase mediated enzymatic browning, in fruits and vegetables.

ABOUT THE AUTHORS

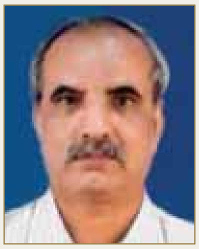

Dr. Ramesh Chander joined the Food Technology Division in 1975 after graduating from BARC Training School. He received his PhD from the University of Mumbai and MSc from H.A.U. both in Microbiology. He was a Post Doctoral fellow at the University of Florida, USA from 1988-1990. He is a fellow of the "Maharashtra Academy of Sciences". He is a recipient of the Outstanding Paper Award in the pharmaceutical field, conferred by the Controlled Release Society at Orlando, Florida (USA) on July 28, 1992. He is the author of more than 40 publications. His work pertains to the development of safe, shelf-stable meat products using hurdle technology. He has invented Vibro-thermal disinfester for disinfestation of food grains. He has also transferred the technology for foldable solar dryer. He has investigated several natural antioxidants for minimizing lipid peroxidation in processed food. His major contribution is development of "Artificial Viral Envelopes" for targeted intracellular delivery of peptides, enzymes, toxins and gene constructs, for which he holds a US and a European patent. He was actively involved in the upgradation of KRUSHAK for meeting the compliance requirements of USDA-APHIS for radiation processing of mangoes for export to USA. As a result of his efforts, Indian mangoes could be exported to USA after a gap of 18 years. He retired from BARC in April, 2009 as Head, Meat & Meat Products Section, Food Technology Division, BARC.

Dr. A.K. Sharma joined the Training School of BARC, Mumbai, in 1975, after finishing Masters degree in Microbiology from National Dairy Research Institute, Karnal. His early work related to aflatoxin biosynthesis and control in food commodities, for which he was awarded a Ph.D. degree from the University of Mumbai in 1984. Dr. Sharma was a DBT Post-Doctoral Associate at the Department of Plant Pathology, University of California, Riverside, USA during 1990-1991, where he worked on the molecular mechanism of host-pathogen interactions in plants. He studied food irradiation at the Royal Institute of Quality Control of Agricultural Products (RIKILT), Wageningen, The Netherlands. Dr. Sharma has made substantial contributions to the field of food irradiation technology with special reference to microbiological safety of foods, radiation processing of food commodities including spices and mango. He was the project manager of KRUSHAK irradiator project at Lasalgaon, set up for demonstrating low dose applications of radiation, for preservation of agricultural commodities. As a result of his efforts, Indian mangoes could be exported to USA after a gap of 18 years. For his outstanding achievements in the field of radiation and radioisotope applications in food technology Dr. Sharma has been awarded INS Award-2006 by the Indian Nuclear Society, and Group Achievement Award-2007 of the Department of Atomic Energy. He has more than 300 publications in the national and international journals, including chapters in books and encyclopedias, and articles in international and national conferences. Dr. Sharma has been the apex coordinator for three plan projects in the field of applications of radiation technology for food preservation and hygienization. He has represented India in the co-coordinated research programmes as well as an expert of the International Atomic Energy Agency. He has been the secretary of the Environmental Mutagen Society of India and Vice-President of the Indian Society for Environmental Science & Technology. Dr. Sharma is currently Outstanding Scientist & Head, Food Technology Division, BARC, and also holds adjunct position of Senior Professor, Homi Bhabha National Institute, Mumbai.

DIFFERENTIAL FREE RADICAL SCAVENGING ACTIVITY AND RADIOPROTECTION OF CAESALPINIA DIGYNA EXTRACTS AND ITS ACTIVE CONSTITUENT

U. Singh, A. Kunwar and K. I. Priyadarsini
Radiation & Photochemistry Division

and

R. Srinivasan and M. J. Nanjan
JSS College of Pharmacy, Udagamandalam

This paper was adjudged as the Best Poster at the Trombay Symposium on Radiation & Photochemistry (TSRP-2008) held at the University of Pune, between 7-11 January, 2008.

ABSTRACT

Two extracts E1and E2 were prepared from the dried root of the plant *Caesalpinia digyna* by extracting with solvents of different polarities. The extracts were standardized with respect to a polyphenol, bergenin, by LC- MS analysis and they were subjected to free radical scavenging activity and *in vitro* radioprotection studies. Free radical reactions were carried out with superoxide, hydroxyl, and peroxyl radicals and DPPH. *In vitro* radioprotecting activity was studied, by following their effect on γ - radiation-induced lipid peroxidation, protein carbonylation and DNA damage. The results indicated that E1 with higher free radical scavenging is also a more potent inhibitor of radiation-induced damage to proteins, DNA and liposomes than E2. Comparing the results with those for bergenin indicated that, bergenin alone is not responsible for the free radical scavenging ability and *in vitro* radioprotection. The studies also confirmed, that the extracts enriched with bergenin are more effective than the isolated polyphenol, bergenin.

Introduction

Currently, there is a growing interest in the development of natural products and plant extracts as antioxidants and anti-cancer agents. It has been postulated and verified by several researchers, that such natural formulations are less toxic and have minimum side effects. It is therefore necessary, to identify important medicinal plants and plant products and evaluate them by modern scientific tools, so that, such plant products can be explored as leads, for the development of novel therapeutic agents.

Members of the species of genus *Caesalpinia* like *Caesalpinia sappan, Caesalpinia bonducella, Caesalpinia pulcherrima* etc are known since ancient times, for their medicinal properties and they are commonly used in Indian folk medicine [1]. *Caesalpinia digyna* belonging to the same family is a large, scandent, prickly shrub growing wild in the shrub forests of the eastern Himalayas, Nilgiris, Sri Lanka, Malaya islands etc [1]. The plant is one of the constituents of an Ayurvedic preparation known as *Geriforte,* used for curing senile purities, antifatigue effect etc. [1]. This plant has many phytochemicals such as caesalpinine A, cellallocinine, ellagic acid, gallic acid, bergenin, bonducellin etc. [1]. In some of our earlier experiments, bergenin was isolated from the root extract of *Caesalpinia digyna*, purified and spectroscopically characterized [1]. Bergenin is a hydrolysable tannin derivative, which exhibits antiulcerogenic, anti-HIV, antioxidant, anti-inflammatory, neuroprotective and immunomodulatory effects [1]. It is an isocoumarin derivative with five hydroxyl groups. The chemical structure of bergenin is given in Scheme 1. Although both the root and the active phenolic constituent are known to exhibit promising antioxidant and medicinal properties [1], they have not been evaluated for their radioprotection capabilities. Therefore, an attempt has been made, to compare the radioprotection and free radical scavenging activities of the root extract, with that of its major active constituent. For this, the root was extracted with methanol and acetone and two extracts E1 and E2 respectively were prepared. They have been standardized with respect to bergenin content. The two extracts along with bergenin have been subjected for free radical scavenging activity and *in vitro* radioprotecting activity.

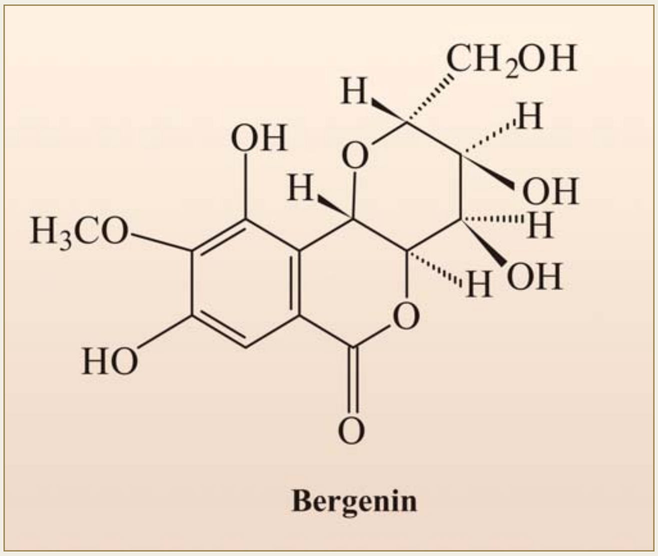

Scheme1: Chemical structure of Bergenin

Materials and Methods

The dried root of *Caesalpinia digyna* was powdered, defatted with 600 ml of petroleum ether (60 – 80°C) and extracted with methanol for 18 – 20 h. The extract was concentrated to dryness, under reduced pressure and controlled temperature (40° – 50° C). This was termed as extract E1. This extract was again fractionated with acetone. This acetone soluble fraction was termed as extract E2. Bergenin, the active constituent of the root was isolated from the E1 and characterized by IR, NMR and mass spectrometry.

The total phenolic content present in the extracts was measured, using a modified colorimetric Folin-Ciocalteu method and compared with a standard calibration curve plotted for gallic acid solution (1-10 μg/ml) and expressed as percent (%) gallic acid equivalents.

The superoxide radical scavenging ability of the extracts and bergenin was studied spectrophotometrically, using xanthine/xanthine oxidase method [2]. Relative rate constants for the scavenging of hydroxyl radical and peroxyl radical by the extracts / bergenin were estimated by pulse radiolysis technique, utilizing 500 ns pulses of 7 MeV electrons, from a linear electron accelerator [3].

Since plant extracts contain many active components whose concentrations are not known correctly, a method was developed to estimate the comparative reactivity of the extracts, based on competition kinetics, using a standard whose rate constant with hydroxyl radicals is known accurately. Here we employed ABTS^{-2}

The reaction of DPPH with the extracts and bergenin was examined by monitoring the absorbance at 517 nm in the presence and absence of different concentrations of extracts / bergenin.

Protein oxidation was carried out in BSA and the formation of carbonyl groups, due to radiolysis in the presence and absence of different concentrations of extracts and bergenin was assayed, by a standard DNPH-coupled spectrophotometric method [4]. Agarose gel electrophoresis was employed, to track the damage to pBR322 DNA, exposed to an absorbed dose of 50 Gy, both in the absence and presence of varying concentrations (82-328 µg/ml) of the extracts bergenin [4].

Lipid PerOxidation (LPO) studies were carried out in phosphatidyl choline liposomal models, according to the methods reported earlier [2]. Percentage protection for lipid peroxidation and protein carbonylation was calculated and used, for the estimation of IC_{50}. The IC_{50} value is defined as the concentration (in µg/ml) required to inhibit protein carbonylation, DNA damage in terms of conversion of SC to OC form and lipid peroxidation, by 50%.

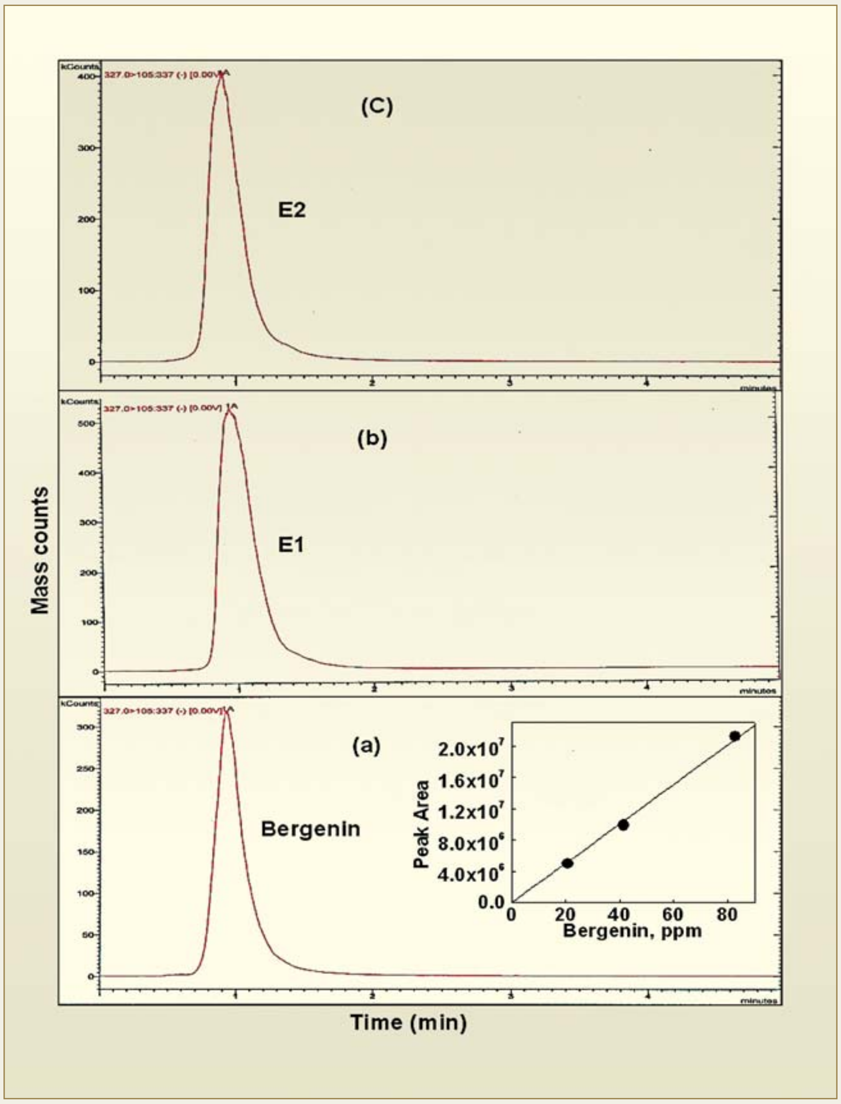

Fig. 1: LC-MS chromatograms of (a) bergenin (b) E1 (C) E2. The chromatograms were recorded by using analytical C18 column, methanol as eluant and mass detector set at mass unit 327.8. Inset shows calibration plot for estimation of bergenin.

Results

Estimation of polyphenols

The total phenolic content in E1 and E2 was estimated in terms of gallic acid, as one µg of the extract equivalent to 0.42 ± 0.04 and 0.34 ± 0.03 µg of gallic acid respectively. To further standardize them, LC-MS analysis was carried out.

Since the *Caesalpinia digyna* plant extracts contain bergenin as one of the major constituents, the two extracts were standardized with respect to the bergenin content, by LC-MS analysis. Initially LC-MS analysis of bergenin in methanol was

A calibration plot was made for the peak area as a function of bergenin concentration in the range of 20 to 100 ppm (Inset of Fig.1) and used to estimate bergenin content in the extracts. Fig.1 shows the LC-MS analysis of the two extracts, confirming the presence of bergenin by mass peak at mass units 327.8 and from the calibration plot, the bergenin content was estimated to be 39 ± 2.2 % and 27 ± 1.9 % respectively in E1 and E2. The extracts thus standardized with bergenin content were studied for free radical scavenging ability and *in vitro* antioxidant activity.

Free radical scavenging studies of the extracts and bergenin

The IC_{50} values for the scavenging of superoxide radicals by the extracts and bergenin were estimated and are listed in Table 2. It can be seen, that E1 is more effective than E2 in scavenging the superoxide radicals and its activity is even more than that of pure bergenin. Using nanosecond pulse radiolysis technique, the rate constant for the reaction of hydroxyl radical with bergenin at pH 7 was independently determined, as $3.3 \times 10^{9}\ M^{-1}s^{-1}$. The reactivity of the extracts with hydroxyl radicals was estimated by employing Competition kinetics and these values are listed in Table 1.

In a similar fashion, the reactivity parameters of the extracts and bergenin with $CCl_3O_2^{\cdot}$ radical [5] were estimated and the results listed in Table 1.

The IC_{50} values for scavenging of DPPH radicals are listed in Table 2 for E1, E2 and bergenin. The relatively large IC_{50} value for bergenin suggests, that bergenin itself in pure form is not a good scavenger of free radicals, but the extracts showed a much better effect. In an independent study, the rate constant for the reaction of bergenin with DPPH was found to be 88.1 $M^{-1}s^{-1}$. Comparing the reactivity of E1 and E2 and the above determined rate constant for bergenin, it was found that one microgram of E1 or E2 respectively is equivalent to 9 and 18.8 μg of bergenin, in exhibiting reaction with DPPH radicals.

In vitro radioprotection studies

In vitro radioprotecting ability of the extracts was evaluated, in terms of inhibition of γ-radiation-induced protein carbonylation in BSA, DNA damage in plasmid pBR322 and lipid peroxidation in liposomes. From these results, the IC_{50} values were estimated and these values are listed in Table 2 along with that for bergenin under similar conditions. The results indicated that both E1 and E2 exhibit almost similar protection towards BSA against radiation-induced damage. E1 is slightly more

Table 1: Reactivity extract values estimated through competition kinetics

Extracts/ Compound	**Hydroxyl radical ($^{\bullet}OH$)** (Times of $ABTS^{-2}$)	**Peroxyl radical ($CCl_3O_2^{\bullet}$)** (Times of $ABTS^{-2}$)	**DPPH radical $k_{obs}(s^{-1})$** (at 125 μg/ml)
E1	0.14 ± 0.09	1.8 ± 0.1	0.92 ± 0.09
E2	0.26 ± 0.10	4.1 ± 0.2	0.66 ± 0.07
Bergenin	$3.3 \pm 0.2 \times 10^{9} M^{-1}s^{-1}$	$4.2 \pm 0.3 \times 10^{6} M^{-1} s^{-1}$	0.14 ± 0.03^{a}

[a] Calculated at 250 mg/ml

potent than E2. Bergenin however is not so effective as compared to either of the extracts tested.

Similarly, effect of the extracts or bergenin on γ-radiation-induced damage in pBR322 DNA was studied. On exposure to γ-radiation, the SC form of DNA got converted to the OC form and in the presence of extracts or bergenin, there is a decrease in the damage to the SC form. Figs. 2 A, B, and C show agarose gel electrophoresis pattern where, lane 1 is the unirradiated control, lane 2 is irradiation control and lanes 3, 4, 5 and 6 show the pattern for

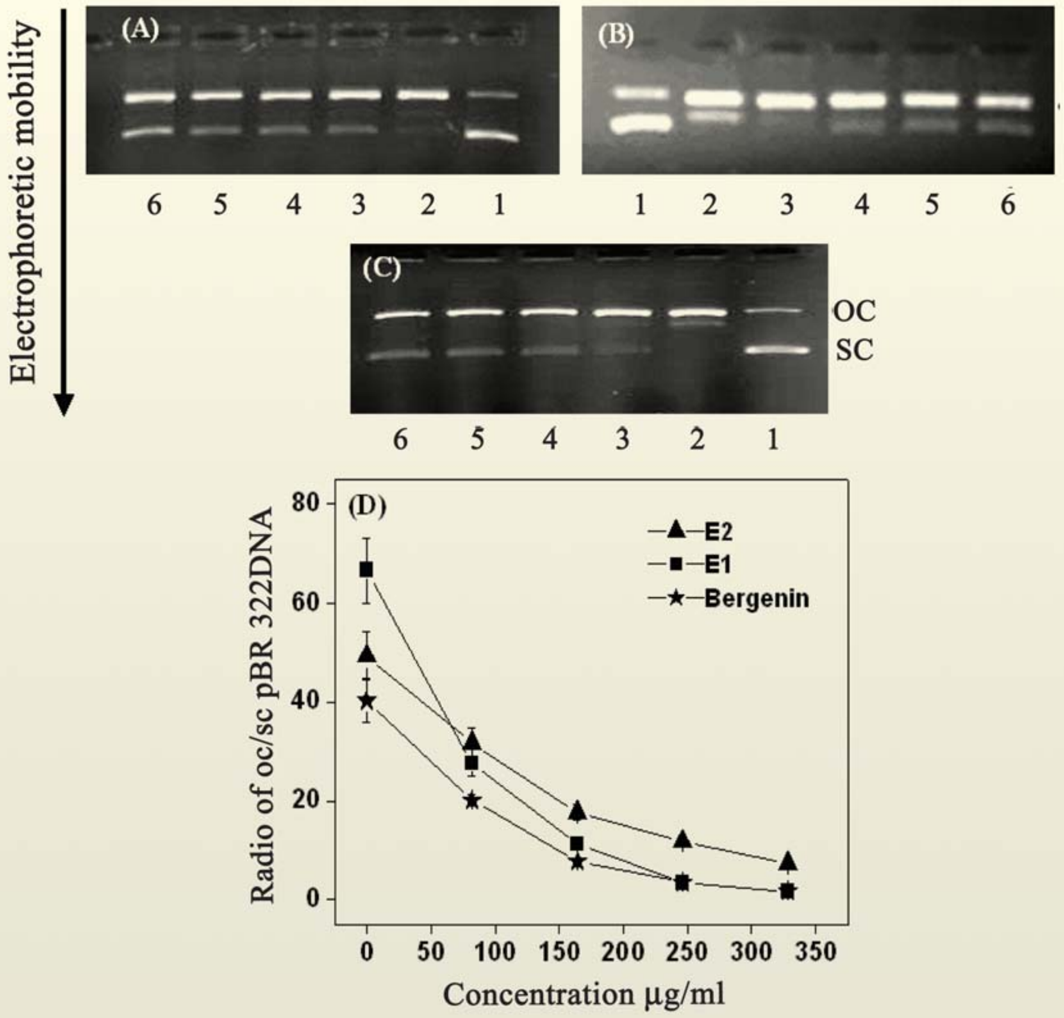

Fig. 2: Agarose gel electrophoretic pattern, depicting super coiled and nicked open circular forms of plasmid DNA protection by varying concentrations of E1 (A), E2 (B) and bergenin (C) against 50 Gy γ-radiation-induced strand breaks. The arrow indicates the direction of electrophoretic mobility. Lane 1: pBR 322 control, Lane 2: pBR 322 exposed to γ-radiation of 50 Gy; lanes 3 to 6 exposed to radiation dose of 50 Gy in the presence of the 82, 164, 246, 328 µg/ml of extracts and bergenin. (D) Line graph showing ratio of OC / SC form as a function of increasing concentrations of E1, E2 and bergenin

Table 2: *In vitro* antioxidant activity of two different extracts of *Caesalpinia digyna root* and bergenin. E1- methanol extract, E2 – acetone extract.

Fractions/ Compound	IC$_{50}$ values (µg/ml) for scavenging/inhibition of free radicals and radiation induced damage to cellular organelles				
	DPPH	DNA Damage (50 Gy)	Inhibition of superoxide radicals	Protein carbonylation (50 Gy))	Lipid peroxidation (240 Gy))
E1	2.66 ± 0.13	69 ± 3.5	6.6 ± 0.3	3.4 ± 0.2	14.6 ± 0.7
E2	4.97 ± 0.24	124 ± 6	8.9 ±0.4	3.7 ± 0.2	27.3 ± 1.4
Bergenin	377.5 ± 18.8	82 ± 4	23.2± 1.2	14.2 ± 0.7	34.0 ± 1.7

the irradiated plasmid DNA, in the presence of varying concentrations of E1, E2 and bergenin. The intensities of OC and SC form of plasmid DNA were measured under different treatment conditions and the ratio of OC / SC was plotted as a function of the concentration of extracts or bergenin (Fig. 2 D). From this the IC$_{50}$ values were estimated and listed in Table 2. In these studies, E1 was found to be superior to E2. However, bergenin under these conditions displayed protection similar to E1.

Inhibition of lipid peroxidation by the extracts was monitored by TBARS formation in liposomal solution in the absence and presence of different concentrations of E1, E2 and bergenin after exposing to γ radiation. The IC$_{50}$ values for the inhibition of TBARS are listed in Table 2.

The results too indicated that among the three, E1 exhibits higher protection towards liposomes than either E2 or bergenin against radiation-induced damage.

Discussion

Caesalpinia digyna, an herb used in Indian folk medicine, is known to possess antioxidant activity and the plant is rich in polyphenols like bergenin. Since herbal extracts are being considered as alternate therapeutic agents, the dried plant root is extracted with solvents of varying polarity and two active extracts were prepared and they were standardized with respect to bergenin. The bergenin content in these extracts was nearly 30%. These extracts were subjected to free radical reactions and *in vitro* radioprotection ability and the results were compared with those of bergenin. The two extracts E1 and E2 and bergenin scavenged free radicals like hydroxyl radicals, superoxide radicals and DPPH to a different extent. Bergenin itself is a good scavenger of hydroxyl radicals but not so effective in scavenging other free radicals like superoxide radical, and DPPH.

Reaction with hydroxyl radicals is non-specific, while reaction with the other radicals is more specific and considered important, in evaluating the antioxidant activity of new compounds. These studies indicate that the extracts are more effective inhibitors of antioxidant-specific free radicals than bergenin. Similarly a comparison of the *in vitro* radioprotecting ability of the extracts indicated, that E1 exhibits higher

Radioprotection than the other extract. Bergenin in comparison is equally effective in inhibiting DNA damage but is less effective than the two extracts in inhibiting radiation-induced damage to proteins and l lipid peroxidation to liposomes. Both protein carbonylation and lipid peroxidation proceed through free radical mechanism, therefore it is not surprising that extracts that scavenge specific free radicals are more effective inhibitors of protein carbonylation and lipid peroxidation. Radiation-induced DNA damage too can be mediated through free radicals. But bergenin showing good protection to DNA and also being a good scavenger of hydroxyl radicals, indicates that, the hydroxyl radical scavenging reaction is more important for the DNA protecting ability. Inhibition of radiation induced DNA damage by bergenin and bergenin rich extracts indicates, that such extracts can be explored as potent radioprotectors and therefore warrants future *in vivo* studies.

Our estimation of total polyphenolic content in the extracts indicate, that they contain some polyphenolic substances other than bergenin and these compounds may be responsible for the higher free radical scavenging power of the extract. Antioxidants derived from polyphenols on reaction with oxidizing free radicals, generate phenoxyl radicals. The reactivity of these phenoxyl radicals depends on the substitution and chemical structure and this determines whether free radical scavenging leads to antioxidant action or not. If the resultant antioxidant radicals are reactive, they can even induce more damage to the biomolecules. In extracts containing mixture of polyphenols, the reactions can lead to synergism and thereby increase the efficacy of the antioxidant mixture. Therefore an antioxidant rich formulation can be more potent than any one of the constituents.

Conclusion

All these results clearly confirm that the two extracts of *Caesalpinia digyna* containing bergenin, exhibit superior free radical scavenging ability and radioprotecting ability than their major polyphenolic constituent, bergenin. These results further support the currently developing concepts that plant extracts in natural formulations, show more potent biological activity, than their active constituents.

Acknowledgement

The authors are thankful to R.S.I.S department, I.I.T, Mumbai for LC-MS analysis of extracts, Dr. T. Mukherjee, Director Chemistry Group, and Dr. S.K. Sarkar, Head, Radiation & Photochemistry Division for their encouragement and support to this work.

References

1. Srinivasan, R., Chandrasekar, M. J. N., Nanjan, M. J., and Suresh, B. (2007) *J. Ethnopharmacol*. **113**: 284-291.
2. Barik, A., Mishra, B., Shen, L., Mohan, H., Kadam, R. M., Dutta, S., Zhang, H-Y., and Priyadarsini, K. I. (2005) *Free Radic*. *Biol. Med*. 39: 811-822.
3. Spinks, J. W. T., and Woods, R. J. (1991) Introduction to radiation chemistry. New York: Wiley, p. 243.
4. Mishra, H. S., Khairnar, N. P., Barik, A., Priyadarsini, K. I., Mohan, H., and Apte, S. K. (2004) *FEBS Lett*. 58: 26-30.
5. Alfassi, Z. B., Mosseri, S., and Neta, P. (1987) *J. Phys. Chem*. 91: 3383–3385.

ABOUT THE AUTHORS

Mr. Umang Singh is working as a research fellow in the Radiation and Photochemistry Division, BARC since January 2007 under the collaboration scheme between University of Mumbai and the Department of Atomic Energy. His area of specialization is free radical reactions, antioxidant and radioprotection studies of plant polyphenols and extracts.

Mr. Amit Kunwar obtained his M. Sc. degree in Biotechnology from the Centre For Plant Molecular Biology, Tamil Nadu Agricultural University in 2003. After graduating from BARC Training School in 2005 (48th Batch, Bioscience discipline), he joined the Radiation & Photochemistry Division, BARC. Since then, he is involved in free radical cellular biochemistry and evaluation of synthetic as well as natural molecules, for their anti-oxidant and pro-oxidant activity, employing spectroscopic and biochemical techniques.

Dr. (Ms.) K. Indira Priyadarsini joined BARC in 1983. She is currently working on the elucidation of mechanisms of antioxidant action involving organoselenium compounds, natural products and herbal extracts with potential application as radioprotectors, employing spectroscopic methods, electron pulse radiolysis and biochemical studies. Dr. Priyadarsini has co-authored more than 135 papers in peer reviewed international journals on radiation chemistry, photochemistry, biophysics and radiation biology. She has been elected as the Fellow of the National Academy of Sciences, India and is the recipient of the Homi Bhabha Science & Technology Award.

STUDY OF GAS SENSING PROPERTIES OF ZnO NANOWIRE SENSOR

R. Mohan
Department of Physics, Barkatullah University, Bhopal,

M. Bharti
Chaudhry Devilal University, Sirsa, Haryana
and
M. Kaur, K. Ganapathi and S.K. Gupta
Technical Physics & Prototype Engineering Division

This paper received the Best Poster Award at the (National Seminar on Physics and Technology of Sensors) NSPTS-13 held at University of Pune, from March 3-5, 2008

ABSTRACT

We have studied the gas sensing properties of thick films prepared using ZnO nanowires. For this purpose, a paste of nanowires was prepared in methanol, painted on Alumina substrate followed by annealing at 500°C. ZnO nanowires were prepared by carbothermal method and characterized by SEM, EDX and XRD. The performance of films as a chemical sensor was studied, as a function of temperature for several toxic gases such as H_2S, NH_3, NO, CO and CH_4. These films were found to be highly sensitive to H_2S and NO gases. It was observed, that at room temperature, the film is more sensitive to H_2S gas as compared to NO gas, but recovery after exposure to NO gas is faster. With increase in temperature, there is not much change in recovery time after NO gas exposure, but on exposure to H_2S gas, recovery time decreases appreciably with increasing temperature.

Introduction

Semiconductor metal-oxide-based gas sensors are commonly used for environmental and emission monitoring, automotive, domestic, industrial and medical applications, due to their advantages such as small dimensions, low cost and inertness. The gas sensing mechanism of these sensors, involves chemisorption of oxygen on the oxide surface, followed by charge transfer during the reactions of oxygen with target gas molecules. The adsorbed oxygen extracts electrons from the semiconducting material, leading to change in carrier density and conductivity, which corresponds to the gas concentration. Since the sensing mechanism is surface reaction which is directly related to the granularity, porosity and surface-to-volume ratio of grains, the performance of the sensors improves with reduction in the size of oxide particles. Among the semiconductor metal oxides, zinc oxide (ZnO) was one of the earliest to be discovered and is one of the most widely used gas sensing material. ZnO gas sensors in various forms have been reported to sense H_2, NO_2, NH_3, CH_4, O_2, CO and ethanol. Recent advances in synthesis and investigation of physical properties of nanostructures, provide an opportunity to greatly improve the performance of these materials, for gas sensing. Variety of ZnO nanostructures such as nanowires, nanobelts, nanospring, nanorod, nanocombs, nanotetrapod, nanotube, nanonail, nanosheet, nanohelics have been synthesized and studied. Better gas sensing properties of nanostructured ZnO have been reported [1-4].

We have synthesized ZnO nanowires by carbothermal method and studied their gas sensing properties, as a function of concentration as well as temperature. It is observed, that at room temperature, these films are reasonably sensitive towards H_2S and NO gases. Recovery time as function of increasing concentration, significantly increases for H_2S, but remains nearly same for NO. With increase in temperature, recovery time for H_2S gas decreases, while it does not have much variation for NO. This suggests a difference in sensing mechanism of the two gases.

Experimental

Synthesis: A conventional horizontal tube furnace was used, for the synthesis of ZnO nanowires. Mixture of ZnO and graphite in 3:1 ratio (by weight) was used as a source material. It was loaded on to a quartz boat and placed in the center of 1 m long quartz tube. High purity gases were introduced through one side of the furnace and other side of the quartz tube was connected to a water bubbler. The flow of gases was controlled with rotameters. The material was heated to 1050°C under a constant flow of 500 sccm argon. On stabilizing the temperature, the gas atmosphere was switched to 98% argon and 2% oxygen at same flow rate. The furnace was maintained under these conditions for 30 mins and then cooled to room temperature at a rate of 6°C / min. White spongy material was deposited all along the tube, in gas flow direction.

Characterization: Surface morphology of the samples was studied using a Scanning Electron Microscope (SEM) VEGA MV2300T/40 (TS 5130 MM, TESCAN). Chemical composition of the nanowires was confirmed, by recording Energy Dispersive X-ray analysis spectrum (Oxford Instruments Inca energy 250 system). The phases present and structure of nanowires were identified by X-ray diffraction (XRD), carried out using Cu-K_α radiation.

Gas sensing: Thick films were made out of nanowires by making a paste of nanowires in methanol, painting them on Alumina substrate, followed by annealing at 500°C. Two gold contacts were thermally evaporated on these films. Silver wires were attached to these gold film contact pads, to measure the resistance change, on exposure to the gases.

For measurement of the response to gases, the films were loaded in a housing having a volume of 250 cm^3 as described earlier [5]. Measured quantity of desired gas (having 1000 ppm gas concentration) was introduced in the housing, using a micro-syringe, so as to yield desired concentration and resistance of the film was measured, as function of time. After steady state was achieved, recovery of sensors was studied by opening the housing to the atmosphere.

Results

Structural Characterization: The Scanning Electron Microscopy images (SEM) in Fig. 1 show, that as grown samples consist of nanowires, with typical lengths in the range of several micrometers and diameter of 50-150 nm. Energy Dispersive X-ray spectrum confirms, that the elements present in the powdered sample are zinc and oxygen (Fig. 2). X-ray diffraction pattern of the nanowires is given in Fig. 3. The diffractogram indicates a standard hexagonal structure of ZnO (JCPDS 80.0075) with lattice parameters $a = b = 0.324$ nm and $c = 0.520$ nm. Traces of metallic Zn is also indicated in the diffraction pattern.

Electrical Characterization

Room temperature: ZnO nanowires were investigated, for their use as gas sensors for several toxic gases (H_2S, NH_3, NO, CO and CH_4). The films were found to exhibit good sensitivity towards H_2S and NO gases (Figs. 4 (a) and (b)) and very little or no response to other gases. The sensor response (defined as $S = R_a/R_g$ for reducing gas and R_g/R_a for oxidizing gases where R_a and R_g are resistances in air and gas respectively) as a function of gas concentration for H_2S and NO gases is shown in Figs. 5 (a) and (b) respectively. Sensor response for 2 and 60 ppm of

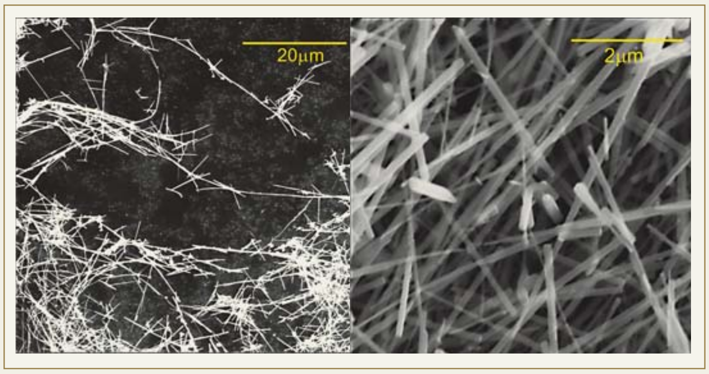

Fig.1: SEM micrographs of ZnO nanowires at lower and higher magnifications

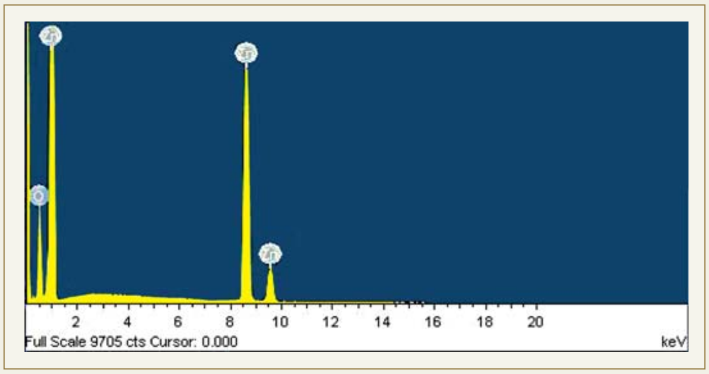

Fig. 2: EDAX spectrum from a bunch of ZnO nanowires

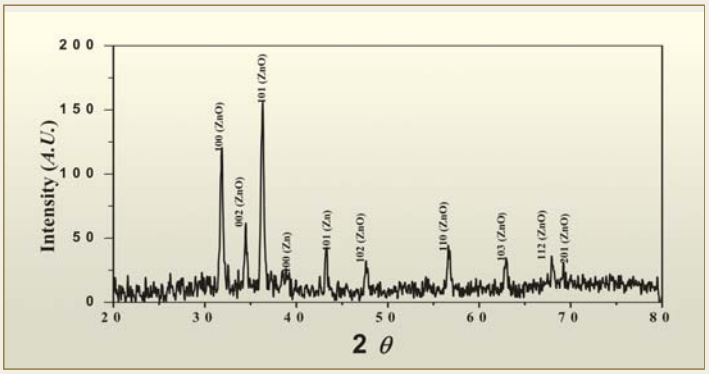

Fig. 3: XRD pattern from a bunch of ZnO nanowires

H_2S gas is ~3 and 16 respectively, as compared to ~1.5 and 8 for NO gas at same concentrations. It is also observed that at higher concentrations (20 ppm in Fig. 4 (a)) recovery is very slow for H_2S gas (~6 hrs). However for NO gas, recovery time is less than 10 minutes even for concentrations as high as 60 ppm.

Elevated temperatures

The dynamic properties of the sensors such as sensitivity, response and recovery times are known to be temperature dependent. Generally the base resistance, response and recovery times of sensors, decrease with increase of temperature. Therefore response-recovery curves were recorded as a function of temperature for both the gases (Figs. 6 (a) and (b)). It is observed, that for 10 ppm of NO gas, response and recovery times decrease from 5 mins to 10 secs and 10 min to 2 min respectively, when temperature is increased from 30 to 300°C. In contrast, for 10 ppm of H_2S gas, response and recovery times decrease from 5 mins to 25 secs and 3 hrs to 3 mins on increasing temperature to 300°C.

Discussion

It can be seen from Fig. 4, that recovery time of the sensor on exposure to H_2S increases with increase in gas concentration, while for NO gas it is small at all concentrations. Even as a function of temperature,there is a huge change in recovery time for H_2S gas (3 hrs to 3 mins), as that compared to NO gas (10 min to 2 min). The different response transients of the sensor to these two gases, might be due to different sensing mechanisms for the two gases.

Oxygen vacancies present in ZnO, acts as electron donors to make it an n-type semiconductor. Oxygen molecules from the ambient are adsorbed at the grain boundaries, which in turn capture electrons from the conduction band, forming adsorbed oxygen ion. This causes a decrease in carrier concentration and increase in resistance of the sample. When the sensors are exposed to a reducing gas, the gas reacts with the adsorbed oxygen,

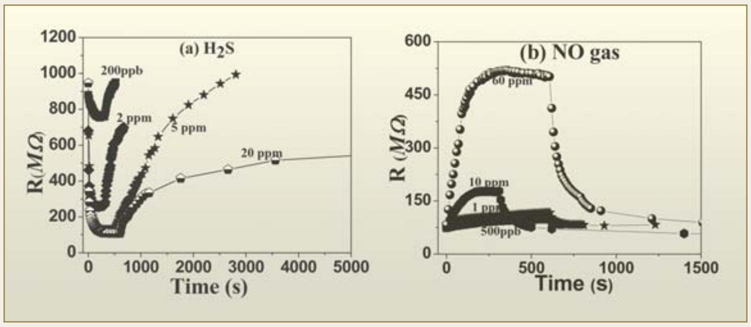

Fig. 4: Response and recovery curves of ZnO nanowires thick film with (a) different concentrations of H_2S gas and (b) different concentrations of NO gas

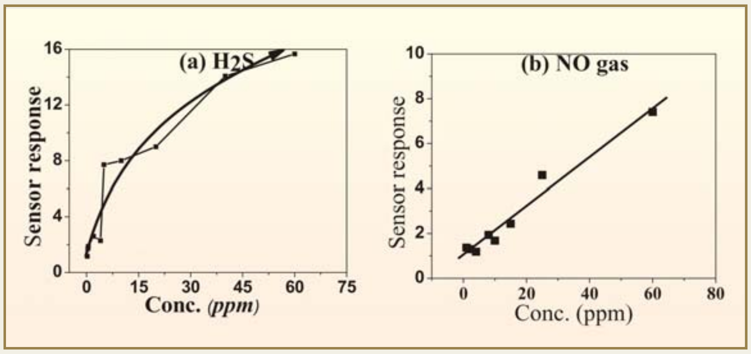

Fig. 5: Sensor response as a function of concentration at room temperature for (a) H_2S gas and (b) NO gas

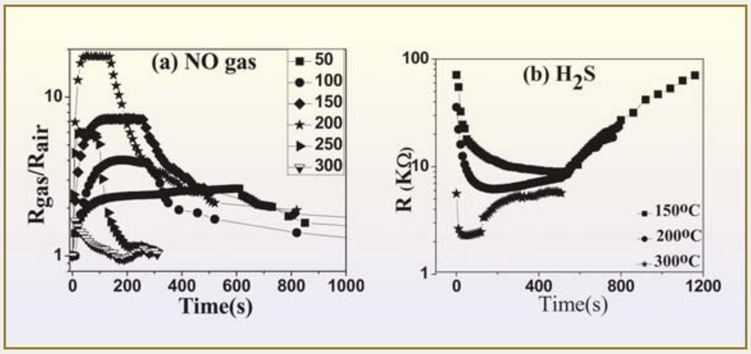

Fig. 6: Response and recovery curves of ZnO nanowire thick film for (a) 10 ppm NO gas as a function of temperature (b) 10 ppm H_2S gas at 150°C, 200°C and 300°C.

resulting in the release of the trapped electrons back into the conduction band. This leads to an increase in carrier concentration and decrease in resistance of the sensor. However on exposure to oxidizing gas, reaction take place directly with the oxide surface, rather than with the oxygen chemisorbed at the surface.

Generally, sensing mechanism of all gases by any metal oxides is explained by this mechanism. As the oxygen adsorption-desorption mechanism is nearly same for two gases, difference in recovery time characteristics, indicates a different mechanism for one of the gases.

Slow response to H_2S at high concentration may arise, due to interaction of ZnO with H_2S, forming ZnS [6-8]. On exposure to low concentration of H_2S, (as discussed earlier) recovery is complete, since the amount of ZnS formed, is small. As we go to higher concentrations, the amount of ZnS formed is more and the desulfurization rate is same, hence there is an increase in recovery time. At room temperature, desulfurization rate is slow resulting in slow recovery, with increase in temperature this rate increases, which helps the sample to recover faster.

The difference in behaviour of recovery time in the case of two gases with increasing concentration as well as temperature, could be attributed to difference in sensing mechanism. In case of NO gas, sensing takes place by adsorption-desorption process and in case of H_2S gas, ZnO reacts with the gas to give ZnS.

Conclusion

A conductometric gas sensor has been fabricated, based on ZnO nanowires synthesized by carbothermal method. Gas sensing properties of this sensor reveal that it is sensitive to both H_2S and NO gases. The response transients of these two gases have been studied, as a function of temperature as well as concentration. The difference in behaviour of recovery time as a function of temperature and concentration has been explained in terms of different interaction mechanisms of the two gases.

References

1. Ge C., Bai Z., Hu M., Zeng D., Cai S., Xie C., Preparation and gas-sensing property of ZnO nanorod-bundle thin films, *Mater. Lett.* 2007.
2. Bie Li-Jian, Yan Xiao-Na, Duan Yue-Qin, Yuan Zhi-Hao, Nanopillar ZnO gas sensor for hydrogen and ethanol, *Sens. Actuat. B*, 126, 2007, 604-608.
3. Wen X., Fang Y., Pang Q., Yang C., Wang J., Ge W., Wong K. S. and Yang S., *J. Phys. Chem. B*, 109, 2005, 15303-15308.
4. Hsueh Ting-Jen, Chang Shoou-Jinn, Hsu Cheng-Liang, Lin Yan-Ru, Chen I.-Cherng, Highly sensitive ZnO nanowire ethanol sensor with Pd adsorption, *Appl. Phys. Lett.*, 91, 2007, 531111-3.
5. Kaur M., Gupta S.K., Betty C.A., Saxena V., Katti V.R., Gadkari S.C. and Yakhmi J.V., *Sens. Actuat. B*, 107, 2005, 360.
6. Wang D., Chu X. and Gong M., *Nanotechnology* 18, 2007, 185601.
7. Li Y., Guo H., Li C. and Zhang S., *Ind. Eng. Chem. Res.* 36, 1997, 3982-3987.
8. Hayter C. E., Evans J., Corker J. M., Oldman R. J. and Williams B. P., *J. Mater.* Chem. 12, 2002, 3172-3177.

ABOUT THE AUTHORS

Dr. Manmeet Kaur received her Ph.D. from Devi Ahilya Vishwavidyalaya, Indore in 1998. Her thesis work involved effect of heavy ion irradiation on high temperature superconductors. She joined BARC, Mumbai in 1999 as Dr. K.S. Krishnan Research associate and is presently working as Scientific Officer. Her present interests include development of metal oxide thin films and nanomaterials for sensing toxic gases.

Ms. Kailasa Ganapathi joined BARC in the year 2006. She is working on development of H_2S gas sensors and growth of nanowires of different materials. She has supplied many H_2S sensors to Heavy Water plants at Manuguru and Kota.

Dr. S. K. Gupta joined BARC in 1975 and is presently Head of Thin Films Devices Section in TPPED. Over the years, he has worked on space quality silicon solar cells, high temperature superconductor thin films and single crystals, gas sensors and thermoelectric materials. He has carried out extensive studies on vortex dynamics in superconductors. He is a member of the National Academy of Sciences, India.

MIGRATION OF METALS INTO GROUNDWATER FROM URANIUM TAILINGS POND

S. Mishra, S. Bhalke, S. T. Manikandan, F. Sunny,
R.N. Nair, G.G. Pandit and V. D. Puranik
Environmental Assessment Division

This paper was awarded the Best Poster Award at the Sixteenth National Symposium on Environment (NSE-16), held at Hisar, during 16-18 July, 2008

ABSTRACT

The migration of metals into the groundwater, due to leaching from a uranium tailings pond, is carried out in the present study. Manganese is taken as a typical example for the study. Manganese concentrations in the inlet of effluent treatment plant, which represent the tailings pond leachate concentration, were used for the calculation of the source term. A finite element based groundwater flow and contaminant transport model (FEFLOW) is used, to simulate the manganese concentrations at different locations around the tailings pond. Site specific K_d values of manganese are determined, using the batch method and applied in the transport model. The distribution coefficient K_d values were found to be varying from 5.0 ml/g (Near Rekha Mines) to 22.0 ml/g (Garanala downstream) with an average of 10.6 ml/g. Model results show that K_d is a sensitive parameter in the contaminant transport prediction. It was found that the model predicted plume pattern of manganese which is comparable with measured manganese concentrations. The particle trajectories generated by the model can be used, to optimize the sampling locations for the future monitoring programme.

Introduction

Uranium milling waste (tailings) containing sulphate, manganese and some trace amounts of radionuclides, are disposed in ponds, specifically selected for this purpose. Any metals or other contaminants that are present in the tailings, may be leached into the soil and enter into the groundwater. The possible pathway of the metals to reach the environment is via the leaching of the metals from tailings, to the aquifer below and subsequent transport in the aquifer. Migration of metals and other tailings constituents occurs through leaching and erosion. The degree of migration is related to numerous factors, including the chemistry of the tailings material; the permeability of the impoundment and liner (if present); the amount of precipitation; the nature of the underlying soils; and the proximity to both surface and groundwater.

In the present study, migration of manganese from a tailings pond to the groundwater has been carried out. The manganese concentrations, in selected observation wells at different locations surrounding the tailing pond were measured experimentally and the results were compared with the simulated manganese concentrations, obtained from a finite element based groundwater flow and contaminant transport model, using site specific distribution coefficient (K_d) values.

Sampling and Analysis

Jaduguda Uranium mine is located at 24 km south of Tatanagar, in Jharkhand State, India. Bulk of the ore processed emerges as tailings (residues from ore processing) and are pumped in to a tailings pond. There are three valley-dam types of tailings ponds at Jaduguda. The first and second stages of the tailings pond are located adjacent to each other in a valley with hills on three sides and engineered embankments on downstream side of natural drainage. These two tailings ponds are nearly filled up and ready for closure. The third stage of the tailings pond which is currently in use, is also located nearby in a similar setting. The precipitates settle down in the tailings pond and the clear liquid is decanted through a series of decantation wells and the decanted effluent is flown to the effluent treatment plant. For the present work, tailings and effluent samples were collected for the calculation of source concentration. It is found, that Mn concentration in tailings pond effluent is 60 mg/l (which is the source for the contaminant model, as the same effluent is leaching downwards to reach the groundwater). Yearly average source concentration values are varying from 47.5 mg/l to 60 mg/l. Groundwater (from 30 different wells) and surface water samples (from 17 locations) were collected covering almost 80 sq km area surrounding the tailings pond. Soil samples were collected for the determination of site specific distribution coefficient (K_d) values. All these samples were processed and analyzed for manganese (Mn) using atomic absorption spectrometer having a detection limit of 0.001mg/l.

Determination of K_d for Manganese

The distribution coefficient, K_d, is the ratio of the mass of solute species adsorbed or precipitated on the solids, per unit of dry mass of the soil, to the solute concentration in the liquids at equilibrium. For estimation of K_d, a batch method, (ASTM 1992j) was used. In this test, a specific solution to geomedium ratio of 4.0 was taken. The soil solution mixture was gently agitated on a shaker for 6 hours/day for three-day contact period.

In the present work, around 2 g of soil (Mn concentration in soil was measured, prior to the experiment) was taken and added to about 8 ml of distilled water which is spiked with 2 mg of Mn. The solution is constantly agitated for 3days. The solution is centrifuged and Mn is estimated in the filtrate.

Distribution coefficient K_d is given by the relation

$$K_d = \frac{C_0 - C_e}{C_e}\frac{V}{m}$$

where,

C_0 and C_e are the concentrations of Mn in water (mg/ml) at the beginning of the experiment (i.e. time t = 0) and at equilibrium condition (i.e. t = 72 hrs), respectively. V is the volume of the liquid phase in ml and m is the weight of the soil in g.

Results and Discussion

Using the batch method, the site specific K_d values are determined for the soil samples collected from Jaduguda near the tailings pond. Eight sites within the study are chosen for determining the distribution coefficient values. The K_d for manganese was found to be varying from 4.97 ml/g to 22.0 ml/g and values at individual locations are shown below.

The literature K_d value for manganese was found to vary from 0.2 ml/g (Baes and Sharp, 1983) to 150 ml/g (Sheppard and Thibault, 1990). This indicates that a one order variation in K_d value is possible in the field. Thus in the Jaduguda study area, the average K_d for manganese could vary from 4 ml/g to 40 ml/g.

Mn concentrations measured in the groundwater ranges from 0.001 to 1.54 mg/l (Fig.1). In eighty percentile of the sites, Mn concentration observed are less than 0.1 mg/l. The measured concentrations

Location	Distribution Coefficient (K_d) ml/g
Suvernarekha River d/s	11.70
Gara nala d/s	22.00
Gara nala u/s	6 .81
Near Rakha mines	5 .28
Bhatin school	8 .49
Bhatin road	4 .97
Titlatiland near TP(1)	13.60
Titlatiland near TP(2)	12.00

were plotted against the latitude and longitude of observation well locations is shown in Fig. 2(a). From the figure it is clear, that there is a movement of Mn around the tailings pond.

Mn plume movement was simulated using FEFLOW, a finite element based groundwater flow and contaminant transport model (Wasy, 2002). Mn source and boundary conditions were applied to the model, with flow parameters taken from other studies. The general flow direction was towards Suvernarekha River with the velocities in the range of 2.0 x 10^{-3} m/day to 3.4 m/day. The K_d values measured at different sites, were imputed in corresponding sub domains representing a heterogeneity. The measured Mn concentration at each observation well is compared with the contaminant model results. This is done with a virtual observation well over the model domain with latitude and longitude values of the actual observed vales. Fig. 2 (a) represents the contour of the measured concentrations in May 2007 with the individual observation shown with a "plus" mark on it. Fig 2. (b) shows the Mn concentration contours obtained from model. It is found that the modeled predicted plume pattern of manganese and the

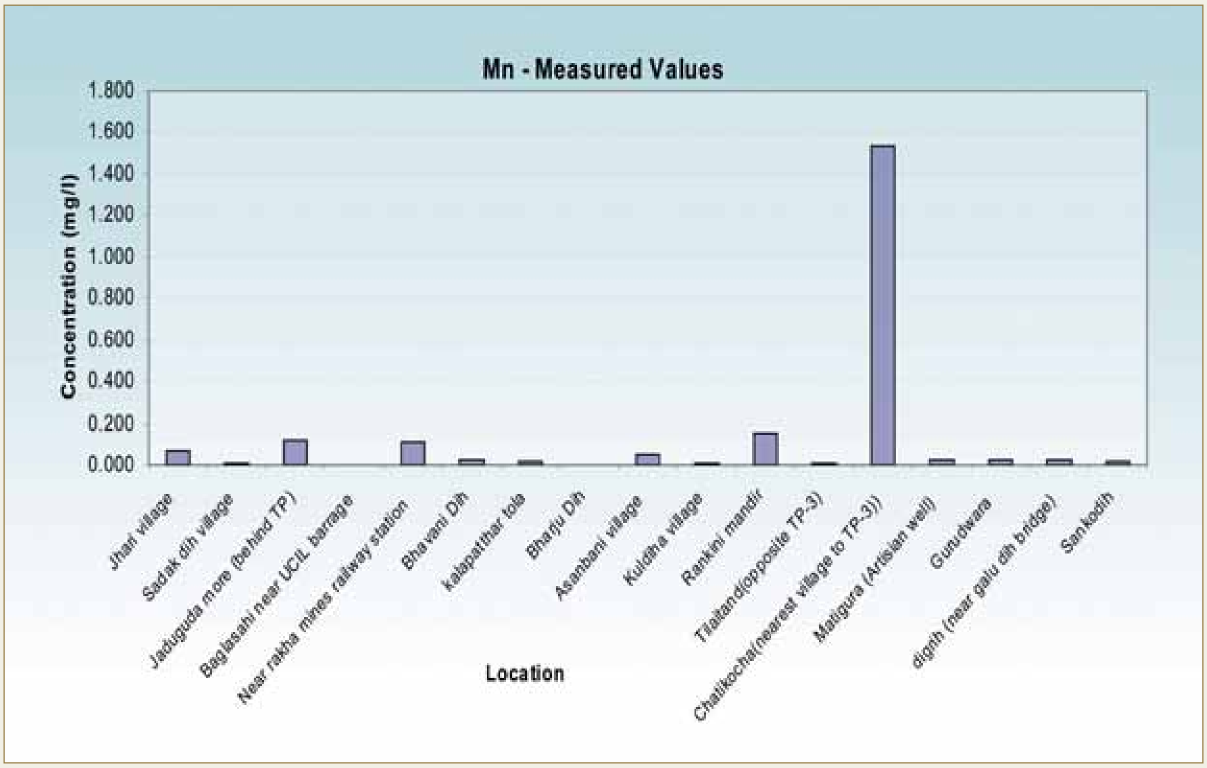

Fig.1: Mn concentration observed in groundwater at different villages

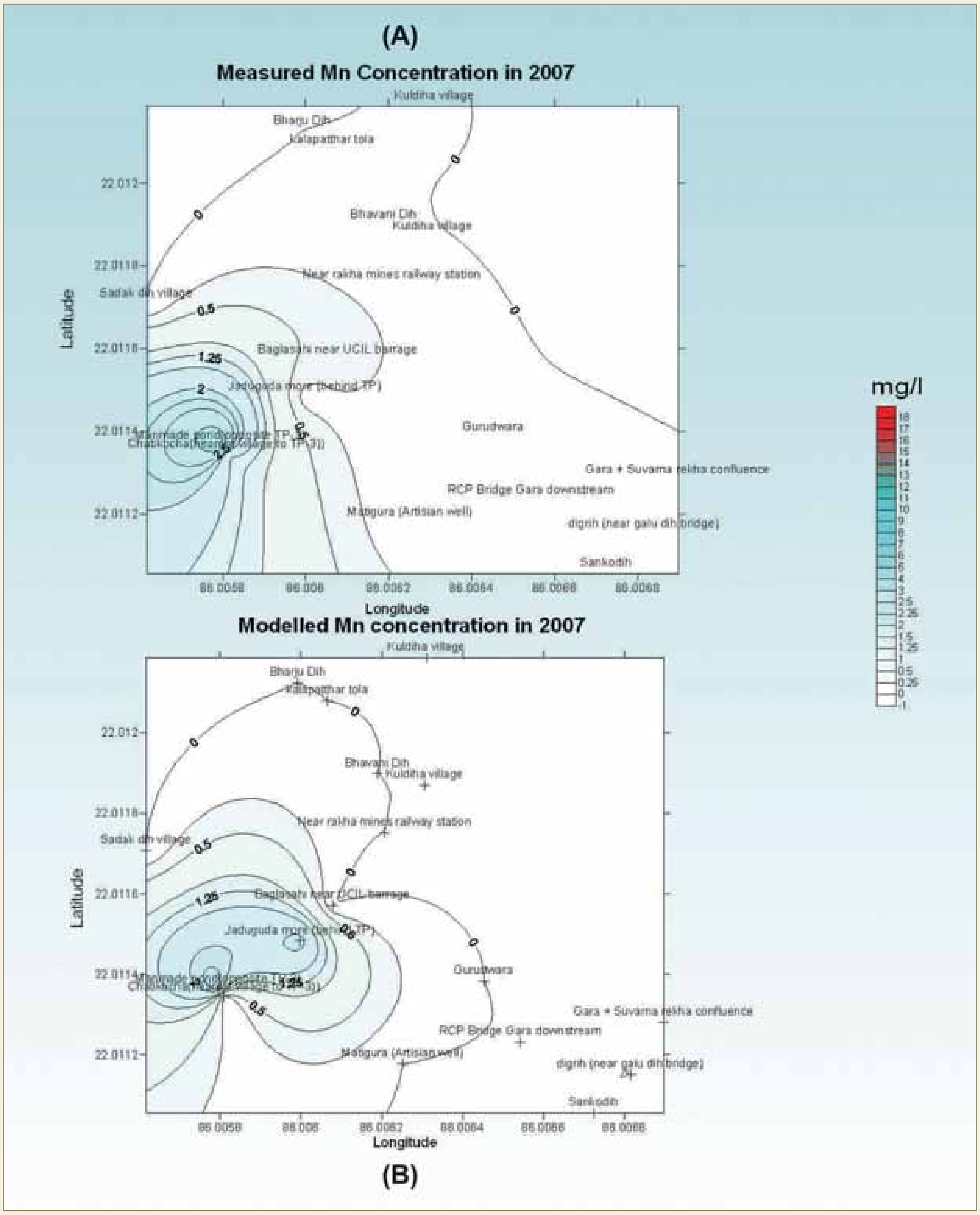

Fig. 2: Manganese concentrations in groundwater at different observation wells during 2007 around the tailings pond (a) measured (b) modelled

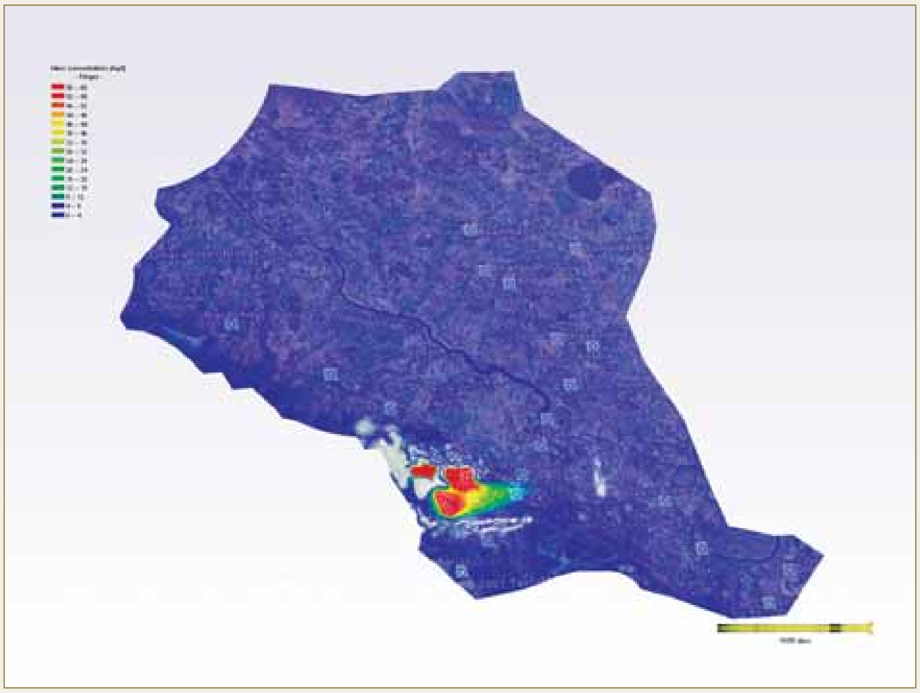

Fig. 3: Simulated manganese contaminant transport from tailings pond

simulated manganese concentrations are almost comparable with the measured values.

The plume of manganese transport is given in Fig. 3. This figure shows the migration after 50 years of simulation. The plume is moving towards south east towards the villages of Karthi kalndhi and Bagla Shai along the line of Gara river. From the plume pattern it is inferred, that the manganese plume is moved up to a distance of 500 m from the tailings pond.

Conclusion

The present work describes the preliminary results of transport of manganese around Jaduguda tailings pond area. It shows that there is a migration of manganese into groundwater up to 500 m distance. However detailed study has to be carried out for more accurate predictions. The distribution coefficient (K_d) values are found to be varying from 5.0 ml/g (Near Rekha Mines) to 22.0 ml/g (Garanala downstream) with an average of 10.6 ml/g. The manganese concentration experimentally measured varies from 0.01 mg/l (Sadak di village) to 1.54 mg/l (Chatikocha village, near Tailings Pond). In eighty percentile of the sites, Mn concentration observed is less than 0.1 mg/l. Model results show that distribution coefficient K_d is a sensitive parameter in contaminant prediction. It is found that the model predicted plume pattern of manganese is comparable with measured manganese concentrations. The particle trajectories generated by the model, can be used to optimize the sampling locations for future monitoring programme.

Acknowledgement

Thanks are due to Mr. V. N. Jha RPS (NF), EAD for his assistance in sample collection at Jaduguda.

References

1. Wasy, 2002, FEFLOW-finite element subsurface flow and transport simulation system, Institute for water Resource Planning and Systems Research ltd., Germany.
2. C. F. Baes, 111 and R. D. Sharp 1983. "A proposal for estimation of soil leaching and leaching constants for use in assessment models". *J. Environ. Qual.*, Vol.12, No.1, pages 17-28.
3. Sheppard, M.I. and Thibault, D.H. 1990. "Default Soil Solid/Liquid Partition Coefficients, Kds, for Four Major Soil Types: A Compendium." *Health Physics, 59,* (4), 471-482. New York, New York: Pergamon Press. TIC: 249329.

ABOUT THE AUTHORS

Dr. (Ms.) Suchismita Mishra completed her M.Sc. (Chemistry) in 1997 from Utkal University, Orissa and joined the Environmental Assessment Division (EAD), BARC, through the 41st batch of BARC training School (Chemistry Discipline) in 1998. She has awarded the Ph.D. Degree from Mumbai University in 2009. Her fields of interest include characterization of heavy metals, organometallics and radionuclides in environmental and biological matrices, speciation analysis, risk assessment and use of sorbents for removal of contaminants. Currently she is involved in characterization and speciation of metals in uranium mill tailings and determination of distribution coefficient for natural radionuclides in geological matrices, to study the migration of radionuclides.

Mr. Sunil Bhalke after completing his B.Sc. from Rani Durgavati Vishwavidyalaya, Jabalpur, joined the Environmental Assessment Division, BARC, through the sixth batch of BARC training course on Health Physics in 1998. He completed his M.Sc. Chemistry (Organic) (by research) from the Institute of Science, Mumbai University, 2003. His fields of interest include estimation, characterization and speciation of heavy metals, organo-pollutants and radionuclides in various environmental and biological matrices, using different analytical techniques.

Mr. S. T. Manikandan of Environmental Assessment Division obtained his M.Tech. degree in Environmental Engineering from IIT Chennai. He joined BARC in 2001 after completing the 10th Orientation Course for Engineering Postgraduate (OCEP) from Training School. He is currently working on groundwater hydraulics and numerical modeling of contaminant transport in subsurface. He is associated with BRNS projects on geohydrological investigations; and groundwater flow and radionuclide transport modeling in uranium mining and tailings pond sites. He was conferred DAE Special Contribution Award for the year 2007.

Dr. (Ms.) Faby Sunny joined BARC in 1985 and is currently working in the Environmental Assessment Division. She obtained her Ph.D. in Chemistry from Mumbai University in 2005. She is involved in the modeling of groundwater flow and contaminant transport using analytical and numerical techniques. She is associated with BRNS projects on geohydrological investigations; and groundwater flow and contaminant transport modeling in uranium mining and tailings pond sites.

ABOUT THE AUTHORS

Dr. R. N. Nair is presently working as Head, Environmental Modelling Section, Environmental Assessment Division. Dr. Nair joined BARC in 1982 after completing MSc from the University of Cochin, Kerala and subsequently completed his Ph.D. from the same university. His major fields of interest and expertise include environmental fluid mechanics, groundwater flow and contaminant transport modelling, surface water flow and contaminant transport modelling, radiological safety assessment of waste disposal facilities, evaluation of waste acceptance criteria, derivation of discharge limits, uncertainty analysis of environmental models, environmental radiation dose assessment and environmental heat transfer from thermal discharge outfalls.

Dr. (Ms.) G.G. Pandit joined BARC in 1981 (24th Batch of Training school, Chemistry). Currently she is heading the Environmental Monitoring and Assessment Section of the Environmental Assessment Division, BARC. Presently her interest of work is on assessment of long term impact from both radioactive and non-radioactive pollutants, released to different compartments of the environment. She is the National Project Coordinator of UNDP/IAEA/RCA project on Characterization and source identification of particulate matter in the Asian Region. She has more than 150 national and international publications to her credit.

Mr. V.D. Puranik joined the 15th batch of BARC Training School in Physics discipline. He worked in the Chemical Engineering Division of BARC and later in the Chemical Technology Division and Machine Dynamics Division on development of processes for isotopic separation. Till the year 2002, he was heading the Process Development Section in Machine Dynamics Division when he joined the Environmental Assessment Division as its Head. Presently his interest of work is radiological and chemical pollutants, their generation and dispersion in air and water, and modeling of such processes. He is looking after the safety of personnel and environmental monitoring of the front end fuel cycle facilities of the department and the radiation monitoring and networking programme in the country.

ROOM TEMPERATURE CHLORINE GAS SENSING PROPERTIES OF POLYPYRROLE-ZnO COMPOSITE THIN FILMS

A. Joshi and S.A. Gangal
Department of Electronic Science, University of Pune, Pune

and

D.K. Aswal, M. Kaur, S.K. Gupta and J.V. Yakhmi
Technical Physics and Prototype Engineering Division

This paper was awarded the Best Poster Prize at the 53rd DAE Solid State Physics Symposium (2008) held at BARC, Mumbai from Dec. 16-20, 2008

ABSTRACT

Chlorine gas sensing characteristics of polypyrrole and Polypyrrole-ZnO nanowire composite thin films have been studied. The composite films were synthesized by drop casting method. The films were characterized for its morphology as well as gas sensing characteristics for different gases such as H_2S, NH_3, CH_4, CO and NO at room temperature. The composite films were found to be more sensitive to chlorine than pure polypyrrole. They were also selective for chlorine gas over other gases. This indicates composite films can be used as room temperature chlorine sensor.

Introduction

Chlorine is a toxic gas with very low toxic limit of 5 ppm in air for 8 hr. It is widely used in various industrial processes as well as to disinfect water. It is desirable to detect chlorine in lower concentrations as it can affect human health. Inorganic materials like semiconducting oxides (SnO_2, ZnO, WO_3) have been used, for sensing of different oxidizing and reducing gases, but the working temperature is generally in the range of 150-400°C [1-3]. It is desirable to develop sensors operable at room temperature. Recently nanostructures in the form of belts, wires and rods have been studied for gas sensing applications [4]. Conducting polymers like polyaniline, polypyrrole and polythiopene are promising candidates for applications in sensor technolgy [5-7], due to their room temperature operation and easy processing. However, they show lack of selectivity and poor thermal and mechanical stability. Suitably processed organic-inorganic hybrid materials may have advantages of both organic and inorganic materials and need to be investigated for gas sensing and other applications [8-9].

In this paper, we report synthesis and gas sensing characteristics of polypyrrole-ZnO nanowire composite. Results have been compared with that of pristine polypyrrole film. It is seen that composite film shows better sensitivity and selectivity for chlorine than pure polypyrrole.

Experimental

ZnO nanowires were synthesized using carbothermal evaporation method [10] with typical diameter of 80-100 nm and length of several microns.

Polypyrrole-ZnO nanowire composite films were synthesized by drop casting method, using a suspension of polypyrrole and ZnO nanowires in ethanol. The films were deposited on glass substrates of 10 mm X 10 mm size. Pure polypyrrole film was synthesized by using aqueous solution of pure distilled Pyrrole (0.1 M) and Ammonium Persulphate (0.05 M) as an oxidizing agent. The films were drop cast on glass substrates. All the films were dried at room temperature. The composite films were characterized by scanning electron microscopy (SEM) (Vega, MV 2300/T40, Tescan). For gas sensing measurements, two gold pads with 1mm spacing were thermally evaporated on the films and silver wires were attached, using silver paint for measurement of resistance. In order to record response to different gases, the films were mounted in a SS housing of 250 cc volume and measured quantity of desired gas (at 2000 ppm concentration) was injected through syringe, so as to yield the desired concentration in the housing. All the films were characterized for response to Cl_2, H_2S, NH_3, CH_4, CO and NO gases by measurement of resistances in air and in the presence of gas. All the measurements were carried out at room temperature.

Results and Discussion

Morphology of the films was determined by SEM. For this purpose, a very thin layer of gold was thermally evaporated on the composite films. Typical micrograph of a film is shown in Fig.1. The image shows formation of island like structure embedding nanowires and polypyrrole. SEM image of ZnO nanowires is also shown in inset of Fig.1.

For gas sensing measurements, composite samples were exposed to 5 ppm concentration of different gases at room temperature. For comparison, gas response of pure polypyrrole film was also studied. It was observed that composite films are more sensitive to chlorine gas, in comparison to polypyrrole. Sensitivity of sensors is defined by:

Sensitivity = R_a / R_g.

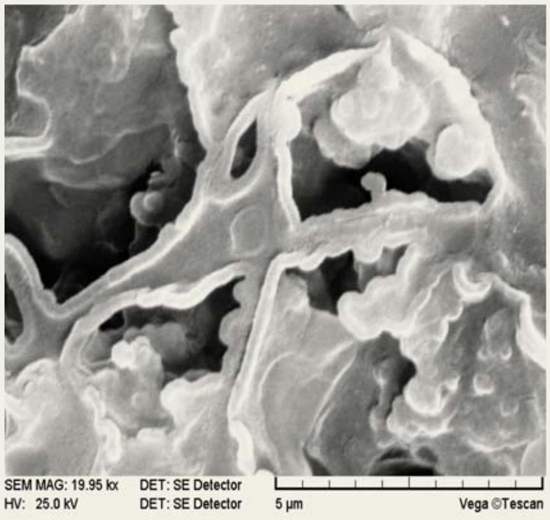

Fig. 1: SEM micrograph of composite films. Inset shows SEM image of ZnO nanowires

Typical response and recovery characteristics for composite and polypyrrole films are shown in Fig. 2. The resistance of all the samples is found to decrease after exposure to chlorine gas. This indicates p-type behaviour of all the samples.

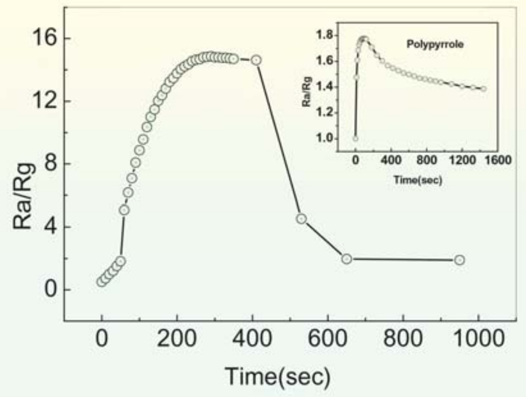

Fig. 2: Response and recovery characteristics of composite films to 5 ppm of Cl_2

Composite films were found to have much higher sensitivity than that of pure polymer films. The response time of composite film was found to be similar to that of pure films (<1min) but the recovery time (25 min) was much less. Cross-sensitivity of

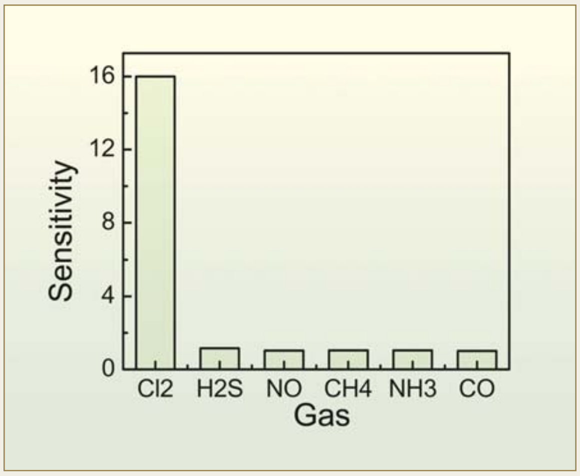

Fig. 3: Sensitivity of composite films for 5 ppm concentration of different gases

composite films for various gases like H_2S, NH_3, CH_4, CO, NO was also measured. The composite films were found to be highly selective towards chlorine as shown in Fig. 3.The higher sensitivity for chlorine gas in composite films, is attributed to localization of electrons on polypyrrole ring from O_2^- surfaces of ZnO nanowires. It reduces polypyrrole films by donating electrons that makes it insensitive to all reducing gases. Chlorine being highly-oxidizing gas, accepts electrons from composite films, thereby showing more sensitivity than pure polypyrrole.

Conclusion

We have synthesized polypyrrole-ZnO nanowire composite films by drop casting method. The films were characterized by SEM and gas response was studied. Composite films were found to be highly sensitive and selective for chlorine gas at room temperature.

References

1. Jun Tamaki, Sens. *Actuators* B 83 (2002) 190.
2. T.V.Belysheva, L.P.Bogovtseva, *J.Analytical Chemistry* 61 (2006) 494.
3. D. R. Patil, L. A. Patil, Sens. *Actuators* B 123 (2007) 546.
4. Q. Wan, Q. H. Li, Y. J. Chen, T. H. Wang, X. L. He, J. P. Li, and C. L. Lin, *Appl. Phys. Lett*. 84 (2004)3654.
5. J.Huang,S.Virji,B.H.Weiller,R.B.Kaner, *J. Am. Chem. Soc*. 125 (2003) 314.
6. Kumaran Ramanathan ,Mangesh A.Bangar et al, *J. Am. Chem. Soc*. 127 (2005) 496.
7. M.Penza,E.Milella, M.B.Alba, *Sens.Actuators*. B 40 (1997) 205-209.
8. P. Gomez-Romero, *Adv. Mater*. 13 (2001) 163.
9. D.B.Mitzi, K.Chondroudis,C.R.Kagan , IBM *J.Res & Dev.* 45 (2001) 29.
10. Manmeet Kaur, S. Bhattacharya, M.Roy, S. K. Deshpande, P. Sharma, S. K. Gupta, J.V.Yakhmi, *Applied Physics* A 87 (2007) 91.

ABOUT THE AUTHORS

Dr. D. K. Aswal joined Technical Physics and Prototype Engineering Division through 30th Batch of Training School. He has made several contributions in the field of thin/thick films and single crystals of various high temperature superconductors and colossal magnetoresistive materials. He has investigated various properties of magnesium-di-boride superconductor, metallic multilayer grown by molecular beam epitaxy and thermoelectric materials. Currently he is working on organic/molecular electronics.

ABOUT THE AUTHORS

Dr. Manmeet Kaur received her Ph.D. from Devi Ahilya Vishwavidyalaya, Indore in 1998. Her thesis work involved effect of heavy ion irradiation on high temperature superconductors. She joined BARC, Mumbai in 1999 as Dr. K.S. Krishnan Research associate and is presently working as Scientific Officer. Her interests include development of metal oxide thin films and nanomaterials for sensing toxic gases.

Dr. S. K. Gupta joined BARC in 1975 and is presently Head of Thin Films Devices Section in TPPED. Over the years, he has worked on space quality silicon solar cells, high temperature superconductor thin films and single crystals, gas sensors and thermoelectric materials. He has carried out extensive studies on vortex dynamics in superconductors. He is a member of the National Academy of Sciences, India.

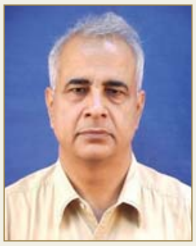

Dr. J.V. Yakhmi, Associate Director (S), Physics Group and Head, Technical Physics and Prototype Engineering Division of BARC, has worked for the past 40 years on diverse areas of research in materials science, such as: high Tc systems, magnetic alloys, molecular materials etc. He is a recipient of several national and international awards / fellowships.

PHASE STUDIES ON Np-Zr-O SYSTEM

N.K. Kulkarni and S.K. Sali
Fuel Chemistry Division
and
D.G. Phal
Radioanalytical Chemistry Division

This paper was conferred the Best Poster Award (2^{nd} Prize) at the 2^{nd} DAE-BRNS International Symposium on Naterial Chemistry (ISMC-2008), held at BARC, Mumbai, from Dec, 2-6, 2008

Extended Abstract

It has been known for a long time, that actinide dioxides ThO_2, UO_2, PuO_2 and AmO_2, form extensive series of mixed crystals with ZrO_2 above 1000°C, which have tetragonal structure at low concentration of actinide oxide and cubic fluorite structure at lower content of zirconium oxide. The solid solubility of ZrO_2 in actinide oxide, forming fluorite type solid solutions $Zr_yM_{1-y}O_2$, increases, with decrease in size of actinide ion (M). The solid solubility of ZrO_2 in ThO_2, UO_2, PuO_2 and AmO_2 is 5, 15, 80 and 82 mol% at 1400°C in air, respectively. Our recent studies on ZrO_2-UO_2 system have shown, that the solubility of ZrO_2 in UO_2 matrix can be increased up to 35 mol% at 1400°C, by slightly modifying the preparation conditions. Fluorite type zirconium-based solid solutions with actinide oxides, are known for their high thermal and irradiation stability and chemical durability under repository conditions.

During the burn-up of nuclear fuels, long-lived lighter actinides (Np, Am and Cm) are accumulated in the fuel; neptunium thus produced, amounts to 60% of these elements. There is no report on NpO_2- ZrO_2 system. The present study describes the phases formed on heating different proportions of ZrO_2 and NpO_2 at 1400°C in air. Neptunium oxide used for solid state reactions with ZrO_2 was obtained, from thermal decomposition of neptunium oxalate in air at 1000°C for 10 h. Homogenous mixtures of NpO_2 and ZrO_2 having Zr : Np ratio ranging from 90:10 to 10:90 with a difference of 10 mol% were prepared, by grinding together in agate mortar. These mixtures were heated at 1400°C for 15 h in flowing dry air with intermittent grinding, to get homogeneous products. The products were characterized by X-Ray powder Diffraction (XRD) analysis, using monochromatized Cu K_α radiation ($l = 1.5406$ Å) on a Diano X-Ray diffractometer, enclosed in a glove box, to handle the radioactive materials. It was found that up to 30 mol% of ZrO_2 dissolves in NpO_2 forming a single fcc phase $Zr_yNp_{1-y}O_2$ ($y = 0$ to 0.3) solid solutions. The lattice parameters of fcc phase decrease with increase in zirconium concentration, from 5.434 Å for pure NpO_2 to 5.383 Å for $Zr_{0.3}Np_{0.7}O_2$. On further increase in Zr concentration i.e. for compositions 0.35 £ $y < 0.8$, tetragonal phase of ZrO_2 separated out along with fcc phase giving a mixture of tetragonal (zirconium rich) and cubic (neptunium rich) solid solutions. For $0 < y \leq 0.2$ a single phase tetragonal solid solution was obtained corresponding to tetragonal phase of ZrO_2 containing NpO_2. Fig.1 shows phases formed along with lattice parameters of fcc solid solutions, as a function of mol% of NpO_2.

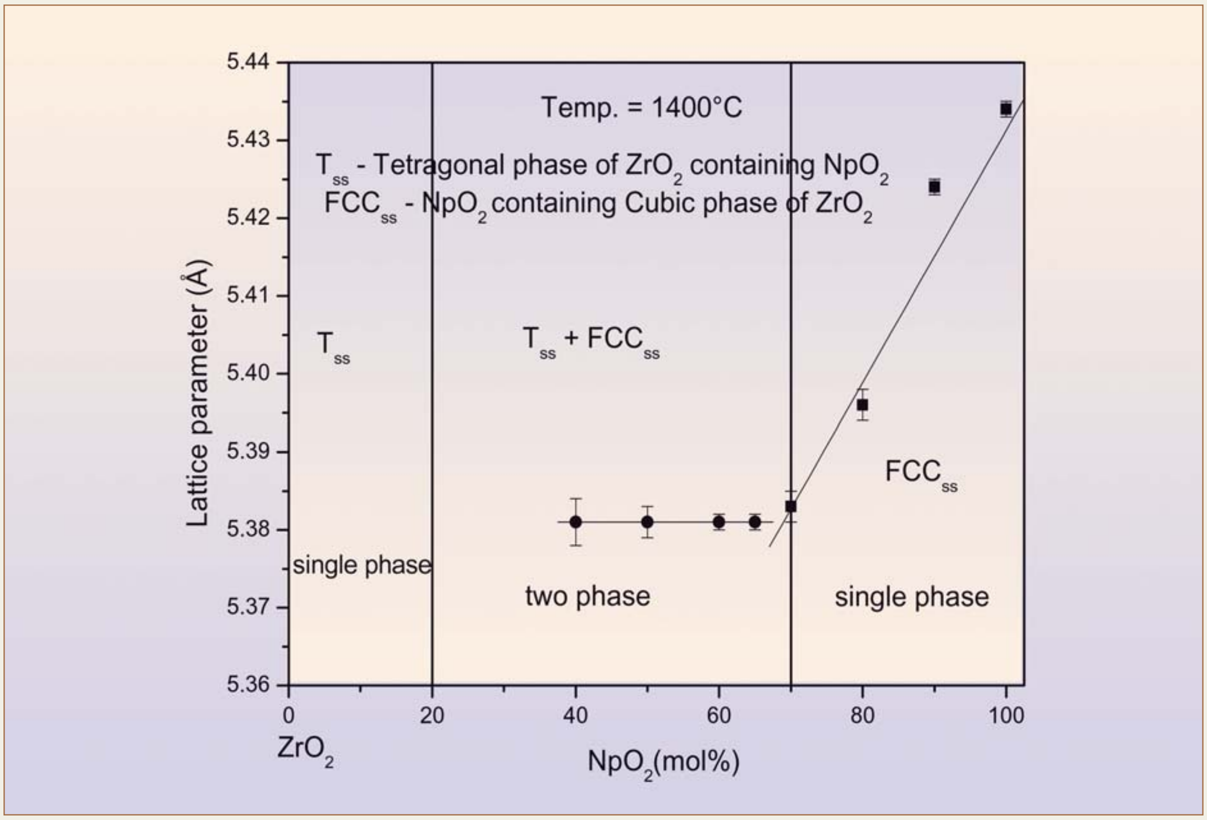

Fig.1: Lattice parameter and extension of solid solutions in $NpO_2 - ZrO_2$ system, 1400°C

ABOUT THE AUTHORS

Dr. N. K. Kulkarni completed his B.Sc. degree from Karnataka University in 1978 and joined Fuel Chemistry Division, BARC in 1981. He obtained his M.Sc. by Research and Ph. D. in Chemistry from Mumbai University in years 1987 and 2002 respectively. He is involved in chemical quality control of nuclear materials. His field of interest is X-ray diffraction and thermal analysis studies of nuclear fuel oxides and different actinide compounds. His other area of interest is fixation of actinides and lanthanides in Zirconia- based ceramic waste forms, their solid solubility and leaching behaviour studies. He has published more than 50 papers in international journals and symposia. He is a member of professional bodies like ITAS and IANCAS.

Dr. S.K. Sali completed his M.Sc. (Physical Chemistry) from Pune University and joined the Fuel Chemistry Division, BARC in 1983. He obtained his Ph.D. from Mumbai University in 1997. He is actively involved in chemical quality control of nuclear fuels. His main areas of research are thermochemical investigations of actinide compounds by X-ray and thermal methods. He has more than 65 publications in international journals and national symposia.

ABOUT THE AUTHORS

Dr. Dilip Ganpatrao Phal joined BARC in 1981 after doing research in Forensic Science Laboratory for three years. He obtained his Ph.D. (Chemistry) in 1992 from University of Mumbai. He has worked extensively on the use of different ion exchange resins for the separation and purification of Plutonium from Americium and Uranium, subsequently this was used for the laboratory processing of plutonium from (I) Oxalate supernatant and (ii) High concentration of Uranium. Large volumes of the above solution were processed. Dr. Phal has extensively studied extraction of Pu (IV) and U (IV) by di-2-ethyl-hexyl phosphoric acid as a function of acidic extractant, neutral donors, diluents and acids. Dr Phal has developed number of methods for Processing and Purification of Plutonium from (a) MOX (UO_2+PuO_2) powder fuel samples. (b) Highly sintered PuO_2 powder. (c) Magnesium crucible slag. (d) Plutonium alloy by (i) wet route and (ii) dry route and (e) Recovery of Americium. He has made significant contribution in setting up a NUMAC Control Laboratory which involves analysis of U and Pu in nuclear materials like UO_2 and (U, Pu)O_2 , Enriched U-alloy, U metal powder, EADU, Enriched UO_3 , Enriched U_3O_8 and Enriched Uranium nitrate solution.

TEMPERATURE PROGRAMMED REDUCTION OF IN$_{2(1-X)}$ NI$_{2X}$TIO$_{5-\delta}$ OXIDES

A. M. Banerjee, M. R. Pai and S. R. Bharadwaj
Chemistry Division

This paper was awarded the Best Paper award (Second Prize) in the Oral Presentation Category at the 16th National Symposium & Workshop on Thermal Analysis, held at Kalpakkam, from Feb. 4-8, 2008.

Abstract

The reduction behaviour of mixed metal oxides with nominal compositions of In$_{2(1-x)}$Ni$_{2x}$TiO$_{5-\delta}$, where 0.0 £ x £ 0.2, has been investigated as a function of the value of x. These compositions were synthesized by ceramic route and characterized using powder X-ray diffraction and Infrared spectroscopic techniques. The In$_{2(1-x)}$Ni$_{2x}$TiO$_{5-\delta}$ samples were single-phased samples, isomorphic with In$_2$TiO$_5$ phase upto 10% Ni content. A secondary phase, identified to be Ni$_{0.75}$Ti$_{0.125}$O phase, was present along with the major phase of indium titanate in In$_{1.7}$Ni$_{0.3}$TiO$_{5-\delta}$ and In$_{1.6}$Ni$_{0.4}$TiO$_{5-\delta}$ samples. Ni substitution at In^{3+} site, induced ease in reducibility, as indicated by lowering of T$_{max}$ and onset reduction temperature in substituted samples, as compared to the In$_2$TiO$_5$ phase. Ni facilitated the reduction of Ti^{4+} in Ni$_{0.75}$Ti$_{0.125}$O to Ni-Ti phase, as indicated by the XRD reflections in the reduced In$_{1.8}$Ni$_{0.2}$TiO$_{5-\delta}$ sample.

Introduction

In view of global energy and environmental issues, photocatalytic water splitting to produce clean energy carrier H$_2$, has been widely regarded as one of the ideal solar energy conversion methods [1]. Much effort has been made to develop the single phased photocatalysts for efficient water splitting. To our knowledge, however, the number of single phased photocatalysts capable of stoichiometric water splitting, especially under visible light irradiation, is still very limited so far [2]. Uptill now, various kinds of indates such as In$_2$O$_3$(ZnO)m [3], MIn$_2$O$_4$ (M=Ca, Sr, Ba) [4], LnInO$_3$ (Ln=La, Nd) and Sr$_{1-x}$M$_x$In$_2$O$_4$ (M=Ca, Ba), [5] have been reported as photocatalysts for water splitting. However, the activities of the aforementioned In^{3+} containing photocatalysts are usually low under visible light irradiation, due to the relatively large band gaps.

Earlier, we have reported the thermal/chemical stability, redox behaviour and catalytic properties of Th(VO$_3$)$_4$ and LaMnO$_3$ oxides, as a function of multiple cationic substitutions, at both A and B sites [6-9]. With the objective to study the thermal and reduction behaviours of certain titania-based single phased compositions, which can serve as prospective photocatalysts particularly for water splitting reactions, studies have been recently taken up in our laboratories on In$_2$O$_3$-TiO$_2$ system, resulting in formation of indium titanate, In$_2$TiO$_5$.An aliovalent substitution by M^{3+} cation [M = Fe^{3+} (0.64 Å), Cr^{3+} (0.63 Å)] at B-cation site, in In$_2$TiO$_5$ was attempted, introducing thereby some micro-structural changes in their lattice.

It is therefore apparent, that the substitution of a lower-valent ion in place of smaller Ti^{4+} (ionic radius = 0.68 Å), is likely to form an anion deficient solid solution with partial loss of oxygen in the lattice (δ). Recently, we studied the effect of B-Site substitution on thermal properties and reduction behaviour of In_2TiO_5, viz., $In_2Ti_{1-x}Fe_xO_{5-\delta}$, $In_2Ti_{1-x}Cr_xO_{5-\delta}$, $(0.0 \le x \le 0.02)$ mixed oxide catalysts [10]. In the present study, we report the A-site substitution-induced effects on indium titanate. For this purpose, $In_{2(1-x)}Ni_{2x}TiO_{5-\delta}$, $(0.0 \le x \le 0.02)$ mixed oxide catalysts were synthesized using solid-state reaction and characterized by powder X-Ray Diffraction (XRD). The thermal and reduction behaviours were studied by recording ThermoGravimetric, Differential Thermal Analysis (TG/DTA) and Temperature-Programmed Reduction (TPR) profiles.

Experimental

Mixed oxides with nominal composition, $In_{2(1-x)}Ni_{2x}TiO_{5-\delta}$, for $0.0 \le x \le 0.2$, were synthesized through ceramic route, by mixing reactant oxides in appropriate stoichiometry and calcining at 1200°C. The powder XRD patterns were recorded on a Philips X-ray diffractometer (model PW 1710), equipped with a graphite monochromator and Ni-filtered Cu-Kα radiation. The thermal behaviour of these samples (~ 20 mg) was monitored by recording their simultaneous DTA/TG profiles both in air and $5\%H_2+Ar$ atmospheres, in the temperature range of 25-1000°C at a heating rate of 10°C min^{-1}.

TPR run was recorded on a TPDRO-1100 analyzer (ThermoQuest, Italy) under the flow of H_2 (5%) + Ar at a gas flow rate of 20 ml min^{-1}, in the temperature range of 25-1000°C, at a heating rate of 6°C min^{-1}. The samples were pretreated at 350°C for about 2.5 h in helium, prior to recording of the first TPR run.

Results and Discussion

X-Ray Diffraction (XRD)

Fig. 1 shows the powder XRD patterns of In_2TiO_5 and corresponding patterns observed due to aliovalent substitution of Ni^{2+} in place of In^{3+} at A-site. The lines due to reactant oxides are missing in these patterns thus confirming the completion of the solid-state reaction. The XRD patterns, of samples with $In_{1.95}Ni_{0.05}TiO_{5-\delta}$, $In_{1.9}Ni_{0.10}TiO_{5-\delta}$ and $In_{1.8}Ni_{0.2}TiO_{5-\delta}$ compositions, match with the XRD pattern of unsubstituted indium titanate sample, as shown in curves b-d of Fig. 1. Thus in these samples,

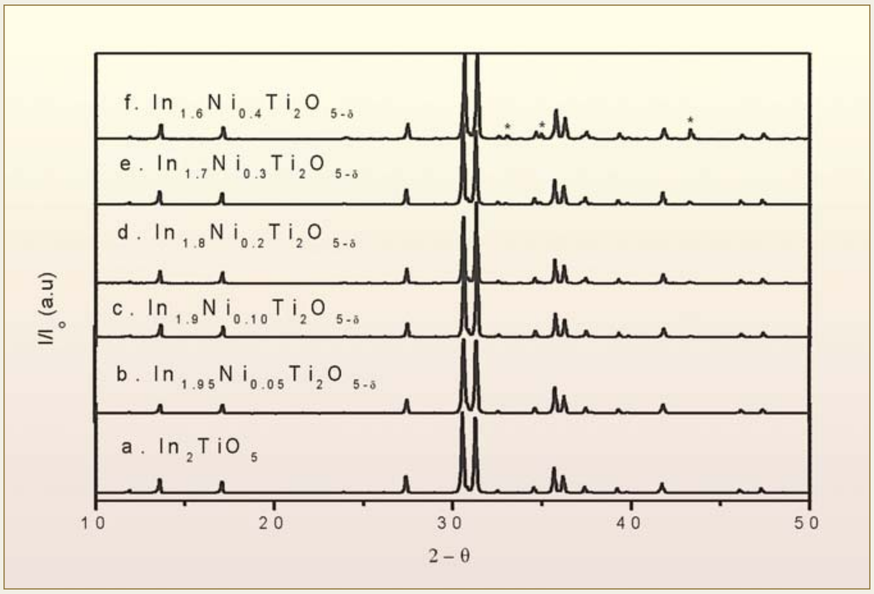

Fig. 1 : XRD patterns of $In_{2(1-x)}Ni_xTiO_{5-\delta}$.

Ni substitution resulted in single phase, due to formation of solid solution of Ni with the lattice of the parent compound, indium titanate. However, for samples having Ni content higher than 10% some low intensity lines (marked with *) in addition to parent phase were also observed (Fig. 1e and f). These weak lines present at $2\theta = 43.33°$, $35.71°$ and $63.02°$ are attributed to the formation of secondary phase in the samples having compositions of $In_{1.7}Ni_{0.3}TiO_{5-\delta}$ and $In_{1.6}Ni_{0.4}TiO_{5-\delta}$. The secondary phase was identified to be $Ni_{0.75}Ti_{0.125}O$ (JC-PDS card No. 31-0916).

Temperature Programmed Reduction behaviour (TPR)

The typical first Temperature Programmed Reduction cycle (TPR) of substituted samples and unsubstituted sample, are shown in Fig. 2. The TPR profile of unsubstituted In_2TiO_5 sample as seen in curve 'a' comprises a prominent band starting at ~600°C and extending beyond 1000°C. This indicated the predominant reduction of one of the species, identified to be In^{3+}, in the temperature range of 600-1100°C, over other reducible species in In_2TiO_5 sample. The temperature maximum (T_m) of the reduction bands corresponds to ~1070°C. However, Ni^{2+} substitution at In^{3+} site, has induced considerable changes in the reduction profile of indium titanate. In case of compositions having higher content of Ni, viz., $In_{1.8}Ni_{0.2}TiO_{5-\delta}$ and $In_{1.6}Ni_{0.4}TiO_{5-\delta}$, TPR profiles (Fig. 2c-d), exhibit two-three weak bands in low temperature range of 450-800°C in addition to main reduction band. The presence of these bands is attributed to reduction of $Ni^{2+} \rightarrow Ni^0$ along with reduction of In^{3+}. At the same time, the T_{max} of the individual peaks was found to be lower in the case of substituted samples. For instance, we observe the lowering of T_{max} around by 80°C in Fig. 2d, as compared to the TPR profile of an unsubstituted phase (Fig. 2a). Also the onset reduction temperature of 625°C in unsubstituted phase has considerably decreased by mere 20% Ni substitution as shown in Fig. 2d. The TPR profile as a whole has shifted to lower temperature as a result of Ni substitution. These results are comparable to our earlier work [10] where Fe and Cr were substituted at B-site. Thus, M (Ni^{2+}, Cr^{3+} and Fe^{3+}) substitution has undoubtedly facilitated the reduction of In_2TiO_5 phase. These changes in the TPR profiles, can be ascribed to the nonstoichiometry and imperfections, generated in the single phased compositions, as a result of A and B-site substitution.

XRD patterns of spent $In_{1.8}Ni_{0.2}TiO_{5-\delta}$ sample, obtained after recording TPR, shows the presence of prominent lines at $2\theta = 33.01°$, $39.0°$, $54.00°$ which conform to reported pattern of In^0 (JC-PDS No.5-642). Other strong lines at 27.44°, 36.08° and 54.32°, match well with rutile TiO_2 phase (JC-PDS No.21-1276). Remaining lines in the residue were at $2\theta = 41.27°$, $43.38°$, $44.23°$, $39.2°$. These lines do not match with the reported XRD pattern of Ni metal alone (JC-PDS. No. 04-0850). However, an alloy formation of Ni-Ti is indicated by these lines, according to JC-PDS card No. 35-1281. This is a very interesting observation as Ti^{4+} is otherwise stable towards reduction, but Ni facilitated its reduction upto 1100°C. The formation of Ni-Ti alloy on reduction of $In_{1.8}Ni_{0.2}TiO_{5-\delta}$ sample is quite plausible, as revealed by the XRD pattern, a secondary phase of $Ni_{0.75}Ti_{0.125}O$, which segregated out in the fresh $In_{1.8}Ni_{0.2}TiO_{5-\delta}$ sample along with major indium titanate phase. This new phase possibly would have facilitated the reduction of titanium along with reduction of nickel. This also suggests that the extent of reduction of Ti and subsequent alloy formation, would depend on the content of secondary phase. Thus TPR results in conjunction with XRD studies, reveal the reduction of $In^{3+} \rightarrow In^0$, while Ni^{2+} facilitated the reduction of non-reducible cation Ti^{4+} and resulted in formation of Ni-Ti alloy.

Thermo-Gravimetric, Differential Thermal Analysis (TG/DTA)

Both substituted and unsubstituted samples did not show any weight loss in TG, thus indicating that all substituted $In_{2(1-x)}Ni_{2x}TiO_{5-\delta}$ oxide samples are stable in air upto 1000°C. However, in H_2+Ar atmosphere, corresponding TG plots exhibited substantial weight loss of all samples. The weight loss in TG plot starts above ~490°C and continues upto ~1050°C in

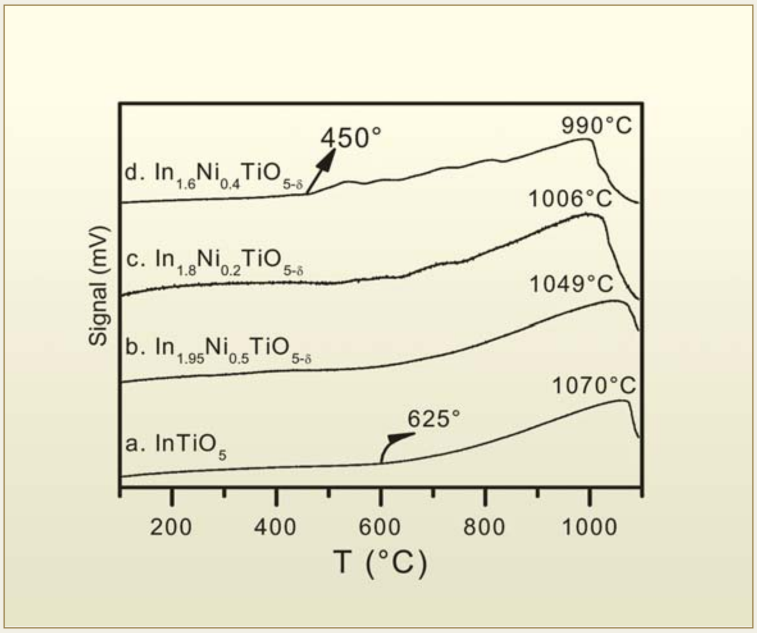

Fig. 2 : First TPR cycle of $In_{2(1-x)}Ni_xTiO_{5-\delta,}$

Ni-substituted samples. As revealed by temperature programmed reduction profiles (Fig. 2) of these oxides, we can infer that this weight loss is due to reduction of these oxides in H_2 atmosphere. Mainly the weight loss is attributed to reduction of species, In^{3+} and Ni^{2+}, to In^0 and Ni^0 respectively. The evidence of the above inference comes from temperature programmed reduction profiles of In_2O_3 and TiO_2 oxides. Their TPR profiles recorded in the range of 25-1000°C under H_2 flow (5% H_2 in Ar) suggest, that In_2O_3 gives single prominent reduction band with T_{max} at 670°C, whereas TiO_2 gives a very weak profile upto 1000°C. The presence of lines due to In^0 in the XRD pattern of residue sample obtained after recording TG, confirms the above result.

Conclusions

A-site substitution by a divalent Ni^{2+} cation at In^{3+} site, resulted in single phase compositions suggesting formation of solid solution of Ni in the lattice of the parent compound, indium titanate. However, for samples having Ni content higher than 10% in indium titanate, it resulted in the segregation of secondary phase, $Ni_{0.75}Ti_{0.125}O$ along with major phase of indium titanate, In_2TiO_5. The secondary phase, identified to be $Ni_{0.75}Ti_{0.125}O$, was present in the samples having compositions of $In_{1.7}Ni_{0.3}TiO_{5-\delta}$ and $In_{1.6}Ni_{0.4}TiO_{5-\delta}$. The temperature programmed reduction and XRD studies establish reduction of In^{3+} and Ni^{2+} to In^0 and Ni^0 metal in the temperature range of 450-1050°C. Ni substitution induced considerable ease in reducibility (T_{max}) of substituted samples as compared to In_2TiO_5 phase. Presence of Ni-Ti alloy is indicated in the reduced $In_{1.6}Ni_{0.4}TiO_{5-\delta}$ sample. The substitution-induced non-stoichiometry and the microstrucural defects, may cause distortion in the lattice, thus facilitating the reduction of oxides.

References

1. A Fujushima and K. Honda, *Nature,* 238 (1972) 37.
2. Z. Zou.; J. Ye, K. Sayama and H. Arakawa, *Nature,* 414 (2001) 6254.
3. A. Kudo and I. Mikami, *Chem. Lett.*, 27 (1998) 1027.
4. J. Sato, S. Saito, H. Nishiyama and Y. Inoue, *J. Phys. Chem.*, 105 (2001) 6061.
5. J. Sato, S. Saito, H. Nishiyama and Y. Inoue, *J. Phys. Chem.*, 107 (2003) 7975.
6. M. R. Pai, B. N. Wani, A. D. Belapurkar and N. M. Gupta, *J. Molec. Catal.* A, 223 (2004) 275.
7. M. R. Pai, B. N. Wani, and N. M. Gupta, *Thermochim. Acta,* 425 (2005) 109.
8. M. R. Pai, B. N. Wani, B. Shreedhar, S. Singh and N. M. Gupta, *J. Molec. Catal. A*, 246 (2006) 128.
9. M. R. Pai, B. N. Wani and N. M. Gupta, *J. Mater. Sci. Lett.*, 21 (2002) 1187.

10. A. M. Banerjee, M. R. Pai, K. Bhattacharya, A. K. Tripathi, V. S. Kamble, S. R. Bharadwaj and S. K. Kulshreshtha, *Internatl. J. Hydrogen Energy,* (Article in press).

11. M. R. Pai, A. M. Banerjee, S. R. Bharadwaj and S. K. Kulshreshtha, *J. Mater. Res.,* 22 (2007) 1787.

ABOUT THE AUTHORS

Mr. Atindra Mohan Banerjee completed his Master of Science in Chemistry from Calcutta University in 2004. He completed a one year Orientation Course in Nuclear Science and Engeneering from BARC Training School (OCES - 48 batch). Subsequently he joined the Chemistry Division of BARC, Mumbai in Sept. 2005. He is involved in the development of catalyst for sulphuric acid decomposition reaction in thermochemical cycle for hydrogen generation by water splitting and photocatalytic water splitting. He has 2 publications in International journals and 6 publications in Symposia/conferences. He is a recipient of the Best Paper Award conferred during ISMC-2006 for the paper titled " Studies for S-I Thermochemical Cycle for Hydrogen production".

Dr. (Ms.) Mrinal R. Pai joined BARC through Training School (40th Batch) after completing her Post graduation in Chemistry from IIT Delhi in 1996. She initiated her research activities in the field of catalysis with development of H_2 mitigation catalyst during year 1999 in Chemistry Division. She was awarded Ph.D degree in Physical Chemistry from Mumbai University in year 2005. Also, she gained experience in synthesizing fine powders of nano-size oxides/mixed oxides with spinels, perovskites and pyrochlore structures and characterizing them by various techniques for their prospective applications in pollution abatement, water splitting by photocatalysis and sulfuric acid decomposition reaction in S-I thermochemical cycle. There are sixteen publications in refereed international journals, several publications in symposium and conferences and invited talks to her credit.

Dr. Shyamala Bharadwaj obtained her B.Sc. Degree from Mumbai University in the year 1976 and joined the Department of Atomic Energy in the year 1977, after graduating from the 20th Batch of BARC Training School. Later she completed her Masters Degree and obtained Ph.D. in Physical Chemistry from Mumbai University. She has been working in the area of high temperature thermodynamics of nuclear as well as other refractory materials for the past 30 years. During the year 2000-2001, she worked as Guest Scientist at the Juelich Research Centre, Juelich, Germany, where she was involved in the investigations of Solid Oxide Fuel Cell materials. Presently, she is heading the Fuel Cell Materials and Catalysis Section of Chemistry Division, BARC. Her current interests are in the field of Intermediate Temperature Solid Oxide Fuel Cells and generation of hydrogen by water splitting by thermochemical and photocatalytic methods. She has more than 180 publications to her credit, with more than 75 publications in reputed international journals. She is a Ph.D. Guide of Mumbai University. She was the Hon. Treasurer of Indian Thermal Analysis Society (ITAS) during 1996-2000 and is currently the Hon. Secretary of ITAS. She was given NETSH-ITAS Award 2006, for her contribution in the field of thermodynamics and thermal analysis.

STUDIES ON ELECTRICAL PROPERTIES OF PZTs CONTAINING VARYING AMOUNTS OF RARE EARTHS (Ce, Pr AND Nd) BY IMPEDANCE SPECTROSCOPY

R. V. Pai and S.K. Mukerjee
Fuel Chemistry Division

R. Mishra
Chemistry Division

V. Venugopal
Radiochemistry & Isotope Group

This paper won the Best Paper Award (2nd prize) in the Poster Session at the Discussion Meet on Electroanylatical (DM-ELANTE-2008) held at Munnar, Kerala, during February 25-28, 2008

Introduction

Lead Zirconate Titanate (PZT) [1] ceramics have been extensively used for various device applications, because of their excellent dielectric, pyroelectric, piezoelectric and electro-optic properties [2]. Doping of PZT with rare earths in A/B sites (perovskite ABO_3), has shown significant bearing in its dielectric and ferroelectric characteristics [3].

Conventional method of preparing these ceramic materials is through solid-state reactions [4, 5]. But the advantages of solution-based routes lie in the formation of the product at much lower temperatures with larger surface area and better micro homogeneity as compared to solid state route. Lower synthesis temperature prevents volatilization of the component oxide, facilitating fixing of required stoichiometry. This paper presents synthesis of PZT powders containing 5, 10 and 15 mole % Ce, Pr and Nd by Gel-Entrapment Technique [6]. AC Impedance spectroscopy has been utilized, to study the electrical properties such as dielectric properties and electrical conductivity of the samples at different temperatures.

Experimental

The oxides $Pb_{1-x}R_xZr_{0.65}Ti_{0.35}O_3$ where R = Ce, Pr and Nd and x= 0, 0.05, 0.1 and 0.15, were prepared by Gel-Entrapment Technique. The samples were characterized by room temperature XRD, TG-DTA (Setaram, Model 92-16.18) and DSC (Setaram, Model 131) techniques. The samples were pelletized into 10 mm diameter disks of thickness 1.5 mm, at a pressure of 250 MPa and sintered in air at 1000°C for 2 h. The pellets were then polished and coated with thin layer of Pt paste on flat ends and fired to 800°C for 2h to have a better contact with the electrode for measurement of electrical properties.

The electrical properties of the samples were measured using a Solatron AC Frequency Analyzer (Model 1260) in the frequency range 10 MHz to 1 Hz. The impedance spectra were recorded in the temperature interval of 350 to 800°C with the step of 25°C for all the samples. The temperature was controlled by a microprocessor and measured by a K-type thermocouple placed very close to the sample. At each temperature, the samples were equilibrated for 20 min before recording the spectra.

Results and Discussion

The room temperature XRD analysis of the samples indicated that, the materials were single phase with cubic lattice structure, except for Nd containing samples in which some pyrochlore phases were also observed. The cell parameters of the compounds obtained from least square fitting of the XRD data, were found to be in good agreement with the reported values. Fig.1 shows the room temperature XRD patterns of these compounds, calcined at 1073 K. The sharp and singlet pattern indicates better phase purity and crystallinity.

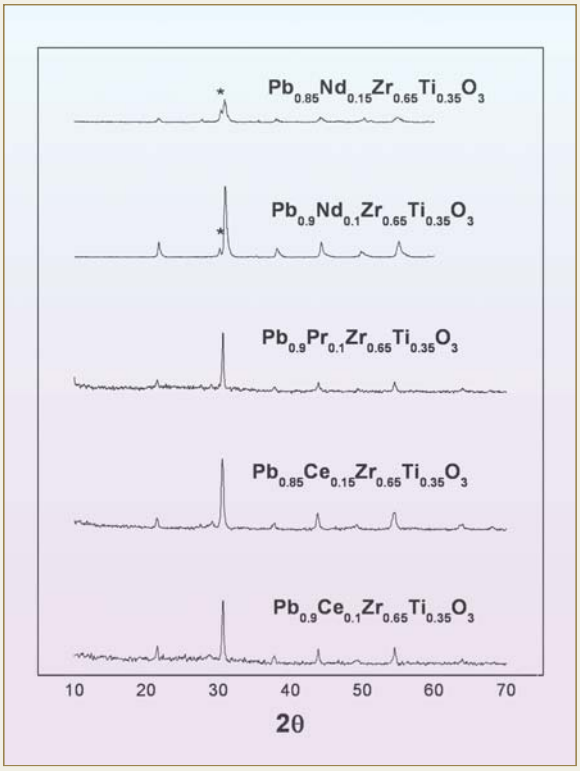

Fig. 1: Room temperature XRD patterns of PZTs doped with Nd, Ce and Pr calcined at 1073 K. (* = pyrochlore phase)

Electrical property measurements by Impedance Spectroscopy

For impedance measurements, the sintered pellets were polished and coated with a thin layer of Ti paste and heated to 1073K for 2 h, to improve contact with the electrode. The electrical properties of the samples were measured using a Solartron AC Frequency Analyzer (Model 1260) in the frequency range 10 MHz – 1 Hz. Fig. 2 gives the Nyquist plot of the compound $Pb_{0.95}Ce_{0.05}Zr_{0.65}Ti_{0.35}O_3$ at various temperatures. The relaxation frequency (f_o) of the material, independently of the geometrical parameter of the sample, was found at the apex of the Nyquist semicircle fulfilling the condition $2pf_oR_bC_b = 1$.

From this relation, the bulk capacitance of the material (C_b), also called the geometric capacitance, can be calculated and the bulk dielectric constant e_b can be determined using $C_b = \varepsilon_b\varepsilon_o .A/l$; where ε_b is the vacuum permittivity.

The semicircular pattern in the impedance spectrum is representative of the electrical processes taking place in the material, which can be expressed as an equivalent electrical circuit comprising of a parallel combination of resistive and capacitive elements. The

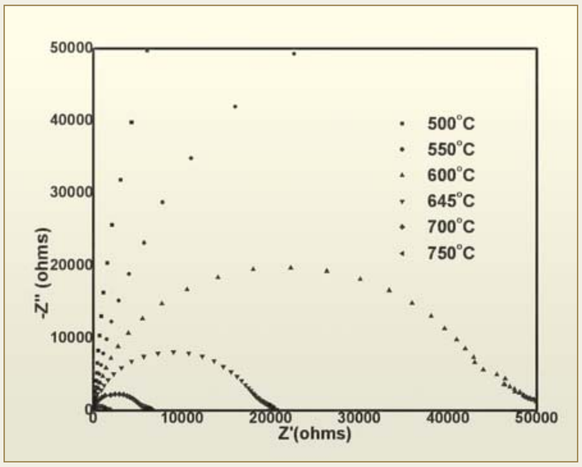

Fig. 2: Nyquist plot of $Pb_{0.95}Ce_{0.05}Zr_{0.65}Ti_{0.35}O_3$ at various temperatures

intercept of the semicircle on the real axis, gives the resistance of the corresponding component contributing towards the impedance of the sample. The graph shows that at lower temperature, the resistance offered for conduction is very high. As temperature increases, the conduction becomes easier. This shows typical semiconductor behaviour in these samples. At lower temperature only conduction through grains prevails where as at higher temperature grain conduction as well as grain boundary conduction is seen. The Nyquist plot for PZT undoped and doped with 5 mole% of Pr, Ce and Nd is presented in Fig. 3. The impedance of the sample decreased with Pr doping whereas the impedance showed increase with doping of Ce and Nd. The large increase of impedance value in the case of Nd containing samples, may be due to the pyrochlore phase present in them.

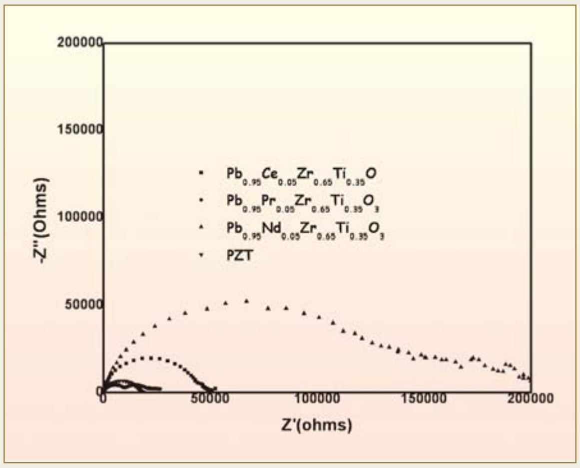

Fig. 3: Nyquist plot of PZT containing 5 mole% of rare earths at 600°C

The frequency (1Hz to 10 MHz) dependent dielectric constants (ε_r) of all the compounds were determined from the capacitance values. Fig. 4 shows the variation of ε_r of $PbZr_{0.65}Ti_{0.35}O_3$ as well as $Pb_{0.9}R_{0.1}Zr_{0.65}Ti_{0.35}O_3$ where R = Ce, Pr and Nd as a function of temperature measured at 1 kHz as well as 10 kHz. It is clear that the ε_r of all the compounds decrease with increase in frequency as the capacitance value of these compounds decreases with increase in frequency. The dielectric constant of these samples increased with increase in temperature as the polarizability of the oxide system increases with temperature. Also, it can be seen from the figure that the e_r increases with Pr doping in the parent PZT sample, whereas the ε_r value remarkably decreases with Ce as well as Nd doping. The sample $Pb_{0.9}Pr_{0.1}Zr_{0.65}Ti_{0.35}O_3$ showed ε_r of ~22489 at 710°C, measured at 1 KHz. The undoped samples (PZT) showed a ε_r of ~ 19600 at this temperature, whereas the ε_r for Ce and Nd containing samples showed ε_r values of 5232 and 3002 respectively. Further the dielectric constants of Ce and Nd doped samples were found to decrease with increase in dopant concentration. Qi-Yue Shao et al

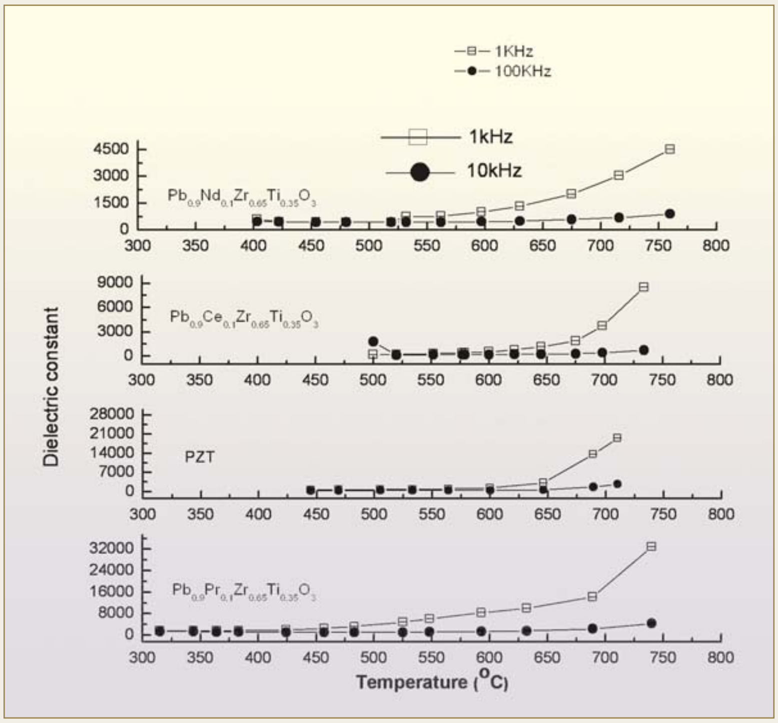

Fig. 4: Variation of ε_r of $PbZr_{0.65}Ti_{0.35}O_3$ as well as $Pb_{0.9}R_{0.1}Zr_{0.65}Ti_{0.35}O_3$ where R = Ce, Pr and Nd as a function of temperature measured at 1 kHz as well as 10 kHz

[7] also reported that the dielectric constant of PZT thin films decreased when the film was doped with Ce. The authors attributed this behaviour to the presence of pyrochlore phase in Ce containing thin films. But in the present study, pyrochlore phase was not observed in the Ce containing samples even for 15 mole% of Ce. Ce has almost equal probability to either replace Pb^{2+} at *A* site or Zr^{4+}/Ti^{4+} ions at *B* sites of ABO_3 perovskite lattice. This is feasible, as Ce can exist both in tri and tetra valence states and can replace Pb^{2+} ($rCe^{3+}=1.43$ Å and $rPb^{2+}=1.63$ Å) or Zr^{4+} ($rCe^{4+}=0.86$ Å and $rZr^{4+}=0.73$ Å), respectively. It is reported in the literature [8] that tendency of Ce to occupy A site (as Ce^{3+}) is more if the Ce ion concentration is less than 1 mole% and beyond 1 mole%, both *A* as well as *B* sites can be occupied by Ce equally (Ce^{3+} in *A* site and Ce^{4+} in *B* site). They further reported that the samples containing Ce in the *A* sites (3+ oxidation state) improve the electrical properties. Similarly, in the present study, 5 to 15 mole % of Ce containing samples, may be occupying a large proportion of *B* sites in the ABO_3 system which might be responsible for the decreased e_r value in the Ce containing PZT. Even though Pr also exhibits tri and tetra oxidation states, tri oxidation state is more stable than tetra oxidation states, whereas in the case of Ce ion, extra stability would be attained by Ce^{4+} ion because of noble gas electronic configuration by removal of 4 electrons. Hence Pr occupancy in *B* sites in place of Zr^{4+}/Ti^{4+} is small and high value of e_r was observed in the present study. Since *A* site substitution can reduce oxygen vacancies by forming *A* site vacancy–oxygen vacancy defect dipoles, increase electric displacements thus increasing the dielectric constant. The donor dopants have been reported to improve the dielectric and ferroelectric properties of PZT thin films [9, 10]. Considering the ionic radius of Nd^{3+} (1.0 Å) the *B* site occupancy by Nd should be the minimum. But in our study, the addition of Nd in PZT reduces the dielectric constant. This may be due to the presence of pyrochlore phase in the Nd containing samples. During sintering, pyrochlore forms usually as a transient phase before the PZT formation. The pyrochlore phase is oxygen deficient and so it is a metastable transient phase [11]. Thus, in the Non crystallite PZTs, the presence of impurity phases such as pyrochlore, play an important role in deciding the dielectric constant.

The DC conductivity of the samples was calculated using the relation, $\sigma = 1/R^*(l/A)$, where R is the electrical resistance, is the thickness of the sample and A the area of cross section of the sample. The activation energy, E_a, for all the samples was calculated from the plot of ln (σT) versus 1/T using the conductivity relation $\sigma T = \sigma_0 \exp(^-E_a/(K_B T))$, where σ_0, is the pre-exponential factor, E_a the activation energy and K_B the Boltzmann constant. The DC conductivity increases with increase in temperature. At higher temperature, PZT as well as rare earth doped PZT samples behave as semiconductors and in semiconducting ceramics, free carriers interact with the charged grain boundaries, giving rise to increase in the ionic conductivity. During the course of motion through the solid, the available limited number of mobile carriers get trapped in relatively stable potential wells. Due to a rise in temperature, the donor cations take a major part in the conduction process and the conductivity increases. At 10 mole% and 15 mole% dopant concentration, PCeZT showed maximum conductivity amongst the same class of samples. It was also observed, that in PCeZT samples, the conductivity increases with increase in dopant concentration, whereas for both the Pr and Nd containing samples the conductivity decreases as we increase the dopant concentration. This may be due to the fact that at higher Ce ion concentration, more cationic vacancies are created at *A* site which contributes more towards the conductivity values. The variation of DC conductivity for PZT and $Pb_{0.85}R_{0.15}Zr_{0.65}Ti_{0.35}O_3$ where R = Ce, Pr and Nd with 1/T is given in Fig. 5. The conductivity in Nd doped samples showed a minimum value among all the samples and decreased with dopant ion concentration. The amount of pyrochlore phase in the Nd containing samples increases with increase in Nd concentration and reduces the conductivity of these samples.

Conclusions

PZT containing 5, 10 and 15 mole% of Ce, Pr and Nd were prepared, by a novel solution-based technique. The dielectric constants of PZT decrease with Ce doping, because of the B site occupancy whereas the polarizability of samples increases with Pr doping. The DC conductivity of the samples increases with increase in Ce concentration, which may be due to the cationic vacancy at *A* site created. The pyrochlore phase in Nd doped samples is found to be responsible for lower conductivity as well as lower dielectric constant values.

Acknowledgements

The authors wish to express their sincere thanks to Dr. S.K.Aggarwal, Head, Fuel Chemistry Division for his constant encouragement throughout the course of the work.

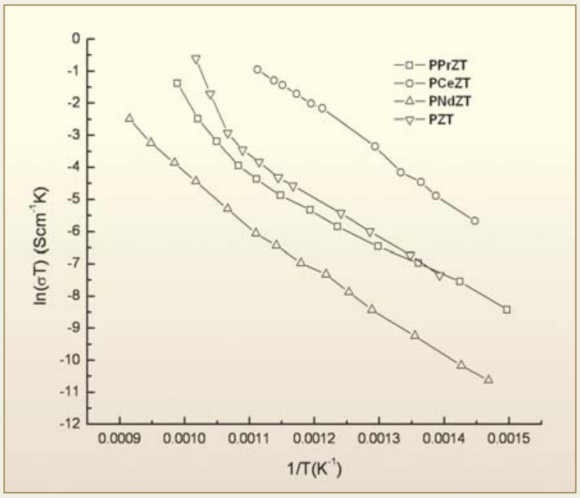

Fig. 5: Variation of DC conductivity for PZT and $Pb_{0.85}R_{0.15}Zr_{0.65}Ti_{0.35}O_3$ where R = Ce, Pr and Nd with 1/T

References

1. J.N. Kim, Michael J. Haun, Sei Jm, L.E. Cross and X.R. Xue. *IEEE Trans. Ultrasonics Ferroelectrics And Frequency Control*. 36 (4) (1989).

2. M.E. Lines, A.M. Glass, *Principles and applications of ferroelectrics and related Materials* Oxford (1979).

3. Ani1 Govindan, H.D. Sharma, A.K. Tripathi, P.K.C. Pillai and T.C. Goel, *Ferroelectrics,* 134 (1992) 217.

4. S.S. Chnadratreya, R.M. Fulrath and J.A. Pask, *J. Am. Ceram. Soc.* 64 (1981) 422.

5. B.V.Hiremath, A.I. Kingon and J.V. Biggers, *J. Am. Ceram. Soc.* 66 (1983) 790.

6. R.V.Kamat, K.T. Pillai, V.N.Vaidya and D.D. Sood , *Material chemi. Phy.* 46 (1996) 67.

7. Qi-Yue Shao, Ai-Dong Li, Yue-Feng Tang, Hui-Qin Ling, Nai-Ben Ming, *Material Chemi.phy,* 75 (2002) 207.

8. S.B. Majumder, D.C. Agrawal, Y.N. Mohapatra, R.S. Katiyar, *Mater. Sci. and EngB,* 98 (2003) 25.

9. S.H. Lee, S.J. Lee, S.H. Kim, B.G. Chae, Y.S. Yang, H.J. Joo, J.P. Kim,W.S. Park, M.S. Jang, *J. Korean Phys. So.* 32(1998) S1670.

10. D.F. Ryder, N.K. Raman, *J. Electron. Mater*. 21 (1992) 971.

11. K.G. Brooks, I.M. Reaney, R. Klissurska, Y. Haung, L. Bursill, N. Setter, *J. Mater. Res*. 9 (1994) 2540.

ABOUT THE AUTHORS

Mr. Rajesh V. Pai joined Fuel Chemistry Division, BARC after graduating from the 40th batch of Training School in the year 1997 after completing his M.Sc. (Applied Chemistry) from Cochin University of Science & Technology. He gained experience in synthesis and characterization of nano-size powders of mixed oxides by various techniques. He is mainly associated with the development of sol-gel process for nuclear materials and high technology ceramics. He is also engaged in the electrical characterization of various ferroelectric and piezoelectric materials by Impedance Spectroscopy.

Dr. S. K. Mukerjee joined Department of Atomic Energy after completing his M.Sc. (Chemistry) from Nagpur University. He has obtained his Ph.D. degree from Mumbai University in the year 1993. Currently he is heading Process Chemistry Section of Fuel Chemistry Division, BARC and is a recognized Ph.D. Guide of Mumbai University and of Homi Bhabha National Institute. His area of interest involves the development of ceramic materials for application of Nuclear Technology. He has extensively studied sol gel processing of nuclear materials for advanced fuel fabrication.

Dr. R. Mishra, Ph.D. (Mumbai University) is working in Chemistry Division, BARC. He specialized in high temperature chemistry and chemical thermodynamics. He derived thermodynamic data on several nuclear materials and intermetallic compounds, phase diagram studies of binary and ternary oxide systems. He was awarded the TA instrument-ITAS Young Scientist Award-2004 and Alexander von Humboldt Fellowship for post-doctoral studies in the University of Munich, Germany.

Dr. V. Venugopal is the Director, Radiochemistry & Isotope Group, BARC. He is a specialist in the field of high temperature thermodynamics and chemical quality control of Pu based fuels. He has worked at Nuclear Research Centre, Julich on the development of Nickel-based binary super alloys required for Rocket Jet Nozzle and turbine blades and also on the development of high intensity metal halide vapour lamps at high temperature. He has been honoured with NETZSCH-ITAS and ISCAS for his outstanding contributions in the field of thermal science and solid state chemistry respectively.

STUDIES ON SQUARE WAVE ANODIC STRIPPING VOLTAMMETRY FOR DETERMINATION OF TRACE LEVELS OF GALLIUM EMPLOYING BI-FILM ELECTRODE

J.V. Kamat, N. Gopinath, H.S. Sharma and S.K. Aggarwal
Fuel Chemistry Division

> This paper was conferred the Best Paper Award (2^{nd} prize) in the Poster Session at the Discussion meet on Electronalytical Technologies DM-ELANTE-2008 at Munnar, Kerala, held during February 25-28, 2008

Introduction

Anodic Stripping Voltammetry is an established electrochemical method and has been exploited in the past, for estimation of metallic impurities at trace as well as sub trace levels, employing mercury-drop electrode [1,2]. However, because of the toxicity of mercury, alternative electrode material, such as Bi-film is being explored, for trace determination. Recently, Wang et al have adopted Bi-film electrode for electroanalytical determination of trace metals [3]. Bi-films can be formed on different carbonaceous substrates such as carbon fibers [4, 5], printed inks [6], carbon paste [7] or glassy carbon [8]. In this communication, we present Square Wave Anodic Stripping Voltammetric (SWASV) studies, on the determination of Gallium at microgram levels, employing Bi-Film on Gc electrode in acetate buffer.

Experimental

All voltammetric experiments were performed with Autolab PGSTAT30 / General-Purpose Electrochemical System. A three electrode voltammetric cell having a GC disc of 3 mm diameter as the working electrode, GC rod as a counter electrode and Ag/AgCl (3M NaCl) as reference electrode was employed and 10 mL of acetate buffer (pH = 4 .6) was used, as a supporting electrolyte in the present studies. The GC working electrode was polished with 0.05 mM alumina slurry on a felt pad, prior to each new set of SWASV experiment. The standard gallium stock solution was prepared, by dissolving high purity gallium metal in AR grade concentrated HCl, under reflux conditions and stocked in a standard glass flask. The test solutions were prepared from this standard Ga solution prior to carrying out SWASV experiments.

Preparation of Bi-film on GC surface

Bi-film on polished GC electrode was prepared by electrodeposition of Bi at -1.1 V from 1mM Bi (III) solution in acetate buffer under stirring conditions. The deposited bismuth was then stripped by sweeping the potential of the electrode from -1.1V to + 0.4V and a stripping peak of Bi was observed at –0.028 V. On the basis of these investigations, a conditioning potential of +0.4V was applied to remove Bi-film from GC surface, prior to each new SWASV experiment.

Results and Discussion

In situ deposition of the Bi film and Ga was carried out on the GC surface, by spiking the acetate buffer with $1\mu g$ of Bi (III) and $0.8\ \mu g$ of Ga. The stripping voltammogram was recorded by scanning the electrode between -1.1V and -0.5V, applying square wave waveform which resulted in the sharp undistorted stripping peak of Ga at -0.9V. Further studies were carried out to optimize experimental parameters, conditioning time (T_c), deposition potential (E_d), deposition time (T_d), SW frequency and SW amplitude. Renewal of GC surface is an essential requirement for obtaining reproducible values of peak current. SWASV experiments were therefore carried out, to optimize the conditioning time for the removal of the Bi-film and target metal from GC surface. It is obvious from Fig.1, that 120 s of conditioning time, is optimum for the removal of the film. Next experiments were performed by varying deposition potential from -1.0 V to -1.5 V. In Fig. 2 SWASV peak current of Ga is plotted as a function of deposition potential. It is seen from the figure, that peak current Ip_a increases initially with $E_{d,}$ up to -1.1 V and then levels off at higher values of E_d. This shows that a deposition potential of -1.1 V is most optimum for preconcentration of gallium. In Fig. 3, effect of deposition time (T_d) on the SWASV peak current is presented. It can be seen that peak current, increases linearly with deposition time from 60 s to 180 s and at higher T_d, Ip levels off. This shows, that deposition time of 180 s is optimum. In the next course of investigation, the effect of SW modulation amplitude (DE) on Ip was studied and the results are presented in Fig. 4. It is seen from the figure, that Ip attains a maximum value at 60 mV amplitude, which is optimum for further studies. On the basis of above mentioned studies, further SWASV experiments were carried out with the optimized parameters; Ed -1.1V, T_c 120 s, T_d 180 s, SW frequency 25 Hz, SW amplitude 60 mV.

Validation of optimized experimental parameters was evaluated, by performing ten individual SWASV experiments at 1mg level of Ga. The relative standard deviation was found to be better than

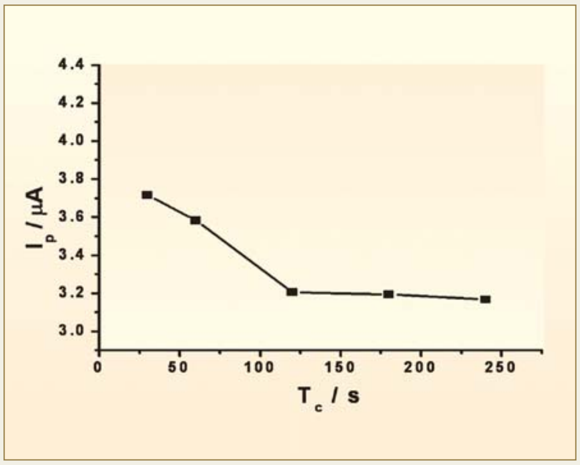

Fig.1: SWASV peak current (I_p) as a function of conditioning time (T_c) for the removal of Bi-film from GC surface at the conditioning potential +0.4 V

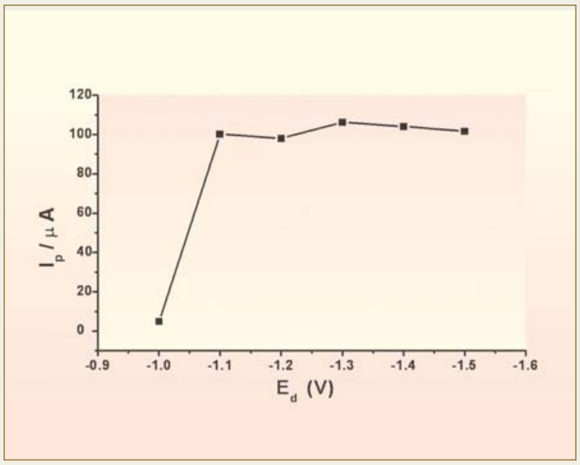

Fig.2: Ip as a function of deposition potential (E_d). Test solution 1µM Ga, deposition time 180 s, equilibration period 30 s, SW frequency 25 Hz, SW modulation amplitude 60 mV, step potential 5mV, scan potential range –1.1V to - 0.5V.

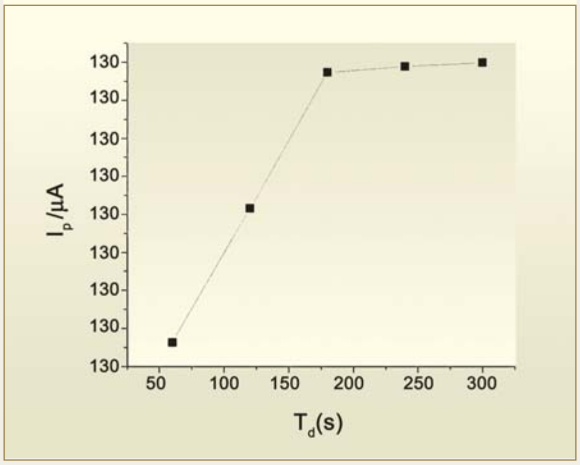

Fig. 3: Ip $_{as}$ a function of deposition time (T_d), under the experimental conditions as shown in Fig. 2 and deposition potential of -1.1V.

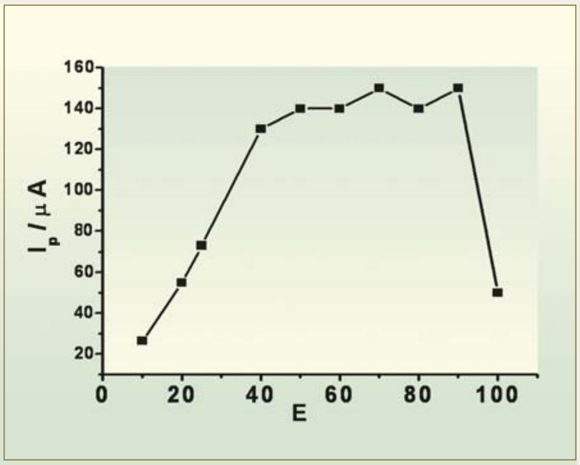

Fig. 4: I_p as a function of SW amplitude (ÄE) under the experimental conditions shown in Fig.3

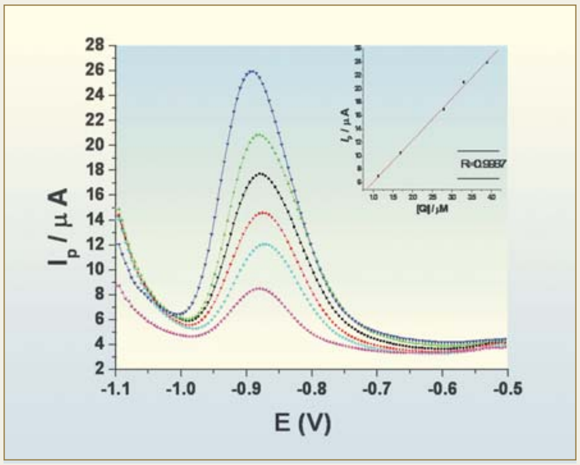

Fig. 5: I_p as a function of Ga concentration in 1μM - 4μM range in acetate buffer, also shown (inset) SWASV for increasing concentration of Ga . Other conditions, as in Fig.3

2%. The proportionality between I_p and concentration of Ga in 1 μM to 4 μM range was verified. Ip was observed to increase linearly with Ga concentration, as shown in Fig. 5 and a correlation coefficient of 0.998 was obtained. A few determinations of Ga at 0.2mg level were carried out by standard addition approach and the results obtained are encouraging. Further work on the determination of gallium at μM concentration of gallium and interference of zinc in gallium determination are being pursued.

Conclusion

SWASV studies, carried out employing Bi-film electrode will be useful for gallium determination at sub microgram level.

References

1. J.V. Kamat, N. Gopinath and S.K. Aggarwal, Nuclear and Radiochemistry Symposium, Amritsar, India (2005) 507.
2. T.K. Bhardwaj, H. S. Sharma and S.K. Aggarwal, *J. Nucl. Materials* 360 (2007) 215.
3. J. Wang, J. M. Lu, S.B. Hocevar, P.A.M. Farias, B.Ogorevc, *Anal. Chem*. 72 (2000) 3218.
4. E.A.Hutton, S.B.Hocevar, B. Ogorevc, *Anal. Chem. Acta* 537 (2005) 285.
5. M.A. Baldo, S.Daniele, C.Bragato, *J. Phys. IV* 107 (2003) 103.
6. J. Wang, J.M.Lu, S.B.Hocevar, B.Ogorevc, *Electroanalysis* 13 (2001) 13.
7. S.A.A. Elsuccary, I. Svancara, R. Metelka, L. Baldrianova, M.E.M. Hassouna, K.Vytras, Sci. Pap. Univ. Pardubice, Ser. A-9 (2003) 5.
8. S.B. Hocevar, B.Ogorevc, J.Wang, B.Pihlar, *Electroanalysis* 14 (2002) 1707.

ABOUT THE AUTHORS

Dr. J. V. Kamat obtained her M. Sc. Degree from Mumbai University. She joined BARC in 1982. After joining, she obtained her Ph. D. (Chemistry) from Mumbai University. Her main field of research is electroanalytical chemistry of actinides. She is involved in developing and employing various Electroanalytical Techniques for different applications in the nuclear fuel cycle. She is the Treasurer of the Indian Society for ElectroAnalytical Chemistry (ISEAC).

Mr. N. Gopinath received M.Sc. degree from Sri Venkateswara University, Tirupati in 1973. He joined Radiochemistry Division, BARC in 1977. Presently he is working in Fuel Chemistry Division, BARC. Since he joined BARC, he has been actively involved in the field of quality assurance of nuclear fuel materials and has developed new electroanalytical methodologies for determination of nuclear fuel materials. He has authored a good number of research papers in the field of electroanalytical chemistry of nuclear materials. Presently he is involved in the studies on exploitation of the significant electro catalytic properties of nanomaterials for analytical purposes. He is the Secretary of the Indian Society for ElectroAnalytical Chemistry (ISEAC).

Dr. H.S. Sharma joined Radiochemistry Division, BARC in 1978, after completing D.Phil. from University of Allahabad and is presently Head, Electrochemistry Section, Fuel Chemistry Division, BARC. His major fields of interest include development of analytical methodologies for precise and accurate determination of actinides in nuclear fuel materials and electrochemical synthesis of conducting-polymers and nano-scale materials and their characterization employing spectroscopic and microscopic techniques. He has contributed significantly to the development of coulometric method for precise and accurate determination of U and Pu in nuclear fuel materials. He has introduced voltammetric and Electrochemical Quartz Crystal Microbalance techniques in electrochemical research. Dr. Sharma was recently awarded Prof. S. S. Sandhu Award (2007- 2008) by the Indian Chemical Society, for his outstanding contribution in Electrical Research.

Dr. S.K. Aggarwal is Head, Fuel Chemistry Division, BARC since July 2005 and is also a Professor of Chemistry at the Homi Bhabha National Institute (HBNI). He joined the 16th Batch of BARC Training School in 1972 and received the Homi Bhabha Award. He did his Ph.D. from Mumbai University and his post-doctoral training at University of Virginia, USA. Dr. Aggarwal was honoured with the Eminent Mass Spectrometrist Award by the Indian Society for Mass Spectrometry (ISMAS) in 1996 and was recently conferred with the DAE Special Contributions award 2006. He is a specialist in the field of atomic mass spectrometry and alpha spectrometry and is interested in various mass spectrometric techniques. His other areas of interest include laser-based analytical techniques, Electrochemistry, X-ray spectroscopy and Separation techniques like HPLC, solvent extraction etc. He has more than 100 publications in reputed International Journals and is a recognized Ph.D. Guide of the Mumbai University and of HBNI.

DEVELOPMENT OF A HIGH TEMPERATURE OXYGEN SENSOR FOR LEAD BISMUTH EUTECTIC

A. Borgohain, N.K. Maheshwari, P.K. Vijayan, D. Saha and R.K. Sinha
Reactor Engineering Division

This paper was awarded the Best Poster Paper Award at the Discussion Meet on Electro Analytical Techniques and their Applications, (DM-ELANTE) held at Munnar, Kerala, from Feb. 25-28, 2008

Introduction

Lead-based alloys are being considered as primary candidates, for nuclear coolants of advanced nuclear energy systems, due to their specific thermal-physical and chemical properties, such as high boiling point, high thermal conductivity, low vapour pressure and no violent reaction with air and water [1]. The amount of dissolved oxygen in liquid lead alloys, should not increase beyond a limit to avoid the contamination of the liquid system by lead and bismuth oxides, as this can affect the ability of the fluid to flow and to extract heat, by clogging in the pipes or by depositing on the heat exchanger surface. There is also a lower limit of dissolved oxygen concentration, which is to be maintained to ensure an efficient corrosion protection of the structure, if the oxide layer self-healing method is chosen. The use of the ionic conduction properties of some solid electrolytes and in particular the Yttria Stabilized Zirconia (YSZ) based ceramic, allows the making of an electrochemical cell assembly for on-line measurement of dissolved oxygen, in a liquid metal system in a wide concentration range. Several studies are available on the development and application of YSZ sensor, for the dissolved oxygen measurement in LBE systems [2,3]. This paper deals with the theory behind the measurement of dissolved oxygen in LBE, by YSZ-based oxygen sensor. The details of construction and experiments on the sensor are described.

Theory

The upper limit of the dissolved oxygen in LBE is defined, as the concentration of oxygen required to form Fe_3O_4 protective oxide layer and the upper limit as the saturation level of oxygen at a particular temperature. The limits are obtained from the following two reactions taking place in LBE [4],

$$Pb + O \rightleftharpoons PbO \qquad \text{...............(1)}$$

$$3Fe + 4O \rightleftharpoons Fe_3O_4 \qquad \text{................ (2)}$$

Using Henry's law, the limits of partial pressure of oxygen can be expressed, using the Eq. (1) & Eq. (2), as follows [4],

$$\frac{1}{2}\Delta F_{Fe_3O_4} < RT\ln P_{O_2} < 2\Delta F_{PbO} - 2RT\ln a_{Pb} \qquad \text{............(3)}$$

Fig. 1 shows an oxygen sensor consisting of a one-end closed YSZ tube as solid electrolyte with $Bi+Bi_2O_3$ mixture as reference electrode. The molten lead alloy in which the tube is immersed, serves as the other electrode. At high temperature (>300°C), the solid electrolyte membrane (i.e. YSZ) is porous to oxygen ion, an imbalance in the oxygen concentration between two electrodes will cause the oxygen ion to migrate, to equalize the concentrations on each side. Oxygen on the higher concentration side will "pick up" two electrons to become ions, travel through

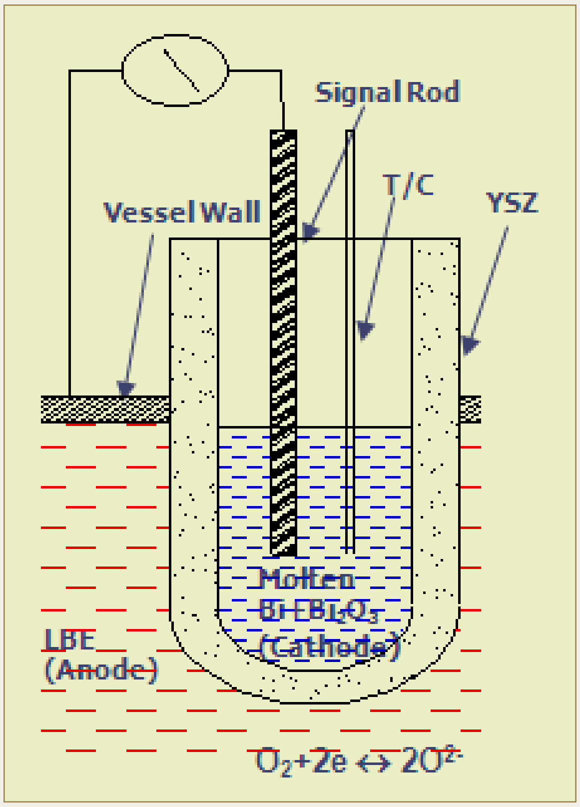

Fig. 1 : YSZ Oxygen sensor

the YSZ and re-form into a neutral molecule at lower oxygen concentration electrode surface, where it will "deposit" two electrons. The potential difference across the electrodes can be calculated from Nernst Equation as [3],

$$E = \frac{RT}{4F}\ln\frac{P'_{O_2}}{P_{O_2}} \qquad \text{...............(4)}$$

$$= \frac{1}{2F}\left(\frac{1}{3}\Delta F_{Bi_2O_3} - \Delta F_{PbO} - RT\ln a_{PbO} + RT\ln a_{Pb}\right)$$

Where P'_{O_2} and P_{O_2} are the partial pressures of the dissolved oxygen in the reference electrode and liquid metal respectively.

For pure lead, $a_{Pb} = 1.0$.
Using Eq (3), Eq (4) and referring to the Oxide Handbook [5] for ΔFs, the limits of the sensor voltage can be expressed as,

$$E_{max} = 8.123\text{x}10^{-5}\ T + 0.4304 \text{ (Volts)} \qquad \text{...........(5)}$$

$$E_{min=} -7.264\text{x}10^{-5}\ T + 0.142 \text{ (Volts)} \qquad \text{...........(6)}$$

Sensor Construction and Testing

An oxygen sensor is developed, to measure dissolved oxygen level in Lead. As shown in Fig. 1 the oxygen sensor consists of a one-end closed YSZ tube, fabricated in Ceramics Materials Section, Materials Group, BARC. The tube is partially filled with laboratory grade Bi+Bi$_2$O$_3$ mixture, which is the reference electrode of the sensor. A Molybdenum rod (signal rod, for electrical connection between molten reference electrode and vessel wall) and a SS sheathed thermocouple (for temperature measurement) are immersed, in the mixture. The tube is sealed with a high temperature Teflon cap and high temperature silicon sealant. The molten lead alloy in which the tube is immersed, serves as the other electrode. A test setup (Fig. 2) is made to test the oxygen sensor. The test setup mainly consists of a SS vessel with oxygen sensor fittings, level sensor, thermocouples and gas inlet and outlet fittings. The sensor is inserted into the vessel through specially designed leak-tight fitting, so that it is partially immersed inside the molten metal. Fig. 3 shows the sensor before installation in the test set-up. The level sensor is a discrete type sensor.

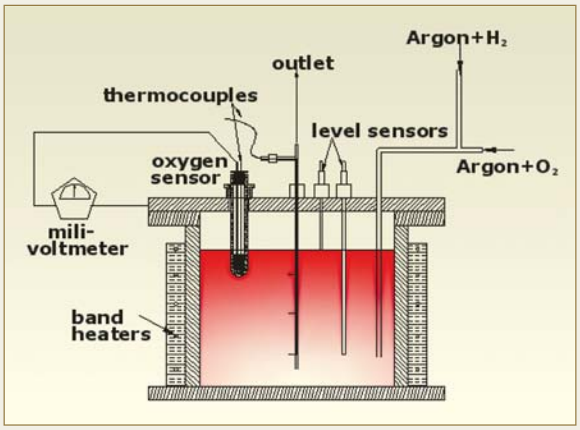

Fig. 2 : Oxygen sensor test set-up

Fig. 3 : Oxygen sensor

When the level sensor tip touches the liquid metal level, the electrical circuit closes between the sensor tip and vessel wall and the indication is given by a LED. A high impedance millivoltmeter is connected between the Molybdenum rod and test vessel body (Fig. 4), to measure the EMF generated across the tube wall, due to difference in oxygen concentration in reference electrode and molten metal. Since the vessel body is in contact with the molten metal, the EMF generated between reference electrode and molten metal will be sensed by the millivoltmeter.

Fig. 4 : View of the Oxygen sensor with the test set-up

The vessel is heated by high temperature ceramic band heaters. The heater power is controlled by dimmer-stat. The temperature of the liquid metal and vessel surface is measured by SS316L sheathed thermocouples. The center temperature of the vessel is measured and ensured that it is well above the melting point of the lead.

High purity argon gas is used as the cover gas of the liquid metal in the vessel, to avoid oxidation of liquid metal at high temperature. Argon+H_2 gas is used as reducing gas, to remove the excess dissolved oxygen in the vessel. Pressure gauge is used to monitor the gas pressure in the vessel and rotameters are used to measure the gas flow rates. The oxygen level in the molten lead is increased by bubbling with air and decreased by bubbling with H_2+Argon gas.

Results and Discussion

Fig. 5 shows the predicted variation of EMF generated in the oxygen sensor with different temperature at different oxygen concentrations (%wt) in LBE. This figure is derived from equations (4), (5) and (6). From the figure, it can be seen that if the EMF value of the sensor goes below 0.1 Volts, then PbO oxide layer formation begins. If EMF goes above 0.45 Volts, the protective oxide layer on the metal surface becomes unstable which may lead to corrosion. For normal operation range (i.e. 350 to 550°C) the safe zone of

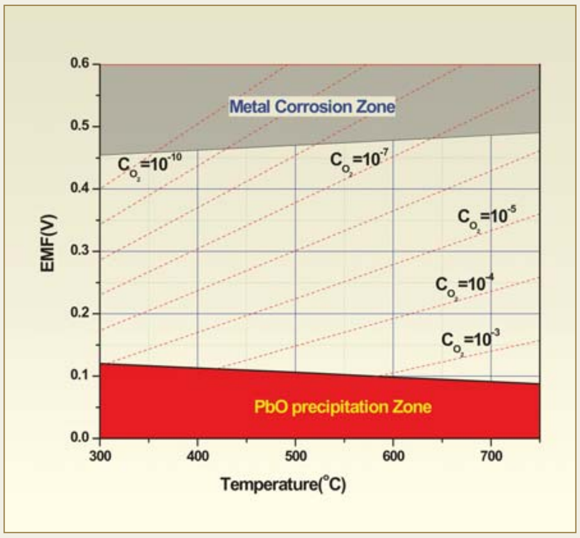

Fig. 5: Variation of EMF in the Oxygen sensor with temperature at different dissolved O_2 concentrations (%wt) in LBE

operation is 10^{-7} to 10^{-5} %wt of oxygen during normal operation. In terms of EMF, it can be inferred that from 0.2V to 0.4V is the safe zone of operation for all temperatures.

In the experimental studies, the molten lead is kept at constant temperature for few hours, to attain a uniform temperature. After that, air is injected in the lead to increase the oxygen partial pressure in the lead, which reduces the EMF [2] in the sensor.

After some time, the oxygen concentration in the lead is reduced by introducing H_2+Argon gas, which is indicated by increase in EMF values of the sensor. This process is repeated and similar trends of EMF values are found, as shown in Fig. 6. The maximum and minimum EMF in the sensor are found to be 0.45V and 0.115V, which are close to the E_{max} and E_{min} predicted by Eq (5) and Eq (6) respectively.

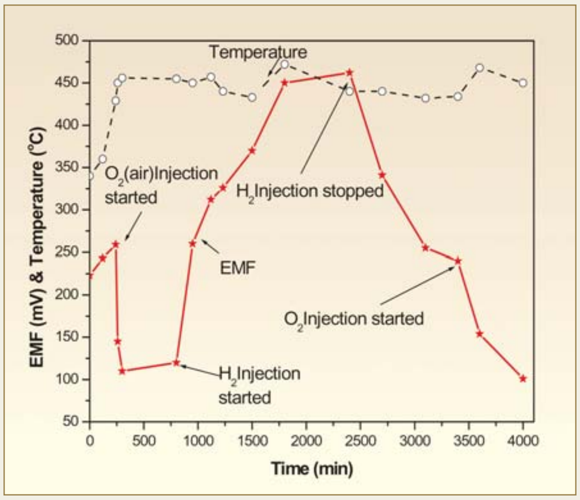

Fig. 6 : Experimental results on the variation of EMF of oxygen sensor with oxygen concentration in molten lead

In the second test, the sensor molten lead is cooled from 525°C to 350°C with high purity argon bubbled in the liquid metal. Fig. 7 shows the variation of EMF of the sensor with temperature. It can be seen that the EMF of the sensor reduces as per prediction from 525°C to 440°C. After that, it drastically reduces to the saturation level in the 440°C to 350°C range. This may be due to the accumulation of oxygen present in the argon gas as impurity. The frequent injection of air in the liquid metal created a thick oxide layer on the liquid metal surface, which could not be removed by reducing environment (bubbling with Argon+H_2).

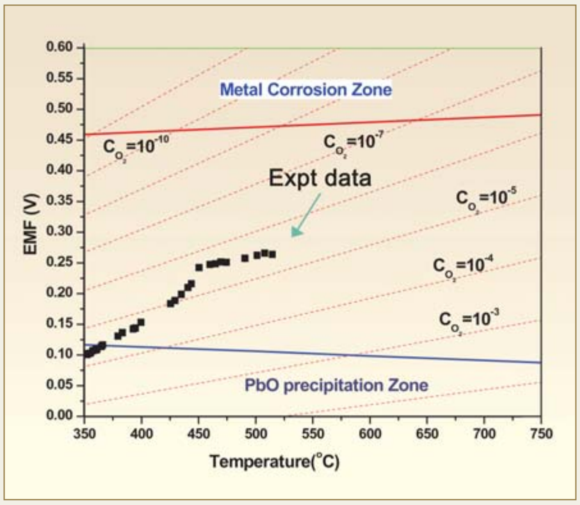

Fig. 7 : Variation of EMF with temperature with pure Argon gas bubbling

Conclusion

The theoretical basis for of the oxygen sensor for molten lead has been elucidated. The construction and testing of an Yttria Stabilized Zirconia (YSZ) probe is described. The oxygen concentration in the liquid metal was varied and the response of the oxygen sensor in terms of EMF is studied. The response of the sensor is similar to the theoretical prediction. But sophisticated temperature control and EMF measurement and recording systems are required, to improve the accuracy of the sensor. Accurate and fine control of dissolved oxygen control system is required to calibrate the Oxygen sensor at different oxygen concentration levels.

Acknowledgement

The authors are thankful to Ceramic Materials Section, Materials Group, BARC for supply of YSZ tube
.

Nomenclature

a	activity constant
E	EMF, Volts
F	Faraday's Constant, C/mol
ΔF	Free energy of formation, can be found for oxide hand book [5], J/mol
P	Partial pressure, Pa
R	Gas constant, $JK^{-1}mol^{-1}$
T	Temperature, K

Subscript

Min	minimum
Max	maximum

References

1. A. Borgohain, N. K. Maheshwari, P. K. Vijayan, D. Saha and R. K. Sinha, Proceedings of DAE-BRNS Topical Symposium on Role of Analytical Chemistry in Nuclear Technology (RACNT), Bhabha Atomic Research Centre, Mumbai, January 4-6, 2007.
2. J. Konys, H. Muscher, Z. V, O. Wedemeyer, "Oxygen measurements in stagnant lead–bismuth eutectic using electrochemical sensors" *J. Nuclear Materials* 335 (2004) 249–253.
3. Jinsuo Zhang, Ning Li, "Review of studies on fundamental issues in LBE corrosion", Las Alomas National Laboratory, Report No: LA-UR-04-0869. 2004.
4. Orlov, Y.I., The main impurities and their condition in the Pb-Bi coolant, contract SSC RF IPPE/CEADRN-DER 5010 6 8 B049630, Substage 2.1, Obninsk (1998).
5. G. V. Samsonov (Ed.), The Oxide Handbook, 2nd Ed., IFI/Plenum, New York, 1982.

ABOUT THE AUTHORS

Mr. A. Borgohain joined the Reactor Engineering Division, BARC in 1998. His research interest is lead-bismuth and molten salt coolant technology development, for High Temperature Reactors. He is actively involved in development of oxygen sensor for liquid metal applications and development of fuel rod simulators for safety related studies of nuclear reactors. He is also involved in experimental as well as theoretical studies on thermal-hydraulics of advanced nuclear reactor systems.

Dr. N. K. Maheshwari joined the Reactor Engineering Division, BARC in 1987. His research interest is passive safety system studies and development of advanced nuclear reactor systems. He is involved in development of indirectly heated fuel rod simulator and flow visualization techniques. He is also actively involved in experimental and theoretical thermal hydraulic studies, related to nuclear reactor systems. He is also an associate professor at the Homi Bhabha National Institute, a deemed university.

ABOUT THE AUTHORS

Dr. P. K. Vijayan joined the Reactor Engineering Division (RED) in 1977. Currently he is the head of thermal hydraulics section of RED. He is a well-known expert in the field of reactor thermo-hydraulics especially in natural circulation phenomenon. He is a member of several professional bodies. He is a recipient of the DAE Technical Excellence award for the year 1998. He is also a Professor at the Homi Bhabha National Institute, a deemed university.

Mr. Dilip Saha joined the Reactor Engineering Division in 1972. Since he joined RED, he has been involved in research and development work in the area of thermal hydraulics and safety of nuclear reactor systems. Right from its inception, Mr. Saha has been involved in the design and development of Advanced Heavy Water Reactor. Currently, he is Head of the Reactor Engineering Division, BARC.

Mr. Ratan Kumar Sinha joined the Reactor Engineering Division of BARC in the year 1973. He is a Distinguished Scientist and had been designated as Director, Reactor Design & Development Group and Director, Design, Manufacturing and Automation Group of BARC. Mr. Sinha has handled several major assignments relating to the Indian research and power reactors. He is currently guiding the design and development of the innovative Advanced Heavy Water Reactor and the Compact High Temperature Reactor. Mr. Sinha has received several awards and honors. Mr. Sinha is a nationally and internationally recognized expert in the area of nuclear reactor technology and a member of several national and international committees.

SOL-GEL PROCESS FOR ALUMINA AND ALUMINA BASED MATERIALS

K.T. Pillai, R.V. Kamat, S.K. Mukerjee and V.N. Vaidya
Fuel Chemistry Division

This paper was conferred the Best Poster Award (2nd Prize) at the Poster Session in ALUMINAS 2008, held at CGCRI, Kolkata, during February 28 - March 01, 2008

ABSTRACT

Alumina and alumina-based materials were synthesized by using different techniques of sol-gel process at Fuel Chemistry Division, BARC. Alumina monoliths, in the form of disc and cylinder, were prepared from alumina sol by physical and chemical gelation. Ruby was obtained by homogeneous mixing of chromium nitrate solution in alumina sol, prior to gelation and then heating the gel in oxy-acetylene flame or heating at high temperature. High-purity yttrium aluminium garnet (YAG) as well as neodymium-doped YAG were prepared from aluminium nitrate solution by developing a simple innovative method, called "Gel Entrapment Technique" (GET). Spherical particles of alumina of desired size and porosity were prepared from aluminium nitrate solution by a process, called "Internal Gelation Process" (IGP) using hexa methylene tetramine (HMTA) and urea as the gelling agents for homogeneous gelation. As a useful modification, the porous alumina spheres were embedded with microcrystalline ammonium molybdo phosphate (AMP) for selective separation of cesium, a major fission product present in irradiated nuclear fuel. Yet another modification was the hydrothermal synthesis of zeolite (mordenite) on alumina spheres for a variety of applications. The preparative conditions of each of the above ceramics and its characterization by TG, DTA, XRD, SEM, porosity, surface area, particle size etc. are described.

Introduction

Sol-gel process is one of the best methods for the synthesis of high-tech materials. The motivations for sol-gel process development are the need for materials with better properties, higher purity, better homogeneity and lower processing temperature. Alumina ceramics prepared by sol-gel process are of great interest, due to their wide range of applications in preparing coatings for different purposes, catalysts, membrane and wafers (in separation technology), chromia-doped alumina and neodymium-doped YAG (in LASER technology), bioceramics (artificial teeth and bones) etc.

Alumina microspheres of controlled size and porosity can be used for a variety of applications such as ion exchangers, base materials for catalysts and other materials. Their thermal and radiation stability, chemical inertness, porous structure with large surface area and presence of large number of exchangeable hydroxyl groups, make them suitable for a variety of applications. Ammonium molybdo phosphate (AMP) is well known for selective adsorption of cesium from acid medium and specifically from fission products solutions. Since AMP is micro-crystalline and impervious to liquid, it cannot be used directly in the separation column. To overcome this, AMP was trapped in alumina gel particles by a novel method known as Gel Entrapment Technique (GET). Zeolites are crystalline alumino silicates which are widely used as sieves, catalysts etc. In nuclear industry they are used to remove cesium and strontium isotopes. Hydrothermal synthesis of zeolite on alumina spheres prepared by IGP was investigated.

Experimental

Preparation of Alumina Monoliths

In order to make alumina sol, aluminium iso-propoxide was prepared by Yoldas [1] method and hydrolized [2] with hot water (80 - 90°C) in the presence of small amount of nitric acid and peptized. The sol was then concentrated to 2.2 M and taken in Teflon moulds coated with paraffin oil. Two sets of gels were prepared. In the first set (GEL-I), gelation was accomplished through dehydration, by evaporation at room temperature (physical gelation). In the second set (GEL-II) 2 ml of 1.1 M aluminium nitrate solution was added to 100 ml of 2.2 M alumina sol, to bring about the controlled chemical gelation in 30 -60 minutes. The gels were dried at room temperature for a few days and heat treated up to 1000°C at a rate of 1°C / minute. The shrinkage (axial and radial) of the gels was studied at various temperatures. The gels were characterized by DTA-TG, at a heating rate 10 °C / minute using a thermo-gravimetric analyzer. The phase analysis of gels heated at various temperatures was done by XRD.

Preparation of chromia-doped alumina

In order to prepare chromia-doped alumina, chromium nitrate solution was added to alumina sol, so as to get chromia 0.1 mole percent and then gelation was accomplished by adding aluminium nitrate solution. The gels were heat treated at 700°C, 1000°C and 1300°C, to get chromia-doped alumina. These samples were studied for their spectroscopic properties. Samples were heated in oxy-acetylene flame, to ascertain ruby formation.

Preparation of YAG by using GET

Yttrium nitrate and aluminium nitrate solutions were mixed at 3:5 mole ratio and then gelled by controlled addition of HMTA solution. At pH 4, the Al^{3+} ions formed the hydrous oxide gel, with Y^{3+} ions entrapped within the gel matrix. The gel was soaked in ammonia solution, to cause a homogeneous precipitation of yttrium. The gel was then washed with dilute NH_4OH solution, to remove water-soluble unwanted compounds. The washed gel was dried in air at 200°C to get the precursor powder which was subsequently heated at various temperatures up to 1400°C, to get the YAG powder. The phase studies of the samples heated at different temperatures were carried out with X-ray diffractometer. The particle size distribution was studied by sedigraph technique and the microstructure by SEM.

Preparation of Alumina Microspheres by Internal Gelation Process

The saturated solution obtained by dissolving the crystals of $Al(NO_3)_3$ in water, has a molarity of ~2.5 M, which is low for obtaining gels of desired strength. Gelling of solution having high nitrate content, requires large quantities of HMTA and urea, which in turn lowers the concentration of aluminium in the feed. By using the $Al(NO_3)_3$ solution, feed solution could be prepared with composition [Al] < 0.8 M and [HMTA, urea]/[Al] (reffered as R) < 2.6. The gel particles obtained from the above solution were soft. To get a strong gel, it is necessary to have a solution with higher aluminium molarity and low nitrate content. Different techniques have been developed to reduce the nitrate content and thereby increase aluminium concentration. Addition of NH_4OH to $Al(NO_3)_3$ solution, can produce acid-deficient conditions. Different ammonia-treated

$Al(NO_3)_3$ solutions were prepared, by adding required amount of NH_4OH to get $[NO_3^-]/[Al]$ ratio (R) 3.00, 2.75, 2.50 and 2.25. Nitrate was destroyed by heating the solution with HCHO and then the $[NO_3^-]/[Al]$ was adjusted to the required ratio with $Al(NO_3)_3$. Similarly, glycerol could be used to get de-nitrated solutions. By pre-treating $Al(NO_3)_3$ solution with HMTA, nitrate can be controlled in two ways. When HMTA decomposes at low pH and high temperature, HCHO and NH_3 are released. The HCHO denitrates while NH_3 neutralizes the nitrate in the solution. Different HMTA pre-treated $Al(NO_3)_3$ solutions were prepared. The above solutions were used to prepare feed solutions having different [Al] = 0.8 to 1.5 M and R = 2.7 to 1.0. Droplets of feed solution were allowed to pass through a vertical column, containing hot (~95°C) silicone oil. The gel spheres were degreased with carbon tetrachloride and then washed with dil. NH_4OH solution, to remove unwanted substances from the gels. The spheres were dried at 100°C and heat-treated at different temperatures. Characterization of the spheres was done at various stages of heating.

Preparation of AMP-trapped Alumina Gel Particles by GET

Feed solution containing aluminium nitrate, urea and HMTA was mixed with AMP powder to form a slurry. Droplets of the slurry were gelled by dispersing in hot silicone oil. The AMP powder was entrapped in the alumina gel particles. Several batches were prepared by varying the amount of AMP up to 20 g/L of the feed solution. Different washing schemes tried for these gels were: washing with 2 M ammonia solution, water at room temperature, hot (80°C) water and dil. NH_4OH (<0.1 M) solution. The gels were heat-treated at 200°C, 300°C and 380°C for 10 hours. For cesium separation from nuclear waste solution, the gel particles should have sufficient acid stability. This was checked by immersing the gels in nitric acid of different strengths (0.1 M, 1.0 M and 2.0 M) for a duration of 24 hours.

Synthesis of Zeolite on Alumina Microspheres

Alumina microspheres were prepared by IGP and heated in three lots at different temperatures, viz. 400°C, 500°C and 700°C. Five gms. each of the above spheres were treated with 18 ml of 0.8 M sodium silicate solution ([Si] = 1.6 M) in Teflon-lined pressure vessel (capacity 24 ml) at 150°C for 100 hours and thereafter at room temperature for another 100 hours. The product obtained was washed with water and dried at 100°C. The material was characterized by DTA-TG and SEM.

Results and Discussion

Alumina Monoliths

In the case of GEL-I, the gelation occurred after several days, depending upon the quantity of the sol. The gels shrank anisotropically, the axial shrinkage was more than radial. Due to this, the gels had warping during drying and sintering (Fig.1).

Less than 2 mm thick monoliths could be prepared by this method of gelation. Nearly isotropic shrinkage of gels without warping was noticed in the case of GEL-II (Fig. 2 & 3). The TG-DTA curves (Figs. 4) of

Fig. 1: Alumina monoliths heated at 1200°C (physical gelation)

GEL-II showed major weight-losses in two stages, with corresponding endothermic peaks. The first stage loss at 100°C was due to the escape of physically bound water, while the second loss around 400°C was attributed to the chemically bound water. Above 450°C, there was a continuous decrease in weight, till the material got transformed into α-alumina. The exothermic peak at 295°C was due to the decomposition of nitrate used for the gelation. In the case of GEL-I, the exothermic peak was absent. The XRD patterns of the gels heated up to 1100°C (Fig. 5) indicated, that the gels were amorphous up to 1000°C and the α-alumina phase was formed after heating at 1100°C for 5 hours.

Chromia-doped Alumina

Uniform doping could be achieved by adding chromium nitrate solution prior to the gelation of alumina sol (Fig. 6). Spectroscopic studies revealed, that luminescence was observed only for sample heated at 1300°C, indicating the formation of ruby.

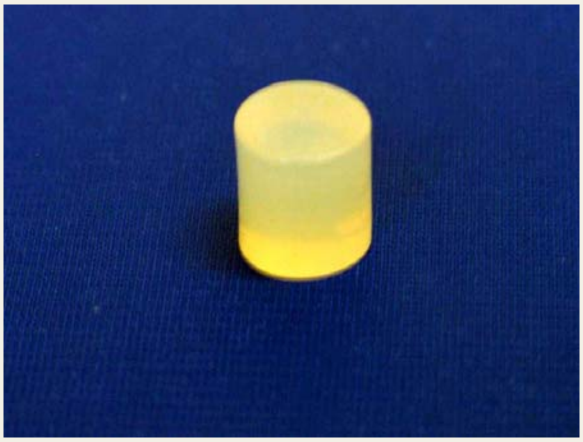

Fig. 2: Alumina gel dried at room temp. (controlled chemical gelation)

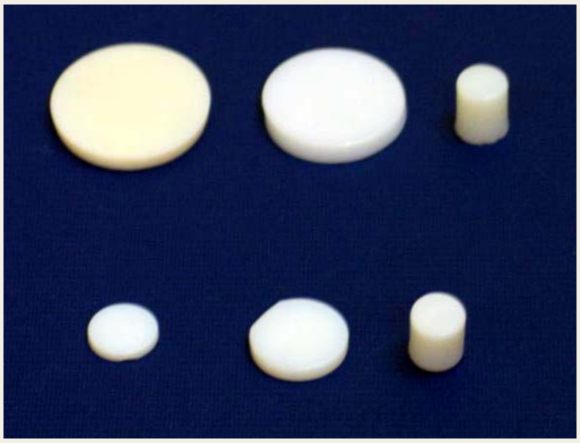

Fig. 3: Alumina monoliths heated at 1200 °C (controlled chemical gelation)

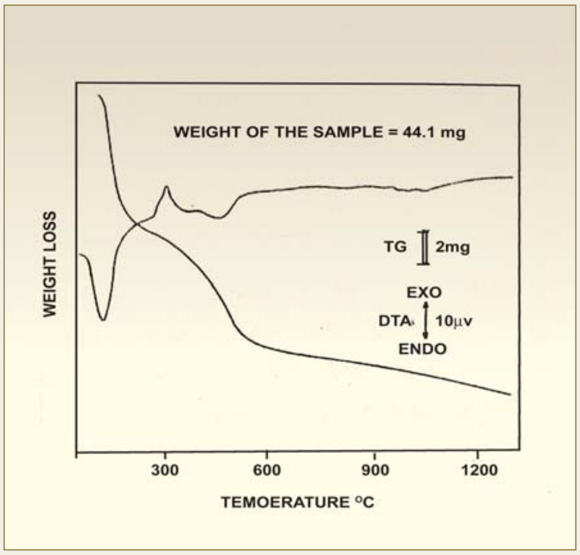

Fig. 4: TG-DTA of GEL-II

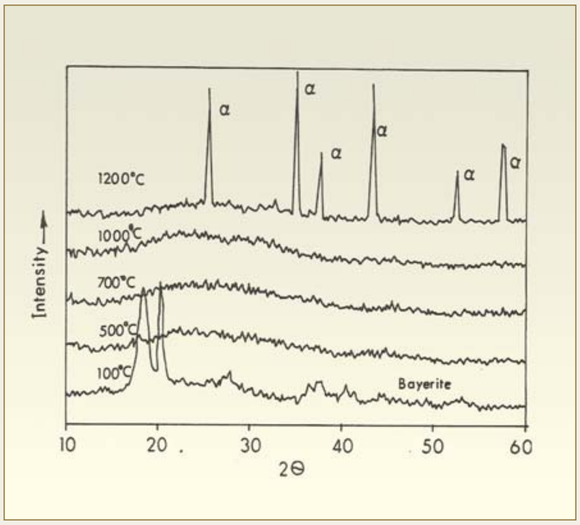

Fig. 5: XRD patterns of alumina gel heated at different temperatures

When the gel was heated in oxy-acetylene flame, ruby formation was observed (Fig. 7).

YAG powder

The XRD patterns of the YAG precursor powder heated at 800, 810, 1000 and 1400°C are shown in Fig. 8. The powder was amorphous at 800°C, whereas the 810°C heated sample showed the formation of YAG phase. Further heating of the samples showed an increase in the intensity of the YAG peaks. The predominant particle size (Fig. 9) of the YAG powder heated at 1000°C was around 400 nm.

The SEM photograph indicated the particles were agglomerates (Fig. 10).

Alumina microspheres

Good alumina microspheres could be prepared from pre-treated $Al(NO_3)_3$ solution, having $[NO_3^-]/[Al]$ mole

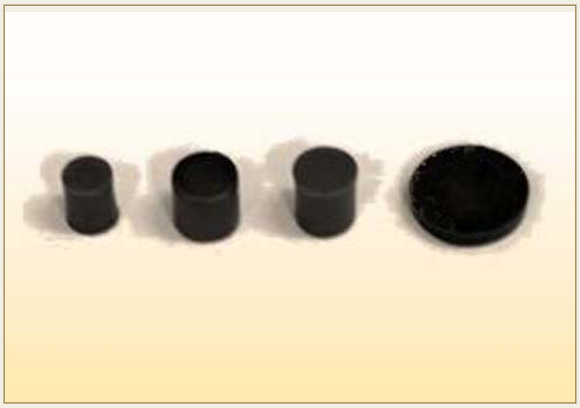

Fig. 6: Chromia-doped Alumina heated at 700°C

Fig. 7: Formation of Ruby after heating in oxy-acetylene flame

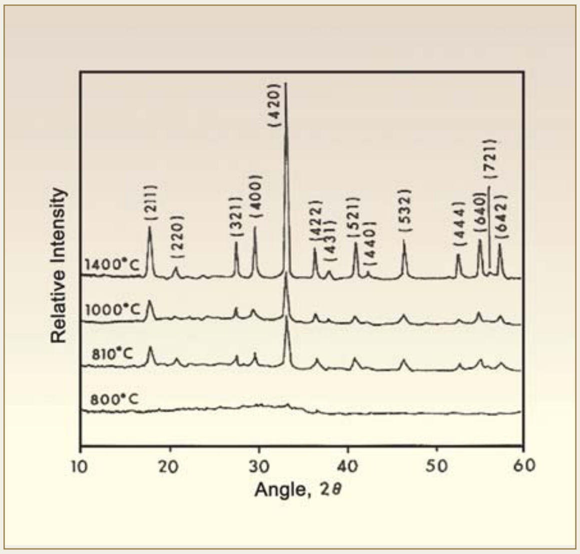

Fig. 8: XRD patterns of YAG precursor heated at different temperatures

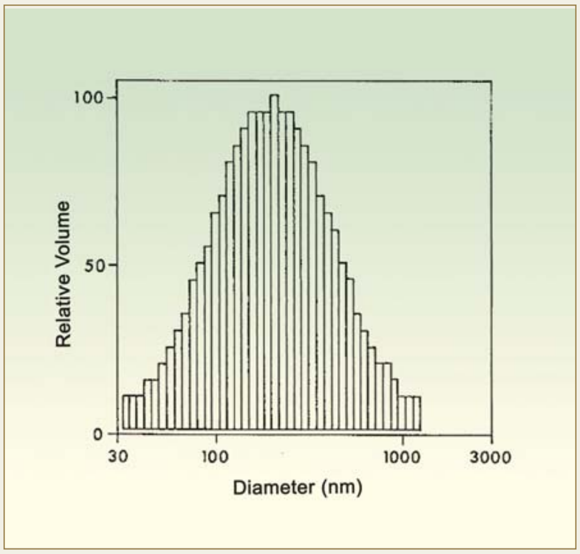

Fig. 9: Particle size distribution of YAG powder heated at 1000 °C

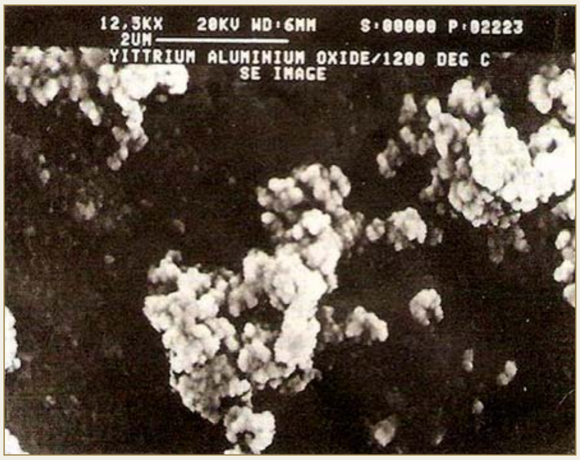

Fig. 10: SEM photograph of YAG powder heated at 1200°C

ratio 2.5 to 2.75 and having feed composition; [Al]= 1.0 M to 1.4M and R = 1.8 to 0.8. The photograph of alumina spheres heated at 700°C is shown in Fig. 11. The gel spheres obtained from insufficient gelation agents and low concentration of aluminium in the feed, resulted in the formation of soft spheres which leached during washing with NH_4OH solution and drying. The gel particles prepared from high content of gelling agents in the feed, cracked catastrophically during drying and heating. These particles were transparent even after soaking in NH_4OH solution for a prolonged time.

The XRD patterns of the sample (prepared from NH_4OH pretreated $Al(NO_3)_3$ solution) heated at various temperatures are given in Fig. 12. The 100°C dried sample showed crystalline $Al(OH)_3$ while the samples heated at 500°C and 700°C showed very weak peak at d = 1.98, indicating the presence of γ-alumina. The 1000°C and 1200°C heated samples indicated that the samples were a mixture of δ- and θ-alumina. But in 1200°C heated sample, the intensity of XRD peaks showed, that the θ-alumina phase was more predominant. Only 1400°C heated sample showed the XRD pattern of a-alumina. The XRD patterns of samples obtained from other denitrated solutions were similar (Fig. 13). Dried (100°C) samples showed bayerite peaks. While at 500°C, 700°C and 1000°C, the samples were X-ray amorphous. After heating at 1200°C for 5 hours, the samples formed α-alumina. The surface area of 700°C heated samples was above 200 m^2/g with pore volume about 0.4 cc/g.

AMP-trapped Alumina Gel Particles

AMP-trapped alumina gel particles are shown in Fig. 14. Washing of the AMP-gel spheres with high concentration of NH_4OH solution, led to the loss of AMP. Washing with either ambient or hot water did not cause AMP loss, but led to severe cracking in the gels during subsequent heat treatment. Hence washing was carried out with <0.1 M NH_4OH solution. The water washed gels were not stable in > 1 M nitric acid solution, whereas the gels obtained with 16 g of AMP per litre of feed solution, washed

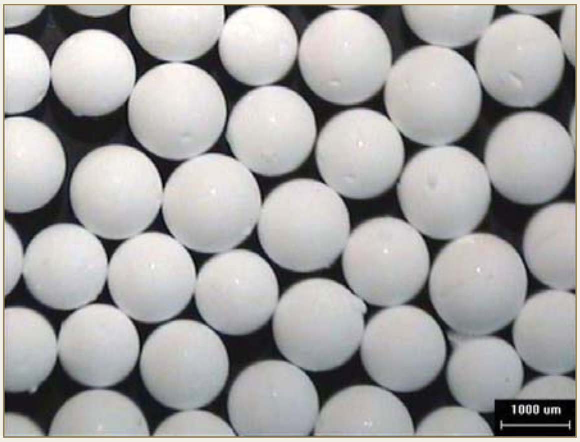

Fig. 11: Alumina microspheres heated at 700 °C

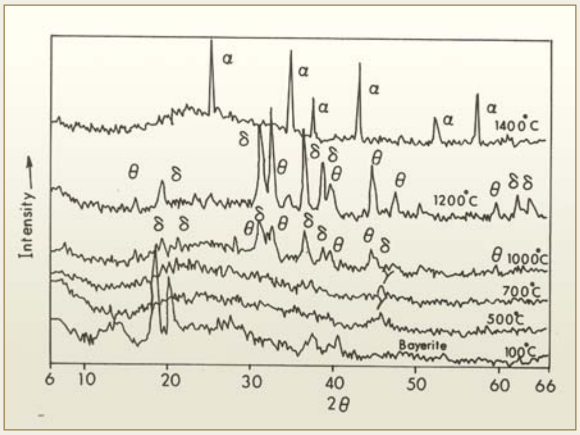

Fig. 12: XRD patterns of alumina samples (from NH_4OH pretreated solution) heated at different temperatures

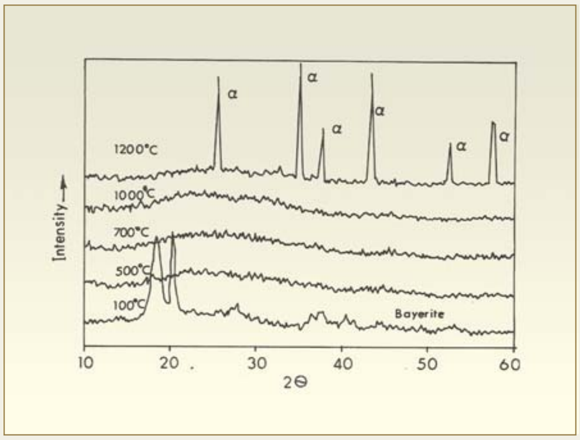

Fig. 13: XRD patterns of alumina samples (from de-nitrated solution) heated at different temperatures

Fig. 14: AMP-trapped alumina gel particles

Table 1: Acid-stability of the gels

Heated for 10 hours at (°C)	Stability of gels when immersed for 24 hours		
	0.1M HNO_3	1.0M HNO_3	2.0M HNO_3
200	Stable	Peptise	Peptise
300	Stable	Peptise	Peptise
380	Stable	Stable	Stable

NH_4OH solution and heated at 380°C for 10 hours, were stable in 2.0 M acid solution (Table1). When the AMP was > 16 g/L, the gel formed was very soft. Pure alumina spheres heated above 700°C are stable in high acidic medium. In case of AMP-trapped with <0.1 M alumina, the heat treatment has to be curtailed below 400°C, to avoid the decomposition of AMP. Consequently such gels showed poor acid-stability. Acid-stability of the gels was improved by prolonged heat treatment at 380°C.

Zeolite on Alumina Microspheres

Out of the three lots of alumina spheres heated at different temperatures, only 400°C heated batch could form Mordenite (zeolite) after the hydrothermal treatment with sodium silicate at 150°C. The DTA-TG curves are shown in Fig. 15. The DTA curve showed endothermic peaks at 150°C and 525°C which were attributed to the loss of loose and bound water respectively. The TG curve showed a continuous weight-loss of 16% up to 550°C, of which a sharp weight-loss of 5% was between 500°C and 550°C. This sharp weight-loss accompanied by an endothermic peak, was mainly due to the loss of zeolite water. The SEM photograph (Fig. 16) indicated the formation of zeolite crystals.

Conclusion

Sol-gel process can be meticulously exploited for the synthesis of different high-tech materials. Controlled chemical gelation of the alumina sol, helped to get

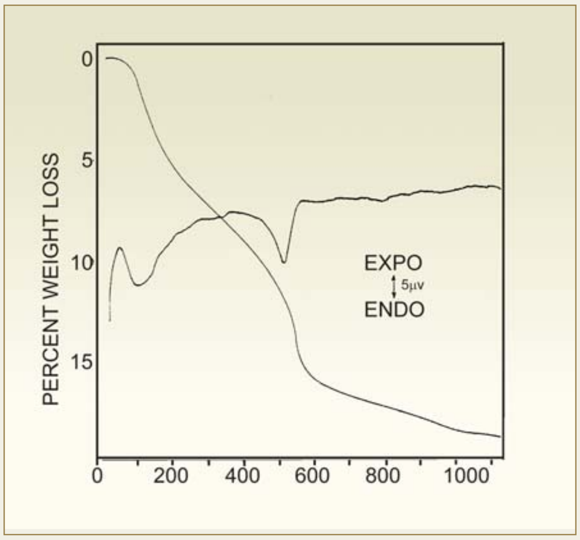

Fig. 15: DTA-TG curves of zeolite-alumina sample

good quality gel. These gels shrank isotropically without warping. Alumina monoliths of different sizes can be prepared by this technique.

Homogeneous doping of chromia in alumina can be achieved, by mixing chromium nitrate in alumina sol, prior to gelation. This method can be adapted to prepare doped materials.

The Gel Entrapment Technique is a novel technique for ultrastructure processing of a variety of high-tech multi-component materials like Nd-doped YAG, YIG etc.

Different phases of alumina, such as γ, δ, θ and α can be prepared, by using suitable feed solutions and heat treatment. Gamma (γ) alumina spheres can be prepared (nitrate neutralized $Al(NO_3)_3$ solution by NH_4OH solution and heating the gels at 700°C. Amorphous alumina spheres can be obtained from denitrated $Al(NO_3)_3$ solutions. High surface area and porosity make these spheres attractive as substrates for catalysts. Since a large number of hydroxyl groups are present in the spheres even at high temperatures (700°C), these spheres can be used as ion exchangers even in harsh environments like high acid medium, high radiation etc. Other uses are in gas and water purification systems.

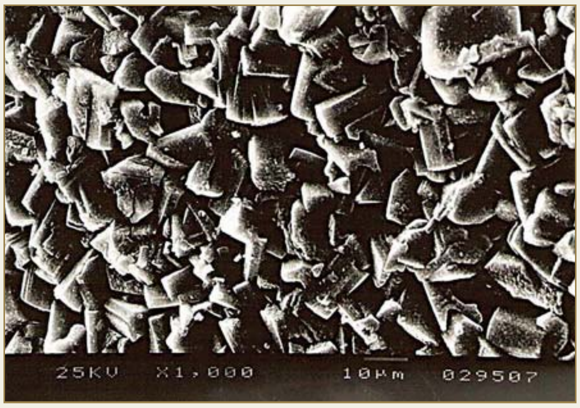

Fig. 16: SEM photograph of zeolite crystals

Uniform trapping of AMP particles in porous alumina has been achieved through GET. The product obtained is suitable for use in column, for the separation of cesium from nuclear waste solution of low acidity. Conditions have been optimized for the hydrothermal synthesis of mordenite on alumina spheres. The thermal stability was found to be good. The material can be used for separation of cesium and strontium from waste solutions.

References

1. H. Okamura and H.K. Bowan, *Ceram. Iter.,* 12 (1986) 163.
2. B.E Yoldas, *Am. Ceram. Soc. Bull.*, 54 (1975) 289.

ABOUT THE AUTHORS

Dr. K.T. Pillai joined the Fuel Chemistry Division of BARC in 1977. Since then he has been working on the development of Sol-gel process for nuclear and non-nuclear high tech materials. In 2002, he obtained his Ph.D. degree from University of Mumbai. He has published more than 63 research papers related to the process development for various materials as well as doped materials in various national and international journals. He is a life member of several scientific associations.

ABOUT THE AUTHORS

Mr. R.V. Kamat obtained his M. Sc. Degree in Chemistry from Karnataka University and joined BARC in 1974. He is currently, Head, Actinides Recovery Section of the Fuel Chemistry Division, BARC. He is a specialist in the processing of plutonium waste. His areas of interest include sol-gel and other solution-based processes, for the production of advanced ceramics.

Dr. S.K. Mukerjee joined the Department of Atomic Energy after completing his M.Sc. (Chemistry) from Nagpur University. He obtained his Ph.D. degree from Mumbai University in the year 1993. Currently he is heading Process Chemistry Section of Fuel Chemistry Division, BARC and is a recognized Ph.D. Guide of Mumbai University and of Homi Bhabha National Institute. His area of interest involves the development of ceramic materials for application in Nuclear Technology. He has extensively studied sol gel processing of nuclear materials for advanced fuel fabrication.

Dr. V.N. Vaidya graduated from the 12th batch of BARC Training School as a Chemistry trainee officer and joined the Radiochemistry Division of BARC in 1969. Dr. Vaidya retired as Head, Fuel Chemistry Division in 2005. Dr. Vaidya is presently engaged as DAE BRNS Raja Ramanna Fellow at BARC. Dr. Vaidya is a Fellow of Maharashtra Academy of Sciences and the Institute of Ceramics. He is a life member of several scientific associations. For the last 24 years he has been working on the development of Sol-Gel process for nuclear fuels and advanced ceramic materials. He has more than 150 publications in international journals and conferences,has given invited talks and edited four books.

LANTHANIDE IONS DOPED $Y_2SN_2O_7$ NANO-PARTICLES: LOW TEMPERATURE SYNTHESIS AND PHOTOLUMINESCENCE STUDY

S. Nigam, V. Sudarsan and R. K. Vatsa
Chemistry Division

This paper received the Second Best Poster Award at the International Symposium on Materials Chemistry, (ISMC-2008), held at BARC, Mumbai, from Dec. 2-6, 2008

ABSTRACT

Nanoparticles of $Y_2Sn_2O_7$ co-doped with lanthanide ions, Tb^{3+} and Ce^{3+}, were prepared at a relatively lower temperature (700°C) in ethylene glycol medium, with narrow size distribution. The crystal structure, particle size were characterized by X-ray diffraction, transmission electron microscopy. As prepared samples show strong blue and green emission, characteristic of Tb^{3+}, on excitation at the wavelength corresponding to the 4f®5d transition of Ce^{3+} due to the energy transfer from Ce^{3+} to Tb^{3+} ions, but very poor luminescence has been observed from samples heated at 700°C. Further, these nanoparticles were prepared and incorporated in silica matrix. It has been observed that incorporation of the nanoparticles in silica matrix improves the luminescence properties of 700°C annealed $Y_2Sn_2O_7$: Ce,Tb nanoparticles. Effective shielding of lanthanide ions from the inhomogeneities by the silica matrix, is the reason for the improved luminescence.

Introduction

During the past decade, pyrochlore-type oxides ($A_2B_2O_7$) have emerged as important host matrices for lanthanide doped luminescent materials, due to their higher thermal stability[1-4]. Among different types of pyrochlores, the ones based on Sn^{4+} ions are applicable as potential hosts for the incorporation of luminescent lanthanide ions.[5,6] Up to now, conventional solid-state reaction is the most commonly used synthetic method for preparation of rare-earth pyrochlore oxides. This synthesis route employs a solid-state reaction of metal-oxide with appropriate rare-earth oxides at high temperature (>1200 %C) for a long time (several days). At this temperature, particle aggregation invariably takes place, leading to the formation of particles having a size more than 100 nm. In the present work, $Y_2Sn_2O_7$ nanoparticles co-doped with lanthanide ions Tb^{3+} and Ce^{3+} were prepared by soft chemical route at relatively low temperature 700%C and investigated for luminescence properties.

Experimental

Preparation of the nanoparticles

For the preparation of lanthanide ions (Tb^{3+} and Ce^{3+}) doped $Y_2Sn_2O_7$ nano-materials, Sn metal, Tb_4O_7, Y_2CO_3, $Ce(NO_3)_3 \cdot 6H_2O$ were used as starting materials. The solution containing Y^{3+}, Sn^{4+} and Ce^{3+}-Tb^{3+} in ethylene glycol medium, was slowly heated up to 100 °C and then subjected to urea hydrolysis. The precipitate obtained after washing was heated to 500°C, 700°C and 900°C. Schematic diagram of the preparation procedure is shown in Fig. 1. For incorporation of the nanoparticles in silica matrix,

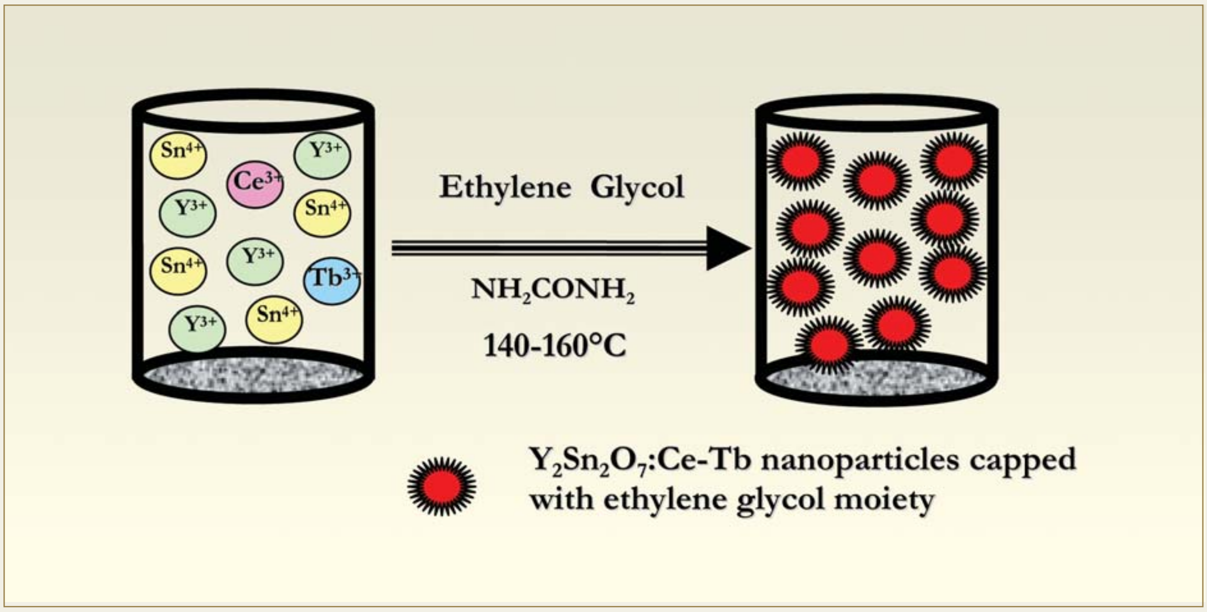

Fig. 1: Schematic diagram for synthesis of $Y_2Sn_2O_7$: Ce^{3+}-Tb^{3+} nanoparticles

tetraethylorthosilicate (TEOS) was added to the reaction mixture, as soon as precipitation started.

Characterization

X-Ray Diffraction (XRD) studies were carried out using a Philips powder X-ray diffractometer (model PW 1071) with Ni filtered Cu-Kα radiation. The lattice parameters were calculated from the least square fitting of the diffraction peaks. The average crystallite size was calculated from the diffraction line width, based on Scherrer relation $D = 0.9\lambda/\beta\cos\theta$, where D is the average particles size, λ is the wavelength of X-rays and β is the full width at half maximum (FWHM). All luminescence measurements were carried out at room temperature with a resolution of 3 nm, using a Hitachi Instrument (F-4500) having a 150 W Xe lamp as the excitation source. Transmission Electron Microscopy (TEM) was performed on a representative $Y_2Sn_2O_7$:Ln sample, using a JEOL JEM 3000F TEM machine.

Result and Discussion

XRD and TEM studies

Fig. 2 shows the XRD patterns of as prepared $Y_2Sn_2O_7$:Ce^{3+}(2.5%),Tb^{3+}(2.5%) sample along with the ones heated at different temperatures. As prepared sample is amorphous, heat treatment below 700 °C, did not induce any crystallization. However, at 700 °C and above, thermal decomposition of the hydroxides leads to the formation of highly crystalline cubic $Y_2Sn_2O_7$:Ce^{3+},Tb^{3+} nanoparticles as can be clearly seen from the XRD pattern shown in part c of Fig. 2. For 900 °C heated sample, crystallinity has been found to improve as revealed by the decrease in line width of the diffraction peaks. Average particle size is calculated from the width of the X-ray diffraction peaks and found to be around 5 nm for the 700 °C heated sample. For nanoparticles incorporated in silica and heated at 700 °C, the XRD pattern (not shown) revealed only a broad peak characteristic of amorphous silica, suggesting that the crystalline nanoparticles are very finely dispersed in amorphous silica matrix. TEM images of the nanoparticles obtained at 700 °C are shown in Fig. 3. The image is characterized by very fine spherical particles having a diameter in the range of 2-5 nm. Very small spherically shaped particles are mainly formed due to the low concentration of the product nuclei (yttrium tin hydroxide) existing in the reaction medium after coprecipitation[7].

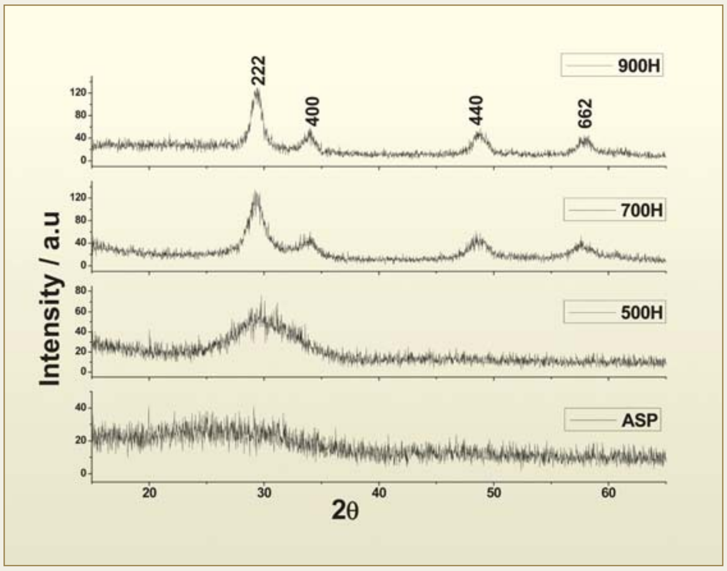

Fig. 2: XRD Pattern of the $Y_2Sn_2O_7$ (5% Tb^{3+} and Ce^{3+} Co-doped) with respect to temperature

Luminescence studies

Luminescence measurements were carried out for as prepared, 700 and 900 °C heated samples. For Ce^{3+} and Tb^{3+} co-doped as prepared samples, strong blue and green emission, characteristic of Tb^{3+}, has been observed from the as prepared nanoparticles on excitation at the wavelength corresponding to the $4f \rightarrow 5d$ transition of Ce^{3+}. These results very clearly demonstrate that there exists strong energy transfer between Ce^{3+} and Tb^{3+} ions. But, very poor luminescence has been observed from Ce^{3+}-Tb^{3+} co-doped samples heated at 700 and 900°C. To improve the luminescence, these nanoparticles were prepared and incorporated in silica matrix. It has been observed that incorporation of the nanoparticles in silica matrix improves the luminescence properties of 700°C annealed $Y_2Sn_2O_7$: Ce,Tb nanoparticles. Effective shielding of lanthanide ion from the inhomogeneities by the silica matrix is the reason for the improved luminescence. The emission scan of these samples has been shown in Fig. 4.

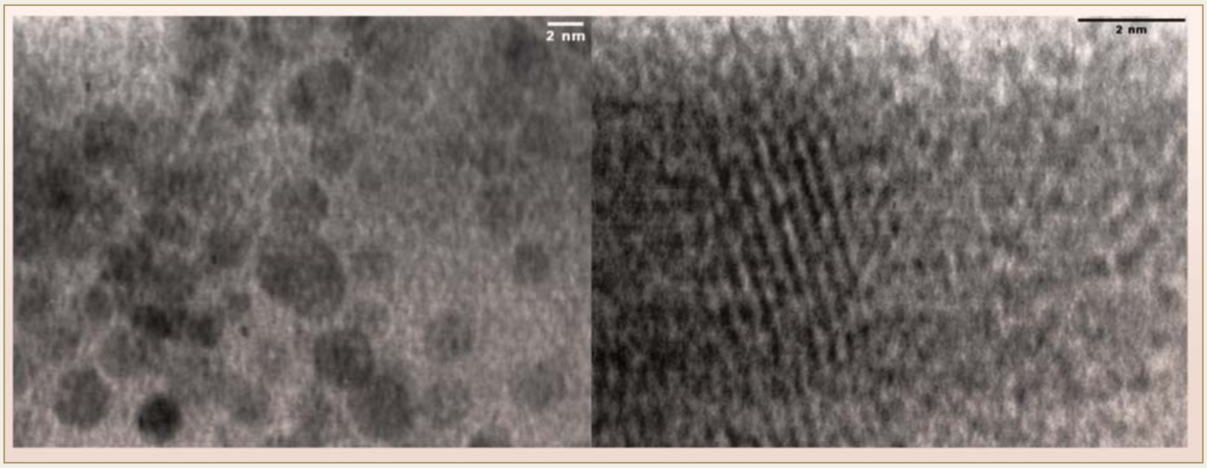

Fig. 3 : TEM Images $Y_2Sn_2O_7$ (5% Tb^{3+} and Ce^{3+} Co-doped) heated at 700 °C

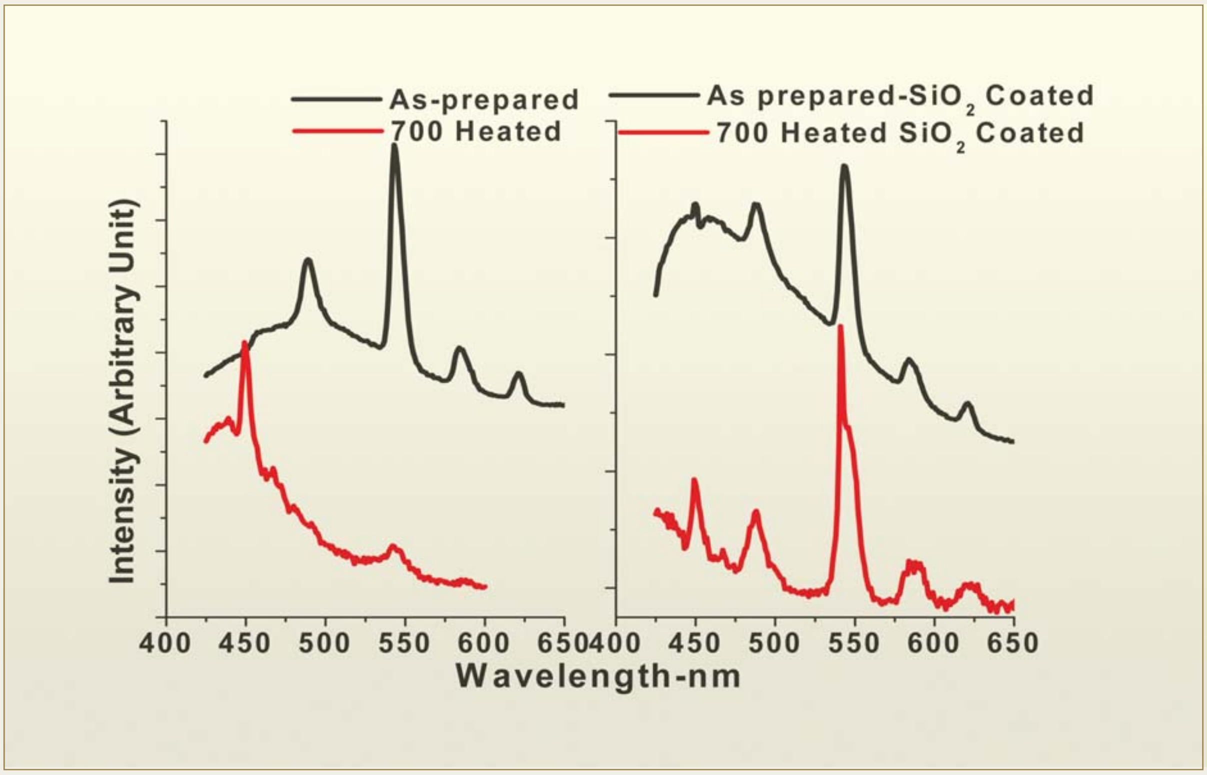

Fig. 4: Emission spectra of $Y_2Sn_2O_7$ (5% Tb^{3+} and Ce^{3+} Co-doped) nanoparticles

Conclusion

$Y_2Sn_2O_7$ nanoparticles co-doped with lanthanide ions Tb^{3+} and Ce^{3+} were prepared by Soft chemical route at relatively lower temperature 700°C and investigated for luminescence properties. Very poor luminescence has been observed from Ce^{3+}-Tb^{3+} co-doped samples heated at 700°C due to poor energy transfer between Tb^{3+} and Ce^{3+} ions and interaction of surface lanthanide ions with ligands. However, the energy transfer and associated luminescence can be significantly improved after dispersing the nanoparticles in silica matrix.

Acknowledgement

The authors thank Dr. T. Mukherjee, Director, Chemistry Group, BARC and Dr. D. Das, Head, Chemistry Division, BARC for their encouragement during this work.

References

1. Lian, J.; Wang, L. M.; Wang, S. X.; Chen, J.; Boatner, L. A.; Ewing, R. C. *Phys. Rev. Lett.* **2001**, *87*, 1459011–4.
2. Zhao, J. H.; Kunkel, H. P.; Zhou, X. Z.; Williams, G.; Subramanian, M. A. *Phys. Rev. Lett.* **1999**, *83*, 219–222.
3. Ali, N.; Hill, P.; Zhang, X.; Willis, F. *J. Alloys Compd.* **1992**, *181*, 281–285.
4. Grey, C. P.; Dobson, C. M.; Cheetham, A. K.; Jakeman, R. J. B. *J. Am. Chem. Soc.* **1989**, *111*, 505–511.
5. Li, K.; Zhang, T.; Wang, H.; Yan, H. *J. Solid State Chem.* **2006**, *179*, 1029–1034.
6. Kang, S. W.; Yoo, J. S.; Lee, J. D. *J. Electrochem. Soc.* **1998**, *145*, 648–651.
7. Burda, C.; Chen, X.; Narayanan, R.; El-Sayed, M. A. *Chem. ReV.* **2005**, *105*, 1025–1102.

ABOUT THE AUTHORS

Dr. Sandeep Nigam joined BARC in 2003 after graduating through the 46th batch of Training School. Since then he has been actively involved in the field of cluster science. He was awarded Ph. D. degree from Mumbai University in year 2008 for his theoretical work on pure and mixed clusters. At present he is working on theoretical studies of noble metal cluster deposited on oxide surfaces and their catalytic behaviour. He has also contributed to the chemical synthesis of mixed oxide nanoparticles and their luminescence studies.

Dr. V. Sudarsan joined the Chemistry Division BARC, in the year 1994 after graduating from the 37th batch of the Training School. He received his Ph. D. from Mumbai University in the year 2002 for his work on structural aspect of inorganic glasses. Currently he is working on optical properties and structural aspects of nanoparticle and glassy materials.

Dr. R. K. Vatsa is currently heading the Structural Chemistry Section of Chemistry Division. He passed M.Sc. from Delhi University in 1986 and graduated from the 30th batch of BARC Training School. He has been involved with the gas phase photodissociation / ionization of atoms, molecules, radical and clusters. He obtained his Ph.D. in 1994 from Mumbai University. He along with other coworkers indigenously developed the Time of Flight Mass Spectrometer (TOFMS) system. His group has recently discovered a simple and cheaper way of generating highly energetic, multiply charged atomic ions. He has more than 75 publications to his credit and is a recognized Ph.D. guide of the University of Mumbai and the Homi Bhabha National Institute.

HYDROGEN STORAGE CHARACTERISTICS OF TICRV ALLOY: EFFECT OF ZR SUBSTITUTION FOR TI

K. Shashikala, S. Banerjee, A. Kumar and C.G.S. Pillai
Chemistry Division

This paper was awarded the 2nd Best Poster Presentation Award at the International Symposium on Materials Chemistry (ISMC-2008) held at Mumbai, during Dec. 2-6, 2008

ABSTRACT

The effect of Zr substitution for Ti on the hydrogen absorption-desorption characteristics of $Ti_{1-x}Zr_xCrV$ alloys (x = 0, 0.05, 0.1 and 1.0) have been investigated. The crystal structure, maximum hydrogen absorption capacity, kinetics and hydrogen desorption properties have been studied in detail. While TiCrV crystallizes in Body Centered Cubic (BCC) structure, ZrCrV is a C15 cubic Laves phase compound and the intermediate compositions with 5 and 10 at% Zr substitutions for Ti (x = 0.05 and 0.1), show the presence of a small amount of $ZrCr_2$ Laves phase along with the main BCC phase. The pressure-composition isotherms have been studied at room temperature. TiCrV shows separation of TiH_2 phase on cycling. A small amount of Zr substitution for Ti is found to have advantageous effects on the hydrogen absorption properties of TiCrV, as it suppresses TiH_2 phase separation and decreases hysteresis. It is found that the hydrogen absorption capacity of $Ti_{1-x}Zr_xCrV$ decreases as the Zr content increases, due to the increased fraction of Laves phase.

Introduction

Ti-V based systems with Body Centered Cubic (BCC) structure, are considered as promising third generation hydrogen storage materials, due to their high hydrogen storage capacity of ~ 3 wt% [1]. Following the discovery of Ti-V-M (M = Cr, Mn, Fe, Co or Ni) alloys by Akiba et al [2], ternary Ti-V based systems have been well explored for their hydrogen storage properties. However, these alloys suffer from disadvantages like difficult activation treatment, poor kinetics, large hysteresis, low cyclic stability and high cost. Substitution of Ti, V or Cr with elements like Zr, Co, Fe or Mn leads to drastic changes in the hydrogen storage properties of the alloys, due to the formation of secondary Laves phases, which coexist along with the BCC phase [3-7]. The presence of a secondary Laves phase, makes the activation procedure easier as compared to pure BCC phase, though the secondary phase decreases the maximum hydrogen storage capacity [8, 9]. These 'Laves phase related BCC solid solution' alloys, are extensively explored for their applications as negative electrode materials in Ni-MH batteries [3].

In our recent work on $Ti_{0.85}VFe_{0.15}$ system, we explored the effect of Zr substitution for V [4]. It was found that Zr substitution (5 at%) in $Ti_{0.85}VFe_{0.15}$ improves the activation procedure, reduces the hysteresis loss and increases the effective hydrogen storage capacity. Zr substitution is reported to improve the hydrogen absorption characteristics of Ti-V based BCC alloys, by forming the grain boundary network of Laves phase [8]. The BCC alloy chosen for the present study is stoichiometric TiCrV from the Ti-V-Cr series, which is reported to exhibit good hydrogen absorption capacity [2]. However, hydrogenation of TiCrV is reported to result in phase separation into TiH_2 and $TiCr_{1.8}H_{5.3}$, when subjected to cyclic hydrogenation-dehydrogenation process [6, 7]. The hydrogen storage properties of some of the alloys of Ti-Cr-V series are found to improve with the substitution of Zr for Ti, though it increases the slope of the P-C isotherm [8]. Here, we report the hydrogen absorption-desorption properties, crystal structure and kinetics of $Ti_{1-x}Zr_xCrV$ ($x = 0, 0.05, 0.1$ and 1.0) alloys. It is found that a small amount of Zr substitution (5 at%), improves the hydrogen absorption-desorption properties by suppressing TiH_2 phase formation, while the saturation capacity decreases only marginally.

Experimental details

The alloys were prepared by arc melting of high purity constituent elements (> 99.9%) in a water-cooled copper hearth under Ar atmosphere. The ingots were turned over and remelted 4-5 times, to ensure homogeneity. Phase purity of the alloys was checked by powder X-Ray Diffraction (XRD) technique using Cu K_α radiation. The composition of the alloys was confirmed by elemental analysis. The hydrogen absorption desorption characteristics were measured, using a Sieverts type set up described in our earlier studies [4, 9]. The alloys were activated by heating under diffusion vacuum (10^{-6} mbar) for 2 hours at 673 K. After activation, the sample was cooled to working temperature under vacuum, followed by introduction of hydrogen into the reaction chamber. The Pressure Composition isoTherm (PCT) was studied in the pressure range of 0.02-25 atm H_2 at ambient temperature. After each cycle, the sample was dehydrogenated by heating at 673 K, under diffusion vacuum. The kinetic study was done at room temperature and a hydrogen pressure of 20 atm after one absorption desorption cycle. The hydride sample was surface poisoned with air at liquid nitrogen temperature, before being taken out.

The total hydrogen storage capacity was estimated, by heating a small amount of the hydride sample, in an evacuated and calibrated quartz chamber [4].

Results and Discussion

Crystal structure of the alloys

Fig. 1 shows X-ray diffraction patterns of the $Ti_{1-x}Zr_xCrV$ alloys with $x = 0, 0.05, 0.1$ and 1.0. The XRD pattern indicates that TiCrV exists as single phase BCC structure, with a lattice parameter 3.051 Å which is in agreement with the values reported earlier for the TiCrV alloy [7, 8].

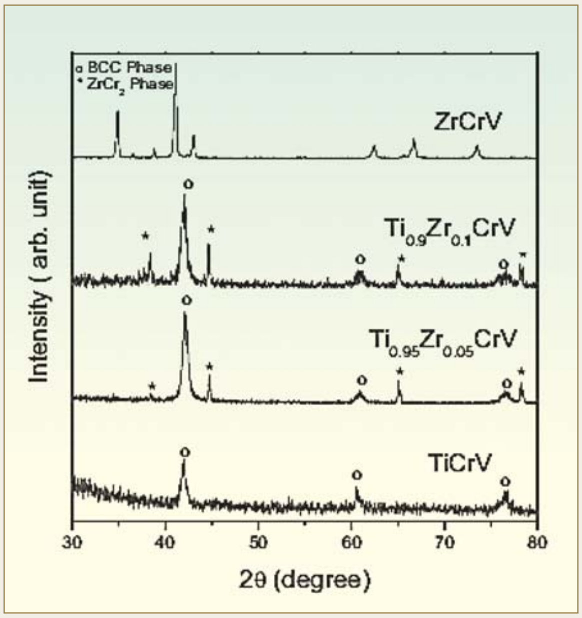

Fig. 1 : X-ray diffraction patterns of the $Ti_{1-x}Zr_xCrV$ alloys ($x = 0.0, 0.05, 0.1$ and 1.0)

When Zr is substituted for Ti, secondary phase formation takes place. The XRD pattern of $Ti_{0.95}Zr_{0.05}CrV$ alloy, consists of a small fraction of a secondary phase besides the main BCC phase, with a lattice parameter $a = 3.067$ Å. The earlier studies on Ti-Zr-V-Cr systems [8], reported the secondary phase as C15 cubic Laves phase compound $ZrCr_2$. The additional lines seen in the XRD patterns of $Ti_{0.95}Zr_{0.05}CrV$ and $Ti_{0.9}Zr_{0.1}CrV$ match with those of $ZrCr_2$ phase. As the Zr content increases, the intensity of the peaks corresponding to the secondary phase increases. When Zr is completely substituted for Ti, single phase ZrCrV is formed with C15 cubic Laves phase structure having lattice parameter a=7.283 Å. The lattice parameters of the alloys are listed in Table 1.

Hydrogen absorption studies on different compositions

The compound TiCrV absorbs a maximum of 5.7 H atoms / formula unit (3.64 wt%) forming a hydride with a composition, $TiCrVH_{5.7}$ at room temperature. This maximum absorption capacity is observed at a hydrogen pressure of 20 atm.

Table 1: Lattice parameters of different alloys

Sample	Phase	Lattice parameter (Å)	Hydride Composition	Hydride Phase	Lattice parameter (Å)	Capacity (Wt%)
TiCrV	BCC	3.05	$TiCrVH_{6.17}$	FCC	4.29	3.93
$Ti_{0.95}Zr_{0.05}CrV$	BCC	3.10	$Ti_{0.95}Zr_{0.05}CrVH_{6.10}$	FCC	4.28	3.83
	C15 Laves Phase	7.02		C15 Laves Phase	-	
$Ti_{0.9}Zr_{0.1}CrV$	BCC	3.70	$Ti_{0.9}Zr_{0.1}CrVH_{5.10}$	FCC	4.26	3.18
	C15 Laves Phase	7.04		C15 Laves Phase	7.68	
ZrCrV	C15 Laves Phase	7.28	$ZrCrVH_{4.65}$	C15 Laves Phase	7.80	2.33

For x=0.05, $Ti_{0.95}Zr_{0.05}CrV$ is found to absorb a maximum of 5.6 H atoms / formula unit, forming a hydride with a composition $Ti_{0.95}Zr_{0.05}CrVH_{5.60}$ at room temperature. This implies, that the maximum hydrogen absorption capacity of TiCrV alloy does not decrease appreciably for x=0.05. However, further increase in the Zr content reduces the hydrogen absorption capacity. $Ti_{0.9}Zr_{0.1}CrV$ absorbs a maximum of 4.7 H atoms/formula unit, forming a hydride with composition $Ti_{0.9}Zr_{0.1}CrVH_{4.7}$. With increase in Zr content to 10% (x=0.1), the peaks corresponding to $ZrCr_2$ phase are seen in the X-ray diffraction pattern. This cubic phase is found to absorb lower hydrogen content as compared to pure BCC phase of TiCrV. The compound ZrCrV absorbs only 4.28 H atoms / formula unit, forming a hydride with composition $ZrCrVH_{4.28}$ at room temperature, and a hydrogen pressure of 20 atm. The maximum hydrogen absorption capacities of different compositions are listed in Table 1. The pressure composition (P-C) isotherms of TiCrV, $Ti_{0.95}Zr_{0.05}CrV$, $Ti_{0.9}Zr_{0.1}CrV$ and ZrCrV are shown in Fig. 2 (a-d), respectively. The plateau pressure is found to be less than 0.02 atm, which is the lowest detection limit of our set up. The BCC alloys generally exhibit two plateaus in the pressure-composition isotherms [10, 11]. The two plateaus observed in the earlier studies on Ti-Cr-V systems [10, 11], need resolution of pressure readings, in the range of 10^{-3} bar. The Zr substituted $Ti_{0.95}Zr_{0.05}CrV$ system shows improved P-C isotherm with low hysteresis loss and relatively flat desorption plateau, which are very important for long term cyclic stability.

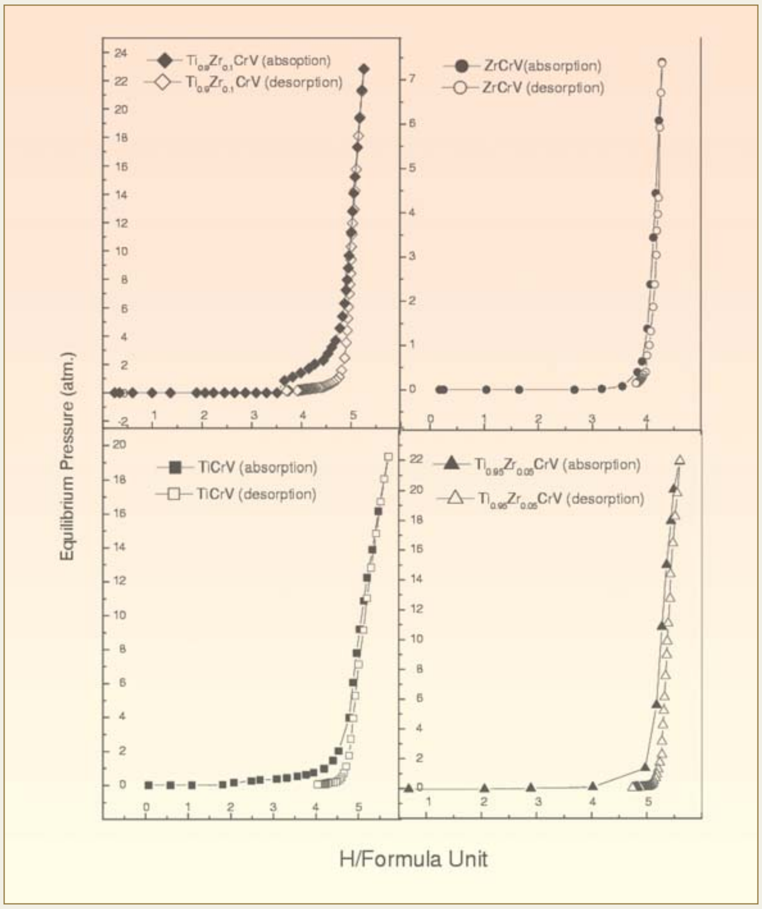

Fig. 2 : P-C isotherms of the $Ti_{1-x}Zr_xCrV$ alloys ((x =0.0, 0.05, 0.1 and 1.0) at room temperature

The rate of hydrogen absorption for TiCrV, $Ti_{0.95}Zr_{0.05}CrV$ and $Ti_{0.9}Zr_{0.1}CrV$ after one absorption-desorption cycleat room temperature is shown in Fig. 3(a-c). All the compositions were dehydrogenated at 673 K under vacuum, before carrying out the kinetic study. It can be seen from Fig. 3, that for all the three alloys, the hydrogen absorption rate is quite fast and the hydrides reach near saturation values in about 80-200 seconds.

Crystal structure of the hydrides

Fig. 4 shows XRD patterns of the hydrides with saturated compositions. The hydride $TiCrVH_{5.7}$ is having Face Centered Cubic (FCC) structure. In general, Ti-V-Fe and Ti-Cr-V and based BCC alloys form monohydride with distorted BCC structure, which subsequently transform into FCC structure, upon further hydrogen changing [10-11].

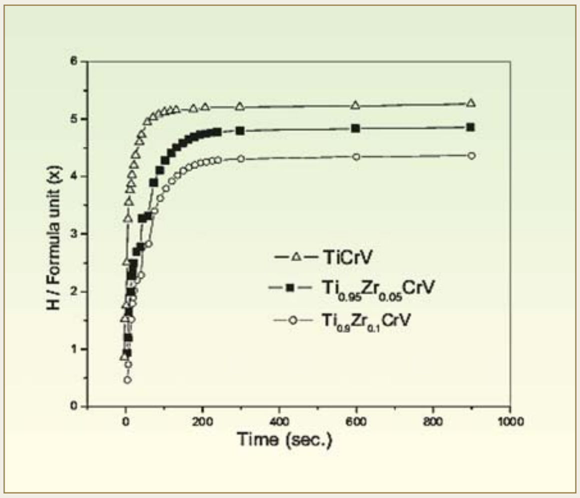

Fig. 3 : Kinetic study on the alloys at room temperature and 20 atm hydrogen pressure. (Recorded after one absorption-desorption cycle.)

The lattice parameter of FCC structured $TiCrVH_{5.7}$ is found to be a = 4.292 Å. Lin et al [7] reported the appearance of $TiCr_{1.8}H_{5.3}$ hydride with FCC structure, when TiCrV is hydrogenated with a hydrogen content of 1.5 wt%. They also observed that further increase in hydrogen content to saturation value of 3.55 wt%, led to TiH_2 phase formation, in addition to $TiCr_{1.8}H_{5.3}$ phase. Wang et al [6] also reported a decrease in the hydrogen absorption capacity of TiCrV alloy, due to phase separation into TiH_2 and $TiCrH_{5.3}$ upon cycling. In our opinion, the phase coexisting with TiH_2 should have been Ti-deficient. Unlike in the work by Lin [7] & Cho [8] wherein TiH_2 formation was reported on hydrogenation, we find the formation of FCC hydride, $TiCrVH_{5.7}$, with lattice parameter a = 4.292 Å as

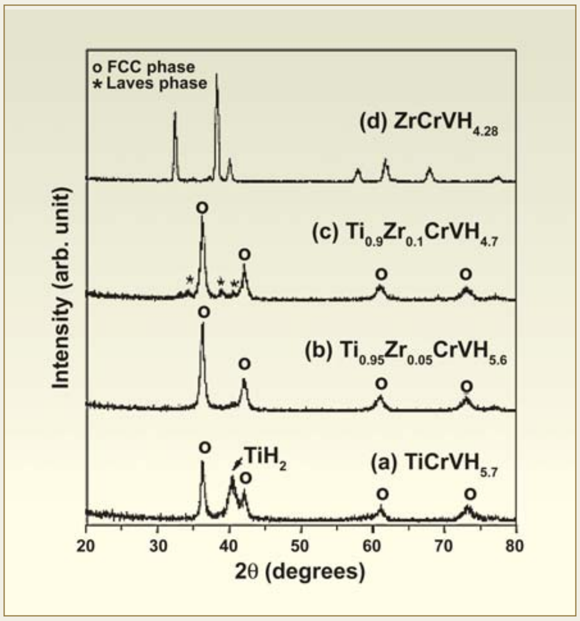

Fig. 4 : X-ray diffraction patterns of the hydrides: (a) $TiCrVH_{5.7}$, (b) $Ti_{0.95}Zr_{0.05}CrVH_{5.6}$, (c) $Ti_{0.9}Zr_{0.1}CrVH_{4.7}$ and (d) $ZrCrVH_{4.28}$.

shown in Fig. 5(a). There are no peaks corresponding to TiH_2 in the XRD pattern of the saturated hydride. The FCC hydride $TiCrVH_{5.7}$ shown in Fig. 5(a) is formed by exposing the activated TiCrV to hydrogen at 298 K and this hydride is not subjected to absorption-desorption cycles. However, on dehydrogenation of $TiCrVH_{5.7}$ at 673 K, followed by second cycle of hydrogen absorption, the peaks corresponding to TiH_2 appear in the XRD pattern, along with the main FCC hydride phase (Fig. 5(b)). It is quite likely that the main FCC phase seen in Fig. 5(b) is Ti-deficient as compared to stoichiometric TiCrV.

For x=0.05, the hydride $Ti_{0.95}Zr_{0.05}CrVH_{5.6}$ is found to have FCC structure with lattice parameter a = 4.280 Å. XRD pattern does not indicate TiH_2 or ZrH_2 phase separation, even after five hydrogenation-dehydrogenation cycles. Thus, the 5 at% Zr substituted sample, is expected to exhibit better cyclic hydrogen absorption capacity than TiCrV. The lattice parameter of $Ti_{0.9}Zr_{0.1}CrVH_{4.7}$ is found to be 4.260 Å. This hydride contains a small amount of $ZrCr_2$ hydride phase. The alloy ZrCrV retains the C15 cubic Laves phase structure upon hydrogenation and the lattice parameter increases due to hydrogen absorption, which can be seen from the decrease in the 2θ values of the peaks, in the XRD pattern. The lattice parameter for $ZrCrVH_{4.28}$ is found to be 7.807 Å.

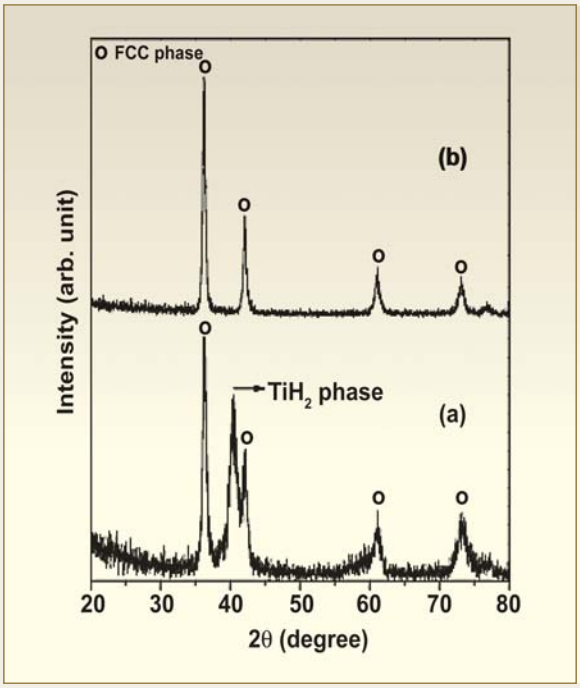

Fig. 5 : X-ray diffraction patterns of (a) FCC $TiCrVH_{5.7}$ formed by hydrogen absorption at 298 K (not subjected to absorption-desorption cycles) and (b) TiCrV hydride formed in the 2nd cycle of absorption (298 K), following one cycle of hydrogen absorption (298 K)-desorption (673 K) showing TiH_2 phase.

Conclusions

In the present study, the hydrogen absorption and desorption characteristics of $Ti_{1-x}Zr_xCrV$ alloys with x = 0, 0.05, 0.10 and 1.0 have been investigated. The maximum storage capacities of these alloys are found to be 3.64, 3.53, 2.93 and 2.16 wt%, respectively. While TiCrV is formed in BCC structure, ZrCrV is a C15 cubic Laves phase compound and the intermediate compositions with x = 0.05 and 0.1 show the presence of a small amount of $ZrCr_2$, along with the main BCC phase. A small amount of Zr substitution (5 at%) for Ti decreases the storage capacity of TiCrV alloy marginally, but TiH_2 phase separation is suppressed, possibly, leading to better cyclic hydrogen absorption capacity. Further increase in the Zr concentration decreases the hydrogen storage capacity considerably, due to the formation of secondary $ZrCr_2$ Laves phase, in addition to the BCC phase.

References

1. Yu X, Wu Z, Li F, Xia B, Xu N, Body-centered-cubic phase hydrogen storage alloy with improved capacity and fast activation, *Appl Phys Lett* 2004;84:3199-3201.
2. Akiba E, Iba H, Hydrogen absorption by Laves phase related solid solution, *Intermetallics* 1998;6:461-470.
3. Miao H, Gao M, Liu Y, Zhu D, Pan H, An improvement on cycling stability of Ti-V-Fe based hydrogen storage alloys with Co substitution for Ni, *J Power Sources* 2008;184:627-632.
4. Basak S, Shashikala K, Kulshreshtha SK, Hydrogen absorption characteristics of Zr substituted $Ti_{0.85}VFe_{0.15}$ alloy, *Int J Hydrogen Energy* 2008;33:350-355.
5. Kuriiwa T, Tamura T, Amemiya T, Fuda T, Kamegawa A, Takamura H, Okada MJ, New V-based alloy with high protium absorption desorption capacity, *J Alloys Compd* 1999;293-295:433-436.
6. Wang J-Y, Jeng R-R, Nieh J-K, Lee S, Lee S-L, Bor H-Y, Comparing the hydrogen storage alloys-TiCrV and vanadium rich TiCrMnV, *Int J Hydrogen Energy* 2007;32:3959-3964.
7. Lin HC, Lin KM, Wu KC, Hsiung HH, Tsai HK, Cyclic hydrogen absorption-desorption characteristics of TiCrV and $Ti_{0.8}Cr_{1.2}V$ alloys, *Int J Hydrogen Energy* 2007;32: 4966-4972.
8. Cho S-W, Han C-S, Park C-N, Akiba E, Hydrogen storage characteristics of Ti-Zr-Cr-V alloys, *J Alloys Compd* 1999; 289: 244-250.
9. Basak S, Shashikala K, Sengupta P, Kulshreshtha SK, Hydrogen absorption properties of Ti-V-Fe alloys: Effect of Cr substitution, Int *J Hydrogen Energy* 2007;32:4973-4977.
10. Akiba E, Okada M, Metallic Hydrides III: Body-centered-cubic solid-solution alloys, *MRS Bulletin* Sept 2002; 699-703.
11. Akiba E, Iba H, Hydrogen absorption by Laves phase related BCC solid solution, *Intermetallics* 1998;6:461-470.

ABOUT THE AUTHORS

Dr. K. Shashikala completed her Master of Science in Chemistry from Mangalore University in 1988. She completed the one year Orientation Course from BARC Training School (OCES-32nd batch) and subsequently joined the Chemistry Division of BARC in 1989. She obtained her Ph.D. from Mumbai University in 1998 and has been working on hydrogen storage materials. Her field of expertise includes intermetallic compounds, development of new hydrogen storage materials and their applications. She has 32 publications in international journals. She is a recipient of Best Paper Award conferred during ISMC-2008 for the paper titled "Hydrogen Storage Characteristics of TiCrV Alloy: Effect of Zr Substitution for Ti".

ABOUT THE AUTHORS

Ms. Seemita Banerjee completed her Master of Science in Chemistry from Calcutta University in 2004. She completed the one year Orientation Course in Nuclear Science and Engineering from BARC Training School (OCES – 48 batch) and subsequently joined the Chemistry Division of BARC, Mumbai in Sept. 2005. Her research work is focused on the development of new solid state hydrogen storage material and determination of hydrogen storage capacities, isotherms and critical thermodynamic and kinetic properties, using different experimental techniques. In order to further explore new materials, with higher hydrogen storage capacity, she is also involved in theoretical modeling using electronic structure theory. She has 6 publications in international journals.

Mr. Asheesh Kumar completed his Graduation in Science from Allahabad University in 2003. He has undergone one year training course in Chemistry from BARC (Cat-I). Subsequently he joined the Chemistry Division of BARC, Mumbai in Feb.2008. He is involved in the preparation of intermetallic compounds and study of their hydrogen storage properties. He is interested in reversible hydrogen storage in alloys and complex hydrides and their applications. He has one publication in an international journal and 7 publications in Symposia/Conferences.

Dr. C.G.S. Pillai is currently the Head, Material Chemistry Section, Chemistry Division, BARC, Mumbai. He obtained his Master's degree from Kerala University and joined BARC in 1976, after graduating from BARC Training School. He obtained his Ph.D. from Bombay University in 1987 and has been working on thermal and electrical transport properties of materials of technological importance. His present interest is in the field of development of diamond for device applications, synthesis and characterization of materials for hydrogen storage and studies on thermo-mechanical properties of thorium-based metallic fuels, for Advanced Nuclear Reactors.

ROTATIONAL DIFFUSION OF PROPYLENE IN Na-ZSM5 ZEOLITE: A MOLECULAR DYNAMICS SIMULATION AND QUASI-ELASTIC NEUTRON SCATTERING STUDY

V. K. Sharma, M.N. Rao, S. Gautam, S. Mitra, S. L. Chaplot and R. Mukhopadhyay
Solid State Physics Division

A. K. Tripathi and V. S. Kamble
Chemistry Division

This paper received the 3rd Best Poster Award at the 2nd International Symposium on Materials Chemistry, (ISMC - 2008) held at BARC, from Dec. 2-6, 2008.

ABSTRACT

Rotational dynamics of propylene adsorbed in ZSM5 zeolite, as studied by using Molecular Dynamics (MD) simulation and QuasiElastic Neutron Scattering (QENS) techniques are reported here. MD simulation studies indicated that the rotational motion is almost an order of magnitude faster than translational motion. While the slower translational motion was studied by QENS spectrometer, the rotational motion was studied using triple axis spectrometer, which has a wider energy window. The variation of the elastic incoherent structure factor showed, that the rotational motion is isotropic in nature. Intermediate scattering function, corresponding to rotational motion obtained from MD simulation, also indicated an isotropic rotation of propylene in Na-ZSM5. However, the trajectory of a CH_3 site of propylene molecules, in the centre of mass frame shows a restricted behaviour for short periods. Migration of the molecule across different channels for longer per covers the entire orientational space, thereby giving rise to isotropic rotation.

Introduction

Zeolites represent a class of technologically important materials, because of their characteristic properties of molecular sieving and catalysis, which makes them indispensable in the petroleum industries [1, 2]. While these properties depend upon many factors including the acidity and the temperature stability of the zeolites, a major role is played by the dynamics of guest molecules, in determining these properties. In order to be able to tailor-make these materials, for use in industry for catalytic and sieving purposes, it is important to understand the dynamical properties of guest molecules, adsorbed in the zeolitic materials. The level of interest that this problem of guest dynamics in zeolitic cavities has generated, can be gauged from the review articles published on the subject[3 – 5]. Over the last few decades, the accessible time and length scales of these dynamics have been enhanced, by the use of several advanced techniques, including QuasiElastic Neutron Scattering (QENS)[6 – 14], Molecular Dynamics (MD) simulation 7, 10, 11, 14 – 17], percolation theory [18], dynamics corrected transition state theory [19], NMR [20].

Recently Neutron Spin Echo (NSE) technique has also been used [21,22]. The technique of QENS has especially found a wide use in this field, for its ability to give spatial as well as temporal information on a wide range of time (10^{-10}-10^{-13} s) and length (few angstroms) scales.

A zeolite particularly important for its use in the catalysis of cracking reactions is ZSM5 zeolite. This zeolite is typified by a network of intersecting channels. In ZSM5 zeolite there are straight channels with an elliptical cross section of approximately 5.7-5.2 Å and parallel to the crystallographic axis *b*. The sinusoidal channels with nearly circular cross section of 5.4 Å run along the crystallographic axes *a* and *c* (Fig. 1 (a)). The resulting intersections are elongated cavities up to 9 Å in diameter.

Here we report the rotational motion of propylene adsorbed in Na-ZSM5 zeolite, as studied by quasielastic and molecular dynamics simulation. The studies were carried out simultaneously. Results are consistent with each other. MD simulations corroborate the experimentally observed properties and predict more detailed insight.

Experimental

The Na-ZSM5 samples used in the QENS study have composition $Na_{2.08}Al_{2.08}Si_{93.92}O_{192}.16H_2O$ and were obtained from Sud-Chemie. For ascertaining the crystalline nature of the samples, we have carried out X-ray diffraction, which revealed that the sample is crystalline with a high degree of order. The zeolite samples were put in two flat rectangular aluminum sample cells and dehydrated by evacuating for a period of about 48 hours, at a temperature 573 K under vacuum (10^{-5} torr). One of them was loaded with propylene gas (purity > 99.99%) to saturation at ambient pressure. Quasieleastic neutron scattering measurements were performed for both dehydrated and propylene adsorbed zeolites, at Triple Axis Spectrometer (TAS) 23], at Dhruva, Trombay. The TAS was used in inverted geometry, in which incident energy E_i was varied and final energy was kept fixed at $E_f = 20$ meV. In this configuration, this instrument has energy resolution ~3 meV in the Q range 0.8 - 2.5 $Å^{-1}$ as obtained from standard vanadium sample. Data from bare zeolite was used, to estimate the contribution from bare zeolite, to the data obtained from propylene loaded zeolite sample.

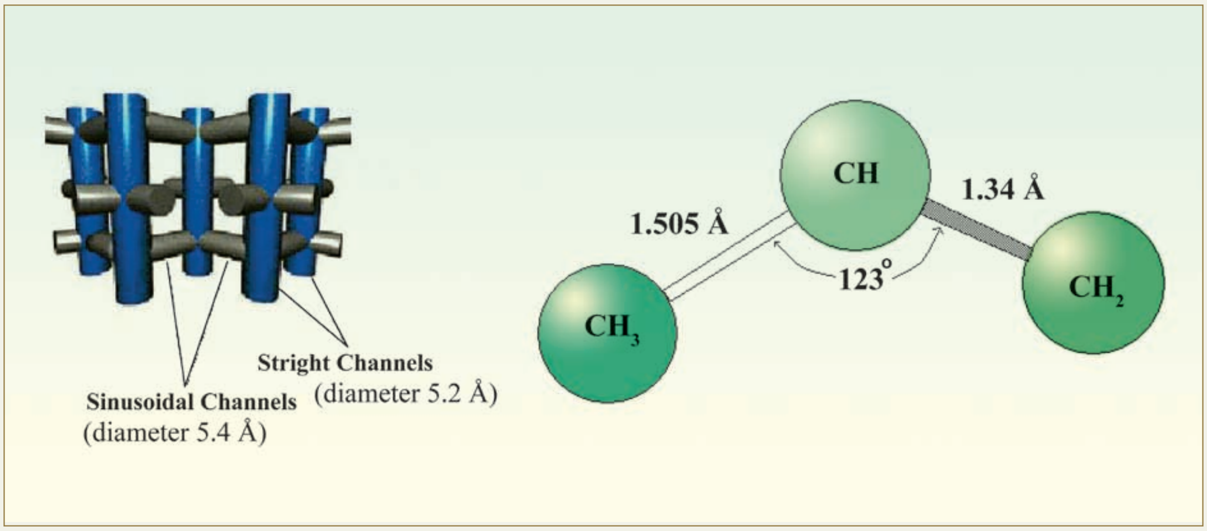

Fig. 1 : (a) Straight and sinusoidal channel structure of ZSM5 zeolite (as described in text) (b) Propylene molecule as a united atom model used in simulation

Computational details

Molecular dynamics simulation of propylene molecules confined in ZSM5 (an isostructural analog of Na-ZSM5) zeolite have been carried out in the micro canonical ensemble. Atomic positions of ZSM5 zeolite were as given by Van Koningsveld [24] The simulation cell consisted of a (2×2×2) unit cell of the ZSM5 zeolite, with 64 propylene molecules at a loading of 8 propylene molecules per unit cell. The zeolite atoms were kept fixed throughout the simulation. Propylene molecule was assumed to be rigid and modeled in united atom model as shown in Fig. 1(b). Lennard-Jones potential parameters between guest-guest and guest-zeolite were taken from literature [25, 26]. Reorientation motion of propylene was studied using quaternion formalism [27].

Theoretical aspects

In a neutron scattering experiment, the scattered intensity is analyzed as a function of both energy and momentum transfer. The quantity measured is the double differential scattering cross section, representing the probability, that a neutron is scattered with energy change *dE* = ħ *d ù* into the solid angle dΩ 6],

$$\frac{d^2\sigma}{\partial\omega\partial\Omega} \propto \frac{k}{k_0}[\sigma_{coh}S_{coh}(\boldsymbol{Q},\omega)+\sigma_{inc}S_{inc}(\boldsymbol{Q},\omega)] \qquad (1)$$

where ó is the scattering cross-section, subscripts *coh* and *inc* denote the coherent and incoherent components and *S*(Q,ω) is the scattering law. **k** and **k**$_0$ are the final and initial wave vectors. **Q** = **k**- **k**$_0$ is the wave vector transfer [Q= 4π sinθ /λ, where 2θ is the scattering angle, in case of elastic scattering] and ħù = *E*-*E*$_0$ is the energy transfer. For systems containing hydrogen atoms, as ó$_{coh}$ (any element) << ó$_{inc}$ (hydrogen), one can write,

$$\frac{d^2\sigma}{\partial\omega\partial\Omega} \propto \frac{k}{k_0}[\sigma_{inc}S_{inc}(\boldsymbol{Q},\omega)] \qquad (2).$$

Therefore, for a hydrogenous system, one is mainly concerned with the incoherent component of the scattering law.

For a molecular system, different kinds of motions – translational, rotational and vibrational – can exist and generally it is assumed that these motions are dynamically independent for mathematically tractable solution. In the quasielastic regime (± 2 meV), the vibrational contribution will be only through the Debye-Waller factor, e^{-2W}, $W=\frac{1}{2}<u^2>Q^2$ where <*u*^{2}> is the mean square displacement. The total *S*(Q,*ù*) can be expressed as a convolution product of the respective scattering functions, under the assumption that the motions are not coupled,

$$S^{tot}_{inc}(Q,\omega)=\exp(-<u^2>Q^2)[S^{trans}_{inc}(Q,\omega)\otimes S^{rot}_{inc}(Q,\omega)] \qquad 3)$$

The scattering law for the rotational motion can be written as [5],

$$S^{rot}_{inc}(Q,\omega)=B(Q)\delta(\omega)+[1-B(Q)]L_R(\omega,\Gamma_R) \qquad (4)$$

where the first term is the elastic part and the second is the quasielastic one. *L*$_R$(*w*,Γ$_R$) is a Lorentzian function,

$$L_R(\omega,\Gamma_R)=\frac{1}{\pi}\frac{\Gamma_R}{\Gamma_R^2+\omega^2} \qquad (5)$$

where Ã$_R$, is the HWHM of the Lorentzian function, inversely proportional to the reorientation time τ. It is convenient to analyse the data in terms of elastic incoherent structure factor (*EISF*), which provides information about the geometry of the molecular reorientations. If *I*$_{el}$(*Q*) and *I*$_{qe}$(*Q*) are the elastic and quasielastic intensities respectively, then *EISF* is defined as [6],

$$EISF=\frac{I_{el}(Q)}{I_{el}(Q)+I_{qe}(Q)} \qquad (6)$$

Therefore, *B*(*Q*) in Eq. (4) is nothing but the *EISF*.

There will be no elastic component for the translational motion and the scattering law will have only a Lorentzian function [5],

$$S_{inc}^{trans}(Q,\omega)=\frac{1}{\pi}\frac{\Gamma_T}{\Gamma_T^2+\omega^2} \tag{7}$$

where Γ_T is Half Width at Half Maximum (*HWHM*) of the Lorentzian function.

Scattering Law, $S_{inc}^{tot}(\mathbf{Q},\omega)$ can also be expressed as the Fourier transform of intermediate scattering function $I_{inc}^{tot}(\mathbf{Q},t)$,

$$S_{inc}^{tot}(Q,\omega)=\frac{1}{2\pi}\int_{-\infty}^{\infty} I_{inc}^{tot}(Q,t)\exp(-i\omega t)\,dt \tag{8}$$

The incoherent intermediate scattering function, $I_{inc}^{tot}(\mathbf{Q},t)$ is a time correlation function for a single particle and can be expressed in terms of the position vector of the scatterer,

$$I_{inc}^{tot}(Q,t)=\left\langle \exp\{i\boldsymbol{Q}.(\boldsymbol{r}(t)-\boldsymbol{r}(0))\}\right\rangle \tag{9}$$

where ***r*** (0) and ***r*** (t) are the positions of scatterer at time *t* = 0 and time *t* respectively and the angular brackets indicate ensemble average. Therefore, Eq. (3) can also be expressed in terms of intermediate scattering function for translational and rotational motion as

$$I_{inc}^{tot}(Q,t)=I_{inc}^{trans}(Q,t).I_{inc}^{rot}(Q,t) \tag{10}$$

where

$$I_{inc}^{trans}(Q,t)=\left\langle \exp\{i\boldsymbol{Q}.(\boldsymbol{r}^{CM}(t)-\boldsymbol{r}^{CM}(0))\}\right\rangle \tag{11}$$

$$I_{inc}^{rot}(Q,t)=\left\langle \exp\{i\boldsymbol{Q}.(\boldsymbol{d}(t)-\boldsymbol{d}(0))\}\right\rangle \tag{12}$$

where $\boldsymbol{r}^{CM}(t)$, $\boldsymbol{r}^{CM}(0)$ is a radius vector of center of mass of propylene molecules, in space-fixed frames at time *t* and time 0 respectively and ***d*** is radius vector of a hydrogen atom with respect to centre of mass of propylene molecule. Therefore, by using Eq. (11) and (12), one can easily calculate the intermediate scattering function from MD simulation trajectories.

Results and Discussion

Intermediate scattering functions, corresponding to translational and rotational motions, are calculated from trajectories of MD simulation from eq.11 and eq.12. In case of a rigid molecule, the information about the rotational motion can be obtained, by following the motion of one interaction site with respect to the centre of mass. In the present case, a CH_3 site was chosen, to provide information about the rotational motion. Thus, ***d*** appearing in eq. 12 is the radius vector of a CH_3 site, with respect to

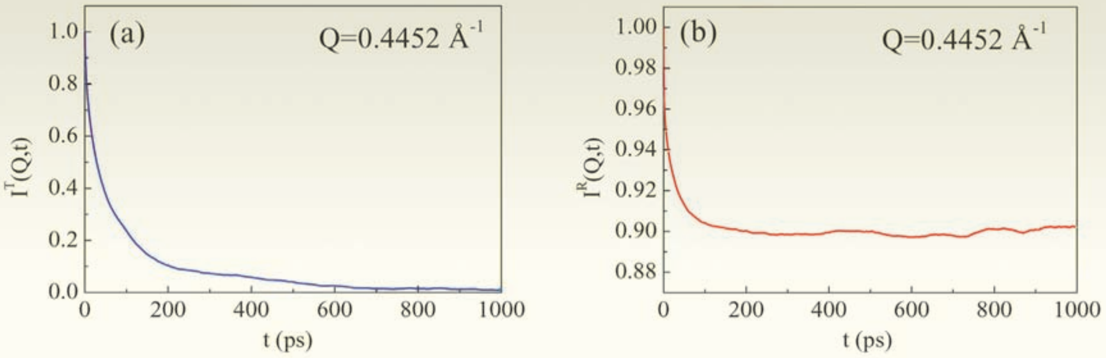

Fig. 2 : Variation of (a) translational and (b) rotational intermediate scattering functions calculated from MD simulation trajectories with time *t* at *Q*=0.4452 Å^{-1}

centre of mass. Very different features can be noted from the behaviour of the calculated intermediate functions, corresponding to translational and rotational motions, as shown in Fig. 2 for a typical value of $Q = 0.4452$ Å^{-1}. The intermediate scattering functions corresponding to the rotational motion reaches a non-zero minimum value within $t \sim 100$ ps, whereas that of the translational goes to zero at $t \sim 900$ ps. A much faster decay of the rotational component, indicates an order of magnitude of faster motion as compared to translation.

The value of $I^R(Q,t)$ functions for longer durations is identical to the *EISF*, a quantity obtained in a QENS experiment. To understand the geometrical aspects of the rotational motion in the present case, the $I^R(Q,t)$ was calculated for different Q values. The variation of *EISF* was compared with various models of rotational motion. The variation of *EISF* for propylene adsorbed ZSM5 zeolites is found to be described well by the isotropic rotational diffusion model as shown in Fig. 3.

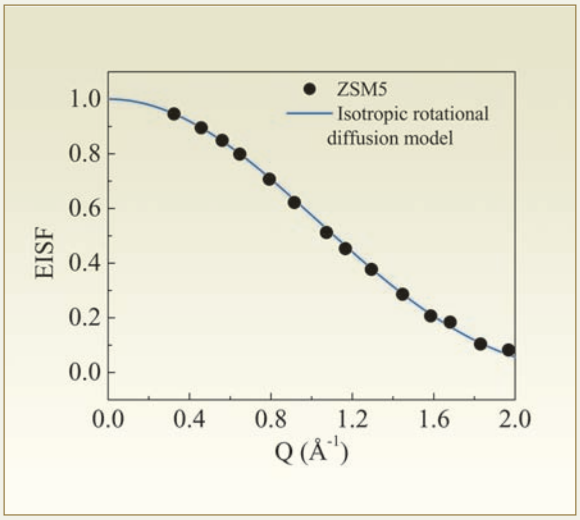

Fig. 3 : Variation of *EISF* obtained from the simulation for propylene and ZSM5 zeolites. The solid curve corresponds to the calculated variation for isotropic rotational diffusion. Note that the curve is calculated for a CH_3 site of the propylene molecule.

The *EISF* in case of isotropic rotational diffusion can be expressed as $j_0{}^2(QR)$ where j_0 is the zero order Bessel function and R is the radiation of gyration. In the present case, R is equal to the distance of CH_3 site from centre of mass of propylene molecules, in body fixed frame.

To investigate the fast rotational dynamics of propylene molecules adsorbed in Na-ZSM5 zeolite, as predicted by the MD simulation results, we have carried out quasi elastic neutron scattering experiment using TAS at Dhruva, Trombay. Significant broadening was observed for the propylene loaded Na-ZSM5 zeolite, whereas no broadening was observed for the bare Na-ZSM5 zeolite. Data for the bare zeolite was subtracted from propylene loaded Na-ZSM5 data, to get the contribution from the propylene molecules alone. Here both the fast and slow components are expected to contribute to the data and therefore the scattering law would have the contribution from both translation and rotation. The solace is the translational contribution is already available from the measurement of the QENS spectrometer [7] and using that information, the contribution of the rotational part can be evaluated.

Here we used the total scattering law as given in Eq. (3). Scattering law for the rotational and translational components is given in Eqs. 4 and 7 respectively. Convoluting the total scattering function with the instrumental resolution function, the parameters of the rotational part ($B(Q)$ and Γ_R) were determined by least squares fit with the measured data. The *EISF* extracted from the fit is shown in Fig. 4. Out of the various plausible models that can be envisaged for describing the rotational motion of the propylene adsorbed in Na-ZSM5, isotropic rotational diffusion described the experimental *EISF* very well as evident in Fig. 3. Radius of gyration was obtained as 1.91 ± 0.01 Å which is equivalent to average distance of all hydrogen atoms, from centre of mass of propylene molecules.

The Scattering Law for isotropic rotational diffusion [28] is given by,

$$S^R(Q,\omega) = j_0^2(Qr)\delta(\omega) + \frac{1}{\pi}\sum_{l=1}^{\infty} A_l(Q)\frac{l(l+1)D_R}{\left(l(l+1)D_R\right)^2 + \omega^2} \qquad (13)$$

where, $A_l(Q) = (2l+1)\,j_l^2(Qr)$ is the weight factor of the quasielastic part and j_l's are the spherical Bessel function of order l, D_R is rotational diffusion coefficient. With the maximum allowed wave vector transfer, Q, as 2.5 Å^{-1} in Triple Axis Spectrometer (TAS), it was found that contribution only up to l=6 towards $A_l(Q)$ in Eq. (16) are sufficient [17].

Using Eqs. 13, 4 and 3, the total scattering function can be written as,

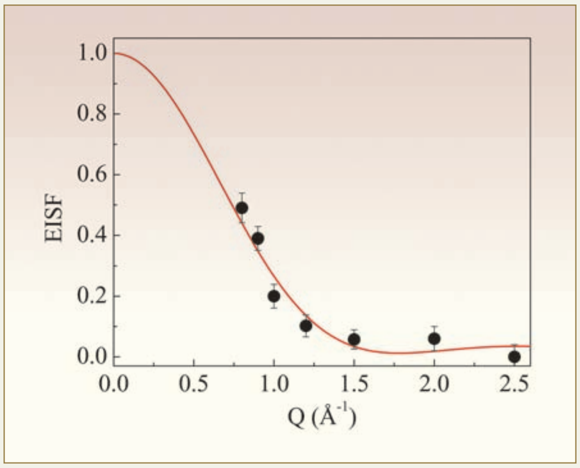

Fig. 4 : Variation of EISF as obtained from QENS data using TAS with respect to wave vector Q. The solid line corresponds to the isotropic rotational diffusion model.

$$S_{Total}(Q,\omega) = j_0^2(Qr)\frac{1}{\pi}\frac{\Gamma_T(Q)}{(\Gamma_T(Q))^2+\omega^2} + \frac{1}{\pi^2}\sum_{l=1}^{\infty}(2l+1)\,j_l^2(Qr)\frac{\left[\Gamma_T(Q)+l(l+1)D_R\right]}{\left[\Gamma_T(Q)+l(l+1)D_R\right]^2+\omega^2} \qquad (14).$$

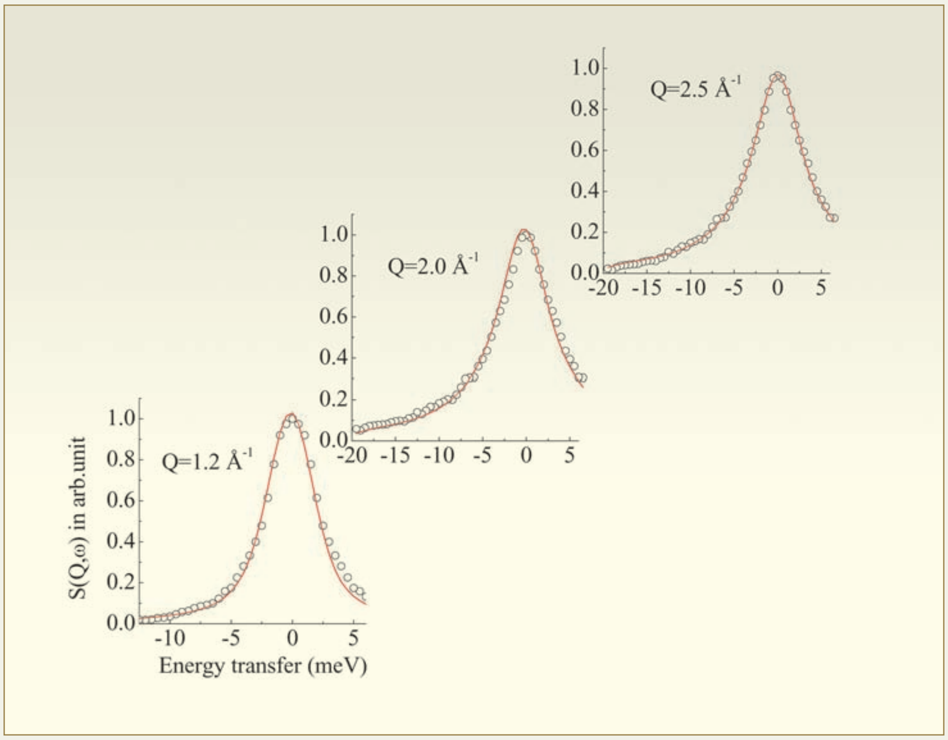

Fig. 5 : Typical fitted experimental data observed with TAS assuming isotropic rotational diffusion model for propylene adsorbed in Na-ZSM5 zeolite at some typical *Q* values.

To compare with the experimental data, Eq. (14) was convoluted with instrumental resolution and the parameters were determined by least squares fit. Here only D_R is to be determined. Typical data with fits obtained are shown in Fig. 5. As evident from the figure, the model has provided very good description of the experimental data. Variation of rotational diffusion coefficients obtained from fits, is shown in Fig. 6. It is found, that rotational diffusion coefficient is more or less constant with respect to *Q*, with an average rotational diffusion coefficient of $D_R = 0.37$ meV.

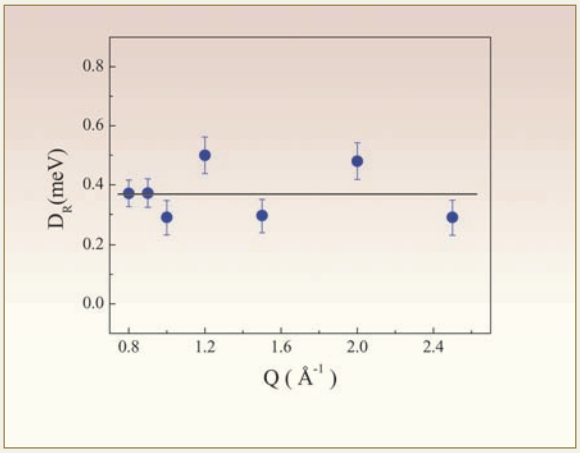

Fig. 6 : Variation of rotational diffusion coefficient with *Q*.

For isotropic rotational motion the trajectory, as obtained from MD simulation of a CH_3 site of the propylene molecule, with respect to the centre of mass should trace a sphere in 3 dimensions. Figs. 7(a) and (b) show the same for time intervals of 1.3 ns and 50 ps in the X-Y plane. It is clearly seen from Fig. 7 (a), that the path traced by the CH_3 site with respect to the centre of mass of the molecule, encompasses the surface of a sphere at longer durations, thereby showing that the molecule has had all the possible orientations, during the time interval of the simulation. This shows that the rotational motion is indeed isotropic on the average over large time. But for shorter periods, the motion is restricted by channel framework and not truly isotropic which is evident in Fig. 7 (b). This is because, as the channel size of the ZSM5 zeolite is comparable with the size of propylene molecule, the molecule does not have the full freedom to rotate in all the directions in a particular channel, for short periods. However, for longer periods, the molecule can migrate to other channels through channel intersection, thereby covering larger orientational space. Therefore, at sufficiently long time, on the average, a molecule can cover all the different orientations.

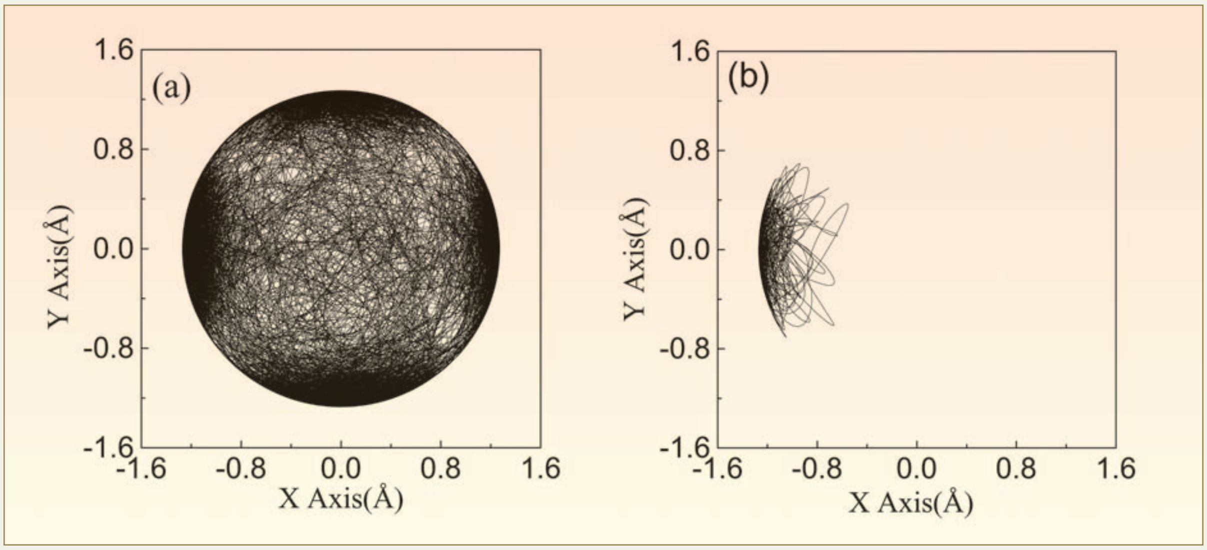

Fig. 7 : Trajectory of the CH_3 site with respect to the centre of mass of the molecule for a) 1311 ps and b) first 50 ps of the simulation production run in X-Y plane.

Conclusion

A study of the rotational motion of propylene confined in channel framework of Na-ZSM5 has been carried out, using QENS measurements and MD simulations. MD simulations predicted faster rotational motion, which was confirmed by QENS measurements carried out at TAS. It was found, that propylene molecule undergoes isotropic rotational diffusion in the channels of ZSM5 zeolite. MD simulation also indicated isotropic rotational diffusion, however, it showed that for short periods, the rotational motion deviates from isotropic behaviour, which is expected from the topology of the ZSM5 zeolite framework. Here experiments and simulation were carried out simultaneously and independently. The results as obtained from these studies not only gave an insight into the rotational dynamical process, but were also consistent with each other.

References

1. G. Tomlinson, Modern Zeolites, *Structure and Function in Detergents and Petrochemicals* (Traw Tech Publications Ltd., Switzerland, 1998).
2. D. L. Bish and D. W. Ming, (Eds.) *Natural Zeolites: Occurrence, Properties, Applications* (Reviews in Mineralogy and Geochemistry Volume 45).
3. D. Dubbeldam and R. Q. Snurr, *Molecular Simulation,* 33 (2007) 305.
4. P. Demontis and G. B. Suffritti, *Chem. Rev.* 97 (1997) 2845.
5. Hervé Jobic and Doros N. Theodorou, *Micropor. Mesopor. Mater.* 102 (2006) 21.
6. Marc Bée, *Quasielastic Neutron Scattering*, (Adam Hilger, Bristol 1988).
7. V. K. Sharma, S. Gautam, S. Mitra, Mala N. Rao, A. K. Tripathi, S. L. Chaplot, and R. Mukhopadhyay, *J. Phys. Chem. B* 113 (2009) 8066.
8. S. Mitra, R. Mukhopadhyay, A.K. Tripathi and N.M. Gupta, *Applied Physics A,* 74 (2002) S1308.
9. V. K. Sharma, Mala N. Rao, Siddarth Gautam, A. K. Tripathi, V. S. Kamble, S. L. Chaplot and R. Mukhopadhyay, *Pramana - J. Phys.*, 71 (2008) 1165.
10. A. Sayeed, S. Mitra, A.V. Anil Kumar, R. Mukhopadhyay, S. Yashonath and S.L. Chaplot, *J. Phys. Chem. B,* 107 (2003) 527.
11. R. Mukhopadhyay, A. Sayeed, S. Mitra, A.V. Anil Kumar, Mala N. Rao, S.L. Chaplot and S. Yashonath, *Phys. Rev. E,* 66 (2002) 061201.
12. S. Mitra, S. Sumitra, A.M. Umarji, R. Mukhopadhyay, S. Yashonath and S. L. Chaplot, *Pramana - J. Phys.* 63 (2004) 449.
13. S. Gautam, S. Mitra, A. Sayeed, S. Yashonath, S.L. Chaplot and R. Mukhopadhyay, *Chem. Phys. Lett.* 442 (2007) 311.
14. S. Mitra, Siddharth Gautam, R. Mukhopadhyay, S. Sumitra, A.M. Umarji, S. Yashonath, S.L. Chaplot, *Physica B* 385-386 (2006) 275.
15. Pradip Kr. Ghorai, Subramanian Yashonath, Pierfranco Demontis and Giuseppe B. Suffritti, *J. Am. Chem. Soc.,* 125 (2003) 7116.
16. Siddharth Gautam, S. Mitra, R. Mukhopadhyay, and S.L. Chaplot, *Phys. Rev. E* 74 041202 (2006).
17. Siddharth Gautam, S. Mitra, S.L. Chaplot and R. Mukhopadhyay, *Phys. Rev. E* 77 (2008) 061201.
18. D. Keffer, alon V. McCormick, and H. Ted Davis, *J. Phys. Chem.* 100 (1996) 967.
19. E. Beerdsen, B. Smit, and D. Dubbeldam *Phys. Rev. Lett.* 93, 248301 (2004).
20. J. Kärger, and D.M. Ruthven, *Diffusion in Zeolites and Other microporous solids* (Wiley –Interscience, New York 1992).
21. Hervé Jobic, Alain Méthivier, and Georg Ehlers, Micropor. Mesopor. Mater. 56 (2002) 27.
22. Hervé Jobic, Harikrishnan Ramanan, Scott M. Auerbach, Michael Tsapatsis and Peter Fouquet, *Micropor. Mesopor. Mater.* 90 (2006) 307.

23. S.L. Chaplot, R. Mukhopadhyay, P.R. Vijayaraghavan, A.S. Deshpande and K.R. Rao, *Pramana-J. Phys*., 33 (1989) 595.
24. H. Van Koningsveld, H. Van Bekkum and J. C. Jansen, *Acta. Cryst*. B, 43 (1987) 127.
25. J.I. Siepmann, M.G. Martin, C. Mundy and M.L. Klein, *Mol. Phys*., 90 (1997) 687.
26. T. J. H. Vlugt, R. Krishana and B. Smit, *J. Phys. Chem.* B 103 (1999) 1102.
27. M.P. Allen and D.J. Tildesley, *Computer Simulation of Liquids* (Oxford University Press, Oxford, 1987).
28. V.F. Sears, *Can. J. Phys*., 44 (1966) 1999.

ABOUT THE AUTHORS

Mr. Veerendra Kumar Sharma graduated from the 50th batch of BARC Training School after completing his M.Sc. (Physics) from Rajasthan University, Jaipur. He received Homi Bhabha Award as overall topper in the 50th batch of BARC Training School. Mr. Sharma has published 5 research papers in international peer reviewed journals and 14 papers in international and national conferences. He is involved in research on stochastic dynamics of molecules in condensed and soft matters using neutron scattering and molecular dynamics simulation techniques.

Dr. Mala N. Rao graduated from the 33rd batch of BARC Training School, after completing her M.Sc. (Physics) from Mumbai University. She is currently working in the area of lattice dynamics of materials, mainly employing the technique of inelastic neutron scattering, in the Solid State Physics Division.

Mr. Siddharth Gautam obtaining his M.Sc. (Physics) degree from Mumbai University in 2002 and working as a lecturer at Thakur Degree College in Mumbai for 2 academic years, Mr. Siddharth Gautam joined the Solid State Physics Division of BARC in 2004, for doing his Ph. D under MU-DAE collaborative programme. His thesis titled “Study of Molecular Motions in Confined media using MD Simulation and Neutron Scattering techniques” was accepted by Mumbai University for award of Ph.D. degree in 2009. He is involved in studying molecular motion using MD simulations and quasielastic neutron scattering.

Dr. Subhankur Mitra joined the Solid State Physics Division in 1994, from the 37th batch of BARC Training School. He received doctorate degree in Physics from Mumbai University in 2005. Dr. Mitra has completed his PostDoctoral fellowship from Laboratoire Leon Brillouin, France. He has published around 40 research papers in international peer reviewed journals. He has been studying molecular motion in condensed matter, using neutron scattering and molecular dynamics simulation techniques.

ABOUT THE AUTHORS

Dr. S. L. Chaplot is from the 18th batch of BARC Training School. He is at present heading the Solid State Physics Division, BARC. He works in the areas of neutron scattering, lattice dynamics and computer simulations.

Ramaprosad Mukhopadhyay joined the 23rd batch of BARC Training School in 1979 after completing his M.Sc (Physics) from Kalyani University. He received the Siddharth Memorial Gold Medal (being topper in M.Sc) and the Homi Bhabha Award for first rank in Physics discipline of 1979 BARC Training School. Since then, he has been associated with the neutron scattering group of Solid State Physics Division. He has worked as: Visiting Scientist at ISIS facility, Rutherford Appleton Laboratory, UK during 1990-91, Visiting Professor at Departamento de Fisica de Materiales, Universidad del Pais Vasco, Spain during 1996-97 and Visiting Scientist at KENS, KEK, Japan in 2000. He has more than 90 papers to his credit in international journals and about 170 papers in international and national conferences.

Dr. A.K. Tripathi joined the Chemistry Division, in 1984 after successful completion of one year Orientation course in Nuclear Science and Engineering from the 27th batch of BARC Training School. He started his research activity in the area of heterogeneous catalysis and has contributed to the development of catalytic solution, for the gas recovery problem in sealed off CW-CO_2 lasers. His research interests include supported metal catalysts, host-guest chemistry including dynamics of adsorbed molecules in micro/mesoporous molecular sieves hosts, entrapment of nanosized oxides in mesoporous materials and evaluation of their catalytic/photocatalytic behaviour towards reactions of environmental importance. Presently, he is actively engaged in studies related to catalyst development for various steps of S-I thermochemical cycle for hydrogen production.

Dr. V.S. Kamble joined the Chemistry Division, in 1974 after his M.Sc. from Nagpur University. He initiated his research career in the area of heterogeneous catalysis, by studying the CO and CO_2 adsorption/methanation over supported metal catalyst and evaluated the role of gamma irradiation in the enhancement of catalytic activity. He also investigated the mode of adsorption and encapsulation of various molecules such as CO, CO_2, methanol, ethylene and benzene in micro / mesoporous molecular sieves, using techniques such as, FTIR, TPD, ESR and microcalorimetry and established structure-activity relationship. He has successfully demonstrated an efficient sun-light assisted photocatalytic oxidation of Volatile Organic Compounds (VOCs) using uranium containing mesoporous molecular sieves. His current interest lies in the S-I processes for hydrogen production specifically in development of catalyst for decomposition of H_2SO_4.

SYNTHESIS OF NANO-SIZED ELECTROLYTE MATERIALS OF SOFC BY GEL COMBUSTION ROUTE

S. Varma, C. Dwivedi, A. N. Shirsat, B. N. Wani and S. R. Bharadwaj
Chemistry Division

This paper was awarded for the 3rd Best Poster Presentation Award at the 2nd International Symposium on Materials Chemistry (ISMC-2008) held at Mumbai, from Dec. 2-6, 2008

ABSTRACT

Rare earth (La, Nd, Gd) doped zirconia were synthesized by gel combustion and co-precipitation route. All compositions were found to stabilise as cubic phase of Zirconia, similar to YSZ, 700 °C. Only Gd doped zirconia retained cubic phase for temperatures upto 1150 °C. Nd and La doped samples exhibited phase separation at 1150 °C. Thermal expansion behaviour of Gd doped zirconia was found to be compatible with that of reported solid oxide fuel cell components.

Introduction

The efficiency of energy conversion and durability of performance of the fuel cell, mainly depend on the oxide ion conducting solid electrolyte activity [1, 2]. YSZ is most commonly used as an electrolyte in SOFCs, because it fulfils several desired criteria (high ionic conductivity, low or nearly zero electronic conductivity and rational strength to stand the mechanical and thermal stresses while operating) [3]. In particular, 8 mol% Y_2O_3–92 mol% ZrO_2 (8YSZ), whose reported conductivity is 0.12 S / cm at 1000^0C, has been widely used. Because a high-temperature operation (about 1000^0C) causes many serious problems, i.e. degradation of the cell performance and a limited choice of materials and so on, it is desirable to operate SOFCs at a moderate temperature around 800^0C. Two approaches for operation temperature reduction have been proposed: one is to use electrolyte membrane to reduce the ohmic loss and the other is to find new electrolyte materials that exhibit high oxygen ion conductivity at reduced temperatures [4]. In the present work, other rare earth (La, Gd and Nd) substituted zirconia were synthesized and evaluated to aid in the development of improved intermediate temperature SOFCs. Most of these electrolyte materials are synthesized using traditional solid state techniques with sintering at 1600–1650 °C, leading to densities of less than 95%, which normally reduce ionic conductivity of the electrolytes. While the wet-chemical synthesis methods produce ceramics single or multi-oxide powders with high sinterability, high surface area, well-defined chemical compositions and homogeneous distribution of the elements [5]. Here gel combustion and co-precipitation synthesis of mentioned multi-component ceramic oxides has been carried out, to produce homogeneous, very fine, crystalline and unagglomerated powders, without the intermediate decomposition step. The structural characterizations of prepared sample were done by XRD and thermal expansion data was generated by dilatometric studies.

Experiment

The solution route adopted in the present work includes combustion and co-precipitation method. The comparisons between the properties of the compound, as to the route of synthesis were also studied.

Synthesis

Various rare earth doped zirconia samples were prepared, by combustion and co-precipitation route and are denoted in Table 1.

Table 1: Synthesis route, composition and sample name for the synthesised oxides

Synthesis route	composition	Sample name
Combustion	$La_{0.2}Zr_{0.8}O_{2-ä}$ $Nd_{0.2}Zr_{0.8}O_{2-ä}$ $Gd_{0.2}Zr_{0.8}O_{2-ä}$	LaSZC NdSZC GdSZC
Co-precipitation	$La_{0.2}Zr_{0.8}O_{2-ä}$ $Nd_{0.2}Zr_{0.8}O_{2-ä}$ $Gd_{0.2}Zr_{0.8}O_{2-ä}$	LaSZP NdSZP GdSZP

Combustion method

In the present work, the nitrate salts of the metals of interest were mixed together in a required stoichiometry, along with glycine in an aqueous media, to produce the transparent mixed metal nitrate solution. Appropriate amount of glycine was added as a fuel, as per the concept of propellant chemistry to obtain ratio of oxidizing to reducing valences as unity [6]. The transparent aqueous solution containing metal nitrates and glycine is then converted to a viscous liquid (gel) by thermal dehydration on a hot plate. The gel with an intimate blending between fuel and an oxidant is then subjected to a temperature in excess of 180 °C by external heating to initiate the combustion reaction. Combustion once initiated is self propagating, resulting in a voluminous powder with a simultaneous evolution of large volume of gaseous product. The powder obtained was further calcined at 600 °C for 24 h. This is to remove the traces of residual fuel, nitrates and their decomposition products, so as to have a chemically pure and crystalline product. The equation for reaction can be written as

$$0.8\, ZrO(NO_3)_2 + 0.2\, RE(NO_3)_3 + \text{fuel} \rightarrow Zr_{0.8}RE_{0.2}O_{2-}\delta + \text{evolution of gases} + H_2O$$

Co-precipitation method

The rare earth substituted samples were prepared by co-precipitation route. A stoichiometric solution with appropriate concentration of the metal nitrates was prepared and mixed. The ammonia solution was then directly added at 90°C with constant stirring. The precipitate was allowed to settle down and then filtered and washed with distilled water.

This precipitate was dried at 100°C. The dried powder (the precursor) was then calcined at 600°C and 1400°C.

Characterization

X-ray Diffraction

Philips 1710 diffractometer based on the Bragg-Brentano reflection geometry with Cu $K_á$ source and Ni foil filter was used for the phase characterization of the obtained powder by X-ray diffraction technique. The diffractometer has a proportional counter (Argon filled) for the detection of X-rays. The X-ray tube rating was maintained at 30 KV and 20 mA in the Philips unit.

The approximate crystallite size is estimated from line broadening of the X-ray peak with the help of Scherrer formula [7].

Thermal Expansion

In the present work, LKB 3185 quartz dilatometer was used for dilatometric measurements. The sample (in the form of sintered pellet of 10 mm diameter and

2-3 mm height) was kept between small quartz discs, which were placed inside the quartz tube. The dilation of the sample was read on a calibrated Mituloyo dial gauge with an accuracy of ± 0.5 ìm. The dilatometric runs on these pellets were carried out in the temperature range of 25 °C to 850 °C at a heating rate of 4°C/min, in air. The dilatometer was calibrated using high density nuclear pure thoria pellets.

Results and Discussion

XRD

Phase identification for the synthesized materials was carried out using Powder XRD technique. Fig. 1 depicts XRD patterns of all the samples as synthesized by combustion and co-precipitation route and heated for 24 h at 700 °C. All the rare earth substituted samples were found to be single phasic in nature and the XRD lines were found to match with the reported pattern for cubic phase of Yttria stabilized Zirconia (JCPDS 30-1468). It is evident from the XRD patterns, that the samples produced by both the routes have stabilised the cubic phase of zirconia. The broadening of the XRD peaks also suggests crystallite size in nanometre range. Crystallite size data as calculated by Scherrer equation are given in Table 1. The samples prepared by combustion route are found to have smaller particle size of 11 – 15 nm as compared to 22 - 25 nm when obtained through co-precipitation route.

The synthesised samples were sintered at two more temperatures, i.e. 1400 °C and 1100 °C. The XRD recorded are given in Fig. 2 and Fig. 3 respectively. As evident from Fig. 5, all the samples underwent phase transition during this sintering. While, La substituted sample was found to match with monoclinic phase of zirconia (JCPDS 37-1484), Nd and Gd substituted samples exhibit the presence of two phases. XRD patterns for NdSZC and NdSZP samples are found to consist of both monoclinic (JCPDS 37-1484) and tetragonal (JCPDS 42-1164) phases of zirconia. GdSZP and GdSZC samples exhibit retention of cubic phase of Zirconia (JCPDS 30-1468) along with traces of tetragonal phase of zirconia (JCPDS 42-1164).

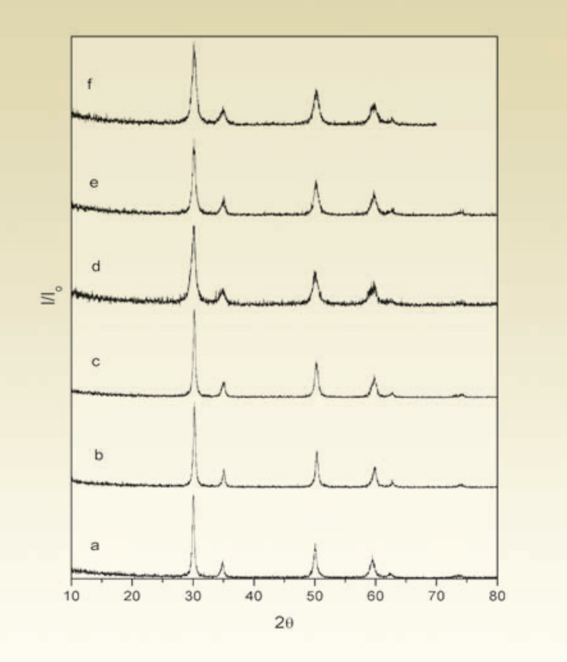

Fig. 1 : XRD patterns for (a) LaSZP, (b) GdSZP, (c) NdSZP, (d) LaSZC, (e) GdSZC and (f) NdSZC samples after calcination at 700 °C for 24h

Samples synthesized by combustion route were also sintered at 1100 °C. Fig. 3 exhibits overlay of XRD patterns recorded for these samples. It is evident that while, Gd substituted sample retains the cubic phase, Nd and La substituted samples exhibit phase transition to Tetragonal (Trace level) and Monoclinic phases, respectively. The overall data for the phases present after sintering at different temperatures is summarized in Table 1.

Dilatometry

The relative thermal expansion was measured in air from room temperature to 850°C on air-sintered circular shaped pellets of 10 mm diameter. Plots for the relative thermal expansion of sintered pellets in Ar flow are shown in Fig. 4. The temperature dependence of relative thermal expansion for all materials shows identical behaviour. The Linear Thermal Expansion Coefficients (TECs) of the compounds for different

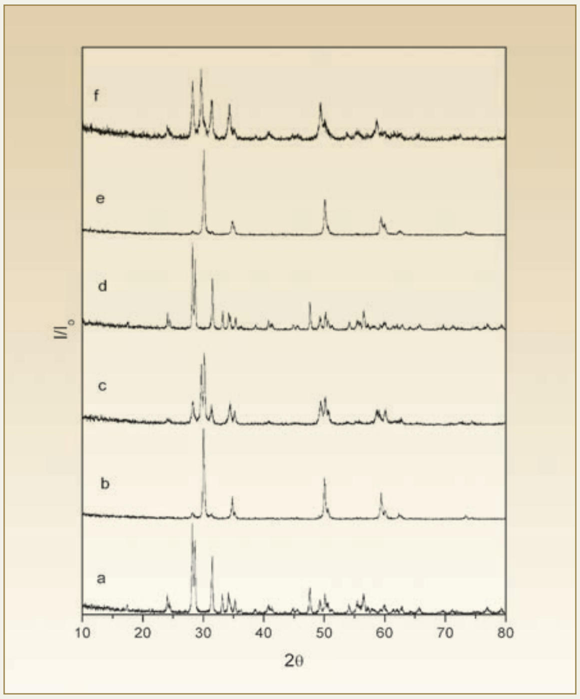

Fig. 2 : XRD patterns for (a) LaSZP, (b) GdSZP, (c) NdSZP, (d) LaSZC, (e) GdSZC and (f) NdSZC samples after sintering for 4h at 1400 °C.

rare earth dopants were deduced from Fig. 4 and are given in Table 3. The TEC value of Gd substituted zirconia was close to that reported for YSZ value whereas the value for La substituted sample was found to be the least. The TEC value increases with decrease in ionic radii of substituted rare earth cation. When these values were compared with those reported for other components of SOFC, as shown in Table 4, the value for GdSZ is found to be in good agreement with the TEC values of all the three components, namely Ni/YSZ cermet anode, the lanthanum manganite cathode and metallic interconnect materials.

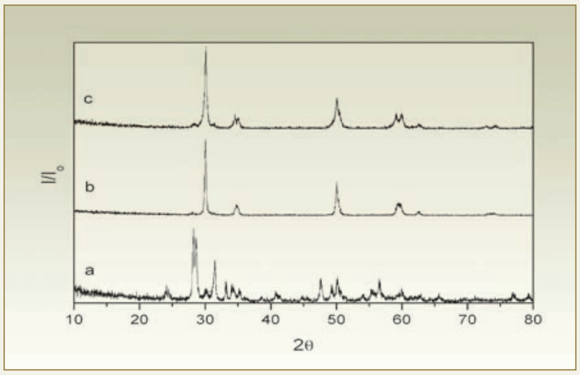

Fig. 3: XRD patterns for (a) LaSZC, (b) GdSZC and (c) NdSZC samples after sintering for 4h at 1100 °C

Discussion

Low temperature synthesized rare earth substituted zirconia showed cubic phase which on heating above 1100°C converts to tetragonal and/or monoclinic phase. In case of GdSZ, cubic phase could be stabilised to a greater extent as compared to other two substituted samples. These could be due to identical ionic radii of Y^{3+} (0.93 Å) and Gd^{3+} (0.94 Å), which also displays similar behaviour. Whereas the ionic size of La^{3+} (1.06 Å) and Nd^{3+} (1.00 Å) being bigger the stabilisation of cubic phase formed at lower temperature was by solution route synthesis, was not possible at temperatures in excess of 1100 °C.

Table 2: Crystallite size and phase identification after sintering at different temperatures

Sample	700°C		1400°C	
	Particle size	Symmetry	Particle size	Symmetry
NdSZC	11nm	C	40nm	C + T
GdSZC	15nm	C	44nm	C + T
LaSZC	11nm	C	66nm	M
NdSZP	23nm	C	45nm	C + T
GdSZP	22nm	C	38nm	C + T
LaSZP	25nm	C	48nm	M

C = Cubic, T = Tetragonal, M = Monoclinic

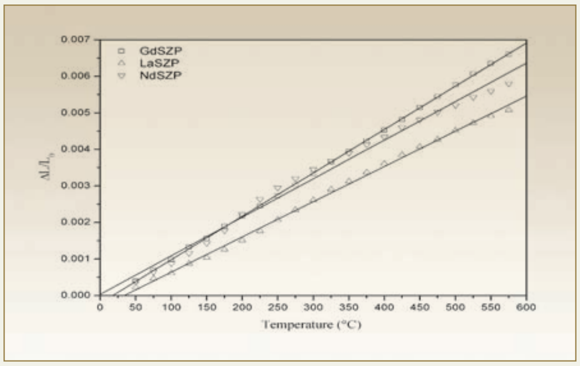

Fig. 4 : Thermal expansion for samples, sintered at 1400 °C

Table 3: Thermal Expansion Coefficient (TEC) values of rare earth doped zirconia

Sample	**TEC**
LaSZP	9.64 X 10^{-6}
NdSZP	10.55 X 10^{-6}
GdSZP	11.87 X 10^{-6}

Table 4: Thermal Expansion Coefficients of components used for commercial Solid Oxide Fuel Cell

Component	**Material**	**TEC/10^{-6}K^{-1}**	**Ref.**
Electrolyte	YSZ	10.5-11.0`	[8]
Anode	Ni/YSZ cermet (30 vol. % Ni)	12.3	[8]
Cathode	$La_{0.79}Sr_{0.2}MnO_3$	12.4	[8]
Ceramic interconnect	$La_{0.9}Sr_{0.1}CrO_3$	10.7	[8]
Metalic interconnect	Fe + Cr (18-24 wt %)	12.2-14.0	[9]

Conclusion

In all the three La, Nd and Gd substituted zirconia, the cubic phase could be achieved at as low as 700°C temperature, when synthesized by gel combustion as well as co-precipitate route. Whereas, this phase could be prepared only above 1700°C by ceramic route. The samples calcined at 700°C showed nano sized particles of 11 -25 nm depending on the synthesis route employed. When heated to 1400°C all the samples exhibited good sintering characteristics with crystallite size in excess of 40 nm. Among the three thermal expansion coefficient value of Gd substituted zirconia was close to YSZ or to other components of SOFC. Whereas, La substituted zirconia showed the value of 8.5 X 10^{-6} which is not compatible with other cell components. Secondly, above 1000°C it showed monoclinic phase, which is not a desirable phase of electrolyte in SOFC. In case of Nd substituted zirconia all the three phases namely cubic, tetragonal and monoclinic were present. Thus among all the three it appears that Gd substituted zirconia can be considered as probable electrolyte material.

References

1. S. C. Singhal, K. Kendall, (Eds.), *High Temperature Solid Oxide Fuel Cells: Fundamentals, design and Applications*, Elsevier, UK.
2. R. Bove, S. Ubertini (Eds.), *Modelling Solid Oxide Fuel Cells Methods, Procedures and Techniques,* Springer, pg. 3, 2008.
3. C. B., Choudhary, H. S Maiti, E. C. Subbarao, *Ed.* E.C. Subbarao, *Solid Electrolytes and their Applications,* Plenum Press, pp. 198034-49.
4. S. P. S. Badwal, K. Foger, *Materials Forum,* 1997, 21, 187.
5. E. Chinarro, J.R. Jurado, M .T. Colomer, *J.Eur.Ceram.Soc.*, 2007, 27, 3619.
6. S. S. Manoharan, K. C. Patil, *J. Am. Ceram. Soc.,* 1992, 75, 1012.
7. A. R. West , *Solid State Chemistry And its Applications*, pg. 19, John Wiley & Sons, 1998.
8. N. Q. Minh, *J. Am. Ceram. Soc.* 1993, 76, 563.
9. F. Tietz, *Ionics,* 1999, 5, 129.

ABOUT THE AUTHORS

Dr. Salil Varma joined BARC through Training School (40th Batch) in 1996. After working in WMPD for planning and commissioning of WIP Process Control Lab, he joined the Chemistry group in 1999 and since then, he has contributed to catalysis group for research on H_2 mitigation catalyst, mixed oxide catalysts for pollution abatement and for various TPD-MS/FTIR techniques for reaction mechanism studies. He was awarded PhD in 2004 by University of Mumbai and did his Post-Doctoral research at University of Leipzig, (Alexander von Humboldt Fellow (2005-2006)) on "Decomposition and selective catalytic reduction of nitrogen oxides on substituted rare earth orthovanadates". Currently he is involved in research on newer materials for their application in SOFC and development of a single cell SOFC test setup.

Ms. Charu Dwivedi did her post graduation in Physical Chemistry from Panjab University, Chandigarh in 2007. After completion of training from 51st batch of BARC training school, she is pursuing her doctoral studies under the aegis of HBNI at Radiation & Photochemistry Division of BARC, under the guidance of Dr. Manmohan Kumar and Mr. P.K. Wattal, BETDD. Her research interests are development of polymer extractant composites for separation of radionuclides and toxic metals from waste solution and synthesis of nanoparticles and their applications.

Mr. A. N. Shirsat joined BARC in 1994 and then obtained M.Sc. in Physical Chemistry from Mumbai University in 2004. He has contributed extensively to thermodynamic studies on nuclear and non-nuclear materials. He has worked on thermodynamic stabilities of various rare earth oxycarbonates and transport properties of volatile fission products pertaining to oxide and metallic nuclear fuels. Currently, he is involved in synthesis, characterisation and property measurements for various mixed oxides with prospective application in IT-SOFC and development of test facility for single cell SOFC setup.

Dr. (Ms) Bina Wani, Ph.D (Mumbai University) joined the Chemistry Division in 1979. She has about 28 years of experience in utilization of various thermo-analytical techniques related to solid-state chemistry, studies on oxyfluoro compounds including superconductors and catalysts based on mixed oxides. She has 54 publications in reputed peer review journals to her credit. She worked as Visiting Scientist at Ames Laboratory, Iowa, USA in 1995. Her current interest lies in the development of various cell component materials for IT-SOFC and mixed oxide based catalysts for pollution control.

ABOUT THE AUTHORS

Dr. (Ms) Shyamla Bharadwaj, M.Sc. and Ph.D from Mumbai University joined BARC in 1977 through 20th Batch of Training School. She has been working in the area of high temperature thermodynamics of nuclear as well as other refractory materials for the past 30 years. During the year 2000 – 01, she worked as Guest Scientist at Juelich Research Centre, Germany. Presently, she is heading the Fuel Cell Materials and Catalysis Section of Chemistry Division, BARC. She is a Ph.D guide of Mumbai University and Professor of Homi Bhabha National Institute, Mumbai. She has been honoured with the NETSH-ITAS Award 2006, for her contribution in the field of thermodynamics and thermal analysis.

STUDIES ON THE PREPARATION OF ^{106}RU SILVER PLAQUE SOURCES FOR THE TREATMENT OF EYE CANCER

R.B. Manolkar, A.R. Mathakar and A. Dash
Radiopharmaceuticals Division

K.P. Muthe
Technical Physics and Prototype Engineering Division

P. Sreeramakrishnan
Isotope Applications Division

C.P. Kaushik
Waste Management Division

This paper received the 3rd Best Prize in the Poster Session at the International Symposium on Material Chemistry held at BARC, Mumbai, from December 2-6, 2008

ABSTRACT

An electrochemical process has been developed, to deposit a layer of ruthenium on the concave surface of a silver plaque of dimension 0.2 mm (t) x 15 mm (ϕ). ^{106}Ru tracer was used, to optimize the parameters for electro-chemical deposition such as current density, acidity and ruthenium ion concentration in the bath. Satisfactory deposition of ^{106}Ru was achieved at a current density of 1mA.cm^{-2} over a period of 18 - 20 hours, with ruthenium concentration of ~ 200 µg/ml and 0.05-0.1M HNO_3 in the electrochemical bath. Leachability of ^{106}Ru bare source in 0.9% saline was found to be < 185 Bq and activity distribution was found to be uniform within ± 5 %. The process of electro-deposition of ruthenium on the plaques was reproducible

Introduction

^{106}Ru transforms into ^{106}Rh with emission of β particles ($E_b$max = 39 keV, $T_{1/2}$ = 368 d) which subsequently decays to stable ^{106}Pd with emission of β particles ($E_b$max 3.54 MeV (79%), 3 MeV (8%), 2.4 MeV (11%) and 2 MeV (2%). ^{106}Ru is one of the attractive radionuclides employed in brachytherapy of eye cancer for more than four decades. Several groups have been involved in the ^{106}Ru/^{106}Rh ophthalmic plaque preparation and used in clinical situations after dosimetric evaluations [1-5]. A plaque with low amount of ^{106}Ru activity of the order of 12 - 26 MBq (0.3 - 0.7 mCi) is adequate for the treatment and the plaque can be used for upto two years. Macro amount of stable ruthenium electrodeposition in different media has been reported [6-8]. In this paper, optimize parameters for the preparation of brachy therapy source of ^{106}Ru on silver plaque using electrochemical method wherein, the ^{106}Ru is deposited on the concave surface and sealed between two layers of 0.7 mm backing and 0.1 mm thick front window of silver, for the treatment of eye cancer.

Experimental

All the reagents used were of analytical grade. A simple digital potentiostat (locally fabricated) was used, to achieve constant current supply. A potentiostat/ galvanostat (AUTOLAB/PGSTAT100), Micro Devices Metrohm Limited, Netherlands was used, to record cyclic voltammogram. All the experiments were carried out at ambient temperature (22 ± 1°C). ^{106}Ru used in this experiment was isolated from intermediate level waste, arising from spent nuclear fuel. The isolation and purification of ^{106}Ru was carried out using the facility available at WIP, Trombay. The solution ^{106}Ru was evaporated to near dryness and reconstituted with 0.4 M sulphamic acid, containing ~ 0.1M nitric acid. GM and HPGe counters were used to determine ruthenium activity. High purity $RuCl_3.nH_2O$ was procured from Aldrich Chemical and used as carrier after dissolving the required quantity in 1 M HNO_3. A H type galvanic cell (20 mm ID × 60 mm h) was fabricated in our Division and the anolyte and catholyte were separated using a G-3 porous frit. The experimental volume of the bath was maintained at 10 mL. High purity silver cicular disks were moulded in the shape of the plaque of 15 mm ϕ and 0.2 mm thick were used as cathode and platinum plate of 10 mm (l) × 0.2 mm (b) × 70 mm (h) as anode. The experimental set-up is shown in Fig. 1. Efforts were made to find out the formal redox potential of ruthenium in sulphamic acid medium, a silver micro electrode was prepared using 2 mm ϕ circular silver rod embedded in the Teflon tube and surface polished with different polish papers (600-1000 grade) followed by diamond paste. A cyclic voltammogram (CV) of ruthenium solution was recorded using silver as working, calomel as reference and platinum as counter electrodes. The cathodic deposition at different ruthenium carrier concentrations (25 – 600 µg/ml) with trace quantities of ^{106}Ru was studied, by passing a constant current of 1 mA/cm^2 at pH ~ 1 for a time period of 2 h. The deposition was also studied for varying deposition time periods up to 24 h, keeping other parameters constant such as current, concentration (~200 µg/ml) and pH ~ 1. The effect of current on deposition was studied at different cathode current densities ranging from 0.5 - 4 mA/cm^2. To estimate the leach rate, the source was placed in 100 mL of 0.9% saline solution for 72 hours and the activity in the solution was measured at 24 hour intervals. The deposition yield was determined indirectly by drawing samples before and after plating from the bath and measuring the activity using GM counter, after proper dilution. The uniformity of the activity distribution of ^{106}Ru in sources was ascertained by autoradiography wherein the sources were exposed to Agfa D-7 film for 1- 6 h.

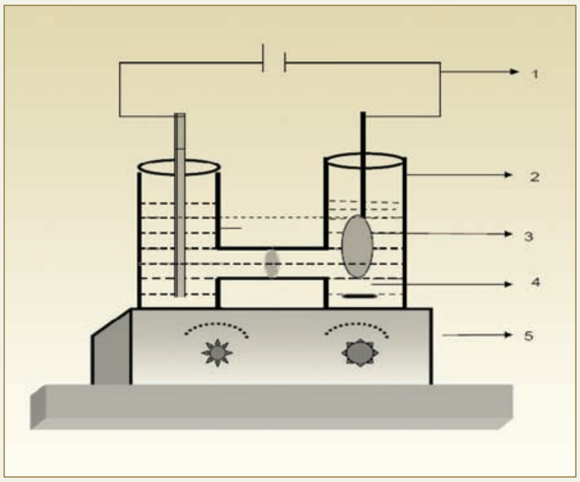

Fig. 1: Electrochemical cell (1) Current supplier, (2) Glass cell (3) Silver plaque (4) Stirring glass rod (5) Magnetic stirrer

Results and Discussion

The aim of this work comprises an investigation of different parameters influencing the electrochemical deposition of ^{106}Ru on circular disks, evaluation of the level of uniformity of the deposited layer, determination of leachability of the deposited layer,

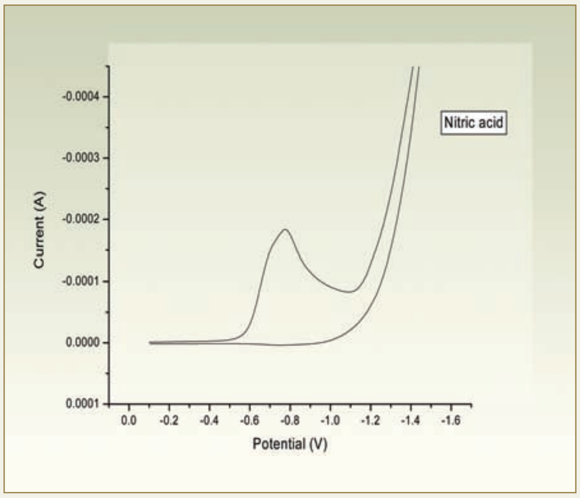

Fig. 2: Cyclic voltammogram of ruthenium in nitric acid and silver microelectrode

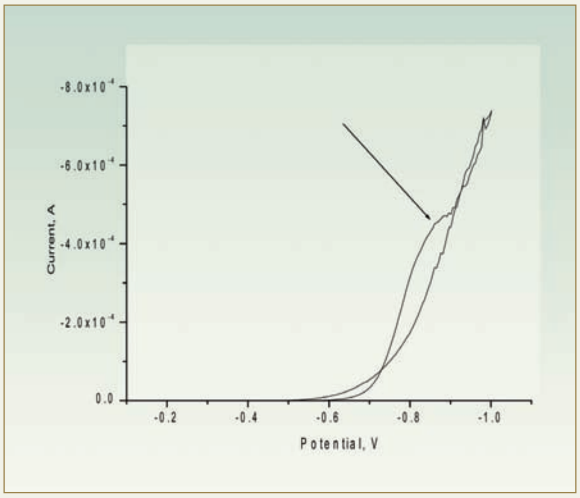

Fig. 3: Cyclic voltammogram of Ru in sulphamic acid and Dropping Hg electrode

for the preparation of ^{106}Ru plaque. The concentration of ^{106}Ru used for this purpose was in micrograms quantity and the electrolysis has to be performed in a custom-made electrochemical cell. Voltammetric studies were performed to study the electrodeposition behaviour of ^{106}Ru in the electrobath.

In cyclic voltammograms (CV) studies, no reduction or oxidation peaks were observed in 0.4M NH_2SO_3H containing ruthenium in the range of 5×10^{-5} to 5×10^{-4} M. When we changed the supporting medium to HNO_3 and KCl instead of sulphamic then a sharp reduction peak was observed and the cyclic voltommogram is shown in Fig. 2. To see the behaviour in dropping mercury electrode in sulphamic acid as supporting medium, a small reduction hump was seen at - 0.86 V instead of a sharp peak and shown in Fig. 3.

Though reduction is not observed in the cyclic voltametric experiments, electrodeposition of ^{106}Ru on the cathode was achieved, by applying constant current (potential) between anode and cathode, as it is two electrode system was used. The results obtained at constant time of 2 h under various carrier concentrations indicating that ~ 12 to 15 % of the ^{106}Ru could be deposited (Fig. 4). Around ~ 50 ± 5% was deposited when the deposition time was subsequently extended to ~ 18 hours (Fig. 5). It was further observed, that if nitric acid is absent in the electrolytic bath or if higher current density > 2 mA/cm^2 is applied, then either the solution became

Table 1: Optical density on autoradiography of the silver plaque sources

S. No.	I	II	III	IV	Average (OD)	SD	C.V. (%)
A	2.34	2.26	2.32	2.38	2.32	± 0.05	2.15
B	2.25	2.17	2.12	2.20	2.18	± 0.047	2.16
C	2.64	2.57	2.46	2.49	2.54	± 0.07	2.75

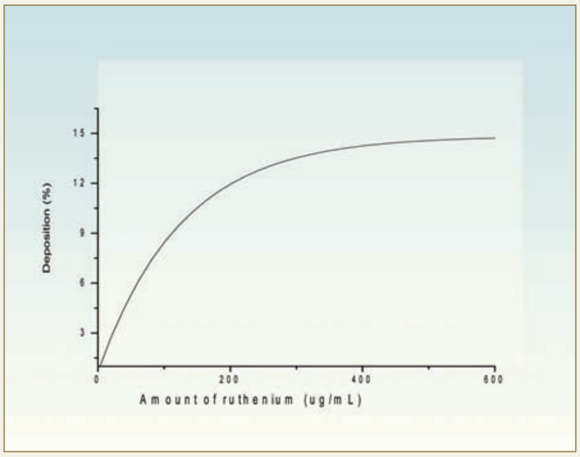

Fig. 4: Deposition (%) vs various carrier concentrations of ruthenium in the bath

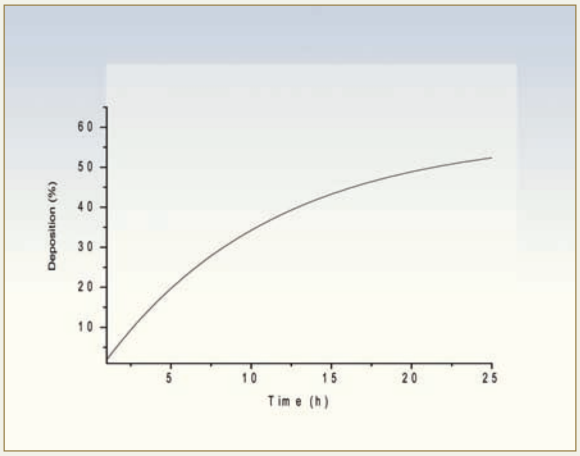

Fig. 5: Deposition (%) vs deposition time (h)

turbid or the coating became black because of silver surface oxidation. Addition of ~ 1mL of 1M HNO_3 along with the NH_2SO_3H into the bath, eliminated these problems and yielded bright silvery deposition.

On placing the source (~ 26 MBq) in saline for 72 h, no measurable activity (< 185 Bq) of was observed. On autoradiography, it was seen that the distribution of activity was uniform within 2.5 % C.V. The data is summarized in Table 1. The Scanning Electron Microscopy (SEM) image of Ru coated silver plaque at 200 times magnification is shown in Fig. 6. This revealed that Ru particles are distributed uniformly throughout the silver matrix. In order to ascertain the homogeneity of Ru in the plaque, the EDX spectra was recorded at various locations and the quantification of results as weight percentage are given in Table 2 which revealed, that the variation in distribution of Ru along the surface of the silver plaque is reasonably uniform within ± 5 %.

This process of making the source is especially advantageous, as it permits 'all- radioactivity' *in situ* approach, allows the control of radioactivity content in the source and the mild experimental conditions of this process, facilitate safe handling of radioactivity. The major advantage of the present method is the simplicity of a single electrolysis step and economy.

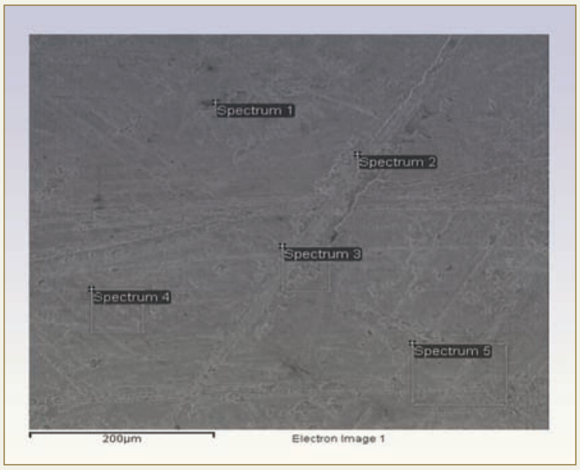

Fig. 6: SEM image of ruthenium coated silver plaque under 200 times magnification

Conclusions

^{106}Ru could be uniformly electrodeposited on silver plaque. The sources prepared were non-leachable and have the potential to be used in brachytherapy for the treatment of eye cancer. The major advantages of this plaque preparation is the ease of deposition, possibility of depositing desired amount of activity, low leachability and long term usability as compared to ^{125}I and ^{103}Pd.

Table 2: The various elements recorded as weight percentage at four different points using Energy Dispersive X-ray (EDX) of ruthenium coated plaque

Spectrum	C	O	S	Ag	Ru	Total
Position 1	4.73	5.11	0.74	65.39	24.03	100
Position 2	4.89	5.12	0.73	65.18	24.07	100
Position 3	3.68	6.02	1.10	54.30	34.89	100
Position 4	3.84	6.29	1.13	54.55	34.19	100
Mean	4.28	5.63	0.92	59.85	29.30	100
S.D. (%)	0.53	0.50	0.19	5.43	5.25	

Acknowledgements

The authors are highly grateful to Dr. (Ms.) Meera Venkatesh, Head, Radiopharmaceuticals Division, BARC, for her continuous encouragement and support for this work. They are also thankful to Dr. A. K. Satpati, Analytical Chemistry Division, for his help in providing cyclic voltametric data.

References

1. P. K. Lommatzsch, *Surv. Ophthalmology*, 19, 1974, 85.
2. Potter, R., Janssen, K., Prott, F. J., Widder J., Haverkamp, U., Busse, H. and Muller, R. P., *Front Radiat. Ther. Oncol.* 30, 1997,143.
3. Lommatzsch, P. K., Werschnik, C. and Schuster, E. Graefes. *Arch. Clin. Exp. Ophthalmology*, 238 (2), 2000, 129.
4. Melvin A Asstran, *Medical Physics*, 30, Issue 6, 2003, 1219.
5. C. G. Soares, S. Vynckier, H. Jarvinen, W. G. Cross, P. Sipila, D. Fluhs, B. Schaeken, and F. A. Mourtada, *Med. Phys.* 28, 2001, 1373.
6. Molnda E., Mielcarski M., *J. Raioanal. Nucl. Chem*. 238, 1998, 159.
7. Mieczyslaw Mielcarski, Izabela Puchalska, *Nukleonika*, 47(2), 2002, 83.
8. Young-Soon Kim, Hyung-Il Kim, M. A. Dar, Hyung-Kee Seo, Gil-Sung Kim, S.G. Ansari, Jay J, Senkevich, and Hyung-Shik Shin, *The Electrochemical Society-State Lett*., 9, Issue 1, 2006, C19.

ABOUT THE AUTHORS

Dr. R.B. Manolkar graduated from Karnataka University, Dharwar and joined the Radiochemistry Division in 1982. His field of specialization was estimation of uranium and plutonium from fuel samples by electrochemical techniques. From 1993 onwards, he has been working in Radiopharmaceuticals Division. He obtained his Ph D. degree in Chemistry from University of Mumbai in 2000. He was involved in the development and supply of brachytherapy sources particularly radioactive phosphorous (^{32}P) coating on stents for the prevention of reblockage (restenosis) after post angioplasty. He was also involved in multi-centric clinical trial programme and the stents were supplied to various hospitals in Mumbai, Pune, Bengaluru, Delhi and Hyderabad etc. He has standardized a method for the production and supply of radioactive ^{125}Iodine for the treatment of eye and prostate cancer and radioimmunoassay (RIA) etc. He has published over 9 papers in international journals and 30 papers in symposia/conferences.

Mr. A.R. Mathakar after completing B.Sc. from Mumbai University joined BARC in 1988 and obtained his M.Sc. degree from Mumbai University in 1994. He was involved in the regular production and supply of ^{99}Mo. He has worked in the development of ^{153}Sm-EDTMP, ^{166}Ho-HA and various ^{99m}Tc-based formulations, for potential medical use, some of which are now routinely supplied to different hospitals through BRIT. Currently he is involved in the regular fabrication of ^{137}Cs-brachytherapy sources, processing of $^{186/188}$Re, ^{166}Ho and ^{90}Y etc. for various applications. He has 7 publications in international and national journals to his credit. He is a life member of NAARRI, IANCAS and INS.

Dr. Ashutosh Dash completed his M.Sc. in the year 1982 and joined the Isotope Group of BARC in 1983 after graduating from the 26th batch (Chemistry) of Training School. He has been engaged in the research and development of therapeutic sources and radiochemical separation techniques since then. Dr. Dash obtained his PhD degree from the Mumbai University in 1995 and is currently Head, Therapeutic and Reference Sources Section of Radiopharmaceuticals Division, BARC. He was deputed to Korean Atomic Energy Research Institute (KAERI) as a Visiting Scientist under the Scientist Exchange Programme during 2002-2003. He has served as Chief Scientific Investigator and Co-Investigator in various coordinated research projects of International Atomic Energy Agency (IAEA) in the area of development of technology for the production of therapeutic sources and radionuclidic generators for industrial and medical applications. He has published over 35 papers in international journals and 60 papers in international and national symposia/conferences.

ABOUT THE AUTHORS

Mr. K.P. Muthe is presently working in the field of thin film growth and characterization. He has studied the growth behaviour of High Critical temperature superconductors using Molecular Beam Epitaxy (MBE). The reference value of this work has fetched him a place in Marquis Who's Who of the world (1997) and Dictionary of International Biography (1999). He has extensively used X-ray Photoelectron Spectroscopy to solve several materials related problems like corrosion and to study mechanisms for detection of gases. His current interests include: i) Synthesis of alumina based radiation sensors for radiation dosimetry and ii) Detection of toxic gases.

Mr. P. Sreeramakrishnan is group leader of NDT & Sealed Source Applications group in the Isotope Applications Division of BARC. After graduating in Physics from University of Calicat, he joined BARC in 1974. Presently he is working on industrial applications of sealed sources for troubleshooting and process optimization. He is actively involved in the training and certification programme of radiography testing, level 1and level 2 personnel.

Dr. C.P. Kaushik, joined the Waste Management Division in 1985, after successful completion from the 28th batch of BARC Training School. Presently he is shouldering the responsibility of Superintendent (Labs, Training & Safety) at Waste Management Facility, Trombay. He is engaged in development of matrices for treatment/conditioning of different types of radioactive wastes and its implementation on plant scale for more than two decades. He is also responsible for characterization of waste and waste forms. Other areas of his research interest include: characterizations of buffer and backfill materials for use in Near Surface Disposal Facilities and Geological Repositories, separation and recovery of valuables from radioactive waste and material issues in the field of radioactive waste management. He has more than 100 publications to his credit. He is a recipient of INS gold medal award in the year 2005 and Group Achievements Award in the year 2006 for his contribution in the commissioning of WIP, Trombay.

STUDIES ON ELECTROPOLYMERIZATION OF INDOLE AND SUBSTITUTED INDOLE IN ACETONITRILE

P. C. Pandey and G. Singh
Department of Applied Chemistry, Institute of Technology,
Banaras Hindu University, Varanasi

and

H. S. Sharma and S. K. Aggarwal
Fuel Chemistry Division

This paper was conferred the Best Paper Award (3rd prize) at the Poster Session of (DM-ELANTE)-2008 held at Munnar, Kerala during February 25-28, 2008

ABSTRACT

Electrochemical polymerization of indole and substituted indole (2-methyl indole, indole-2-carboxylic, indole-5-carboxylic acid and indole-6-carboxylic acid) have been studied in acetonitrile, containing 0.1M tetraethylammonium tetrafluoroborate under potentiodynamic conditions at platinum electrode. It has been observed that substituting methyl and carboxylic acid groups at position-2 in the heterocyclic ring of indole, makes the oxidation relatively difficult as compared to the electrooxidation of unsubstituted indole. It is understood that substitution at position-2 with the methyl or carboxylic group creates steric hindrance in the electropolymerization taking place through 1,3 positions. Further, relatively better electropolymerization of methyl substituted indole at position-2 compared as to that of carboxylic substituted monomer at position-2 is attributed to lower steric hindrance of methyl group than the carboxylic acid group due to the bulky nature of the latter group. Substitution of carboxylic acid at position -5 or -6 in the benzene ring of indole on the otherhand, facilitates electropolymerization of substituted indole monomers.

Introduction

Electropolymerization of indole[1-9] is of importance, as it has found attractive applications as redox capacitors[10-11], modified electrodes[12], in rechargeable battery[6] and chemical sensors[13]. Experimental conditions especially on the choice of solvent to be used during electropolymerization of indole, have been reported by several authors and the crucial point of attention in this regard, is the content of water if organic solvents are used for electropolymerization. In the earlier studies on electropolymerization of indole [6,7], it was suggested that the polymer formation proceeds through 1-3 positions of indole, however, polymerization through 2-3 positions is also reported[3]. In view of this, it is still of interest to study electropolymerization of indole, by blocking the 2-position in the heterocyclic ring of indole, that eliminates the possibility of polymerization through 2-3 positions and to study the effect of hydrophobicity and steric hindrance of 2-subtituent group on polymer growth. The substituted indole monomers, 2-methyl indole, indole-2-carboxylic acid, indole-5-carboxylic acid and indole-6-carboxylic acid are chosen in present studies in order to make a comparative study on the electropolymerization in acetonitrile. Additionally, the comparison on the electrochemical performances of hexafluorophosphate-doped polyindole and tetrafluoroborate-doped polyindole on platinum electrode surface, has also been carried out.

Experimental

Indole-2-carboxylic acid, 2-methy indole, indole-5-carboxylic acid, indole-6-carboxylic acid and dry acetonitrile (HPLC grade) were obtained from E. Merck, Germany; indole and tetraethylammonium tetrafluoroborate were obtained from Aldrich Chem.; tetrabutylammonium perchlorate was made from tetrabutylammonium bromide and $HClO_4$ followed by re-crystallization and drying of the electrolyte via conventional process. A three-electrode single-compartment electrochemical cell with a platinum working electrode, a Ag/AgCl reference electrode and a platinum gauze auxiliary electrode, as described elsewhere[6,7], were used in the present studies. Each polymer-modified electrode was characterized by recording CV of modified indole electrode in the monomer- free solution made in same non-aqueous solvent, containing similar concentrations of supporting electrolytes, used during the electropolymerization process of the polymer film formation.

Results and Discussion

In order to study the effect of the functional group in heterocyclic ring and benzene ring of indole on electropolymerization, we have recorded CVs of 0.2M indole and its substituted monomers by scanning Pt working electrode potential at a scan rate of 100 mV S^{-1}, in acetonitrile containing 0.1 M tetraethylammonium tetrafluoroborate. The CV's recored for indole, indole-5-carboxylic acid and indole-6-carboxylic acid are presented in Fig. 1, Fig. 2 and Fig. 3, respectively. In Fig. 4 responses obtained in the first forward scan of corresponding to Fig. 1, Fig. 2 and Fig. 3, indicating oxidation potential of each monomer and depicting early stages of nucleation during electropolmerization of different monomers, is presented. It can be seen from Fig. 4 that oxidation of indole onsets around 0.7 V and that of 2-methyl indole and indole 2- carboxylic acid at 1.1 V and 1.3 V, respectively. This suggests that substituting methyl and carboxylic acid at position-2 in the heterocyclic ring makes the electrooxidation process relatively difficult and consequently electropolymerization of the respective monomer sluggish. It is understood that substitution of methyl and carboxylic acid at position-2 creates steric hindrance in the electropolymerization taking place through 1, 3 positions. This view point also gets support from the observation, that the extent of steric hindrance is higher for indole 2-carboxylic acid as compared to 2-methyl indole because carboxylic group is relatively bulky in comparison to methyl. In contrast to this, oxidation of indole 5-carboxylic acid takes place at relatively less positive potentials, 0.3 V and 0.85 V, suggesting that electropolymerization becomes easier and steric hindrance to polymerization through 2,3 positions is ruled out during the process of electropolymerization. These observations also demonstrate contribution of steric hindrance during polymer chain propagation and stability of the radical cation formed. Carboxylic acid is a relatively bulky group in comparison to methyl group and its presence at position -2 in the heterocyclic ring created higher steric hindrance in the polymer chain propagation during early stages of polymerization as compared to the methyl group. 5- and 6-substituted indole monomers follow entirely different rout as the rate of polymerization is faster as compared to that of indole monomer and is triggered at two different oxidation potential, the first one close to 0.3 V much lower as compared to indole (0.7 V) and the second one at 0.9 V little high as compared to indole monomer.

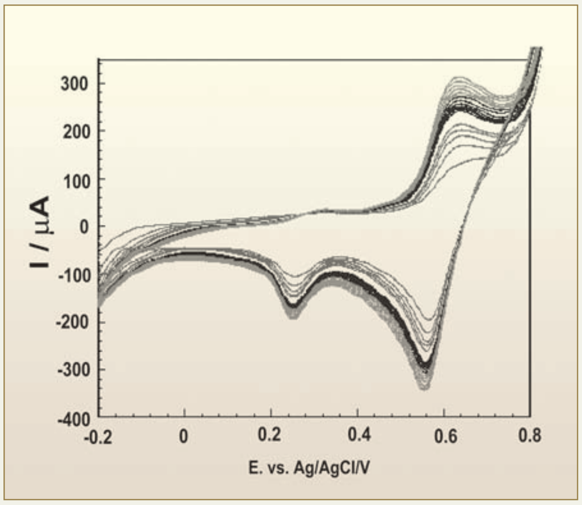

Fig. 1: CVs of 0.2 M indole recorded by scanning potential between –0.2 to 1.0 V vs Ag/AgCl at a scan of 100 mV s-1 in acetonitrile containing 0.1 M tetraethylammoniu tetrafluoroborate, at Pt electrode

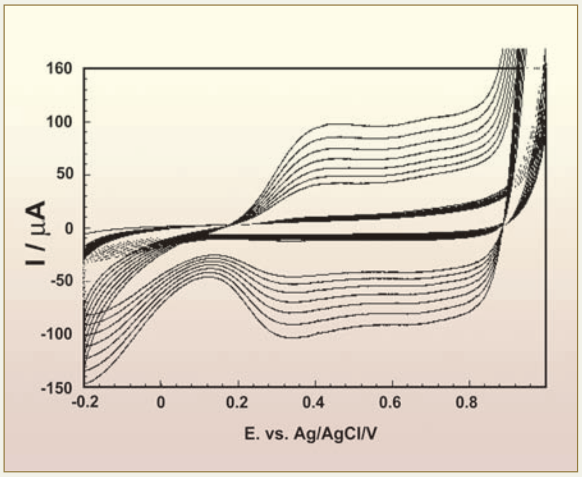

Fig. 2: CVs of 0.2 M indole-5 carboxylic acid recorded under the experimental shown in Fig. 1

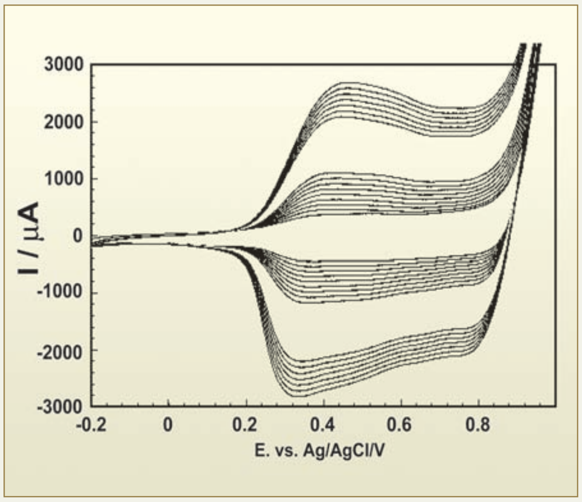

Fig. 3: CVs of 0.2 M indole-5 carboxylic acid recorded under the experimental shown in Fig. 1

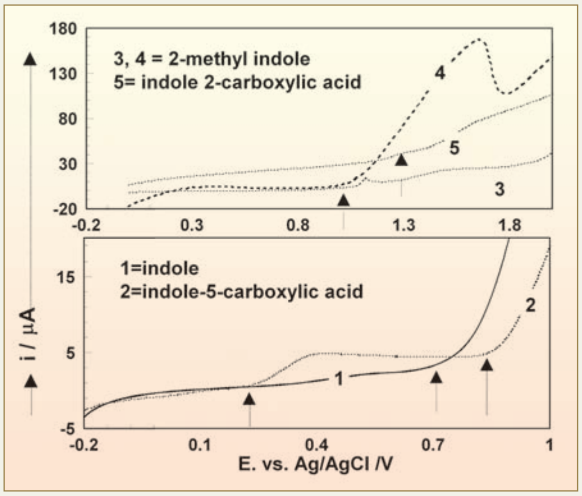

Fig. 4: CV responses taken from first CV scan recorded during electropolymerization of indole and its substituted monomers (0.2M) in acetonitrile containing 0.1 M tetraethylammonium tetrafluoroborate.

It is of significance to study the effect of dopants on the redox behaviour of polyindole-modified electrode. Accordingly, we have recorded CVs of tetrafluoroborate-doped polyindole and hexafluorophosphate doped polyindole in acetonitrile containing respective supporting electrolytes, tetraethylammonium tetrafluoroborate and tetrabutylammonium hexafluorophosphate. Hexafluorophosphate-doped modified polyindole electrode shows superior reversible redox behaviour as compared to tetrafluoroborate-doped polyindole and could be attributed to the enhanced polarity of the former dopant.

Conclusions

Studies on electrochemical polymerization of indole and substituted indole (2-methyl indole, indole-2-carboxylic, indole-5-carboxylic acid and indole-6-carboxylic acid) in acetonitrile containing 0.1M tetraethylammonium tetrafluoroborate under potentiodyanamic conditions at platinum electrode, described herein have shown, that substituting methyl or carboxylic acid groups at position-2 in the heterocyclic ring of indole makes electropolymerization relatively difficult, whereas substitution of carboxylic acid at position 5- or 6- in the benzene ring of indole, promotes electropolymerization as compared to that of unsubstituted indole. The studies carried out support that mechanism of electropolymerization proceeds through 1, 3 positions of indole.

Acknowledegment

Authors are thankful to Dr. V. Venugopal, Director, Radiochemistry and Isotope Group, BARC, for his keen interest in this work. G. Singh gratefully acknowledges DST, New Delhi, for financial assistance.

References

1. R. J. Waltman, A. F. Diaz, and J. Bargon, *J. Phys. Chem., 88*, 4343 (1984).
2. P. C. Pandey, *J. Chem. Soc., Faraday Trans. 1, 84*,2259 (1988).
3. K. M. Choi, C. Y. Kim, and K. H. Kim, *J. Phys. Chem., 96*, 3782 (1992).
4. K. M. Choi, and K. H. Kim, *J. Appl. poym. Sci. , 44*, 751 (1992).
5. G. Zotti, S. Zecchin, and G. Schiavon, *Chem. Mater., 6,* 1742 (1994).
6. P. C. Pandey,and R. Prakash, *J. Electrochem. Soc., 145,* 999 (1998).
7. P. C. Pandey,and R. Prakash, *J. Electrochem. Soc., 145*, 4301 (1998).
8. Jingkun Xua,, Weiqiang Zhou, Jian Hou, Shouzhi Pu, Liushui Yan, Jingwu Wang, *Materials Letters 59*, 2412 (2005).
9. A, Sezai Saraç ^{A1} and ^{a}erife O¨zkara, *Int. J. Polymeric Materials 53*, 587 (2004).
10. Shunzo Suematsu, Takashi Ishikawa, Mika Hanada, Hideaki Takenouchi, and Katsuhiko Naoi, *Electrochemistry, 71* ,695 (2003).
11. Kenji Machida, Hideaki Takenouchi, Remi Hiraki, and Katsuhiko Naoi, *Electrochemistry, 73*, 489 (2005).
12. Mihaela Ghitaa,1, Damien W.M. Arrigan, *Electrochimica Acta 49*, 4743 (2004).
13. D. Tyler McQuade, Anthony E. Pullen, and Timothy M. Swager, *Chem. Rev., 100*, 2537 (2000).

ABOUT THE AUTHORS

Dr. H.S. Sharma joined the Radiochemistry Division, BARC in 1978, after completing D.Phil. from University of Allahabad and is presently Head, Electrochemistry Section, Fuel Chemistry Division, BARC. His major fields of interest include development of analytical methodologies for precise and accurate determination of actinides in nuclear fuel materials and electrochemical synthesis of conducting-polymers and nanoscale materials and their characterization employing spectroscopic and microscopic techniques. He has contributed significantly to the development of coulometric method for precise and accurate determination of U and Pu in nuclear fuel materials. He has introduced voltammetric and Electrochemical Quartz Crystal Microbalance techniques in electrochemical research. Dr. Sharma has been recently awarded, "Prof. S. S. Sandhu Award" (2007-08) by the Indian Chemical Society, for his outstanding contributions in Electrochemical Research.

Dr. S.K. Aggarwal is Head, Fuel Chemistry Division, BARC and is also a Professor of Chemistry at the Homi Bhabha National Institute (HBNI). He joined the 16th Batch of BARC Training School in 1972 and received the Homi Bhabha Award. He did his Ph.D. from Mumbai University and his Post-doctoral training at University of Virginia, USA. Dr. Aggarwal was honoured with the Eminent Mass Spectrometrist Award by the Indian Society for Mass Spectrometry (ISMAS) in 1996 and was recently conferred with the DAE Special Contributions award 2006. He is a specialist in the field of atomic mass spectrometry and alpha spectrometry and is interested in various mass spectrometric techniques. His other areas of interest include laser-based analytical techniques, Electrochemistry, X-ray spectroscopy and Separation techniques like HPLC, solvent extraction etc. He has more than 100 publications in reputed international journals and is a recognized Ph.D. Guide of the Mumbai University and of HBNI.

CHARACTERIZATION OF ALUMINA CERAMICS UNDER SHOCK LOADING

A.K. Mukhopadhyay and S.Bhattacharyya
Mechanical Test Section, Analytical Facility Division
Central Glass and Ceramic Research Institute, Kolkata

and

K.D. Joshi, A. Rav and S.C. Gupta
Applied Physics Division

and

S. Biswas
Non-Oxide Ceramic Section
Central Glass and Ceramic Research Institute, Kolkata

This paper received the Poster Award 2008 at the 53rd DAE Solid State Physics Symposium held at BARC and TIFR, Mumbai during December 16-20, 2008

ABSTRACT

This work reports the characterization of sintered Alumina ceramics, before and after shock loading, in a Gas Gun facility indigenously developed at BARC, Mumbai. The Nanoindentation technique was utilized, to reflect the decrease in hardness and Young's modulus of Alumina ceramics due to shock loading. Detailed Scanning Electron Microscopy (SEM) and Field Emission Scanning Electron Microscopy (FESEM) was utilized, to understand the nature and degree of failure propagation and the interrelation between such damage evolution and the degradation in local mechanical properties, in these brittle ceramics. This study demonstrated for the first time, that shear stress dominated failure, could play a major role in damage evolution, in shock loaded alumina ceramics.

Introduction

Alumina is the most well established, commercially utilized ceramic, for armour applications. The preferred experimental technique to determine properties of materials under shock-loading conditions, is that of plate impact. Here a flat and parallel plate of known shock response is impacted onto an equally flat and parallel plate of the material of interest. The mechanical response can be determined by a number of methods, including rear surface velocity measurements such as VISAR (velocity interferometry system for any reflector), or stress gauges, mounted in various orientations to the loading axis. The mechanical properties that can be extracted include the dynamic yield strength—the Hugoniot Elastic Limit (HEL), the dynamic tensile spall strength due to interactions between release waves from the rear of the flyer and target plates, and shear strength. Several researchers have investigated the behaviour of alumina ceramics under plate and / or rod impact conditions; however, there has not been a significant effort so far, to compare the nanomechanical properties of shocked and unshocked alumina ceramics. This is precisely the aim of the present report. One of the established experimental techniques, for evaluation of mechanical properties at the ultra-structural low dimension of the sample, is nanoindentation. Here the mechanical disturbance made by the external probe, can be made to span length scales comparable to or even less than the microstructural length scale of the sample.

In recent times, the nanoindentation technique has proved to be a powerful means of characterizing near-surface mechanical properties, such as Young's modulus (E), hardness (H) etc. of materials. This technique relies on high-resolution instruments that continuously monitor the loads, *P*, and displacements, *h*, of an indenter, usually a Berkovich type, as it is pushed into and withdrawn from a material. Important information obtained from the resultant *P*–*h* curve, are the peak load, P_{max}, the maximum penetration depth, h_{max}, final penetration depth, h_f, and the contact stiffness, *S*. The nanoindentation load–displacement curve, is usually described by a power law function of the form $P = \alpha(h - h_f)^m$ where, α and *m* are empirically determined fitting parameters. Based on the observation that predicted m values are 1 for plat punch, 1.5 for paraboloid of revolution and 2 for conical indenter [1] whereas the experimentally determined *m*-values vary from 1.25 to 1.51 and have an average value of 1.40 [2], it was decided to check out first, how α and *m* would vary with the nanoindentation load, for the un-shocked alumina samples.

Materials and Methods

99.99% pure alumina powder (Morimura Bros. Inc., Tokyo, Japan) was pressureless-sintered at 1310^0C, to a density of 97.5% of theoretical (4.02 gm/cc) and an average grain size of 10.1 ± 0.23 μm. Both as prepared and shocked samples were characterized by conventional XRD, SEM and Image Analysis techniques. Micromechanical characterization of polished samples was done, using a nanoindentation machine in a load range between 0.4 and 1000 μN, with force and depth sensing resolutions of 0.2 μN and 0.1μm. All the shock experiments were conducted at the Gas Gun facility available at BARC, Mumbai. Details of the standard experimental facilities are reported elsewhere [3] and will be only briefly described here. Two types of shock experiments were conducted. In the first type of experiment, the alumina sample was shock loaded to peak pressure for complete destruction. This experiment though, provided a data point on the Hugoniot but due to complete destruction of the sample, no post shock analysis was possible. For this experiment, alumina disk of diameter 25 mm and thickness 2.5 mm was fitted in a matching hole, made on a Perspex disc of diameter 60 mm and thickness 5 mm. The sample was placed in the central hole of this disc in such a way that one surface of the sample was flushed with one surface of the Perspex disc. This surface was used as the impact surface. Two shock arrival sensors were used to measure the shock arrival at the impact surface and the back surface of the sample. For this purpose the two sensors were placed in such a way, that the sensing end of one of the sensors was flushed with the impact surface, however, the same of the other sensor was resting on the back surface of the sample. The second type of experiments were recovery experiments in which, the samples after unloading from peak shock pressures were recovered for post shock analysis. In two separate shock recovery experiments similar alumina disks as mentioned above were shocked to impact pressures, of 6.5 and 12 GPa, respectively and subsequently collected through a dedicated catcher arrangement [3].

In the first type of experiment, from the measured shock arrival times at the two surfaces and the measured thickness, the shock velocity (U_s) in sample could be determined. The impactor plate used in the experiment was of SS304, whose shock Hugoniot was already known. The velocity of the impacting plate (V_p) just before the impact was measured, using (Up) electrical pins connected to the input of a pulse forming network. From the measured U_s (in the sample), V_p and known Hugoniot of SS304, the particle velocity and shock pressure in the sample could be derived, by using the impedance match method. In second type of experiments, the samples could reach peak pressures through a number of revervations.

Results and Discussion

In the first type of experiment, the measured impact velocity and shock velocity in the sample, were 0.48 km/s and 7.03 km/s, respectively. The Up determined from these measurements and known Hugoniot of SS304 was 0.28 km/s. The shock pressure (P) in the sample evaluated by substituting the initial density of 3.89 g/cc, measured Us and Up in second jump condition was 7.6 GPa. The compression ratio (V/V_0) was evaluated as 0.96. These values of P, Us, Up and V/V_0 agree well with published Hugoniot data .

The samples recovered from recovery experiments were analyzed through nanoindentation, XRD and SEM techniques. The XRD data of both unshocked and shocked sintered alumina was taken and the main intense peak was compared with standard data of α-alumina (JCPDS-43-1484). It was found that the major peaks of sintered alumina disc, matched with the standard peaks of α -Alumina, but a little shift of peaks of the shocked sample occurred, with respect to those of the unshocked alumina, possibly suggesting the presence of a strained lattice. The nanoindentation data of the unshocked alumina, showed a small indentation size effect at depths, less than 300 nm (eg. the hardness decreased at the rate of 0.03 GPa/nm) but at higher depths the hardness was nearly constant at about 20 GPa. Attempt was made to analyze this data in terms of the famous Nix and Gao model [4].

Interestingly, both h_f and h_{max} showed an empirical power law dependence of the type $h - \beta P^n$ on load where β and n are empirical fitting parameters. However, β, n were very different e.g. ~ (18 and 0.56) for h_f and (1.58 and 0.80) for h_{max}. The reason for variation of hardness with depth could be rationalized in terms of the load dependencies of the elastic (W_E/W_T) and plastic (W_P/W_T) components of the energy spent in the indentation process. While at lower loads, most of the energy spent in indentation involved elastic deformation energy, the scenario changed at higher load of indentation, where most of the energy spent in indentation process involved the irreversible deformation or the plastic component. Preliminary nanoindentation experiments on alumina, deformed at shock levels of 6.5 and 12 GPa, showed a trend of drastically decreased hardness, especially at higher loads e.g. 1000 μN. We could not compare our results with published data because no data was available on nanoindentation hardness of shock loaded alumina ceramics. Also, the evaluation results of α and *m* parameters showed interesting behaviour with respect to variation in nanoindentation load. The typical brittle failure pattern observed in the fracture surface of the as-received alumina, was in sharp contrast to the localized plastic deformation zones observed in the fracture surface of the shocked alumina, where a large number of microcracks along with a macrocrack were present. Both intergranular and transgranular fractures had occurred during the shock-induced failure process. An attempt is made here to develop a plausible picture of mechanisms involved in the shock failure process.

Summary and Conclusion

In our work, SEM and FESEM evidence provides for the first time, a plausible picture of shear dominated failure that affects the damage evolution and consequent failure, propagation process, in shock loaded alumina ceramics, which shows drastic reduction in mechanical properties as evaluated by the nanoindentation technique.

References

1. I. N. Sneddon, *Int. J. Engg. Sci.* **3** (1965) 47.
2. W.C. Oliver and G. M. Pharr, *J. Matter. Res.* **7** (1992) 1564.
3. K. D. Joshi et al, *Proceedings of DAE Solid State Physics Symposium* (2007).
4. W. D. Nix and H. Gao, *J. Mech. Phys. Solids* 46 (1998) 411.

ABOUT THE AUTHORS

Mr. K.D. Joshi joined BARC after graduating from the 36th batch of BARC training school. He was awarded the prestigious DAE Special Contribution award. He has contributed to about 50 publications in various journals and conference proceedings. He is involved in theoretical as well as experimental studies on response of materials to high pressures.

Mr. A. Rav completed his B.E. in electronics from Gujarat University and joined BARC from the 44th batch of BARC training school. He is engaged in development of instrumentation, required for diagnostics in shock wave experiments.

Dr. Satish C. Gupta joined BARC in 1972 through the 15th batch of BARC training school. He has published a large number of publications in reputed international journals. He is a recipient of the prestigious DAE Special Contribution award. His research interests are in the field of behaviour of high energy density matter and response of materials to dynamic compression, at high strain rate using shock wave. Presently he is leading the activities of the Applies Physics Division.

Author Index

Kumar, U. 34
Kumbhakar, M. 149
Kunwar, A. 241, 311
Kutty, T.R.G. 90

Sayings of Homi J Bhabha

- *No power is costlier than no power!*
- *A scientific institute, be it a laboratory or an academy, has to be grown with great care like a tree.*
- *No country intending to play a leading part in the world can afford to neglect pure or long-term research.*
- *If an item of equipment is imported from abroad, all one gets is a particular instrument. But if one builds it oneself, an all important lesson in expertise is learnt as well.*
- *Art, music, poetry and everything else that I do, have this one purpose-increasing the intensity of my consciousness of life.*
- *For each man can do best and excel in only that thing which he is passionately fond, in which he believes-that he has the ability to do it.*
- *My success will not depend on what A or B thinks of me. My success will be what I make of my work.*
- *No exam was ever a test of original or creative ability in anybody.*

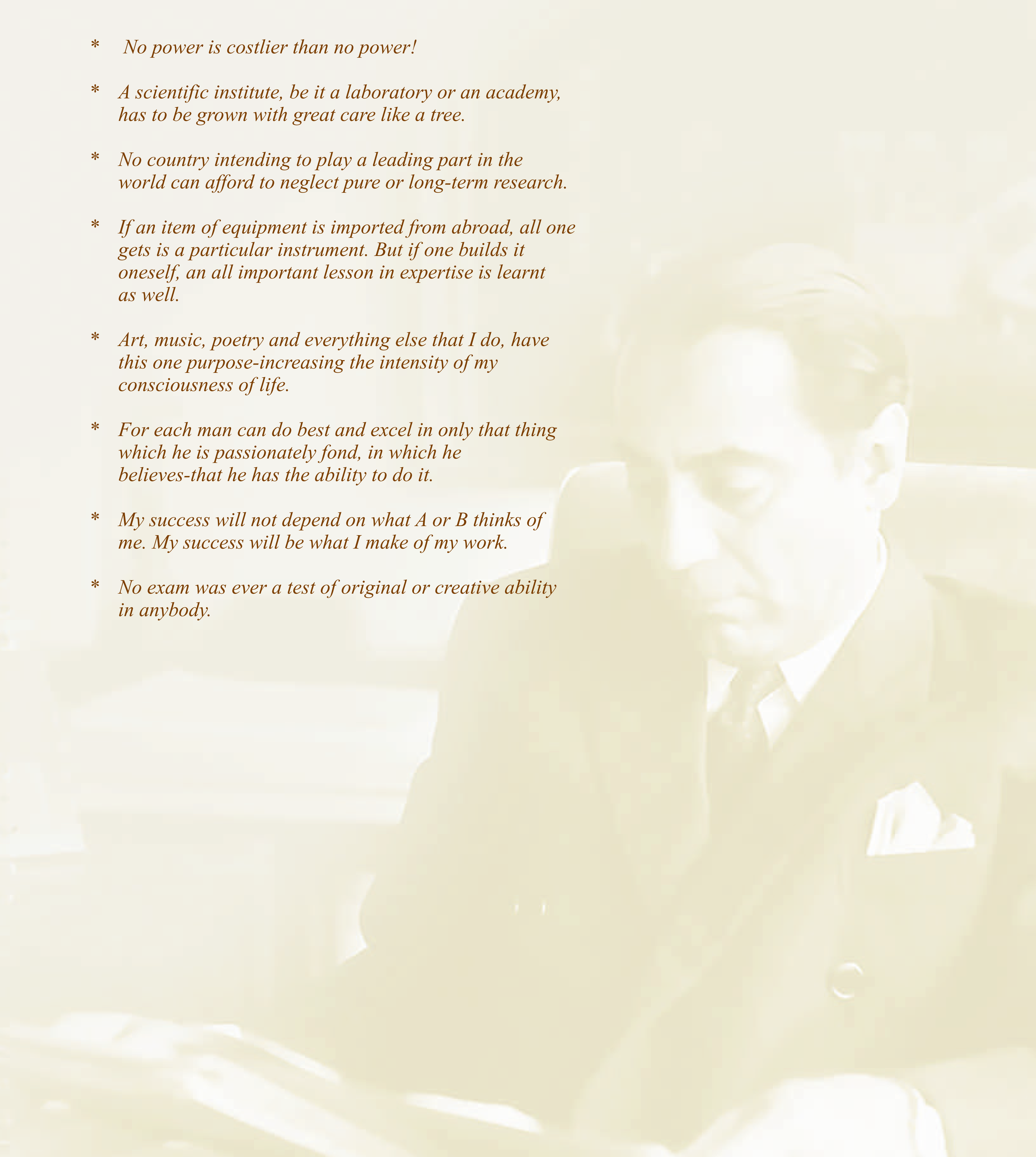

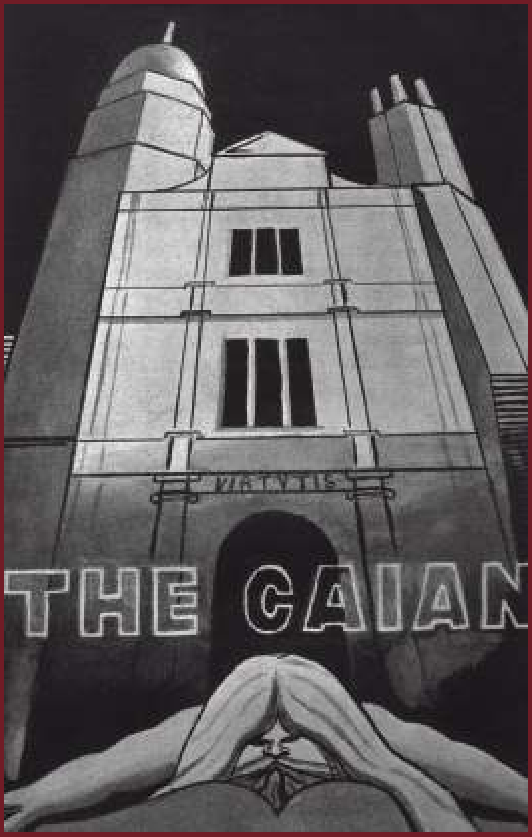

Sketch drawn by Dr. H.J. Bhabha
for the cover of the college magazine
"The Caian," when Dr. Bhabha was at the Gonville
and Caius College, Cambridge University.

(Reproduced with permission from
the Masters and Brothers of the
Gonville and Caius College, Cambridge University, UK.)

Edited & Published by:
Dr. Vijai Kumar,
Associate Director, Knowledge Management Group &
Head, Scientific Information Resource Division,
Bhabha Atomic Research Centre, Trombay, Mumbai 400 085, India.
Editorial Management: Dr. (Ms.) S. C. Deokattey,
Computer Graphics & Layout: Mr. N. Kanagaraj and Mr. B.S. Chavan, SIRD, BARC
BARC Newsletter is also available at
URL: http://www.barc.gov.in